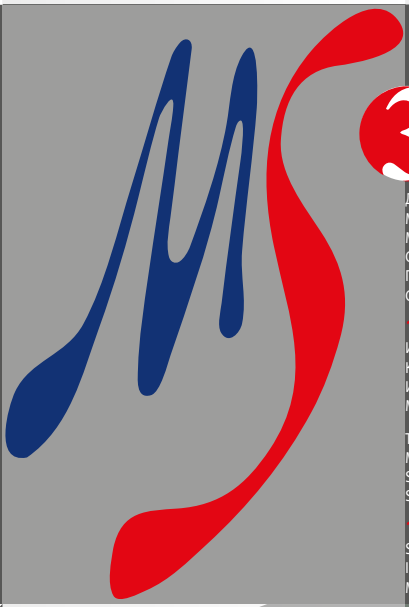


ДВЕНАДЦАТЫЙ
МОСКОВСКИЙ
МЕЖДУНАРОДНЫЙ
СИМПОЗИУМ
ПО ИССЛЕДОВАНИЯМ
СОЛНЕЧНОЙ СИСТЕМЫ

11–15 ОКТЯБРЯ 2021
ИНСТИТУТ
КОСМИЧЕСКИХ
ИССЛЕДОВАНИЙ
МОСКВА

THE TWELFTH
MOSCOW
SOLAR SYSTEM
SYMPOSIUM

11–15 OCTOBER 2021
SPACE RESEARCH
INSTITUTE
MOSCOW

12

ИКИ
SPACE
RESEARCH
INSTITUTE
OF RAS

ГЕОХИ

BROWN

ДВЕНАДЦАТЫЙ МОСКОВСКИЙ СИМПОЗИУМ ПО ИССЛЕДОВАНИЯМ СОЛНЕЧНОЙ СИСТЕМЫ 12M-S^3

октябрь 11-15, 2021
ИНСТИТУТ КОСМИЧЕСКИХ ИССЛЕДОВАНИЙ
РОССИЙСКОЙ АКАДЕМИИ НАУК
МОСКВА, РОССИЯ

THE TWELFTH MOSCOW SOLAR SYSTEM SYMPOSIUM 12M-S^3

october 11-15, 2021
SPACE RESEARCH INSTITUTE
OF RUSSIAN ACADEMY OF SCIENCES
MOSCOW, RUSSIA

спонсоры:
- Институт космических исследований РАН
- Институт геохимии и аналитической химии им. Вернадского РАН
- Брауновский университет (США)

sponsored by:
- Space Research Institute RAS
- Vernadsky Institute of Geochemistry and Analytical Chemistry RAS
- Brown University, USA

ISBN: 978-5-00015-015-3
DOI: 10.21046/12M-S3
© Федеральное Государственное Бюджетное Учреждение Науки
ИНСТИТУТ КОСМИЧЕСКИХ ИССЛЕДОВАНИЙ РОССИЙСКОЙ АКАДЕМИИ НАУК (ИКИ РАН)
2021

TABLE OF CONTENT

INTRODUCTION

PROGRAM COMMITTEE

PROGRAM
overview PROGRAM
scientific PROGRAM

ABSTRACTS

INFORMATION
ADDRESS
METRO MAP
REGISTRATION AND INFORMATION DESK
ORAL SESSIONS, location
POSTER SESSIONS, location
INTERNET ACCESS AND WiFi
SOCIAL PROGRAM
LUNCH POINTS

THE TWELFTH MOSCOW SOLAR SYSTEM SYMPOSIUM 12M-S^3

SPACE RESEARCH INSTITUTE
MOSCOW, RUSSIA
october 11-15, 2021

Starting from 2010, the Space Research Institute holds annual international symposia on Solar system exploration. Main topics of these symposia include wide range of problems related to formation and evolution of Solar system, planetary systems of other stars; exploration of Solar system planets, their moons, small bodies; interplanetary environment, astrobiology problems. Experimental planetary studies, science instruments and preparation for space missions are also considered at these symposia.

The Twelfth Moscow international Solar System Symposium (12M-S^3) will be held from October 11 till 15, 2021.

Subject matter of this symposium will cover many problems of the Solar system science with the central topic "Moon, Mars and Venus research". This topic relates to scientific problems of several missions: "Mars Express", "Venus Express", the missions under development in Russia: "Luna-Glob ", "Luna-Resource", "Venera-D", "ExoMars".

THE FOLLOWING SESSIONS WILL BE HELD DURING THE SYMPOSIUM:

OPENING SESSION

- Session. MARS
- Session. VENUS
- Session. MOON AND MERCURY
- Session. SMALL BODIES (INCLUDING COSMIC DUST)
- Session. GIANT PLANETS
- Session. EXTRASOLAR PLANETS
- Session. ASTROBIOLOGY

In light of COVID-19 travel restrictions the Symposium will be held both «face-to-face» and «virtual» formats.

For all «face-to-face» participants in Space Research Institute (IKI) the masks as well as social distancing will still be obligatory!

Space Research Institute holds this symposium with participation of the following organizations:

- Vernadsky Institute of Geochemistry and Analytical Chemistry RAS, Russia
- Brown University, USA
- Schmidt Institute of Physics of the Earth RAS, Russia
- Keldysh Institute of Applied Mathematics RAS, Russia
- Kotelnikov Institute of Radio-engineering and Electronics RAS, Russia
- Sternberg Astronomical institute, Moscow State University, Russia

Symposium website: **https://ms2021.cosmos.ru**
Contact email address: **ms2021@cosmos.ru**

PROGRAM COMMITTEE

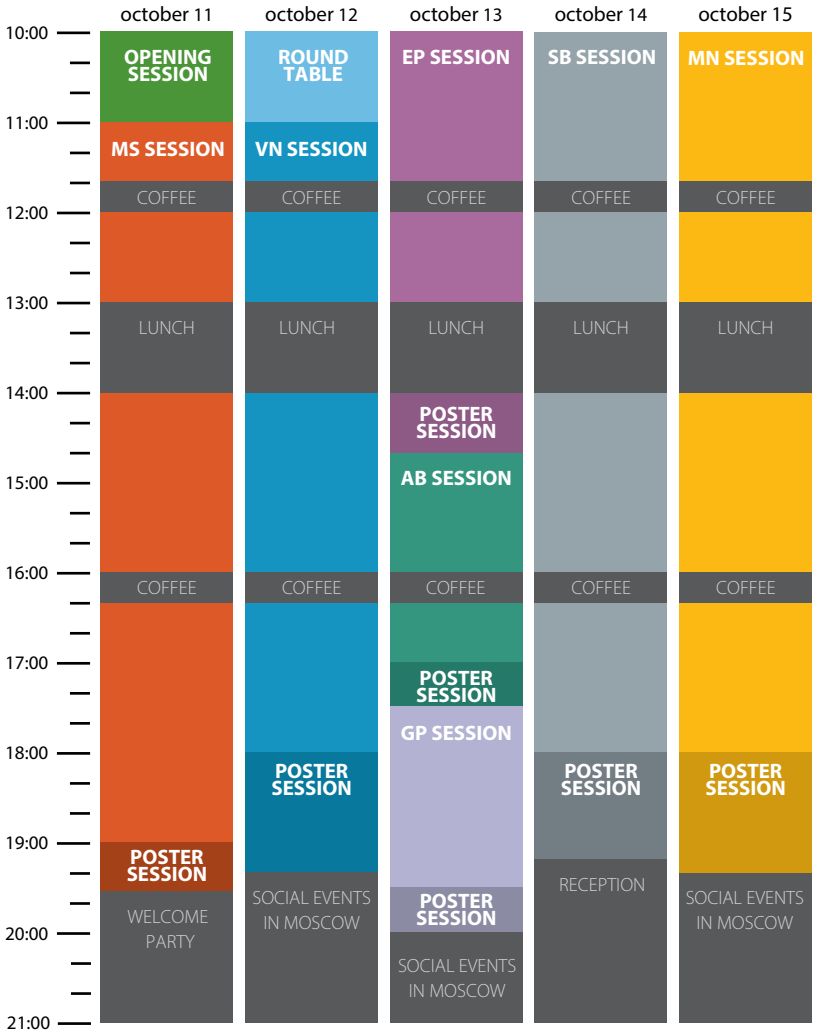
chair:
acad. **ZELENYI L.M.** IKI RAS

members:
BAZILEVSKIY A.T. GEOHI RAS
BIBRING J.-P. IAS,CNRS, France
BOLTON S.J. Southwest Research Institute, USA
BOROVIN G.K. Keldysh AMI RAS
DUXBURY T. George Mason University, USA
HEAD III J. Brown University, USA
KORABLEV O.I. IKI RAS
KOSTITSYN Y.A. GEOHI RAS
MAROV M.Ya. GEOHI RAS
MITROFANOV I.G. IKI RAS
RODIN A.V. IKI RAS
SHEVCHENKO V.V. GAISH MSU
SMIRNOV V.M. IRE RAS
SVEDHEM H. ESTEC, ESA
TAVROV A.V. IKI RAS
TITOV D. ESTEC, ESA
VAISBERG O.L. IKI RAS
VOROBYOVA E.A. MSU
WU Ji National Space Science Center, China
ZAKHAROV A.V. IKI RAS
ZASOVA L.V. IKI RAS

secretary:
ROSTE O.Z. IKI RAS, ms3@iki.rssi.ru

overview 12M-S³ program
THE TWELFTH MOSCOW SOLAR SYSTEM SYMPOSIUM

IKI RAS, 11–15 october 2021



MS SESSION: MARS SESSION
VN SESSION: VENUS SESSION
EP SESSION: EXTRASOLAR PLANETS SESSION
AB SESSION: ASTROBIOLOGY SESSION
GP SESSION: GIANT PLANETS SESSION
SB SESSION: SMALL BODIES SESSION
MN SESSION: MOON AND MERCURY SESSION
ROUND TABLE: DISCUSSION «PH3 ON VENUS?»

12M-S³ SCIENTIFIC PROGRAM

MONDAY, 11 OCTOBER 2021

10.00–11.00

OPENING SESSION

Convener: **Lev ZELENY**
conference hall, second floor

11.00–19.35

MARS SESSION

Convener: **Oleg KORABLEV**
conference hall, second floor

11.00–11:20	**Thomas DUXBURY et al**	Mariner Mars 1969 image restoration archive	12MS3-MS-01
11.20–11.40	**Francesca FERRI et al**	AMELIA, The EDL Science Experiment for the ExoMars 2022 Mission	12MS3-MS-02
11.40–12.00		COFFEE-BREAK	
12.00–12:20	**Mariano SASTRE et al**	Luminescence technique applied to Martian sediments in-situ dating: the IN-TIME project	12MS3-MS-03
12.20–12.40	**Boris IVANOV**	Tracks in Martian dust – dust devils and air shock waves footprints	12MS3-MS-04
12.40–13.00	**Elena PODOBNAYA et al**	Trajectory estimations for fresh impacts on Mars	12MS3-MS-05
13.00–14.00		LUNCH	
14.00–14.20	**Sergei NIKIFOROV et al**	Water and chlorine estimation in the martian subsurface according to DAN measurements onboard the NASA Curiosity rover	12MS3-MS-06
14.20–14.40	**Gonzalo BARDERAS et al**	Martian CO_2 polar caps deposits derived with GEANT4-PLANETO-COSMICS from neutron flux variations	12MS3-MS-07
14.40–15.00	**Benjamin BOATWRIGHT and James HEAD**	Mars Crater Modification in the Late Noachian II: Updated Criteria for Identifying Cold-Based Crater Wall Glaciation	12MS3-MS-08
15.00–15.20	**James HEAD**	Zhurong landing site in southern Utopia Planitia, Mars: global geologic context, stratigraphy and outstanding questions	12MS3-MS-09
15.20–15.40	**Anton SALNIKOV et al**	Constructing an analytical model of the magnetic field of Mars using satellite data and modified S-approximations	12MS3-MS-10
15.40–16.00	**Valery SHEMATOVICH**	Atomic oxygen loss during proton auroral events at Mars	12MS3-MS-11
16.00–16.20		COFFEE-BREAK	
16.20–16.40	**Valery SHEMATOVICH and D. BISIKALO**	Kinetic modeling of proton aurora at Mars	12MS3-MS-12
16.40–17.00	**David PACIOS et al**	Some applications of the space data analysis + cloud computing: from the Martian auroras to the COVID-19 Pandemic evolution	12MS3-MS-13

17.00–17.20	**Mikhail LUGININ et al**	CO_2 clouds on Mars from ACS solar occultations onboard TGO	12MS3-MS-14
17.20–17.40	**Anna FEDOROVA et al**	Seasonal and spatial variations of the CO vertical distribution on Mars based on ACS TGO measurements	12MS3-MS-15
17.40–18.00	**Alexey PANKINE**	Vertical distribution of water vapor in the Martian atmosphere retrieved from MGS TES day and night observations	12MS3-MS-16
18.00–18.20	**Vladimir A. KRASNOPOLSKY**	Seasonal and Latitudinal Variations of the HDO/H_2O Ratio in the Martian Atmosphere	12MS3-MS-17
18.20–18.40	**Alexander TROKHIMOVSKIY et al**	Hydrogen chloride (HCl) and its isotopologues in the atmosphere of Mars	12MS3-MS-18
18.40–19.00	**Denis BELYAEV et al**	Temperature and density climatology of the Martian middle/upper atmosphere from the ACS/TGO CO_2 spectroscopy	12MS3-MS-19
19.00–19.35	**POSTER SESSION, SESSION MARS** 8 posters * 4 min		
	Alexander ZAKHAROV et al	Dust Complex instrument onboard ExoMars-2020 Surface Platform	12MS3-MS-PS-01
	Anatoly MANUKIN et al	Seismometer for measurements on Mars	12MS3-MS-PS-02
	Ekaterina STARICHENKO et al	Activity of the gravity waves in the Martian atmosphere from the ACS/TGO solar occultations experiment	12MS3-MS-PS-03
	Vladimir OGIBALOV	Heating rate due to the NIR CO_2 and CO bands emissions in the daytime Martian atmosphere	12MS3-MS-PS-04
	Vladimir GUBENKO and I. KIRILLOVICH	Determining the characteristics of internal gravity waves in terrestrial atmospheres using an analysis of the vertical temperature or density profiles recovered from radio occultation satellite measurements	12MS3-MS-PS-05
	Tamara GUDKOVA and A. BATOV	Non-hydrostatic stresses and the location of marsquakes' sources	12MS3-MS-PS-06
	Sergey PAVLOV et al	Towards Martian Moons Exploration: micro-Raman and VIS-MIR reflection spectroscopy of the Phobos surface simulants	12MS3-MS-PS-07
	Natalia BULATOVA	The phenomenon lightning, possible transport of electrons and cosmic rays to Earth	12MS3-MS-PS-08

10.00–11.00

ROUND TABLE:
Discussion «PH3 on Venus?»

Moderator: **Oleg KOTSYURBENKO**
conference hall, second floor

11.00–19:20

2 VENUS SESSION

Conveners: **Ludmila ZASOVA**, **Richard ERNST**
conference hall, second floor

11.00–11.15	**Richard ERNST et al**	Assessing a Large Igneous Provinces (LIPS) Context for Volcanism on Venus	12MS3-VN-01
11.15–11.30	**Ekaterina ANTROPOVA et al**	Analysis of Multiple Impact "Splotches" in HinemoaPlanitia, NW and W of Phoebe Regio, Venus	12MS3-VN-02
11.30–11.45	**Carlos BRAGA et al**	Preliminary Geology & Stratigraphy of the Volcanic Center Atira Mons, Beta-Atla-Themis Region, Venus	12MS3-VN-03
11.45–12.00		COFFEE-BREAK	
12.00–12.15	**Carlos SANCHEZ et al**	Dyke Swarm History of Nabuzana Corona, Scarpellini Quadrangle (V-33), Venus	12MS3-VN-04
12.15–12.30	**Hafida EL. BILALI et al**	Dyke Swarm History of Atla Regio, Venus	12MS3-VN-05
12.30–12.45	**Abdelhak AITLAHNA et al**	Window into 4-km Cross Section of Venusian Crust Exposed by Normal Faults of Dali Chasma, SW of Atla Regio	12MS3-VN-06
12:45–13:00	**Rachid OUKHRO et al**	Characteristics, Orientation and Origin of Structural Components of Jokwa Linea Groove Belt, SE Stanton Quadrangle (V-38), Venus	12MS3-VN-07
13.00–14.00		LUNCH	
14.00–14.15	**Ludmila ZASOVA**	"Venera-D" and Decade of Venus Exploration	12MS3-VN-08
14.15–14.30	**Mikhail IVANOV et al**	Geological characterization of the Venera-D landing sites	12MS3-VN-09
14.30–14.45	**Mikhail IVANOV et al**	Criteria for Venera-D Mission Lander Site Selection	12MS3-VN-10
14.45–15.00	**Anastasia KOSENKOVA**	Investigation of the Capabilities of a Maneuverable Lander to the Venus Surface	12MS3-VN-11
15.00–15.15	**Vladislav ZUBKO et al**	Using of a resonant orbit in the problem of extension landing areas on the Venus surface	12MS3-VN-12
15.15–15.30	**Sanjay LIMAYE and R. MOGUL**	Venus cloud cover puzzles	12MS3-VN-13

15:30–15:45	**Daria EVDOKIMOVA et al**	Night distribution of the O_2 (A1ΔG) airglow on Venus observed by SPICAV IR/VEX in 2006-2014	12MS3-VN-14
15:45–16:00	**Dmitry GORINOV et al**	O_2 night airglow and dynamics of Venus atmosphere around 100 km from VIRTIS-M/VEx	12MS3-VN-15
16.00–16.20		COFFEE-BREAK	
16.20–16.35	**Michael WAY et al**	Large Scale Volcanism and the possible heat-death of Venus like worlds	12MS3-VN-16
16.35–16.50	**James HEAD et al**	Contributions of Volatiles to the Venus Atmosphere from the Observed Extrusive Volcanic Record: Implications for the History of the Venus Atmosphere	12MS3-VN-17
16.50–17.05	**Mikhail IVANOV et al**	Pit Crater Chains, Graben and Related Features in OvdaTessera, Venus: Implications for Dike Emplacement and Volatile Loss	12MS3-VN-18
17.05–17.20	**Jihane OUNAR et al**	Origin and Evolution of Lineaments in NW Wawalag Planitia, Stanton Quadrangle (V-38), Venus	12MS3-VN-19
17.20–17.35	**Rico FAUSCH et al**	Mass spectrometic measurements of complex molecules during hypervelocity planetary flybys	12MS3-VN-20
17.35–17.50	**Kirill ZAKHARCHENKO et al**	High-temperature detector of space radiation based on diamond sensitive elements	12MS3-VN-21
17:50–18:00		**DISCUSSION**	
18.00–19:20		**POSTER SESSION, SESSION VENUS** 16 posters * 5 min	
	Tamara MENSHCHIKOVA and Tamara GUDKOVA	On Load Love Numbers for Venus	12MS3-VN-PS-01
	Jordan SHACKMAN et al	Reconnaissance geological mapping of the Latmikaik Corona and associated dyke swarms, Henie Quadrangle (V-58), Venus	12MS3-VN-PS-02
	James HEAD and Mikhail IVANOV	Erosion of Tessera Terrain on Venus: Criteria for Recognition of Effects of the Presence of an Earth-Like Atmospheric Erosional Environment	12MS3-VN-PS-03
	James HEAD and Mikhail IVANOV	Global Geological Mapping of Venus: Identification of Challenges & Opportunities for Future Venus Mapping	12MS3-VN-PS-04
	Evgeniya GUSEVA and Mikhail IVANOV	Dome-Shaped Coronae of Venus: Spatial Distribution, Relationship with Rifts and Lobate Plains	12MS3-VN-PS-05
	Mikhail IVANOV and James HEAD	Morphometric characteristics of large volcanoes on Venus	12MS3-VN-PS-06

Lauren MACLELLAN and Richard ERNST	Structural Map of Northern Astkhik Planum and Selu Corona, Lada Terra, Venus	12MS3-VN-PS-07
Vladimir OGIBALOV and Yuliya BORDOVSKAYA	Influence of wind fields with macroscopic velocity gradients on the IR CO2 bands emissions outgoing from a planetary atmosphere	12MS3-VN-PS-08
Mahanoor RIAZ et al	Developing a Dyke Swarm History for Bell Regio, Venus	12MS3-VN-PS-09
Anoushka SINGHAL et al	Magmatic Feeder Systems of the Lo Shen Region, Southern Margin of Eastern Ovda Regio, Venus	12MS3-VN-PS-10
Mohamed Achraf MEDIANY et al	Developing a Detailed Magmatic History of Eastern Rusalka Planitia, Venus	12MS3-VN-PS-11
Abderrazzak HASANAINE et al	Detailed Mapping of a Corona Cluster within Dali-Diana Chasmata 1000 km SW of Atla Regio, Venus	12MS3-VN-PS-12
Kamal MGHAZLI et al	Dyke Swarms of the Maram Corona Area, along Parga Chasmata, SE of Atla Regio, Venus	12MS3-VN-PS-13
Ismail HADIMI et al	Detailed Mapping of Graben-Fissure Systems of Nott Corona Region, Isabella Quadrangle (V-50), Venus	12MS3-VN-PS-14
Fatima Ezzahrae NAJIB et al	Evaluation of the Cluster Of Anemone Type Volcanoes Located South of Atla Regio, Venus	12MS3-VN-PS-15
Raiden DEAN et al	Mapping of Graben Systems ("Ribbon Fabrics") in Western Ovda Tessera, Venus: Interpretation as Dyke Swarms	12MS3-VN-PS-16

10.00–14.40

3 EXTRASOLAR PLANETS SESSION

Convener: **Alexander TAVROV**
conference hall, second floor

10.00–10.15	**Shingo KAMEDA et al**	Ultraviolet Spectrograph for Exo-planet (UVSPEX) onboard WSO-UV for Earth-like exoplanets	12MS3-EP-01
10.15–10.30	**Vlada ANANYEVA et al**	Properties of RV-exoplanet distributions by masses and by orbital periods	12MS3-EP-02
10.30–10.45	**Oleg YAKOVLEV et al**	Comparison of the mass distributions of short-period exoplanets detected by transit and by RV methods	12MS3-EP-03
10.45–11.00	**Valery SHEMATOVICH and A. AVTAEVA**	Non-thermal atmospheric loss for hot sub-neptune π Men c	12MS3-EP-04
11.00–11.15	**Shiva ZAMANPOUR et al**	Light curve analysis of ten exoplanets	12MS3-EP-05
11.15–11.30	**Marina RUMENSKIKH et al**	Modeling transit absorptions of hot Jupiters in the metastable helium line	12MS3-EP-06
11.30–11.45	**Ahmad MAZIDABADI FARAHANI et al**	Refined ephemeris for three hot Jupiters using ground-based and TESS observations	12MS3-EP-07
11.45–12.00		COFFEE-BREAK	
12.00–12.15	**Ildar SHAIKHISLAMOV et al**	3D MHD modeling of hot Jupier' magnetosphere and onservational manifastations	12MS3-EP-08
12.15–12.30	**Igor SAVANOV**	Activity of two young stars of solar type with planetary systems from the Ursa major moving group of stars and the stream Psc-Eri	12MS3-EP-09
12.30–12.45	**Vladislav SIDORENKO and A. IVANOVA**	Secular evolution of orbital motions in planetary system consisting of a star and two planets	12MS3-EP-10
12.45–13.00	**Sergei IPATOV**	Migration of bodies in the Proxima Centauri planetary system	12MS3-EP-11
13.10–14.00		LUNCH	
14.00–14.40		**POSTER SESSION, SESSION EXTRASOLAR PLANETS** 8 posters*4 min	
	Valery KOTOV	Motion of superfast exoplanets and solar system	12MS3-EP-PS-01
	Fatemeh HASHEMINASAB	Revealing exoplanet's atmosphere composition with high resolution spectroscopy	12MS3-EP-PS-02
	Tabassom MADAYEN et al	Investigation of the period-mass relations for W UMA-Type contact binary systems by using machine learning method	12MS3-EP-PS-03

Artem BEREZUTSKY et al	Simulation of a system with two hot exoplanets TOI 421	12MS3-EP-PS-04
Farzaneh AHANGARANI FARAHANI et al	Refined Ephemeris for Hot Jupiter WASP-12 b using Ground-Based and TESS Observations	12MS3-EP-PS-05
Anastasiya IVANOVA et al	Correction of observation selection in statistics of RV-exoplanets. From the number of detected planets to the occurrence rate	12MS3-EP-PS-06
Andrei YUDAEV and Alexander TAVROV	Wavefront correction for direct imaging of exoplanets. Phase retrieval by LCSLM and Interfero-Coronagraph	12MS3-EP-PS-07
Ilia MIROSHNICHENKO et al	Absorption in the Hα line by outleting atmospheres of hot Jupiters	12MS3-EP-PS-08

14.40–17.30

4 ASTROBIOLOGY SESSION

Conveners: **Oleg KOTSYURBENKO**, **Elena VOROBYOVA**
conference hall, second floor

14.40–15.00	**Sohan JHEETA**	Where were the molecules of life made?	12MS3-AB-01
15.00–15.15	**Vladimir KOMPANICHENKO**	Origin of life on a planet by efficient response of prebiotic systems to high-frequency oscillations in the environment	12MS3-AB-02
15.15–15.30	**Daniil MIRONOV**	Prospects for the use of lichens in astrobiological and astroecological research	12MS3-AB-03
15.30–15.45	**Ximena ABREVAYA et al**	UV radiation from stellar flares: a constraint for life?	12MS3-AB-04
15.45–16.00	**Eduardo CORTON et al**	Microbial fuel cells as extraterrestrial microbial life sensors	12MS3-AB-05
16.00–16.20		COFFEE-BREAK	
16.20–16.40	**Richard HOOVER et al**	Extraterrestrial & intraterrestrial diatoms & cyanobacteria: implications to the origin and distribution of biospheres	12MS3-AB-06
16.40–17.00	**Janusz PETKOWSKI et al**	Phosphine and other Venusian cloud anomalies	12MS3-AB-07
17.00–17.30	**POSTER SESSION, SESSION ASTROBIOLOGY** 7 posters * 4 min		
	Richard HOOVER et al	Extraterrestrial cyanobacteria and diatoms in the Orgueil (CI1) and Murchison (CM2) carbonaceous chondrites	12MS3-AB-PS-01
	Oleg KOTSYURBENKO et al	Succession of hypothetical microbial communities on Venus during planetary climate change	12MS3-AB-PS-02
	Dmitry SKLADNEV et al	Aerosol or foam – which structure of Venusian clouds is better for survival of hypothetical microbial communities	12MS3-AB-PS-03
	Sergey BULAT et al	Resistance of DNA(Microbial) to radiation damage on the frosty Jovian Europa surface	12MS3-AB-PS-04
	Hamidreza GUILANI and Aila PORO	The Necessity of Developing ML and AI for Future Astronomy	12MS3-AB-PS-05
	Vladimir CHEPTSOV et al	Perchlorate tolerance of soil microbial communities	12MS3-AB-PS-06
	Andrey BELOV and Vladimir CHEPTSOV	Resistance and metabolic activity of soil prokaryotic communities under conditions of water deficiency: astrobiological implications	12MS3-AB-PS-07

17.30–20.00

5 GIANT PLANETS SESSION

Convener: **Scott BOLTON**
conference hall, second floor

17.30–17.50	**Scott BOLTON**	Juno's Extended Mission	12MS3-GP-01
17.50–18.10	**Heidi BECKER et al**	Trapped GeV Heavy Ions in Jupiter's Inner Radiation Belts at High Latitudes	12MS3-GP-02
18.10–18.30	**Nimrod GAVRIEL and Yohai KASPI**	The number and location of Jupiter's circumpolar cyclones explained by vorticity dynamics	12MS3-GP-03
18.30–18.50	**Alesandro MURA et al**	Infrared observations of Jupiter's Aurorae, Atmosphere and Moons	12MS3-GP-04
18.50–19.10	**Alexander PERMINOV and E. KUZNETSOV**	The semi-analytical four-planetary motion theory of the third order in masses	12MS3-GP-05
19.10–19.30	**Peter WURZ et al**	Measurement of Io's Atmosphere during the IVO Mission	12MS3-GP-06
19.30–20.00	**POSTER SESSION, SESSION GIANT PLANETS**		
	7 posters * 4 min		
	Satoshi TANAKA et al	Jupiter and lunar seismograms	12MS3-GP-PS-01
	Vladimir VDOVICHENKO et al	The first experience of studying latitudinal variations of a weak absorption band NH3 550nm on Jupiter	12MS3-GP-PS-02
	Ekaterina KRONROD et al	Estimates of the possible dehydration of hydrated silicates in the cores of large icy satellites	12MS3-GP-PS-03
	Andrey KHARITONOV	Some data confirming the hypotheses of the formation of silicate and iron-hydrocarbon-containing shells of giant planets	12MS3-GP-PS-04
	Victor KRONROD et al	The content of hydrated silicates in the primordial rocky core of Ganymede	12MS3-GP-PS-05
	Anna DUNAEVA et al	Condensed phases of carbon dioxide in Titan's icy crust: influence on rheological properties	12MS3-GP-PS-06
	Alexander SUKHANOV	Repeatability of a given configuration of planets	12MS3-GP-PS-07

10.00–19.10

6 SMALL BODIES SESSION including cosmic dust

Conveners: **Alexander BASILEVSKY**, **Alexander ZAKHAROV**
conference hall, second floor

10.00–10.20	**Evgenij ZUBKO et al**	Negative polarization of distant Comet C/2017 K2 (PANSTARRS)	12MS3-SB-01
10.20–10.40	**Ekaterina CHORNAYA et al**	Fast variations of polarization maximum in comet C/2020 S3 (Erasmus)	12MS3-SB-02
10.40–11.00	**Vladimir BUSAREV et al**	Reflectance spectra of asteroids with simultaneous sublimation activity: registration and models	12MS3-SB-03
11.00–11.20	**Boris SHUSTOV and R. ZOLOTAREV**	Near-Earth asteroids: Depletion time scales, escape routes and estimate of share of interstellar bodies	12MS3-SB-04
11.20–11.40	**Nikolai KISELEV et al**	Recent progress in studying polarization of the Jupiter's and Saturn's satellites and NEAs in the Crimean Astrophysical Observatory and the Peak Terskol Observatory	12MS3-SB-05
11.40–12.00		COFFEE-BREAK	
12.00–12.20	**Tatyana GALUSHINA et al**	Study of the nonlinearity problem for the near-Sun asteroids	12MS3-SB-06
12.20–12.40	**Maxim ZHELTOBRYUKHOV et al**	The Umov effect in the near-earth asteroids	12MS3-SB-07
12.40–13.00	**Ricardo GIL-HUTTON**	The CASLEO polarimetric survey of the main belt asteroids	12MS3-SB-08
13.00–14.00		LUNCH	
14.00–14.20	**Vladislav ZUBKO et al**	Using optimal number of asteroids on the resonance orbits to construct the planetary defense shield	12MS3-SB-09
14.20–14.40	**Maryam HADIZADEH et al**	Calculating period and the rotation speed of the asteroids by using observational data collection	12MS3-SB-10
14.40–15.00	**Sergei IPATOV and Mikhail MAROV**	Collisions of planetesimals with the Earth and the Moon	12MS3-SB-11
15.00–15.20	**Vladimir TCHERNYI and S. KAPRANOV**	How the third force of diamagnetic expulsion and the mechanism of magnetic anisotropic accretion allowed Saturn to create rings by itself	12MS3-SB-12
15.20–15.40	**Fatemeh NAJAFI KODINI et al**	Study of Pluto's atmosphere based on 2020 stellar occultation light curve results	12MS3-SB-13
15.40–16.00	**Sergey POPEL et al**	Dust dynamics at the Moon: Levitation or lofting	12MS3-SB-14
16.00–16.20		COFFEE-BREAK	

16.20–16.40	**Yulia REZNICHENKO et al**	Ionization properties of dusty Martian ionosphere	12MS3-SB-15
16.40–17.00	**Ute BÖTTGER et al**	The Raman spectrometer RAX as an analytical instrument for the JAXA MMX sample return mission	12MS3-SB-16
17.00–17.20	**Andrei DMITROVSKII et al**	Tidal deformation modeling as a potential means of constraining the interior structure of Phobos	12MS3-SB-17
17.20–17.40	**Yuriy CHETVERIKOV et al**	Monitoring of space precipitation at the Vostok antarctic station using the example of collecting magnetite microparticles from may to september 2017	12MS3-SB-18
17.40–18.00	**Alexey PANKINE**	Reconciling estimates of endogenic power emitted from the southern polar region of Enceladus	12MS3-SB-19
18.00–19.10	**POSTER SESSION, SESSION SMALL BODIES (INCLUDING COSMIC DUST)** 18 posters * 4 min		
	Vladimir ZUBKO et al	Possible space mission to Sedna at launch in 2029-2037	12MS3-SB-PS-01
	Manue l DOMINGUEZ-PUMAR et al	Preliminary tests with a 3D thermoprobe for measuring the thermophysical properties of regolith	12MS3-SB-PS-02
	Yuri SKOROV and V. RESHETNYK	Transport characteristics of the near-surface layer of the nucleus of comet 67P	12MS3-SB-PS-03
	Andrey SHUGAROV et al	System of observation of day-time asteroids (SODA)	12MS3-SB-PS-04
	Arina SAVELOVA et al	On the possibility to study the surface matter composition of primitive main belt asteroids near perihelion	12MS3-SB-PS-05
	Anna KARTASHOVA et al	Investigation of (159402) 1999 AP10 asteroid with observations and simulation data	12MS3-SB-PS-06
	Dmitry PETROV and E. ZHUZHULINA	Features of the phase dependence of the degree of linear polarization of sungrazing comet C/1965 S1	12MS3-SB-PS-07
	Vladimir EFREMOV et al	Application of small meteor ablation model to Perseid observations	12MS3-SB-PS-08
	Yulia IZVEKOVA et al	Dust acoustic waves in Martian atmosphere	12MS3-SB-PS-09
	Alexey ROSAEV	Dwarf planet Ceres resonance perturbations	12MS3-SB-PS-10
	Tatiana MOROZOVA and Sergey POPEL	Modulational interactions in the dusty plasmas of meteoroid tails	12MS3-SB-PS-11
	Victoria SAFRONOVA and Eduard KUZNETSOV	Estimation of the age of young asteroid pair (21436) Chaoyichi – (334916) 2003 YK39	12MS3-SB-PS-12
	Sergey KOPNIN et al	Dust acoustic solitons in the magnetosphere of Saturn	12MS3-SB-PS-13

	Inna SHASHKOVA et al	Investigation of the dust particles dynamics under the airless bodies' conditions: experimental set-up	12MS3-SB-PS-14
	Ilia KUZNETSOV et al	Investigation of the lunar near-surface dusty plasma exosphere interaction with spacecraft with PiC method simulation	12MS3-SB-PS-15
	Andrey DIVIN et al	Collisional cooling of electrons at comet 67p/Churyumov–Gerasimenko as viewed from 3D particle-in-cell simulations	12MS3-SB-PS-16
	Tatiana DROZHZHOVA et al	Simulating the reflectance observed on macroscopic scale planetary surfaces by a GPU ray-tracing technique	12MS3-SB-PS-17
	Azariy BARENBAUM	On the nature of observed comets and the mechanism of their formation	12MS3-SB-PS-18
19.10–21.10	**RECEPTION**		

10.00–19.20

7 MOON AND MERCURY SESSION

Conveners: **Igor MITROFANOV**, **Maxim LITVAK**
conference hall, second floor

MERCURY			
10.00–10.20	**Johannes BENKHOFF et al**	BepiColombo en route to Mercury – Results from some investigations during cruise	12MS3-MN-01
10.20–10.40	**Alexander KOZYREV et al**	MGNS flight to Mercury: status repot	12MS3-MN-02
LUNAR SCIENCE			
10.40–11.00	**James HEAD et al**	Geologic Context for Lunar South Circumpolar Region Exploration: Implications for Goals, Site Selection and Operations Strategy	12MS3-MN-03
11.00–11.20	**Alexandr GUSEV et al**	Geological exploration of the Moon: regolith, volatile and rare elements	12MS3-MN-04
11.20–11.40	**Alexander BASILEVSKY et al**	Impact-caused regolith reworking within the polar regions of the Moon	12MS3-MN-05
11.40–12.00		COFFEE-BREAK	
12.00–12.20	**Igor ALEINOV et al**	Transient volcanically-induced lunar atmosphere: basic properties and effect on volatile transport	12MS3-MN-06
12.20–12.40	**Marina DÍAZ MICHELENA et al**	In situ determination of multiple physical properties of planetary surface rocks and soils through a single measurement of their complex susceptibility	12MS3-MN-07
12.40–13.00	**Yugi QIAN et al**	Provenance of Materials at the Chang'e-5 Landing Site	12MS3-MN-08
13.00–14.00		LUNCH	
LUNAR MISSIONS			
14.00–14.20	**Vladislav TRET'YAKOV et al**	Science program of Luna-25 and Luna-27 missions	12MS3-MN-09
14.20–14.40	**Maxim LITVAK et al**	Tests of Lunar Robotic Arm with lunar polar regolith simulant	12MS3-MN-10
14.40–15.00	**Alexander ZAKHAROV et al**	Lunar near-surface dusty plasma investigations with PmL instrument	12MS3-MN-11
15.00–15.20	**Oleg VAISBERG et al**	Instruments ARIES-L and LINA-R for investigation of space plasma interaction with the lunar regolith.	12MS3-MN-12
15.20–15.40	**Dave HEATHER et al**	The ESA PROSPECT Payload for Luna 27: Development Status and Science Activities	12MS3-MN-13

15.40–16.00	**Tatiana KOZLOVA et al**	Extraction of Soil Samples from Subsurface: Instrument GZU for Lunar Robotic Landers	12MS3-MN-14
16.00–16.20		COFFEE-BREAK	
16.20–16.40	**Maxim LITVAK et al**	Future Lunar Sample Return mission	12MS3-MN-15
16.40–17.00	**Sergey KRASILNIKOV et al**	Data improvement of geological and morphological structure of the Luna-25 landing sites	12MS3-MN-16
		CONCEPT OF FUTURE EXPERIMENTS	
17.00–17.15	**Egor SOROKIN et al**	Laser experimental modeling of the formation of nanophase iron (np-Fe0).	12MS3-MN-17
17.15–17.30	**Andrey KIM et al**	The concept of Lunar Printer for Future Robotic Missions	12MS3-MN-18
17.30–17.45	**Andrey SHUGAROV et al**	The concept of Lunar-based UV-Optical-IR Telescope for ILRS	12MS3-MN-19
17.45–18.00	**Mikhail MALENKOV et al**	Directions of research and achievements of the school for the creation of locomotion systems of planetary rovers. To the 100th anniversary from the birth of A.L. Kemurdjian	12MS3-MN-20
18.00–19.20		**POSTER SESSION, SESSION MOON AND MERCURY** 25 posters * 3 min	
	Jinsong PING et al	A Mission Suggestion: Dynamics of Lunar Rotation & Frame Tie of Astronomy for ILRS	12MS3-MN-PS-01
	Sergey KRASILNIKOV et al	Geological investigation of the South pole of the Moon	12MS3-MN-PS-02
	Mohamad ESSAM ABDELAAL et al	Study the trajectory of dust particles by simulating the plasma environment on the Moon's surface	12MS3-MN-PS-03
	Imant VINOGRADOV et al	Sensor DLS-L of the GC-L instrument of the "Luna-Resource" mission: calibration results and perspective discussion	12MS3-MN-PS-04
	Boris EPISHIN and Michael SHPEKIN	Lunar territories with direct visibility of the Earth	12MS3-MN-PS-05
	Artem KRIVENKO et al	The setup for studying the sublimation of water ice on the mineral composition at lunar conditions	12MS3-MN-PS-06
	Andrey KHARITONOV	Results of spectral analysis of the magnetic and gravitational fields of the moon according to the data of the Apollo spacecraft	12MS3-MN-PS-07
	Valeriy BURMIN	Optimal Systems of Recording Acoustic Signals on Spacecraft of the Cylindrical Form	12MS3-MN-PS-08

Elena BELENKAYA et al	Excess of sodium ions density required to create a wide current at the Hermean magnetopause	12MS3-MN-PS-09
Jingyi ZHANG et al	The Origin of the Lunar Procellarum KREEP Terrane (PKT): Stratigraphic Evidence and Implications for Lunar Geological and Thermal Evolution	12MS3-MN-PS-10
Ekaterina FEOKTISTOVA et al	Morphological and morphometric features of Mercurian craters	12MS3-MN-PS-11
Negal MAHDAVI et al	O-C Analysis of 545 Lunar Occultations	12MS3-MN-PS-12
Alexander KRASILNIKOV et al	The Model Estimates of the Craters Ejecta Thickness in the Southern Polar Region of the Moon	12MS3-MN-PS-13
Azariy BARENBAUM and Michael SHPEKIN	On origin and age of Mare Orientale on Moon	12MS3-MN-PS-14
Mohammad MADANI and Atila PORO	A study on the Visibility Limit of Stellar Occultations with the Moon at Sunset and Sunrise	12MS3-MN-PS-15
Yuan LI et al	Analysis of Topographic Roughness vs WEH Concentration in the Regolith of the Lunar South Polar Area	12MS3-MN-PS-16
Vladimir ROTARU et al	Morphometric parameters for the new catalog of Mercury craters	12MS3-MN-PS-17
Ekaterina GRISHAKINA and Mikhail IVANOV	Geological analysis of the lunar crater Plaskett	12MS3-MN-PS-18
Elnaz BOZORGZADEH et al	Analyses of observational parameters in the timing accuracy of Lunar occultiation	12MS3-MN-PS-19
Nikolay SLODARZH and Zhanna RODIONOVA	Comparison of the cratering of the north and south polar regions of the Moon	12MS3-MN-PS-20
Gennady KOCHEMASOV	Earth and Moon: different ages of similar wave tectonics reflecting their unequal masses	12MS3-MN-PS-21
Gennady KOCHEMASOV	Chang'E-5 confirms globe-wide distribution of the centimeter-scale rippling caused by coupling two Lunar frequencies (near Earth and in Galaxy)	12MS3-MN-PS-22
Vladimir CHEPTSOV et al	Laser ionization mass spectrometer LASMA-LR onboard Luna-25 and Luna-27 spacecraft	12MS3-MN-PS-23
Vladimir AFANASYEV and G. PECHERNIKOVA	On the capture of protoplanetary bodies during the formation of the Earth–Moon system	12MS3-MN-PS-24
Nadezhda CHUJKOVA et al	Density, stress, and gravitational field anomalies inside the Moon, Mars, and Earth: a comparative analysis.	12MS3-MN-PS-25

SESSION 1. MARS (MS)
ORAL SESSION

MARINER MARS 1969 IMAGE RESTORATION ARCHIVE

T.C. Duxbury [1], J.G. Ward [2], B.V. Semenov [3], K.E. Herkenhoff [4], S.H. Slavney [2], C.H. Acton [3], R.A. Jacobson [3], B.S. Zhukov [5], N.V. Seregina [1]

[1] *George Mason University, Department of Physics and Astronomy, Fairfax, VA, 22030, USA, tduxbury@gmu.edu;*

[2] *Washington University, Earth and Planetary Sciences Department, Saint Louis, MO, 63130, USA;*

[3] *California Institute of Technology, Jet Propulsion Laboratory, Pasadena, CA, 91109, USA;*

[4] *US Geological Survey, Astrogeology Science Center, Flagstaff, AZ, 86001, USA;*

[5] *US Russian Academy of Sciences, Space Research Institute, Moscow, Russia*

KEYWORDS:
Mariner, Mars, Images, PDS, SPICE, MOLA.

INTRODUCTION:
The Mariner 6 and 7 spacecraft of the Mariner Mars 1969 mission each took a few hundred images [1] during their approaches to and flybys of Mars in July – August 1969. Until now these images were not on-line, searchable and did not have NAIF SPICE kernels needed to analyze them. Now, after a few years of development and detailed peer review for validation, they are on-line at the NASA Planetary Data System Geosciences Node at Washington University https://pds-geosciences.wustl.edu/missions/mariner/duxbury_mariner69.htm

IMAGE ARCHIVE:
Ancillary to the images, NAIF SPICE kernels (.bsp, .bc, .tf, .ti, .tsc) were reconstructed from Mariner Mars 1969 documents [2] and [3], processing the reseau locations in each image and registering the actual images to derived digital image models (DIMs) from the Mars Orbiter Laser Altimeter global digital terrain model (MOLA DTM — [4]) and SPICE kernels [5]. The archive bundle of restored images (Figure 1 — in PDS4 format) contains: 1) the original Level – 2 Experiment Data Record image; 2) the image in 1) but with all blemishes, noise spikes and reseaux removed and missing lines filled; 3) a high-pass filtered version of 2); 4) a simulated image derived from the MGS MOLA global DTM; and 5) a latitude /longitude gridded version of 2) or 3) with also indications where landers/rovers, Phobos, Deimos and stars might be for each image.

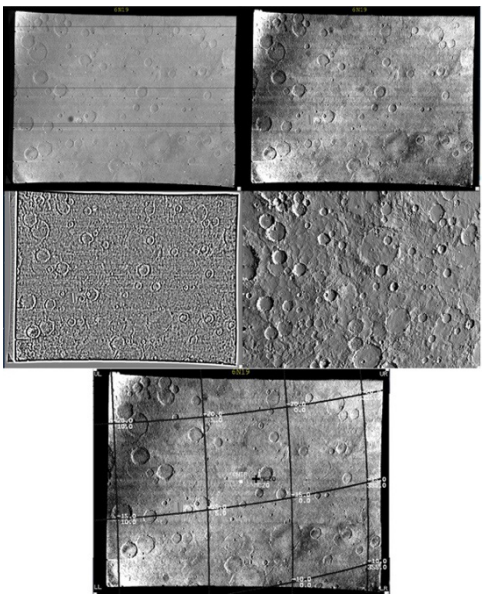


Fig. 1. Example of the 5 versions of a restored image.

REFERENCES:

[1] Collins, S.A.. 1971. The Mariner 6 and 7 pictures of Mars, NASA SP, 263, Washington, D.C..
[2] Campbell, J.K., Mariner Mars 1969 Simulated TV Pictures, JPL Document 605—237, 15 June 1970. DOI10.1016. j.pss.2017.02.013.
[3] Danielson, G.E., and D.R. Montgomery. 1971, Calibration of the Mariner Mars 1969 television cameras, J. Geophys. Res., V. 76, P. 2..
[4] D.E. Smith, M.T. Zuber, H.V. Frey, J.B. Garvin, J.W. Head, D.O. Muhleman, G.H. Pettengill, R.J. Phillips, S.C. Solomon, H.J, Zwally, B. Banerdt, T.C. Duxbury, M.P. Golombek, F.G. Lemoine, G.A. Neumann, D.D. Rowlands, O. Aharonson, P.G. Ford, A.B. Ivanov, C.L. Johnson, P.J. McGovern, J.B. Abshire, R.S. Afzal, and X. Sun. 2001, Mars orbiter laser altimeter: experiment summary after the first year of global mapping of Mars, J. Geophys. Res., V106, El0, 23, P. 689–23, 722.
[5] C. Acton, N. Bachman, B. Semenov, and E. Wright. A look toward the future in the handling of space science mission geometry. 2017. Planetary & Space Sci., V. 44, No. 1, P. 65–70.

AMELIA, THE EDL SCIENCE EXPERIMENT FOR THE EXOMARS 2022 MISSION

F. Ferri [1], A. Aboudan [1], G. Colombatti [1], C. Bettanini [1], S. Debei [1], O. Karatekin [2], S. Lewis [3], F. Forget [4], S. Asmar [5], A. Lipatov [6], I. Polyanskiy [6], A.M. Harri [7], G.G. Ori [8], A. Pacifici [8], P. Withers [9], K. Marchenkov [6], D. Rodionov [6], N. Modzhina [10]

[1] *Università degli Studi di Padova, Centro di Ateneo di Studi e Attività Spaziali "Giuseppe Colombo" (CISAS), francesca.ferri@unipd.it;*
[2] *Royal Observatory of Belgium (ROB), Brussels, Belgium;*
[3] *School of Physical Sciences, The Open University, Milton Keynes, UK;*
[4] *Laboratoire de Météorologie Dynamique, Paris, France;*
[5] *Jet Propulsion Laboratory, California Institute of Technology — NASA, USA;*
[6] *IKI, Moscow, Russia;*
[7] *Finnish Meteorological Institute (FMI), Helsinki, Finlandia;*
[8] *IRSPS, Pescara, Italy;*
[9] *Boston University, USA;*
[10] *TsNIIMASH, Russia*

KEYWORDS:
Mars; *ExoMars* mission; Entry, Descent & Landing; *in situ* measurements, observations, modelling, trajectory, attitude, atmospheric profile.

The entry, descent and landing of *ExoMars* Descent Module (EDM) offer a rare (once-per-mission) opportunity to perform an *in situ* investigation of the martian environment over a wide altitude range. The main objective of the *Atmospheric Mars Entry and Landing Investigations and Analysis* (AMELIA) experiment was the assessment of the atmospheric science and landing site by exploiting the Entry Descent and Landing System (EDLS) sensors of *Schiaparelli* beyond their designed role of monitoring and evaluating the performance of the EDL technology demonstrator.

The AMELIA – EDL science experiment of the *ExoMars* program aims at exploiting the EDLS engineering measurements for scientific investigations of Mars' atmosphere and surface [1].

On the 19th October 2016, Schiaparelli, the Entry Demonstrator Module (EDM) of the ESA ExoMars Program entered into the martian atmosphere. Despite the ultimate failure of ExoMars – 2016 Schiaparelli to land safely, it transmitted data throughout its descent to the surface, until the loss of signal at 1 minute before the expected touch-down on Mars' surface. The entry phase and the initial descent under parachute were nominally operated until an anomaly in the navigation system (the unexpected saturation of one GNC sensor) caused the catastrophic conclusion of the mission. The radio signal and the flight data, although more limited than expected, have been essential to investigate the anomaly the caused the crash landing (e.g. [2, 3]) and for the achievement of the AMELIA scientific objectives. From the limited returned EDL flight data, AMELIA managed to reconstruct the correct trajectory and attitude of Schiaparelli EDM and to retrieve the atmospheric profiles and low altitude wind profiles [4].

As per the previous mission, the experiment AMELIA 2022 will rely on the EDL measurements of the ExoMars 2022 descent module encapsulating the Russian surface platform, Kazachok and the European rover, and Rosalind Franklin during entry and descent into Mars' atmosphere and at landing. Because of the increased mass of the ExoMars 2022 EDM with reference to Schiaparelli, the EDL scenario is more complex and foresee the deployment of two parachutes, one supersonic and one subsonic, to slow it down prior to landing on Mars.

The in situ measurements will be performed by the GNC (Guidance, Navigation and Control) sensors of the descent module: 2 Inertial Platforms (IMU) and the Radar Altimeter (RDA) and also by the Kazachok Surface Platform (SP) payload (namely, the meteorological package MTK – L

and the television camera system TSPP) and from the tracking of the radio signal during EDL both by Mars' relay orbiters and direct to Earth link. An essential set of the EDL flight data will be transmitted in real time through Mars relay orbiters, while the whole data set will be retransmitted after landing.

From the measurements recorded during entry and descent, we will retrieve an atmospheric vertical profile along the entry and descent trajectory. Different algorithms, methods, data sets and their assimilation will be used for simulation and reconstruction of the EDM trajectory and attitude during the entry and descent phases to retrieve the most accurate atmospheric profile. A near real time reconstruction of the trajectory will be done using the radio communication link between the EDM and the radio receiver on board the Mars orbiters and by the carrier signal detection by ground telescopes. Atmospheric vertical profiles in terms of density, pressure, and temperature, will be derived directly from deceleration measurements, by matching atmospheric standard model with Extended Kalman filtering (EKF) of a 6 DoF EDM dynamic model. The dynamical behaviour of the EDM during the descent under parachute will be modeled, simulated, and reconstructed using different data, methods, and data assimilation (e.g., IMU, radio link, radar, imaging and auxiliary data). Wind profile along the entry probe path will be retrieved by using the Doppler shift in the radio link between the Descent Module and a radio receiver and by modeling the dynamic response of the pendulum system composed by the EDM and the parachute line.

Scientific analysis of the landing measurements and descent images will be aimed at the determination of the landing site context (e.g., surface mechanical characteristics, geomorphology, etc.), its characterization and assessment also in combination with remote sensing imaging.

ExoMars – 2022 will provide the opportunity for new direct in situ measurements exploring an altitude range not covered by remote sensing observations from an orbiter. AMELIA results together with the measurements of the meteorological package MTK – L at the surface of Mars will provide a surface and atmosphere "ground truth" for remote sensing observations and important constraints for validation of Mars atmosphere models.

The experience and lessons learned in the framework of the Schiaparelli EDM and expertise in Mars observations and modelling are being put in perspective for the AMELIA ExoMars – 2022 Entry, Descent and Landing (EDL) science experiment.

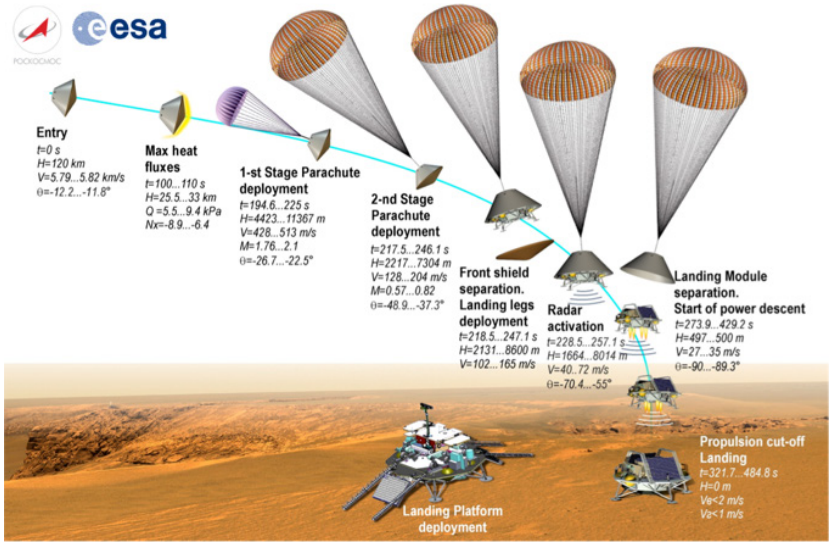


Fig. 1. ExoMars 2022 EDL scenario.

ACKNOWLEDGEMENTS:
AMELIA is an experiment for scientific investigations of Mars' atmosphere and surface by means of the ExoMars measurements during its entry, descent, and landing on Mars. The International AMELIA team led by Francesca Ferri (CISAS-Univ. Padova) as Principal Investigator, includes scientists and experts from Italy, Belgium, France, UK, Finland, USA, and Russia. The support of the national funding agencies of Italy (ASI, grant no. 2017-03-17, I/018/12/3 and 2020-21-HH.0), Belgium (BELSPO and PRODEX), UK (UKSA, grant no. ST/M00306X/1) and France (CNES) is gratefully acknowledged.

REFERENCES:
[1] Ferri, F. et al. 2019. Space Science Review 215: 8. https://doi.org/10.1007/s11214-019-0578-x;
[2] Portigliotti S., et al. 2017. 14th International Planetary Probe Workshop IPPW#14, The Hague, The Netherlands, June 2017;
[3] Bonetti, D., et al 2018. Acta Astronautica. V. 149, P. 93–105;
[4] Aboudan, A., et al. 2018. Space Science Reviews, 214, doi: 10.1007/s11214-018-0532-3

LUMINESCENCE TECHNIQUE APPLIED TO MARTIAN SEDIMENTS IN-SITU DATING: THE IN-TIME PROJECT

M. Sastre [1], M.L. Martín [2,3], J.L. Vázquez-Poletti [4], F. Valero[1,3], L. Vázquez[3,4], A. di Iorio[5]

[1] *Facultad de Ciencias Físicas, Universidad Complutense de Madrid, Madrid, 28040, Spain;*
[2] *Escuela de Ingeniería Informática de Segovia, Universidad de Valladolid, Segovia, 40005, Spain;*
[3] *Instituto de Matemática Interdisciplinar, Universidad Complutense de Madrid, Madrid, 28040, Spain;*
[4] *Facultad de Informática, Universidad Complutense de Madrid, Madrid, 28040, Spain;*
[5] *ALMA Sistemi Srl, Guidonia, 00012, Italy*

KEYWORDS:
Martian sediments; luminescence; geochronology; in-situ instrument; Martian analogue.

INTRODUCTION:
The "In situ instrument for Mars and Earth dating applications" (IN – TIME) project aims to build a leading-edge instrument to be able to date the Martian surface sediments using the luminescence method. Such an instrument needs to meet several technological requirements for in-situ examination, and to be successfully selected for a mission to Mars it must be miniaturized.

A geochronology for recent events on Mars can be a complex issue because the uncertainties associated with the current most frequent methodology (crater counting) are typically around one million years. This value is comparable to the younger ages obtained. Therefore, using the luminescence method may be very helpful to overcome this problem.

The luminescence technique applied to date geological strata has been successfully employed on the Earth, dating the last exposure to the daylight of some specific grains. It is based on the fact that certain types of materials, under appropriate conditions, can absorb, store and afterwards release energy from environmental ionizing radiation. Among these materials, the most useful ones for our purposes are quartz and K-feldspar. Anyway, to date any kind of rock using the luminescence method, some requirements must be met, namely: a) the rock shall be composed of minerals which behave as dosimeters; b) the luminescence energy stored in the minerals must have been zeroed at the time of sediment deposition and burial; c) saturation of the energy storage in the minerals should not have been reached at the time of analysis.

Several characteristics, including geological, mineralogical, and climatic aspects need to be considered before choosing a Martian analogue for luminescence dating. With these constrains, a terrestrial area where these features can be comparable to those on Mars surface is found in Lanzarote (Spain). For this reason, a team from the IN-TIME project has performed a field study in this island. Naturally, the radiation environment needs to be taken into account too [1].

Here we present a panoramic view of the use of the luminescence method in the context of the IN-TIME project.

REFERENCES:
[1] Schetakis, N., Crespo, R., Vázquez-Poletti, J. L., Sastre, M., Vázquez, L., and Di Iorio, A. Overview of the main radiation transport codes. Geosci. Instrum. Method. Data Syst. 2020. V. 9. P. 407 – 415. https://doi.org/10.5194/gi-9-407-2020

TRACKS IN MARTIAN DUST — DUST DEVILS AND AIR SHOCK WAVES FOOTPRINTS

B.A. Ivanov[1]
[1] *Institute of Geosphere Dynamics, Russian Academy of Science, Leninsky Prospect 38-1, Moscow, Russia, 119334, baivanov@idg.chph.ras.ru*

KEYWORDS:
Mars, impact craters, atmospheric shock waves, dust devils, HiRise.

INTRODUCTION:
Thin dust layers on the surface of Mars are very mobile. The wind action changes the albedo, creating various patterns on the surface. Some of these patterns are elongated curved tracks, located along the path of dust devils [1]. Orbital and surface images revealed the formation of many tracks during the passage of dust devils. The exact mechanism of track's formation is under study now [2]. The most elaborated models are air swirl entertainment [3] and a pressure depression in a center of air vortex [4].

Impact generated atmospheric shock waves have been proposed as a source of surface albedo changes near new impact craters years ago – e.g. [5, 6]. In the current project we investigate a possibility that air shock wave interactions (refraction, reflection, collision) near dusty surface could produce elongated curvilinear albedo features [7]. To advance the study we compare some properties of dust devil tracks (DDT) with albedo contrast of air-blast related features (parabolas and scimitars). The goal is to compare assumed pressure impulse values for dust devil swirls and atmospheric shock waves.

ALBEDO CONTRAST:
In the variety of DDT's types, we are interested in long dark (a majority) and bright (locality-depended) tracks [1]. The preference is shifted toward DDT formed near new impact craters with parabolas and scimitars. The general statistics for the albedo contrasts of DDT is published in [8, 9]. For most of studied locations with the Lambert albedo from ~ 0.18 to 0.25 the typical albedo decrease for dark DDT's is in the range from ~ 0.005 to 0.03 [8], and depends on the location and a season. The DDT average width is about 20 to 40 m with maxima up to 100-300 m [9].

For impact related parabolas [7] the width varies with a distance from a crater (what is interpreted with geometry of a pair collided hemispheric air shocks of limited length) in the range of 1 to 10 impact crater diameters. For scimitars the geometry is still poorly modeled. Generally, the scimitar width increased with a distance from the "parent" crater and could be as large as ~ 10 crater diameters.

Fig. 1 presents a rare example of a new impact, where both a parabola and a scimitar were formed. Occasionally, the dust devil crossed the site after the impact, so we can compare general features of all three albedo features. The impact site image was obtained 04.24.2019, the age is bounded with CTX images 12.29.2018 and 2.28.2019. Hence the imaged impact scene is a few months old. The scimitar is brighter than surroundings, while the parabola and the DDT is darker.

The parabola albedo contrast with surroundings is about - 0.2 %. The profile across the scimitar is non-symmetric with the albedo contrast about + 3 % relative to the surrounding halo margins. The parabola geometry is well reproduced with the model of two hemispherical air wave crossing provided that crater's 2 impact occur 0.64 s after crater's 1 impact.

The scimitar bilateral symmetry indicates the direction of projectile's flight (roughly form the upper right to the lower left in Fig. 1). Going from the crater side in the up-range direction, the reflectivity I/F shows a leading dark strip (comparable with the parabola profile) and a wider brighter zone approximately of 10 m width (the visible width of simitars typically increases with the distance to the crater). The darker strip I/F amplitude contrast is about - 1 %, while the brighter strip I/F amplitude is about + 2 % brighter than surroundings. The I/F (albedo) finally approach the background level.

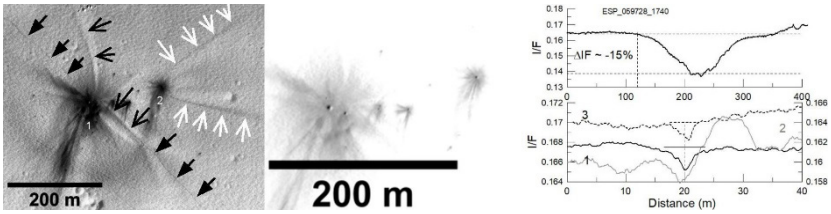


Fig. 1. The impact crater cluster at ESP – 059728 – 1740. The left panel shows location of main craters (1 and 2), a scimitar (open black arrows), a parabola (white open arrows) and a possible dust devil track (filled black arrows). The image is processed with the "enhance contrast" ImageJ plugin. The middle panel shows the stretched image of craters. The right panel shows brightness profiles through the main halo about 200 m wide (the upper plot), and across the parabola (1, the left vertical axis), the scimitar (3, the left vertical axis), and the DDT (3, the right vertical scale). Profiles are 40 m long, centered at the darkest point, and are obtained with the ImageJ tool for a 40 × 40m rectangular with the centerline along the albedo feature. The non-mapped image is used.

The dust devil track looks like to be formed after the impact event. This DDT has a continuous length of ~ 1 km, starting and ending on local slopes, and a visible width of 2 to 3 m. The dark DDT I/F (albedo) contrast with surroundings is about - 1 %.

The model of scimitar's formation reproduces the crater-faced arc geometry as the impact of a projectile fragment with the velocity of 4 to 5 km s^{-1} and the impact angle 45 ^{o} to 50 ^{o} above the horizon depending on the assumed fragment's density.

Totally we have accumulated a few dozen measured impact cites of various ages (from a few months to several years). The first impression is that parabolas, well resembling DDT, could survive to be recognized by HiRISE up to ~ 10 terrestrial years.

MECHANISMS OF FORMATION:

The formation mechanism of parabolas and scimitars is still unclear. Parabolas have close to a perfect bilateral symmetry relative to the connecting line between the "parent" crater pair. When the time delay between impacts in a cluster is small enough, we see the "simultaneous" formation of two or three parabolas. The closeness of albedo profiles across DDT and parabolas witnesses into a favor to some similarity of the formation mechanism. We take into account both negative pressure excursions and eddies formation due to collision of air shock waves.

For scimitars the formation mode seems to be more complicated. While we could assume the collision of hemispherical and ballistic atmospheric shock fronts from the close to a perfect bilateral symmetry relative to the flight direction, the opposite sign of the albedo contrast (relative to parabolas and most DDT's), the mechanism which block a wide area against the dust darkening demands more study in a future.

CONCLUSIONS:

The Martian dust activation by dust devils and by short action of assumed atmospheric shock waves seems to have some similarity in mechanisms. The idea to convert this apparent similarity into numerical values of particle sizes, pressure excurse amplitudes and durations still has some potential for a future progress.

ACKNOWLEDGMENTS:

The work is a part of an official assignment from the Russian Federation Ministry of Science and Higher Education to the Institute of Geosphere Dynamics, Russian Academy of Sciences (project No AAAA-A17-117112350020-9).

REFERENCES:

[1] Reiss D., Fenton L., Neakrase L., Zimmerman M., Statella T., Whelley P., Rossi A.P., Balme M. Dust Devil Tracks // Space Science Reviews. 2016. V. 203. No 1, P. 143–181.
[2] Klose M., Jemmett-Smith B.C., Kahanpää H., Kahre M., Knippertz P., Lemmon M.T. Lewis S.R., Lorenz R.D., Neakrase L.D.V., Newman C., Patel M.R.,

Reiss D., Spiga A., Whelley P.L. Dust Devil Sediment Transport: From Lab to Field to Global Impact // Space Science Reviews. 2016. V. 203. No. 1. P. 377–426.
[3] Kurgansky M.V. To the theory of particle lifting by terrestrial and Martian dust devils. Icarus. 2018. V. 300. P. 97–102.
[4] Balme M., Hagermann A. Particle lifting at the soil-air interface by atmospheric pressure excursions in dust devils // Geophysical Research Letters. 2006. V. 33. No. 19. P. L19S01, doi:10.1029/2006GL026819.
[5] Ivanov B.A., Melosh H.J., McEwen A.S. New Small Impact Craters in High Resolution HiRISE Images – III // Proceedings of 41st Lunar and Planetary Science Conference. The Woodlands, Texas. 2010. Abstract No. 2020.
[6] Burleigh K.J., Melosh H.J., Tornabene L.L., Ivanov B., McEwen A.S., Daubar I.J. Impact airblast triggers dust avalanches on Mars // Icarus. 2012. V. 217. P. 194–201.
[7] Ivanov B. Martian dust activation due to air shock waves from small impacts // Proceedings of the 11th Moscow Solar System Symposium. Moscow. 2020. No. 11MS3-MS-13.
[8] Statella T., Pina P., Silva E.A.. Extensive computation of albedo contrast between martian dust devil tracks and their neighboring regions // Icarus. 201. V. 250. P. 43–52.
[9] Statella T., Pina P., da Silva E.A.. Automated width measurements of Martian dust devil tracks // Aeolian Research. 2016. V. 20. P. 1–6.

TRAJECTORY ESTIMATIONS FOR FRESH IMPACTS ON MARS

E.D. Podobnaya[1], O.P. Popova[1], D.O. Glazachev[1]
[1] *Institute for Dynamics of Geospheres RAS, Moscow, Russia, epodobnaya@gmail.com*

KEYWORDS:
Meteoroids, Mars, , impacts, cluster of craters, fragmentation, strewn fields.

INTRODUCTION:
In recent years, about 700 fresh dated meteoroid impact sites have been discovered on Mars [1 - 3]. Meteoroid impacts resulted in the formation of single craters and crater fields, with crater sizes up to 50 m.

The study of craters on Mars allows us to study the Martian impactors population and the fragmentation details that cannot be detected in terrestrial conditions [4].

CRATERS STREWN FIELDS:
The paper is dealing with craters strewn fields (cluster of craters). Azimuth and entry angle of meteoroid trajectory are found by constructing scattering ellipses [3, 5]. Azimuths and entry angle are connected with orbital parameters of the impactor [3]. Azimuth is calculated as inclination angle of scattering ellipse major axis; flight direction is chosen as the direction from the scattering ellipse center along its major axis towards the maximal crater. Comparison of estimates [5] with previous results [3] shows good correlation for scattering ellipses calculated azimuth. In the case of oblique impacts, the crater ejecta is distributed asymmetrically and permits to determine the direction of flight [6]. For meteoroids under consideration ejecta distribution and corresponding azimuth are found based on Mars images, submitted by HiRISE project [2]. In some cases, parabolic features which are treated as surface records of atmospheric shock wave interaction [7, 8] are used to determine the azimuth. Ejecta-based estimates of azimuth for 41 from 55 of considering clusters are compared with azimuths obtained by constructing scattering ellipses [3, 5]. For azimuths calculated by craters ejecta inclination of meteoroid trajectory projection fits the estimations [3] for about 70 % of clusters, direction of meteoroid flight fits in about third of clusters.

REFERENCES:
[1] Malin, M.C., Edgett, K.S., Posiolova, L.V., McColley, S.M., Noe Dobrea, E.Z. Catalog of New Impact Sites on Mars Formed May 1999 – March 2006. Malin Space Science Systems // Inc., San Diego, California. 2006.
[2] Daubar I.J., McEwen A.S., Byrne S., Kennedy M.R., Ivanov B. The current Martian cratering rate // Icarus. 2013. V. 225. No. 1. P. 506 - 516.
[3] Daubar I.J., Banks M.E., Schmerr N.C., Golombek M.P. Recently Formed Crater Clusters on Mars // Journal of Geophysical Research: Planets. 2019. V. 124. No. 4. P. 958 - 969.
[4] Hartmann W.K., Daubar I.J., Popova O., Joseph E.C. Martian cratering 12. Utilizing primary crater clusters to study crater populations and meteoroid properties // Meteoritics & Planetary Science. 2018. V. 53. No. 4. P. 672 - 686.
[5] Podobnaya E.D., Popova O.P., Glazachev D.O. Scattering ellipses for recently formed crater clusters on Mars. Dynamic processes in geospheres. Issue 12 // IDG RAS, Moscow, 2020. In Russian. P. 89 - 98.
[6] Shuvalov, V. Ejecta deposition after oblique impacts: An influence of impact scale // Meteoritics &Planetary Science. 2011. V. 46. No. 11. P. 1713 - 1718.
[7] Ivanov, B.A., Melosh, H.J., McEwen, A.S., Team, H., New Small Impact Craters in High Resolution HiRISE Images – III. // Proc. 41at Lunar and Planetary Science Conference, The Woodlands, Texas, 2010, abstract No. 2020.
[8] Burleigh, K.J., Melosh, H.J., Tornabene, L.L., Ivanov, B., McEwen, A.S., Daubar, I.J., Impact airblast triggers dust avalanches on Mars // Icarus. 2012. V. 217. P. 194–201.

WATER AND CHLORINE ESTIMATION IN THE MARTIAN SUBSURFACE ACCORDING TO DAN MEASUREMENTS ONBOARD THE NASA CURIOSITY ROVER

S.Y. Nikiforov[1], I.G. Mitrofanov[1], M.V. Dyachkova [1], A.B. Sanin[1], M.L. Litvak[1], D.I. Lisov[1]
[1] *Space Research Institute of the Russian Academy of Sciences (IKI), 84/32 Profsoyuznaya Str, Moscow, Russia, 117997, nikiforov@np.cosmos.ru*

KEYWORDS:
Mars exploration, rover, neutron spectroscopy, water.

INTRODUCTION:
This work presents updated results for water and chlorine content in the soil of Gale crater based on active and passive measurements by the Dynamic Albedo of Neutron (DAN) instrument onboard the NASA Curiosity rover [1].

Analyzed data are derived both from DAN active and passive measurements made at local surface areas (pixels) along traverse of the rover [2, 3]. The contents of water and equivalent chlorine are studied separately for distinct geomorphological units along the traverse, the mean values and sample variances are evaluated for each of the unit.

In our work, we will present the latest results on DAN observations in these areas.

REFERENCES:
[1] Mitrofanov, I.G., et al., 2012. Dynamic Albedo of Neutrons (DAN) experiment onboard NASA's Mars Science Laboratory. Space Science Reviews, V. 170 (1–4), P. 559–582. https://doi.org/10.1007/s11214-012-9924-y.
[2] Nikiforov, S.Y., et al., 2020. Assessment of water content in martian subsurface along the traverse of the Curiosity rover based on passive measurements of the DAN instrument. Icarus, 346, 113818. https://doi.org/10.1016/j.icarus.2020.113818.
[3] Lisov, D.I., et al., 2018. Data processing results for the active neutron measurements by the DAN instrument on the curiosity Mars rover. Astron. Lett. V. 44 (7), P. 482 – 489. https://doi.org/10.1134/S1063773718070034.

MARTIAN CO_2 POLAR CAPS DEPOSITS DERIVED WITH GEANT4 - PLANETOCOSMICS FROM NEUTRON FLUX VARIATIONS

G. Barderas[1,3], L. Yubero[1], L. Vázquez[2,3]
[1] *Facultad de Matemáticas, Universidad Complutense de Madrid, Spain;*
[2] *Facultad de Informática, Universidad Complutense de Madrid, Spain;*
[3] *Instituto de Matemática Interdisciplinar, Facultad de Matemáticas, Universidad Complutense de Madrid gbardera@ucm.es*

KEYWORDS:
Mars, Mars Odyssey, HEND, GEANT4, PLANETOCOSMICS.

INTRODUCTION:
Mars shows a seasonal CO_2 cycle through condensation and sublimation processes, by exchanging significant amounts of CO_2 from each polar cap with the atmosphere. Neutron spectroscopy data gathered with HEND / GRS instrument on-board Mars Odyssey have been widely used to study local and global variations of Martian CO_2 seasonal caps, as well as to develop global maps of Martian neutron flux and subsurface water ice distribution [1 - 4].

The efficiency of the moderation of the fast and epithermal neutrons produced by Galactic Cosmic Rays in the subsurface layer depends on the presence of hydrogen atoms in the Martian soil, leading to a lower neutron albedo at Polar Regions [1 - 6]. However, when the water ice is covered by the seasonal CO_2 polar caps, the efficiency of the moderation of the fast neutrons in the subsurface layer decreases, and an increase of the flux of fast and epithermal neutrons emanating from the Martian surface is expected. Thus, providing the possibility of using neutron data as a sensitive method to study the seasonal caps and their inter - annual variations [1–7].

Monte Carlo codes are often used to simulate the passage of particles through the Martian soil and atmosphere, and the subsequent neutron production, scattering or capture processes under different seasonal scenarios. Then, the resulting neutron leakage could be compared to the HEND counting rate to estimate CO_2 effective thickness, mass or density.

In this work, we intend to use an adapted version of the GEANT4 [8] toolkit Planetocosmics [9] to estimate the CO_2 polar deposits from HEND neutron flux data and analyze its consistency with prior studies [1–4] and the dependency of the involved parameters.

REFERENCES:
[1] Feldman, W.C. et al. Science. 2002. V. 297. No. 5578. P. 75–78.
[2] Mitrofanov, I.G et al. Science. 2002. V. 297. No. 5578. P. 78 – 81.
[3] Boynton, W.V. et al. 2002. Science. V. 297. No. 5578. P. 81–85.
[4] Litvak, M.L. et al. ICARUS. 2006. V. 180. No. 1. P. 23–37.
[5] Kelly, N.J. et al. J. Geophys. Res. 2006. E03S07.
[6] Litvak, M.L. et al. J. Geophys. Res. 2007. E03S13.
[7] Prettyman, T.H. et al. J. Geophys. Res. 2009. 114, CiteID E08005.
[8] Agostinelli, et al. Nucl. Instrum. Methods Phys. Res. A. 2003. Vol. 506. P 250 – 303.
[9] Desorgher, L. et al. In: 36th COSPAR Scientific Assembly. 2006. Vol. 36. P. 2361–2361.

MARS CRATER MODIFICATION IN THE LATE NOACHIAN II: UPDATED CRITERIA FOR IDENTIFYING COLD-BASED CRATER WALL GLACIATION

B.D. Boatwright[1], J.W. Head[1]
[1] *Dept. of Earth, Environmental and Planetary Sciences, Brown University, Providence, RI 02912 USA, benjamin_boatwright@brown.edu; james_head@brown.edu*

KEYWORDS:
Mars climate, fluvial processes, glaciation, crater modification, Noachian.

INTRODUCTION:
We previously described a degraded Noachian-aged crater in Terra Sabaea, provisionally named "B," that contained inverted fluvial channel networks and lacustrine deposits [1–2]. Crater B is not breached by fluvial channels and lacks depositional morphologies such as fans or deltas, which sets it apart from previously described open- and closed-basin lakes on Mars that are hydrologically connected to their surroundings [3–4]. This "closed-source drainage basin" (CSDB) therefore represents a new type of paleolake on Mars. The lack of hydrologic connectivity, along with additional evidence of remnant cold-based glacial morphologies within the crater, led us to hypothesize top-down melting of a cold-based crater wall glacier as the source of runoff and sediment for the fluvial and lacustrine deposits, which produced one or more proglacial lakes within the crater [1–2]. This interpretation is consistent with model predictions of the early Mars climate [5–7] and is the first potential geomorphic evidence of Noachian cold-based glaciation, sedimentation, and proglacial lake formation found on Mars.

Using the geomorphic criteria established by our initial studies of crater B, we conducted a wider regional survey in Terra Sabaea to search for further evidence of cold-based glaciation and glacially sourced fluvial and lacustrine deposits within degraded craters [8]. Here, we highlight an additional example from our survey that suggests geologic processes similar to those in crater B were acting at regional scales, and how this second example may shed light on aspects of this era of Mars crater modification that we had not previously observed.

GEOLOGY OF THE SECOND CRATER:
Our regional survey revealed 42 distinct inverted fluvial channel systems within a ~ 500 km radius of crater B [8]. Among these, approximately half were located in other unbreached (CSDB) craters that lacked evidence of either inflow or outflow channels as potential drainage sources. Of the unbreached craters, approximately one in three fell within the Type II classification of Mangold et al. [9] that are modified by fluvial activity but maintain faintly visible ejecta deposits, in contrast to Type I, whose ejecta deposits have been completely removed. Type I craters are thought to have formed mostly in the Noachian while Type II craters formed in the Hesperian [9].

The unnamed second crater we highlight here is located at 22.46˚S 46.19˚E, or ~ 250 km southeast of crater B (Fig. 1A; Robbins crater ID 21–000144 [10]). It is slightly smaller than B, with a diameter of 47 km. Despite being located in an Early Noachian highlands unit (eNh) [11], visible ejecta to the southwest suggests this crater is Type II and thus younger than B, which is Type I. Below we describe the notable geologic features within this crater and then compare them to our previous observations of crater B.

CROSS-CUTTING RIDGES:
A single large, sinuous ridge network is exposed in the southwest floor of the crater (Fig. 1B). It is partly interrupted by multiple small, fresh impacts, but in the unobscured areas there is a clear distinction between the higher, flat-topped tributaries and the surrounding floor that suggests a downslope flow direction toward the center of the crater. As in crater B, these ridg-

es appear to be inverted fluvial channels with distinct proximal and distal morphologies. An isolated branch further to the south contains two superposed ridges. HiRISE images show a higher ridge flowing approximately N – S with two branches that curve off to the east (Fig. 1C). These branches superpose a lower pair of subparallel N – S ridges at a ~ 90 ˚ angle. Although individual ridges may represent channel belts with multiple avulsions, the intersection of two stratigraphically distinct ridges is more likely representative of two separate channel-forming events [12]. Unlike in crater B, the channel cross-cutting in the second crater strongly suggests that multiple episodes of fluvial activity occurred during this period of crater modification on Mars.

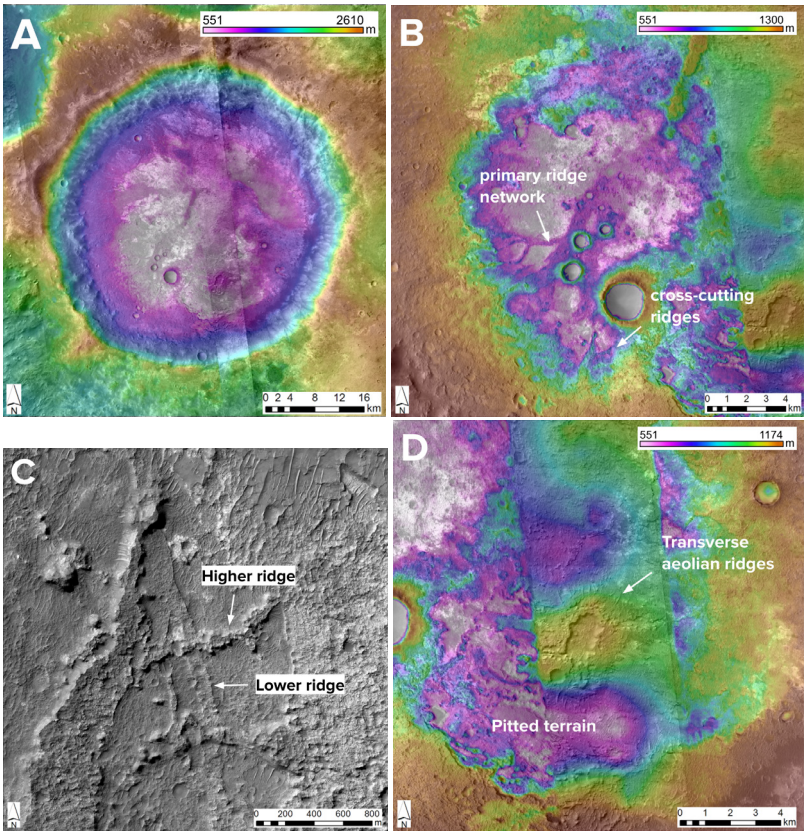


Fig. 1. (**A**) 47 km crater located ~ 250 km southeast of crater B; blended CTX/MOLA DEM. (**B**) Southwest part of the crater floor with primary ridge network. (**C**) Multiple generations of cross-cutting ridges; HiRISE visible image. (**D**) Pitted terrain and transverse aeolian ridges in southeast crater floor.

AEOLIAN ACTIVITY:

The southeast floor of the crater has a more chaotic texture, although smaller inverted channels are visible here as well. The overall appearance of this area at HiRISE resolution is rough and pitted. The pit boundaries often have perpendicular sets of small linear ridges extending outward from them (Fig. 1D). These ridges closely match the description of topographically influenced transverse aeolian ridges (TARs) [13], linear dune-like features that form normal to the local wind field. Topographically influenced TARs do not readily appear in crater B, where they mostly occur as topographically independent ridges in wide, low-slope plains. In some instances the TARs in the second crater are found in close proximity to the inverted channels. While both TARs and inverted fluvial channels can appear as quasi-linear ridges conforming to topography, the inverted channels tend to be flat-topped with some amount of sinuosity and branching, while the TARs are typically sharp-crested, linear, and subparallel. On average, the inverted channels we observe also have longer length scales (~ 1–5 km) than TARs (< 1 km).

DISCUSSION:
We have described in detail a second example of a crater containing features similar to those identified in the closed-sourced drainage basin crater "B" [1–2] as further demonstration of this style of crater modification on Mars. Major differences between this second crater and the original crater B include the identification of cross-cutting inverted fluvial channels and the close interrelationship between some inverted channels and transverse aeolian ridges, or TARs. In crater B, we interpreted the inverted channels as alluvial sediment lags that had become indurated, making them resistant to erosion as surrounding unconsolidated material was removed. Widespread deflation surfaces in crater B suggested that later aeolian activity was primarily responsible for the removal of sediment within the crater. Thus, our overall interpretation of crater modification in the Late Noachian can be updated in the following ways:

1. Fluvial channel formation within craters occurred in multiple episodes. The identification of inverted fluvial channels within a Type II crater suggests that this type of crater modification on Mars continued at least into the early period of Type II crater formation, beyond the end of the Noachian [9].
2. Alluvial sediment lags underwent topographic inversion due to removal of surrounding material, possibly through aeolian deflation. Such activity could have provided a source of sediment for nearby transverse aeolian ridges.
3. The identification of inverted fluvial channels within an unbreached CSDB crater outside the original crater B suggests that the processes that led to the formation of inverted fluvial channels and lacustrine deposits in the first crater — namely, cold-based crater wall glaciation and top-down melting — may have been active at wider regional scales in the southern highlands.

FUTURE WORK:
Beyond the two CSDB craters we have now described, we are continuing to study inverted fluvial channels that occur in breached craters and within non-crater topographic basins [8]. By applying the criteria we first formulated for crater B and now have broadened by incorporating a second example, we are working toward characterizing the full range of ancient glacial environments in the southern highlands in order to further test hypotheses of Mars climate evolution.

REFERENCES:
[1] Boatwright B.D., Head J.W. (2020) 11MS3.
[2] Boatwright B.D., Head J.W. (2021) PSJ 2.
[3] Fassett C.I., Head J.W. (2008) Icarus 198.
[4] Goudge T.A. et al. (2015) Icarus 260.
[5] Forget F. et al. (2013) Icarus 222.
[6] Wordsworth R. et al. (2013) Icarus 222.
[7] Wordsworth R. et al. (2015) JGR 120.
[8] Boatwright B.D. et al. (2021) LPSC 52.
[9] Mangold N. et al. (2012) JGR 117.
[10] Robbins S.J., Hynek B.M. (2012) JGR 117.
[11] Tanaka K.L. et al. (2014) USGS SIM 3292.
[12] Hayden A.T. et al. (2019) Icarus 332.
[13] Balme M. et al. (2008) Geomorph. 101.

ZHURONG LANDING SITE IN SOUTHERN UTOPIA PLANITIA, MARS: GLOBAL GEOLOGIC CONTEXT, STRATIGRAPHY AND OUTSTANDING QUESTIONS*

J.W. Head[1]
[1] *Department of Earth, Environmental and Planetary Sciences, Brown University, Providence, RI 02912 USA, james_head@brown.edu*

KEYWORDS:
Mars, China, Tianwen – 1, Zhurong, Borealis, Utopia, oceans, climate, glaciation, volcanism, eolian, sedimentary, impact craters, pitted cones.

INTRODUCTION:
The geologic record of the Northern Lowlands/Utopia Basin of Mars spans the entire history of the planet, and includes evidence for processes such as impact basins, oceans, extrusive and explosive volcanism, tectonics, glaciation, lahars, eolian and cryospheric. We describe this geologic history, some of the many outstanding questions, and how the Zhurong rover exploration can help to resolve some of these questions.

PHASES IN THE HISTORY AND EVOLUTION OF THE NORTHERN LOWLANDS: Following the initial era of accretion, magma ocean formation and crustal solidification [1], the impact flux declined sufficiently such that the major physiographic provinces and most heavily cratered terrains began to be preserved (the Pre-Noachian period) [2, 3]. During this period, the fundamental northern lowlands-southern uplands dichotomy occurred. Once thought to be related to basic mantle convection, possibly even seafloor spreading, on the basis of its irregular shape compared to the Utopia Basin, an alternative view of origin by a large oblique impact finally gained general acceptance [4, 5]. Thus, the formation of the Borealis impact basin and the dichotomy boundary is generally considered be the beginning of preserved martian history [6] (Fig. 1). Below we review the highlights in this history.

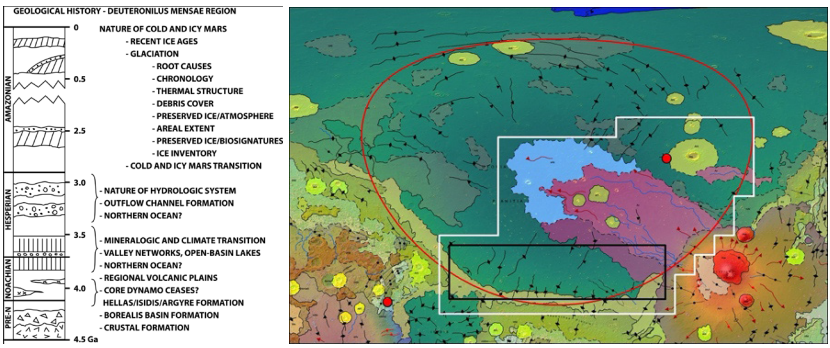


Fig. 1. Left: Stratigraphic Column of the Northern Lowlands/Utopia Basin. Right, Geologic Map of Utopia Planitia [3] Black box, Zhurong landing area, red dot VL-2; red oval, Utopia Basin. Green is Vastitas Borealis Formation.

PHASE 1: PRE-NOACHIAN-EARLY TO MID-NOACHIAN: Formation of the Northern Lowlands topographic depressions: Borealis Basin, followed by Utopia Basin, followed by heavy cratering [2, 3]. The last three impact basins (Hellas, Isidis, Argyre) formed, creating new topoogrpahy, emplacing huge quantities of ejecta, causing substantial erosion and changing the atmosphere and climate [7].

***QUESTIONS*:** What is the age of the Borealis and Utopia basins and how did their sequence influence Utopia Basin evolution/northern lowlands history? Did they sample martian mantle material?

PHASE 2: MID-LATE NOACHIAN-EARLY HESPERIAN: In the "Warm & Wet" early Mars model [8], climate was dominated by MAT > 273 K, low rainfall rates, water infiltration and diffusive degradation and a vertically integrated hydrological system [9]; in the LN-EH a 'Climate Optimum' occurred [10], and fluvial valley networks, open/closed-basin lakes, and possibly a Noachian ocean (VN-OBL/CBL/FO) formed? Alternatively, the climate may have been "Cold & Icy" [11] with transient heating, melting and drainage events.

***QUESTIONS*:** Under what climate conditions did the VN/CBL/OBL form? Was there a Noachian NL/UB ocean? Search for erosion, sediments, mineral alteration (phyllosilicates), shorelines. Where did the water go?

PHASE 3: LATE NOACHIAN-EARLY HESPERIAN CLIMATE AND ATMOSPHERIC TRANSITION: During this period, the climate began transitioning toward the current "Hypothermal/Hyperarid" conditions, a millibars-level atmosphere, MAT ~ 215 K, and minimal atmospheric water vapor. A global cryosphere formed and the hydrological system became horizontally stratified [9]. Formation of the transition unit [3] along the dichotomy boundary.

***QUESTIONS*:** Why, when and how did the LN/EH 'Climate Optimum' transition to the "Hypothermal/Hyperarid" climate of today?

PHASE 4: EARLY HESPERIAN: Massive extrusive volcanism resurfaced 30 % of the planet (Hr-ridged plains) and paved the northern lowlands including Utopia [12]. Tharsis and Elysium (abundant explosive volcanism) active. Fretted terrain and dichotomy boundary modification initiates.

***QUESTIONS*:** How thick was Hr in NL and UB [12]? What were its sources: local, Elysium/Tharsis, global? On what substrate was it emplaced? Noachian Ocean ice? Cratered terrain? Evidence for volcano-ice [13] interactions?

PHASE 5: LATE HESPERIAN-EARLY AMAZONIAN: Circum-Tharsis outflow channels (OC) and a 'second ocean' (SO) formed [2]. OCs have a wide range of ages, residence times and fates [14–16]. Evidence exists both for and against oceans [17]. The NL/UB Vastitas Borealis Formation (VBF) [3] may be a sublimation residue of outflow channel effluent [18].

***QUESTIONS*:** Why no OCs into Utopia despite evidence for shorelines, etc. [19, 20]? What is lander/rover evidence for the nature of oceans, shorelines, tsunamis, and related predictions? Where did OC water come from, and go? Any evidence for cryospheric cracking and groundwater release [21]?

PHASE 6: EARLY AMAZONIAN: WHERE IS THE MISSING WATER? LYOT CRATER: Extensive surface water seems to have disappeared: Where did it go? To the poles? Is it still buried in NL/UB [22], lost to space? How to balance the water budget [23]? Early Amazonian Lyot Crater (47 N), surrounded by Late Valley Networks, lies near Utopia; is source of water for the VN an ancient frozen ocean or surface snow and ice [24]?

***QUESTIONS*:** Where did the water go? Where are the ancient polar deposits? Is there evidence for buried ice in Utopia?

PHASE 7: MIDDLE TO LATE AMAZONIAN: UNUSUAL IMPACT CRATERS: Morphology of impact craters suggests excavation of wet sediment, groundwater or surface snow/ice? Lobate debris aprons, lineated valley fill, concentric crater fill all suggest mid-latitude debris-covered glaciation [25]. Could spin-axis/orbital changes cause latitude-dependent glaciation in Utopia Planitia [26] and possible glaciovolcanism [13]?

***QUESTIONS*:** Is the Vastitas Borealis Formation reworked outflow channel effluent, further processed by sequential latitude-dependent glaciation? What is the role of Mie crater ejecta at the VL-2 site?Is there evidence for glacial sediments and layering at the Zhurong landing site?

PHASE 8: MIDDLE TO LATE AMAZONIAN: BASIN FLOOR TECTONICS, LAHARS, GLACIOVOLCANISM, PITTED CONES, MUD FLOWS AND VOLCANOES: During this period, the floor of Utopia underwent deformation to produce giant polygonal graben, mud flows are associated with the graben [19–20], lahars were emplaced from Elysium [27], evidence for glacial ice

* This paper is based on an invited keynote talk given at the TIanwen–1 Mission Review Meeting in Zhuhai, China, June, 2018.

and volcano-ice interactions abound [28]: Is the water from a residual ocean or latitude-dependent glaciation? How often did ice come and go and how much is still there?

QUESTIONS: What is the origin of the polygonal graben? How much buried ice is there and at what depth? Where did the lahars come from and why?How and why did the mud flows form? Did water flood the Utopia basin floor? What is the origin of the pitted cones [29]?

PHASE 9: LATE AMAZONIAN: THE ORIGIN AND EVOLUTION OF THE NPLD: The North Polar Layered Deposits are young [2–3]. Why, when, how did they form and where was the water before this? Does the NPLD come and go with obliquity variations? Does the NPLD ever completely go away?

***QUESTIONS*:**Over what time period does the NPLD form? Is there evidence for episodic deposition of snow and ice and related deposits in Utopia Planitia?

PHASE 10: LATEST AMAZONIAN: THE LAST 20 MA AND THE LDM: How much did emplacement of the Latitude-Dependent Mantle [30] influence northern and southern Utopia Planitia? Did it modify the surface and what is the residual record. What is the difference between LDM at higher and lower latitudes?

***QUESTIONS*:** Where is the residual ice and what role does it play in the NL-Utopia basin. Does the geological record at the Zhurong site record the LDM or is it dominated by it? How does the geology of the Viking 2 Northern Utopia Site compare to the Southern Utopia Zhurong landing site?

KEY QUESTIONS FOR ZHURONG EXPLORARION:
On the basis of this global geological setting for the Tianwen–1 Zhurong Rover Utopia Basin landing site, we pose the following 14 specific questions for exploration during the Zhurong traverses: 1. Origin of the Pitted Cones? Volcanic, volcano-ice interactions, dewatering, glacial (pingo, morainal) etc.? 2. Origin of graben?: Tectonic, volcanic, cryospheric, different at different scale? 3. Evidence for ancient oceans? Mineralogy, salts, sedimentary structures, grain size distribution? 4. Evidence for mudflows? Scale, internal structure, origin? Relation to graben? 5. Surface/Near Surface Rocks: Sedimentary (ocean, fluvial, glacial, eolian?), volcanic (lava flows, volcanic ash). 6. Stratigraphic Sequence: Nature of crater ejecta as function of crater size. 7. Amazonian Climate Record: Polygons, substructure, cryoturbation, pits (deflation, sublimation?), plateaus/mesas, pedestal craters, pitted rocks [31], etc. 8. Impact Craters: Substructure, pedestals, ejecta, wall stratigraphy, etc. 9. Transverse Aeolian Ridges (TARS)/Dunes: Evidence for changing climate? 10. Surface unit ages: Validating impact crater size-frequency distribution measurements. Role of climate resurfacing? 11. Are the rocks magnetized? Do they show differences? 12. Exotic Mineralogy: Martian mantle excavated by Utopia? 13. Evidence for geologically recent climate change (< 20 Ma)? 14. Evidence for life: Fossils or trace fossils?

REFERENCES:
[1] Elkins-Tanton et al. 2003. MAPS 38, 1753.
[2] Carr & Head. 2010. EPSL 294, 185.
[3] Tanaka et al. 2014. USGS Map3092..
[4] Marinova et al. 2008. Nature 453,1216.
[5] Nimmo et al. 2008. Nature 453, 1220.
[6] Fassett & Head. 2014. PSS 91, 60.
[7] Palumbo & Head. 2017. MAPS 53, 687.
[8] Craddock & Howard. 2002. JGR 107.
[9] Irwin et al. 2005. JGR 110.
[10] Head. 2012. LPSC 43 2137.
[11] Wordsworth et al. 2013. JGR 120, 1201.
[12] Head et al. 2002. JGR 107.
[13] Head & Wilson. 2007. Ann. Glac. 45, 1.
[14] Carr. 1978. JGR 84, 2995.
[15] Carr & Head. 2019. Icarus 319, 433.
[16] Turbet et al. 2017. Icarus 288, 10.
[17] Head et al.. 2018. LPSC 49 2194.
[18] Kreslavsky & Head. 2002. JGR 107, 2151.
[19] Ivanov et al. 2014. Icarus 228, 121.

[20] Ivanov et al. 2015. Icarus 248, 383.
[21] Palumbo & Head. 2020. GRL 47.
[22] Clifford & Parker. 2001. Icarus 154, 40.
[23] Carr & Head. 2015. GRL 42, 1.
[24] Weiss et al.. 2017. GRL 44, 5336.
[25] Head et al.. 2010. EPSL 294, 306.
[26] Madeleine et al. 2009. Icarus 203, 390.
[27] Russell & Head. 2003. JGR 108, 5064.
[28] Pederson & Head. 2010. PSS 58, 1953.
[29] De Pablo & Komatsu. 2009. Icarus. 199, 49.
[30] Head et al.. 2003. Nature 426, 797.
[31] Head et al. 2011. JGR 116.

CONSTRUCTING AN ANALYTICAL MODEL OF THE MAGNETIC FIELD OF MARS USING SATELLITE DATA AND MODIFIED S – APPROXIMATIONS

A.M. Salnikov[1,2], A.V. Batov[1,2], I.E. Stepanova[2], T.V. Gudkova[2]
[1] *Trapeznikov Institute of Control Sciences RAS, Profsoyuznaya, 65, Moscow, Russia, salnikov@ipu.ru;*
[2] *Schmidt Institute Physics of the Earth RAS, B.Gruzinskaya, 10, Moscow, Russia*

KEYWORDS:
Mars, magnetic field, grid, approximation, integral representation.

INTRODUCTION:
The relevance and scientific significance of developing numerical and analytical methods for constructing a new high-resolution model of the Martian magnetic field based on large-volume satellite measurements using the modified S-approximation method [1, 2] has several reasons. From the theoretical point of view, such work is due to the permanent need to create methods for constructing global models of the physical fields of planets based on aggregate, including heterogeneous and multi-precision, publicly available large-volume satellite measurements (e. g. [3–5]). From the practical side, such work is interesting because of the need to create modern software libraries and packages that calculate approximation models of physical fields with modified versions of linear integral representations. The latter has proven itself well in finding analytical approximations of the planet potential fields [6, 7] and continuous functions that are not harmonic but take values at the boundary of the harmonic region of a field.

MAIN RESULTS:
According to the method of S-approximations based on the method of so-called linear integral representations, we specify the valid signal in the form of an integral representation of a harmonic function in a specific region. The main computational stage in the framework of the S-approximation method used is the solution of a high-dimensional SLAE. The main manually selected parameters of the model are the total number and parameters of carriers of simple and double layers that approximate the magnetic field. Since the initial measurements always contain some error, it is also necessary to introduce the upper and lower bounds of the residual norm to solve the problem with the required accuracy. For the formation of grids of samples, we used spherical rectangular equal-area grids [8].

Using the structural-parametric approach, of which the three-dimensional method of S – approximations is a part, we carried out a series of experiments where we approximated the known measured components of the magnetic field by the sum of simple and double layers distributed on two carriers of magnetic masses equivalent in the external field. We obtain data of measurements of the magnetic field of Mars by the magnetometer of the MAVEN station from the PPI PDS public website [9]. Based on samples of satellite measurements from large data arrays on arbitrary grids according to various criteria, models of the Martian magnetic field were constructed using a modified method of S–approximations at satellite heights and on the planet's surface in the areas of operation of the InSight [10] and the Tianwen–1 missions.

REFERENCES:
[1] Strakhov V.N., Stepanova I.E. Solution of gravity problems by the S-approximation method (regional version) // Izvestiya. Physics of the Solid Earth. 2002. V. 38. № 7. P. 535–544.
[2] Stepanova I.E. On the S–approximation of the Earth's gravity field // Inverse Problems in Science and Engineering V. 16. P. 5. P. 547–566
[3] Mittelholz A., Johnson C. L., Morschhauser A. A new magnetic field activity proxy for Mars from MAVEN data // Geophysical Research Letters. 2018. V. 45. P. 5899–5907.

[4] Langlais, B., Thébault, E., Houliez, A. & Purucker, M.E. A new model of the crustal magnetic field of Mars using MGS and MAVEN // J. Geophys. Res. Planet. 2019. V. 124. P. 1542–1569.
[5] Connerney, J.E.P., Espley, J., Lawton, P. et al. The MAVEN Magnetic Field Investigation // Space Science Reviews 2015. V. 195. P. 257–291.
[6] Gudkova T.V., Stepanova I.E., Batov A.V., Shchepetilov A.V. Modified method S-, and R–approximations in solving the problems of Mars's morphology // Inverse Problems in Science and Engineering. 2020, P. 1–15. DOI:10.1080/17415977.2020.1813125.
[7] Gudkova, T.V., Stepanova, I.E., Batov, A.V. Density Anomalies in Subsurface Layers of Mars: Model Estimates for the Site of the InSight Mission Seismometer // Sol Syst Res. 2020. V. 54, P. 15 – 19. DOI: 10.1134/S0038094620010037.
[8] Malkin, Z.A. New Equal-area Isolatitudinal Grid on a Spherical Surface // The Astronomical Journal. 2019. № 158(4). doi:10.3847/1538-3881/ab3a44.
[9] https://pds-ppi.igpp.ucla.edu/search/?sc=MAVEN&i=MAG.
[10] Johnson, C.L., Mittelholz, A., Langlais, B. et al. Crustal and time-varying magnetic fields at the InSight landing site on Mars. Nat. Geosci. 2020. V. 13, P. 199–204.

ATOMIC OXYGEN LOSS DURING PROTON AURORAL EVENTS AT MARS

V.I. Shematovich[1]
[1] *Institute of Astronomy of the Russian Academy of Sciences, Moscow, Russia, shematov@inasan.ru*

KEYWORDS:
Mars, solar wind, high-energy proton and hydrogen atom precipitation, proton auroral events, atmospheric escape, kinetic Monte Carlo model.

INTRODUCTION:
Proton auroral events are observed in the dayside atmosphere of Mars and are caused by the high-energy hydrogen atom fluxes (ENA-H) penetrating into the neutral atmosphere [1]. Such events also cause the loss of neutral atomic oxygen from the Martian atmosphere. The processes of formation, kinetics, and transport of suprathermal oxygen atoms in the transition region (from the thermosphere to the exosphere) during proton auroral events at Mars were considered. An additional source of hot oxygen atoms — momentum transfer collisions of the precipitating high-energy H atoms with atomic oxygen in the upper atmosphere of Mars, namely, $Q_{Oh}: H(E) + O_{th} \rightarrow H(E' < E) + O_{sth}(E'' = E - E')$ — was taken into account in the Boltzmann kinetic equation for suprathermal *O* atoms, which was solved using the kinetic Monte Carlo model [2]. As a result, the estimates of the hot oxygen population in the Martian corona were obtained and it was shown that proton auroral events are accompanied by atmospheric loss of the atomic oxygen with value varying in the range (3.5 - 5.8) × 10^7 cm^{-2} s^{-1} (see Figure).

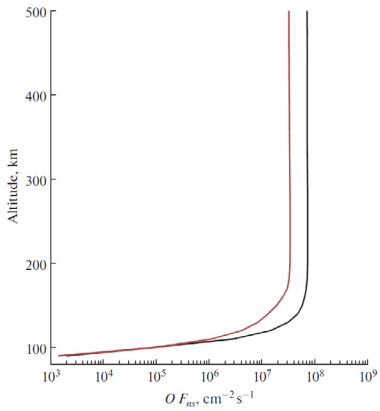


Fig. 1. Height profiles of the calculated upward flux of suprathermal oxygen caused by the precipitation of high-energy hydrogen atoms into the Martian atmosphere through the induced magnetosphere boundary at an altitude of 820 km (black line) and 1260 km (brown line). In the latter case, the content of hydrogen atoms in the corona of Mars is 2 times higher than the analogous value for the basic calculation with The IMB an altitude of 820 km.

The calculated values of the atmospheric loss rate of oxygen atoms caused by the ENA-H precipitation during proton auroral events on Mars are comparable to the values of the atmospheric *O* loss due to photochemistry [3, 4]. It should be noted that although the proton auroras at Mars are sporadic events, the escaping flux of the suprathermal oxygen atoms induced by the precipitation processes can become even dominant under conditions of extreme solar events — solar flares and coronal mass ejections-as it was found in the recent observations of the MAVEN spacecraft [4]. It seems that the loss of the Martian atmosphere due to the forcing by the solar wind plasma and, in particular, the precipitation of high-energy proton and hydrogen atom fluxes during solar flares may play an important role in the atmospheric loss on astronomical time scales [5].

ACKNOWLEDGMENTS:
This study was supported by the Russian Science Foundation (project 19-12-00370).

REFERENCES:

[1] Deighan J., Jain S.K., Chaffin M.S., et al. Discovery of proton aurora at Mars // Nature Astronomy. 2018. V. 2. P. 802.
[2] Shematovich V.I., Marov M.Ya. Escape of planetary atmospheres: physical processes and numerical models // Physics Uspekhi. 2018. V. 61. P. 217.
[3] Groeller H., Lichtenegger H., Lammer H., Shematovich V.I.Hot Oxygen and Carbon Escape from the Martian Atmosphere // Planet. Space Sci. 2014. V. 98, P. 93–105.
[4] Jakosky B.M., Brain D., Chaffin M., and 129 more. Loss of the Martian atmosphere to space: Present-day loss rates determined from MAVEN observations and integrated loss through time // Icarus. 2018. V. 315. P. 146.
[5] Shematovich V., Bisikalo D. (2021, February 23). Hot planetary coronas // In: Oxford Research Encyclopedia of Planetary Science. Oxford University Press, 2021.

KINETIC MODELING OF PROTON AURORA AT MARS

V.I. Shematovich[1], D.V. Bisikalo[1]
[1] *Institute of Astronomy of the Russian Academy of Sciences, Moscow, Russia, shematov@inasan.ru*

KEYWORDS:
Mars, solar wind, high-energy proton and hydrogen atom precipitation, proton aurora, kinetic Monte Carlo model.

INTRODUCTION:

Recently discovered proton auroras [1] are the ones of a few observed phenomena on Mars that arise as a result of direct interaction of solar wind protons with an extended hydrogen corona. Proton aurorae are considered as an excess of atomic hydrogen Lyα emission in the upper atmosphere caused by fluxes of high-energy hydrogen atoms penetrating into the atmosphere through the induced magnetosphere boundary (IMB) [1, 2]. They were measured [1] with the IUVIS spectrograph on board the MAVEN spacecraft, and observed [2] on the dayside of Mars. Hydrogen atoms with kinetic energies of up to several keV are formed due to the charge exchange of protons of the unperturbed solar wind with thermal hydrogen atoms in the extended corona of Mars. The efficiency of this process depends on the radial concentration of hydrogen atoms in the corona [3]. Hydrogen atoms, in contrast to the solar wind protons, easily penetrate into the daytime upper atmosphere through the IMB and cause proton auroral phenomena. The developed kinetic Monte Carlo models [3, 4] of the precipitation of high-energy protons and hydrogen atoms into the planet's upper atmosphere are used to study auroral proton phenomena at Mars.

The fluxes and energy spectra of high-energy hydrogen atoms and protons penetrating deep into the Martian thermosphere were calculated [4] using the kinetic Monte Carlo model [3]. This makes it possible to estimate all the necessary parameters of proton auroral phenomena in the upper atmosphere of Mars. For example, in Figure the height profiles of the volume excitation rate of atomic hydrogen emission in the Lyα line due to the precipitation of high-energy hydrogen atoms with penetrating into the Martian atmosphere through the IMB are shown in Figure for two cases describing the basic (model A1 — black line) and excess (model A2 — red line) content of hydrogen atoms in the corona. These calculated excitation rates together with the radiation transfer model make it possible to estimate the excess hydrogen emission in the Lyα line for a proton aurora in the Martian atmosphere, which was done in the test calculations in [5], and could be compared with the results of measurements [2] by the IUVIS spectrograph on board the MAVEN spacecraft.

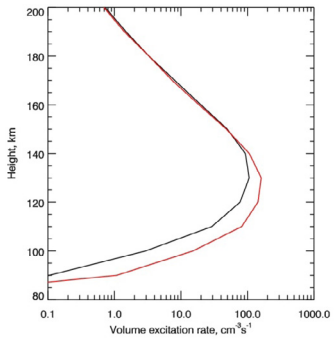


Fig. 1. Height profiles of the volume excitation rates of the Lyα emission of atomic hydrogen caused by the precipitation of high-energy hydrogen atoms into the Martian atmosphere through the induced magnetosphere boundary at an altitude of 820 km (black line) and 1260 km (red line). In the latter case, the content of hydrogen atoms in the corona of Mars is 2 times higher than the analogous value for the basic calculation with the IMB an altitude of 820 km.

ACKNOWLEDGMENTS:
This study was supported by the Russian Science Foundation (project 19-12-00370).

REFERENCES:

[1] Deighan J., Jain S.K., Chaffin M.S., et al. Discovery of proton aurora at Mars // Nature Astronomy. 2018. V. 2. P. 802.
[2] Hughes A., Chaffin M., Mierkiewicz J., et al. Proton Aurora on Mars: A Dayside Phenomenon Pervasive in Southern Summer // J. Geophys. Res.: Space Physics. 2019. V. 124. P. 10,533.
[3] Shematovich V.I., Bisikalo D.V., Zhilkin A.G. Effects of column density variations of extended hydrogen corona of Mars on the charge exchange efficiency with solar wind protons // Astronomy Reports. 2021. V. 65. P. 203–208.
[4] Shematovich V.I., Bisikalo D.V. Kineticcalculations of the charge exchange efficiency between solar wind protons and extended hydrogen corona of Mars // stron. Reports. 2021. V. 65. No. 10 (in press).
[4] Gérard J.-C., Hubert B., Ritter B., Shematovich V.I., Bisikalo D.V. The Martian proton aurora: a model of the Lyman-α emission line profile and intensity distribution // Icarus. 2019. V. 321. P. 266–271.

SOME APPLICATIONS OF THE SPACE DATA ANALYSIS + CLOUD COMPUTING: FROM THE MARTIAN AURORAS TO THE COVID–19 PANDEMIC EVOLUTION

D. Pacios[1], L. Vázquez[1], J.L. Vázquez-Poletti[1]
[1] *Facultad de Informática, Universidad Complutense de Madrid, Spain*

KEYWORDS:
Martian Auroras, Cloud Computing, Artificial Intelligence, Machine Learning, Modelling, Economy, Covid – 19.

INTRODUCTION:
We present the preliminary results related to the identification of Martian auroras with great precision. We consider the data crossing from two instruments (Spicam and Marsis of Mars Express) in real time. Both instruments may not be operating at the same time. We implement a computational solution describing the state-of-the-art technology, in the framework of the cloud computing strategy. Up to 200GB of data are processed and stored by using cloud computing technologies. Such approach is going to be used in the joint recently started European project, EYE, to follow the evolution of Covid – 19 Pandemic with the satellite data basis from Copernicus.

REFERENCES:
[1] Aguirre C., Franzese G., Esposito F., Vázquez L., Caro-Carretero R., Vilela-Mendes R., Ramírez-Nicolás M., Cozzolino F. and Popa C.I.: Signal-adapted tomography as a tool for dust devil detection. Aeolian Research, 2017, 39, P. 12–22.
[2] Vazquez-Poletti J.L.,Velasco M.P., Jiménez S., Usero D., Llorente I.M., Vázquez L., Korablev O., Belyaev D., Patsaeva M.V. and Khatuntsev I.V.. Public "Cloud" Provisioning for Venus Express VMC Image Processing. Communications on Applied Mathematics and Computation. 2019, https://doi.org/10.1007/s42967-019-00014-z.
[3] Schetakis N., Crespo R., Vázquez-Poletti J.L., Sastre M., Vázquez L., Di Iorio A. Overview of Main Radiation Transport Codes. Geoscientific Instrumentation Methods and Data Systems, 2020,V. 9, P. 407 – 415.

CO_2 CLOUDS ON MARS FROM ACS SOLAR OCCULTATIONS ONBOARD TGO

M. Luginin[1], N. Ignatiev[1], A. Fedorova[1], A. Trokhimovskiy[1], D. Belyaev[1], A. Grigoriev[2, 1], A. Shakun[1], F. Montmessin[3], O. Korablev[1]
[1] *Space Research Institute (IKI), Moscow, Russia, mikhail.luginin@phystech.edu;*
[2] *Australian National University (ANU), Canberra, Australia;*
[3] *LATMOS-UVSQ, Guyancourt, France*

KEYWORDS:
Mars, aerosols, CO_2 clouds, ACS, TGO.

Carbon dioxide is the major constituent of the Martian atmosphere. Its seasonal cycle plays an important role in atmospheric dynamics and climate. Formation of the polar CO_2 frost deposits results in up to 30 % of atmospheric pressure variations as well as in dramatic change in surface reflectance and emissivity. Another case of carbon dioxide condensation is formation of a CO_2 clouds that are still poorly studied, despite the fact that they have been observed by a number of instruments [1–6] on the orbit of Mars.

The Atmospheric Chemistry Suite (ACS) is a set of three infrared spectrometers (NIR, MIR, and TIRVIM) featuring high accuracy, high resolving power and a broad spectral coverage (0.7–17 μm) onboard the Trace Gas Orbiter (TGO). To separate CO_2 aerosols from dust and water ice particles and characterize them, we use spectra of TIRVIM and MIR located inside the CO_2 absorption feature at 2.7 μm (Figure 1), accompanied by visible and IR spectra from NIR (0.7–1.7 μm).

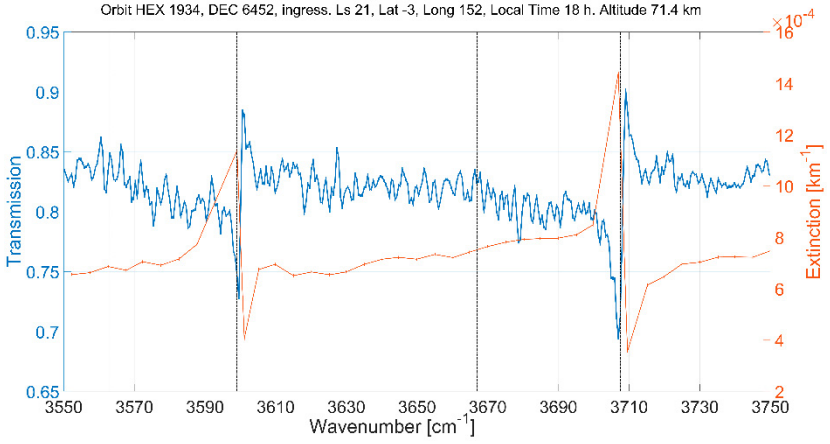


Fig. 1. Transmission (blue) and extinction (orange) spectra measured by TIRVIM at 71 km during the ingress solar occultation observation #6452. Two extinction peaks located at 3600 and 3707 cm^{-1} show presence of CO_2 clouds.

In this work, we will present preliminary results of CO_2 ice clouds observations performed by ACS in the period from May 2018 to June 2021 covering more than a full Martian year.

ACKNOWLEDGMENTS:
This work was funded by Russian Science Foundation, grant number 20-42-09035.

REFERENCES:

[1] Montmessin et al. 2006. Subvisible CO_2 ice clouds detected in the mesosphere of Mars. Icarus, V. 183, P. 403–410. https://doi.org/10.1016/j.icarus.2006.03.015.
[2] Montmessin et al. 2007. Hyperspectral imaging of convective CO_2 ice clouds in the equatorial mesosphere of Mars. Journal of Geophysical Research, V. 112, E11S90. https://doi.org/10.1029/2007JE002944.
[3] Määttänen et al. 2010. Mapping the mesospheric CO_2 clouds on Mars: MEx/OMEGA and MEx/HRSC observations and challenges for atmospheric models. Icarus, V. 209, P. 452–469. https://doi.org/10.1016/j.icarus.2010.05.017.

[4] McConnochie et al. 2010. THEMIS-VIS observations of clouds in the Martian mesosphere: Altitudes, wind speeds, and decameter-scale morphology. Icarus, V. 210, P. 545–565. https://doi.org/10.1016/j.icarus.2010.07.021.
[5] Vincendon et al. 2011. New near-IR observations of mesospheric CO_2 and H_2O clouds on Mars. Journal of Geophysical Research, V. 116, E00J02. https://doi.org/10.1029/2011JE003827.
[6] Jiang et al., 2019. Detection of Mesospheric CO_2 Ice Clouds on Mars in Southern Summer. Geophysical Research Letters, V. 46(14), P. 7962–7971. https://doi.org/10.1029/2019GL082029.

SEASONAL AND SPATIAL VARIATIONS OF THE CO VERTICAL DISTRIBUTION ON MARS BASED ON ACS TGO MEASUREMENTS

A. Fedorova[1], A. Trokhimovskiy[1], F. Lefevre[2], O. Korablev[1], F. Forget[3], N. Ignatiev[1], A. Lomakin[1], K. Olsen[4], D. Belyaev[1], F. Montmessin[2], J. Alday[4], M. Luginin[1] and the ACS Team

[1] *Space Research Institute RAS, Moscow, Russia;*
[2] *UVSQ Univ Paris Saclay, Sorbonne Univ, CNRS, LATMOS, Paris, France;*
[3] *LMD IPSL Jussieu, Paris, France;*
[4] *Physics Department, Oxford University, Oxford, UK*

KEYWORDS:
Mars, atmosphere, spectroscopy, carbon monoxide.

Carbon monoxide (CO) is an incondensable species of the Martian atmosphere produced by the photolysis of CO_2. Its mixing ratio responds to the condensation and sublimation of CO_2 from the polar caps which results in seasonal variations of the CO abundance in polar regions. Since 2018 ACS spectrometers on Trace Gas Orbiter have measured CO in infrared bands by solar occultation method. Here we present the first long-term monitoring of the CO vertical distribution at the altitude range from 0 to 60 km for 1,5 Martian years from Ls = 163 of MY 34 to the end of MY35 on the seasonal and spatial scales. We obtained a mean CO VMR of about 950 ppm in the range of altitude of 0–40 km and latitudes from 60° S to 60° N to exclude extreme polar region that is mostly consistent with previous observations. We found a strong enrichment of CO near the surface during the southern winter and spring in high southern latitudes with a layer at 10–20 km corresponding to local depletion of the CO_2 up to 85 %. In the equinox seasons both in the northern and southern spring, we found an increase of CO mixing ratio above 50 km to 3000–4000 ppm. This enrichment of CO is related to the downwelling flux of the equinox Hadley circulation on Mars above the Poles unreached of CO molecules. Comparison with the chemical model demonstrates the strong overestimation of the intensity of this process with the model where the abundance of CO is 1.5–3 times higher at the same altitudes. The minimum of CO has been observed in the southern summer in the high and middle southern latitudes in good agreement with the nadir measurements. The CO mixing ratio at Ls = 180–240 of MY34 during the GDS has shown depletion of about 10 % compared with claim MY35 that indicates the impact of the HO_x chemistry on the CO abundance.

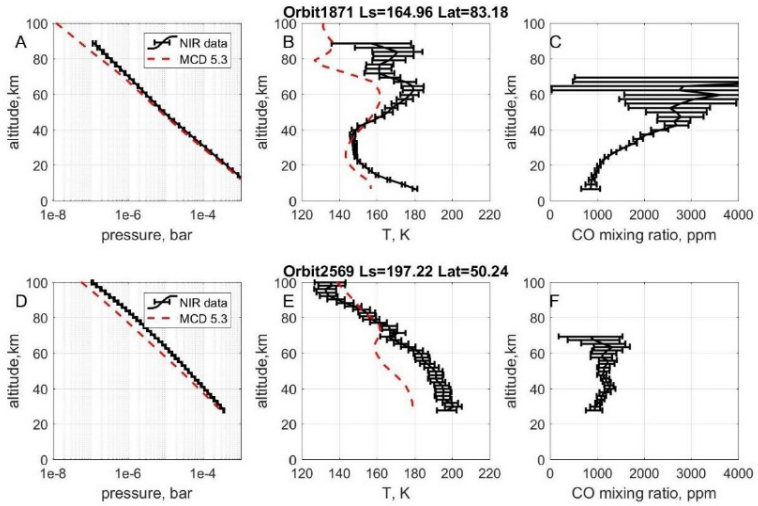


Fig. 1. Two examples of ACS NIR retrievals.

A and D panels: pressure, derived from the CO_2 number density; B and E panels: atmospheric temperature; C and F panels: CO profiles (black lines), compared to MCD5.3 “climatology” (*37*) prediction (dashed red line). The measurements in orbits 1876 and 2569 occurred before the global dust storm and during the storm, respectively. The error bars (one-sigma) are given by the retrieved covariance matrix.

VERTICAL DISTRIBUTION OF WATER VAPOR IN THE MARTIAN ATMOSPHERE RETRIEVED FROM MGS TES DAY AND NIGHT OBSERVATIONS

A. Pankine[1]

[1] *Space Science Institute, Boulder, CO, USA, apankine@spacescience.org*

KEYWORDS:
Mars atmosphere, water vapor, vertical distribution, MGS TES.

INTRODUCTION:

Water vapor is present in the Martian atmosphere in only trace amounts, but is an important factor in the current Martian climate system. Any mass exchange between the largest reservoirs of frozen water on Mars (polar caps and permafrost) can only occur by vapor transport through the atmosphere. The evolution of the polar caps and formation of mantled deposits is intimately related to water vapor transport [1]. Condensation of water vapor in the Martian atmosphere leads to the appearance of ubiquitous water ice clouds that can significantly influence the thermal state of the atmosphere [2]. Water vapor abundances on Mars undergo regular seasonal changes that reflect changes in planetary insolation, atmospheric dynamics, surface-atmosphere exchange and other planetary processes [3]. Column abundances of the water vapor in the Martian atmosphere have been measured by multiple orbiting spacecraft over several Martian years and are fairly well understood. On the other hand, the vertical distribution of the water vapor — while being an important characteristic of the Martian water cycle — has not been systematically observed. Solar occultations and limb observations by orbiting spacecraft provide the most accurate views of the vapor vertical distribution. However, limb and occultation observations of Martian atmosphere are only available for limited locations and seasons, and retrievals below heights of ~10 km, where the bulk of the atmospheric water vapor resides, are generally not possible [e.g. 4, 5].

A new methodology to retrieve water vapor vertical distribution from combined day and night observations of infrared nadir spectra is proposed. The methodology is applied to the Mars Global Surveyor (MGS) Thermal Emission Spectrometer (TES) spectral dataset. Due to the TES dataset's near-global spatial coverage and multi-annual temporal coverage, the resultant dataset of vapor vertical distribution promises to significantly expand our understanding of the Martian water vapor cycle. Details of the new methodology and some preliminary results are discussed below.

RETRIEVAL OF WATER VAPOR VERTICAL PROFILE FROM TES NADIR SPECTRA:

MGS TES spectra were collected at two local times — at ~ 2 am and ~ 2 pm. Atmospheric water vapor spectral bands appearing in TES daytime spectra at wavenumbers 230–400 cm^{-1} have been previously used to retrieve vapor column abundances [3, 67]. The new methodology to retrieve vertical distribution of water vapor from TES nadir spectra is based on the observation that vapor spectral signature in the daytime spectra is only weakly dependent on the vertical profile of vapor (constraining only column abundance), while in the nighttime spectra it is strongly dependent on the vapor profile below ~ 20 km. Figure 1 illustrates this sensitivity by showing changes in the TES water vapor band depth index (BDI) in response to changes in the vapor content at different atmospheric altitudes (vertical axis) for daytime and nighttime observations. Atmospheric temperature profiles in this example are those typical for northern mid-latitudes during early northern summer (Ls = 100 - 105 °). For daytime observations the BDI is equally sensitive to the changes in vapor content (relative to the uniform distribution) at any altitude below the altitude of vapor condensation (~ 17 km). On the other hand the BDI calculated using nighttime observations behaves differently

depending on where in the atmosphere the change in vapor is taking place. The night BDI increases if the vapor is removed from the atmosphere at heights below ~ 8 km, and decreases if the vapor is removed above ~ 8 km (Figure 1). By using this difference in the sensitivity to vapor vertical distribution, the proposed methodology can constrain vertical distribution of the vapor in the lower ~ 20 km of the atmosphere with vertical resolution ~ 10 km. (The sensitivity of the method depends on atmospheric temperatures and varies with location and season). To carry out the retrieval, the TES day and night spectra are averaged on 3 ° × 7.5 ° latitude-longitude spatial grid on temporal intervals of 5 ° L_s. For each spatial grid point the average day and night spectra provide two observations that allow determining two water vapor mixing ratio values below vapor condensation height. Diurnal variability in vapor abundances near surface (associated with possible nighttime frost formation or regolith adsorption / desorption) and at higher altitudes (associated with ice cloud formation) is assumed to be small compared to total column abundance and not significantly affecting vapor distribution on vertical scales ~ 10 km. The methodology relies on the existence of sufficient thermal contrast between the surface and the atmosphere, and between the atmospheric regions below and above ~ 10 km.

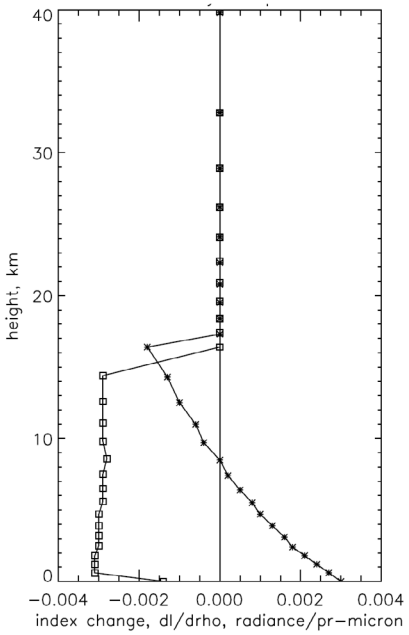


Fig. 1. Sensitivity of the TES water vapor band depth index (BDI) to vapor vertical distribution (Northern midlatitudes, L_s = 100 - 105 °). Open squares — daytime, asterisks — nighttime observations.

PRELIMINARY RESULTS:

Figure 2 shows examples of the water vapor vertical distributions retrieved for MY24 L_s = 135–140 °, L_s = 175–180 °, and MY25 L_s = 45–50 °, L_s = 80–85 °. This range of L_s corresponds to seasons of northern spring and summer, when highest values of water vapor abundances on Mars are observed. Retrievals show vapor distributions that are remarkably consistent with vapor distributions simulated by Global Circulation Models (GCM) [e.g. 8]. During early northern spring (L_s = 45–50°, Figure 2A) vapor distribution is vertically non-uniform in the northern tropics with mixing ratios increasing with altitude and peaking at pressure levels ~ 2 mbar (5–15 km above surface). This enhanced vapor layer is capped by the water ice clouds forming the Aphelion Cloud Belt (ACB). Vapor in the northern mid-latitudes is found close to the surface and is likely released from sublimating seasonal surface deposits. Close to the beginning of the northern summer (L_s = 80–85 °, Figure 2B) highest vapor mixing ratios are found near surface in the northern polar region, consistent with the sublimation of polar ice deposits. The enhanced layer of vapor at pressure levels 2–4 mbar above northern tropics is still present. In the middle of the northern summer (L_s = 135–140 °, Figure 2C) vapor mixing ratios in the northern hemisphere continue to increase and vapor is now concentrated near surface. High vapor concentrations extend from the surface to pressure levels 2–3 mbar in the northern tropics consistent with the atmospheric transport of the vapor by global circulation. Near time of the autumnal equinox (L_s = 175–180 °, Figure 2D) water vapor becomes concentrated at pressure levels 0.5–3 mbar above tropics, reflecting southward vapor transport by global circulation.

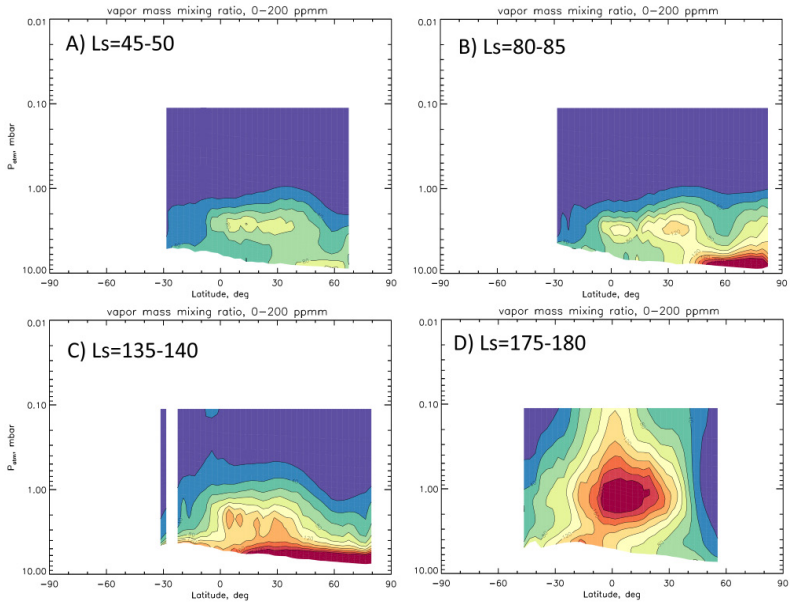


Fig. 2. Examples of water vapor retrievals in MY24 – 25. Vertical distribution of zonally-averaged water vapor mass mixing ratios during **A**) L_s = 45–50 °; **B**) L_s = 80–85 °; **C**) L_s = 135–140 °; **D**) L_s = 175–180 °. Color scale from 0 (black) to 200 ppmm (red).

The example retrievals shown in Figure 2 are consistent with predictions of vapor distributions and transport by GCMs and thus demonstrate the validity of the new retrieval methodology. Application of this retrieval methodology to the MGS TES dataset promises to add significant details to our understanding of the Martian water vapor cycle and to validate numerical models. Future plans include constraining MGS TES limb retrievals of water vapor with the vapor profiles in the lowest 10–20 km retrieved from nadir observations.

ACKNOWLEDGMENTS:
The MGS TES spectral dataset was obtained from the Planetary Data System (PDS). This research was funded by NASA Grant 80NSSC19K1488.

REFERENCES:

[1] Head J.W. et al.. 2003. Nature, V. 426(6968), P. 797–802.
[2] Madeleine J.B. et al.. 2012. Geophys. Res. Lett., V. 39(23).
[3] Smith M.D.. 2008. Annu. Rev. Earth Planet. Sci., V. 36, P. 191–219.
[4] Fedorova A.A. et al.. 2009. Icarus, V. 200(1), P. 96–117.
[5] Korablev, O. et al.. 2018. Space Sci. Rev., V. 214(1), P. 1–62.
[6] Pankine A.A. et al.. 2010. Icarus, V. 210(1), P. 58–71.
[7] Pankine A.A. and Tamppari L.K.. 2019. Icarus, V. 331, P. 26-48.
[8] Steele L.J. et al.. 2014. Icarus, V. 237, P. 97–115.

SEASONAL AND LATITUDINAL VARIATIONS OF THE HDO/H_2O RATIO IN THE MARTIAN ATMOSPHERE

V.A. Krasnopolsky[1]
[1] *Moscow Institute of Physics and Technology, Vlad.Krasn@verizon.net*

KEYWORDS:
Mars; Martian atmosphere; isotope fractionation; seasonal and latitudinal variations; Martian water; evolution.

SUMMARY:
Here we present the IRTF/CSHELL observation of latitudinal variations of HDO / H_2O in northern midsummer at L_S = 128 °. The observed high correlation with the mean atmospheric temperature is discussed. Seven latitudinal profiles of HDO / H_2O observed at various L_S from 20 ° to 145 ° in our decadal campaign are combined in a map of seasonal-latitudinal variations of HDO / H_2O on Mars. Our map is compared with the similar GCM map by Montmessin et al. (2005).

OBSERVATION AND SPECTRAL FITTING

Our long-term campaign to observe variations of HDO/H_2O on Mars using ground-based high-resolution spatially-resolved spectroscopy is presented in Krasnopolsky (2015) and include six latitudinal profiles of HDO/H_2O measured at various seasons. The observations were made using IRTF/CSHELL with resolving power of $\nu / \delta\nu = 4 \times 10^4$. We observed absorption lines of HDO and H_2O at 2722 and 2994 cm^{-1}, respectively (Fig. 1).

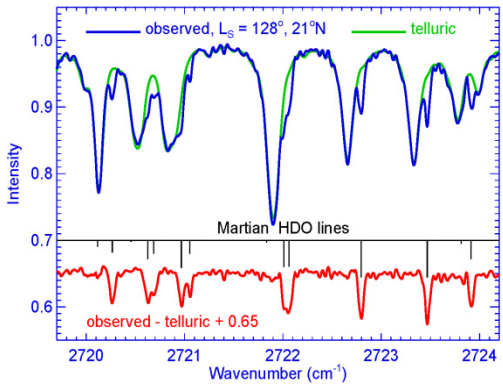


Fig. 1. Spectrum of HDO is compared with the best fit telluric spectrum. Their difference reveals martian HDO lines; their strengths and positions are shown.

To transform the observed spectra of 256 pixels to a uniform scale with a step of 0.001 cm^{-1}, we correct bad pixels and apply a parabolic fitting to get 8 sampling points from each pixel. Then strong lines are identified to get wavenumber scale interpolated to this step. The foreground spectra beyond Mars' spectra are interpolated to the positions of Mars' spectra and subtracted from those, removing thermal and nightglow emissions of the overhead air. Then we apply parabolic and sinusoidal corrections (≈ 1 % each) and wavenumber corrections (nine parameters total).

Synthetic spectra are calculated using the ATMOS solar spectrum (Kurucz 2011, http://kurucz.harvard.edu/sun/atmos/) and the HITRAN database. Free parameters are the solar-to-thermal emission ratio, telluric water (abundance, mean T and p), telluric methane abundance, martian HDO or H_2O abundance, and the instrument spectral resolution (7 parameters). The martian water lines are calculated using the Voigt line shape with T and p from the MGS/TES (Smith 2004). The H_2O spectra are corrected for the martian CO_2 and telluric ozone. The difference between the observed and bets-fit telluric spectra in Fig. 1 perfectly agrees with the strengths and Doppler-shifted positions of the martian HDO lines.

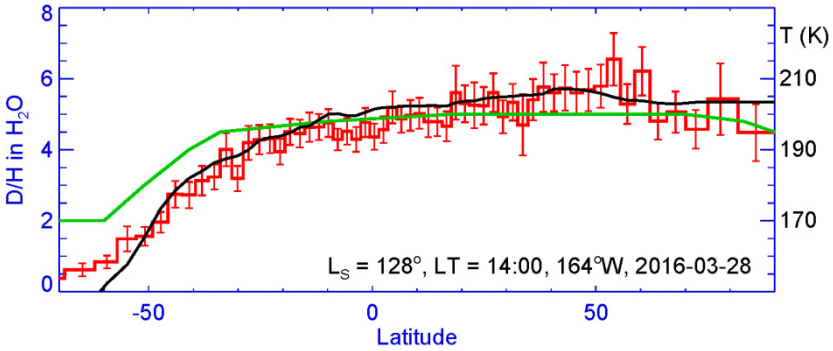


Fig. 2. Latitudinal variations of HDO / H_2O in midsummer (L_S = 128 °) on Mars are compared to the GCM data (Montmessin et al. 2005) and mean T from MGS / TES.

RESULTS:
Similar to Krasnopolsky (2015), Encrenaz et al. (2018) and Aoki et al. (2015), we do not involve aerosol extinction in our retrieval, because its effect mostly cancels out in the HDO/H_2O ratio. The observed HDO/H_2O (Fig. 2) is rather constant in the northern hemisphere, decreasing significantly to the southern subpolar latitudes. It is in reasonable agreement with the GCM data (Montmessin et al. 2005).

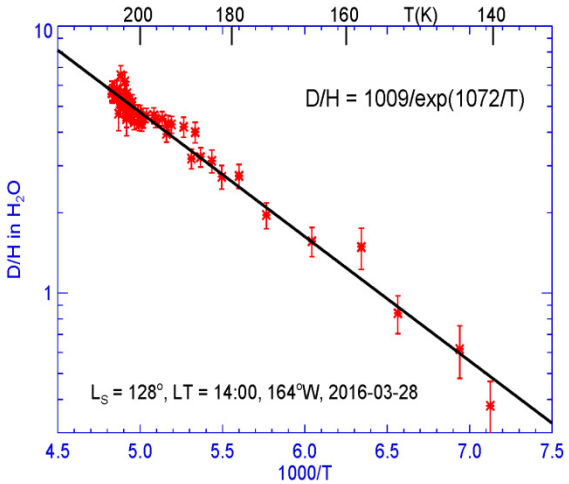


Fig. 3. The Arrhenius plot of the observed HDO/H_2O.

TEMPERATURE DEPENDENCE:
The observed HDO/H_2O are compared in Fig. 2 to temperature variations at the half pressure level measured by the MGS/TES (Smith 2004) at the similar conditions. There is a strong correlation between the values with the coefficient of 0.955. The preferential condensation of HDO at low temperatures explains the correlation. Fig. 3 depicts the Arrhenius plot of HDO / H_2O, where this ratio in the log scale is shown as a function of 1000 / T. The linear fit agrees with the observations, indicating activation energy of 1072 ± 50 K. However, the similar plots for our observations at L_S = 42 and 70 ° (Krasnopolsky 2015) result in activation energies of 2123 and 819 K. Therefore activation energy is not a proper tool to explain the complicated seasonal and latitudinal isotope fractionation on Mars.

MAP OF SEASONAL-LATITUDINAL VARIATIONS OF HDO/H_2O:
Our decadal campaign results in latitudinal profiles of HDO / H_2O at seven seasonal points from L_S = 20 to 145 °. These data are shown as a map in Fig. 4. This is the only observational map of this type that can be compared with the GCM map by Montmessin et al. (2005). Their map is zonally mean, and similar observational maps are currently impossible. However, variations of HDO/H_2O with longitude and local time were within uncertainties of the observations by Aoki et al. (2015).

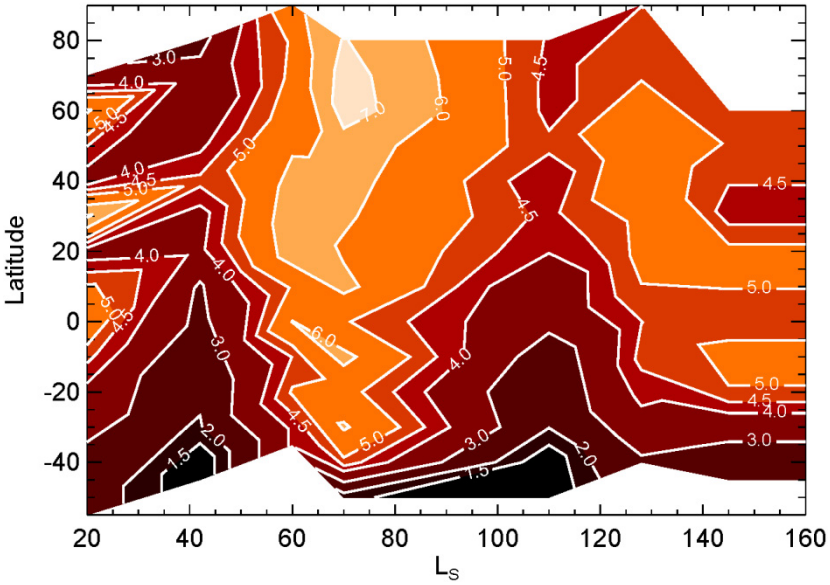


Fig. 4. Map of seasonal and latitudinal variations of HDO / H_2O based on the observations at L_S = 20, 42, 60, 70, 110, 128, and 145 °.

Overall, the variations of HDO/H_2O in our map are larger than those in the GCM and include true variations, longitudinal variability, and uncertainties of the observations. On the other hand, the GCM map is based on condensation/sublimation of water and does not involve adsorption / desorption by the regolith. Some differences between the maps are real. HDO/H_2O is rather constant at 4.5 between 60 °N and 40 °S in the GCM, while our map gives 5 ± 1 in the northern hemisphere with a significant decrease to ≈ 2 at 40 °S.

REFERENCES:

[1] Aoki, S., et al., 2015. Icarus. V. 260, P. 7–22.
[2] Encrenaz, T., et al.., 2018. Astron. Astrophys. V. 612, P. A112.
[3] Krasnopolsky, V.A., 2015. Icarus. V. 257, P. 377–386.
[4] Montmessin, F., Fouchet, T., Forget, F., 2005. J. Geophys. Res. V. 110, P. E03006.
[5] Smith, M.D., 2004. Icarus. V. 167, P. 148–165.

HYDROGEN CHLORIDE (HCL) AND ITS ISOTOPOLOGUES IN THE ATMOSPHERE OF MARS

A. Trokhimovskiy[1], A. Fedorova[1], O. Korablev[1], K.S. Olsen[2], F. Lefèvre[3], F. Montmessin[3]
[1] *Space Research Institute (IKI), Moscow, Russia, a.trokh@gmail.com;*
[2] *Department of Physics, University of Oxford, Oxford, UK;*
[3] *Laboratoire Atmosphères, Milieux, Observations Spatiales (LATMOS / CNRS), Paris, France*

KEYWORDS:
Mars, atmosphere, hydrogen chloride, isotopologues, ACS.

INTRODUCTION:
A major quest in Mars' exploration has been the hunt for atmospheric gases potentially unveiling ongoing activity of geophysical or biological origin [1]. First detection of a halogen gas, HCl, was made with the ACS instrument within ~ 3.2–3.8 μm [2], onboard the ExoMars Trace Gas Orbiter. Hydrogen chloride might originate from contemporary volcanic degassing or chlorine released from gas-solid reactions. Later is more likely because we reveal similar wide distribution of the HCl in the 1–4 ppbv range during southern summer in Martian years 34 and 35 [3]. This season features highly distributed water vapour and noticeable dust load in the atmosphere, both cases potentially participating in the HCl production from the airborne dust. We also succeeded in measuring ratio of hydrogen chloride two stable isotopologues, $H^{35}Cl$ and $H^{37}Cl$ [4]. Unlike other volatiles in the Martian atmosphere, because it is enriched with heavier isotopes, the $\delta\,^{37}Cl$ is measured to be - 7 ± 20 ‰, which is almost indistinguishable from the terrestrial ratio for chlorine. We conclude that chlorine in observed HCl likely originates from dust and is not involved in any long-term, surface-atmosphere cycle.

REFERENCES:
[1] Vago J., Witasse O., Svedhem H., et al., ESA ExoMars program: The next step in exploring Mars. Sol. Syst. Res.. 2005. V. 49, P. 518–528.
[2] Korablev O., Montmessin F., Trokhimovskiy A., et al., The Atmospheric Chemistry Suite (ACS) of Three Spectrometers for the ExoMars 2016 Trace Gas Orbiter. Space. Sci. Rev.. 2018. V. 214, P. 7.
[3] Olsen, K.S., Trokhimovskiy, A., Montabone, L., et al., Seasonal reappearance of HCl in the atmosphere of Mars during the Mars year 35 dusty season. Astron. Astrophys. 2021. V. 647, P. A161.
[4] Trokhimovskiy A., Fedorova A.A., Olsen K.S., et. al., Isotopes of chlorine from HCl in the Martian atmosphere. Astron. Astrophys. 2021.V. 651, P. A32.

TEMPERATURE AND DENSITY CLIMATOLOGY OF THE MARTIAN MIDDLE/UPPER ATMOSPHERE FROM THE ACS/TGO CO_2 SPECTROSCOPY

D.A. Belyaev[1], A.A. Fedorova[1], O.I. Korablev[1], A. Trokhimovskiy[1], E. Starichenko[1], A. Patrakeev[1], F. Montmessin[2], J. Alday[3], M. Lopez-Valverde[4]
[1] *Space Research Institute of the Russian Academy of Sciences (IKI), Moscow, Russia;*
[2] *LATMOS/IPSL, UVSQ University Paris-Saclay, CNRS, Guyancourt, France;*
[3] *Department of Physics, University of Oxford, Oxford, UK;*
[4] *IAA-CSIC, Granada, Spain*

KEYWORDS:
Martian atmosphere, temperature, density, mesosphere, thermosphere, solar occultation.

INTRODUCTION:
The middle and the upper atmosphere of Mars, altitudes above ~ 50 km, includes layers of the mesosphere and the thermosphere (above 100–120 km). This altitude range hosts the mesopause at 90–120 km with the temperature minimum, and the homopause situated 10–20 km higher, where the atmosphere leaves off being well-mixed [1]. Temperature variations in the thermosphere are defined either by seasonal and solar activity trends [2] or by energy transport forced by global circulation and vertical atmospheric waves [3, 4].

So far, a limited number of experiments explored structure of the Martian upper atmosphere: either from in situ mass-spectroscopy or from the orbital limb sounding at emission or absorption spectrometry. The climatology study requires regular measurements, for instance the up-to-date NGIMS probing above 120 km [5, 6] or occultation experiments by IUVS onboard MAVEN [7] and by SPICAM / Mars Express [8]. Those stellar occultations in the UV CO_2 absorption band (110–200 nm) sounded vertical structure of the nightside atmosphere in the altitude range from 30 to 150 km. At the same time, a solar occultation could provide higher sensitivity for the CO_2 absorption above 150 km when measuring in strong infrared (IR) bands with a high spectral resolution.

In this paper, we report highly sensitive measurements of the temperature and density vertical distribution by Atmospheric Chemistry Suite (ACS) on board ExoMars Trace Gas Orbiter (TGO) in the regime of solar occultation [9]. The middle – IR channel (ACS – MIR) has been performing the experiment since April 2018 in the spectral range from 2.3 to 4.2 μm with the resolving power exceeding 25 000. In the occultation mode, the instrument senses CO_2 absorption band around 2.7 μm in an extremely wide altitude range, from 20 to 180 km, encompassing the troposphere, the mesosphere and the thermosphere of Mars. In the paper, we discuss our scheme of the temperature and density retrievals [10] validating with atmospheric models and with simultaneous measurements by ACS – NIR [11]. The climatology is provided by the seasonal and latitude coverage of observations that counts about 600 vertical profiles spreading over 1.5 Martian Years (MY), from the middle of MY34 to the end of MY35. The dataset allows observing long-term and latitudinal variations of the thermal structure in the middle / upper atmosphere at the dawn and dusk terminators. Thanks to the appropriate vertical resolution of the retrieved profiles, 1–3 km, one can reveal gravity waves activity in the atmosphere and characterize their parameters depending on seasons [12].

MEASUREMENTS AND RETRIEVALS:
In this paper, we utilize the data retrieved from the cross-dispersion echelle spectrometer ACS-MIR operating in the solar occultation mode at the wavelength range of 2.3–4.2 μm [9]. This spectral coverage can be achieved thanks to the presence of a secondary diffraction grating, which can be adjusted to one of 12 angular positions. For our study, we observe the Martian atmosphere at the grating position № 4 with the echelle diffraction orders №222 and 223

that correspond to the 2.66–2.7 μm range. This spectral interval contains strong absorption lines of CO_2 (and H_2O) that allow for retrieving temperature and density in the Martian atmosphere with a good sensitivity. Every occultation measurement is recorded at the 640 × 512 pixels focal plane array (FPA), which accommodates up to 20 echelle orders dispersed over FPA by the secondary grating and covers a spectral range of 0.15–0.3 μm. The instrumental resolving power is $\lambda / \Delta\lambda \sim 25\,000$ and the signal-to-noise ratio varies between 2000 and 4000. The vertical resolution of MIR depends on the integration time (~ 100 msec per image) and ranges from 1 to 3 km. The analyzed transmission is obtained by division of the solar spectrum passed through the atmosphere to the reference one, which is measured above the altitude of 200 km where an influence of the atmospheric gases is negligible.Our measurements cover several Martian seasons including the second half of MY34 and the whole MY35, which correspond to ACS MIR observations from May 2018 to January 2021. The selected data set comprises 308 occultation sessions in the Northern Hemisphere and 301 sessions in the Southern Hemisphere, encompassing seasonal periods from LS 180 ° to 355° in MY34 to LS 356° in MY35.

Retrieving CO_2 density and temperature at a specified altitude, we applied a multi-iteration procedure with fitting a modeled transmission spectrum to the measured one. The model around 2.7 μm contains CO_2 rotational lines with intensities significantly dependent on temperature that allows retrieving density and temperature simultaneously. In parallel, the pressure is derived from the retrieved temperature profile under the assumption of hydrostatic equilibrium (see details in [10] and [12]).

ACKNOWLEDGEMENTS:
The analysis of temperature and density profiles and wave structures at IKI are funded by the grant №20-42-09035 of the Russian Science Foundation.

REFERENCES:

[1] Bougher et al., 2017. Chapter 14: Upper Atmosphere and Ionosphere, in The Atmosphere and Climate of Mars, ed. B. Haberle, M. Smith, T. Clancy, F. Forget, R. Zurek, Cambridge University Press, doi:10.1017/9781107016187.
[2] Bougher et al., 2015. Mars Global Ionosphere-Thermosphere Model: Solar cycle, seasonal, and diurnal variations of the Mars upper atmosphere. // Journal of Geophysical Research: Planets. V. 120(2), P. 311–342.
[3] González-Galindo et al., 2015. Variability of the Martian thermosphere during eight Martian years as simulated by a ground-to-exosphere global circulation model. // Journal of Geophysical Research: Planets. V. 120(11),P. 2020–2035.
[4] Medvedev et al., 2015. Cooling of the Martian thermosphere by CO_2 radiation and gravity waves: An intercomparison study with two general circulation models. // Journal of Geophysical Research: Planets, V. 120(5), P. 913–927.
[5] Bougher et al., 2017. The structure and variability of Mars dayside thermosphere from MAVEN NGIMS and IUVS measurements: Seasonal and solar activity trends in scale heights and temperatures. // J. Geophys. Res. Space Physics, V. 122, P. 1296–1313. doi:10.1002/2016JA023454.
[6] Stone et al., 2018. Thermal structure of the Martian upper atmosphere from MAVEN NGIMS. // Journal of Geophysical Research: Planets. V. 123, P. 2842–2867. https://doi.org/10.1029/2018JE005559.
[7] Groller et al., 2018. MAVEN/IUVS stellar occultation measurements of Mars atmospheric structure and composition. // Journal of Geophysical Research: Planets. V. 123, P. 1449–1483. https://doi.org/10.1029/2017JE005466.
[8] Quemerais et al., 2006. Stellar occultations observed by SPICAM on Mars Express. // Journal of Geophysical Research, 111, E09S04. https://doi.org/10.1029/2005JE002604.
[9] Korablev et al., 2018. The Atmospheric Chemistry Suite (ACS) of three spectrometers for the ExoMars 2016 trace gas orbiter. // Space Science Reviews, V. 214(1). https://doi.org/10.1007/s11214-017-0437-6.
[10] Belyaev et al., 2021. Revealing a high water abundance in the upper mesosphere of Mars with ACS onboard TGO. // Geophysical Research Letters, V. 48, e2021GL093411. https://doi.org/10.1029/2021GL093411.
[11] Fedorova et al., 2020. Stormy water on Mars: The distribution and saturation of atmospheric water during the dusty season. // Science, V. 367(6475), P. 297–300. https://doi.org/10.1126/science.aay9522.
[12] Starichenko et al., 2021. Gravity wave activity in the Martian atmosphere at altitudes 20–160 km from ACS/TGO occultation measurements. // Journal of Geophysical Research: Planets, 126, e2021JE006899. https://doi.org/10.1029/2021JE006899.

SESSION 1. MARS (MS)
POSTER SESSION

DUST COMPLEX INSTRUMENT ONBOARD EXOMARS – 2020 SURFACE PLATFORM

A.V. Zakharov[1], G.G. Dolnikov[1], I.A. Kuznetsov[1], A.N. Lyash[1], I.A. Shashkova[1], F. Esposito[2], E. Seran[3], M. Godefroy[3], V.M. Gotlib[1], C. Molfese[2], F. Cortecchia[2], F. Cozzolino[4], B. Saggin[5], A.S. Bychkova[1], A.E. Dubov[1], A.A. Kartasheva[1], A.V. Shekhovtsova[1]

[1] *Space Research Institute (IKI), Moscow, Russia, kia@iki.rssi.ru;*
[2] *INAF – Osservatorio Astronomico di Capodimonte, Napoli, Italy;*
[3] *LATMOS, Guyancourt, France;*
[4] *University of Naples 'Federico II', Napoli, Italy;*
[5] *Politecnico di Milano, Milano, Italy*

KEYWORDS:
Martian dust, Mars, dusty storms, dust devils, saltation, dust instrument.

INTRODUCTION:
The load of suspended dust in the Martian atmosphere varies dramatically but never drops entirely to zero. Effects of airborne dust contribute to the dynamic and thermodynamic evolution of the atmosphere and its large-scale circulation processes on diurnal, seasonal and annual timescales. Suspended dust plays a key role in determining the present climate of Mars and probably influenced the past climatic conditions and surface evolution. Atmospheric dust and windblown dust are responsible for erosion, redistribution of dust on the surface, and surface weathering.

The mechanisms for dust entrainment in the atmosphere are not completely understood, as the current data available so far do not allow us to identify the efficiency of the various processes. Dust-grain transport on the surface of Mars has never been directly measured despite great interest in and high scientific and technological ramifications of the associated phenomena. This paper describes planned, future investigations of the Martian dust environment made possible by the proposed scientific payload Dust Complex (DC) of the ExoMars – 2020 mission's landing platform.

DUST COMPLEX INSTRUMENT:
DC is a suite of four sensors devoted to the study of Aeolian processes on Mars with a primary aim of monitoring the diurnal, seasonal, and annual dust-environment cycles by Martian-ground-based measurements of dust flux in situ, i.e., in the near-surface atmosphere of Mars.

This suite includes:

1) an *Impact Sensor*, for the measurement of the sand-grain dynamics with possibility of the dust particle's mechanical momentum, electrical charge and speed measurement, located on the Surface platform body (~ 1,5 m from the martian surface) and on the deployable *Boom* (~ 0.1 m from the martian surface);
2) a particle-counter sensor, *MicroMED*, for the measurement of airborne dust size distribution and number density;
3) an *Electric Field* sensors, for the measurement of the ambient electric field potentials on two different levels from the surface, mounted on the deployable *Boom;*
4) a radiofrequency antenna *EMA* for the detection and measurement of the atmospheric electrostatic discharges, mounted on *the* deployable *Boom;*
5) a *Conductivity Sensor* for the atmospheric conductivity measurement.

Besides outlining design details of DC and the characterization of its capabilities, this presentation reviews various dust effects and dust phenomena that are anticipated to occur in the near-surface environment on Mars and that are possible to observe with DC. The negative consequences of these effects and phenomena may limit the ExoMars – 2020 mission and future human development of Mars. Mechanisms associated with the influence

of dust in atmosphere processes are discussed. Scientific outcomes of DC have future meteorological and environmental applications on Mars, for example, for the study of the evolution dynamics of the atmospheric aerosols and near-ground stratification. The primary objective of DC is to provide direct measurements of atmosphere aerosols parameters and connected electrical properties not attainable by other techniques with following additional goals:

- Measurement of the daily and seasonally variability and dynamic of the atmosphere dust;
- Detection of the windblown particles and their parameters such as mass distribution and possible charge appearance;
- Measurement of the electrostatic field, electric conductivity of the Martian near surface environment and its correlation with the dust turbidity;
- Detection of micro discharges and electric perturbations in the radiofrequency range.

SEISMOMETER FOR MEASUREMENTS ON MARS

A.B. Manukin[1,2], I.I. Kalinnikov[2], V.P. Matyunin[2], N.F. Saykina[1], A.K. Tonshev[1], N.A. Chernogorova[1]
[1] *Space Research Institute of the Russian Academy of Sciences;*
[2] *Institute of Earth Physics of the Russian Academy of Sciences*

KEYWORDS:
Seismic vibrations, uniaxial sensor, mechanical oscillator, test mass, magnetic stiffness, capacitive sensor, thermal fluctuations, conversion coefficient, slopes.

In order to be able to measure seismic impacts in three mutually orthogonal directions, using the same single-coordinate sensors, we can apply the well-known scheme [1], when each sensor is installed along the edge of an imaginary cube placed on a vertex so that its main diagonal drawn from this vertex is directed along the vector of the local gravitational vertical. Each sensor is installed at an angle of ≈ 0.955 rad or 54.736 deg. arcs to the vertical.

A special feature of this development is a significant expansion of the device's capabilities, which allows measurements to be carried out not only in the classical seismic spectral region, but also in the long-period, quasi-static frequency region. This allows us to study the processes that manifest themselves in variations of the slopes of the base of the device caused by deformation phenomena, in variations of the acceleration of gravity *g*, the cause of which is primarily tidal processes.

The main difficulty in creating this device is the development of a uniaxial sensor based on a mechanical oscillator, with which it would be possible to measure small vibrations of the base. The presence of three sensors allows you to measure the vibrations of the base in three mutually perpendicular directions in the frequency range of 0.1–10 Hz with a sensitivity of 10^{-9} m in the range of 10^{-3} m. Measure slow slopes of the base in the range of periods from 10 c to 10^{7} c with a sensitivity of 10^{-8} rad in the range of 10^{-3} rad, measure *g* variations with a sensitivity of 10^{-8} m/s^2 in the range of 10^{-2} m/s^2.

Such a uniaxial sensor was developed and manufactured. It is distinguished by the fact that the uniaxiality is ensured by means of stretch marks reinforced near the ends of the test mass of a cylindrical shape. (Fig. 1). Stretch marks (2) made of a thin beryllium bronze foil provide high rigidity in the transverse direction and low-along the axis of the cylinder.

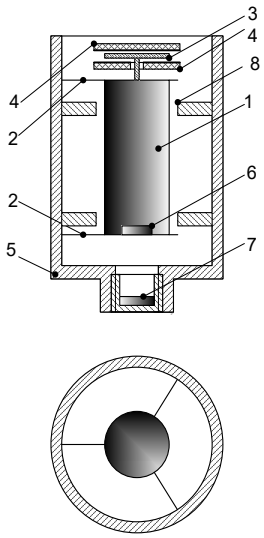


Fig. 1

When measuring on the surface of planets, including on Earth, the test mass is affected by the projection of the acceleration of free fall. The stiffness of the stretch marks is not enough to hold the test mass and it is necessary to introduce additional stiffness.

This problem was solved with the help of cylindrical permanent magnets installed in the sensor housing and on the test mass with the same poles facing each other. The fluctuations of the test mass (1) are measured using a capacitive converter. The rotary plate 3 of the measuring differential tank is connected to the test mass, 4 — the stator plates of the measuring tanks. The magnet 6 is mounted on the test mass, the magnet 7 is in the sensor housing, and the magnet 7 can be moved vertically using a cylindrical cup with an external thread, thereby changing the distance between the magnets. By moving the magnet 7, it is possible to achieve a position where the repulsive force of the magnets will be equal to the weight of the test mass.

As a consequence of the dipole — dipole nature of the interaction [2], the interaction force between magnets is inversely proportional to the fourth power of the distance between them *z*.

$$F=\frac{3\mu_0 J_1 V_1 \cdot J_2 V_2}{2\pi \cdot Z^4}=\frac{B}{z^4} \quad (1)$$

Here μ_0 is the absolute magnetic permeability, *J* is the magnetization of the magnets, *V* is their volume, *z* is the distance between the magnets. By moving the magnet 7, we achieve that $F = mg$ at some z_0. Assuming that the stiffness created by the stretch marks is *k*, the equation of vibrations of the test mass can be written as:

$$m\ddot{x}+h\dot{x}+kx=\frac{B}{(z_0+x)^4}-mg+\sum f \quad (2)$$

x is the coordinate of the test mass relative to z_0. Since $x/z_0 << 1$, equation (2) can be decomposed into a series by a small parameter x/z_0. Using the condition $\frac{B}{z_0^4}=mg$, up to the terms of the first order of smallness, equation (2) is transformed to the form:

$$m\ddot{x}+h\dot{x}+\left(k+\frac{4mg}{z_0}\right)x=\sum f \ .$$

The value $4\frac{mg}{z_0}=k_{mag}$ is the "magnetic" stiffness. The corresponding frequency of natural oscillations of the test mass will be:

$$\omega_0=2\sqrt{\frac{g}{z_0}} \quad (3)$$

For Mars, given that the cosine of the angle between the sensor's sensitivity axis and the vector of the local gravitational vertical is 1/√3, at z_0 = 2 cm, ω_0=20.7 rad/s, which corresponds to approximately $f_0 \approx 3.3$ Hz.

By moving the magnet (7) , you can configure the device to work on the planet with its own acceleration of free fall.

The capacitive converter, built using the AD7746 chip, allows you to measure the differential measuring capacitance with an error of several $aF = 10^{-6}\ pF$. In addition, this chip provides information about the temperature and the value of the supply voltage.

The limit value of small accelerations measured using this sensor is determined by the level of thermal equilibrium fluctuations. .The corresponding value of the minimum measured acceleration determined by thermal noise, [3]:

$$a_{min}\approx\omega_0\sqrt{\frac{\Theta}{m}} \quad (4)$$

for these parameters will be ~ 10^{-8} m/s^2. (Θ is the product of the Boltzmann constant κ and the absolute temperature *T*) These simple estimates show that a high-sensitivity seismic accelerometer with relatively small dimensions and total mass can be implemented on the basis of the described design of the mechanical system.

For testing, the device was installed on a 30 mm thick duralumin tilt plate. The pitch of the plate inclination was $3.6 \cdot 10^{-3}$ rad. The step for changing the acceleration value along the sensitivity axis of the sensor when the plate is tilted was $2.88 \cdot 10^{-2}$ m/s^2. The performed calibration by the slope method showed that the average conversion coefficient was 4.3 pF/m/s^2. A change in the measuring capacity of 1 a_F corresponds to a change in the acceleration of ~ $2.3 \cdot 10^{-7}$ m/s^2. At a frequency of about 1 Hz, this corresponds to vibrations of the base with an amplitude of ~ $5 \cdot 10^{-9}$ m. The level of man-made noise in a ground laboratory is several orders of magnitude higher.

REFERENCES:

[1] Shnirman G.L. Astasis of pendulums. Moscow: Nauka, 1982. P. 168.
[2] Landau L.D. Electrodynamics of continuous media // L.D. Landau, E.M. Lifshits. Nauka. 1992. P. 621.
[3] Gusev G.A. Limiting sensitivity of gravitational-inertial devices when measuring quasi-static processes // G.A. Gusev, A.B. Manukin. Physics of the Earth. No. 9. 1985. P. 90–95.

ACTIVITY OF THE GRAVITY WAVES IN THE MARTIAN ATMOSPHERE FROM THE ACS/TGO SOLAR OCCULTATIONS EXPERIMENT

E.D. Starichenko[1,2], D.A. Belyaev [1,2], A.S Medvedev[3], A.A. Fedorova[1], O.I. Korablev[1], F. Montmessin[4], A. Trokhimovskiy[1]

[1] *Space Research Institute of the Russian Academy of Sciences, Moscow, Russia;*
[2] *Moscow Institute of Physics and Technology, Dolgoprudniy, Russia;*
[3] *Max Planck Institute for Solar System Research, Göttingen, Germany;*
[4] *LATMOS/IPSL, UVSQ Université Paris-Saclay, UPMC Univ. Paris 06, CNRS, Guyancourt, France;*

KEYWORDS:
Gravity waves, Martian atmosphere, Trace Gas Orbiter, Atmospheric Chemistry Suite, solar occultation.

INTRODUCTION:
Gravity waves (GWs) are omnipresent in planetary atmospheres and originate from air parcels vertical displacement. Due to their transfer of energy and momentum throughout the whole atmosphere, GWs have a great influence on an atmosphere's dynamics. In this work, we study the GWs parameters [1] in the Martian troposphere, mesosphere and thermosphere. We process the data of the vertical profiles of temperature and density [2] obtained from the solar occultation experiment conducted by the Russian set of spectrometers Atmospheric Chemistry Suite (ACS) [3] on board the Trace Gas Orbiter (TGO).

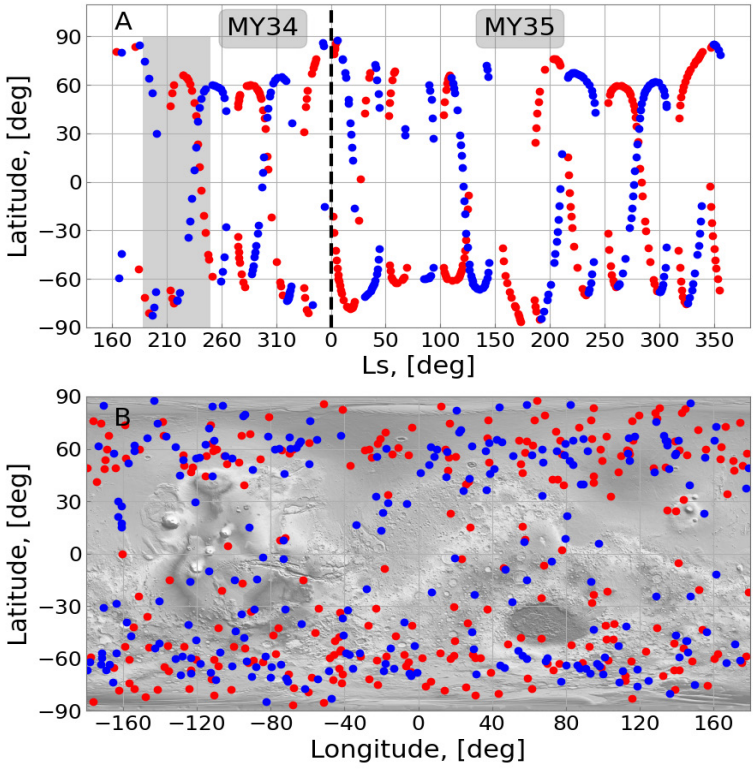


Fig. 1. A) Latitude-solar longitude (*Ls*) **B**) latitude-longitude distributions of the ACS-MIR occultation profiles used in this study. Morning and evening measurements are shown in red and blue, correspondingly. By gray rectangle in Fig. 1A the period of global dust storm is represented.

OBSERVATIONS:
ACS is the part of the TGO, which represents the ESA-Roscosmos ExoMars 2016 collaborative mission. It consists of the three infrared channels: near – NIR (0.73–1.6 μm) [4], middle – MIR (2.3–4.2 μm), and thermal – TIR-VIM (1.7–17 μm). In this work we use the data obtained from the MIR instrument: cross-dispersion spectrometer with the high resolving power ~ 25000, signal to noise ratio more than 1000 and vertical resolution ~ 0.5–2.5 km. Those characteristics allow us to retrieve the temperature and density vertical profiles with small altitude sampling from 10 to 180 km from the 2.7 μm strong band of the CO_2 spectra.

RESULTS:
In this work we present the climatology of GWs and its parameters since the start of the ACS-MIR operations (April, 2018, Ls – 16° MY34) till the end of the MY35 (January, 2021) (see Fig. 1). The amount of processed vertical temperature/density profiles in this study is approximately 500.

We determine and analyze such characteristics of GWs as the wave drag (acceleration), vertical flux of horizontal momentum, potential energy, and Brunt-Väisälä frequency, which characterizes the stability of GWs propagation.

ACKNOWLEDGEMENTS:
The data analysis in IKI is supported by the RSF grant #20-42-09035.

REFERENCES:
[1] Starichenko E. et al., 2021. Gravity wave activity in the Martian atmosphere at altitudes 20–160 km from ACS/TGO occultation measurements. Journal of Geophysical Research: Planets, 126, e2021JE006899. DOI: 10.1029/2021JE006899
[2] Belyaev D. et al., 2021. Revealing a high water abundance in the upper mesosphere of Mars with ACS onboard TGO. Geophysical Research Letters, 48, e2021GL093411. DOI: 10.1029/2021GL093411
[3] Korablev O., Montmessin F., and ACS Team, 2018. The Atmospheric Chemistry Suite (ACS) of three spectrometers for the ExoMars 2016 Trace Gas Orbiter. Space Sci. Rev., 214:7. DOI 10.1007/s11214-017-0437-6.
[4] Fedorova A. et al., 2020. Stormy water on Mars: The distribution and saturation of atmospheric water during the dusty season. Science, eaay9522. DOI: 10.1126/science.aay9522.

HEATING RATE DUE TO THE NIR CO_2 AND CO BANDS EMISSIONS IN THE DAYTIME MARTIAN ATMOSPHERE

V.P. Ogibalov[1,2,3]

[1] *Admiral Makarov state university of maritime and inland shipping, Dvinskaya str., 5/7, Saint-Petersburg, 198035, Russia, vpo563@mail.ru;*

[2] *Saint-Petersburg state marine technical university, Lotsmanskaya str., 3, Saint-Petersburg, 190121, Russia;*

[3] *Saint-Petersburg state forest technical university, Institutskiy per., 5 letter B, Saint-Petersburg, 198264, Russia*

KEYWORDS:

Please suggest 5–10 keywords that describe the content of the abstract. If possible, each keyword should appear in the accompanying abstract.

INTRODUCTION:

The problem of radiative transfer in the IR ro- vibrational bands of the CO_2 molecules is the fundamental one for the atmosphere of Mars, since the heating due to the emissions in these bands has a dominant value in establishing the energy balance, structure, and dynamic properties throughout the entire atmosphere of this planet. Also, the emissions in some bands of the CO_2 and CO molecules are used for remote sensing of the Martian atmosphere. So, a development of more sophisticated models for estimating the values of the Martian atmosphere emissions in the IR bands of the CO_2 and CO molecules is required.

The Martian atmosphere consisting for 95% of the CO_2 molecules has a rather low density. Therefore, both a rarity of molecular collisions, on one hand, and the high rate of excitation of the vibrational states of the CO_2 and CO molecules due to an absorption of the solar radiation in the near- IR spectral range, on another hand, result in a breakdown of the Boltzmann distribution of the excited vibrational state populations of these molecules within wide altitude intervals of the Martian atmosphere, i.e. the vibrational non-local thermodynamic equilibrium (vibrational NLTE) takes place. In the paper [1], the model used for solving the NLTE problem of radiative transfer in the CO_2 bands in the Martian atmosphere has included the 321 excited vibrational states belonging to 7 isotopologues of CO_2 molecules and 779 radiative vibrational transitions (about 100 000 lines). The most upper state is 2003 of the principal isotopologue with energy of about 9500 cm^{-1}.

In this work [2–3], the problem of radiative transfer in the ro-vibrational bands of the CO_2 molecules (near 4.3, 2.7, 2.0, 1.6, 1.4, 1.25, 1.2 and 1.05 μm) and of the CO molecules (near 4.7, 2.3, 1.6 and 1.2 μm) under conditions of the vibrational NLTE in the Martian atmosphere has been solved for the first time taking account for both scattering and absorption of radiation by the Martian aerosols. The 545 ro-vibrational bands rising between the 206 vibational states of 7 isotopologues of the CO_2 molecules and the 10 ro-vibrational bands rising between the 8 vibrational states of 2 isotopologues of the CO molecules are included into the NLTE model. Using the accelerated lambda-iteration approach [4], an original method for solving the problem of radiative transfer in molecular bands under vibrational NLTE in a planetary atmosphere taking account for an accurate treating of the frequency overlapping of all the ro-vibrational lines within the 1.05–15 μm spectral range, which were included into the model, and a reflection of radiation by a planetary surface has been developed. Also this method allows to take into account the processes of scattering (with a phase function of general type) and absorption of radiation by aerosols at the frequencies belonging to the spectral ranges of the CO_2 and CO ro-vibrational bands.

The radiative transfer in all the bands of the CO_2 and CO molecules within the 15–1.02 μm spectral interval with taking into account the overlapping over frequency of lines within a given ro- vibrational band as well as lines belonging to different bands was considered. A visible influence on values

of the non-equilibrium populations of the excited CO_2 vibrational states due to an adoption of the approximation of spectral line isolation in frequency was found within wide layers of the Martian atmosphere.

The contribution into the heating rate from some vibrational transitions were estimated for daytime conditions on Mars. In particular, a visible contribution of vibrational transitions belonging to the spectral region of the 4.3μm CO_2 band, which rise from high excited CO_2 vibrational states, was found for the altitude range of 80–120 km.

Both for a number of profiles representing various conditions in the atmosphere of Mars and for different solar zenith angles, the non-equilibrium populations of the excited vibrational states of the CO_2 and CO molecules were obtained with high accuracy followed by calculating the radiative flux divergence (RFD) in all the IR ro- vibrational bands included into the model. For the first time, the contribution into the RFD values due to a number of radiative vibrational transitions of the CO_2 and CO molecules were estimated for daytime conditions on Mars. Taking into account a reflection of the IR radiation by the planetary surface can result in an increase of the RFD values in all the bands of the CO_2 molecules up to 1.5 K/day within the 0–20 km altitude layer of the Martian atmosphere.

REFERENCES:

[1] Ogibalov, V.P., and Shved, G.M. // Solar System Res., 2003, V. 37, No. 1, P. 23–33,.
[2] Ogibalov V.P., Shved G.M. An improved model of radiative transfer for the NLTE problem in the NIR bands of CO_2 and CO molecules in the daytime atmosphere of Mars. 1. Input data and calculation method // Solar Syst. Res. 2016. V. 50. No. 5. P. 316–328. doi:10.7868/S0320930X16050042.
[3] Ogibalov V.P., Shved G.M. An improved model of radiative transfer for the NLTE problem in the NIR bands of CO_2 and CO molecules in the daytime atmosphere of Mars. 2. Population of vibrational states // Solar Syst. Res. 2017. V. 51. No. 5. P. 373–385. doi:10.1134/S0038094617050070.
[4] Kutepov A.A., Gusev O.A., Ogibalov V.P. Solution of the non-LTE problem for molecular gas in planetary atmospheres: Superiority of the accelerated lambda iteration // J. Quant. Spectrosc. Radiat. Transfer, 1998. V. 60. No. 2. P. 199-220.

DETERMINING THE CHARACTERISTICS OF INTERNAL GRAVITY WAVES IN TERRESTRIAL ATMOSPHERES USING AN ANALYSIS OF THE VERTICAL TEMPERATURE OR DENSITY PROFILES RECOVERED FROM RADIO OCCULTATION SATELLITE MEASUREMENTS

V.N. Gubenko[1], I.A. Kirillovich[1]
[1] *Kotel'nikov Institute of Radio Engineering and Electronics RAS (Fryazino branch), Vvedensky square 1, Fryazino 141190, Moscow region, Russia, vngubenko@gmail.com; gubenko@fireras.su*

KEYWORDS:
Internal gravity waves; internal wave saturation due to shear instability; terrestrial atmospheres; radio occultation satellite measurements; vertical temperature or density profiles.

INTRODUCTION:

The main task of physics of planetary atmospheres is to study wave processes that determine the atmospheric dynamics at all altitudes. A key role of internal gravity waves (IGWs) is primarily connected with the fact that they provide an effective mechanism for energy and momentum transfer upward from the lower atmosphere. A lot of ionospheric processes are well explained through atmospheric waves. So, the traveling ionospheric disturbances (TIDs) and sporadic E-layers are ionospheric manifestations of internal waves in the Earth's neutral atmosphere [1, 2]. Wave generation sources in the atmosphere may be near-surface thermal contrasts, topography, wind shear instability, convection, frontal processes and others. In the absence of IGW energy dissipation, the amplitudes of wave disturbances of wind speed and temperature increase approximately exponentially with altitude. Near-surface low-amplitude perturbations can therefore produce significant effects at large altitudes, where IGWs break down and the wave energy and momentum are transferred to the undisturbed flow. Since internal waves represent a characteristic feature of stably stratified atmospheres, then similar effects can be observed in the atmospheres of Mars and Venus. Internal gravity waves in the Martian atmosphere are thought to play a more important role than those in Earth's atmosphere because the wave amplitudes in the Martian atmosphere are usually greater than their terrestrial counterparts [3].

Radio occultation (RO) satellite observations in the atmosphere of planet are an effective tool of the IGW activity investigations throughout the planet based on nearly uniform and high-quality experimental data. The radio occultation method allows obtaining the vertical profiles of atmospheric parameters (pressure, density and temperature) at a global scale with high vertical resolution in any weather conditions [4–6]. An advantage of the RO measurements in studying internal atmospheric waves is a wider geographical and temporal coverage of areas of interest, which enables global monitoring of wave activity in a planetary atmosphere [7, 8]. Early, an analysis of the vertical profiles of temperature variations, determined from the RO experiments, has revealed some statistical characteristics (i.e. wave potential energy per unit mass) of internal waves in the Earth's atmosphere [9–11]. However, until recently, researchers believed that the vertical temperature and density profiles, reconstructed from the RO measurements, are not enough to quantify the wave effects in planetary atmospheres.

In this regard, we have developed an original method for identifying the discrete wave events and reconstructing the IGW parameters from an analysis of the individual vertical temperature, density, or Brunt-Vaisala frequency squared profile in a planetary atmosphere [12–15]. The method does not require any additional information not contained in the profile and can be used to analyze vertical profiles obtained by various techniques. We have formulated and

justified a threshold discrimination criterion for identifying wave events, and its fulfillment assumes the analyzed variations to be manifestations of internal waves [12]. This method relies on the analysis of the relative wave amplitude, determined from the vertical profile of temperature or density, as well as on the concept of the linear IGW theory, which suggests that the actual wave amplitude is limited by threshold value due to shear instability in the atmosphere. When the IGW amplitude reaches a shear instability threshold as the wave propagates upward, the energy dissipation occurs so that the wave amplitude stays at the atmospheric instability threshold (saturation of internal wave amplitude). For testing the method, we have used simultaneous balloon measurements of temperature and wind speed in the Earth's stratosphere [16]. By analyzing the wind speed hodograph and temperature measurements, Cot and Barat [16] identified the saturated internal wave and determined its characteristics. Using our original method and temperature data only, we independently reconstructed all characteristics of the identified internal wave with errors not exceeding 30 % [12]. Results of wave activity monitoring in the Earth's atmosphere can be useful in constructing numerical circulation models involving parameterization of wave effects. The developed method of identifying the wave events and reconstructing the IGW characteristics in atmospheres of planets [12–15] has been widely recognized by scientific community. It is now being successfully used for the internal wave investigations in atmospheres of Earth [17–22] and Venus [23, 24]. Rechou et al. [19] have found that numerical simulation data and an analysis of the collocated radar and balloon measurements in the Earth's atmosphere demonstrate good efficiency of developed method and high reliability of results it yields.

The aim of this work is: I) the description of the method for identifying the discrete wave events and determining the IGW parameters based on analysis of the individual vertical temperature profile in a planetary atmosphere; II) demonstration of scientific results of its practical application to the temperature data retrieved from atmospheric measurements of the RO satellite missions CHAMP (Earth) and Mars Global Surveyor (Mars).

DISPERSION AND POLARIZATION EQUATIONS FOR IGWS AND DESCRIPTION OF ANALYSIS TECHNIQUE BASED ON SATURATED WAVE ASSUMPTION (SWA – METHOD):

Dispersion equation relates the intrinsic frequency ω (IGW frequency determined in the reference frame that moves with undisturbed wind) to the spatial wave characteristics (horizontal k_h and vertical m wave numbers) and to the stability parameter N_b (Brunt-Vaisala frequency) of atmospheric stratification. When hydrostatic regime holds for internal waves: $N_b^2 \gg \omega^2 > f$, $m^2 \gg k_h^2$, and $m^2 \gg (2H)^{-2}$, the dispersion equation is given by following expression [12–15, 25]:

$$(c-\bar{u})^2 = \frac{\omega^2}{k_h^2} = \frac{N_b^2}{m^2}\frac{1}{1-\frac{f^2}{\omega^2}}, \quad (1)$$

where $(c-\bar{u})$ is the intrinsic horizontal phase speed, c is the ground-based horizontal phase speed, $\bar{u}$ is the wind speed projection in the direction of horizontal wave propagation and H is the scale height of planetary atmosphere. Coriolis parameter (inertial frequency) f is equal to $f = 2\Omega\sin\varphi$, where Ω is planetary rotation rate and φ is latitude. Wave vector or propagation vector (k_h, m) determines the phase propagation direction of an internal wave. For an internal wave whose energy is transferred upward, the phase is directed downward and vice versa. Intrinsic wave frequency ω is defined as positive value.

In the case when one of the axes of Cartesian coordinate system is selected in the direction of the horizontal component of propagation vector, the polarization equations for hydrostatic internal waves take a very simple form [12–15, 26]:

$$v' = -i\frac{f}{\omega}u', \quad (2) \qquad w' = \frac{-k_h}{m}u, \quad (3) \qquad u' = i\frac{g}{N_b}\frac{\hat{T}'}{\sqrt{1-\frac{f^2}{\omega^2}}}, \quad (4)$$

where u' and v' are complex perturbations of wind speed components in the propagation direction and perpendicular to the horizontal wave vector, respectively; w' is the complex wind speed perturbation in the vertical direction; $\hat{T}' = \frac{T'}{T_b}$ is the normalized complex perturbation of absolute temperature; i is imaginary unit. It follows from equation (2) that the phase difference between u' and v' complex perturbations is 90 °, and the ratio $\frac{|v'|}{|u'|}$ is equal to $\frac{f}{\omega}$. So, a low-frequency IGW at $\omega \sim f$ is elliptically polarized transverse wave, because the horizontal wind speed hodograph describes an ellipse and the motion occurs in a plane perpendicular to the wave vector [27]. At higher intrinsic wave frequencies ω when $\frac{f}{\omega} \ll 1$, the ellipse transforms into a straight line and IGWs become linearly polarized. Note that polarization equation (4) holds for internal waves whose energy is transferred upward ($m < 0$), otherwise ($m > 0$) it needs to change sign from plus to minus in this equation [28].

For calculating values of the Brunt-Vaisala frequency N_b, we use measurements of vertical temperature profile $T_b(z)$ and the following expression [12–15]:

$$N_b^2 = \frac{g}{T_b}\left(\frac{\partial T_b}{\partial z} + \frac{g}{c_p}\right) \quad (5)$$

where g is acceleration of gravity, $\frac{g}{c_p}$ is adiabatic temperature gradient in the atmosphere, T_b is mean (undisturbed) temperature, z is vertical coordinate.

Gubenko et al. [12] proposed a novel technique (SWA-method) to identify fluctuations as wave-induced in the analyzed vertical temperature or density profile assuming the IGW amplitude saturation due to shear instability in a planetary atmosphere. They introduced a parameter a_e (relative actual amplitude of a wave) that can be determined from a vertical temperature profile according to [12]:

$$a_e = \frac{|u'|}{|c-\bar{u}|} = \frac{g|m|}{N_b^2}|\hat{T}'| = \frac{2\pi g}{\lambda_z N_b^2}|\hat{T}'| \quad (6)$$

where $\lambda_z = \frac{2\pi}{|m|}$ is the vertical wavelength. In the case when analyzed temperature or density fluctuations are due to a saturated monochromatic wave, the value a_e should be equal to the relative threshold amplitude a of shear instability in the atmosphere [12, 29]:

$$a = \frac{|u'_{sat}|}{|c-\bar{u}|} = \frac{2\sqrt{1-\frac{f^2}{\omega^2}}}{1+\sqrt{1-\frac{f^2}{\omega^2}}} \quad (7)$$

where $|u'_{sat}|$ is a saturated wave amplitude of horizontal wind speed disturbances parallel to the horizontal wave vector. It is obviously that the value a must be smaller than unity. The actual wave amplitude a_e is controlled by processes of shear instability in a planetary atmosphere. Indeed, when wave amplitude ae exceeds a threshold value a, then this leads to shear instability and generation of turbulence that prevents further growth of the wave amplitude (IGW amplitude saturation).

A discrimination criterion for IGWs states that the experimentally determined actual wave amplitude a_e should correspond to the threshold amplitude a of shear instability in the atmosphere. Thus, we find that analyzed temperature or density fluctuations can be considered as wave manifestations, when the value ae satisfies the following inequality [12]:

$$1>a=a_e^0>0 \quad (8)$$

This inequality represents a necessary condition for identification of internal waves. Otherwise, analyzed variations can be associated with the influence of regular thin layers or turbulence in an atmosphere. Gubenko et al. [12] have shown for the first time that such important IGW parameters as the intrinsic frequency (ω) and period (T^{in}), amplitudes of vertical ($|w'|$) and horizontal ($|u'|$ and $|v'|$) perturbations of wind speed, vertical (λ_z) and horizontal (λ_h) wavelengths, intrinsic vertical (c_{pz}^{in}) and horizontal (c_{ph}^{in}) phase speeds can be derived from observed RO temperature profiles in the case of positive IGW identification.

A modified version of the developed SWA – method allows us to reconstruct a complete set of wave characteristics, including such important parameters as densities of kinetic (E_k) and potential (E_p) energy, vertical fluxes of wave energy and momentum [13]. An analysis of height variations of the Brunt-Vaisala frequency squared allows us to calculate the relative wave amplitude, to identify IGWs and reconstruct their characteristics in a planetary atmosphere, and to determine the localization of thin layers of intermittent turbulence occurring when propagating saturated IGWs in the atmospheres [13, 15]. It was shown that in the case of harmonic wave disturbances, the amplitude $A_{N^2}^{rel}$ of relative fluctuations of the Brunt-Vaisala frequency squared $(N^2-N_b^2)/N_b^2$ coincides with the value a_e and has form [13]:

$$A_{N^2}^{rel}=a_e=\frac{g|m|}{N_b^2}\cdot\frac{|T'|}{T_b}=1-\frac{N_{min}^2}{N_b^2} \quad (9)$$

where $N_{min}^2=minN^2$ is the magnitude of the local minimum in the vertical profile $N^2(z)$. Thus, the value of actual wave amplitude can be obtained from an analysis of the data on T or N^2, and these two estimates of actual wave amplitude a_e and $A_{N^2}^{rel}$ should be consistent with each other. Note that local shear instability and atmospheric turbulence caused by it are intensified due to the vertical shear of the transverse component of wind speed induced by the IGWs, which reaches a maximum at levels where there are local minima of the Brunt-Vaisala frequency squared [29–31].

CONCLUSION:

An original SWA-method for the identification of discrete wave events and determination of IGW parameters from an analysis of the vertical temperature profile in a planetary atmosphere has been developed. A discrimination criterion for the identification of wave events has been formulated and argued. In the case when this criterion is satisfied, the analyzed temperature variations can be considered as wave-induced. The developed technique is based on the analysis of actual wave amplitudes and IGW saturation theory in which these amplitudes are restricted by shear instability in a planetary atmosphere. Application of the developed SWA-method to the RO temperature profiles of satellite missions CHAMP (Earth) and Mars Global Surveyor (Mars) has given a possibility to identify discrete wave events in the Earth's and Martian atmospheres and to determine key wave parameters such as the intrinsic frequency and period, amplitudes of the vertical and horizontal wind speed perturbations, vertical and horizontal wavelengths, intrinsic vertical and horizontal phase speeds, kinetic and potential energy of IGWs per unit mass.

ACKNOWLEDGEMENTS:

This study was made in the framework of state task and it was supported by the Russian Foundation for Basic Research (project no. 19-02-00083 A).

REFERENCES:

[1] Gossard E.E, Hooke W.H. Waves in the atmosphere. Elsevier Scientific Publishing Co., Amsterdam-Oxford-New York, 1975.

[2] Gubenko V.N., Pavelyev A.G., Kirillovich I.A., Liou Y.-A. Case study of inclined sporadic E layers in the Earth's ionosphere observed by CHAMP/GPS radio occultations: Coupling between the tilted plasma layers and internal waves // Adv. Space Res. 2018. V. 61. No. 7. P. 1702–1716, doi: 10.1016/j.asr.2017.10.001.
[3] Creasey J.E., Forbes J.M., Hinson D.P. Global and seasonal distribution of gravity wave activity in Mars' lower atmosphere derived from MGS radio occultation data // Geophys. Res. Lett. 2006. V. 33. L01803, doi: 10.1029/2005GL024037.
[4] Gorbunov M.E., Gurvich A.S. Microlab-1 experiment: Multipath effects in the lower troposphere // J. Geophys. Res. 1998. V. 103. D12. P. 13819–13826.
[5] Liou Y.A., Pavelyev A.G., Huang C.Y., Igarashi K., Hocke K., Yan S.K. Analytic method for observation of the gravity waves using radio occultation data // Geophys. Res. Lett. 2003. V. 30. No. 20. CiteID 2021, doi: 10.1029/2003GL017818.
[6] Liou Y.A., Pavelyev A.G., Wickert J., Huang C.Y., Yan S.K., Liu S.F. Response of GPS occultation signals to atmospheric gravity waves and retrieval of gravity wave parameters // GPS Solutions. 2004. V. 8. No. 2. P. 103–111.
[7] Gavrilov N.M., Karpova N.V., Jacobi Ch., Gavrilov A.N. Morphology of atmospheric refraction index variations at different altitudes from GPS/MET satellite observations // J. Atmos. Sol.-Terr. Phys. 2004. V. 66. No. 6–9. P. 427–435.
[8] Gavrilov N.M., Manuilova R.O. Long-term global distributions of mesoscale variations in atmospheric radio refraction obtained from the GPS Champ Satellite Data // Radiophysics and Quantum Electronics. 2016. V. 59. No. 7. P. 535–545, doi: 10.1007/s11141-016-9721-7.
[9] Steiner A.K., Kirchengast G. GW spectra from GPS/MET occultation observations // J. Atmos. Ocean. Tech. 2000. V. 17. P. 495–503.
[10] Tsuda T., Nishida M., Rocken C., Ware R.H. A global morphology of GW activity in the stratosphere revealed by the GPS occultation data (GPS/MET) // J. Geophys. Res. 2000. V. 105. D6. P. 7257–7273.
[11] Tsuda T., Hocke K. Vertical wave number spectrum of temperature fluctuations in the stratosphere using GPS occultation data // J. Meteorol. Soc. Jpn. 2002. V. 80. No. 4B. P. 1–13.
[12] Gubenko V.N., Pavelyev A.G., Andreev V.E. Determination of the intrinsic frequency and other wave parameters from a single vertical temperature or density profile measurement // J. Geophys. Res. 2008. V. 113. D08109, doi: 10.1029/2007JD008920.
[13] Gubenko V.N., Pavelyev A.G., Salimzyanov R.R., Pavelyev A.A. Reconstruction of internal gravity wave parameters from radio occultation retrievals of vertical temperature profiles in the Earth's atmosphere // Atmos. Meas. Tech. 2011. V. 4. No. 10. P. 2153–2162. doi: 10.5194/amt-4-2153-2011.
[14] Gubenko V.N., Pavelyev A.G., Salimzyanov R.R., Andreev V.E. A method for determination of internal gravity wave parameters from a vertical temperature or density profile measurement in the Earth's atmosphere // Cosmic Res. 2012. V. 50. No. 1, P. 21–31, doi: 10.1134/S0010952512010029.
[15] Gubenko V.N., Kirillovich I.A., Pavelyev A.G. Characteristics of internal waves in the Martian atmosphere obtained on the basis of an analysis of vertical temperature profiles of the Mars Global Surveyor mission // Cosmic Res. 2015. V. 53. No. 2. P. 133–142, doi: 10.1134/S0010952515020021.
[16] Cot C., Barat J. Wave-turbulence interaction in the stratosphere: A case study // J. Geophys. Res. 1986. V. 91. D2. P. 2749–2756.
[17] Horinouchi T., Tsuda T. Spatial structures and statistics of atmospheric gravity waves derived using a heuristic vertical cross section extraction from COSMIC GPS radio occultation data // J. Geophys. Res. 2009. V. 114. D16110, doi: 10.1029/2008JD011068.
[18] Xiao C.Y., Hu X. Analysis on the global morphology of stratospheric gravity wave activity deduced from the COSMIC GPS occultation profiles // GPS Solutions. 2010. V. 14. P. 65–74, doi: 10.1007/s10291-009-0146-z.
[19] Rechou A., Kirkwood S., Arnault J., Dalin P. Short vertical-wavelength inertia gravity waves generated by a jet-front system at Arctic latitudes — VHF radar, radiosondes, and numerical modeling // Atmos. Chem. Phys. 2014. V. 14. P. 6785–6799, doi: 10.5194/acp-14-6785-2014.
[20] Sacha P., Foelsche U., Pisoft P. Analysis of internal gravity waves with GPS RO density profiles // Atmos. Meas. Tech. 2014. V. 7. P. 4123–4132, doi: 10.5194/amt-7-4123-2014.
[21] Noersomadi N., Tsuda T. Comparison of three retrievals of COSMIC GPS radio occultation results in the tropical upper troposphere and lower stratosphere // Earth, Planets and Space. 2017. V. 69. P. 125, doi: 10.1186/s40623-017-0710-7.
[22] Zagar N., Jelic D., Blaauw M., Bechtold P. Energy spectra and inertia–gravity waves in global analyses // J. Atmos. Sci. 2017. V. 74. No. 8. P. 2447–2466, doi: 10.1175/JAS-D-16-0341.1.

[23] Altieri F., Migliorini A., Zasova L., Shakun A., Piccioni G., Bellucci G. Modeling VIRTIS/VEX $O_2(a_1\Delta g)$ nightglow profiles affected by the propagation of gravity waves in the Venus upper mesosphere // J. Geophys. Res. 2014. V. 119. P. 2300–2316, doi: 10.1002/2013JE004585.
[24] Peralta J., Sanchez-Lavega A., Lopez-Valverde M.A., Luz D., Machado P. Venus's major cloud feature as an equatorially trapped wave distorted by the wind // Geophys. Res. Lett. 2015. V. 42, doi: 10.1002/2014GL062280.
[25] Fritts D.C., Alexander M.J. Gravity wave dynamics and effects in the middle atmosphere // Rev. Geophys. 2003. V. 41. No. 1. P. 1–59. doi: 10.1029/2001RG000106.
[26] Zink F., Vincent R.A. Wavelet analysis of stratospheric gravity wave packets over Macquarie Island. 1. Wave parameters // J. Geophys. Res. 2001. V. 106. D10. P. 10275–10288.
[27] Gill A.E. Atmosphere-Ocean Dynamics. New York, London, Paris: Academic Press, 1982.
[28] Pfister L., Chan K.R., Bui T.P., Bowen S., Legg M., Gary B., Kelly K., Proffitt M., Starr W. Gravity waves generated by a tropical cyclone during the STEP tropical field program: A case study // J. Geophys. Res. 1993. V. 98. D5. P. 8611–8638.
[29] Fritts D.C. A review of gravity wave saturation processes, effects, and variability in the middle atmosphere // Pure Appl. Geophys. 1989. V. 130. P. 343–371.
[30] Fritts D.C., Rastogi P.K., Convective and dynamical instabilities due to gravity motions in the lower and middle atmosphere: Theory and observations // Radio Sci. 1985. V. 20. No. 6. P. 1247–1277.
[31] Dunkerton T.J., Inertia-gravity waves in the stratosphere // J. Atmos. Sci. 1984. V. 41. P. 3396–3404.

NON-HYDROSTATIC STRESSES AND THE LOCATION OF MARSQUAKES' SOURCES

T.V. Gudkova[1], AV. Batov[1,2]
[1] *Schmidt Institute Physics of the Earth RAS, B.Gruzinskaya, 10, Moscow, Russia, gudkova@ifz.ru;*
[1, 2] *V.A. Trapeznikov Institute of Control Sciences of RAS, 65, Profsoyuznaya street, Moscow, Russia*

KEYWORDS:
extension-compression stresses, shear stresses, gravity and topography data, marsquakes, Mars

INTRODUCTION:
The seismic experiment of the InSight mission (Interior Exploration using Seismic Investigations Geodesy and Heat Transport) [1] is going on Mars. Mars is seismically active, there have been identified subcrustal events of magnitude M_w 3–4, while most of the largest detected marsquakes being located near the Cerberus Fossae fracture system [2], to the East of the InSight länder (Fig. 1). Below we give a possible reason of this phenomenon.

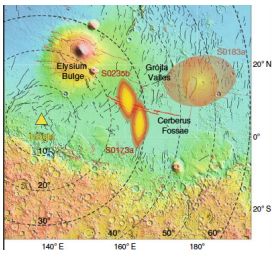


Fig. 1. The estimated locations of events S0173a, S0235b and S0183a relative to the InSight landing site (yellow triangle) (taken from [2])

METHOD:
Mars strongly differs from the equilibrium state [3]. We have modeled the non-hydrostatic stresses arising due to the deviation of a planet from the state of hydrostatic equilibrium, and assume that these stresses could lead to the detected marsquakes. An equilibrium ellipsoid is taken as a reference surface. We consider two levels of loads (Fig. 2): the surface relief ($R^1_{t,n,m}$) and $R^2_{t,n,m}$ — some mass anomalies distributed on the crust-mantle boundary. The amplitudes of the loads $R^1_{t,n,m}$ and $R^2_{t,n,m}$ are selected in such a way as to provide the observed values of the gravity field C_{gnm} [4] and topography C_{tnm} [5] (the coefficients of the Legendre polynomial expansion for the gravity field and topography, here we take them relative the equilibrium surface). A map of the gravity anomalies relative to the equilibrium figure at the surface is shown in Fig. 3.

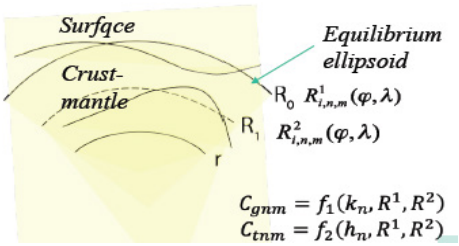


Fig. 2. The two-level loading model.

The static method that uses Green's functions technique (or the load coefficients method) was developed in [6–8]. The detailed description of the method is given in [9].

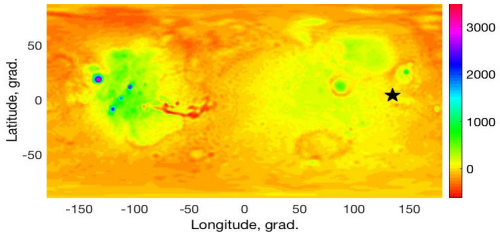


Fig. 3. Gravity anomalies relative to the equilibrium figure in mGal.

RESULTS:

Calculations of tension-compression and maximum shear stresses are carried out for a test model of Martian internal structure, with a step of 1° × 1° over latitude and longitude down to the depth of 1000 km. We take the distribution of density, gravity acceleration, compression modulus K and shear modulus μ for Mars' interior structure model from [9].

Our numerical experiments show the following pattern of stresses (Fig. 4): shear stresses (on the left) and extensional-compression stresses (on the right). An example is given for the 50 km depth. We assume that the extensional stresses more likely lead to the quakes sources. One can see compression stresses (blue color, on right panels) beneath the Tharsis and the area to the West of the Elysium. The area of extensional stresses (red color) is to the East of the lander. The extentional areas in the West direction are located much further.

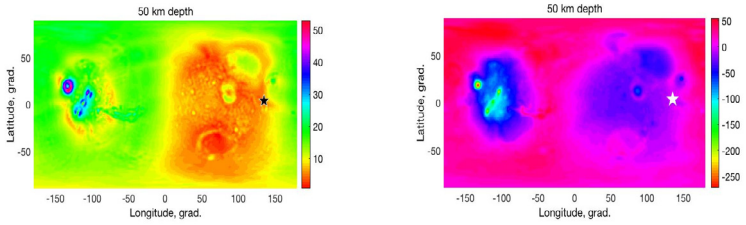


Fig. 4. Shear (left) and extensional-s compression non-hydrostatic stresse (right) in MPa at the depth of 50 km.

ACKNOWLEDGEMENTS:

This work is financially supported by Budget funding of Schmidt Institute of Physics of the Earth RAS.

REFERENCES:

[1] Banerdt B. et al. Initial results from the InSight mission on Mars // Nat. Geosci. 2020. https://doi.org/10.1038/s41561-020-0544-y.
[2] Giardini D. et al. The seismicity of Mars // Nat. Geosci. 2020. https://doi.org/10.1038/s41561-020-0539-8.
[3] Zharkov V.N., Gudkova T.V. On model structure of gravity field of Mars // Sol. Syst. Res. 2016. V. 50. P. 250–267.
[4] Smith D.E., Zuber M.T., Frey H.V. et al. Mars Orbiter Laser Altimeter: Experimental summary after the first year of global mapping of Mars // J. Geophys. Res.. 2001. V. 106. No. E10. P. 23689–23722.
[5] Konopliv A.S., Park R.S., Folkner W.M. An improved JPL Mars gravity field and orientation from Mars orbiter and lander tracking data // Icarus. 2016. V. 274. P. 253–260.
[6] Marchenkov K.I., Lyubimov V.M., Zharkov V.N. Calculation of load factors for deeply buried density anomalies // Doklady Earth Science Sections. 1984. V. 279. P. 14–16.
[7] Zharkov V.N., Marchenkov K.I., Lyubimov V.M. On long-waves shear stresses in the lithosphere and the mantle of Venus // Sol. Syst. Res. 1986. V. 20. P. 202–211.
[8] Marchenkov K.I., Zharkov V.N. Stresses in the Venus crust and the topography of the mantle boundary // Sol. Astron. Lett. 1989. V. 16. No. 1. P. 77–81.
[9] Gudkova T.V., Batov A.V., Zharkov V.N. Model estimatesof non-hydrostatic tresses in the Martian crust and mantle: 1. Two-level model // Solar System Research, 2017. V. 51. No. 6. P. 490–511.

TOWARDS MARTIAN MOONS EXPLORATION: MICRO-RAMAN AND VIS-MIR REFLECTION SPECTROSCOPY OF THE PHOBOS SURFACE SIMULANTS

S.G. Pavlov[1], U. Böttger[1], I. Weber[2], A. Stojic[2], T. Säuberlich[1], A. Pohl[3], S. Rodd-Routley[1], Y. Cho[4], F. Rull[5], H.-W. Hübers[1,3], T. Belenguer[6], A. Börner[1], M. Buder[1], Y. Bunduki[1], E. Dietz[1], T. Hagelschuer[1], S. Kameda[7], E. Kopp[1], A.G. Moral Inza[6], S. Mori[4], C. Perez Canora[6], M. Pertenais[1], G. Peter[1], O. Prieto-Ballesteros[8], S. Rockstein[1], P.Rodriguez Perez[6], C. Ryan[1], P. Santamaria[6], F. Schrandt[1], S. Schröder[1], S. Ulamec[9], T. Usui[10], K. Westerdorff[1]

[1] *Institute of Optical Sensor Systems, German Aerospace Center (DLR), Rutherfordstr. 2, 12489 Berlin, Gemany;*

[2] *Institut für Planetologie, Westfälische Wilhelms-Universität Münster, Wilhelm-Klemm-Str. 10, 48149 Münster, Germany;*

[3] *Institut für Physik, Humboldt Universität zu Berlin, Newtonstr. 15, 12489 Berlin, Germany;*

[4] *Department of Earth and Planetary Science, The University of Tokyo, 7-3-1 Hongo, Bunkyo, Tokyo 113-0033, Japan;*

[5] *Universidad de Valladolid — GIR ERICA, Av. Francisco valles, 8, Parque Tecnólogico de Boecillo, Parcela 203, E-47151 Boecillo, Valladolid, Spain;*

[6] *Instituto Nacional de Técnica Aerospacial (INTA), Ctra. Ajalvir, Km 4, 28850 Torrejón de Ardoz, Spain;*

[7] *Department of Physics, College of Science, Rikkyo University, 3-34-1 Nishiikebukuro, Toshima, Tokyo 171-8501, Japan;*

[8] *Centro de Astrobiología (CAB-INTA-CSIC), Ctra. Ajalvir, Km 4, 28850 Torrejón de Ardoz, Spain;*

[9] *Deutsches Zentrum für Luft- und Raumfahrt e.V. (DLR), Linder Höhe, 51147 Cologne, Germany;*

[10] *Japan Aerospace Exploration Agency (JAXA), Institute of Space and Astronautical Science, Department of Solar System Sciences, 3-1-1 Yoshinodai, Chuo, Sagamihara, Kanagawa, 252-5210, Japan*

KEYWORDS:
Phobos, MMX mission, Raman spectrometer, Surface Simulant.

INTRODUCTION:

The Japan Aerospace Exploration Agency (JAXA)' Martian Moons eXploration (MMX) remote sensing, robotic and sample return mission [1], scheduled to be launched in 2024 and to return in 2029, will have a strong focus on studying Phobos, including close-up surface analysis and collecting samples for Earth return. A rover, provided by CNES and DLR, will be deployed to Phobos [2]. Its payload includes the Raman spectrometer (RAX) for in-situ characterization of the surface composition [3]. Characterization of payload instrumentation by measurements of planetary simulants is a crucial test for performance and prediction of scientific yield. Controversial conclusions on similarity of infrared reflection and imaging of Phobos to those of low-albedo asteroids imply that combined optical spectroscopy studies will prepare a set of possible clues shortly before the MMX mission. Different Phobos simulants were selected and have been used for Raman and broad range (visible-to-mid-infrared) reflection spectroscopy in order to provide critical parameters on detectivity of mineral phases in the sample matrix as well as to compare the close-up spectroscopy with the known remote sensing of Phobos surface by previous Earth-based observatories and planetary missions.

EXPERIMENTAL DETAILS

The Phobos surface simulants were of two main types, prepared assuming different scenarios governing the moon formation and surface weathering:

1) a "captured asteroid", (CM1, C2 – 1 – TL) Phobos Simulants — mixes of Mg-rich phyllosilicates, olivine (Ol), magnetite, Fe-Ni sulfides and carbon-bear-

ing Fe – Ca – Mg and carbon (C) nm-particles [4], based on a composition similar to the Tagish lake meteorite (CI/CM2 carbonaceous chondrite), that exhibits similar featureless, near-infrared reflectance spectra as that of the Phobos surface (appearing as dark in visible spectral range);

2) a "giant impact" scenario simulants with the compositions similar to those developed in [5]: (PGI – 1*): a mix of pyroxene (Px), olivine, antigorite (Atg), magnetite representing CI-type of material; (PGI – 1**): the PGI – 1* with pyrite. A C-free PGI-1* simulant was aimed to distinguish between the contributions and interplay of organic and inorganic components i both Raman and reflectance spectra.

Raman spectra (100–4000 cm^{-1} in Stokes shift) were taken by the RAX breadboard spectrometer (532 nm excitation wavelength; spatial resolution on a sample of ~ 50 μm) and compared with the spectra of single mineral phases taken by a commercial Raman microscope (WiTEC alpha 300 : 532 nm; spatial resolution of ~ 1.5 μm). A Bruker Fourier Transform Vertex 80 v spectrometer was used for the broad visible to mid-infrared range (0.5–27 μm) bi-directional diffuse reflectance measurements (light spot on a sample ~ 0.5–2 mm, ambient air pressure of ~ 2 mbar). The grain size in the original powders was 25–63 μm, corresponding to the expected uppermost surface layer of the Phobos regolith [4].

RESULTS

Raman spectra of the Phobos simulants CM1 and PGI – 1* are generally accompanied with a strong luminescence (PL) signal, which is stronger for the C – bearing samples. After the PL correction, the main spectral features of Ol, Px, Atg phases are distinguishable in the RAX spectra for PGI-1* (Fig. 1a, b) together with the strongest bands specific for silicate minerals. Possible appearance of a serpentine phase (Chrysotile, Ctl, Fig. 1a, b) could point on natural alteration of Px phase at ambient laboratory conditions.

Visible to near-infrared diffuse reflectance spectra exhibit vanishing to absent features, similar to the analysis of the Phobos 2 ground-based observations [6] and as from the Compact-Reconnaissance-Imaging-Spectrometer-for-Mars (CRISM) onboard of the Mars Reconnaissance Orbiter mission [7]. Note that both, C-bearing and C – free Phobos simulants exhibit very similar, low-intense diffuse reflection in the entire VIS – MIR spectral range, obviously governed by the grain size, slowly decreasing towards mid-infrared and with increase of the incident or reflectance angle. Most of the characteristic bands, enabling determination of individual minerals, fall into the mid-infrared (2–30 μm), with prominent long-wavelength MIR features for sulfides (S); C – O vibration modes of C – bearing compounds and strong structural – OH (hydrated minerals) and Si – O (silicates) vibrational modes. For the PGI-1* simulant, the overall slope is governed by most abundant Px+Ol phases with the spectral features of Atg (Fig. 1c). Reflectance spectra of the CM – 1, C2 – 1 – TL simulants (Fig. 1d) are dominated by phyllosilicate (Atg) + C slope and broad bands with enhanced overlapping vibrational modes of carbon and silicon networks in the long-wavelength part of spectra (7–11 μm) and, apparently, a sulfide band (S) at ~ 24 μm. Iron oxide, having relatively weak Fe – O stretching and bending modes, spectrally overlapping with the stronger silicate' bands, was not resolved in our diffuse reflectance measurements.

Generally, carbon-bearing components (in CM1, C2-1TL samples) conceal most of prominent mineral bands in both Raman scattering and infrared reflectance spectra. The RAX breadboard instrument demonstrated its capability to identify major characteristic bands of silicate minerals. Infrared reflectance spectra show gained capability of mineral differentiation by resolving distinguished characteristic bands in the long-wavelength mid-infrared range (7–26 μm), that could be a crucial step in development of future instrumentation for infrared sensing of surfaces of solar system bodies experiencing strong space weathering. Regardless the spatial resolution (*μm* for Raman and mm for IR spectroscopy) all main mineral phases can be identified by complementary Raman scattering and mid-infrared reflection spectroscopies.

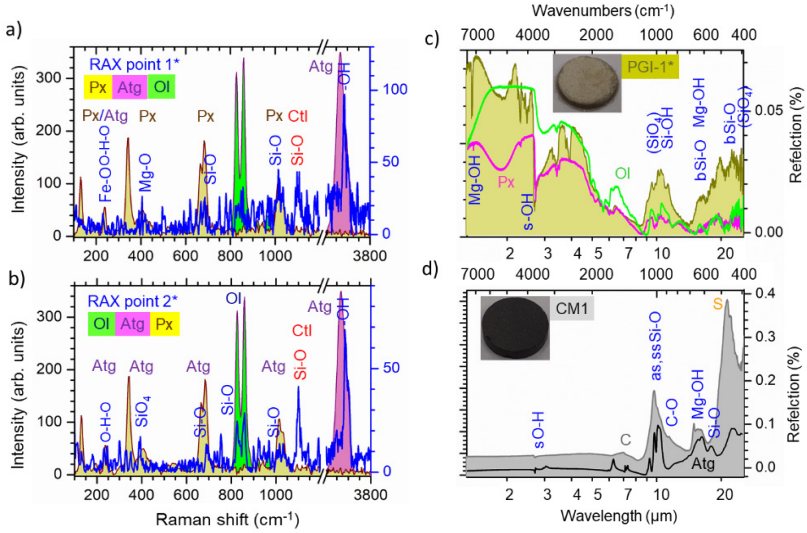


Fig. 1. Raman spectra (**a**, **b**) acquired by the RAX breadboard collected from the Phobos surface simulant PGI-1* at two different locations (blue) and compared with the single mineral phases (shown by filled areas) dominant in the simulant: Ol, Px, Atg, taken from polished rock surfaces by a commercial Raman microscope.
Mid-infrared part of bi-directional (15 ° for both incident and collected reflected light) diffuse reflectance spectra (filled areas) of: **c**) PGI-1* and **d**) CM1 simulants (images in insets), parts of the characteristic single-mineral phase spectra, collected from the powdered Ol, Px, as well as from a bulk Atg, are shown as solid curves (not to scale with the simulant reflectance).

REFERENCES:

[1] Kawakatsu Y., Kuramoto K., Ogawa N., Ikeda H., Ono G. et al. Mission definition of Martian Moons Exploration (MMX) // 70th Int. Astronautical Congress (IAC), 21–25.10. 2019, Washington D.C., USA. P. 495.
[2] Michel, P., Ulamec, S., Böttger U. et al., The MMX rover: performing in-situ surface investigations on Phobos, Earth, Planets and Space, 2021 (in print)
[3] Cho Y., Böttger U., Rull F. et al. In-situ science on Phobos with the Raman spectrometer for MMX (RAX): Preliminary Design and Feasibility of Raman measurements // Earth, Planets, and Space. 2021 (under review).
[4] Miyamoto H., Niihara T., Wada K. et al. Surface Environment of Phobos and Phobos Simulant UTPS // Earth, Planets and Space. 2021 (under review).
[5] Cannon K.M., Britt D.T., Metzger P.T. et al. New high fidelity Martian and Phobos regolith simulant: Enabling tools for exploring the Mars system and ISRU development // 49th LPSC, The Woodlands, Texas, USA, March 19-23, 2018. Abstract No. 2086.
[6] Murchie S., Erard S. Spectral Properties and Heterogeneity of Phobos from Measurements by Phobos 2 // Icarus. 1996. V. 123. Issue 1. P. 63–86.
[7] Fraeman A.A., Murchie S.L., Arvidson R.E. et al. Spectral absorptions on Phobos and Deimos in the visible/near infrared wavelengths and their compositional constraints // Icarus. 2014. V. 229, P. 196–205.

THE PHENOMENON LIGHTNING, POSSIBLE TRANSPORT OF ELECTRONS AND COSMIC RAYS TO EARTH

N.P. Bulatova[1]
[1] *Schmidt Institute of the Earth physics, RAS, Moscow*

KEYWORDS:
Lightning, electric discharges, spherical codensator, electrons and cosmic rays.

The phenomenon of lightning has been studied most fully on the planet Earth, but there are cases of their observation on other planets of the solar system. According to Benjamin Franklin (1706–1790), lightning — an electric discharges that transfer a negative charge the current, amplitude when struck lightning is from 20 to 100 kA. High-speed photography showed that the lightning discharge lasts several tenths of a second and consists of several even shorter discharges. This is the difficulty of studying them [1].

The Earth's atmosphere with non-ionized air molecules does not have the properties of an electric current conductor, but the Earth's lithospheric shell and the upper part of the atmosphere — the ionosphere, containing charged particles , turn the Earth into a kind of spherical codensator, where they serve as plates. In the atmosphere, thunderclouds can act as assistants to the electrical breakdown. (The top of a thundercloud can be at an altitude of 6–7 km, and the bottom can hang over the ground at an altitude of 0.5–1 km.) [1].

However, the cloud itself is not able to electrify in such a way as to cause a discharge between its lower part and the earth. The electric field strength in a thundercloud never exceeds 400 kV/m, and an electric breakdown in the air occurs at a voltage exceeding 2500 kV/m. Therefore, for lightning to occur, something else is needed besides an electric field. If there is an air breakdown, then the negative charge from the lower part of the thundercloud flows to the Ground, we observe this in the in the image of lightning.

In 1992, the Russian scientist A.V. Gurevich from the Institute of Physics. Lebedeva RAS (FIAN) suggested that a kind of ignition for lightning can be cosmic rays — high-energy particles that fall to the Earth from space at a speed close to light. (Thousands of such particles bombard every square meter of the Earth's atmosphere every second.) They are sources of X-ray radiation [2].

Often, lightning is not a brightly glowing straight line connecting the cloud and the earth, but a broken line. Therefore, the process of forming a conducting channel for lightning discharge is called its "step leader". Each of these "steps" is a place where the electrons accelerated to near-light speeds stopped due to collisions with air molecules and changed the direction of movement.

The proof of this interpretation of the stepped nature of lightning is the flashes of X-ray radiation that coincide with the moments when the lightning, as if stumbling, changes its trajectory. Recent studies have shown that lightning serves as a fairly powerful source of X – ray radiation, the intensity of which can be up to 250 000 electron volts [1].

When lightning is discharged, 109–1010 joules of energy are released. Most of it is spent on creating a shock wave(thunder), heating the air, a light flash and other electromagnetic waves. Lightning can heat up the channel through which it moves, five times higher than the temperature on the surface of the Sun. The temperature inside the lightning is much higher than the temperature of 1600–2000 °C, which can range from tens of microseconds to https://agu.confex.com/agu/21workshop/ [3] tenths of a second. The amplitude of the lightning current pulse is usually equal to several tens of kiloamps, but sometimes it can exceed 100 kA.

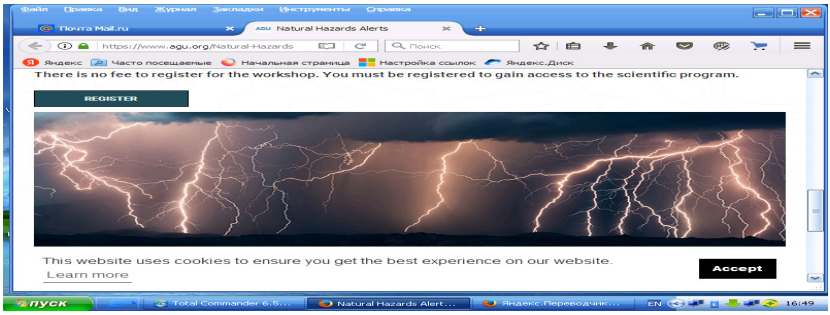


Fig. 1.

According to Gurevich, (2007), a particle of cosmic radiation, colliding with an air molecule, ionizes it, resulting in the formation of a huge number of high-energy electrons. Once in the electric field between the cloud and the earth, the electrons accelerate to near-light speeds, ionizing the path of their movement and, thus, causing an avalanche of electrons moving with them to the earth. The ionized channel created by this avalanche of electrons is used by lightning to discharge.

Since the electric field of the Earth is the field of a spherical capacitor with an applied voltage of about 400 kV. Under the influence of this voltage, a current of 2–4 kA flows from the upper layers to the lower ones all the time, the density of which is $1^{-2} \times 10^{-12}$ A/m^2, and energy is released up to 1.5 GW. And this electric field would disappear if there were no lightning! Therefore, in good weather, the electric capacitor-the Earth-is discharged, and in a thunderstorm it is charged. The charge carrier in the Earth's atmosphere is ions, the concentration of which increases with altitude and reaches a maximum in the ionosphere at an altitude of 50 km, where an electrically conductive layer was formed under the influence of cosmic radiation.

Difficulties in interpreting the obtained observations do not yet make it possible to describe the phenomenon of lightning in its entirety. So, for example, in the Earth's atmosphere, blue, pink, purple lightning was detected, which moved not down to the Earth, but on the contrary up, called elves, etc.

In the optical, radio and gamma ranges, lightning was recorded on Jupiter and its satellite Io, Venus, Uranus and Saturn by spacecraft from flight and orbital trajectories and descent modules.

REFERENCES:

[1] K. Bogdanov, Lightning: More questions than answers // Science and Life. 2007. No. 2.
[2] Gurevich A.V. // Science and Life. 1993. No. 7.
[3] Natural Hazards Alerts Workshop // Video Content Now Available, Bringing Land, Ocean, Atmosphere and Ionosphere Data to the Community for Hazard Alerts will take place virtually from 24–28, May 2021. https://agu.confex.com/agu/21workshop.

SESSION 2. VENUS (VN)
ORAL SESSION

ASSESSING A LARGE IGNEOUS PROVINCES (LIPS) CONTEXT FOR VOLCANISM ON VENUS

R.E. Ernst [1,2], K.L. Buchan [3], H. El Bilali [2], J.W. Head [4]
[1] *Department of Earth Sciences, Carleton University, Ottawa, Ontario, Canada, richard.ernst@ernstgeosciences.com, hafidaelbilali@cunet.carleton.ca;*
[2] *Faculty of Geology and Geography, Tomsk State University, Tomsk, Russia;*
[3] *273 Fifth Ave., Ottawa, Ontario, Canada;*
[4] *Department of Earth, Environmental and Planetary Sciences, Brown University, Providence, RI 02912, U.S.A*

KEYWORDS:
Large Igneous Provinces, LIPs, mantle plumes, plate tectonics, climate transition, magma reservoirs

INTRODUCTION:
Voluminous Venusian magmatism is analogous to Large Igneous Provinces (LIPs) on Earth [1–3]. We consider implications of applying a terrestrial LIP paradigm to Venus:

1) Group magmatic units into LIPs: On Earth each LIP event comprises multiple magmatic units (flows, dykes, sills, intrusions, magmatic underplate) and tectonic features (uplift, associated rifting) [3–5]. Different LIP events (with distinct ages) can spatially overlap. For Venus we are developing strategies to similarly assess grouping units into discrete events.

2) Link to mantle plumes: A variety of models have been proposed for terrestrial LIP and other intraplate magmatism, including rifting, lithosphere delamination, edge convection, meteorite impact, melting of water-enriched mantle, and supercontinent thermal blanketing [3]. However, mantle plumes arguably have a role in the majority of terrestrial LIPs. For Venusian LIPs (by comparison with Earth), we aim to distinguish a plume centre, a broader plume head region, and beyond-plume regions, each with their own magmatic and tectonic expression. Given the absence of plate tectonics, Venus provides an opportunity to assess the size distribution of candidate underlying plumes from the sizes of radiating and circumferential swarms.

3) Assess the graben-fissure systems as the surface expression of underlying dyke swarms [4, 6–7]: Radiating and circumferential graben-fissure systems on Venus, are interpreted to mark radiating and circumferential dyke swarms. We are assessing the proposal that Venusian coronae are analogues of terrestrial circumferential dyke swarms [4].

4) Identify magma reservoirs: On Earth erosion and geophysics reveals the distribution of magma reservoirs of a LIP plumbing system [4, 5]. On Venus (given the absence of erosion), magma reservoirs can be located in at least three ways: a) local uplifts due to filling of a magma reservoir, b) central depressions within coronae, which in some (many?) cases may indicate down-sag caldera collapse associated with expulsion of magma; and c) surface depressions which may mark roof collapse above sill-like and dyke-like layered intrusions [8].

5) Identify sources of lava flows: From a terrestrial perspective, lava flows can be fed from fractures along the edges of a caldera, from lateral injection of dykes intersecting surface topography and from circumferential fractures [9]. Given the absence of erosion, Venus provides a remarkable opportunity for linking specific lava flows to specific sources, thus providing insight into the distribution of buffered vs unbuffered magma reservoirs [10] within an overall magmatic system

6) Consider the effect on climate: Terrestrial LIPs are responsible for dramatic climate change and mass extinctions [11]. We are assessing whether the proposed Great Climate Transition on Venus [12–14] may be associated with stochastic overlap of multiple LIPs [15].

REFERENCES:

[1] Head, J.W., Coffin, M.F. Large Igneous Provinces: a planetary perspective. // In: AGU Geophysical Monograph, 1997, V. 100, P. 411–438.
[2] Hansen, V.L. (2007). LIPs on Venus. // Chemical Geology, 2007, V. 241, P. 354–374.
[3] Ernst, R.E. Large Igneous Provinces. // Cambridge U. Press, 2014, 653 P.
[4] Buchan, K.L., Ernst, R.E. Plumbing systems of large igneous provinces (LIPs) on Earth and Venus: Investigating the role of giant circumferential and radiating dyke swarms, coronae and novae, and mid-crustal intrusive complexes // Gondwana Research*, 2021* (in press).
[5] Ernst, R.E., Liikane, D.A., Jowitt, S.M., Buchan, K.L., Blanchard, J.A. A new plumbing system framework for mantle plume-related continental Large Igneous Provinces and their mafic-Ultramafic intrusions. // Journal of Volcanology and Geothermal Research. 2019. V. 384. P. 75–84.
[6] Grosfils, E.B., Head, J.W. The global distribution of giant radiating dike swarms on Venus: Implications for the global stress state. // Geophys. Res. Lett., 1994, V. 21, P. 701–704.
[7] Ernst, R.E., Head, J.W., Parfitt, E. Grosfils, E., Wilson, L. (1995). Giant radiating dyke swarms on Earth and Venus. // Earth Science Reviews, 1995, V. 39, P. 1 - 58.
[8] MacLellan L.M., Ernst R.E., El Bilali H., Ghail R., Bethell E. Volcanic history of the Derceto large igneous province, Astkhik Planum, Venus // Earth-Science Reviews. 2021. V. 220, No. 103619.
[9] El Bilali, H., Ernst, R.E., Buchan, K.L. Maat Mons, Atla Regio, Venus: Magmatic and tectonic history from detailed mapping. // 52nd Lunar and Planetary Science Conference, 2021, No. 2529.
[10] Partitt, E.A., Head, J.W., Buffered and unbuffered dike emplacement on Earth and Venus: Implications for magma reservoir size, depth, and rate of magma replenishment. // Earth Moon Planets, 1993, V. 61, P. 249–261.
[11] Ernst, R.E., Dickson, A., Bekker, A. (eds.). Large Igneous Provinces: A Driver of Global Environmental and Biotic Changes. // American Geophysical Union Geophysical Monograph, 2021, V. 255, 508 P.
[12] Way, M.J., DelGenio, A.D., Kiang, N.Y., Sohl, L.E., Grinspoon, D. H., Aleinov, I., Kelley, M., Clune, T. Was Venus the first habitable world of our Solar System? // Geophysical Research Letters, 2016, V. 43, P. 8376–8383.
[13] Way, M.J., Del Genio, A.D. Venusian habitable climate scenarios: Modeling Venus through time and applications to slowly rotating Venus-like exoplanets. // Journal of Geophysical Research: Planets, 2020, V. 125 (5), No., e2019JE006276.
[14] Khawja, S., Ernst, R.E., Samson, C., Byrne, P.K., Ghail, R.C., MacLellan, L. Tesserae on Venus may preserve evidence of fluvial erosion. // Nature Communications, 2020, V. 11, No. 5789
[15] Way, M.J., Ernst, R.E., Scargle, J.D. Large Scale Volcanism and the heat-death of terrestrial worlds. // American Geophyical Union Annual Fall Meeting, 2021.

ANALYSIS OF MULTIPLE IMPACT "SPLOTCHES" IN HINEMOA PLANITIA, NW AND W OF PHOEBE REGIO

E.G. Antropova [1], C.H.G. Braga [1], R.E. Ernst [1,2], K.L. Buchan [3], H. El Bilali [2], J.W. Head [4]

[1] *Faculty of Geology and Geography, Tomsk State University, Tomsk, Russia carloshenrique_gb@hotmail.com;*
[2] *Department of Earth Sciences, Carleton University, Ottawa, Canada;*
[3] *273 Fifth Ave., Ottawa, Ontario, Canada;*
[4] *Department of Earth, Environmental and Planetary Sciences, Brown University, Providence, RI 02912, U.S.A.*

KEYWORDS:
Venus Mapping, Magellan SAR, BAT Region, Splotches.

INTRODUCTION:

Impact craters are a common feature of most planetary bodies in the Solar System. Almost a 1000 impact features of various types are distinguished on the surface of Venus, and were classified by [1] into six main types. In addition to the main types, a number of other classes of objects are distinguished, including the so-called "splotches" (also termed "craterless blast haloes") [1–4]. "Over 90 % of the patterns consist of dark splotches with or without (15% versus 85 %) a central bright disturbance and with or without (70 % versus 30 %) a surrounding bright annulus" [1]. The number of recognized splotches on Venus is estimated to be about 500 [1].

The favoured hypothesis for the origin of such splotches is air-burst of meteors [1–4]. The shockwave from such an air-blast could affect the surface in different ways, leading to both radar darkening and brightening [1, 2]. In other cases when these meteors reach the surface, a small crater (or cluster) in the center is observed at the splotches. The type of splotches largely depends on the characteristics of the meteors itself – its size, mass, speed, angle of incidence, etc. An alternative (volcanism) interpretation is that the bright halo could be the result of explosive eruption of pyroclastic material that was redistributed by wind, forming circular structures. However, the absence of any central features of volcanic origin argues against such a hypothesis.

On the basis of our mapping in Hinemoa planitia, NW of Phoebe Regio in the eastern part of the Beta-Atla-Themis region, we have studied and mapped multiple bright splotches in detail. The absence of craters within these splotches is a good indicator that the meteors were destroyed in the atmosphere and did not reach the surface. However, the shockwaves from these meteors were sufficient to form large features. The centers of these splotches are dark and they are surrounded by wide radar-bright annuli. The characteristics of these splotches are summarized in Figures 1–2. The sizes of the splotches vary from 70 to 180 km. The minimum diameter of the inner, dark center varies from 10 to 35 km, and of the bright annulus, from < 50 to 80 km or more. Note that because of diffuse boundaries these numbers are approximate. The concentration of splotches in this area is anomalously high [4].

We have been investigating the possible interpretation that these alignments might represent atmospheric breakup of a large projectile during an oblique impact event. We note that the splotches are distributed along two slightly arcuate NNE trending lines suggesting oblique trajectory from the north or south. There are 4 splotches along the eastern line and at least 5 splotches along the western line (the three shown in Figures 1–2 and at least another two further south, shown in Figure 33 of [1]). The 4 splotches along the eastern line decrease in size to the NNE suggesting and oblique trajectory from the south. The elevation of the splotches varies over about 2 km but no correlation in properties with elevation is observed. We have observed no instances of younger units/structures embaying or cross-cutting splotches.

All these splotches appear to be superposed on underlying geological units (representing a wide range of geologic history [5])

We are currently mapping out the more detailed characteristics of each individual splotch in preparation for assessing more quantitatively an oblique projectile breakup model.

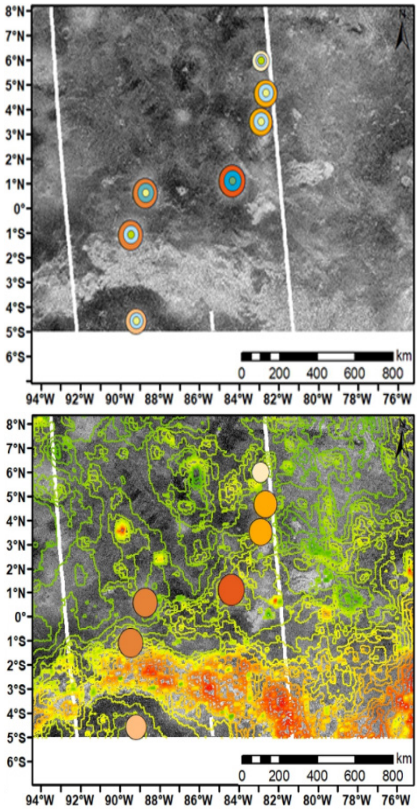


Fig. 1. Distribution of "splotches" on Magellan image. (Upper) Embedded circles explained in Fig. 2. (Lower). superimposed topography with green to red colours representing low to high elevation. Contour values (with respect to mean planetary radius) provided in Fig. 2.

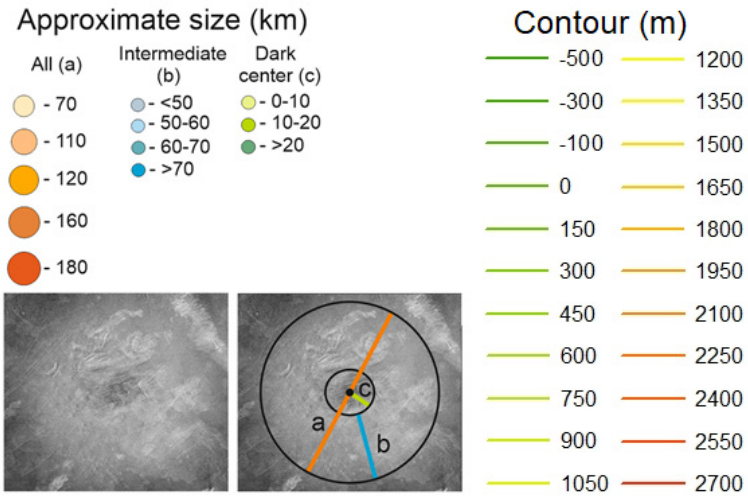


Fig. 2. (Left) Legend for measured characteristics of splotches observed in this study. (Right) Topographic contours values for Figure 1.

REFERENCES:

[1] Schaber, G.G., Strom, R.G., Moore, H.J., et al. Geology and distribution of impact craters on Venus: What are they telling us? // Journal of Geophysical Research, 1992, V. 97, P. 13257–13301.
[2] Schultz, P.H., Atmospheric effects on ejecta emplacement and crater formation on Venus from Magellan. // Journal of Geophysical Research. 1992, V 97, P 16183–16248.
[3] Soderblom, L.A., Chadwick, D.J., Schaber, G.G. Surface effects of impacts into Venus' atmosphere. // Lunar and Planetary Science Conference (LIPSC XXIII), 1992, Abstract number #1652
[4] Kirk, R.L., Chadwick, D.J. Splotches on Venus: Distribution, properties and classification. // Lunar and Planetary Science Conference (LIPSC XXV), 1994, Abstract number #1353
[5] Ivanov, M.A., Head, J.W.. Global geological map of Venus. // Planetary and Space Science, 2011, V. 59, P. 1559–1600.

PRELIMINARY GEOLOGY & STRATIGRAPHY OF THE VOLCANIC CENTER ATIRA MONS, BETA-ATLA-THEMIS REGION, VENUS

C.H.G. Braga [1], E.G. Antropova [1], R.E. Ernst [1,2], K.L. Buchan [3], H. El Bilali [2], J.W. Head [4]

[1] *Faculty of Geology and Geography, Tomsk State University, Tomsk, Russia carloshenrique_gb@hotmail.com;*
[2] *Department of Earth Sciences, Carleton University, Ottawa, Canada;*
[3] *273 Fifth Ave., Ottawa, Ontario, Canada;*
[4] *Department of Earth, Environmental and Planetary Sciences, Brown University, Providence, RI 02912, U.S.A.*

KEYWORDS:
Volcano, Atira Mons, Venus, BAT Region, Stratigraphy, Dyke swarm.

INTRODUCTION:
Atira Mons is a large volcano with an average diameter of ~ 600 km, a height of ~ 1,1 km and capped with a central caldera ~ 100 km across (Fig. 1a) (base altitude, ~ 0,6 km; summit altitude, ~ 1,5 km). It is centered at 52,2°N, 267,6°E (92,4°W) in the NE portion of the BAT region between Kawelu and Guinevere Planitiae. When compared to previous geological mapping [1, 2], our work provides a more detailed map on a scale of 1 : 500 000 of the volcanic edifice region, in order to reconstruct its stratigraphy and geological history. Geological units, including lava flows, grabens, fractures, fissures, wrinkle ridges, fracture belts, shield volcanoes and lava channels, are distinguished based on differences in radar brightness, topography and morphology. Relative ages of units are assessed from embayment and cross-cutting relationships.

GEOLOGICAL SETTING AND RELATIONSHIP WITH OTHER NEARBY FEATURES:
Regional analysis shows that Atira Mons and its apron of flows occupy an area of ~ 350 000 km^2 (Fig. 1 and Fig. 2). They partially overlie the older regional plains (rp; [2]) on the N and terminate against topographic barriers (fracture belts) on the E and W.

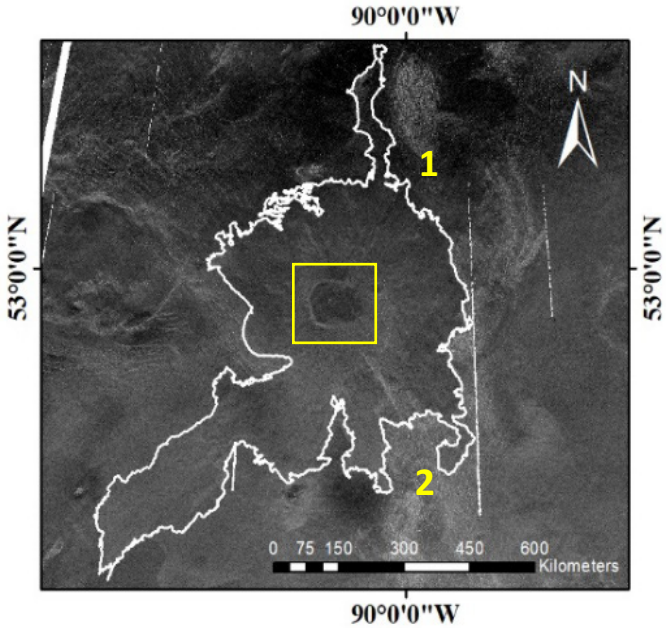


Fig. 1. a) General view of the study area (white line). The yellow box locates Fig. 4a and the red line – Fig. 4b; **1** – Field of shield volcanoes; **2** – Cluster of coronae and corona-like features.

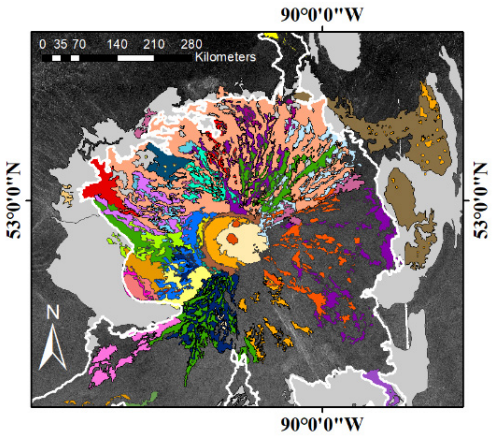


Fig. 2. Currently mapped geological units. Different colors inside the white frame indicate different generations of lava flows associated with Atira Mons. Grey units represent material that is older than Atira Mons and its flows. Brown and orange units outside the frame correspond to shield fields and its volcanic edifices, respectively.

A field of small shield volcanoes is located immediately NE of the Atira Mons' flows (Fig. 1, No 1). These small volcanoes and their associated flows appear to be younger than the regional plains, but have an uncertain age relationship with respect to Atira Mons.

On the south flank, Atira Mons flows partially cover a cluster of coronae and corona-like features, including Davies Patera (Fig. 1, 2). SW-trending flows (Fig. 1) can also be traced ~800 km away from the Atira Mons summit, where they partially cover older plains with wrinkle ridges (pwr; [2]).

FLANK FLOW APRON:

Most of the mapped lava flow units extend radially downslope away from Atira Mons' summit region (**mA**, Fig. 3) until they reach a topographic barrier such as the fracture belts on the E (**fbE**, Fig. 3), W and SW sides (**fbW**, Fig. 3). The W-, NW- and N-trending flows start radially from outside the caldera rim, but eventually swing 40-50º to the W and converge towards a local bowl-shaped depression of unknown origin (**bs**, Fig. 3) ~ 300 km NW of the summit. The E flank flows are fed from the eastern side of the caldera interior, crossing its low rim. However, the W and SW flows are not fed from the caldera interior, but more likely from buried circumferential dykes outside the caldera rim. Radar bright landslides can be seen on the W and NW flanks of the caldera (Fig. 4a), partly covering and obscuring the assumed sources of the W-trending flank flows.

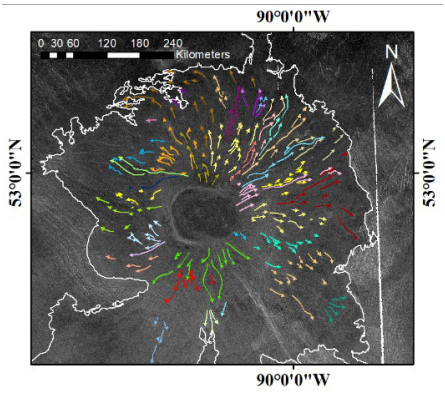


Fig. 3. Flows on the flanks of Atira Mons. Colors indicate different generations of flows mapped on the basis of embayment and cross-cutting relationships. The white line shows the full extent of the flows. **mA** – Atira Mons' summit; **fbW** – Western fracture belt; **fbE** – Eastern fracture belt; **bs** – local depression (basin).

CENTRAL SUMMIT HISTORY:
From our mapping in the summit region (Fig. 4a), we propose the following sequence of events: 1) caldera formation with greater collapse on the east side (Fig. 4b); 2) emplacement of flows on the floor of the caldera, which were later deformed by polygonal fractures [3] and a small set of arcuate fractures; 3) emplacement of younger flows covering part of the summit floor and fed from small shield volcanoes; 4) formation of a set of wrinkle ridges deforming the youngest flows.

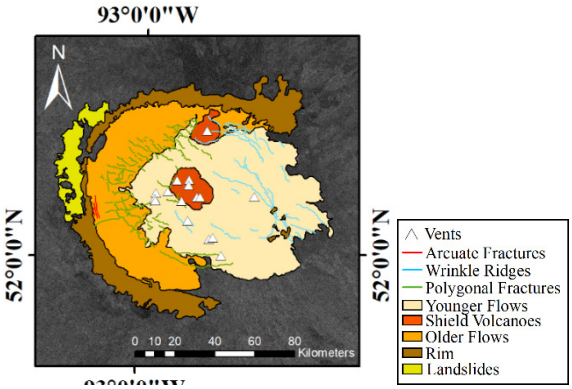


Fig. 4. a) Geological map of Atira Mons' summit (above); **b)** Atira Mons' topographic profile (below) on the red line in Fig. 1a.

ARCUATE FRACTURE SYSTEMS:
A major arcuate fracture system, which is interpreted to overlie a circumferential dyke swarm [4], is located on the E flank of Atira Mons (Fig. 5). This could suggest that late in its history Atira Mons started to develop corona-like characteristics. This arcuate fracture system cuts across the majority of the E-trending radial flows (**fE**, Fig. 5), indicating that most of these fractures are younger than the flows. However, the northern end of this fracture system is completely covered by a younger set of NE-trending flank flows (**fNE**, Fig. 5). The presence of these arcuate fractures only on the E side could reflect formation of a partial (< 360°) circumferential fracture system [5]. Two smaller arcuate fracture systems on the SW portion of Atira Mons (Fig. 5) may form part of a large elliptical system that also incorporates the eastern fracture system. We are currently assessing these patterns and their relation to caldera subsidence and similar features seen in coronae.

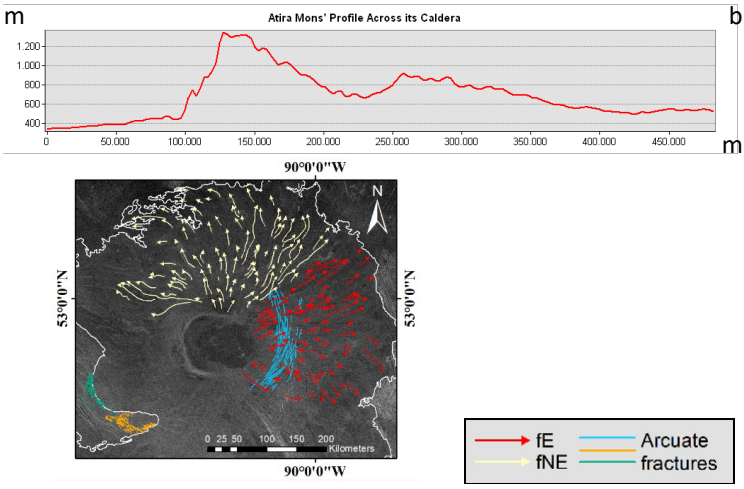


Fig. 5. Eastern arcuate fracture system (blue lines) cutting older E trending flank flows (**fE**) but cut by younger N-NE trending flank flows (**fNE**). On the SW portion are located two other systems of arcuate fractures.

REFERENCES:

[1] Dohm, J.M., Tanaka, K.L., Skinner, J.A. Geologic Map of the Metis Mons Quadrangle (V – 6), Venus // U.S. Geological Survey Scientific Investigations. 2011. Map 3158.
[2] Ivanov, M.A., Head, J.W., Global geological map of Venus. // Planetary and Space Science. 2011. V. 59. P. 1559–1600.
[3] Smrekar S.E., Moreels P., Franklin B.J. Characterization and formation of polygonal fractures on Venus // Journal of Geophysical Research. 2002. V. 107. I. E11. P. 8–1 to 8–17.
[4] Buchan, K.L., Ernst, R.E. In: Srivastava et al. (eds) Dyke Swarms of the World – A Modern Perspective // Springer. 2019. P. 1–44.
[5] Ernst, R.E., Liikane, D.A., Jowitt, S.M., Buchan, K.L., Blanchard, J.A. A new plumbing system framework for mantle plume-related continental Large Igneous Provinces and their mafic-Ultramafic intrusions // Journal of Volcanology and Geothermal Research. 2019. V. 384. P. 75–84.

DYKE SWARM HISTORY OF NABUZANA CORONA, SCARPELLINI QUADRANGLE (V-33), VENUS

J.C. Sanchez [1], R.E. Ernst [1,2], K.L. Buchan [3], H. El Bilali [1]
[1] *Department of Earth Sciences, Carleton University, Ottawa, Ontario, Canada, jcsan13@my.yorku.ca, richard.ernst@ernstgeosciences.com;*
[2] *Faculty of Geology and Geography, Tomsk State University, Tomsk, Russia;*
[3] *273 Fifth Ave., Ottawa, Ontario, Canada, kbuchan33@gmail.com*

KEYWORDS:
Nabuzana corona, nova, dyke swarm, graben system, canali.

INTRODUCTION:
In a previous Lunar and Planetary Science Conference presentation [1] we mapped the distribution of canali in the volcanic plains W and SW of Salus tessera, and demonstrated that two canali segments represent volcanic flows emanating directly from graben of Nabuzana corona. This indicates that these graben are underlain by dykes. Here we extend this work [1] by mapping at a scale of 1 : 500 000 the complex graben (dyke) systems of Nabuzana corona and its surroundings, in order to determine the magmatic and structural evolution of the corona, and further assess the links with the canali [1].

NABUZANA CORONA:
Nabuzana corona [2] has been identified as the more northerly of two adjacent coronae with diameters between 500 and 600 km (Fig. 1–3). Its southern neighbour is called Mukylchan corona [3]. Nabuzana is located in Scarpellini Quadrangle (V – 33) south of Salus tessera and west of western Ovda Regio.

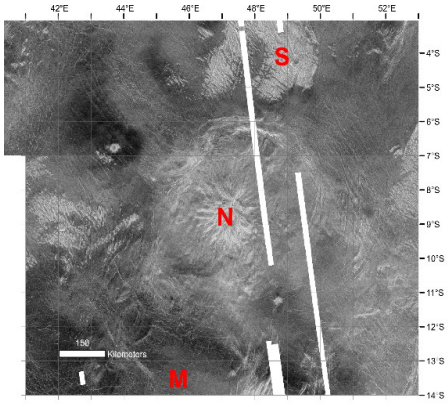


Fig. 1. Magellan SAR image of region of interest with Nabuzana corona (N), the focus of this study, and nearby Mukylchin corona (M). S = Salus tessera. NNW trending white bands are missing data.

MAPPING:
Figure 1 provides a summary of the current mapping of graben in the study area. In Figure 2 the graben are separated into radiating, circumferential and linear systems, that we interpret to be underlain by dykes [4–6].

The circumferential system on the northern and eastern side of the Nabuzana corona follows an elevated rim and inner moat, as typical of many other coronae. One of the canali, Canali A, identified in our earlier study [1] was seen to emanate directly from the graben of this circumferential swarm (Fig. 3), and Canali B [1] emanates from the NW-trending blue swarm (Fig. 3)

Three prominent radiating graben systems (or novae) are also mapped (Fig. 3). The two most northerly focus within the Nabuzana corona annulus. Their foci are only ~ 50 km apart. It is not uncommon for novae to be roughly centred on coronae, in which case they are usually interpreted

to genetically related and part of a single coupled corona-nova system. The third nova focusses 200 km further south of the others. Its relationship to Nabuzana is uncertain, as its centre is on the southern margin of Nabuzana, but also on the northern margin of the adjacent Mukylchan corona (not mapped in the present study).

Some graben sets beyond the Nabuzana corona annulus may be distal portions of the radiating graben systems of the novae. An example is NW-trending dykes located northwest of the corona. Others, however, are likely laterally-injected regional swarms that are simply passing by the corona. An example is the broad NE-trending (orange) swarm located to the southwest of Nabuzana); these likely have no relation to the emplacement of the corona or novae.

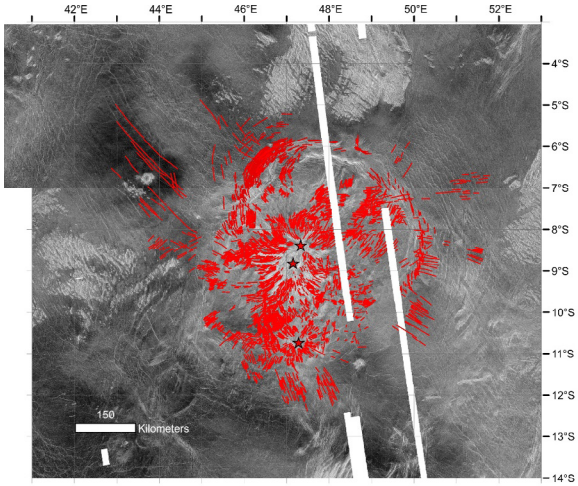


Fig. 2. Currently mapped grabens associated with Nabuzana corona. Stars locate magmatic centres recognized on the basis of radiating graben systems, interpreted to reflect dyke swarms.

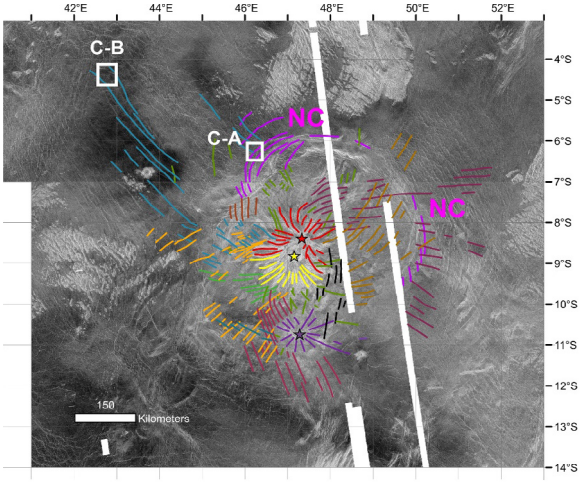


Fig. 3 Generalized distribution of the inferred dyke swarms with stars marking their foci. Red and yellow swarms and their foci represent two phases of Nabuzana corona magmatism and the purple radiating swarm and focus identifies an additional centre near the southern part of Nabuzana corona. NC is a large circumferential swarm associated with Nabuzana corona. White boxes, C-A, and C-B, indicate the location of links between canali “A” and “B” (described in [1]) and the circumferential (purple) swarm and linear (light blue) NW-trending swarm, respectively.

CONCLUSIONS:

The current mapping indicates Nabuzana is a complex corona-nova system with a ~ 600 km diameter annulus of graben located along the corona's rim and inner moat. Nabuzana has two novae that focus within its annulus and are likely related. A third nova is located on its southern margin and of less certain origin. Further study is needed to clarify the age relationships of the various graben systems (interpreted as dyke swarms) that have been identified.

REFERENCES:

[1] Sanchez, J.C., Ernst, R.E., Buchan, K.L., El Bilali, H. Canali W-SW of Salus tessera and link with Nabuzana corona. // Lunar and Planetary Science Conference 52, 2021, abstract No. 1324.
[2] Crumpler, L.S., Aubele, J.C.. Volcanism on Venus // In Sigurdsson, H. (ed.), Encyclopedia of Volcanoes. San Diego, CA: Academic Press, 2000, P. 727–769.
[3] Christensen, P.R. et al. // AGU Fall Meeting, Abstract #IN22A-06, 2009.
[4] Grosfils, E.B., Head, J.W. The global distribution of giant radiating dike swarms on Venus: implications for the global stress state. // Geophysics Research Letters, 1994, V. 21, P. 701–704.
[5] Ernst, R.E., Grosfils, E.B., Mège, D. Giant dike swarms: Earth Venus and Mars // Annual Review of Earth and Planetary Sciences,2001. V. 29, P. 489–534.
[6] Buchan, K.L., Ernst, R.E. Plumbing systems of large igneous provinces (LIPs) on Earth and Venus: Investigating the role of giant circumferential and radiating dyke swarms, coronae and novae, and mid-crustal intrusive complexes // Gondwana Research, 2021 (in press).

DYKE SWARM HISTORY OF ATLA REGIO, VENUS

H. El Bilali [1] R.E. Ernst [1,2], K.L. Buchan [3], J.W. Head [4]
[1] *Department of Earth Sciences, Carleton University, Ottawa, Ontario, Canada; hafidaelbilali@cunet.carleton.ca*
[2] *Faculty of Geology and Geography, Tomsk State University, Tomsk, Russia;*
[3] *273 Fifth Ave., Ottawa, Ontario, Canada;*
[4] *Department of Earth, Environmental and Planetary Sciences, Brown University, Providence, Rhode Island, USA*

KEYWORDS:
Dyke swarm, Graben, Maat Mons, Ozza Mons, Ongwuti Mons, Sapas Mons, Zemina corona

INTRODUCTION:
Atla Regio is a major mantle plume concentration featuring multiple volcanic centres (notably Ozza, Maat and Ongwuti Montes, and likely also Sapas Mons), associated coronae, topographic highs, a geoid high and radiating rift systems, all classic signatures of Large Igneous Province (LIP)-style magmatism associated with an active mantle plume (e.g. [1–3]). Comparable LIP magmatism on Earth consists of major volcanism in the form of shield and plateau basalts, and giant radiating and giant circumferential dyke swarms (e.g. [4–5]). Dyke swarms on Venus are expressed as sets of long narrow graben (and also pit chains) inferred to overlie blind dykes that were, for the most part, laterally emplaced (e.g. [6 - 7]). There have been several detailed studies of graben systems (interpreted in the context of dykes) in multiple regions of Venus (e.g. [8 - 11]) and other planetary bodies (e.g., [12–13]). In these studies, linear, radiating and circumferential swarms have been recognized, with the former associated with rift zones and the radiating and circumferential systems associated with mantle plumes. These regional dykes are interpreted to be fed from buffered magma reservoirs [14].

We undertook detailed mapping of graben systems across Atla Regio in order to distinguish different radiating, circumferential and linear graben sets (interpreted to mark different dyke swarms) and link them with the known magmatic centres of Atla Mons, other magmatic centres of Atla Mons that lack a central magmato-tectonic expression, or magmatic centres outside Atla Regio. Furthermore, crosscutting relationships between the different graben sets can provide the relative ages of the associated dyke swarms and, hence, the relative ages of the magmatic centres to which they belong, providing critical information on regional mantle convection patterns and geodynamics.

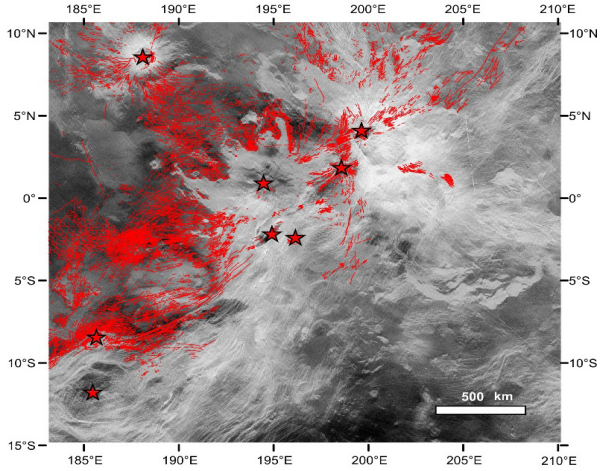


Fig. 1. Mapped graben of Atla Regio. Stars represent magmatic centres.

Initial mapping of the graben interpreted as dykes is shown in Figure 1 (with 16,000 lineaments traced to date). Preliminary analysis of the data (Fig. 2) suggests that there are giant radiating graben systems (interpreted as dyke swarms) linked to 4 Mons (Maat, Sapas, Ozza, Ongwuti), Zemina corona, and unnamed centre #1. Circumferential graben swarms are associated with Sapas and Ozza Mons, and unnamed centres # 2 and # 3.

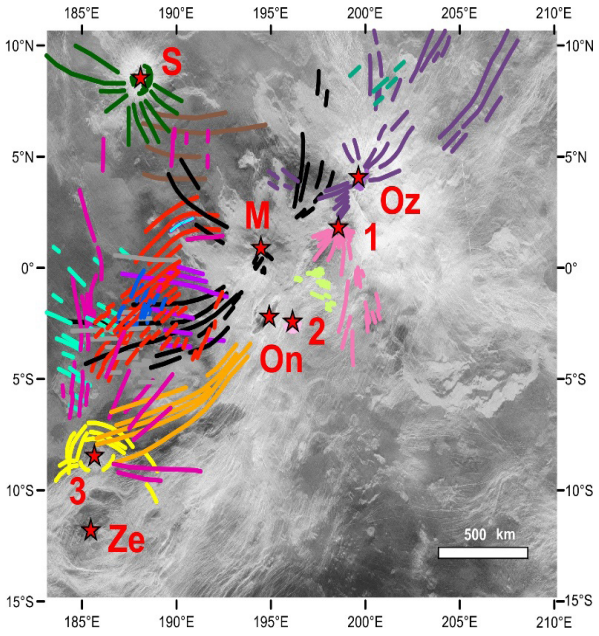


Fig. 2. Generalized distribution of the inferred dyke swarms and their links to specific centres. S = Sapas Mons, M = Maat Mons, Oz = Ozza Mons, On = Ongwuti Mons, Ze = Zemina corona. Numbers 1-3 locate additional centres recognized by associated graben systems (radiating and / or circumferential).

This work is important in providing additional context for the interpretation of the detailed 1 : 500,000 map of the volcanic history of Maat Mons [15], which builds on the earlier more reconnaissance-type mapping of [16].

REFERENCES:

[1] Senske, D.A., Schaber, G.G., Stofan, E.R. Regional topographic rises on Venus: geology of western Eistla Regio and comparison to Beta Regio and Atla Regio. // Journal of Geophysical Research, 1992, V. 97, P. 13395–13420.

[2] Smrekar, S.E., Evidence for active hotspots on Venus from analysis of Magellan gravity data. // Icarus, 1994, V. 112, P. 2–26.

[3] Shalygin, E.V., Basilevsky, A.T., Markiewicz, W.J., et al., 2012. Search for on-going activity on Venus: Case study of Maat Mons, Sapas Mons and Ozza Mons volcanoes. // Planet Space Sci., 2012, V. 73, P. 294–301.

[4] Ernst, R.E., Grosfils, E.B., Mège, D. Giant dike swarms: Earth Venus and Mars // Annual Review of Earth and Planetary Sciences, 2001. V. 29, P.489–534.

[5] Buchan, K.L., Ernst, R.E. Plumbing systems of large igneous provinces (LIPs) on Earth and Venus: Investigating the role of giant circumferential and radiating dyke swarms, coronae and novae, and mid-crustal intrusive complexes // Gondwana Research*, 2021* (in press).

[6] Grosfils, E.B., Head, J.W. The global distribution of giant radiating dike.swarms on Venus: implications for the global stress state. // Geophysics Research Letters, 1994, V. 21, P. 701–704.

[7] Ernst, R.E., Head, J.W., Parfitt, E. Grosfils, E., Wilson, L. Giant radiating dyke swarms on Earth and Venus // *Earth Science Reviews*, 1995, V. 39, P. 1 - 58

[8] Ernst, R.E., Desnoyers, D.W., Head, J.W., Grosfils, E.B. Graben-fissure systems in Guinevere Planitia and Beta Regio (264-312°E, 24-60°N), Venus, and implications for regional stratigraphy and mantle plumes // Icarus, 2003, V. 164, P. 282 - 316.

[9] Studd, D., Ernst, R.E., Samson, C. Radiating graben-fissure systems in the Ulfrun Regio area, Venus // I*carus*, 2011. V. 215, P. 279 -291, doi: 10.1016/j.icarus.2011.06.026.

[10] Davey, S.C., Ernst, R.E., Samson, C., Grosfils, E.B. Hierarchical clustering of pit crater chains on Venus // *Canadian Journal of Earth Sciences*, 2013, V. 50, P. 109–126.
[11] Graff, J.R., Ernst, R.E., Samson, C. Evidence for triple-junction rifting focussed on local magmatic centres along Parga Chasma, Venus. // Icarus. *2018.* V. 306, P. 122–138.
[12] Head, J.W., Wilson, L. Lunar graben formation due to near-surface deformation accompanying dike emplacement. // Planet. Space Sci., 1993, 41, 719–727.
[13] Head III, J.W., Wilson, L. Generation, ascent and eruption of magma on the Moon: New insights into source depths, magma supply, intrusions and effusive/explosive eruptions (part 2: observations) // Icarus, 2017, V. 283, P. 176–223, doi: 10.1016/j.icarus.2016.05.031.
[14] Partitt, E.A., Head, J.W. Buffered and unbuffered dike emplacement on Earth and Venus: Implications for magma reservoir size, depth, and rate of magma replenishment. // Earth Moon Planets, 1993, V. 61, P. 249–261.
[15] El Bilali, H., Ernst, R.E., Buchan, K.L. Maat Mons, Atla Regio, Venus: magmatic and tectonic history from detailed mapping // Lunar and Planetary Science Conference 52, 2021, abstr. No. 2529
[16] Mouginis-Mark P.J. Geomorphology and volcanology of Maat Mons, Venus // Icarus, 2016, V. 277, P. 433–441.

WINDOW INTO 4-KM CROSS SECTION OF VENUSIAN CRUST EXPOSED BY NORMAL FAULTS OF DALI CHASMA, SW OF ATLA REGIO

A. Ait Lahna [1], H. El Bilali [2], R.E. Ernst [2,3], N. Youbi [1,3]
[1] *Department of Geology, Faculty of Sciences-Semlalia, Cadi Ayyad University, Marrakesh, Morocco, aitlahna.abdelhak@gmail.com, youbi@uca.ac.ma;*
[2] *Department of Earth Sciences, Carleton University, Ottawa, Ontario, Canada; hafidaelbilali@cunet.carleton.ca, richard.ernst@ernstgeosciences.com;*
[3] *Faculty of Geology and Geography, Tomsk State University, Tomsk, Russia*

KEYWORDS:
Dali Chasma, Asymmetric rift system, detailed mapping, cross section.

INTRODUCTION:
Dali Chasma a 4000 km long rift system extending SW from Atla Regio. Dali Chasma together with its continuation to the SW, Diana Chasma, extends 7,500 km and connects Thetis Regio in the west with Atla Regio in the east. Diana Chasma and the western portion of Dali Chasma were mapped at 1 : 5,000,000 scale as part of mapping of Diana Chasma Quadrangle (V-37) [1]. The eastern portion of Dali Chasma in Stanton quadrangle (V - 38) has not been previously mapped.

Figure 1 shows the location of our research on Dali Chasma within Stanton quadrangle (V - 38). Mapping of volcanic and tectonic features of this rift is being done at 1 : 500,000 scale. Within our map area we note a structural feature of interest that is the focus of the remainder of this abstract. This feature is interpreted to represent an up to 4 km thick section of Venusian crust exposed through normal faulting associated with asymmetric rifting (Figs. 3 and 4).

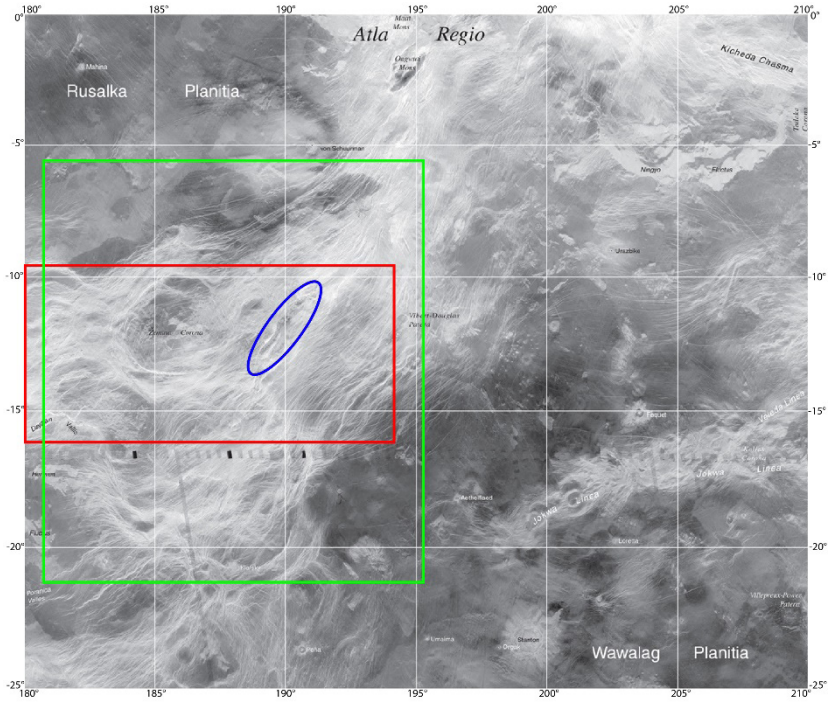


Fig. 1. Stanton quadrangle (V – 38) Red box locates Figure 2. Green box locates Figure 3, Blue ellipse locates structural feature of interest (Figs. 3 and 4). (Mercator Venus projection).

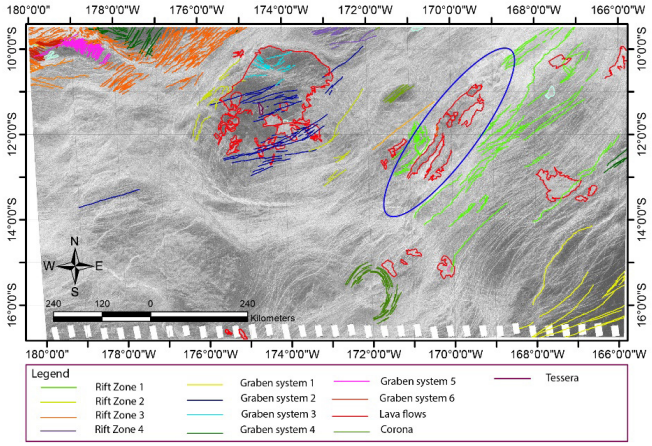


Fig. 2. Mapping of graben systems and flows in progress of Stanton quadrangle (V – 38). Blue ellipse locates structural feature of interest, with detailed analysis in Figures 3 and 4. (Sinusoidal Venus projection).

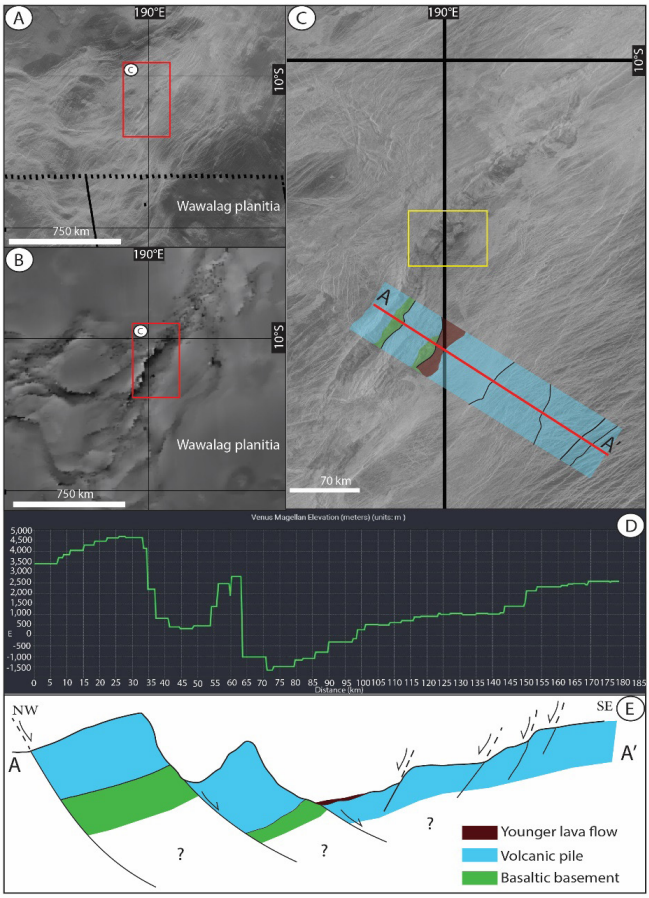


Fig. 3. (A) Magellan SAR image of the studied part of Dali Chasma rift system. Yellow box indicates Figure 4, (B) Magellan topography image for the same system, (C) Magellan SAR image with superimposed geological mapping along a section across Dali Chasma asymmetric rift, (D) Topographic profile across Dali chasma asymmetric rift system generated from JMARS, and (E) Interpreted geologic cross section shows western margin of asymmetric rift with major normal faults exposing about 4 km of crust. (Magellan images in Mercator Venus projection).

EXPOSED 4 KM SECTION OF VENUSIAN CRUST:

The unusual feature (500 km long and 20 - 70 km wide) is centered at 190° E/ 12° S and trends NE, parallel to the overall trend of the Chasmata. It stands out from the rest of the Chasmata by exhibiting a distinct decrease in lineaments. A cross section (Fig. 3C – E) shows that this portion of Dali Chasma represents an asymmetric rift bordered to the north-west by major normal faults and by many less extended normal faults to the south-east. These faults expose a 4 km section through the crust with a radar brighter ~ 3 km thick section overlying a radar darker ~ 1 km thick section. The radar brighter section locally exhibits parallel lineations (Fig. 4) which can be interpreted as horizontal layering, potentially reflecting a flood basalt sequence (or sequence of sills). The radar dark section beneath (see Fig. 4) could represent an older unit (basement?) of basaltic rocks.

In Figure 4 we interpret irregular-shaped areas with mottled radar texture to represent talus accumulated through mass wasting at the base of the exposed escarpment.

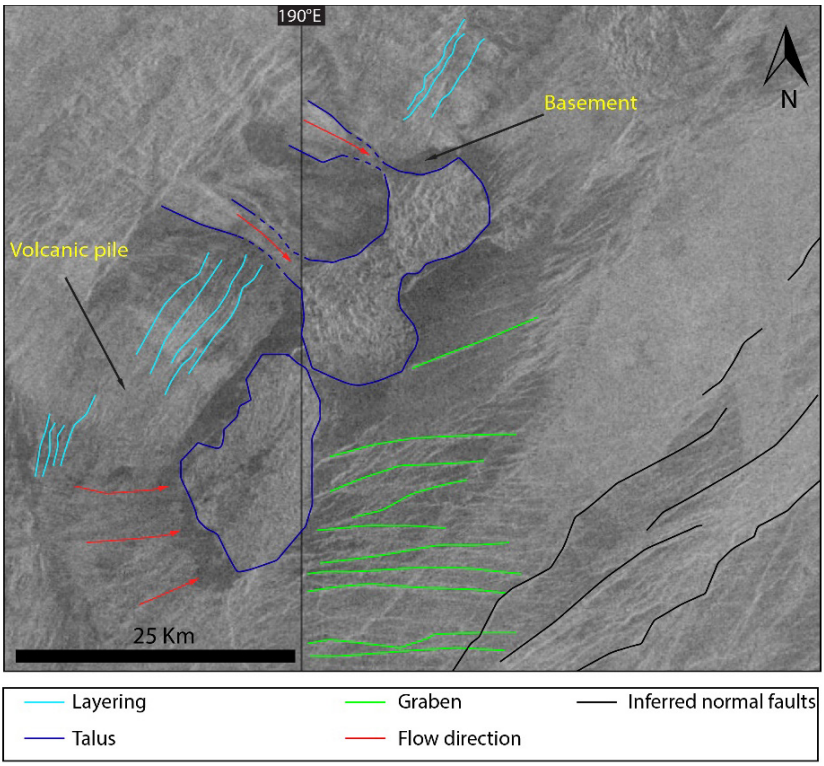


Fig. 4. Detailed map showing accumulation of talus at the base of the escarpment with direction of mass wasting shown by red arrows. Green lines indicate extensional lineaments which developed prior to the asymmetric rifting.

REFERENCES:

[1] Hansen V.L., DeShon H.R., 2002. Geologic map of the Diana Chasma Quadrangle (V – 37), Venus. U.S. Geological Survey Sci. Inv. Map I–2752.

CHARACTERISTICS, ORIENTATION AND ORIGIN OF STRUCTURAL COMPONENTS OF JOKWA LINEA GROOVE BELT, SE STANTON QUADRANGLE (V – 38), VENUS

R. Oukhro [1], H. El Bilali [2] R.E. Ernst [2,3], J.W. Head [4], N. Youbi [1]
[1] *Department of Geology, Faculty of Sciences-Semlalia, Cadi Ayyad University, Marrakesh, Morocco, oukhro.rachid@gmail.com;*
[2] *Department of Earth Sciences, Carleton University, Ottawa, Ontario, Canada, richard.ernst@ernstgeosciences.com;*
[3] *Faculty of Geology and Geography, Tomsk State University, Tomsk, Russia*
[4] *Department of Earth, Environmental and Planetary Sciences, Brown University, Providence, Rhode Island, USA*

KEYWORDS:
Jokwa Linea, corona, nova, Fracture belts, dyke swarm, rift.

INTRODUCTION:
Linea are elongated and topographically elevated features that are associated with abundant lineaments parallel to the topographic elongation. Twenty-two are listed on JMARS [1]. Lineae have also been termed fracture belts, densely lineated material, and more recently, groove belts (see summary of nomenclature in [2, 3]. Excellent examples of groove belts (Antiope, Hippolyta, and Molpadia Lineae) are described from Lavinia Planitia (e.g. [4, 5].

A major question related to these groove belts is their origin: 1) Are they of tectonic extensional origin?, 2) do they represent the surface manifestation of dyke swarms? or 3) are they a combination of these origins? Another important question is why do groove belts have elevated topography?

Regarding the latter point, [6] interpreted the groove belts ("fracture belts") as old rifts and suggested an explanation for the topographic difference between young 'rifts' (trough-like) and groove belts / "fracture belts" (topographic highs embayed by plains units). [6] interpret that "what we see now is a biased sample of those parts of old rifts which stood high enough not to be flooded. Many young rifts have high-standing portions typically on their flanks so that what we see now as fracture belts may be analogs of these elevated portions of old rifts."

Detailed mapping at a 1 : 500 000 scale (much higher than most previous mapping) should provide new insights into addressing the above questions.

JOKWA LINEA GROOVE BELT:
We have selected Jokwa Linea Groove Belt for detailed mapping at a scale of 1 : 500,000. Jokwa Linea (Fig. 1) extends for 1700 km from within southeastern Stanton quadrangle, V-38 eastward into the adjacent Taussig quadrangle, V – 39 which has been mapped at 1 : 5 000 000 scale [7].

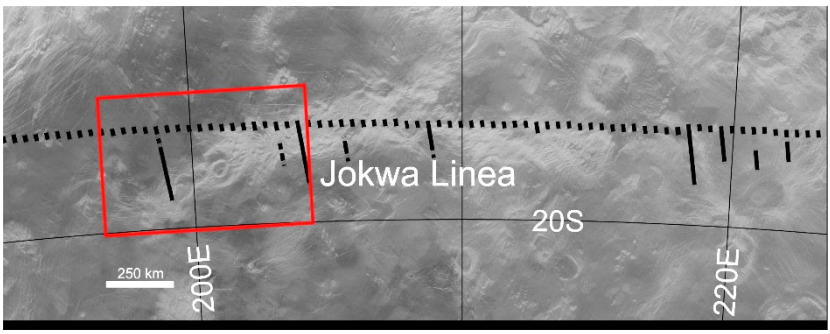
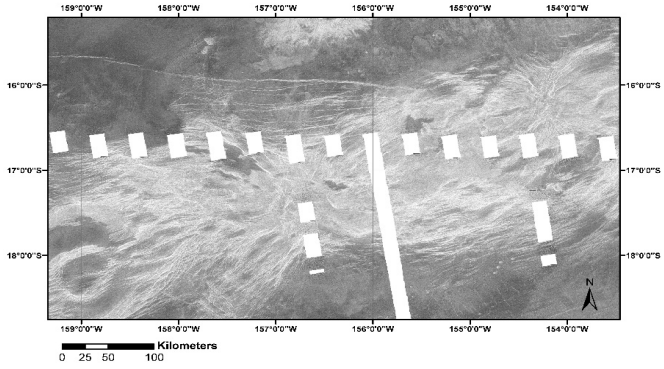


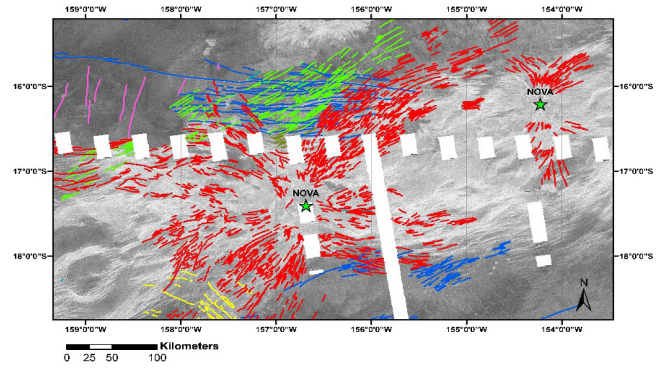
Fig. 1. Location and context of the 1700 km Jokwa Linea. Red box locates Figs. 2 - 3.

Our mapping of the portion of Jowka linea within the Stanton Quadrangle V – 38 is part of the mapping of the entire V-38 quadrangle at 1 : 2 500 000 scale by our Moroccan Venus group (see other abstracts in this conference).

Our initial mapping (reported herein) is from a 620 km long segment of Jokwa Linea (Fig. 2B). Multiple sets of lineaments are identified and shown in different colours. Our mapping includes identifying and distinguishing rift faulting using criteria in [8] and the characterization of corona and nova and corona-nova [9].



A



B

Fig. 2. A) Magellan image of an approximately 620 km long segment of Jokwa Linea. B) Magellan image with preliminary mapping of extensional lineaments. Different colors represent a preliminary grouping into distinct sets. Those with radiating patterns are interpreted to identify radiating dyke swarms. The nature of the other sets of extensional lineaments is being evaluated.

Current investigations are focused on 1) distinguishing the radial and belt parallel features in more detail, 2) assessing their dyke-related versus purely tectonic origin (e.g., presence of pit craters, volcanic flow sources, small shields, etc.), 3) examining stratigraphic and morphological relations to the more regional components of the groove belts (mapped in green and blue in Figure 2), and 4) assessing the relationship of this central features to coronae, novae and related features located in adjacent areas along the groove belt.

Our preliminary mapping (Fig. 2B) shows: 1) that the components of the groove belt here are composed of narrow graben-like structures; 2) that these graben show distinct radial orientations around the 'nova feature' in a pattern very similar to radiating dyke swarms around terrestrial LIP centres and around many edifices of volcanic origin on Venus [10]; and 3) that major parts of these radiating graben systems curve toward the strike of the broader groove belt and join this regional trend.

REFERENCES:

[1] Christensen, P. R. et al. 2009. AGU Fall Meeting, Abstract #IN22A-06
[2] Ivanov, M.A., Head, J.W. Global geological map of Venus // Planet. Space Sci., 2011, V. 59, P. 559–1600.
[3] Ivanov, M.A., Head, J.W. The history of tectonism on Venus: A stratigraphic analysis. Planetary and Space Science, 2015, V. 113–114, P. 10–32

[4] Ivanov, M.A., Head, J.W., Geologic Map of the Lavinia Planitia Quadrangle (V – 55), Venus. // USGS Scientific Investigations Map 2684, 2001.
[5] Fernández, C., Anguita, F., Ruiz, J., Romeo, I., Martín-Herrero, Á.I., Rodríguez, A., Pimentel, C. Structural evolution of Lavinia Planitia, Venus: Implications for the tectonics of the lowland plains. // Icarus, 2010, V. 206, P. 210–28.
[6] Basilevsky, A.T., Head, J.W. 2000. Rifts and large volcanoes on Venus: global assessment of their age relations with regional plains. // Journal of Geophysical Research, 2000, V. 105, P. 24583 – 24611.
[7] Brian, A.W., Stofan, E.R., Guest, J.E. Geologic Map of the Taussig Quadrangle (V - 39), Venus. // United States Geological Survey, Scientific Investigations Map 2813.
[8] Graff, J.R., Ernst, R.E., Samson, C. 2018. Evidence for triple-junction rifting focussed on local magmatic centres along Parga Chasma, Venus. // Icarus, 2018, V. 306, P. 122–138.
[9] Buchan, K.L., Ernst, R.E. Plumbing systems of large igneous provinces (LIPs) on Earth and Venus: Investigating the role of giant circumferential and radiating dyke swarms, coronae and novae, and mid-crustal intrusive complexes // Gondwana Research, 2021 (in press). https://doi.org/10.1016/j.gr.2021.02.014
[10] Grosfils, E.B., Head, J.W. The global distribution of giant radiating dike swarms on Venus: implications for the global stress state. // Geophysics Research Letters, 1994, V. 21, P. 701–704.

VENERA-D AND DECADE OF VENUS EXPLORATION

L.V. Zasova [1]
[1] *Space research institute, RAS,Profsoyuznaya 84/32 Moscow 117997, lzasova@gmail.com*

KEYWORDS:
Space mission, lander, orbiter, atmosphere, surface, clouds

Venus is the Earth-sized terrestrial planet, which has taken a completely different evolutionary path: its surface and atmosphere are strongly different from those on Earth. To understand Venus it needs to solve some important problems:

Extreme greenhouse effect — to understand what drives the atmospheric processes; Composition of surface materials—what is the variability across the planet and what are the implications for interior processes? What is the history of water? — how much did Venus have it and where did it go? What mechanism drives the superrotation? Why does Venus not possess its own magnetic field? Moreover, as most of the Earth-sized exoplanets resemble Venus, a study of Venus is extremely important to understand better their evolution and habitability. Venus, covered by 20 km — thickness cloud layer is challenging for researching its surface. To understand why it is so different from Earth, to clarify its origin and evolution, we need *in situ* measurements in the atmosphere and on the surface. Last time the such measurements were fulfilled 35 years ago by Vega balloons and soviet landers. The IKI/Poscosmos - NASA Joint Science Definition Team (JSDT), after 3.5 years of activity, published the final report on the concept of joint Roscosmos — NASA mission to Venus (http://www.iki.rssi.ru/events/2019/Venera-DPhaseIIFinalReport.pdf).

It includes obiter and lander (Roscosmos) , aerial platform (balloon with variable altitude of floating), a long-lived surface meteo (LLISSE) and seismic and atmospheric (SAEVe) stations (NASA). Phase A of Venera-D started in 2021. The project is under development in accordance with the concept, created by JSDT. The launch date is 2029 (2031) from launch facility Vostochnyi using Angara-5 rocket. Indeed, we live in the “Decade” of Venus exploration: Akatsuki (JAXA) missions is functioning successfully around Venus; Indian (IRSO) orbiter mission Shukrayaan is planned to be launch in 2026; except Venera – D (2029), NASA selected two missions VERITAS (2028–2029) and DAVINCI (2029–2031) as a part of the Discovery Program; EnVision orbital mission was selected as the fifth medium mission (M5) of ESA’s Cosmic Vision programme with launch planned for 2031.

Thus, five – six missions may be working simultaneously at Venus at the end of 20^{th} – beginning 30^{th}. A discussion of synergism between the missions of different agencies will help to solve many puzzles of Venus.

GEOLOGICAL CHARACTERIZATION OF THE VENERA-D LANDING SITES

M.A. Ivanov [1], J.W. Head [2], O.Yu. Segykh [3], A. Simonov [4]
[1] *Vernadsky Inst., RAS, Moscow, Russia;*
[2] *Brown Univ., Providence RI, USA;*
[3] *Lavochkin Association., Khimki, Russia*

KEYWORDS:
Venus, Venera-D, landing sites, geological settings.

INTRODUCTION

Current configuration of the Venera-D mission, specifically, separation of the landing module at encounter of the circum-Venus orbit, introduces strong limitations on the selection of the landing sites. These points are predetermined by the mission ballistics and are located at the northern- and southernmost points of the approach arcs, the position of which depends upon the launch dates. So far, three landing dates (windows) have been selected for each launch year of 2027, 2029, 2031, and 2034. Each window has two landing points, the northern and southern ones, and, thus, 24 potential landing spots exist. Here we describe the geological context that characterize landing ellipses (LE, a circle 300 km diameter) at each landing point using the global geological map of Venus [1–3].

LAUNCH YEAR 2027, WINDOW 1, NORTHERN POINT (158.9W, 25.9N): The LE at this point includes mostly occurrences of shield plains (psh, ~ 46 %; here and everywhere, percent of the ellipse area) and the lower unit of regional plains (rp1, ~ 46 %). Smaller areas at the northern and southern edges of the ellipse are occupied by densely lineated plains (pdl, 8 %). **SOUTHERN POINT (160.2W, 65.3S):** The LE at this point includes mostly unit pr1 (~ 89 %) with small fractions of psh (~ 8 %), ridged plains (pr, ~ 2 %), and pdl (~ 1 %) that occur at the eastern edge of the ellipse.

LAUNCH YEAR 2027, WINDOW 2, NORTHERN POINT (147.1W, 20.1N, FIG. 1): The LE at this point covers a variety of units. Heavily tectonized units include pdl (~ 2 %), groove belts (GB, ~ 4 %), and rift zones (RZ, ~ 16 %). Volcanic plains include psh (~ 23 %), rp1 (~ 22 %), and lobate plains (pl, ~ 24 %). **SOUTHERN POINT (147.6W, 79.9S, FIG. 2):** In contrast to the northern point, the southern LE consists almost completely of rp1 (~ 94 %) and is crossed by a branch of the ridge belt unit (pr/RB, ~ 5 %). An impact crater, Isolde (12 km diameter, ~ 1 %), is near the center of the LE.

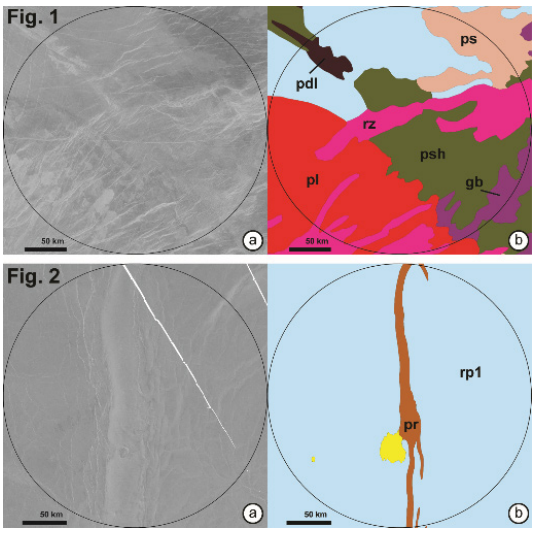


Fig. 1, Fig. 2 Illustrate different geological settings of the proposed landing ellipses. In both images: lef — AR images, right — pieces of the global geological map.

LAUNCH YEAR 2027, WINDOW 3, NORTHERN POINT (134.7W, 16.5N): A large portion of the LE at this point consists of heavily tectonized units such as GB (~ 4 %) and RZ (~ 34 %). Almost the entire eastern portion of the ellipse is covered by lavas of unit pl (~54%) and only a small fraction of the LE is occupied by unit rp1 (~ 8 %). **SOUTHERN POINT (133.5W, 81.4S):** Unit rp1 completely covers the LE at this point.

LAUNCH YEAR 2029, WINDOW 1, NORTHERN POINT (109.95W, 10.4N): More than half of the LE at this point is dissected by branches of rift zones (~ 64 %). Both units of regional plains (rp1, rp2) dominate in the southern portion of the LE and comprise ~ 33 % of its area. An insignificant area of the LE in its southern half is occupied by a narrow branch of GB (~ 3 %). **SOUTHERN POINT (129.1W, 89.3S):** This point is outside of both the SAR coverage and the geological map and cannot be characterized adequately.

LAUNCH YEAR 2029, WINDOW 2, NORTHERN POINT (110.2W, 13.5N): Three units dominate in the LE at this point: rp2 (~ 43 %), pl (~ 25 %), and RZ (~ 18 %). Much smaller fractions of the LE are occupied by psh (~ 8 %), rp1 (~ 4 %) and smooth plains (ps, ~ 3 %). **SOUTHERN POINT (109.8W, 81.3S):** The LE at this point is almost completely covered by rp1 unit (~ 96 %) and the rest of the LE is made up of the pr unit (~ 4 %).

LAUNCH YEAR 2029, WINDOW 3, NORTHERN POINT (112.3W, 22.7N): The psh unit represents the most abundant materials in the LE at this point (~ 59 %). Small occurrences of tessera (t, ~ 0.5 %), pdl (~ 6 %), and GB (~ 14 %) are seen throughout the LE. Materials of unit rp1 make up ~ 20 % of the LE area. **SOUTHERN POINT (112.1W, 69.1S):** The LE at this point is completely covered by unit rp1.

LAUNCH YEAR 2031, WINDOW 1, NORTHERN POINT (107.4W, 38.6N): The southern third of the LE at this point is covered by pl (~ 26 %) and the northern portion of the ellipse is divided between both regional plains units (rp1, ~ 20 % and rp2, ~ 37 %). Small fractions of the LE are occupied by psh (~ 8 %), GB (~ 7 %), pdl (~ 1 %) and t (~ 0.1 %). **SOUTHERN POINT (106.7W, 50.7S):** Two units dominate the LE at this point. The northern half of the ellipse is covered by psh (~ 53 %) and its southern potion is covered by rp1 (~43%). Branches of GB make up ~4% of the ellipse area.

LAUNCH YEAR 2031, WINDOW 2, NORTHERN POINT (108.9W, 37.2N): Unit pl of Zipaltonal Fluctus dominates the LE at this point and makes up ~ 86 % of its area. At the northern and southern edges of the LE there are small occurrences of psh (~ 7 %), GB (~ 5 %), and pdl (~ 2 %). **SOUTHERN POINT (109.5W, 51.7S):** Three units almost completely cover the LE at this point, psh (~ 20 %), rp1 (~ 70 %), and rp2 (~ 9 %). Small occurrences of pdl (~ 0.1 %) and GB (~ 0.9 %) are seen at the southern edge pf the ellipse.

LAUNCH YEAR 2031, WINDOW 3, NORTHERN POINT (112.0W, 36.3N): About 65 % of the LE at this point is covered by pl of Zipaltonal Fluctus. The rest of the ellipse is made up of psh (~ 21 %), GB (~ 8 %), RZ (~ 3 %), pdl (~ 2 %), and t (~ 1 %). **SOUTHERN POINT (113.6W, 53.7S):** The most abundant unit in the LE at this point is psh (~ 46 %) that occupies the central portion of the ellipse. To the West, a branch of GB (~ 19 %) is seen; to the East units rp1 (~ 15 %) and rp2 (~ 17 %) cover the ellipse. The impact crater Trollope (~ 27 km diameter, ~ 3 %) is near the southern edge of the ellipse.

LAUNCH YEAR 2034, WINDOW 1, NORTHERN POINT (154.7W, 37.3N): Units of psh (~ 39 %) and rp2 (~ 33 %) dominate the LE in this region. The rest of the ellipse is made up of rp1 (~ 15 %), GB (~ 11 %), and pdl (~ 2 %). **SOUTHERN POINT (154.6W, 51.7S):** The LE at this point is almost completely covered by unit rp1 (~ 97.5 %) The rest of the ellipse is comprised of rp2 (~ 2.5 %).

LAUNCH YEAR 2034, WINDOW 2, NORTHERN POINT (145.6W, 49.7N): The LE at this point covers only volcanic units of pl (~ 51 %), ps (~ 18 %), rp2 (~ 15 %) rp1 (~ 8 %), and shield clusters (sc, ~ 8 %). **SOUTHERN POINT (145.4W, 37.7S):** About 97% of the LE at this point is covered by materials of rp1,and the rest of the ellipse is made up by psh (~ 3 %).

LAUNCH YEAR 2034, WINDOW 3, NORTHERN POINT (137.1W, 66.95N): The LE at this point is dominated by tectonized units, the most abundant of which is pr that forms the ridge belt of Akuanda Dorsa (~ 43 %).

Branches of GB (~ 7.5 %) occur in spatial association with the ridge belt. The rest of the ellipse is covered by psh (~24%), rp1 (~ 12 %), rp2 (~ 8 %), and pdl (~ 5.5 %). **SOUTHERN POINT (136.7W, 23.1S):** The most abundant unit in the LE at this point is psh (~35%). Unit rp1 covers ~ 27 % of the ellipse area. Units GB (~ 24 %), rp2 (~ 13 %) and pdl (~ 1 %) make up the remainder of the ellipse.

CONCLUSIONS:

Percentage of the LE occupied by different units are summarized in Table 1. Because mission safety has the highest priority, the heavily tectonized units (t, pdl, pr/RB, GB, and RZ) and lobate plains whose radar brightness suggests a rough surface (potentially rough aa lavas) appear as inappropriate regions for landing. For example, within the LEs at the northern points of the launch windows 2 and 3 of 2031, and window 3 of 2027, the percentage of the dangerous units exceeds 90 % and these sites should be excluded from the list of potential landing sites. In contrast, the lower unit of regional plains appear to be the safest unit of a high scientific value and, thus the most attractive as a landing surface. The southern spots of the launch widows 1, 2, and 3 of 2027, 2029, and 2034 are characterized by high percentages of unit rp1 (over 90 %) and the lack/small fraction of rough units and, thus, should be considered as sites of higher priority.

Table 1. Percentage of units in landing ellipses of the Venera-D mission

Year		LS	Units, %											
			t	pdl	pr	gb	psh	rp1	rp2	sc	ps	pl	rz	c
2027	1	N		8.1			45.9	46.1						
		S		0.6	2.3		7.8	89.3						
	2	N		1.8	4.1		23.0	21.8			6.8	26.4	16.0	
		S			4.8			94.1						1.1
	3	N				4.4		8.0				53.7	33.9	
		S						100.0						
2029	1	N				2.8	0.1	23.4	9.7				64.0	
		S	n/a	n/a	n/a	n/a	n/a	n/a	n/a	n/a	n/a	n/a	n/a	n/a
	2	N					7.9	3.7	43.0		2.6	24.7	18.1	
		S			4.4			95.6						
	3	N	0.4	6.0		13.8	58.9	20.3			0.6			
		S						100.0						
2031	1	N	0.1	0.8		6.7	8.2	21.1	37.0			26.1		
		S				4.3	53.4	42.4						
	2	N	0.3	1.8		5.0	7.4					85.5		
		S		0.1		0.9	19.3	70.4	9.3					
	3	N	0.8	1.9		7.9	21.2					65.2	3.0	
		S				19.2	46.2	15.3	16.5					2.7
2034	1	N		2.2		10.7	39.1	15.0	33.0					
		S						97.5	2.5					
	2	N						8.2	15.1	7.9	18.4	50.4		
		S					3.1	96.9						
	3	N	5.5		43.0	7.5	23.6	12.2	8.3					
		S		0.5		24.1	34.9	27.3	13.1					

REFERENCES:

[1] Ivanov, M.A., Head, J.W. Global geological map of Venus. // Planet. Space Sci. 2011. V. 59, P. 1559–1600.
[2] Ivanov, M.A., Head, J.W. The history of volcanism on Venus. // Planet. Space Sci. 2013. V. 84, P. 66–92.
[3] Ivanov, M.A., Head, J.W. The history of tectonism on Venus: A stratigraphic analysis. // Planet. Space Sci. 2015. V. 113–114, P. 10–32.

CRITERIA FOR VENERA-D MISSION LANDER SITE SELECTION

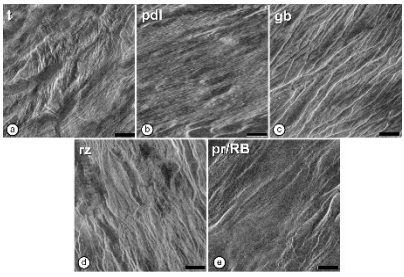
M.A. Ivanov [1], J.W. Head [2], L.V. Zasova [3], O.Yu. Segykh [4], A. Simonov [4]
[1] *Vernadsky Inst., RAS, Moscow, Russia;*
[2] *Brown Univ., Providence RI, USA;*
[3] *Space Research Institute, RAS, Moscow, Russia;*
[4] *Lavochkin Association., Khimki, Russia*

KEYWORDS:
Venus, Venera – D, landing sites, geological settings.

INTRODUCTION: Three criteria can be applied to constrain the selection of a range of landing sites for the Venera – D mission lander: (1) landing safety on specific geologic units and landforms, (2) global representativeness of materials at the landing spot, (3) simplicity of the geological/geochemical characteristics at the landing spot. We use the set of these criteria to assess priorities of landing sites proposed from the ballistic constraints of the Venera-D mission.

SAFETY CONSTRAINS: A safe landing is the most important requirement for landing site selection. We used the safety constraints to isolate areas where landing is too risky because of enhanced roughness of the surface at the scale of meters-decameters. Landforms that make up the surface of Venus can be divided into three categories: tectonic [*1], volcanic [2*], and impact-related [*3] terrains that are characterized by different short-wavelength roughness.

The tectonic terrains are dissected by numerous tectonic structures that cut the surface into isolated blocks often surrounded by steep scarps. The tectonic terrains include tessera (t), densely lineated plains (pdl), groove belts (GB), rift zones (RZ), and ridged plains/ridge belts (pr/RB) (Fig. 1).



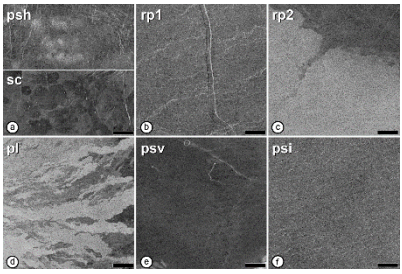


Fig. 1 (left). Examples of tectonized terrains on Venus. Each scale bar is 10 km; north is up. **Fig. 2** (right). Examples of volcanic units on Venus. Each scale bar is 10 km; north is up.

TESSERA (T, FIG. 1A) occupies about 8 % of the surface of Venus and represents the oldest material unit on the planet. Tessera may represent a "window" into Venus' geological past and, thus, is a target of extreme scientific importance. However, tessera surfaces usually show at least two sets of intersecting contractional (ridges) and extensional (graben, fractures, scarps) structures and resemble, both morphologically and by scale, the interiors of terrestrial rift zones where an uncontrolled safe landing is practically impossible.

DENSELY LINEATED PLAINS (PDL, FIG. 1B, ~ 2 % OF THE SURFACE OF VENUS) is a material unit that is characterized by numerous closely spaced linear and curvilinear lineaments (fractures) that are few hundred meters wide and a few tens of kilometers long.

GROOVE BELTS (GB, FIG. 1C, ~ 8.7 % OF THE SURFACE OF VENUS) are defined as zones of densely packed extensional structures (fractures and graben) up to 1 - 2 km wide and several tens of kilometers long. Groove belts form zones many hundredsof kilometers long and tens of kilometers wide.

RIFT ZONES (RZ, FIG. 1D, ~ 5.0 % OF THE SURFACE OF VENUS) also consist of numerous and densely packed fractures and graben. In contrast to groove

belts, structures of rift zones on average are broader, longer, and somewhat less densely packed than structures of groove belts. However, vertical topographic relief is quite variable.

The extensional structures of pdl, GB, and RZ form a specific pattern that resembles the surface of the Canyonlands region in Utah. These types of the tectonized terrains are obviously extremely dangerous for landing.

RIDGED PLAINS/RIDGE BELTS (PR/RB, FIG. 1E, ~ 2.2 % OF THE SURFACE OF VENUS) is a material unit the surface of which is cut by linear and curvilinear ridges (5^{-10} km wide, several tens of kilometers long). The ridges are often collected into prominent belts (ridge belts) hundreds of kilometers long and tens of kilometers wide. Morphologically, this type of tectonized terrain of Venus resemble the mature terrestrial mountain ranges such as Southern Urals and may not be appropriate for the safe landing because of the presence of long and rocky slopes.

The volcanic terrains on Venus include a variety of lava plains with either mildly- or non-tectonized surfaces.

SHIELD PLAINS (PSH, FIG. 2A UP, ~ 18.5 % OF THE SURFACE OF VENUS) have a great number of small (1–10 km) shield- and cone-like mounds that are interpreted as volcanic edifices.

SHIELD CLUSTERS (SC, FIG. 2A BOTTOM, ~ 0.7 % OF THE SURFACE OF VENUS): the surface of this unit is morphologically similar to that of shield plains. In contrast to psh, however, shield clusters are mostly tectonically non-deformed and often display small lava flows superimposed on the surrounding regional plains. Morphologically, shield plains and shield clusters resemble terrestrial shield fields and may have similar origins.

REGIONAL PLAINS, LOWER UNIT (RP1, FIG. 2B, ~ 33.0 % OF THE SURFACE OF VENUS), have a morphologically smooth surface with relatively homogeneous and low radar backscatter; the surface is cut by widely separated sets of wrinkle ridges. This unit is the most abundant and ubiquitous one on Venus and its occurrences can be traced almost continuously around the globe.

REGIONAL PLAINS, UPPER UNIT (RP2, FIG. 2C, ~ 9.8 % OF THE SURFACE OF VENUS), are characterized by a morphologically smooth surface that is deformed by the same populations of wrinkle ridges that cut the surface of rp1. In contrast to the relatively low albedo of rp1, the albedo of rp2 is noticeably higher.

LOBATE PLAINS (PL, FIG. 5D, ~ 8.8 % OF THE SURFACE OF VENUS) usually have morphologically smooth surfaces that are occasionally disturbed by a few extensional features. The radar albedo of lobate plains consists of numerous interleaved bright and dark flow-like features.

SMOOTH PLAINS OF VOLCANIC ORIGIN (PSV, FIG. 5E, ~ 2.3 % OF THE SURFACE OF VENUS) have a morphologically smooth, tectonically undisturbed, and featureless surface that typically has low radar albedo.

SMOOTH PLAINS OF IMPACT ORIGIN (PSI, FIG. 5F) form radar-dark parabolas and haloes around impact craters [4, 5] and likely represent deposits of fine - grained materials with smooth surfaces, some of which extend for hundreds of kilometers [*6].

The significantly lower abundance of tectonic structures on the volcanic units makes their surfaces to be more even compared to the tectonized terrains. However, units such as rp2 and pl are characterized by higher radar albedo and, thus, may have enhanced short-wavelength roughness [7] resembling rough aa lavas. Landing on such rough surfaces will very likely result in lander overturn and/or serious structural damage.

The surfaces of shield plains (psh), shield clusters (sc), the lower unit of regional plains (rp1) and smooth plains (both volcanic and impact, psv, psi) are either mildly - or non - tectonized and their radar albedo is noticeable lower than that of rp2 and pl. This means that these units may provide surfaces appropriate for safe landing.

REPRESENTATIVENESS:
Among units appropriate for safe landing, only psh, rp1, and psi are pervasive and have significant lateral extent. These units formed by processes acting at the global scale and, thus, composition of their materials may provide clues to the understanding of some of the most important processes in the observable geologic history of Venus.

SIMPLICITY OF GEOCHEMICAL SIGNAL:
In order to prioritize units psh, rp1, and psi, we apply the criterion of the potential complexity/simplicity of the geochemical signal that can be received after analysis of materials of these units. In this respect, shield plains represent a less desirable type of terrains. The characteristic features of shield plains are small volcanic co structs that formed from numerous and isolated sources. Melts in these reservoirs may have a complex history that depends upon several factors such as: (1) degree of fractional differentiation of melts, (2) degree of the melt contamination by the wall rocks, (3) frequency of replenishment of the reservoirs by fresh melts, (4) degree of partial melting in the fresh melt source regions, (5) degree of mixing of the fresh melts and evolved magmas in the transient reservoirs. As a result, the erupted lavas in shield fields may have a broad spectrum of compositions that reflect a complex pre-eruption history. Numerous samples are needed to estimate the role and influence of factors involved in formation of the shield field lavas and a single analysis of the shield field materials are likely to result in non-representative measurements that may be difficult to interpret. The potentially large ambiguity in interpretation of the chemical analysis made on the surface of shield plains significantly lowers the scientific priority of this unit.

The smooth plains of impact origin appear to be less complicated geochemical target because they likely consist of fine-grained materials that have been well mixed within the convective impact plume. Materials of the radar-dark parabolas/haloes, however, have travelled through atmosphere as small particles with the higher surface to volume ratio and may be the subject of enhanced alteration. The results of analysis of these materials potentially may be altered from their original composition due to the solid/gas interaction.

Unit rp1 represents a better candidate for a single chemical analysis because of the following characteristic: (1) The uniform morphology of the plains suggests that they have the same mode of origin everywhere on Venus. (2) The lack of volcanic constructs on the surface indicates that the plains formed by high degrees of melting in the source regions and rapid delivery of melts to the surface. This reduces the chances of either fractional differentiation or contamination by crustal materials. (3) The small number of impact craters obviously embayed by materials of the plains suggests that they formed during a relatively short time. All these characteristics of regional plains suggest that their mode of origin is similar to that of terrestrial plateau-basalts and that the plains may represent an uncontaminated sample of the upper fertile mantle of Venus.

CONCLUSIONS:
The sequential application of the above criteria to the morphological units that make up the surface of Venus suggests that only one unit (rp1) represents a target of very high scientific importance that is both representative and provides a candidate safe landing. Thus, the high percentage of unit rp1 in a landing ellipse increases its priority among the other potential landing sites. For example, the southern spots of the launch widows 1, 2, and 3 of 2027, 2029, and 2034 are characterized by a high percentages of unit rp1 (over 90 %) and the lack/small fraction of rough units, and thus should be considered as landing sites of higher priority [8].

REFERENCES:
[1] Ivanov, M.A., Head, J.W. The history of volcanism on Venus. // Planet. Space Sci. 2013. V. 84, P. 66 - 92.
[2] Ivanov, M.A., Head, J.W. The history of tectonism on Venus: A stratigraphic analysis. // Planet. Space Sci. 2015. V. 113–114, P. 10–32.
[3] Schaber, G.G., Strom, R.G., Moore, H.J. (7 others). Geology and distribution of impact craters on Venus: What are they telling us? // Journ. Geophys. Res. 1992. V. 97. P. 13257–13301.

[4] Campbell, D.B., Stacy, N.J.S., Newman, W.I. (5 others). Magellan observations of extended impact crater related features on the surface of Venus // Journ. Geophys. Res. 1992. V. 97, P. 16249–16278.
[5] Izenberg, N.R, Arvidson, R.E., Phillips, R.J. Impact crater degradation on Venusian plains // Geophys. Res. Lett. 1994. V.21, P. 289-292.
[6] Basilevsky, A.T., Head, J.W., Abdrakhimov, A.M. Impact crater air fall deposits on the surface of Venus: Areal distribution, estimated thickness, recognition in surface panoramas, and implications for provenance of sampled surface materials. // Journ. Geophys. Res. 2004. V. 109, E12003, doi:10.1029/2004JE002307
[7] Ford, P.G. Plaut, J.J., Weitz, C.M., Farr, T.G., Senske, D.A., Stofan, E.R., Michaels, G., Parker, T.J. Guide to Magellan image interpretation. JPL publication 93–24. 1993. 148 p.
[8] Ivanov, M.A., Head, J.W., Sedykh, O.Yu., Simonov, A. Geological characterization of the Venera-D landing sites // The 12th Moscow Solar System symposium. Moscow. Russia. 2021, this issue.

INVESTIGATION OF THE CAPABILITIES OF A MANEUVERABLE LANDER TO THE VENUS SURFACE

A.V. Kosenkova [1]
[1] *Lavochkin Association, Russia, Khimki, Leningradskaya 24, 141402, Kosenkova.AV@yandex.ru*

KEYWORDS:
Venus, Spacecraft, Maneuver, Design, Atmosphere, Surface.

At present, the question of Venus research becomes relevant. The exploration of Venus as a terrestrial planet is interesting not only from the standpoint of fundamental science, but also from the standpoint of comparative planetology. And despite the impressive results of previous missions such as Soviet spacecraft of "Venera" and "Vega" series, American spacecraft of "Mariner", "Pioneer – Venus" series, "Magellan", some other flyby missions and more recent spacecraft of other agencies: Japanese spacecraft "Akatsuki", the spacecraft of the European Space Agency "Venus Express", many questions still need to be answered. So currently American and European space agencies are working on scientific programs for various missions to Venus, such as "Venus Flagship", "VERITAS", "DAVINCI +" and "EnVision". The concept of the "Venera – D" mission with international cooperation is being worked out in Russia. Projects "Venera-D" and "DAVINCI +", among other elements of the mission, assume lander for making measurements on the surface.

Nowadays in addition to the simplest task of the descent to the surface, the lander may face the task of achieving the required landing area, the most rational from the view point of making research, which is a separate task need to be solved by the scientific community.

"Venera-D" mission has the lander design similar to the Soviet landers "Venera" and "Vega", which relate to the ballistic type of a lander with zero lift-to-drag ratio at hypersonic velocity range that do not provide the possibility of making maneuvers during the descent in order to choose the required landing site.

This paper discusses various types of landers for the descent to the Venus surface, including those with the ability of making maneuvers during the descent in the atmosphere for increasing the latitude of coverage of the landing zones and for landing in the required areas. A comparative analysis of these landers is carried out and their design capabilities are determined in terms of maneuverability and mass characteristics. Aerodynamic characteristics of these landers are calculated, as well as the investigation of ballistic and thermal modes of the descent for various entry angles into the planet's atmosphere, the possibility of maneuvering during the descent in the atmosphere and its range are assessed. The advantages of using maneuverable "lifting body" type of a lander over a ballistic type of a lander, which does not have the ability of making maneuvers during the descent, are shown, which imposes some restrictions on the range of reachable landing sites for the expected launch dates in 2029–2034 years. In addition, the use of such maneuverable landers will expand the range of tasks and scientific research that can be carried out not only on the surface, but also at the stage of descent in the atmosphere before reaching the surface.

REFERENCES:

[1] Abdrakhimov A.M., Geochemical comparison of volcanic rocks from terrestrial intraplate oceanic hot spots with Venusian surface material. *Geochem. Int.*, 2005, V. 43, no. 8, P. 732–747.
[2] Limaye S.S., Kossin J.P., Rozoff C., Piccioni G., Titov D.V. and Markiewicz W.J. Vortex circulation on Venus: Dynamical similarities with terrestrial hurricanes. *Geophys. Res. Lett.*, 2009, vol. 36, no. 4, L04204, http://dx.doi.org/10.1029/2008GL036093.
[3] Marov M.Y., Hantress U.T. (2013) Soviet robots in the solar system Technology and discoveries. Moscow: PHYSMATLIT, 612 p.
[4] Phase II repot of the Venera-D Joint Science Definition Team. Available at: https://www.lpi.usra.edu/vexag/reports/Venera-DPhaseIIFinalReport.pdf (accessed January 31, 2019)

[5] Report of the Venera-D Joint Science Definition Team. Available at: http://www.iki.rssi.ru/events/2017/venera_d.pdf (accessed January 20, 2017)
[6] Ghail R.C. et. al. VenSAR on EnVision: Taking earth observation radar to Venus. Int. J. App. Earth Obs. Geoin., 2018, vol. 64, pp. 365–376, https://doi.org/10.1016/j.jag.2017.02.008.
[7] Limaye S.S. et al. The thermal structure of the Venus atmosphere: Intercomparison of Venus Express and ground based observations of vertical temperature and density profiles. Icarus, 2017, V. 294, P. 124–155, https://doi.org/10.1016/j.icarus.2017.04.020.
[8] Ivanov M.A. and Head J.W. Global geological map of Venus. Planet. Space Sci., 2011, vol. 59, pp. 1559 - 1600, doi:10.1016/j.pss.2011.07.008.
[9] Venera-D Landing Sites selection and Cloud Layer Habitability Workshop. October 2–5, 2019. IKI, Moscow, Russia. URL: http://www.venera-d.cosmos.ru/index.php?id=workshop2019&L=2
[10] A.V. Kosenkova. Investigation of the possibilities of aerodynamic forms of a lander capable of maneuverable descent in the Venus atmosphere / AIP Conference Proceedings, 2171, 160005 (2019); https://doi.org/10.1063/1.5133309
[11] Kosenkova, A.V., Minenko, V.E., Bykovsky, S.B., and Yakushev, A.G., 2018, Investigation of aerodynamic characteristics of lander alternative forms to study Venus. Inzhenernyi zhurnal: nauka i innovatsii — Engineering Journal: Science and Innovations, no. 11. URL: http://engjournal.ru/eng/catalog/arse/ahtp/1826.html

USING OF A RESONANT ORBIT IN THE PROBLEM OF EXTENSION LANDING AREAS ON THE VENUS SURFACE

V.A. Zubko [1], N.A. Eismont [1], A.A. Belyaev [1], R.R. Nazirov [1], K.S. Fedyaev [1], Zasova L.V. [1], D.A. Gorinov [1], A.V. Simonov [2]

[1] *Department of Space Dynamics and Mathematical Information Processing, Space Research Institute of the Russian Academy of Sciences (IKI), 84/32 Profsoyuznaya Str, Moscow, 117997, Russia;*

[2] *Lavochkin Research and Production Association, 24 Leningradskaya St., Khimki, Moscow Region, 141402*

KEYWORDS:
Venera-D project, resonant orbit, gravity assist maneuver, Venus, space mission.

The Venera-D project has the objective of studying the surface and atmosphere of Venus [1–3]. The mission is planned to be launched in 2029. The spacecraft will include a lander and an orbital module. The descent vehicle will also include a long-lived (about 1 month) and short-lived (a few hours) science stations [3].

A noticeable part of the planning of the mission is to identify areas on the Venus surface that would be reachable for landing. While determining accessible landing areas we are limited, at first, by only one lander per one mission, so that means that only a small part of the Venus surface would be studied. Because of that it is needed to focus only on surface areas that would satisfy the requirements of the planet's researchers in the most way. But from another hand we are also limited by the possibility of landing to only that points that would be accessible by the orbital position of Venus relative to the Earth. The dense atmosphere of Venus also serves as the constraint that needs to be considered, because it restricts the maximum allowable overload during the descent. Due to the listed above factors ensuring landing accessibility of every point on the surface of Venus proves to be very difficult. The obtained accessible landing areas would be relatively small due to the imposed restrictions on the re-entry angle into the dense layer of atmosphere and the short period of the orbital position of Venus.

The easiest way to extend the accessible landing areas may simply consist of increasing the launch delta-v budget required for flight to Venus. However, such possibilities are strongly restricted, primarily by the value of ΔV. The current study proposes a different way of choosing and reaching any point on the Venus surface. The launch of a spacecraft to Venus during the launch windows in 2029–2034 is considered for this purpose. The constraints for the method are the re-entry angle and the maximum possible overload. The key-point of the proposed method is to use the Venus gravity field itself for transferring the spacecraft to a resonant orbit to planet with return through one Venusian year. The direction of spacecraft relative velocity would be changed during the gravity assist, due to that landing would occur into the different point on the Venus surface in the next close encounter the spacecraft with Venus. The total landing sites would increase, because Venus gravity field can provide a bunch of the different relative trajectories that would transfer the spacecraft onto resonant orbits. This method allows one to provide an access to any point on the surface of Venus, but the time of flight will be increased on the one Venusian year. Results of the research showed that the new strategy provides an essential extension of accessible landing areas and makes any point on Venus surface accessible with a small increasing ΔV for launch from the Earth and duration of the flight.

REFERENCES:

[1] Zasova, L.V.. Issledovanie Venery kosmicheskimi missiyami: ot «Venery – 4» k «Venere – D». K 80-letiyu so dnya rozhdeniya akademika M.YA. Marova. M., IKI RAN, Mekhanika, upravlenie i informatika, 2015. (in Russian)

[2] Zasova, L.V.. Iz istorii Missii Venera-Ekspress. M., IKI RAN, Mekhanika, upravlenie i informatika, 2014. (in Russian)

[3] Zasova, L.V. ,Gorinov, D.A., Eismont, N.A., Kovalenko, I.D. Abbakumov, A.S. and Bober, S.A.. Venera-D: A Design of an Automatic Space Station for Venus Exploration. Sol. Syst. Res., 2019, vol. 53, no. 7, doi: 10.1134/S0038094619070244.

VENUS CLOUD COVER PUZZLES

S.S. Limaye [1], R. Mogul [2]
[1] *Space Science and Engineering Center, University of Wisconsin, 1225 W. Dayton St., Madison, WI 53806, USA, sslimaye@wisc.edu;*
[2] *Chemistry & Biochemistry Department, California State Polytechnic University, Pomona, CA, USA, rmogul@cpp.edu*

KEYWORDS:
Venus, Clouds, aerosols, composition

INTRODUCTION:
The global cloud cover of Venus, which reaches as high as high as 72 km in equatorial latitudes and about 67 km in polar latitudes (Ignatiev *et al.* 2009), shrouds the variations in cloud properties and chemical abundances down to the bottom of the cloud layer around 47 km. Nearly featureless at visible wavelengths, the global cloud cover shows large contrasts at UV wavelengths (day side) and near infrared wavelengths, where variations in cloud opacity can additionally be observed through the CO_2 windows on the night side. The few measurements of cloud properties from probes that descended into the atmosphere reveal a surprising consistency in the layered structure with distinct particle size distributions, at least in the equatorial and mid-latitudes between ~ 48 - 70 km altitude range. The origins of the day and night side contrasts are poorly understood. The day side contrasts require local variations of multiple absorbers across wavelengths, while the night side contrasts require local variations from the surface, lower atmosphere, and clouds to explain temporal changes in the emitted radiation, as it escapes to space through the CO_2 windows.

While an adopted global cloud model (Ragent *et al.* 1985; Zasova *et al.* 2007) has been used extensively to analyze the observations of Venus clouds from spacecraft and Earth-based telescopes, the impact of the local variations in the cloud properties and abundances of trace species has been rarely considered. Recent reports and analyses of past data are also revealing gaps in our knowledge and understanding of the clouds on Venus.

There are several fundamental questions regarding origins and dynamics of Venus' clouds and atmosphere that remain to be sufficiently addressed through current in situ measures, remote measures, or theoretical models. These puzzle pieces include: (I) Why is there a spatial and temporal variability of water vapor in the atmosphere?, (II) What other substances may be dissolved or suspended in the cloud aerosols, besides sulfuric acid, and what are the impacts to the physicochemical properties of the aerosols?, (III) What are the vertical profiles for acidity and abundances of acids such as sulfuric acid, phosphoric acid, and HCl in the cloud droplets?, (IV) What are the vertical profiles for the abundances of potential trace species such as HNO_2, PH_3, and NH_3?, (V) What are the abundances of phosphorus-containing species (such as phosphates) and transition metals in the clouds and lower atmosphere?, (VI) What are the identities of the unknown absorbers, and are they formed in the clouds, lower atmosphere, or below the surface?, (VII) Do the clouds or lower atmosphere harbor any chemical trends, such as redox or mixing disequilibria, and do any of these trends match the UV or NIR contrasts?, and (VIII) What are the fluxes of chemical input into the atmosphere and clouds from surface out-gassing and/or volcanic output?

REFERENCES:
[1] Ignatiev N.I., Titov D.V., Piccioni G., Drossart P., Markiewicz W.J., Cottini V., Roatsch T., Almeida M., and Manoel N. (2009) Altimetry of the Venus cloud tops from the Venus Express observations. *Journal of Geophysical Research: Planets*, 114.10.1029/2008je003320
[2] Ragent B., Esposito L.W., Tomasko M.G., Marov M.Y., Shari V.P., and Lebedev V.N. 1985. Particulate matter in the Venus atmosphere. *Advances in Space Research*, 5: 85–115.https://doi.org/10.1016/0273-1177(85)90199-1
[3] Zasova L.V., Ignatiev N., Khatuntsev I., and Linkin V. (2007) Structure of the Venus atmosphere. *Planetary and Space Science*, 55: 1712–1728, http://adsabs.harvard.edu/abs/2007P%26SS...55.1712Z.

NIGHT DISTRIBUTION OF THE O_2 (A1ΔG) AIRGLOW ON VENUS OBSERVED BY SPICAV IR/VEX IN 2006–2014

D. Evdokimova [1], A. Fedorova [1], M. Zharikova [1,2], D. Belyaev [1], F. Montmessin [3], O. Korablev [1], J.-L. Bertaux [3]

[1] *Space Research Institute of the Russian Academy of Sciences, Moscow, Russia, evd.dar@yandex.ru;*

[2] *National Research University Higher School of Economics, Moscow, Russia;*

[3] *CNRS/IPSL/UVSQ/UPMC, LATMOS, Guyancourt, France*

KEYWORDS:
Oxygen 1.27 - μm emission, nightglow, Venus upper mesosphere, infrared spectroscopy, Venus Express.

INTRODUCTION:

One of the tracers of atmospheric circulation in the Venus upper mesosphere at night is the infrared O_2 ($\alpha^1\Delta_g$) airglow at 1.27 μm. It was firstly identified in ground-based observations in 1975 [1]. Maximal intensity of the emission is reached at about 96 km. Thus, it indicates in particular the atmospheric dynamics of a transitional region in-between two regimes of global circulation: the cloud zonal super-rotation below 70 km and the subsolar to anti-solar (SSAS) transfer of air masses over 110 km. The SSAS circulation supplies the night atmosphere of Venus by oxygen atoms produced by photodissociation in the daytime hemisphere. The atoms downwelling to deeper atmospheric layers at night recombine to exited O_2 ($\alpha^1\Delta_g$) molecules which radiative relaxation to the ground state involves the IR emission at 1.27 μm. Statistically, the maximum of emission brightness was observed around the anti-solar point by ground-based and orbital measurements. This result shows a domination of the SSAS circulation at 90-100 km.

Venus Express, the recent ESA space mission, carried two instruments that were able to observe the O_2 ($\alpha^1\Delta_g$) airglow in details from the Venus orbit. One of them was the imaging spectrometer of VIRTIS-M; its IR channel studied the morphological features of the airglow in 2006-2009 [2 - 5]. The full analysis of VIRTIS-M limb and nadir observations by Soret et al. [4] concluded that the location of emission statistical maximum corresponds to the anti-solar point. Intensity of the maximum reached 1.6 MR. However, the independent analysis by Shakun et al. [5] revealed a slight shift of the nightglow's statistical maximum towards the evening terminator and a latitude of ~10° N.

The current work is based on the dataset of the SPICAV instrument with a high resolution channel in the IR (0.65–1.7 μm) [6]. SPICAV IR nadir observations accumulated a dataset in 2006–2014 that allowed to observe a major part of the Venus globe. The spatial resolution depended on the spacecraft distance to the planet due to the orbit elongation [6] and it is in range of 50-1000 km. SPICAV IR dataset extends the long-term and latitudinal coverage of the VIRTIS – M experiment, which rarely observed the Northern Hemisphere of Venus at night.

DATA ANALYSIS:

The SPICAV IR spectral range covers the O_2 ($\alpha^1\Delta_g$) airglow band and several transparency windows where the thermal emission originating bellow the Venus clouds escapes to space. The O_2 ($\alpha^1\Delta_g$) emission band at 1.27 μm is overlapped by the transparency window at 1.28 μm. The robust extraction of the O_2 ($\alpha^1\Delta_g$) spectrum is possible because of the high resolving power of the spectrometer (~ 1400). We optimize a thermal emission spectrum by a 1-D radiative transfer model with multiple scattering for each measurement. Direct model is computed by the SHDOMPP program solving the radiative transfer equation by the method of discrete ordinates and spherical harmonics in a plane-parallel atmosphere. The algorithm is an adjusted routine developed by Bézard et al. [7] and Fedorova et al. [8], it is used in this study with a cloud layer model by Haus et al. [9]. In order to increase the accura-

cy, the thermal emission model is computed for three atmospheric windows at 1.1, 1.18 and 1.28 μm. And there are three optimizing parameters: a scaling factor applied to mode 2 and 3 particle distributions of the cloud layer model, the H_2O mixing ratio in the lower atmosphere of Venus and the surface emissivity.

RESULT:

This study analyses more than 800 sessions of nadir observations (~ 10000 spectra) with chosen emission angle ≤ 2°. The observed intensities have significant variations over the detection limit estimated at 0.13 MR and the measured values reach 5.0 ± 0.1 MR. The local time and latitude distribution of the O_2 ($\alpha^1\Delta_g$) airglow at night was obtained based on these observations. The statistical maximum corresponds to the anti-solar point with the intensity value of 1.6 - 1.7 MR. In general, the distribution is fairly symmetrical about the equator. The result is in good correspondence with the analysis of the VIRTIS-M data [4, 5].

REFERENCES:

[1] Connes, P. et al. $O_2(1\Delta)$ emission in the day and night airglow of Venus // The Astrophysical Journal. 1979. V. 233. P. L29–L32.
[2] Gérard, J. C., et al. Distribution of the O2 infrared nightglow observed with VIRTIS on board Venus Express // Geophysical research letters. 2008. V. 35. No. 2.
[3] Piccioni, G., et al. Near-IR oxygen nightglow observed by VIRTIS in the Venus upper atmosphere. // J. Geophys. Res. Planets. 2009. V. 114.
[4] Soret, L., et al. Atomic oxygen on the Venus nightside: Global distribution deduced from airglow mapping // Icarus. 2012. V. 217. No. 2. P. 849–855.
[5] Shakun, A.V., et al. Investigation of oxygen O2 (a1Δg) emission on the nightside of Venus: Nadir data of the VIRTIS-M experiment of the Venus Express mission // Cosmic Research. 2010. V. 48. No. 3. P. 232–239.
[6] Korablev, O., et al. SPICAV IR acousto-optic spectrometer experiment on Venus Express. // Planetary and Space Science. 2012. V. 65. No. 1. P. 38–57.
[7] Bézard, B., et al. The 1.10 and 1.18 μm nightside windows of Venus observed by SPICAV-IR aboard Venus Express // Icarus. 2011. V. 216. No. 1. P. 173–183.
[8] Fedorova, A., et al. The CO_2 continuum absorption in the 1.10 and 1.18 μm windows on Venus from Maxwell Montes transits by SPICAV IR onboard Venus express // Planetary and Space Science. 2015. V. 113. P. 66–77.
[9] Haus, R., et al. Radiative energy balance of Venus based on improved models of the middle and lower atmosphere // Icarus. 2016. V. 272. P. 178–205.

O_2 NIGHTGLOW AND DYNAMICS OF VENUS ATMOSPHERE AROUND 100 km FROM VIRTIS-M/VEX

D.A. Gorinov [1], L.V. Zasova [1], A.V. Shakun [1], I.V. Khatuntsev [1]
[1] *Space Research Institute of the Russian Academy of Sciences, dmitry_gorinov@rssi.ru*

KEYWORDS:
Venus, atmosphere, oxygen, nightglow, dynamics.

INTRODUCTION:
The infrared spectra observed in the IR channel of VIRTIS (M-IR) cover a spectral range of 1–5.1 μm with the spectral resolution of 14 nm. The observations were carried out in two different modes, nadir and limb. The 1.27 μm oxygen airglow forms bright "patches" on Venus nightside an it was monitored by VIRTIS from 2006 to 2008.

RESULTS:
From nadir observations it was found that intensity and position of the maximum of emission on the night side are strongly variable: intensity changes up to maximal observed value of 6.5 MR with an averaged over the Southern hemisphere value of 0.35 ± 0.3 MR. Bright spots can be observed at any nightside local time, from morning to evening terminators. Accurate retrieval of the thermal emission [1] allows obtaining more detailed average map than published earlier [2, 3]. The general high intensity area was found in the exact antisolar point. The O_2 airglow intensity substantially decreases to terminators. Both these facts demonstrate the significant role of the subsolar-antisolar (SS-AS) circulation.

However, maximum of the O2 airglow intensity in the average map is observed at 22 – 23 hours, and the minimum – at the morning terminator. The shift is explained by the thermal tides, which have a peak at 1 – 2 hours before midnight [4, 5]. Asymmetry between the evening and morning part on the nightside can be related to the horizontal wind speed asymmetry in [6]: the speed of horizontal wind in the midnight direction from the morning side exceeds the flow moving in the opposite direction by 10 – 30 m/s. Asymmetry of the SS - AS was found at 120 - 140 km from the observations of NO local time distribution on night side: maximum emission was found around 2 h local time (from Pioneer Venus and SPICAV/VEx data). From those results it was concluded that the zonal superrotation above 100 km still has an impact on dynamics, up to 60 m/s [7]

From limb observations it was found that the altitude of the O_2 peak is located at 97 ± 3 km, with a halfwidth of 8 ± 3 km and average intensity of 0.45 ± 0.3 MR [3].

REFERENCES:
[1] Shakun, A.V., Zasova, L.V., Piccioni, G., Drossart, P., & Migliorini, A. Investigation of oxygen O2(a1Δg) emission on the nightside of Venus: Nadir data of the VIRTIS-M experiment of the Venus Express mission // Cosmic Research. 2010. V. 48(3), P. 232 – 239
[2] Gérard, J. - C., Saglam, A., Piccioni, G., Drossart, P., Cox, C., Erard, S., et al. Distribution of the O2 infrared nightglow observed with VIRTIS on board Venus Express // Geophysical Research Letters. 2008. V. 35, L02207
[3] Piccioni, G., Zasova, L., Migliorini, A., Drossart, P., Shakun, A., García Muñoz, A., et al. Near-IR oxygen nightglow observed by VIRTIS in the Venus upper atmosphere // Journal of Geophysical Research. 2009. V. 114, E00B38
[4] Zasova, L., Khatountsev, I.V., Ignatiev, N.I., Moroz, V.I., Local time variations of the middle atmosphere of Venus: Solar-related structures // Advances in Space Research. 2002. V. 29, I. 2, P. 243 - 248
[5] Zasova, L. V., Ignatiev, N. I., Khatuntsev, I. V., & Linkin, V. M. Structure of the Venus atmosphere // Planetary and Space Science. 2007. V. 55(12), P. 1712 – 1728.
[6] Gorinov, D.A., Khatuntsev, I.V., Zasova, L.V., Turin, A.V., Piccioni, G. Circulation of Venusian Atmosphere at 90 – 110 km Based on Apparent Motions of the O_2 1.27 μm Nightglow From VIRTIS-M (Venus Express) Data // Geophysical Research Letters. 2018. V. 45
[7] Brecht, A.S., Bougher, S.W., Gérard, J. - C., Parkinson, C.D., Rafkin, S., Foster, B. Understanding the variability of nightside temperatures, NO UV and O_2 IR

LARGE SCALE VOLCANISM AND THE POSSIBLE HEAT-DEATH OF VENUS LIKE WORLDS

M.J. Way [1], R.E Ernst [3,4], J.D. Scargle [5]

[1] *NASA Goddard Institute for Space Studies, 2880 Broadway, NY NY, USA, Michael.J.Way@nasa.gov;*

[2] *Theoretical Astrophysics, Department of Physics and Astronomy, Uppsala University, Sweden 3 Department of Earth Sciences, Carleton University, Ottawa, Canada K1S 5B6;*

[4] *Faculty of Geology and Geography, Tomsk State University, Tomsk, 634050, Russia;*

[5] *Astrobiology and Space Science Division, NASA Ames Research Center, MS 245, Moffett Field, USA*

KEYWORDS:
Large Igneous Provinces, Runaway Greenhouse, Venus, Earth.

INTRODUCTION:

Large scale volcanism has played a critical role in the long-term habitability of Earth and possibly Venus. Large Igneous Provinces (LIPs) are in fact the cause of most major extinction events in Earth's history, contrary to the popular belief about the devastation from large bolides. We examine the timing of Large Igneous Provinces (LIPs) through Earth's history [1] to estimate the likelihood of nearly simultaneous events that could drive a planet into an extreme moist or runaway greenhouse, quenching subductive plate tectonics. Such events would end volatile cycling and may have driven Venus from a cool temperate state into the heat-death we see today. Using the Earth's LIP [1] we have found that LIP events are distributed randomly throughout the past 3 billion years. A conservative estimate of the rate of LIPs in a random history statistically the same as Earth's, pairs and triplets of LIPs closer in time than 0.1–1 million years are likely. This simultaneity threshold is significant to the extent that it is less than the time over which environmental effects have been shown to persist, for example in the Siberian Traps record [2, 3]. With the recent mission selections of VERITAS and EnVision it may be possible for their high resolution radar maps to distinguish LIPs in the surface record we can see today on Venus.

ACKNOWLEDGMENTS:

This work has been submitted to Geophysical Research Letters: https://doi.org/10.1002/essoar.10506641.1

REFERENCES:

[1] Ernst, R.E. et al. 2021. Large Igneous Province Record Through Time and Implications for Secular Environmental Changes and Geological Time-Scale Boundaries. In: Ernst, R.E., Dickson, A.J., Bekker, A. (eds.) Large Igneous Provinces: A Driver of Global Environmental and Biotic Changes. AGU Geophysical Monograph 255 P. 3–26.

[2] Burgess, S.D. et al. 2014. High-precision timeline for Earth's most severe extinction. Proceedings of the National Academy of Sciences, 111: 3316–3321 [correction 2014, 111: 5050].

[3] Burgess, S.D. & Bowring, S.A. 2015. High-precision geochronology confirms voluminous magmatism before, during and after Earth's most severe extinction. Sci. Adv. 1 (7), e1500470. http://dx.doi.org/10.1126/sciadv.1500470.

CONTRIBUTIONS OF VOLATILES TO THE VENUS ATMOSPHERE FROM THE OBSERVED EXTRUSIVE VOLCANIC RECORD: IMPLICATIONS FOR THE HISTORY OF THE VENUS ATMOSPHERE

J.W. Head [1], L. Wilson [1,2], M.A. Ivanov [3] & R. Wordsworth [4]
[1] *Brown Univ., Providence RI, USA, james_head@brown.edu;*
[2] *Lancaster Univ., Lancaster, UK;*
[3] *Vernadsky Institute, Moscow, Russia;*
[4] *Harvard Univ., Cambridge MA, USA*

KEYWORDS:
Venus, atmospheric history, volatiles, geologic history, volcanism, effusive eruptions, explosive eruptions.

INTRODUCTION:
The nature of the geologically recent runaway greenhouse Venus atmosphere, its relation to Venus geologic and geodynamic history, and why it is so different from that of the Earth, are all questions that have perplexed planetary scientists since the early Space Age [1]. A number of recent studies have focused on *forward-modeling* of the origin and evolution of the Venus atmosphere with the current atmosphere as the end-product, defining and assessing the nature and abundance of volatiles derived from the interior and from space, their influence on the atmosphere and interaction with the surface, and the rates of their loss to space [2 - 4]. Several *forward models* have found that more Earth-like clement conditions [2], with oceans and an N_2-dominant atmosphere [3 - 4], may have existed into the last ~ 20 % of the history of Venus (Fig. 1), the age of the oldest observed geologic units [5], the tesserae [6], and the global volcanic plains that followed [7].

Critical to the assessment of these models is the role of volcanism, the primary process of transfer of volatiles from the Venus mantle to the surface and atmosphere. In this study, we use the current atmosphere as a baseline and work *backward* in time, assessing the nature and magnitude of the major phases of volcanism revealed in the geological record [5], their style and magnitude of volatile output [7], and the candidate effects of their volatile release on the observed atmosphere. The atmospheric pressure of the current Venus atmosphere (93 bars) is sufficient to significantly inhibit the exsolution of key volatile species during effusive eruptions [8 - 9] and to preclude explosive volcanic activity that could deliver exsolved volatiles high into the atmosphere, except in extreme cases where the volatile content exceeds several wt% [9].

We specifically address the following questions: 1. Does the eruption of the *total volume of extrusive deposits observed on Venus contribute significantly* to the current atmosphere? 2. How does the volume of the most recent phase of volcanism (lobate plains; large shield volcanoes) affect the interpretation that observed atmosphere SO_2 levels are related to current ongoing volcanism? 3. Could the period of near-global volcanic resurfacing (psh, $rp_{1,2}$) have *produced* the current atmosphere? 4. Do the characteristics of the oldest units (tesserae) shed any light on whether the current atmosphere largely predates the observed geologic record (dating from sometime in the first 80% of Venus history) or was produced during the last 20 % of the history of Venus? Addressing these questions provides a framework on which to define the array of evolutionary pathways that Venus and Earth might have followed, refine further the future questions and approaches to the exploration of Venus, and assist in the interpretation of the dozens of new Venus-like exoplanets.

The Magellan mission provided global image coverage that enabled identification of geologic units and their stratigraphic relationships, the construction of a global geologic map [5], assessments of the nature and role of volca-

nism [7] and tectonism [10] with time, and estimates of the absolute timescale of these events [13]. The observed geological record provides an estimate of the nature of volcanic units, their areal coverage, their stratigraphic relationships and thicknesses, and estimates of the time scale of their emplacement. A summary of the key data for volcanism is presented in [7], their Fig. 26 and Table 5, Table 1 here.

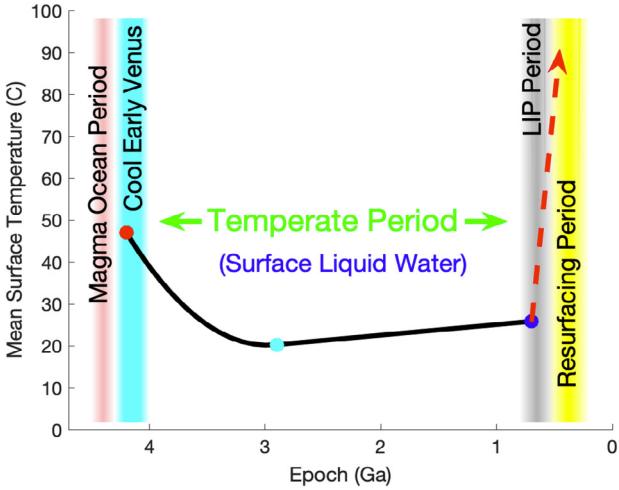


Fig. 1. Possible climate history (Way & Del Genio, 2020).

Table 1.

Unit	Exposed Area (10^6km^2)	Max Area (10^6km^2)	Mass (10^{20} kg) at specific thickness (km)					
			0.1	0.2	0.3	0.4	0.5	N/A
psh	84.5	320.3	0.96	1.92				
rp1	150.7	235.8				2.82	3.54	
rp2	44.8	85.1	0.27	0.51				
pl (lobate plains)	40.3	40.3			0.36		0.60	
pl (large volcanoes)[a]								0.255
pl (large volcanoes)[b]								0.51
total eruptives				2.43			4.14	0.765

We converted the volumes of the main volcanic units [7; Table 1] to lava/magma masses using a density of 3000 kg·m^{-3}. Next, we chose the *upper* value where there is a choice of 2 possible thicknesses, and added the contributions from *all* of the units ("total eruptives" in Table 1); summing the values of the "total eruptives" gives the absolute upper limit estimate of the mass of documented volcanics that could contribute to the atmosphere, 7.335×10^{20} kg. We then compare this with the current mass of the Venus atmosphere (4.8×10^{20} kg). We find that in order to make the current atmosphere from the above volcanics, *the magma would have to consist of 65.4% by mass volatiles*, which is, of course, impossible. We conclude that the *grand total* of the currently documented volcanics can not have produced other than a very small fraction of the current atmosphere.

Exsolution of volatiles during volcanic eruptions is significantly dependent on surface atmospheric pressure [8 - 9]. As a specific example, we next looked at the contributions of SO_2 to the current atmosphere. The current SO_2 content of the 4.8×10^{20} kg atmosphere is 150 ppm, so there is a mass of 7.2×10^{16} kg in the atmosphere. Gaillard and Scaillet [3; their Fig. 3] shows that the amount of S released from their typical basalt, even if it is decompressed to the lowest Venus surface pressure, 40 bars in the highest terrains, is only ~ 1.6 % of the assumed inventory, 1000 ppm, i.e., 16 ppm of S. SO_2

has a molecular mass of 64, double that of S, so this represents 32 ppm of SO_2. The total erupted volcanic mass is 7.335×10^{20} kg; 32 ppm of that is 2.35×10^{16} kg. In summary, the *total mass of all volcanics* could have released 2.35×10^{16} kg of the current 7.2×10^{16} kg, i.e. 32.6 % of the current SO_2 in the atmosphere. Taking only the recent volcanism total amount (pl, 1.365×10^{20} kg) shows that this is only 18.6% of the grand total. We conclude that it is highly unlikely that a significant amount of SO_2 is being constantly supplied to the atmosphere by recent volcanic activity, particularly in the period of eruption of pl emplacement, representing the vast majority of the total observed geological record.

DISCUSSION AND CONCLUSIONS:

On the basis of these data and simple calculations we present the following findings and explore their implications for the climate history of Venus:

1. The current high atmospheric pressure severely inhibits the degassing of mantle-derived S, H_2O and CO_2 brought to the surface by volcanism and its contribution to the atmosphere [8–9].
2. The current high atmospheric pressure severely inhibits plinian explosive eruptions that can deliver volatiles directly into the atmosphere on Earth and in Mars-like low-atmosphere density environments [9].
3. The *total volume* of lava erupted in the stratigraphically youngest period of the observed record (pl, rift-related, volcanic edifices) is insufficient to account for the current abundance of SO_2 in the atmosphere; thus, it seems highly unlikely that current and recently ongoing volcanism could be maintaining the currently observed 'elevated' levels of SO_2 in the atmosphere [11].
4. The *total volume* of lava erupted in the period of *global volcanic resurfacing* (psh, rp_1, rp_2) is insufficient to produce the CO_2 atmosphere observed today, even if the ambient atmospheric pressure at that time was only 50 % of what it is today. Therefore, a very significant part of the current CO_2 atmosphere must have been inherited from a time prior to the observed geologic record, sometime in the first ~ 80 % of Venus history.
5. The amount of water degassed to the atmosphere during the period of *global volcanic resurfacing* would have been minimal, even if the atmospheric pressure was only 10 % of what it is today. Therefore, the current low atmospheric water content may be an inherent characteristic of the ambient atmosphere and not necessarily require enhanced loss rates to space in at least the last 20 % of Venus history.
6. Because of the fundamental effect of atmospheric pressure on the quantity of volatiles that will be degassed, varying the nature of the mantle melts over a wide range of magma compositions and mantle fO_2 has minimal influence on the outcome.
7. If the period of *global volcanic resurfacing* was insufficient to produce the current atmosphere, then it seems unlikely that the immediately preceding period of tessera deformation could have occurred in the presence of a more clement, Earth-like atmosphere and climate with an active surface water cycle [12]. Higher resolution documentation of any types of atmospheric erosion patterns in the tessera terrain will be a critical test.
8. The current Venus atmosphere may be a "fossil atmosphere", largely inherited from a previous epoch in Venus history, and if so, may provide significant insight into the conditions during the first 80% of Venus history.
9. If episodic periods of *global volcanic resurfacing* (such as seen in the observed recent geologic record) were responsible for building up the "fossil atmosphere", then assuming an initial 1 bar atmosphere, more than 90 similar *global volcanic resurfacing periods* would be required to produce the currently observed CO_2 atmosphere.
10. A critical question is: What was the atmospheric pressure/water content/solar insolation 'tipping point' that led to the general stabilization of this "fossil atmosphere"?

On the basis of these preliminary conclusions, we are now exploring 1) volatile contributions with time, using the range of estimates for volumes [7], the several suggested time-scales for the observed geologic record [13], and the pressure-dependence of volatile exsolution and speciation [8], 2) an updated model for the ascent and eruption of magma under different surface pressures, using the lunar end-member as a baseline [14], 3) a wider range of mantle compositions and fO_2 [15], 4) a wider range of candidate fluxes in individual eruptions, 5) improving the definition of parameter space for the occurrence and nature of explosive eruptions and the nature, interaction and dispersal of volatiles and tephra, and 6) assessing the predictions of these sets of results for the fate of the volatile species that are produced during eruptions (interaction with both the surface [15] and existing atmosphere).

REFERENCES:

[1] Taylor et al., 2018, SSR, 214, 34;
[2] Bullock & Grinspoon, 1996, JGR, 101, 7521;
[3] Way et al., 2016, GRL, 43, 8376;
[4] Way & Del Genio, 2020, JGR, 125;
[5] Ivanov & Head, 2011, PSS, 59, 1559;
[6] Ivanov & Head, 1996, JGR, 101, 14861;
[7] Ivanov & Head, 2013, PSS, 84, 66;
[8] Gaillard & Scaillet, 2014, EPSL 403, 307;
[9] Head & Wilson, 1986, JGR 91, 9407;
[10] Ivanov & Head, 2015, PSS, 113, 10;
[11] Esposito, 1984, Science 223, 1072;
[12] Khawja et al., 2020, Nat. Comm., 11, 5789;
[13] Kreslavsky et al., 2015, Icarus 250, 438;
[14] Wilson & Head, 2018, GRL 45, 5852;
[15] Zolotov, 2018, Rev. Min. Geochem. 84, 351.

PIT CRATER CHAINS, GRABEN AND RELATED FEATURES IN OVDA TESSERA, VENUS: IMPLICATIONS FOR DIKE EMPLACEMENT AND VOLATILE LOSS

M.A. Ivanov [1], J.W. Head [2], L. Wilson [3]
[1] *Vernadsky Institute, RAS, Moscow, Russia, mikhail_ivanov@brown.edu;*
[2] *Brown University, Providence RI, USA;*
[3] *Lancaster University, Lancaster, UK*

KEYWORDS:
Venus, Ovda Region, volcanism, pit chains, graben, dikes.

INTRODUCTION:
The stratigraphically oldest exposed terrain on Venus, the highly tectonically deformed radar-bright tesserae, form uplands and highlands embayed and partly covered by radar-dark volcanic plains. At issue is the extent of volcanism within the tesserae, the volcanic or sedimentary origin of many occurrences of these radar-dark plains, the relation of volcanic and weathering processes to the sequence of tesserae tectonic deformation, and the mechanism of tesserae radar-dark plains formation. We report here on the discovery and documentation of tesserae pit crater chains and graben complexes in Ovda Regio, (Fig. 1), a class of features that occur at different altitudes in the tesserae terrain and elsewhere on Venus [1, 2].

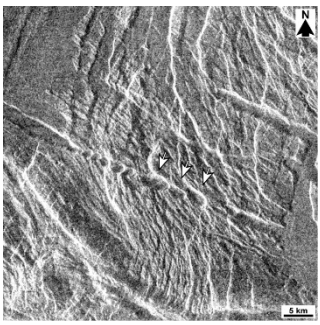


Fig. 1. An example of pit chains and graben identified in Ovda Regio. Arrows indicate elongated, graben-like pits formed by coalescent of individual pits. Graben segments on the left and right are at the lower elevations and the pit chain (center) is relatively higher. Graben on the left cur the surface of intratessera plains.

ABUNDANCY, DIMENSIONS, SPATIAL AND TOPOGRAPHIC DISTRIBUTIONS OF PIT CHAINS AND GRABEN:
We conducted our study in an area of Ovda Region covering ~ $4.5 \cdot 10^6$ km^2, using mosaics of the F-MIDR images (75 m/px resolution) and identified 435 pit chains that consist usually of 2 to 4 pits (up to ~ 30 pits, the total number of the documented chained pits is 2241) in the diameter range 0.3 - 2.9 km with the mean diameter of ~ 0.78 ± 0.35 km. The chain length depends upon the number of pits and varies from 0.6 to 57.3 km with the mean length of ~ 6.2 ± 7.1 km. Many of the chains are arranged along the same trend that can be traced for a few hundred kilometers. Within the chains, pits can be separated from each other and appear as circular features with the mean spacing of ~ 1.5 ± 0.9 km. Quite often, however, the pits coalesce each other and in these cases some of them form elongated graben-like features.

The pit chains in Ovda Regio occur over a wide range of elevations, from ~ 0 to ~ 6 km (Fig. 2a) with the mode of the topographic distribution between 3 - 4.5 km and the mean elevation of ~ 3.4 ± 1.0 km. Although the pit chains occur throughout Ovda, their spatial distribution is non-random and they preferentially are concentrated at the northern and southern edges of central Ovda. In these regions, the density of the pit chains can reach ~ 6.5 chains per 10^5 km^2.

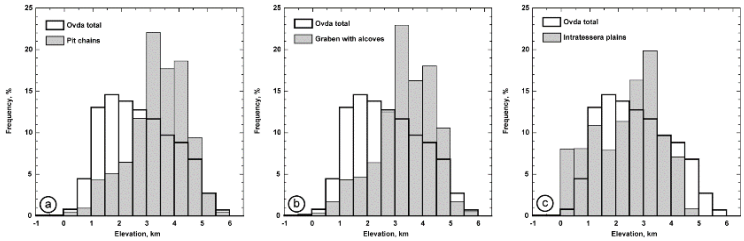


Fig. 2. Hypsograms of the pit chains (a), graben (b), and intratessera plains (c) showing the topographic distribution of these features relative to the topographic variations of tessera in Ovda Regio.

The pit chains usually occur in a tight spatial association with graben that often begin in broad U-shaped troughs with rounded tips and scalloped edges. These graben and pit chains usually are aligned along same trends in which the graben segments are alternating with the pit chains (Fig. 1). In our study, we have identified and mapped 1015 such graben that are either completely within the Ovda highland or cross its boundary

The length of the graben that display associated pit craters varies broadly from ~ 1 to ~ 315 km with the mean value of ~ 14.6 ± 20.2 km. In many cases, however, the shorter individual graben form chains that can extend up to 600 km. The maximum visible width of the graben varies from the resolution limit of the F-MIDR mosaics to ~ 14 km with a mean value of ~ 1.5 ± 1.4 km. The topographic distribution of the graben almost exactly coincides with that of the pit chains (Fig. 2b) and the spatial distribution of the graben mimics that of pit chains.

In rare cases, the graben represent sources of sinuous channels that have no tributaries and that sometimes demonstrate braided pattern. On the basis of their morphologic characteristics, the channels differ significantly from fluvial features either on Earth or Titan, and the channels that form the valley networks on Mars. These channels most closely resemble the population of sinuous rilles on the Moon [3] and we interpret the channels in Ovda as volcanic features.

STRATIGRAPHIC POSITION OF THE PIT CHAINS/GRABEN COMPLEXES IN OVDA TESSERA:

As we mapped the pit chains and graben, we paid special attention to their age relationships relative to the surrounding features. Given that the graben represent long and contiguous features, they are an excellent cross-cutting structure to aid in the relative age analysis. We identified three situations in which the stratigraphic position of the graben can be assessed: (1) *Younger graben*: these cut tessera-forming structures and intratessera plains; (2) *Older graben*: these are deformed by tessera-forming structures; (3) *Pre-plains graben*: materials of the intratessera plains embay the graben.

In our study, we have found only 16 graben (~ 2 % of the total population) that are deformed. The other documented graben postdate the tessera-forming structures. Out of 661 graben that are in contact with the intratessera plains, only 19 (~ 3%) appear as partly embayed by material of the intratessera plains. Thus, the absolute majority of the graben are among the youngest features of Ovda Tessera that postdate both the main tectonic episodes of the tessera formation and emplacement of the intratessera plains.

DISCUSSION/CONCLUSIONS:

The following characteristics of the pit chains and graben suggest that the pits and graben have a common origin: (1) coincidence of the spatial and topographic distributions of the pit chains and graben; (2) their alignment along the same trends in which the pit chains and graben segments are alternating; (3) existence of transitional morphologies between individual pits and graben (Fig. 1).

Similarly looking pit chains in association with graben on Mars [Wyrick et al., 2004 and references therein] were usually interpreted as having either a pure tectonic or a volcanotectonic origin. In the framework of the tectonic model, pits represent collapse structures above voids formed due to crustal exten-

sion [4–6]. In the volcanotectonic models, pits and graben represent the surface manifestations of stalled, hear-surface ascending dikes [8–12]. Although both mechanisms can be applied to the formation of the pit chain/graben complexes in Ovda Regio, the association of some graben with lava channels favors the volcanotectonic interpretation. In framework of the volcanotectonic model, the graben are the result of the surface subsidence between fault planes formed in crustal rocks as a dike ascends and stalls [see summary in 13–15] and the pits are the results of the surface collapse in voids left after exsolution and diffusion of magmatic gases.

If this interpretation is correct, then the pit chains and graben represent specific stages of dike emplacement and volcanism within a large tessera region. At earlier stages, extensive radar-dark plains (the intratessera plains) formed in broad topographic depressions. Although these plains occur at different elevations, the mode of their topographic distribution is shifted toward lower elevations relative to that of the pit chains and graben (Fig. 2c) and on average the surface of the plains (~ 2.42 ± 1.10 km) is ~ 1 km lower than the mean elevation of the pit chains and graben (~ 3.40 ± 1.00 km). The mean graben width, ~ 1.5 km, suggest that the depth to the dike tip is ~ 1.3 km and, thus, the upper edges of the dikes are at about the same elevation as the average elevation of the intratessera plains surface.

The dikes that are marked by the pit chains and graben, however, cannot be the sources of the intratessera plains because they postdate most of the plains (Fig. 1). In fact, except for the rare lava channels that occur at the topographically lower ends of some graben, there is no evidence for volcanic deposits in association with both the pits and graben. This means that the later dikes were able to cause deformation of the surface and only in exceptional cases erupted magmatic material on the surface. According to theory [16, 17], this could occur in Ovda Tessera due to the fact that more gas was exsolved in the stalled dike at higher elevation and lower overburden pressure of the ambient atmosphere, together with effects from neutral buoyance zone migration due to the same altitude-dependent pressure effect.

This increased exsolved gas abundance in the later dikes is consistent with the abundant chained pit craters/graben found in Ovda Regio toward higher elevations (Fig. 2a) and the usual alternation of the pit chains and graben along a single trend. Thus, such alternation may reflect local topographic variations along the dike strike and preferential formation of the pits at relatively higher elevations where the atmospheric pressure is lower. In these areas, the lower ambient pressure may cause enhanced degassing of magma, gas diffusion to the surface and subsequent collapse into the void space to form pits. Fig. 1 clearly shows that the pits preferentially occur at higher elevations in Ovda Regio, supporting this hypothesis. We are currently modelling magma degassing as a function of elevation and reduced atmospheric pressure in order to assess this hypothesis further.

REFERENCES:

[1] Davey S.C., Ernst R.E., Samson C., Grosfils E.B. Hierarchical clustering of pit crater chains on Venus. Can. J. Earth Sci. // 2013. V.50. P. 109–126.
[2] Sawford C., Ernst R.E., Samson C., Davey S.C. Pit crater chains in the Nyx Mons region, Venus. LPSC 46. // 2015. #1283.
[3] Hurwitz D.M., Head J.W., Hiesinger H. Lunar sinuous rilles: Distribution, characteristics, and implications for their origin. Planet. Space Sci. // 2013. V. 79–80. P. 1–38.
[4] Wyrick D., Ferrill D.A., Morris A.P., Colton S.L., Sims D.W. Distribution, morphology, and origins of Martian pit crater chains. Journ. Geophys. Res.. // 2004. V.109. E06005.
[5] Tanaka K.L., Golombek M.P. Martian tension fractures and the formation of grabens and collapse features at Valles Marineris. Proceedings of LPSC. // 1989. V. 19. P. 383–396.
[6] Ferrill D.A., Morris A.P., Waiting D.J., Franklin N.M., Sims D.W. Influence of gravity on the geometry of Martian normal faults. LPSC 34. // 2003. #2050.
[7] Ferrill D.A., Morris A.P. Dilational normal faults. J. Struct. Geol. // 2003. V. 25. P. 183–196.
[8] Greeley R. Lava tubes and channels in the Lunar Marius Hills. The Moon. // 1971. V.3. P. 289–314.
[9] Greeley R. The role of lava tubes in Hawaiian volcanoes. in: U.S. Geol. Surv. Prof. Pap., 1350. // 1987. PP. 1589–1602.

[10] Head J.W., Lunar volcanism in space and time. Reviews of geophysics and space physics. // 1976. V. 14. P. 265–300.
[11] Haruyama J., Hioki K., Shirao M. et al. (11 others). Possible lunar lava tube skylight observed by SELENE cameras. Geophys. Res. Lett. // 2009. V. 36, L21206.
[12] Robinson M.S., Ashley J.W., Boyd A.K., Wagner R.V., Speyerer E.J., Hawke B.R., Hiesinger H, van der Bogert C.H. Confirmation of sublunarean voids and thin layering in mare deposits. Planet. Space Sci.. // 2012. V. 69. P. 18–27.
[13] Rivalta E., Taisne B., Bunger A.P., Katz R.F. A review of mechanical models of dike propagation: Schools of thought, results and future directions. Tectonophysics. // 2015. V. 638. P.1–42.
[14] Head J.W., Wilson L. Lunar graben formation due to near-surface deformation accompanying dike emplacement. Planet. Space Sci.. // 1993. V. 41. P. 719–727.
[15] Head J.W., Wilson L. Generation, ascent and eruption of magma on the Moon: New insights into source depths, magma supply, intrusions and effusive/explosive eruptions (part 2: observations). Icarus. // 2017. V. 283. P. 176–223.
[16] Head J.W., Wilson L. Volcanic processes and landforms on Venus: Theory, predictions, and observations. Journ. Geophys. Res. // 1986. V. 91. P. 9407–9446.
[17] Head J.W., Wilson L. Magma reservoirs and neutral buoyancy zones on Venus: Implications for the formation and evolution of volcanic landforms. Journ. Geophys. Res. // 1992. V. 97. P. 3877–3903.

ORIGIN AND EVOLUTION OF LINEAMENTS IN NW WAWALAG PLANITIA, STANTON QUADRANGLE (V-38), VENUS

J. Ounar [1], H. El Bilal i[2] R.E. Ernst [2,3] J.W. Head [4], N. Youbi [1]
[1] *Department of Geology, Faculty of Sciences-Semlalia, Cadi Ayyad University, Marrakesh, Morocco, jihaneounar@gmail.com;*
[2] *Department of Earth Sciences, Carleton University, Ottawa, Ontario, Canada, richard.ernst@ernstgeosciences.com;*
[3] *Faculty of Geology and Geography, Tomsk State University, Tomsk, Russia;*
[4] *Department of Earth, Environmental and Planetary Sciences, Brown University, Providence, Rhode Island, USA*

KEYWORDS:
Wawalag planitia, wrinkle ridges, dykes, Stanton Quadrangle, lineaments

INTRODUCTION:
In the global stratigraphic framework of [1–2], planitia host volcanic plains and represent the oldest units after the tesserae.

OUTSTANDING QUESTIONS ON LINEAMENTS IN REGIONAL VOLCANIC PLAINS:
1) What is the origin and sequence of lineaments in the regional plains that make up the planitia?, 2) What is the sense of deformation (e.g., extension, compression, shear)?, 3) Do the lineaments decrease in abundance as a function of time (distribution in older versus younger units)?, 4) What is their orientation (particularly in relation to regional structure)?, 5) Do any of these lineaments show radial or circumferential structure that might be linked to potential centres of magmatism [3]?, and 6) Is there any evidence for aqueous erosion affecting their morphology and sequence that might be related to global climate change (e.g. [4–6]?

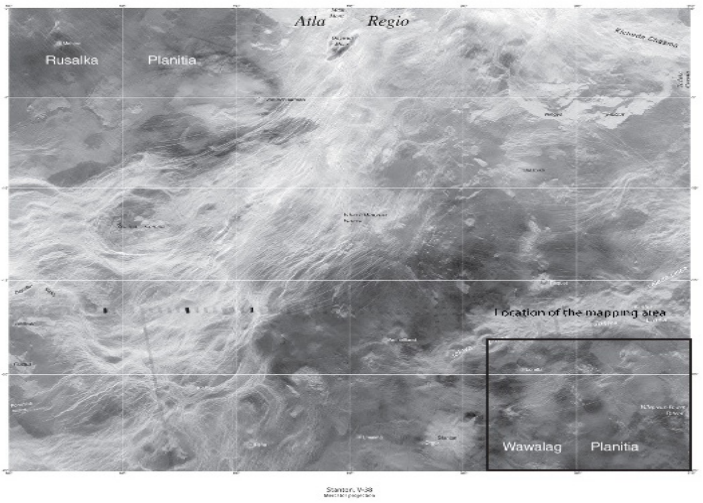


Fig. 1. Magellan image with labelling of Stanton quadrangle (V-38) with black box showing the location of detailed mapping in Figure 2.

WAWALAG PLANITIA:
We have selected Wawalag Planitia for similar detailed mapping (1 : 500,000) in order to attempt to provide insights into the above questions. Wawalag Planitia spans southeast Stanton (V – 38) southwest Taussig (V-39), northeast Isabella (V – 50) and northwest Imdr Regio (V – 51). Of these, only V – 39 has been mapped at the quadrangle scale [7]. Preliminary geological mapping results for V-50 are reported in [8–9]. Preliminary mapping results for V – 51 are reported in [10].

PRELIMINARY LINEAMENT MAPPING:

Initial mapping of the portion of Wawalag Planitia in southeast Stanton Quadrangle (Fig. 2) reveals a complex pattern of extensional lineament systems and these are provisionally interpreted to represent dyke swarms [3]. Both radiating and circumferential swarms have been identified and these both are associated with magmatic centres.

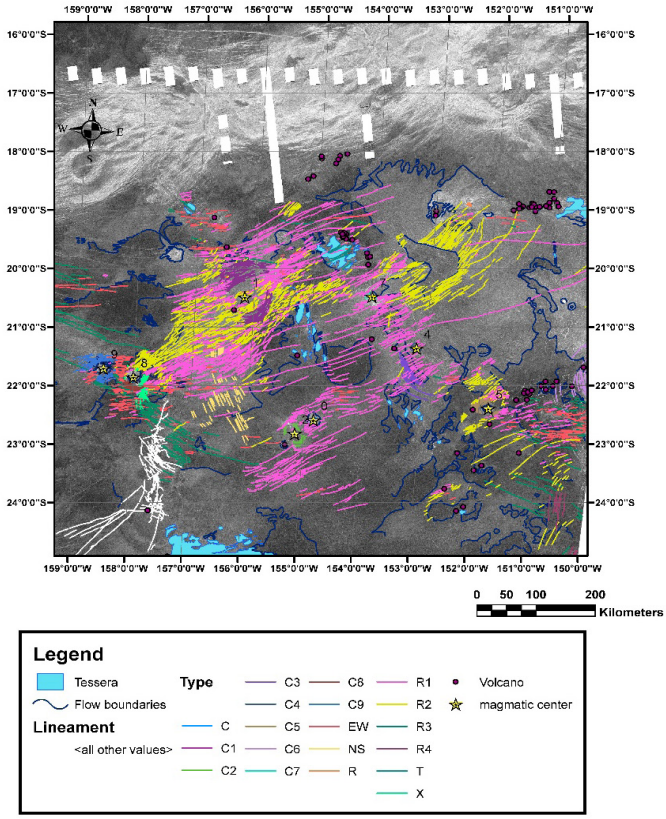


Fig. 2. Initial mapping results in the SE Stanton quadrangle (see location in Figure 1). Lines indicate different extensional lineament systems. R-labels indicate recognized radiating systems, C-labels indicate circumferential systems. Additional labels are for systems with currently uncertain overall geometry. Areas of tesserae are outlined and some plains flow boundaries are shown.

In addition, we have begun the mapping of flow unit boundaries as part of this detailed mapping project, also at 1 : 500 000 scale).

REFERENCES:

[1] Ivanov, M.A., Head, J.W. Global geological map of Venus // Planet. Space Sci., 2011, V 59, P. 1559–1600;

[2] Ivanov, M.A., Head, J.W. The history of tectonism on Venus: A stratigraphic analysis. Planetary and Space Science, 2015, V. 13–114, P. 10–32;

[3] Buchan, K.L., Ernst, R.E. Plumbing systems of large igneous provinces (LIPs) on Earth and Venus: Investigating the role of giant circumferential and radiating dyke swarms, coronae and novae, and mid-crustal intrusive complexes // Gondwana Research, 2021 (in press). https://doi.org/10.1016/j.gr.2021.02.014;

[4] Ernst, R.E., Samson, C., Kuiper, Y.D., Khawja, S. (2019). Geological testing of climate change models on Venus. 50th Lunar and Planetary Science Conference 2019 (LPI Contrib. No. 2132), abstract no. 2382;

[5] Ernst, R.E., Samson, C., Bethell, E., Khawja, S. (2020) Geological constraints on the timing of the extreme warming climate transition on Venus, Extended Abstract No. 1174, 51st Lunar and Planetary Science Conference, Houston, USA;

[6] Khawja, S., Ernst, R.E., Samson, C., Byrne, P.K., Ghail, R.C., MacLellan, L. Tesserae on Venus may preserve evidence of fluvial erosion. // Nature Communications, 2020, V. 11, Article No. 5789. https://doi.org/10.1038/s41467-020-19336-1;

[7] Brian, A.W., Stofan, E.R., Guest, J.E. Geologic Map of the Taussig Quadrangle (V – 39), Venus. // United States Geological Survey, Scientific Investigations Map 2813;
[8] Bleamaster, L.F. Geologic mapping of Isabella quadrangle (V 50), Venus. // Lunar and Planetary Science Conference XXXVII, 2006, abstr. Number 2233;
[9] Bleamaster, L.F. Geologic Mapping of Isabella Quadrangle (V – 50) and Helen Planitia, Venus // Abstracts of the Annual Meeting of Planetary Geologic Mappers, Flagstaff, AZ, 2008;
[10] Lang, N.P., Thomson, B.J. Volcanic geology of the Imdr Regio (V – 51) Quadrangle, Venus: An initial look. // Planetary Geologic Mappers 2020 (LIP Contrib. No. 2357), abstract no. 7037.

MASS SPECTROMETIC MEASUREMENTS OF COMPLEX MOLECULES DURING HYPERVELOCITY PLANETARY FLYBYS

R. Fausch [1], P. Wurz [1], and M. Tulej [1]
[1] *Physics Institute, University of Bern, Sidlerstrasse 5, 3012 Bern, Switzerland, rico.fausch@unibe.ch*

KEYWORDS:
Mass spectrometry; In situ analysis during hypervelocity flybys; Chemical Composition; Nobel gases; Venus; Intact bio signatures; Ocean Worlds.

Sensitive chemical composition analyses during planetary flybys remain challenging because of the high velocities of the spacecraft with respect to the atmospheric gas, with typical encounter velocities of about 2 to 20 km/s. This results in both fragmentation and fractionation of the molecules in the mass spectrometers used so far. In deep space exploration, mass spectrometers are the instrument of choice to analyse the chemical composition of celestial bodies' atmosphere to improve our understanding of the origin and evolution of Solar System objects. The growing interest in complex molecules, especially biomolecules and biomarkers has fostered the development of specialised instruments that can analyse them.

Current instrumentation uses two modes to analyse the fast flow of neutral gas (and ions) streaming into the instrument. In open source mode, species entering the instrument are directly ionised and the formed ions need to be deflected into the mass analyser by electrostatic means to be mass analysed, which limits the relative encounter velocities to about 5 km/s. In closed source mode, the gas is first thermalized by many collisions with the wall of the antechamber, and the thermalised gas is then passed on to the ionisation stage. Closed sources are considered for higher relative encounter velocities but the species may fragment or chemically alter during these hypervelocity impacts at the wall of the antechamber. Thus, inferring the original molecules' identity is difficult if not impossible, especially the larger the investigated molecules become.

We discuss the possibility of analysing complex chemical species during hypervelocity flybys without the limitations of open and closed ion sources. Our novel ion optical system directly measures the atmospheric species with a direct entrance source system [1]. This system combines the advantages of the open and closed source system namely preserving the chemical nature of the molecules and enabling measurements at hypervelocity. The promising results of this ion optical system provides new possibilities for the analysis of complex (bio) molecules during flybys of Venus, Enceladus, Io, Europa, Ganymede, and others [2].

REFERENCES:

[1] Fausch R., Wurz P., Tulej M., and Rohner U. CubeSatTOF: Planetary Atmospheres Analyzed with a 1U High-Performance Time-Of-Flight Mass Spectrometer. Proceedings of the Small Satellite Conference. 2020.
[2] Fausch R., Wurz P., Cotting B., Rohner U., and Tulej M. Direct Measurement of Neutral Gas during Hypervelocity Planetary Flybys. 2022 IEEE Aerospace Conference. (submitted).

HIGH-TEMPERATURE DETECTOR OF SPACE RADIATION BASED ON DIAMOND SENSITIVE ELEMENTS

K.V. Zakharchenko [1], A.A. Altukhov [1], R.F. Ibragimov [2], V.A. Kolyubin [1], E.M. Tyurin [2]

[1] *Industrial Technological Center "UralAlmazInvest", Ltd. 121108, 4, Ivana Franko str., Moscow, Russia, nanophys@mail.ru;*

[2] *National Research Nuclear University "MEPhI", 115409,31, Kashirskoe sh., Moscow, Russia*

KEYWORDS:
Space radiation, electrons, protons, heavy ions, neutrons, diamond, detector, high temperature.

INTRODUCTION:
Space radiation detector based on diamond sensitive elements for high-temperature applications has been developed. Preliminary tests of the detector have been carried out. The detector effectively registers electrons, gamma radiation and neutrons up to 200 °C. The detector is perspective to be used in the missions aimed to Venus research and in long-term space missions.

PECULIARITIES OF HIGH TEMPERATURE SPACE RADIATION DETECTOR:
High temperature is one of the factors affected the operation characteristics and the reliability of spacecraft equipment. The working ability at high temperatures is of great importance for the equipment used not only in the missions aimed to hot objects like Venus but also in long-term missions because of high requirements to the reliability (the resource of the equipment exponentially falls as the temperature increases[1]). Also high radiation hardness is required for the spacecraft equipment for long-term missions

Conventional space radiation detectors based on silicon electronics can hardly be exploited at the temperatures greater than plus 100 °C [2]. The sensors based on CVD diamond plates demonstrate excellent performance at the temperatures greater than 200 °C and in hard radiation environment [3, 4]. But not only the sensor itself but all electronic components must work at high temperatures. We have used high-temperature materials for the printed circuit board and sealing. The output of diamond sensor was carried to the charge sensitive amplifier (CSA) based on high-temperature transistor and operational amplifier. The output of the CSA was transformed to the amplitude spectrum by conventional pulse signal processor "GreenStar".

Space radiation detector must be also resistant to mechanical action. We have chosen the configuration of the apparatus taking into account the results of modeling the action of wide-band random vibration.

TESTING THE SPACE RADIATION DETECTOR:
We have performed preliminary test of the detector under action of beta, gamma and neutron radiation at room temperature and at high temperature. Sr-90+Y-90 and Cs-137 sources have been used to obtain beta and gamma radiation and deuterium-tritium neutron generator was the source of neutron radiation. The detector has been placed into the thermostat equipped with the heater and the temperature meter.

The spectra of output signal of the detector at room temperature and at 200° C are shown at the Figures 1, 2, 3 (the spectra have been obtained under action of beta, gamma and neutron radiation, consequently).

One can see from the figures that the detector registers beta, gamma and neutron radiation at room temperature and at plus 200 °C. The spectra obtained at room and at high temperature coincide within the uncertainty of the experiment. The spectrum of neutron radiation at plus 200 °C is shifted towards smaller energies by ~ 100 keV compared to that obtained at room temperature. This is probably caused by changes in neutron energy (the spectra have been obtained at different sessions of generator work).

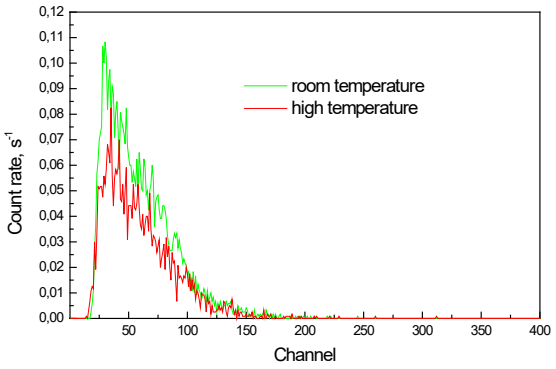


Fig. 1. Detector output spectra under action of beta radiation at room temperature and at plus 200 °C.

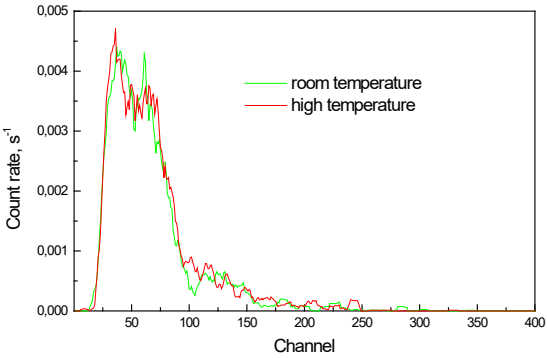


Fig. 2. Detector output spectra under action of gamma radiation at room temperature and at plus 200 °C.

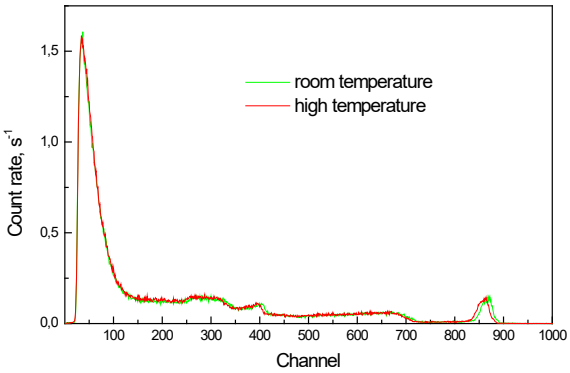


Fig. 3. Detector output spectra under action of neutron radiation at room temperature and at plus 200 °C.

CONCLUSIONS:

We have developed and tested the space radiation detector based on diamond sensitive elements operable at high temperatures. The test has shown that the detector effectively registers beta, gamma and neutron radiation at high temperatures up to 200 °C. The detector is perspective for using in long-term space missions and in the missions aimed to the research of hot objects like Venus.

ACKNOWLEDGMENTS:

The work has been partially supported by Federal State Budgetary Institution "Fund for Promoting the Development of Small Forms of Enterprises in the Scientific and Technical Sphere" (Innovation Assistance Fund), Project No61893.

REFERENCES:

[1] EEE parts reliability manual. Ministry of Defense of Russian Federation. 2006. P. 641
[2] Baranochnikov M.L.. Receptors and detecros of radiation manual. Moscow: DMK Press. 2012. 640 p.
[3] Amosov V.N., Meshchaninov S.A., Rodionov N.B., Rodionov R.N. Development the radiometer of gamma radiation based on synthetic diamond material // Prikladnaya fizika. 2012. No. 3. P. 79-85.
[4] Kadilin V.V., Kolyubin V.A., Lvov S.A., Nedosekin P.G., Idalov V.A., Tyurin E.M., Kolesnikov S.V., Samosadnyi V.T. The prospects of Application of diamond detectors for registration of charged space radiation particles// Yadernaya fizika I injiniring. 2014. V. 5. No. 2. P. 138–144.

SESSION 2. VENUS (VN)
POSTER SESSION

ON LOAD LOVE NUMBERS FOR VENUS

T.I. Menshchikova [1], T.V. Gudkova [2]
[1] *Schmidt Institute Physics of the Earth RAS, B.Gruzinskaya, 10, Russia, ms.tamm@mail.ru*

KEYWORDS:
Venus, load Love coefficients, topography, gravity field, rheological models.

INTRODUCTION:
We are on the eve of the seismic experiment on Venus [1]. There is little knowledge of Venus' seismic activity. Magellan data reveal such signs of tectonic activity as extensional fractures and wrinkle ridges on the Venusian surface. Current seismic activity could be expected in the areas of Beta, Atla, Phoebe régions, which are strongly supported by upwelling mantle plumes. The evidence for current volcanism is confirmed [2]. Since there is no sign of plate boundaries or their motions on Venus like on the Earth, areas with high stresses could be potencial sources of quakes. Boundary conditions for streses' modeling are based on both the topography and gravity field data, and the values of load Love numbers. For this purpose, we calculate load Love numbers for different rheological models of Venus.

DATA:
The gravity and topography data provided by the Magellan mission: the spherical harmonic global topography model (SHTJV360u) [3] and gravity field model (SHGJ180u) [4] are available at the Planetary System data (http://pds-geosciences.wustl.edu). We have used these data up to the spherical harmonic degree and order 70, based on the accuracy of the gravity field at the moment. The surface of an effectively equilibrium Venus [5], which survives from an earlier epoch, is chosen as a reference.

METHOD:
The distribution of non-hydrostatic stresses in a planet can be obtained by considering the planet as an elastic spherically symmetric body under the influence of both surface (relief on the surface of the planet) and internal (buried density anomalies) loads. The amplitudes of loads that serve as boundary conditions for solving the system of equations of elastic equilibrium of a gravitating planet are determined according to the topography and gravitational field and load Love numbers. Load Love numbers (load coefficients) are functions of the planet's response to loads.

Load numbers $k_n(r)$ and $h_n(r)$ for the density anomaly located at a given depth r are obtained from the solution of the system of equations of elastic equilibrium of a gravitating planet (the equation of motion of a deformed body, the Poisson equation, Hooke's law for an isotropic medium), which can be represented as six first-order differential equations [6] and solved by the fourth-order Runge-Kutta method. These values depend on the depth of the load location, the degree of harmonics n and the rheological model of the planet. Load Love numbers (or load coefficients) are calculated for a given model of the planetary interior.

MODEL:
The reaction of the planet in response to the applied load depends on the behavior of the material. The rheological properties of Venus, at present, are not precisely established. We consider several variants of models of inhomogeneous elasticity of Venus. As a first approximation, we take an elastic model — Model A. In the second case (Model B) we assume the presence of an elastic lithosphere. Beneath the lithosphere there is a softened layer, which partly lost its elastic properties. Spreading till the core, softened layer is characterized by a reduced (to one-tenth of the initial value) shear modulus. In the third model — Model C — the shear modulus is changing gradually: one-tenth of the initial value of shear modulus just beneath the crust is increasing up to its elastic value at the core-mantle boundary. In the absence seismic measurements, there is no exact knowledge how thick the Venusian lithosphere is. The thickness the lithosphere is varied from 100 to 500 km according to the results of [7].

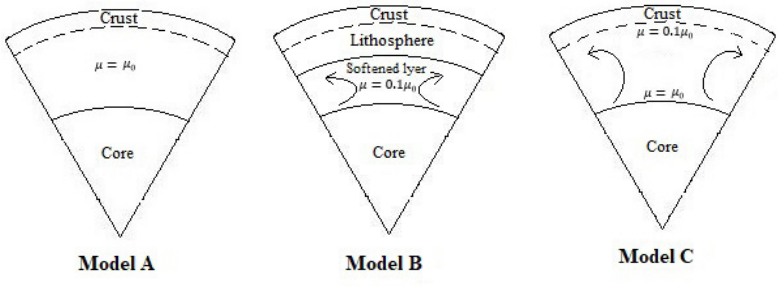


Fig. 1 Rheological models of Venus: Model A – an elastic model. Model B – a model with the lithosphere of various thickness values (100 – 500 km) located on a softened layer, which partially lost its elastic properties. The softening is modeled by the reduced (to one-tenth of the initial value) shear modulus μ in the layer beneath the lithosphere, stretching down to the core. Model C – a model with a reduced shear modulus value just beneath the crust, while its value increasing up to its elastic value the core-mantle boundary.

RESULTS:

Load Love numbers $k_n(r)$, $h_n(r)$ have been calculated for different rheological models of Venus (Models A, B and C, see Fig. 1). Load numbers $k_n(r)$ and $h_n(r)$ (with opposite sign) for a test interior model are shown in Fig. 2 for degree and order n = 2-70 and various load depths: at the surface, at the crust-mantle boundary and some depths in the mantle.

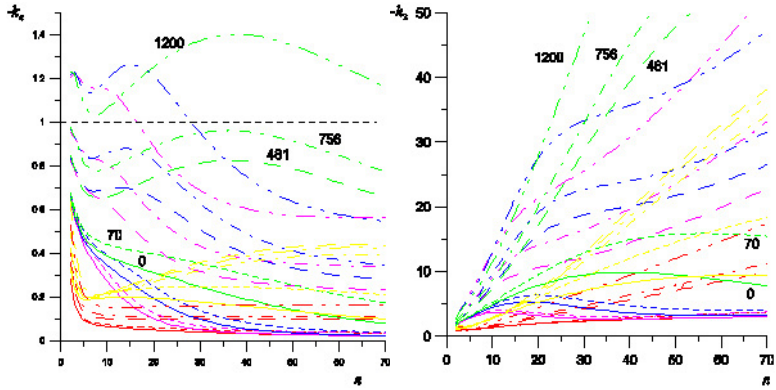


Fig. 2. Load numbers $k_n(r)$ and $h_n(r)$ (with opposite sign) for the elastic Venusian model of type A (red lines); type B models with a lithospheric thickness of 100 km (green lines), 300 km (blue lines) and 500 km (pink lines), and type C models (yellow lines) as a function of the spherical harmonic number n for different depths of anomalous density waves: at the surface of 0 km, at the crust-mantle depth of 70 km, at depths of 481 km, 756 km and 1200 km. The horizontal dashed line corresponds to the value $k_n(r) = -1$ (isostasy).

The value of $k_n(r_j)$ determines the response of the external gravity field on anomalous density wave with some amplitude. At $k_n(r_j) = 0$ the interiors of a planet behaves as «undeformed», while there is a bounding of layers: light material is replaced by heavier one and heavy material – by lighter one. The value $(-k_n(r_j)) = 1$ corresponds to full isostatic compensation, the physical reason is the effects of deformation and bounding of elastic shells of the mantle, located above softened layers. At $0 < (-k_n(r_j)) < 1$ there is a partial compensation of anomalous density wave. It is seen from Fig. 2, that the response function (the load coefficients) is sensitive to a rheological structure of the planet, this fact can be used to discriminate between the rheological models of Venus.

ACKNOWLEDGMENTS:

The study was performed under a government contract of the Schmidt Institute of Physics of the Earth of the Russian Academy of Sciences.

REFERENCES:

[1] Kremic T., Ghail R, Gilmore M., Hunter G., Kiefer W., Limaye S., Pauken M., Tolbert C., Wilson C. Long-duration Venus lander for seismic and atmospheric science // Planetary and Space Science. 2020. V. 190. Pp.104961

[2] Shalygin, E.V., Markiewicz W.J., Basilevsky A.T., Titov D.V., Ignatiev N.I., Head J.W. Active volcanism on Venus in the Ganiki Chasma rift zone // Geophys. Res. Lett. 2015. V. 42. P. 4762–4769. doi:10.1002/2015GL064088.

[3] Rappaport N. J., Konopliv A. S., Kucinskas A. B. Animproved 360 degree and order model of Venus topography // Icarus. 1999. V. 139. P. 19 – 31. doi:10.1006/icar. 1999. 6081.

[4] Konopliv et al., 1999 Konopliv A. S., BanerdtW. B., SjogrenW. L. Venus gravity:180th degree and order model // Icarus. 1999. V. 139. P 3 – 18. doi:10.1006/ icar.1999.6086.

[5] Zharkov V.N., Gudkova T.V. On Parameters of the Earth-like model of Venus // Sol. Syst. Res. 2019. V.53. N 1. P. 1 - 4

[6] Marchenkov K.I., Lyubimov V.M., and Zharkov V.N. Calculation of load factors deeply buried density anomalies, Doklady Earth Science Sections, 1984, V. 279, pp. 14–16.

[7] Orth C.P., Solomatov V.S. Constraints on the Venusian crustal thicknes variations in the isostatic stagnant lid approximation // Geochem. Geophys. Geosyst. 2012. V. 13. P. Q11012. doi:10.1029/2012GC004377.

RECONNAISSANCE GEOLOGICAL MAPPING OF THE LATMIKAIK CORONA AND ASSOCIATED DYKE SWARMS, HENIE QUADRANGLE (V - 58), VENUS

J. Shackman [1], R.E. Ernst [2,3], E.M. Bethell [4], K.J.E. Boggs [1], B. Beckie [1], K. Tardiff [1], and R.C. Dietrich [1]

[1] *Department of Earth and Environmental Sciences, Mount Royal University, 4825 Mount Royal Gate se, Calgary, Alberta, Canada T3E 6K6;*

[2] *Department of Earth Sciences, Carleton University, 1125 Colonel By Drive, Ottawa, Ontario, Canada K1S 5B6;*

[3] *Faculty of Geology and Geography, Tomsk State University, 36 Lenin Avenue, Tomsk, Russia 634050;*

[4] *Department of Earth and Environmental Sciences, University of Ottawa, 75 Laurier Avenue E, Ottawa, Ontario, Canada K1N 6N5*

KEYWORDS:
Latmikaik Corona, Xcacau Corona, Tellervo Chasma, Henie Quadrangle, Venus

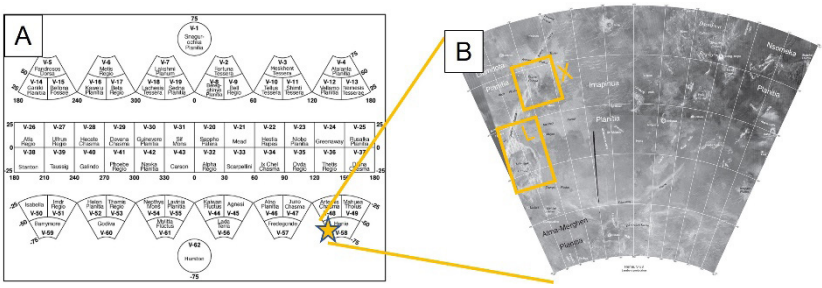
INTRODUCTION:
Venusian coronae typically appear as irregular landforms, ranging from circular to ovular in shape, with diameters up to 2500 km. Coronae have annulus borders composed of densely packed grooves [2], potentially grabens overlying dykes [3], mottled material and frequently lava flows that extend outwards from the annulus [4]. Phillips et al. [5] proposed that the concentric geometry of coronae with the accompanying volcanic features support the interpretation that the coronae are the surficial expression of mantle diapirs. The topographic expression of coronae may reflect different stages of corona evolution, specifically, elevated core regions are thought to represent retrogressive stage evolution while sunken core regions represent progressive stage evolution [6].

Here we present reconnaissance mapping of the Latmikaik and Xcacau Coronae, Tellervo Chasma, and associated graben systems, in the Henie (V – 58) Quadrangle in the southern hemisphere of Venus (Fig. 1).

METHODOLOGY:
Detailed mapping of geological features were traced out in ArcGIS (1 : 500 000) on files downloaded from the Planetary Data System for Magellan data. Mapped geological features were then categorized by defining characteristics such as orientation and trend.

RESULTS:
Both Coronae are elongated in the north-south orientation (Latmikaik: 345 km wide, 650 km long; Xcacau 120 km wide, 165 km long), and constrained by the annulus material, which are defined by dense swarms of radar bright, linear, and curvilinear subparallel lineaments (Figs. 2, 3). The Latmikaik Corona core consists of radar dull mottled material, which is nearly devoid of fractures and radar bright flow material, with small scale wrinkle ridges. Annulus material constructs a topographically high region around the edge of the Latmikaik Corona, and with the core material slightly raised, defines an overall W-profile [6]. At least three dense graben systems cross the Xcacau Corona which has a less defined annulus (Fig. 3). The core of the Xcacau Corona is sunken.

A complex series of at least seven graben systems of different trends cross Xcacau Corona and the northeastern end of the Tellervo Chasma (Fig. 3). The Tellervo Chasma extends from the Xcacau to the Latmikaik Coronae (striking 050 - 230°). A radiating graben system converges on an enigmatic feature at the south end of Xcacau Corona. One graben system (025 - 205°) extends the length of the Chasma but does not appear to extend significantly past the margins of the Chasma. Six densely packed graben swarms (striking 011–191°; 010–190°; 340–160°; 325–145°; 337–157°) appear to be slightly deflected as they cross Xcacau Corona and the northern end of Tellervo Chasma. Two other graben systems (331 – 151°; 015–195°) were mapped south Xcacau Corona.


A
B
Ovda Regio
Thetis Regio
Imdr Regio
Ganiki Chasma
Parga Chasma
Hecate Chasma
Diana Chasma
Guinevere Planitia
Eistla Regio
Atla Regio
Beta Regio
Phoebe Regio
Devana Chasma
Rhea Mons
Sapas Mons
Maat Mons
Sif Mons
Carson
Gula Mons
Sacajawea Patera
Innini Mons
Ozza Mons
Ushas Mons
Tinatin Planitia
Lada Terra
Lavinia Planitia
Aphrodite Terra
Atla Regio
Helen Planitia
Thetis Regio
Ganiki Chasma
Parga Chasma
Hecate Chasma
Diana Chasma
Guinevere Planitia
Eistla Regio
Atla Regio
Beta Regio
Phoebe Regio
Devana Chasma
Rhea Mons
Sapas Mons
Maat Mons
Sif Mons
Carson
Gula Mons
Sacajawea Patera
Innini Mons
Ozza Mons
Ushas Mons
Tinatin Planitia
Lada Terra
Lavinia Planitia
Aphrodite Terra

FUTURE WORK:

Our team plans to complete mapping of the entire Henie Quadrangle at a scale of 1 : 2 500 000 during 2022 in order to examine outstanding questions regarding the relationship between Large Igneous Province plumbing systems (dyke swarms) and coronae [3]. Volcanic lava flows will be examined in detail to identify their origin, quantity, and their relative relationships between coronae, chasma, shield volcanoes, dyke swarms and wrinkle ridges. Graben systems will be traced across the entire quadrangle to examine the extent of the influence of Artemis Corona which is located north of the Henie Quadrangle (cf. [7]).

REFERENCES:

[1] Barsukov, V.L., Volkov, V.P., Planeta Venera (atmosfera, poverkhnost', vnutrennee stroenie) (Planet Venus (Atmosphere, Surface, Internal Structure), // Moscow: Nauka, 1989.

[2] Stofan, E.R., Sharpton, V.L., Schubert, G., Baer, G., Bindschadler, D.L., Janes, D.M., Squyres, S.W. Global distribution and characteristics of coronae and related features on Venus: Implications for origin and relation to mantle processes. // Journal of Geophysical Research. 1992. V. 97. No. E8. P. 13347 – 13378.

[3] Buchan, K.L., Ernst, R.E. Plumbing systems of large igneous provinces (LIPs) on Earth and Venus: Investigating the role of giant circumferential and radiating dyke swarms, coronae and novae, and mid-crustal intrusive complexes. // Gondwana Research. 2021. (in press).

[4] Ivanov, M.A., Head, J.W. Geology of Venus: Mapping of a global geotraverse at 30N latitude. // Journal of Geophysical Research. 2001. V. 106. N. E8. P. 17515–17566.

[5] Phillips, R.J., Raubertas, R.F., Arvidson, R.E., Sarkar, I.C., Herrick, R.R., Izenberg, N., Grimm, R.E. Impact craters and Venus resurfacing history. // Journal of Geophysical Research. 1992. V. 97. N. E10. P. 15,923 – 15,948.

[6] Guseva, E.N., Ivanov, M.A. Structures of Coronae on Venus: Results of Topographic and Geologic Analysis. // Solar System Research. 2020, V. 54. N. 6. P. 529–536.

[7] Hansen, V.L., Olive, A. (2010). Artemis, Venus: the largest tectonomagmatic feature in the Solar System? // Geology, 2010, V. 38: P. 467–470

EROSION OF TESSERA TERRAIN ON VENUS: CRITERIA FOR RECOGNITION OF EFFECTS OF THE PRESENCE OF AN EARTH-LIKE ATMOSPHERIC EROSIONAL ENVIRONMENT

J.W. Head [1], M.A. Ivanov [2]
[1] *Department of Earth, Environmental and Planetary Sciences, Brown University, Providence RI 02912 USA, james_head@brown.edu;*
[2] *Vernadsky Institute of Geochemistry, Russian Academy of Sciences, Moscow, Russia, mikhail_ivanov@brown.edu*

KEYWORDS:
Venus, tessera, atmosphere, hydrology, fluvial, lacustrine, erosion.

INTRODUCTION:
Fundamental questions concerning the nature of the current atmosphere of Venus include: 1) Why is it so different than that of Earth? Did it start with an Earth-like, more clement environment and transition to the inhospitable atmosphere observed today? If so, when in its geologic history did this occur and what were the factors that caused this transition? Could the current Venus atmosphere be a "fossil atmosphere", dating back to much earlier in its geologic history? What insights can be gained from the multitude of "Venus-like" exoplanets that have been recently documented? Addressing these questions requires a very wide range of disciplines and approaches in order to understand 1) planetary dynamics, 2) accretion, magma ocean formation and early evolution, 3) origin, composition and evolution of primary and secondary atmospheres (including the origin of volatiles from accretion, subsequent impacts, and mantle degassing), their climate and atmospheric circulation history, and the relative importance of factors such as loss rates to space, impact bombardment, surface chemical alteration, and crustal and lithospheric recycling processes, 4) geological and geodynamic history and evolution, including core formation, origin and evolution of a magnetic field, and lithospheric stability and evolution, and 5) the implications of all of these factors on environments conducive to the origin and evolution of life.

Critically important is the integration of these and other factors into a coherent paradigm as a framework for testing the role of these multiple factors and explanations for current and future observations. A major step in this direction was taken with a comprehensive review and analysis by Way and Del Genio [1], who explored three competing scenarios for the history of the Venus atmosphere: 1) Earth-like Until Recent History: Venus spent much of its history with surface liquid water, plate tectonics, and a stable temperate climate (as suggested in part by the high D/H ratio measured by Pioneer-Venus, interpreted to imply sufficient water for a shallow ocean throughout much of its history) (Fig. 1, 2) Early Magma-Ocean Dominant: A long-lived primordial magma ocean and associated CO_2/steam atmosphere dissociated the water vapor, causing significant hydrogen escape and magma ocean oxidation; 3) Early Runaway Greenhouse: Venus had surface water for a short period early in its history, but a gradually warming Sun induced a moist/runaway greenhouse, leaving Venus desiccated after about the first billion years. Way and Del Genio [1] employ the sparse available constraints and an atmospheric general circulation model to show that the first scenario, 1) Earth-like Until Recent History, is a viable option. But when did this more Earth-like Venus atmosphere transition to the current, decidedly non-Earth like current atmosphere? Way and Del Genio [1] "further speculate that large igneous provinces and the global resurfacing hundreds of millions of years ago played key roles in ending the clement period in its history and presenting the Venus we see today."

In summary, the excellent and comprehensive Way and Del Genio [1] contribution offers an array of testable hypotheses that can be further addressed with analysis of existing data and data from the several missions in the upcoming international Venus armada. As a contribution to this effort,

we develop here criteria for the recognition of the hypothesized transition from an earlier "clement period in its history …[to]…the Venus we see today." (Fig. 1). Elsewhere [2] we have assessed the prediction that "… large igneous provinces and the global resurfacing hundreds of millions of years ago played key roles in ending the clement period in its history and presenting the Venus we see today." Here we focus on developing criteria for the recognition of the effects of a "clement period in its history" that is predicted to have been in effect during the formation and evolution of the highly deformed tessera terrain, terrain that has been shown [1, 3] to predate "…the global resurfacing hundreds of millions of years ago…." [1] (Fig. 1).

CRITERIA FOR RECOGNITION OF A CLEMENT PERIOD DURING TESSERA FORMATION AND EVOLUTION:

Among the clear predictions of the model (Fig. 1) is the presence of liquid water on the surface and in the atmosphere prior to "…the global resurfacing hundreds of millions of years ago…." [1]. Thus, the climate history prior to the transition (during tessera time) has been characterized by Way and Del Genio [1] as 'clement" and we use the general term "warm and wet" (to describe this condition. We use the term "hot and dry" to refer to the current climate. We then explore the predicted geological effects of the clement "warm and wet" climate as a framework for testing of the presence of climate during tessera time, prior to the "global resurfacing".

THE MARTIAN CLIMATE EVOLUTION DEBATE:

Development of criteria for the recognition of the nature and intensity of an atmospheric water cycle from its erosional and depositional signatures and remnants has been an ongoing discussion on Mars for many decades [4] and provides a framework for assessing a "warm and wet" climate on Venus. At issue is whether the Mars ambient climate in the ~ 400 Ma-long Late Noachian was "warm and wet" [5], or "cold and icy" [6 - 7]. The "warm and wet" paradigm is characterized by Mean Annual Temperatures (MAT) > 273 K, atmospheric pressure (Patm) ~ 1 bar, a vertically integrated hydrological system, rainfall, infiltration and runoff, possible northern lowland oceans and a Late Noachian 'climate optimum' during which runoff exceeded infiltration resulting in extensive fluvial erosion. Evidence for fluvial and lacustrine activity is interpreted to characterize the *ambient* climate.

The "cold and icy" paradigm" is characterized by Patm < ~ 500 mbar, MAT ~ 225 K, a horizontally stratified hydrological cycle (global cryosphere), and an adiabatic cooling effect that transported water vapor to the uplands and deposited it there as snow and ice. Evidence for fluvial and lacustrine activity is interpreted to represent transient heating events that melted the accumulated snow and ice in the "cold and icy highlands", causing short-term fluvial and lacustrine activity.

Although the appropriate interpretive paradigm is at issue for Mars [4], the evidence for fluvial and lacustrine activity is accepted in both scenarios and provides a basis for recognition of long-term ambient climate conditions on Venus. Key geomorphologic indicators are: 1) *fluvial features* in the form of 'valley networks' [8], 2) *lacustrine features* in the form of > 220 open-basin lakes (both an inlet and outlet channel) [9] and > 200 closed-basin lakes (inlet channel only) [10]. Debated is the presence/absence of Noachian northern lowland oceans, an area largely covered by later events [11]. Additional evidence for a "warm and wet" ambient Noachian climate is the presence of phyllosilicates (strong evidence for extensive alteration of rocks in a warm and wet environment) [12], but at issue is whether this environment was at the surface and linked to climate, or occurred in a deep groundwater -hydrothermal environment subsequently brought to the surface by impact cratering.

SUMMARY AND CONCLUSIONS:

In summary, if the earlier climate of Venus was characterized by a water-rich "warm and wet" ambient climate with oceans that transitioned during the emplacement of global regional plains [1] to a "hot and dry" ambient climate deficient in water, then the stratigraphically oldest exposed terrain on Venus, the tessera terrain [1, 3], should be characterized by the following evidence for erosional and hydrological cycles: 1) *pluvial features*, evidence

for rainfall, infiltration and runoff, 2) *fluvial features*, and an integrated fluvial system including sediment sources, transport systems and sinks, 3*) lacustrine features*, open and closed-basin lakes representing localized water catchment and storage areas, 4) *fans and deltas*, localized features and deposits associated with differences in the abundance, velocity and transport ability of water (e.g., debris fans, deltas, lacustrine and oceanic shorelines, concentrations of chemical weathering and evaporative products, etc.), 5) *oceanic areas*, lowland regions representing the final sink for water and sediment, and 6) *phyllosilicates* and related chemical alteration products.

Key to the assessment and testing of the Way and Del Genio model [1] is the resolution of currently available image and topography data (Magellan and Venera 15/16) for the tessera and surrounding pre-regional-global volcanic resurfacing units, and what features can only be recognized with higher-resolution data from the upcoming international armada of Venus missions. Next steps in our research is the application of these criteria to the existing image, topography and compositional data to assess further the Way and Del Genio paradigm [1] (Fig. 1).

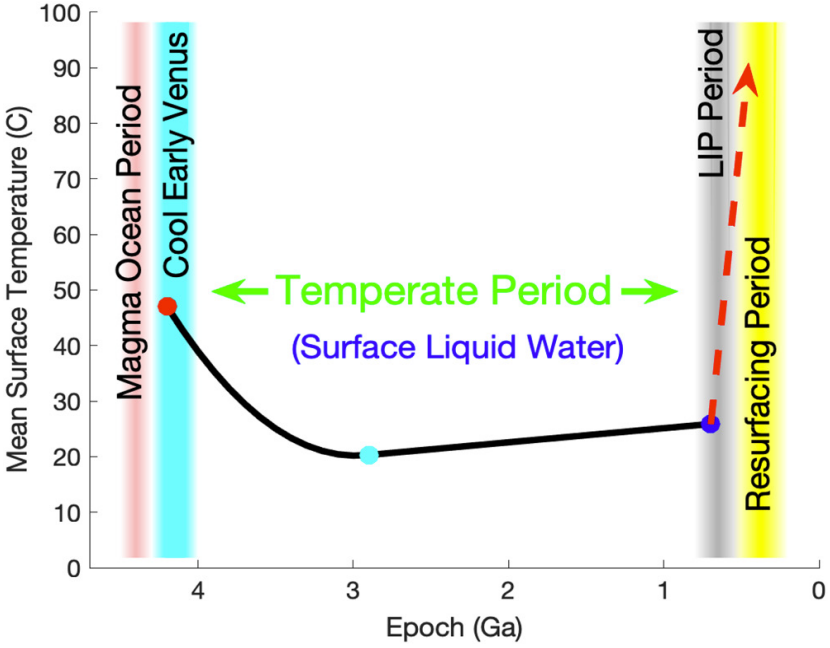


Fig. 1. Possible Venus climate history and transition to the period of the observable geolgic record [3]. The *Earth-like Until Recent History* paradigm of Way and Del Genio (2020) [1].

REFERENCES:

[1] M. Way & A. Del Genio (2020) JGR 125;
[2] J. Head et al. (2021) LPSC 52 #2143;
[3] M. Ivanov & J. Head (2011) PSS 59, 1559;
[4] R. Wordsworth et al. (2018) Nat. Geosci. 11, 888;
[5] R. Craddock & A. Howard (2002) JGR-P 107, 5111;
[6] R. Wordsworth et al. (2013) Icarus 222, 1;
[7] R. Wordsworth et al. (2015) JGR-P 120, 1201;
[8] B. Hynek et al. (2010) JGR-P 115, E09008;
[9] T. Goudge et al. (2012) Icarus 219, 211;
[10] T. Goudge et al. (2015) Icarus 260, 346;
[11] J. Head et al. (2019) 9th Internat. Mars Conf. #6108;
[12] J-P Bibring et al. (2005) Science 307, 1576.

GLOBAL GEOLOGICAL MAPPING OF VENUS: IDENTIFICATION OF CHALLENGES & OPPORTUNITIES FOR FUTURE VENUS MAPPING

J.W. Head [1], M.A. Ivanov [2],
[1] *Dept. of Earth, Environmental and Planetary Science, Brown University, Providence, RI 02912 USA, james_head@brown.edu;*
[2] *V.I. Vernadsky Institute of Geochemistry and Analytical Chemistry, Russian Academy of Sciences, Moscow, Russia*

INTRODUCTION AND BACKGROUND:
A global geologic map of Venus was compiled [1] at a scale of 1 : 10 M, using Magellan radar image and altimetry data, supplemented by Venera-15 / 16 radar images. The map (Fig. 1) covers the entire surface of Venus (460×10^6 km^2), 90% of the surface area of Earth. The associated documentation [1] outlined the history of Earth and planetary geological mapping to illustrate the importance of utilizing the dual stratigraphic classification approach to geological mapping. On the basis of this well-established approach, thirteen distinctive units and a series of structures and related features were identified on the surface of Venus. Included were discussions of 1) the history and evolution of the definition and characterization of these units, 2) exploration and assessment of alternative methods and approaches that have been suggested, and 3) an outline of the pathway from the sequence of mapping of small areas, to regional and global scales. As seen in Fig. 1, the contribution outlined the specific definition and characterization of these units, mapped their distribution, and assessed their stratigraphic relationships.

On the basis of these data, [1] then compared local and regional stratigraphic columns and compiled a global stratigraphic column, defining rock-stratigraphic units, time-stratigraphic units, and geological time units. Superposed craters, stratigraphic relationships and impact crater parabola degradation were used to assess the geologic time represented by the global stratigraphic column. On the basis of these data and the unit characteristics, [1] interpreted the geological processes that were responsible for their formation, and then, on the basis of unit superposition and stratigraphic relationships, interpreted the sequence of events and processes recorded in the global stratigraphic column.

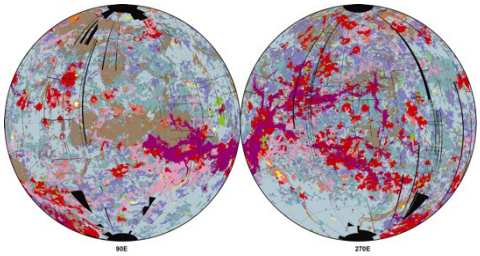
The earliest part of the history of Venus (Pre-Fortunian) predates the observed surface geological features and units, although remnants may exist in the form of deformed rocks and minerals. The observable geological history of Venus was subdivided into three distinctive phases (Fig. 1). The earlier phase (Fortunian Period, its lower stratigraphic boundary cannot be determined with the available data sets) involved intense deformation and building of regions of thicker crust (tessera). This was followed by the Guineverian Period. Distributed deformed plains, mountain belts, and regional interconnected groove belts characterize the first part and the vast majority of coronae began to form during this time. The second part of the Guineverian Period involved global emplacement of vast and mildly deformed plains of volcanic origin. A period of global wrinkle ridge formation largely followed the emplacement of these plains. The third phase (Atlian Period) involved the formation of prominent rift zones and fields of lava flows unmodified by wrinkle ridges, often associated with large shield volcanoes and, in places, with earlier-formed coronae. Atlian volcanism may continue to the present. About 70 % of the exposed surface of Venus was resurfaced during the Guineverian Period and only about 16% during the Atlian Period. Estimates of model absolute ages (Fig. 1) [2] suggest that the Atlian Period was about twice as long as the Guineverian and, thus, characterized by significantly reduced rates of volcanism and tectonism. The three major phases of activity documented in the global stratigraphy and geological map [1], and their interpreted temporal relations [1, 2], provide a basis for assessing

the geological, atmospheric and geodynamical processes operating earlier in Venus history [e.g., 3 - 5] that led to the preserved record [1]. In addition, detailed analysis of the preserved volcanic [6] and tectonic [7] records permit a more in-depth understanding of the recent geological history, the associated geological processes [8 - 10] and the major unknowns and questions that can be addressed with continuing geologic mapping at a wide range of scales. Below we list some of compelling questions (see also [11]) and opportunities for future geological mapping.

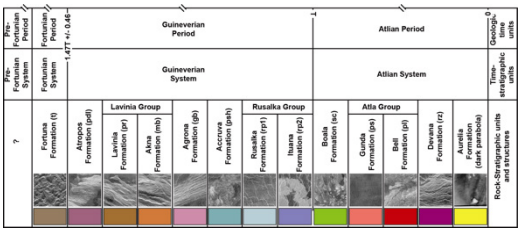
SOME FUNDAMENTAL QUESTIONS FOR FUTURE GEOLOGICAL MAPPING OF VENUS:

1. **IS THERE EVIDENCE FOR EXTENSIVE PYROCLASTIC ACTIVITY? WHEN, WHERE AND HOW ABUNDANT?:** This question is of critical importance for determining the history of the present atmosphere and links to the potential volatile content of eruptive magmas.
2. **WHAT IS THE RELATIONSHIP OF CORONAE, NOVAE, ARACHNOIDS, AND SHIELD VOLCANOES IN SPACE, TIME AND ALTITUDE?:** Are these apparently disparate features related in origin, in space, in time? This is a critical question to assess the nature and evolution of mantle dynamics (e.g., mantle plumes, broader mantle upwellings, etc.) and how this might have changed with time.
3. **WHAT CONSTRAINTS DOES THE DISTRIBUTION AND VOLUME OF VOLCANIC PLAINS OF DIFFERENT AGES PLACE ON THE ORIGIN AND EVOLUTION OF THE ATMOSPHERE?:** Estimates of the areal coverage, embayment relationships, thickness, and volumes of units of extrusive volcanic origin is key to assessing the input of magmatic volatiles into the atmosphere.
4. **HOW DOES THE CURRENT ATMOSPHERIC ENVIRONMENT INFLUENCE THE ASCENT AND ERUPTION OF MAGMA?:** Clearly, the very high Venus atmospheric pressure inhibits magmatic gas exsolution, concentration and explosive volcanic eruptions. Is there any evidence for widespread pyroclastic deposit in the past and could such deposits signal the presence of a very different, lower-atmospheric-pressure environment?
5. **WHAT IS NATURE AND RELATIONSHIPS OF FESTOONS AND PANCAKE DOMES?:** Are they silica-rich volcanism, viscous magmatic foams, or both? How do they differ in terms of their age and geologic setting?
6. **HOW DO TESSERA PATTERNS OF DEFORMATION COMPARE AMONG THE DIFFERENT OCCURRENCES AND HOW DO SIMILARITIES AND DIFFERENCES INFORM US ABOUT TESSERA ORIGIN (E.G., LATERAL COLLISION, UPWELLING, DOWNWELLING ETC.)?:** In order to span the gap between the preserved geologic record (e.g., [1]) and the earlier "cryptic" history, this question requires detailed and comprehensive geologic mapping.
7. **HOW MUCH STRAIN IS REPRESENTED BY DEFORMATIONAL FEATURES IN THE TESSERA, AND HOW DOES THIS VARY IN SPACE AND TIME?:** These are critical issues in understanding earlier "cryptic" Venus history and the transition to the current record (see details in [10]). Detailed geologic mapping of deformation features in the tessera and integrations across different tessera occurrences is essential.
8. **WHAT IS THE HISTORY OF TOPOGRAPHY ON VENUS AND HOW DOES THIS INFORM US ABOUT THE VENUS THERMAL AND GEODYNAMIC EVOLUTION?:** When and how did the current topography form and what are the relative roles of Pratt and Airy isostacy? How can geologic mapping and topography be combined to address this question?
9. **WHAT ARE THE CRITERIA FOR RECOGNIZING TECTONICALLY MODIFIED IMPACT CRATERS IN THE TESSERA AND CAN ADDITIONAL CRATERS BE RECOGNIZED?:** Do any tessera elements represent much more ancient terrain dating back into the "cryptic" period of Venus history? Can we develop additional criteria for recognizing tectonically and volcanically modified craters and comprehensively map the tessera in search for any evidence of these?

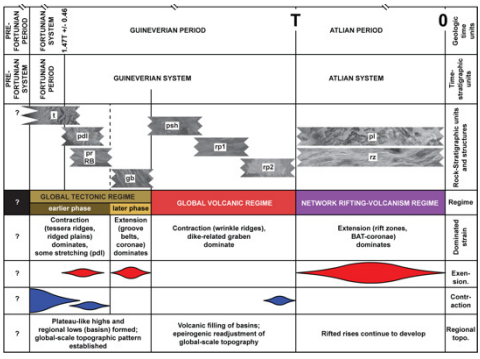
10. **WHAT ARE THE RELATIONSHIPS OF GRAVITY HIGHS AND RECENT VOLCANISM?:** Where on Venus is the most likely recent geological deformation and volcanism [12]? How do these relate to the several positive gravity anomalies suggesting active mantle upwelling?
11. **HOW CAN WE DISTINGUISH BETWEEN TECTONIC AND VOLCANIC FEATURES AND PROCESSES?:** Graben and fractures of tectonic origin abound on Venus, but some are radial and concentric to coronae, and related central volcanic features. How many of these are due to near-surface dikes of volcanic origin? Which have associated pits, domes and flows?
12. **WHAT IS THE RELATIONSHIP BETWEEN RIFT ZONES AND THE MAJOR LOBATE FLOWS THAT ORIGINATE THERE?:** Detailed documentation the relationships (time and space) is essential to understand the global rifting system and implications for mantle convective patterns.



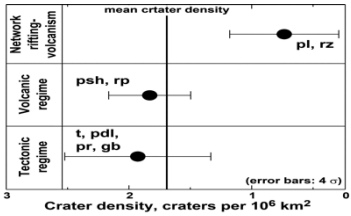
a



b



c



d

Fig. 1. (a) Geologic map; **(b)** Stratigraphic column; **(c)** Interpreted 3 phases of geologic evolution and events [1]. **(d)** Buffered impact crater density data [1, 2].

REFERENCES:

[1] Ivanov & Head, 2011, PSS 59, 1559;
[2] Kreslavsky et al., 2015, Icarus 250, 438;
[3] Bullock & Grinspoon, 1996, JGR, 101, 7521;
[4] Way et al., 2016, GRL, 43, 8376;
[5] Way & Del Genio, 2020, JGR, 125;
[6] Ivanov & Head, 2013, PSS 84, 66;
[7] Ibid, 2015, PSS 113, 10;
[8] Head & Wilson, 1986, JGR 91, 9407;
[9] Gaillard & Scaillet, 2014, EPSL 403, 307; 9.
[10] Hanmer, 2020, ESR 201, 103077;
[11] Byrne et al., 2019, LPSC 50, 2853;
[12] Shalygin et al., 2015, GRL 42, 4762.

DOME-SHAPED CORONAE OF VENUS: SPATIAL DISTRIBUTION, RELATIONSHIP WITH RIFTS AND LOBATE PLAINS

E.N. Guseva [1], M.A. Ivanov [2]
[1] *Vernadsky Institute of Geochemistry and Analytical Chemistry, RAS, Kosygin str., 19, 119991, Moscow, Russia, guseva-evgeniya@ya.ru*

KEYWORDS:
Venus, coronae, topography, rifts, lobate plains, evolution of mantle diapirs.

INTRODUCTION:
Coronae — large (up to 2500 km across) circular structures with annulus consisting of densely packed grooves and sometimes ridges [1 - 4]. Topography of the coronae, the associated volcanic and tectonic activity, and their non-random spatial distribution [5] indicate that the coronae represent the surface manifestation of mantle diapirs [6-9]. Due to the practical absence of erosion on Venus, the topography of coronae can be at various stages of the evolution of their parental diapirs, expressed by successive change of the shape of the corona topographic profiles [10].

We studied all cataloged coronae of Venus [3; 11] and have found [12–13] that they are characterized by three class of topographic profiles: D, W, and U [13]. The D-class profile has a dominating central dome and probably reflects progressive stage of a diapir evolution associated with the rise of the dome-shaped uplift. The W-class profile is characterized by a central uplift surrounded by one or more concentric depressions and, apparently, reflects the transition from progressive to regressive stages of evolution – the uplift loses its thermal support from the diapir and subsides. The U-class profile, a topographic depression, may reflect the final stages of evolution of a diapir.

Some coronae with the D-class profile are concentrated in the Beta – Atla – Themis region, BAT. This area is bounded by large branches of rift zones and is characterized by abundant young volcanism in the form of lobate plains [3, 7, 12–13]. Rifts and lobate plains — the major features of endogenous activity during the late network rifting-volcanism regime of resurfacing on Venus [14–15].

THE PURPOSE OF THE STUDY:
In this work, we studied in more detail the spatial association of dome-shaped coronae with rift zones and lobate plains to understand the possible genetic relationship between the initial stage of coronae formation (dome formation) with the formation of rifts and young volcanic plains.

OBSERVATIONS AND RESULTS:
We studied 81 coronae with the D-class topographic profile and analyzed their stratigraphic relationship with lobate plains (pl) (Fig. 1). It was found that 39 structures (about half of the population of dome-shaped coronae) are spatially associated with the plains. Out of these, 31 coronae (~ 80 %) are embayed by lobate plains, and in 8 cases (~ 20 %) the annulus of the coronae, consisting of rift fractures, cuts the lobate plains.

About half of the dome-shaped coronae are located in rift zones - 43 structures or 53 % of the population (Fig. 1). We analyzed the stratigraphic relationship of these coronae with lobate plains and found that most of them, 26 structures (or 60 %), are spatially associated with pl. Of these, 18 coronae (or about 70 %) are embayed by lobate plains (Fig. 2), and in 8 cases (about 30 %) the annulus of the coronae, consisting of rift fractures, cut the plains.

CONCLUSIONS:
1. Dome-shaped coronae compose only 15 % of the entire studied population of Venus coronae - 81 coronae out of 550 structures, of which less than half (39 coronae) are spatially associated with young lobate plains. The annulus of these coronae are mainly embayed by the material of the plains external to the coronae. Thus, the dome-shaped coronae only in rare cases are the centers of young volcanism.

2. About half (43 coronae or 53% of this population) of the dome-shaped coronae are located in rift zones. This indicates that rifting is not the dominant factor in the formation of dome-shaped coronae.

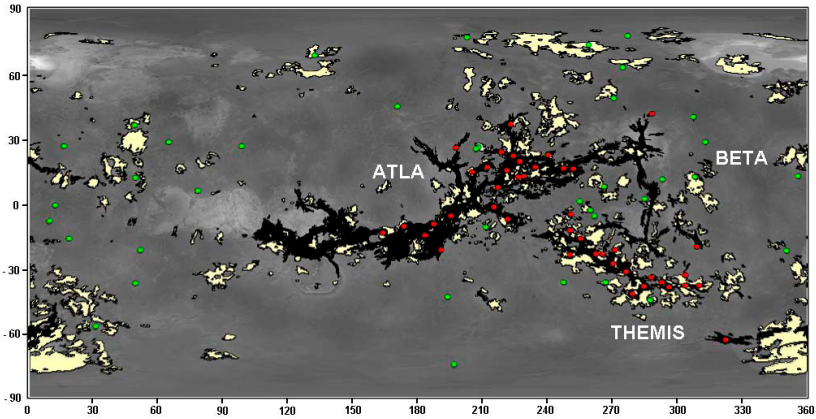


Fig. 1. Dome-shaped coronae are shown in green: those coronae in rift zones – red, the rift zones in black and the lobate plains in yellow (geological base from [16]).

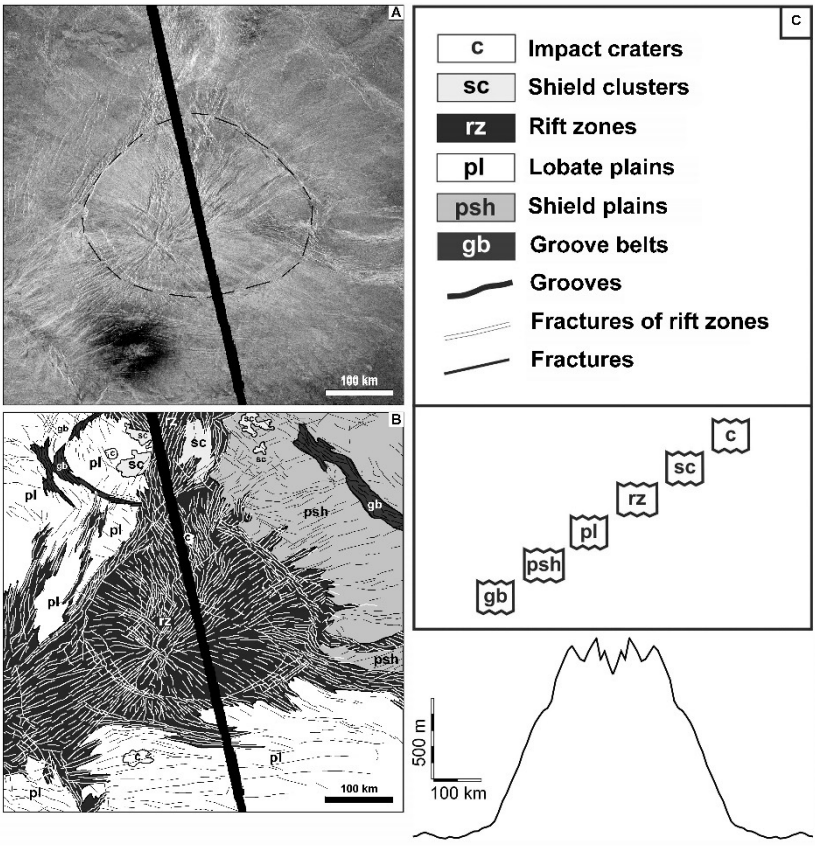


Fig. 2. Shulamite Corona are located in a rift zone, center coordinates 38.7ºS, 284.4ºE; diameter 285 km, image in sinusoidal projection, resolution ~ 352 m/px. **A** – the corona annulus consists of structures of the rift zone (dashed line); **B** — geological map; **C** — sequence of events during the formation of the corona and its averaged topographic profile.

REFERENCES:

[1] Barsukov V.L., Basilevsky A.T., Burba G.A. et al (27 others) The geology and geomorphology of the Venus surface as revealed by the radar images obtained by Venera 15 and 16 // J. Geophys. Res. 1986. v. 91. NB4. p. D378–D398.

[2] Pronin A.A., Stofan E.R. Coronae on Venus: Morphology and distribution // Icarus. 1990. V. 87. P. 452–474.
[3] Stofan E.R., Sharpton V.L., Schubert G., Baer G., Bindschadler D.L., Janes D.M., Squyres S.W. Global distribution and characteristics of coronae and related features on Venus: Implications for origin and relation to mantle processes // J. Geophys. Res. 1992. V. 97. N. E8. P. 13347–13378.
[4] Head J.W., Crumpler L.S., Aubele J.C., Guest J., Saunders R.S. Venus Volcanism: Classification of volcanic features and structures, associations, and global distribution from Magellan data // Journal of Geophysical Research. 1992. V. 97. P. 13.153–13.197.
[5] Phillips R. J., Raubertas R. F., Arvidson R. E., Sarkar I. C., Herrick R. R., Izenberg N., Grimm R. E. Impact craters and Venus resurfacing history // J. Geophys. Res. 1992. V. 97. N. E10. P. 15.923–15.948.
[6] Nikishin A.M. Hot sport tectonics on Venus: implications for rifting and doming // Lunar and Planetary Science XVII. 1986. P. 615–616.
[7] Squyres S.W., Janes D.M., Baer G., Bindschandler D.L., Shubert G., Sharpton V.L., Stofan E.R. The morphology and evolution of coronae on Venus // J. Geophys. Res. 1992. V. 97. P. 13.611–13.634.
[8] Jellinek A.M., Lenardic A., Manga M. The influence of interior mantle temperature on the structure of plumes: Heads for Venus, tails for the Earth // Geophys. Res. Lett. 2002. V. 29. N. 11. P. 27–1–27–4.
[9] Johnson C.L., Richards M.A. A conceptual model for the relationship between coronae and large-scale mantle dynamics on Venus // J. Geophys. Res. 2003. V. 108. N. E6. P. 12–1–12–18
[10] Smrekar S.E., Stofan E.R. Corona formation and heat loss on Venus by coupled upwelling and delamination // Science. 1997. V. 277. P. 1289–1294.
[11] Crumpler L. S., Aubele J. Volcanism on Venus // in: Encyclopedia of Volcanoes. Bruce Houghton, Hazel Rymer, John Stix, Steve McNutt, and Haraldur Sigurdson eds. Acad. Press. San Diego, San Francisco, New York, Boston, London, Sydney, Toronto. 2000. P. 727–770.
[12] Guseva E. N., Ivanov M.A. Spatiotemporal Relationships of the Groove Belts, Coronal Structures, and Rift Zones of Venus // Solar System Research. 2019. V. 53. No 6. p. 411–422.
[13] Guseva E. N., Ivanov M.A. Structures of Coronae on Venus: Results of Topographic and Geologic Analysis // Solar System Research. 2020. V. 54. No 6. p. 497 - 503.
[14] Ivanov M.A., Head J.W. The history of volcanism on Venus // Planetary and Space Science. 2013. V. 84. P. 66–92.
[15] Ivanov M.A., Head J.W. The history of tectonism on Venus: A stratigraphic analysis // Planetary and Space Science. 2015. V. 113–114. P. 10–32.
[16] Ivanov M.A., Head J.W. Global geological map of Venus // Planetary and Space Science. 2011. V. 59. P. 1559–1600.

MORPHOMETRIC CHARACTERISTICS OF LARGE VOLCANOES ON VENUS

M.A. Ivanov [1], J.W. Head [2]
[1] *Vernadsky Institute, RAS, Moscow, Russia, mikhail_ivanov@brown.edu;*
[2] *Brown University, Providence RI, USA*

KEYWORDS:
Venus, volcanism, large volcanoes, volcano height, volcano size-frequency distribution.

INTRODUCTION:
Among terrestrial planets, large volcanoes are known on Venus, Earth, and Mars and represent an important component of volcanological history of these planets. The number and sizes of the large volcanoes vary significantly. On Mars, there are only a few such features but they have enormous dimensions (e.g., Olympus Mons is ~ 600 km across and ~ 25 km high). The largest volcanoes on Earth are numerous but their dimensions are much smaller [e.g., 1, 2]. On Venus, the largest volcanoes are about as abundant as on Earth, their basal width can reach dimensions of the largest volcanoes on Mars [3], but their height is comparable with that of the volcanoes on Earth. Thus, studies of morphometric characteristics of the large volcanoes (e.g., basal width and height) provide important data that help to constrain/test volcanological theories. Here we report on the results of the morphometric study of a list of large volcanoes on Venus revised after [3].

DATA AND METHOD:
In the catalogue of volcanic landforms on Venus (features ≥ 100 km in diameter [3]), the basal width of the large volcanoes was determined by the extent of the lava apron around the central edifice. This approach overestimates dimensions of the central construct. In our study, we estimated diameter of the volcano main body using the Magellan topographic data. As a first step, we determined an apparent center of a volcano under study. Then we calculated the mean elevation in zones that are concentric to the established center. The width of each zone was measured at a resolution of the size of a pixel of the global topographic map of Venus, ~ 4.641 km. This method allows construction of an average topographic profile of a feature under study [e.g. 4] whose width is significantly larger than resolution of the topographic map. The large volcanoes satisfy this requirement. The radius of a volcano under study was determined on a topographic profile by finding the most prominent break of slope near the volcano base with verification by visual inspection of the SAR images. Using this method, we have determined the following primary morphometric and topographic parameters of the large volcanoes (Fig. 1): diameter of the volcano, $D_v = 2R_v$ (R_v - mean radius of the volcano), mean diameter of the lava apron, $D_a = 2R_a$ (R_a - mean radius of the apron), maximum elevation at the volcano summit, H_{max}, mean elevation of the volcano summit, h_s, elevation of the volcano base, h_b, height of the construct, $h = h_s - h_b$.

SIZE-FREQUENCY DISTRIBUTION OF LARGE VOLCANOES ON VENUS:
A curve of the size-frequency distribution of the large volcanoes suggests that there are three subpopulations of these features (Fig. 2).

1. The first consists of the largest volcanoes with diameters from ~ 425 to ~ 750 km. There are 20 such structures; their mean diameter is ~ 560 ± 100 km (1σ). The slope of approximating the linear fit of these volcanoes, ~0.07, is about twice smaller than the slope of a model random distribution, ~ 0.139. Thus, these features are not only the largest but also show greater variations in their sizes. These characteristics suggest that the formation of these volcanoes requires unusual combinations of factors favoring growth of volcanic constructs (e.g., higher magma supply rate during prolonged episodes). The largest volcanoes are characterized by the smallest D_a / D_v ratio, ~ 1.2 ± 0.3. This suggests that during the formation of the largest volcanoes, the eruption points were more broadly

distributed within the area of actual volcano and about equally contributed to the formation of the apron and the central edifice, which correspond to the case of unbuffered dike emplacement [5]. About 50% of these volcanoes occur in a spatial association with the Beta-Atla-Themis (BAT) region and several others are associated with the eastern Eistla rise.

2. The second subpopulation includes 27 volcanoes in a diameter range ~ 230 - 400 km. The mean diameter of such volcanoes is ~ 310 ± 55 km and their size-frequency distribution mimics the model random distribution (Fig. 2). This suggests that although volcanoes of these sizes are less frequent in comparison with the random distribution, they likely formed by a random combination of factors both favoring and disfavoring edifice growth. The D_a/D_v ratio of these volcanoes is distinctly higher ~ 1.7 ± 0.5, which suggests that during their formation the eruption points were more concentrated in a region of a future edifice and contributed more to the edifice growth. These volcanoes are also mostly associated with the BAT region and occur on the Eistla, Ulfrun, and Bell volcanic rises.
3. The most abundant subpopulation of large volcanoes includes 42 structures, the diameters of which vary from about 90 to 200 km; their mean diameter is ~ 140 ± 35 km. The slope of the approximating linear fit of these volcanoes, ~ 0.428, is significantly steeper that of the model random distribution (Fig. 2), which means that diameters of these volcanoes are more tightly clustered at the mean value. The narrower diameter range of these volcanoes and their larger number (~ 47 % of the total population of the large volcanoes) suggest that these structures represent the most common large volcanic constructs on Venus. These volcanoes occur at the lower background elevations (mean is ~ 0.64 ± 0.56 km) and have the largest D_a / D_v ratio, ~ 2.0 ± 1.0, which suggests a higher concentration of the eruption points in the area below the volcano and prevalence of the buffered dike emplacement [5] during the formation of these volcanoes. The BAT region apparently did not control the spatial distribution of these volcanoes and they preferentially occur within the vast plains eastward of the BAT.

HEIGHT OF THE LARGE VOLCANOES:

The cumulative frequency distribution of the heights of the large volcanoes shows that among these features there are four (~ 4.5 % of total population) unusually tall volcanoes (Fig. 3). These are Maat (Atla Regio), Polik-mana (western Beta Regio), Yunya-mana (northern Themis Regio), and Tepev (Bell Regio) Montes. Their heights vary from ~ 2.9 to 6.1 km. The first three volcanoes mark vertices of the BAT triangle and occur in spatial association with broad rift zones; Tepev crowns rift-free Bell Regio. The other large volcanoes (95.5 % of the population) are characterized by rather narrow range of heights between ~ 0.1 and 2.5 km with the mean height of ~ 1.1 ± 0.6 km. The strong clustering of the majority of the large volcanoes at single and relatively low value is likely a consequence of the higher atmospheric pressure on Venus that suppresses degassing of ascending magma and favors locking the neutral buoyancy zone below the surface [6, 7].

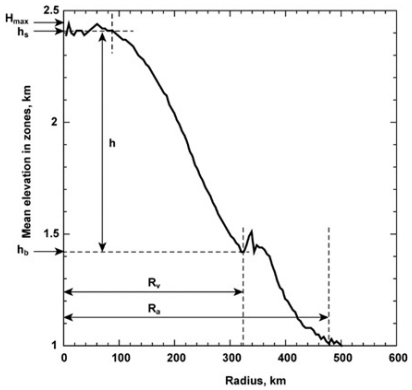


Fig. 1. Morphometric parameters of large volcanoes in this analysis.

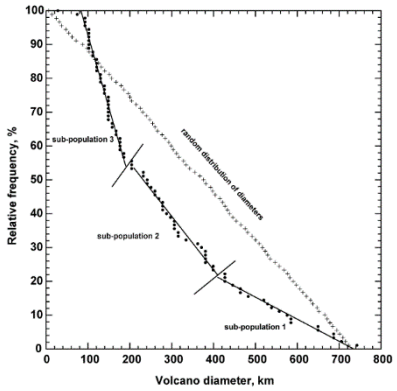


Fig. 2. SFD of large volcanoes on Venus.

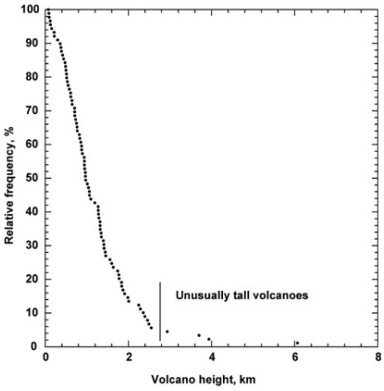


Fig. 3. Frequency distribution of heights of large volcanoes on Venus.

REFERENCES:

[1] Pike, R.J., Clow, G.D. Revised classification of terrestrial volcanoes and catalog of topographic dimensions, with new results of edifice volume. // USGS OFR 81 - 1038. 1981.
[2] Grosse, P., Euillades, P.A., Euillades, L.D., van Wyk de Vries, B. A global database of composite volcano morphometry. // Bull. Volcanol. 2014. 76 : 784.
[3] Crumpler L. S., Aubele J. Volcanism on Venus. // in: Encyclopedia of Volcanoes, Bruce Houghton, Hazel Rymer, J. Stix, S. McNutt, H. Sigurdson eds., Acad. Press. 2000. P. 727–770.
[4] McGovern, P.J., Solomon, S.C., Head, J.W., Smith, D.E., Zuber, M.T, Neumann, G.A. Extension and uplift at Alba Patera, Mars: Insights from MOLA observatios and loading models. // Journ. Geophys. Res. 2001. V.106. P. 23769–23908.
[5] Parfitt, E.A., Head, J.W. Buffered and unbuffered dike emplacement on Earth and Venus — Implications for magma reservoir size, depth, and rate of magma replenishment. // Earth, Moon, and Planets. 1993. v. 61, NO. 3, p. 249–281.
[6] Head, J.W., Wilson, L., Volcanic processes and landforms on Venus: Theory, predictions, and observations. // Journ. Geophys. Res. 1986. V. 91. P. 9407–9446.
[7] Head, J.W., Wilson, L., Magma reservoirs and neutral buoyancy zones on Venus: Implications for the formation and evolution of volcanic landforms. // Journ. Geophys. Res. 1992. V. 97. P. 3877–3903.

STRUCTURAL MAP OF NORTHERN ASTKHIK PLANUM AND SELU CORONA, LADA TERRA, VENUS

L.M. MacLellan [1], R.E. Ernst [1,2]
[1] *Department of Earth Sciences, Carleton University, Ottawa, ON, Canada;*
[2] *Faculty of Geology and Geography, Tomsk State University, Tomsk, Russia*

KEYWORDS:
Venus, planetary geology, Selu Corona, Astkhik Planum, graben, Yenkhoboy Fossae, Brynhild Fossae, dyke swarm, Fatua Corona

INTRODUCTION:
We present preliminary 1 : 500,000 scale structural mapping of the northern portion of Astkhik Planum as part of a continuation of same-scale geological mapping completed in southern Astkhik Planum [1]. The mapped area falls within the Kaiwan Fluctus (V – 44) quadrangle and spans 4.5° – 23° E, 36° – 44.5° S. Our mapping expands on the previous 1 : 5 000 000 scale mapping [2] done as part of the Quadrangle Series by separating the "grabens" (consisting of grabens, fractures and fissures and interpreted to overlie dykes) into sets and tracing them back to their sources; thus far, we have identified 24 graben sets with sources consisting of Selu Corona, cryptic centers and potentially Fatua Corona and Eve Corona (Fig. 1).

GRABEN SETS (DYKE SWARMS):
Twenty-four distinct graben sets, overlying dyke swarms, have been identified in northern Astkhik Planum (Fig. 1). Herein graben sets will be referred to by the numbering found within the legend for Figure 1.

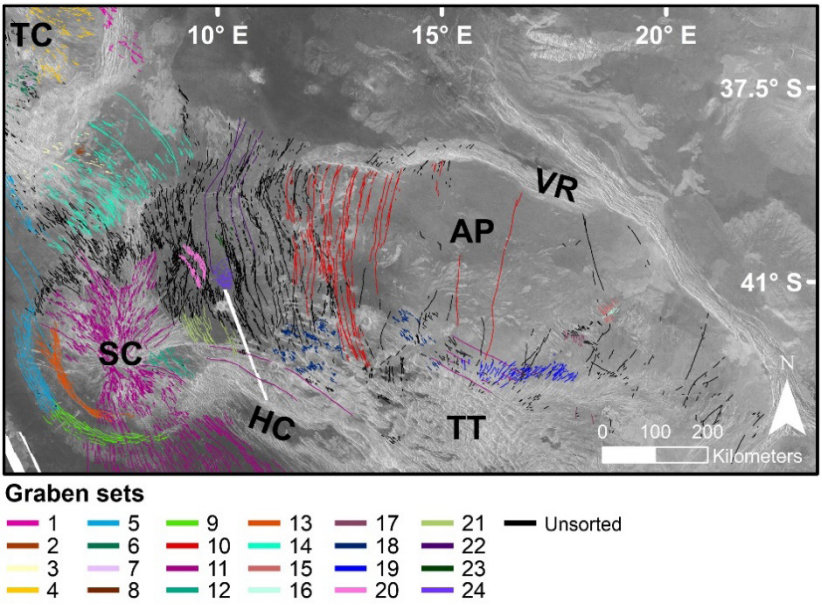


Fig. 1. Structural map of the graben sets and unsorted graben in Northern Astkhik Planum. AP = Astkhik Planum, SC = Selu Corona, VR = Vaidilute Rupes, HC = Hanghepiwi Chasma, TC = Tamfana Corona, TT = Tyche Tessera. NW-trending white lines represent missing Magellan data.

SELU CORONA GRABEN:
Selu Corona, located at 42.5°S, 6°E, is a part of the NW-trending Alpha-Lada extensional belt and marks the NW corner of Astkhik Planum. It is considered a corona-nova and is composed of a radiating center (graben set 11) and two elevated annuli; the outer annulus (graben sets 5 and 9) is ~ 50 % intact, whereas the inner annulus (graben set 13) is ~ 25 % intact, and both

are located on the western side of the corona (Fig. 2). Through our detailed mapping, we found that the corona center hosts multiple distinct radiating centers. Furthermore, the outer annulus (rim) can be divided into two parts: (1) the western portion (graben set 5) has a constant SE-trend, despite the overall annulus curving around Selu Corona. We propose that the graben in this section of the outer annulus actually belong to a set originating from another corona (Eve) centered 1230 km to the NW; these graben are only visible in the Selu corona annulus due to its high topography allowing escape from lava flooding; (2) the southern portion (graben set 9) has a continuously changing trend that follows around the southern portion of Selu Corona and thus graben set 9 is a circumferential graben system belonging to Selu Corona.

The majority of the radiating graben set from Selu Corona are flooded. Only those located within the topographic high (inward from the outer annulus) are preserved. However, there are some large Selu radiating "master" graben that were preserved (probably because they were deep enough to avoid been completely flooded by the younger flows). Yenkhoboy Fossae are master graben that extend ~ 1500 km south from Selu Corona, towards Eithinoha Corona. There are several other master graben that radiate east from Selu Corona. Some of these graben are continuously visible throughout Tyche Tessera and can be traced for distances up to 660 km. Others cannot be directly seen for large distances throughout Astkhik Planum due to flooding, but their continuation is inferred from flooded narrow valleys (originally Selu graben) cutting through remnants of tessera; these graben can be traced for up to 900 km (Fig. 2).

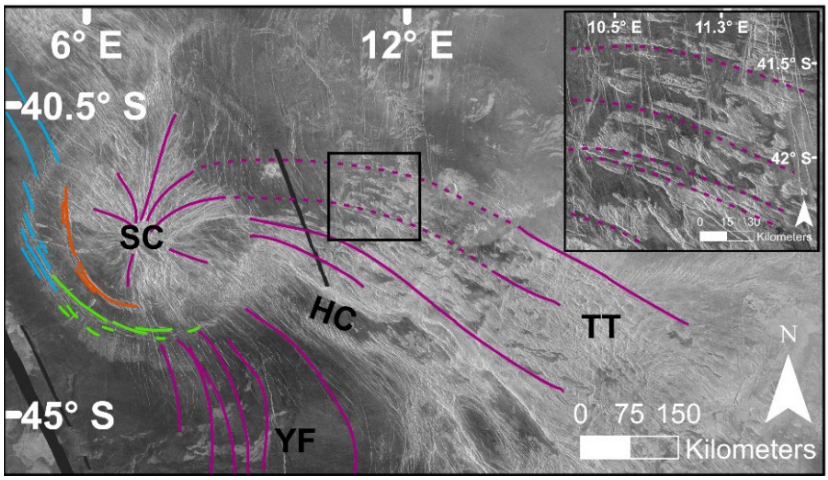


Fig. 2. Schematic diagram of the graben sets belonging to Selu Corona. The outer annulus consists of graben sets 5 (blue) and 9 (green), the inner annulus is graben set 13 (orange) and the radiating set is graben set 11 (purple). SC = Selu Corona, HC = Hanghepiwi Chasma, TT = Tyche Tessera, YF = Yenkhoboy Fossae. NW-trending black lines represent missing Magellan data.

NS-TRENDING GRABEN:

Graben sets 14 and 22 have trends SE and SW, respectively. However, once they enter into Astkhik Planum, both of their trends change to become NS-trending; graben set 14 experiences a gradual change, whereas graben set 22 experiences an abrupt "kink" in its trend (Fig. 3). Neither set appears to be influenced by the nearby Selu Corona, so we assume Selu Corona was not tectonically active or did not exist at this time. Furthermore, the kink in trend of graben set 22 perfectly aligns with the topographic change associated with Astkhik Planum, which is raised a few hundred meters above the surrounding planes. The change in graben set trends is likely due to a change in the stress field that is local to Astkhik Planum. The cause of such a N-S sigma 1 stress across Astkhik Planum is unknown.

We are evaluating the possibility that graben set 22 is a continuation of Brynhild Fossae and is sourced from Fatua Corona [3, 4]. Before these graben enter Astkhik Planum, they have the same trend as Brynhild Fossae but are seperated by a 660 km gap of younger volcanism (Fig. 3). This interpretation is supported by the presence of partially flooded remnants of similar trending grabens throughout the volcanic plain (dotted region in Fig. 3).

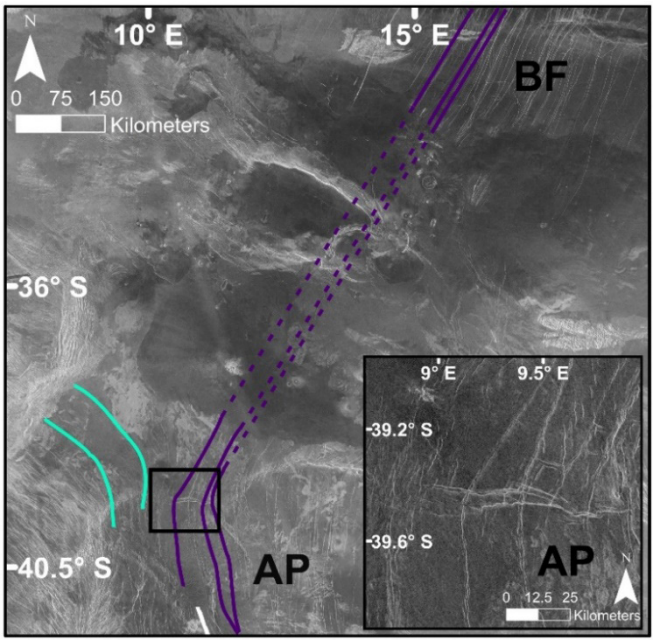


Fig. 3. Schematic diagram of graben sets 14 (blue) and 22 (purple) changing to a NS-trend once entering Astkhik Planum. The inset image highlights the abrupt kink in graben set 22's trend. AP = Astkhik Planum, BF = Brynhild Fossae. NW-trending white line represents missing Magellan data.

FUTURE WORK:

Further structural mapping still needs to be conducted, as well as sorting the unsorted graben into sets and identifying their sources. Mapping of the flows in northern Astkhik Planum is also underway in order to determine the flow emplacement history, their sources, and their timing/link with the graben sets. Both the structural mapping and flow mapping will be linked to previous detailed mapping done in southern Astkhik Planum centering on Derceto Corona [1] to gain insights into the history of the entirety of Astkhik Planum, and also its connection to Vaidilute Rupes, Hanghepiwi Chasma, surrounding coronas and the adjacent lowlands.

REFERENCES:

[1] MacLellan L.M., Ernst R.E., El Bilali H., Ghail R., Bethell E. Volcanic history of the Derceto large igneous province, Astkhik Planum, Venus // Earth-Science Reviews. 2021. V. 220.

[2] Bridges N.T., McGill G.E. Structure/Volcano Map of the Kaiwan Fluctus Quadrangle (V – 44), Venus // U.S. Geological Survey Geologic Investigations Series I-2747. 2005.

[3] Bethell E.M., Ernst R.E., Samson C., Buchan K.L. Detailed Mapping od Graben-Fissure Systems Associated with Fatua Corona, Venus: Implications for Magmatism and the Regional Stress Field // Lunar and Planetary Science XLVIII. 2017.

[4] Bethell E.M., Ernst R.E., Samson C. The Geological Map of Alpha Regio (V – 32) Quadrangle // Journal of Maps. 2019. V. 15. No. 2. P. 474–486.

INFLUENCE OF WIND FIELDS WITH MACROSCOPIC VELOCITY GRADIENTS ON THE IR CO_2 BANDS EMISSIONS OUTGOING FROM A PLANETARY ATMOSPHERE

V.P. Ogibalov [1,2,3], Yu.I. Bordovskaya [4]

[1] *Admiral Makarov state university of maritime and inland shipping, Dvinskaya str., 5/7, Saint-Petersburg, 198035, Russia, vpo563@mail.ru;*

[2] *Saint-Petersburg state marine technical university, Lotsmanskaya str., 3, Saint-Petersburg, 190121, Russia;*

[3] *Saint-Petersburg state forest technical university, Institutskiy per., 5 letter B, Saint-Petersburg, 198264, Russia;*

[4] *Saint-Petersburg state university, Universitetskaya nab., 7/9, Saint-Petersburg, 199034, Russia, bordovskayay@gmail.com*

KEYWORDS:
radiative transfer, planetary atmospheres, wind field gradient, Venus, molecular bands, carbon dioxide.

INTRODUCTION:

Modeling radiation fields in planetary atmospheres is an important task of atmospheric optics. For example, its results are important when considering the energy balance of the atmosphere and the surface, and are also necessary when modeling measurements of optical devices in the problem of remote sensing of the atmosphere and the underlying surface.

In recent decades, there have been successful missions of automated interplanetary stations to Venus (Venus Express) and to the borders of the Solar system (Voyager). The phenomenon of superrotation which consists in a presence of wind currents with significant velocities in the narrow altitude region above the top of cloud layer at low latitudes in the Venusian atmosphere was found [1 - 2]. Also significant wind speeds on Neptune were also measured [3]. Until now, a number of issues related to the energy and dynamics of the atmosphere of Venus remain unclear.

At angles of view that differ from the direction of viewing in the nadir, there is a non-zero projection of wind speed on the beam of view, and as a result of the Doppler effect, there is a shift in the volume absorption coefficient of radiation in frequency. There are two things to consider: 1) the spectral dependence of the absorption coefficient in the core of the spectral line of atmospheric gases is very strong and 2) its values themselves at frequencies near the central frequency of the line are the largest. Therefore, even small frequency shifts can lead to a significant change in the volume absorption coefficient of radiation and, consequently, to a change in the radiation transfer pattern. Thus, the study of the possible influence of large-scale vertical gradients of horizontal wind speed is an urgent task for the optics of planetary atmospheres.

In previous studies, the problem of radiation transfer in molecular bands of carbon dioxide was also solved for the atmosphere of Venus. But the influence of velocity gradients of large-scale wind currents on the characteristics of the radiation field at the frequencies of spectral lines of atmospheric gases has not yet been studied.

MODEL AND RESULTS:

In the framework of the simplified model, the problem of radiation transfer in the spectral lines of infrared CO_2 bands in the planet's atmosphere is considered for the first time, taking into account the frequency shift of the volume absorption coefficient of radiation due to the Doppler effect. This shift occurs when the projection of the velocity of large-scale wind movements on the sighting beam is not zero. For different viewing angles, the variability of the values of the radiation intensity leaving the atmosphere at the upper boundary was studied, depending on a number of parameters of both the model of the vertical gradient of the horizontal wind speed and the spectral parameters of the line (band).

It is shown that the presence of a layer moving in the atmosphere can significantly affect the intensity of radiation leaving the atmosphere at the upper boundary, for a certain frequency range. In particular, if there is a temperature gradient, the intensity of outgoing radiation at some frequencies may increase, and at others it may decrease several times, but without compensation.

The main conclusions are as follows. 1) the effect of large-scale gradients is most noticeable when the visual beam is almost parallel to the horizontal velocity vector, i.e. along or against the moving layer (the azimuth angle values are close to 0 or 180) and/or strongly inclined (the Zenith angle is close to 90). At the same time, even when the visual beam is directed almost perpendicular, the effect of taking into account the Doppler effect is noticeable, especially in the red wing of the spectral line.

The analysis of the results of the present study allows us to conclude that further investigations of the above mentioned radiative transfer problem for more realistic models would be fruitful.

REFERENCES:

[1] Lebonnois, S., F. Hourdin, V. Eymet, A. Crespin, R. Fournier, and F. Forget. Superrotation of Venus' atmosphere analyzed with a full general circulation model // J. Geophys. Res. 2010. Vol. 115. E06006. doi:10.1029/2009JE003458.

[2] Mendonça, J.M., Read, P.L.. Exploring the Venus global super-rotation using a comprehensive general circulation model // Planetary and Space Science. 2016. Vol. 134. P. 1 - 18. doi: 10.1016/j.pss.2016.09.001.

[3] Mousis, O., Atkinson, D.H., Cavalie, T. L.N., et al. Scientific rationale for Uranus and Neptune in situ explorations // Planetary and Space Science. 2018. V. 155. P. 12 - 40. doi: 10.1016/j.pss.2017.10.005.

DEVELOPING A DYKE SWARM HISTORY FOR BELL REGIO, VENUS

M. Riaz [1], R.E. Ernst [1,2], H. El Bilali [2]
[1] *Department of Earth Sciences, Carleton University, Ottawa, Ontario, Canada, MahanoorRiaz@cmail.carleton.ca, richard.ernst@ernstgeosciences.com, hafidaelbilali@cunet.carleton.ca;*
[2] *Faculty of Geology and Geography, Tomsk State University, Tomsk, Russia*

KEYWORDS:
Nyx Corona, dyke swarm, giant radiating dyke swarm, giant circumferential dyke swarm, Bell Regio, Tepev Mons, Nefertiti Mons, Otafuku Tholus

INTRODUCTION:
Bell Regio is a broad rise approximately 1500 km in diameter with several main volcanic centres, Tepev Mons, Nyx Mons, Nefertiti Mons and Otafuku Tholus (e,g, [1–3]).

The goal of our mapping is to provide a detailed dyke swarm history of Bell Regio. There are abundant graben fissures lineaments and also pit chains [4] in Bell Regio (Fig. 1) which can be grouped into distinct sets on the basis of their distribution and trends (Fig. 2). Such sets can be interpreted to mark radiating and circumferential dyke swarms [5] and which can be associated with known volcanic centres or unnamed cryptic centres within Bell Regio or potentially linked to more distal magmatic centres outside Bell Regio.

Our preliminary work reported herein (Figs. 1–2) will be extended across Bell Regio in order to develop the full dyke swarm history. A dyke swarm framework for Bell Regio will then allow a second stage of research focused on the volcanic flow history and determining the specific sources for each flow. As an example, Fig. 3 shows an important package of radar bright flows being fed from circumferential dykes associated with Nyx Mons.

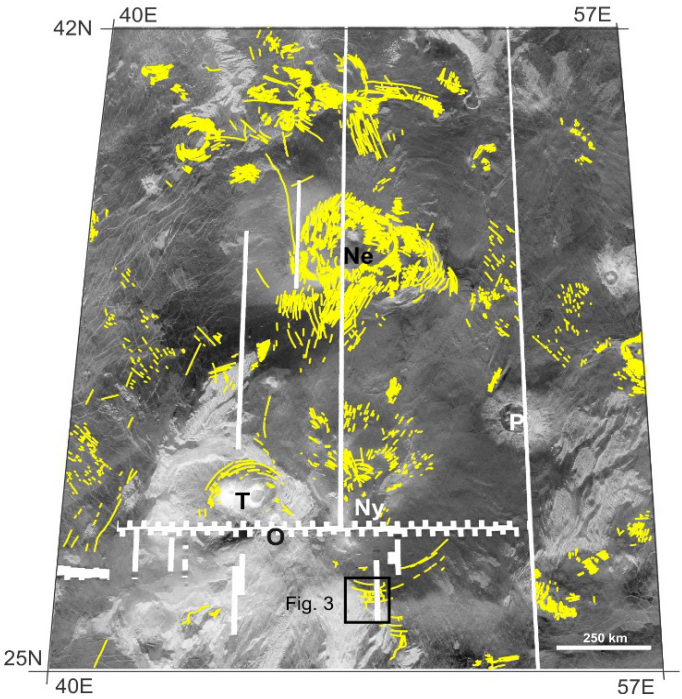


Fig. 1. Preliminary map of graben fissure systems of Bell Regio (interpreted as dyke swarms). Ny = Nyx Mons, T = Tepev Mons, O = Otafuku Tholi, Ne = Nefertiti Corona, P = Potanina Crater. Box locates Figure 2. All lineaments are shown in yellow.

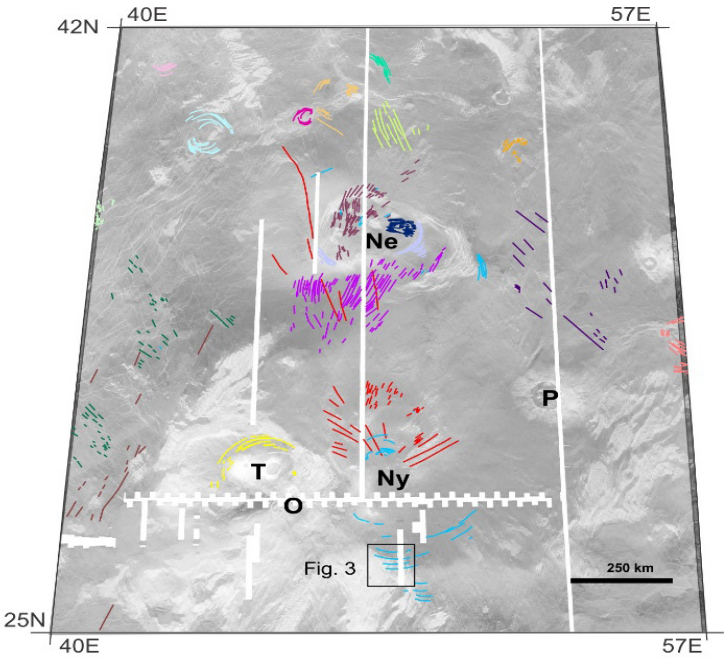


Fig. 2. Extensional lineaments of Fig. 1 generalized and colour-coded to represent different swarms. Note the radiating (red lines) and circumferential (blue lines) sets associated with Nyx Mons, and the yellow set that circumscribes the central portion of Tepev Mons.

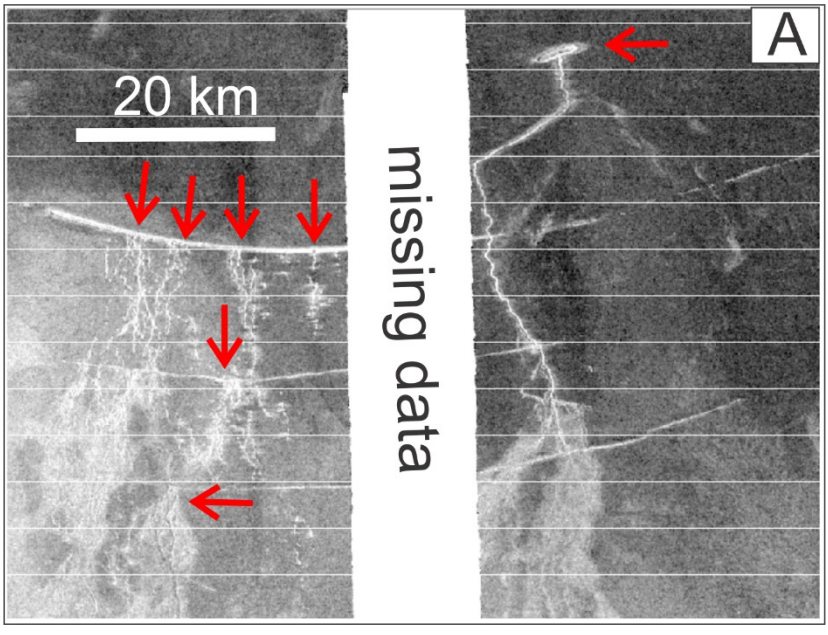


Fig. 3. Circumferential dykes of Nyx Mons feeding radar bright flows. Location of image given in Figures 1 and 2.

REFERENCES:

[1] Campbell, B.A., Campbell, P.G. Geologic Map of the Bell Regio Quadrangle (V – 9), Venus // USGS Geologic Investigations Series Map I-2743, 2002.
[2] Campbell, B.A., Rogers, P.G. Bell Regio, Venus: Integration of remote sensing data and terrestrial analogs for geologic analysis. // Journal of Geophysical Research, 1994, V. 99, P. 21153–21171

[3] Rogers, P.G., Zuber, M.T. Tectonic evolution of Bell Regio, Venus: lithospheric flexure, and edifice stresses. // Journal of Geophysical Research, 1998, V. 103, No. E7, P. 16841–16,853
[4] Sawford, W.C., Ernst, R.E., Samson, C., Davey, S.C. Pit crater chains in the Nyx Mons region, Venus. // 46th Lunar and Planetary Science Conference, 2015, abstr. 1283.
[5] Buchan, K.L., Ernst, R.E. Plumbing systems of large igneous provinces (LIPs) on Earth and Venus: Investigating the role of giant circumferential and radiating dyke swarms, coronae and novae, and mid-crustal intrusive complexes // Gondwana Research, 2021 (in press).

MAGMATIC FEEDER SYSTEMS OF THE LO SHEN REGION, SOUTHERN MARGIN OF EASTERN OVDA REGIO, VENUS

A. Singhal [1], R.E. Ernst [1,2], H. El Bilali [1]
[1] *Department of Earth Sciences, Carleton University, Ottawa, Ontario, Canada, AnoushkaSinghal@cmail.carleton.ca; richard.ernst@ernstgeosciences.com, hafidaelbilali@cunet.carleton.ca;*
[2] *Faculty of Geology and Geography, Tomsk State University, Tomsk, Russia*

KEYWORDS:
Valles, lava channel, domal uplift, Lo Shen

INTRODUCTION:
Lo Shen Valles is located on the southern margin of eastern Ovda Regio and is more than 225 km long. The upper portion of Lo Shen Valles region (Fig. 1) is the locus of sources for the channelized lava flows of Lo Shen Valles and for additional smaller lava channel systems.

In the present study we are interested in: 1) determining the relative timing of the channelized systems and characterizing their magma reservoir sources; 2) and developing a geological history for the region.

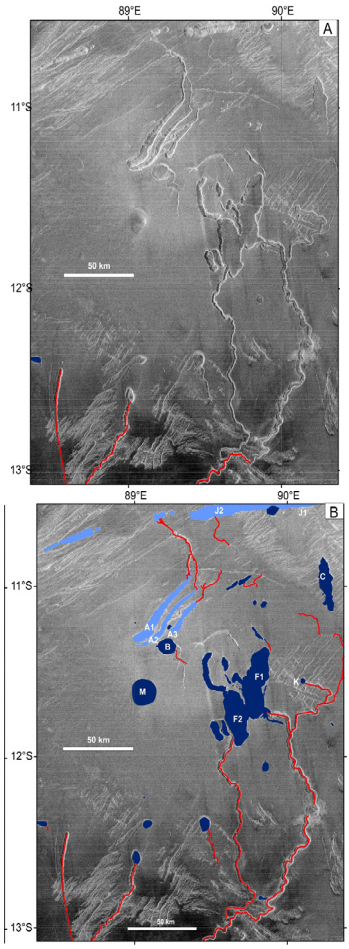


Fig. 1. Upper portion of Lo Shen Valles region, showing distribution of pit chains (light blue) and other depressions (regular or irregular in shape) (dark blue), and lava channels fed from them (red).

INTRUSIONS AS FEEDERS FOR THE CHANNELIZED FLOWS:
The lava sources in our study area are marked by extensive shallow depressions from which channelized flows originate (Fig. 1). Some sources are small and sub-circular (e.g., labelled M in Fig. 1b) and some are more elongate to irregular in shape (e.g. labelled F1 and F2), and all seem to have flooded floors and are provisionally interpreted to represent roof-collapse above shallow magma reservoirs (see similar interpretation in [1]. Those reservoirs that have an elongate shape or distribution (C) are suggested to be associated with dykes (e.g. [2 - 3]) while those of more irregular shape (e.g. F1 and F2) may represent more sill-like reservoirs.

In addition, there are pit chains/troughs (e.g. J1, J2, A1 - A3) representing collapse features above underlying dykes [4], some of which (i.e. A1 - A3) are also sources for channelized flows (Fig. 1).

GEOLOGICAL HISTORY:
These depressions and their channelized flows (Fig. 1) were emplaced onto a smooth surface, representing a lava flooding event that is bordered by unflooded tesserae on the north and east, suggesting flooding of a broad topographic low. However, the area of lava flooding actually corresponds to a topographic high (about 140 × 80 km, and about 300 - 500 m high) (Fig. 2). We suggest that uplift must have occurred after regional lava flooding; otherwise, the adjacent tesserae (which are located downhill in the present topography) would have been flooded. We speculate that this elongate domical uplift was caused by filling of an underlying sill like magma reservoir more than 50 km across and 100 s of m thick.

ASSESSING MAGMA LEVEL IN INTRUSIONS:
This inferred magma reservoir under the broad uplift could also be responsible for feeding magma upward into dykes with surface expression as pit chains (A1 - A3 in Figs. 1b, 2). These pit chains have a maximum elevation of about 4700 m, indicating a 200 - 300 m difference in elevation from that at which the channelized flows started: 4313, 4489 and 4458 m (Fig. 2). This would suggest that the level of magma in dykes A1 - A3 was 200 - 300 m below the surface. We are applying this approach (comparing the elevation at which channelized flows begin with the topographic changes) to more broadly assess magma level in the different reservoirs in the study area, both spatially and through time.

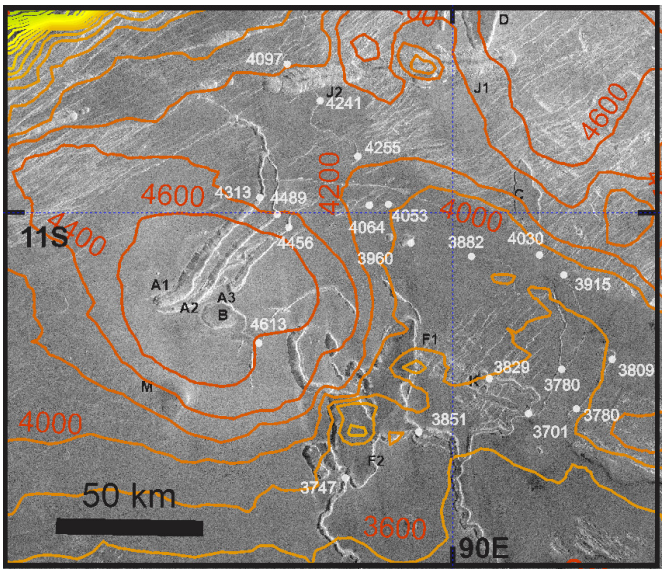


Fig. 2. Upper portion of Lo Shen Valles with shallow intrusions (labels in black), elevation contours and labels in red/orange, and elevation at key points along channelized flows (white lettering). Background image is from Cycle 1 left looking Magellan SAR.

LINKING DYKE-LIKE INTRUSIONS TO REGIONAL SWARMS

An additional aspect in progress is detailed mapping of the graben-fissure systems in the unflooded adjacent areas to identify regional dyke swarms which could potentially be linked with the dyke-like near surface intrusions in our study area.

REFERENCES:

[1] MacLellan, L.M., Ernst, R.E., El Bilali, H., Ghail, R., Bethell, E. Volcanic history of the Derceto large igneous province, Astkhik Planum, Venus // Earth-Science Reviews. 2021. V. 220, No. 103619.

[2] Ernst, R.E., Buchan, K.L. Layered mafic intrusions: a model for their feeder systems and relationships with giant dyke swarms and mantle plume centres. // South African Journal of Geology, 1997, V. 100, P. 319–334.

[3] Ernst, R.E., Liikane, D.A., Jowitt, S.M., Buchan, K.L., Blanchard, J.A. A new plumbing system framework for mantle plume-related continental Large Igneous Provinces and their mafic-Ultramafic intrusions. // Journal of Volcanology and Geothermal Research. 2019. V. 384. P. 75–84.

[4] Davey, S.C., Ernst, R.E., Samson, C., Grosfils, E.B. Hierarchical clustering of pit crater chains on Venus // Canadian Journal of Earth Sciences, 2013, V. 50, P. 109–126.

DEVELOPING A DETAILED MAGMATIC HISTORY OF EASTERN RUSALKA PLANITIA, VENUS

M.A. Mediany [1], H. El Bilali [2,3], R.E. Ernst [3,4], N. Youbi [1]
[1] *Department of Geology, Faculty of Sciences-Semlalia, Cadi Ayyad University, Marrakesh, Morocco; acheraf17@gmail.com;*
[2] *Department of Earth Sciences, Carleton University, Ottawa, Ontario, Canada;hafidaelbilali@cunet.carleton.ca, richard.ernst@ernstgeosciences.com;*
[3] *Faculty of Geology and Geography, Tomsk State University, Tomsk, Russia*

KEYWORDS:
Rusalka Planitia, Dali-Diana Chasmata, Atla Regio, Sith Corona, graben-fissure lineaments, dyke swarms, rifts, Zaryanitsa Dorsa

INTRODUCTION:
The Dali-Diana Chasmata (rift zone) trends SW from Atla Regio (Fig. 1) and is bordered on the north side by Rusalka Planita. Trending from the chasma into the planitia is a NNW-trending line of coronae, spatially associated with Zaryanitsa Dorsa (e.g. [1, 2]). This region is part of Quadrangle V – 37 which was mapped at 1 : 5 000 000 scale [1]. There has also been detailed structural analysis focused on the dorsum in the region [2]. These two studies [1, 2] provide an important framework for the focus of the present study.

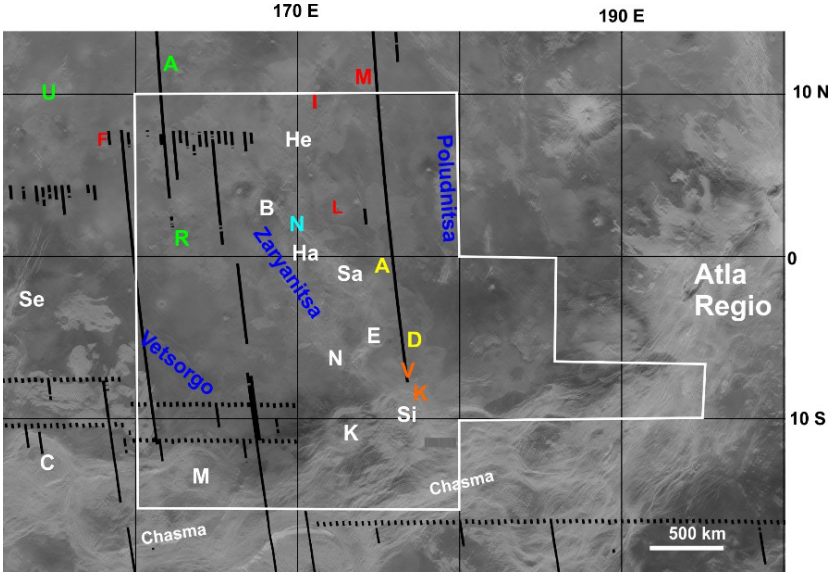


Fig. 1. Distribution of named volcanic and structural units in the map region. Location of Figs. 2 and 3 is given by white outline.
Corona (in white): B = Bil, C = Ceres, E = Eigin, Ha = Hannahannas, He = Heqet, K = Khabuchi, M = Miralaidji, N = Nirmali, Sa = Saunau, Se = Seia, and Si = Sith.
Colles (in green): A = Asherat, R = Ran, U = Urutonga.
Mons (in red): F = Fand, I = Iseghey, L = Lamashtu, M = Muhongo.
Tholus (in orange): K = Khotal-Ekva, V = Vilakh
Fluctus (in yellow): A = Argimpasa, D = Dotetem
Dorsa: Poludnitsa, Zaryanitsa, Vetsorgo
Farra (light blue): Nammu

The present detailed 1 : 500 000 scale study focuses on the magmatic components: 1) mapping of lava flow distributions and identification of their sources; and 2) mapping graben-fissure systems, which can be interpreted to overlie dyke swarms [e.g. [3]). The goal is to integrate the distribution of flows and dyke swarms with known magmatic centres (coronae, mons, etc.) in order to develop the magmatic history for this eastern portion of Rusalka Planitia and understand the relationship with dorsum and chasmata. Fig. 1 shows the numerous magmat-

ic centres (mainly coronae and, mons), and associated flow fields (flucti) recognized for the region, each of which can potentially have an associated radiating and/or circumferential graben-fissure system [3]. Fig. 2 provides a preliminary geological map of the study area with colours coded in terms of relative age. Fig. 3 provides the current progress in mapping of graben-fissure system (interpreted to represent dykes) in the southern half of the study area.

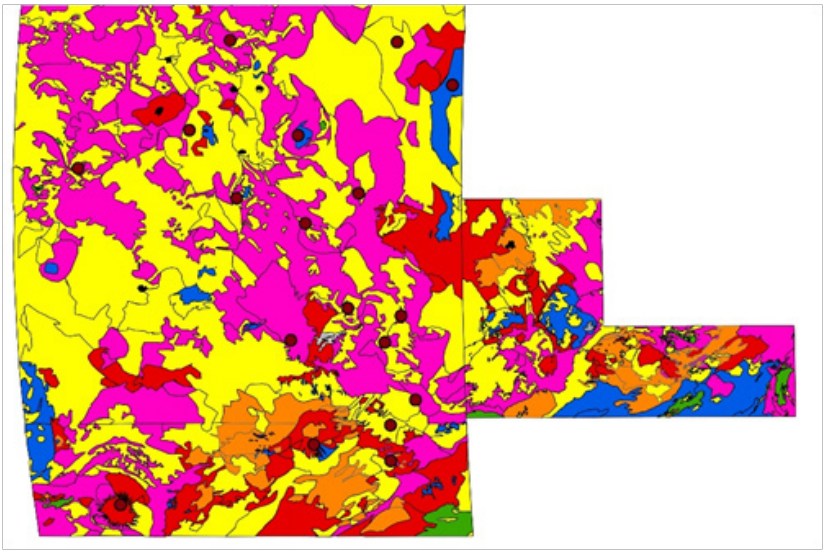


Fig. 2. Distribution of units in the area. Oldest to youngest have the colours: green, blue, yellow, orange, red, pink. Brown dots locate named features (Fig. 1).

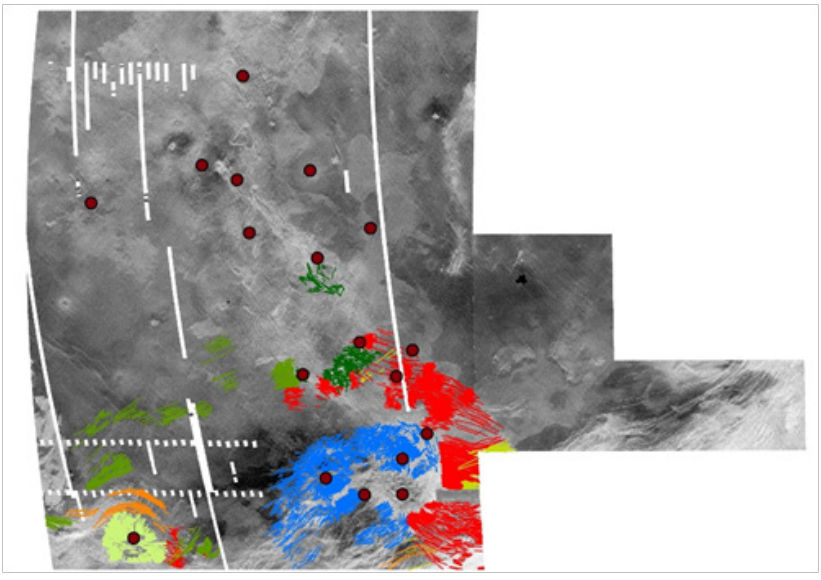


Fig. 3. Graben-fissure distribution.

REFERENCES:

[1] Hansen, V.L., DeShon, H.R. Geologic map of the Diana Chasma Quadrangle (V. 37), Venus. // USGS Geologic Investigations Series I-2752, 2002
[2] Young, D.A., Hansen, V.L. Poludnista Dorsa, Venus: History and context of a deformation belt. // Journal of Geophysical Research, 2005, V. 110, N. E03001.,
[3] Buchan, K.L., Ernst, R.E. Plumbing systems of large igneous provinces (LIPs) on Earth and Venus: Investigating the role of giant circumferential and radiating dyke swarms, coronae and novae, and mid-crustal intrusive complexes // Gondwana Research, 2021 (in press).

DETAILED MAPPING OF A CORONA CLUSTER WITHIN DALI-DIANA CHASMATA 1000 KM SW OF ATLA REGIO, VENUS

A. Hasanaine [1], H. El Bilali [2], R.E. Ernst [2,3], N. Youbi [1]
[1] *Department of Geology, Faculty of Sciences-Semlalia, Cadi Ayyad University, Marrakesh, Morocco; rziki.23kech@gmail.com;*
[2] *Department of Earth Sciences, Carleton University, Ottawa, Ontario, Canada;hafidaelbilali@cunet.carleton.ca, richard.ernst@ernstgeosciences.com;*
[3] *Faculty of Geology and Geography, Tomsk State University, Tomsk, Russia*

KEYWORDS:
Atla Regio, Chasma, dyke swarm, graben-fissure lineament, magmatic centre

INTRODUCTION:
Although, corona can be abundant along chasma (rifts) (e.g. [1–6]), the role of corona in the evolution of chasma is not well understood. The present contribution aims to apply detailed (1 : 500,000 scale) geological mapping to a section of a chasma about 1000 km to the SW of Atla Regio (Fig. 1). The mapping will include graben-fissure systems (interpreted to overlie dykes), normal faults associated with rifting, and associated flows, all integrated with topographic data. The goal of this high resolution (1 : 500 000 scale mapping) is an improved understanding of the relationships between corona and rift segments and to test the model of [6]. Based on detailed mapping of graben fissure systems and interpreted rift faults along a 1500 km long segment of Parga Chasma, [6] recognized that many coronae represent the locus of local triple junction rift centres, and extrapolated this observation to the entire length of both Parga and Hecate Chasmata. Current progress in graben-fissure mapping is shown in Figure 2.

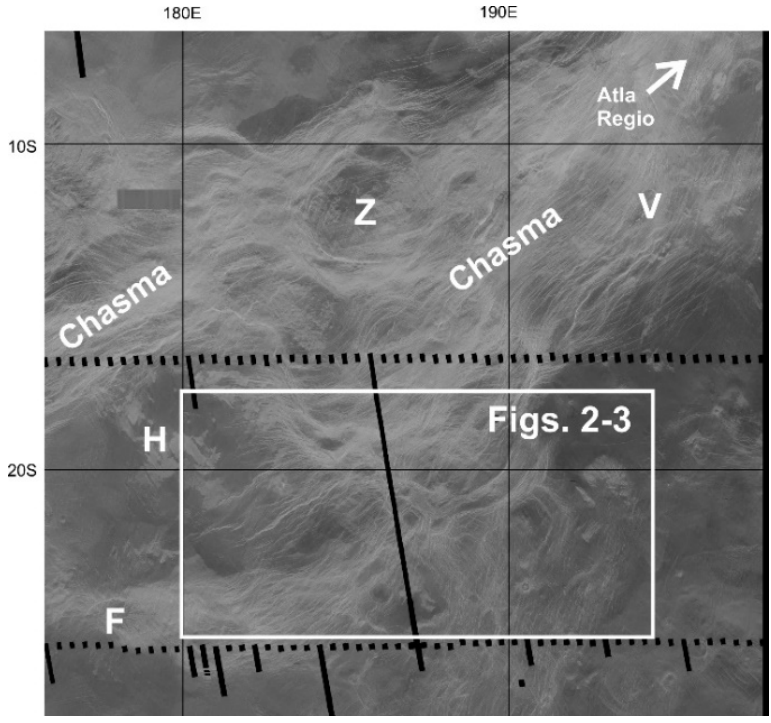


Fig. 1. Location of the study area along the southern margin of Dali Chasma about 150 km SW of Atla Regio. Named corona are: F = Flidais Corona, V = Vibert-Douglas Patera, and Z Žemina Corona. Additional unnamed corona-like features are also present (recognized by their circular appearance). H = Henwen fluctus

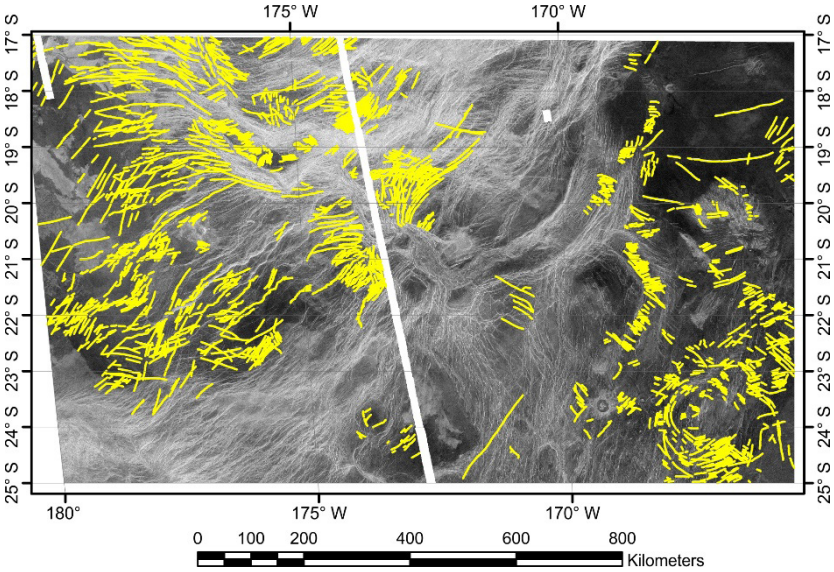


Fig. 2. Initial mapping of graben fissure lineaments. Location of study area is shown in Fig. 1.

REFERENCES:

[1] Hamilton, V.E., Stofan, E.R. The geomorphology and evolution of Hecate Chasma, Venus. // Icarus 1996, V. 121, P. 171–194

[2] Martin, P., Stofan, E.R. Coronae of Parga Chasma, Venus. // 35th Lunar Planet. Sci., 2004, Abstract 1576 .

[3] Martin, P., Stofan, E.R., Glaze, L.S. , Smrekar, S. Coronae of Parga Chasma, Venus. // J. Geophys. Res. 2007, V. 112, No. E04S03 .

[4] Smrekar, S.E., Hoogenboom, T., Stofan, E.R., Martin, P. Gravity analysis of Parga and Hecate chasmata: Implications for rift and corona formation. // Journal of Geophysical Research, 2010, V. 115, No. E07010, doi:10.1029/2009JE003435.

[5] Ivanov, M.A., Head, J.W. The history of tectonism on Venus: A stratigraphic analysis. // Planetary and Space Science, 2015, V. 113 - 114, P. 10 - 32.

[6] Graff, J.R., Ernst, R.E., Samson, C. Evidence for triple-junction rifting focussed on local magmatic centres along Parga Chasma, Venus. // Icarus, 2018, V. 306, P. 122–138.

DYKE SWARMS OF THE MARAM CORONA AREA, ALONG PARGA CHASMATA, SE OF ATLA REGIO, VENUS

K. Mghazli [1], H. El Bilali [2], R.E. Ernst [2,3], N. Youbi [1]
[1] *Department of Geology, Faculty of Sciences-Semlalia, Cadi Ayyad University, Marrakesh, Morocco; mghazli.k@gmail.com;*
[2] *Department of Earth Sciences, Carleton University, Ottawa, Ontario, Canada;hafidaelbilali@cunet.carleton.ca, richard.ernst@ernstgeosciences.com;*
[3] *Faculty of Geology and Geography, Tomsk State University, Tomsk, Russia*

KEYWORDS:
Maram Corona, Ya-Yerv Corona, Repa Corona, Ulgen-ekhe Coronae, dyke swarm, Parga Chasmata

INTRODUCTION:
The relationship between coronae and chasmata has been extensively discussed (e.g. [1–6]). One such region is along the 10 000 km long Parga Chasma which connects Atla Regio with Themis Regio. Based on detailed mapping of graben fissure systems and interpreted rift faults along a 1500 km long segment of Parga Chasma, [6] recognized that many corona represent the locus of local triple junction rift centres. [6] extrapolated this observation to the entire length of Parga Chasmata (and also Hecate Chasmata) and produced a map of local centres of triple junction rifting focussed on coronae. This was further compared to the Atlantic rift system of Earth.

We have selected a region along Parga Chasmata for detailed study. This area is about 2000 km SE from the centre of Atla Regio (Fig. 1) and for this area the grouping by [6] of rift segments and coronae into local triple junction centres is shown in Fig. 2. The goal of this present research is to provide detailed mapping (1 : 500 000 scale) of the graben fissure systems, lava flows and rift faults integrated with the topographic changes in order to provide insights into setting of these corona within the corona. Our mapping builds on the previous reconnaissance mapping (1 – 5 000 000 scale) of Taussig Quadrangle (V. 39) by [7].

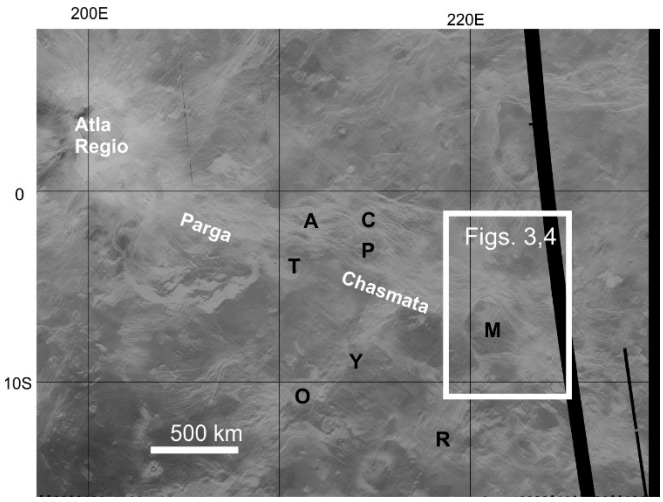


Fig. 1. Location map of present study along Parga Chasma. Named corona (in black letters) are: A = Attabeira, C = Chantico, **M = Maram**, O= Oduduwa, P= Pazar-ana, R = Repa, T = Tadaka, and Y = Ya-Yerv.

Initial mapping of the graben-fissures is shown in Fig. 3 and these graben-fissures are provisionally grouped into distinct sets in Fig. 4 which we interpret to represent dyke swarms. Notably there is an impressive radiating swarm (red

lines) centred on Maram corona, a possible radiating swarm (white lines) centred on location 2, and a circumferential system (pink lines) surround location 1, and more mapping is needed to test which could be associated with location 3. Additional extensive linear sets (e.g., green, yellow, pink, and blue lines) are present which may belong to magmatic centres outside the map area.

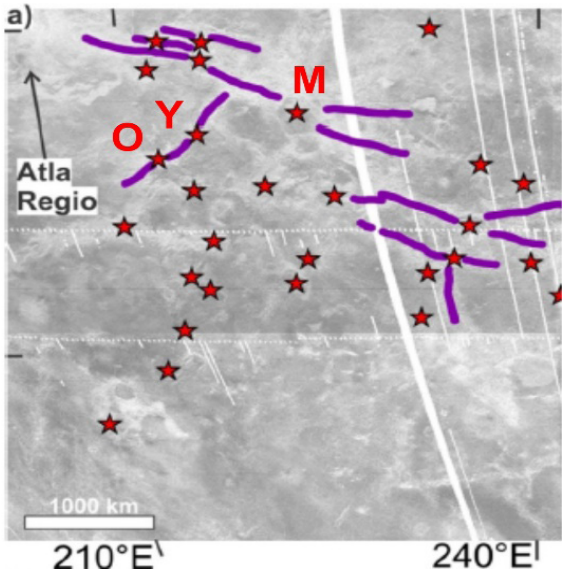


Fig. 2. Interpretation of rift segments. Location of rifts along NW end of Parga chasmata from [6]. M = Maram, O = Oduduwa and Y = Ya-Yerv coronae.

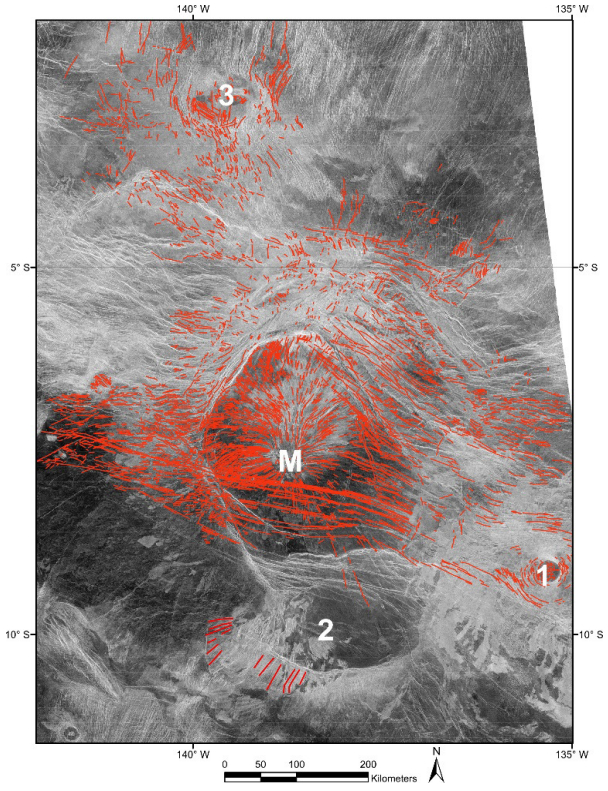


Fig. 3. Initial mapping of graben-fissure systems in the vicinity of Maram Corona (M). 1 and 2 represent additional unnamed magmatic centres.

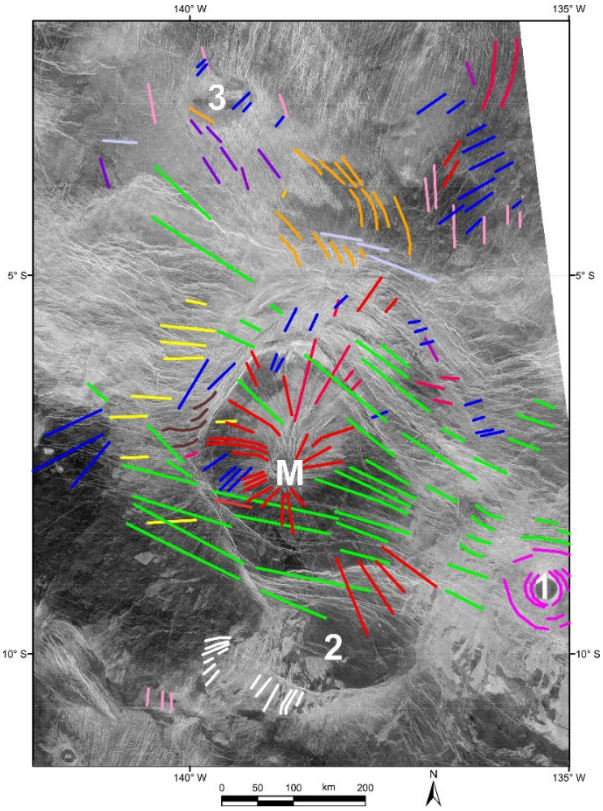


Fig. 4. Initial grouping of graben fissures linework of Fig. 1 into potential distinct dyke swarms based on trend.

REFERENCES:

[1] Hamilton, V.E., Stofan, E.R. The geomorphology and evolution of Hecate Chasma, Venus. // Icarus 1996, V. 121, P. 171–194
[2] Martin, P., Stofan, E.R. Coronae of Parga Chasma, Venus. // 35th Lunar Planet. Sci., 2004, Abstract 1576 .
[3] Martin, P., Stofan, E.R., Glaze, L.S. , Smrekar, S. Coronae of Parga Chasma, Venus. // J. Geophys. Res. 2007, V. 112, No. E04S03 .
[4] Smrekar, S.E., Hoogenboom, T., Stofan, E.R., Martin, P. Gravity analysis of Parga and Hecate chasmata: Implications for rift and corona formation. // Journal of Geophysical Research, 2010, V. 115, No. E07010, doi:10.1029/2009JE003435.
[5] Ivanov, M.A., Head, J.W. The history of tectonism on Venus: A stratigraphic analysis. // Planetary and Space Science, 2015, V. 113-114, P. 10-32.
[6] Graff, J.R., Ernst, R.E., Samson, C. Evidence for triple-junction rifting focussed on local magmatic centres along Parga Chasma, Venus. // Icarus, 2018, V. 306, P. 122–138.
[7] Brian, A.W., Stofan, E.R., Guest, J.E. Geologic Map of the Taussig Quadrangle (V. 39), Venus. // USGS Scientific Investigations Map 2813, 2005.

DETAILED MAPPING OF GRABEN-FISSURE SYSTEMS OF NOTT CORONA REGION, ISABELLA QUADRANGLE (V–50), VENUS

I. Hadimi [1], H. El Bilali [2,3], R.E. Ernst [3], N. Youbi [1]
[1] *Department of Geology, Faculty of Sciences-Semlalia, Cadi Ayyad University, Marrakesh, Morocco, ismail.hadimi@gmail.com;*
[2] *Department of Earth Sciences, Carleton University, Ottawa, Ontario, Canada;hafidaelbilali@cunet.carleton.ca, richard.ernst@ernstgeosciences.com;*
[3] *Faculty of Geology and Geography, Tomsk State University, Tomsk, Russia*

KEYWORDS:
Nott corona, Libby Patera, Tursa Tholus, Epona corona, dyke swarms. Isabella crater

INTRODUCTION:
Nott corona is within Isabella Quadrangle (V–50), located south of Atla Regio east of Aditi Dorsa, west of Wawalag Planitia and north of Nsomeka Planitia. Nott corona has a central depression with dimensions of 110 × 80 km and a depth of about 250 m. Nott Corona has been described in initial reconnaissance mapping of Quadrangle V-50 (e.g., [1 - 2]), and briefly discussed in [3]. Isabella (with a 175 km diameter) is the second largest impact crater on Venus and has been characterized in detail [4].

The region has abundant magmatic features such as Nott and Epon Corona, Libby Patera, Tursa Tholus, as well as graben-fissure systems. We have selected the Nott corona region for detailed (1 : 500 000 scale) geological mapping to produce a geological history that integrates the volcanic features (lava flows and magmatic centres) along with graben fissure systems, marking dyke swarms (c.f. [5])

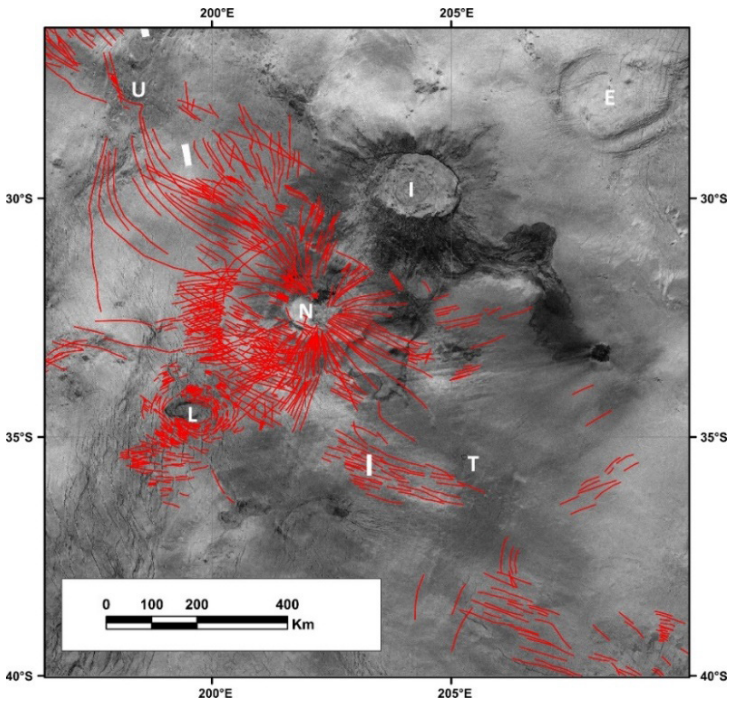


Fig. 1. initial detailed graben-fissure mapping for parts of the study area. N = Nott corona, L = Libby patera, E = Epona corona, T = Tursa tholus, U = unnamed centre, and I = Isabella impact crater. Background is inverted Cycle 1 Magellan SAR image. NW-trending narrow white rectangular regions indicate missing data.

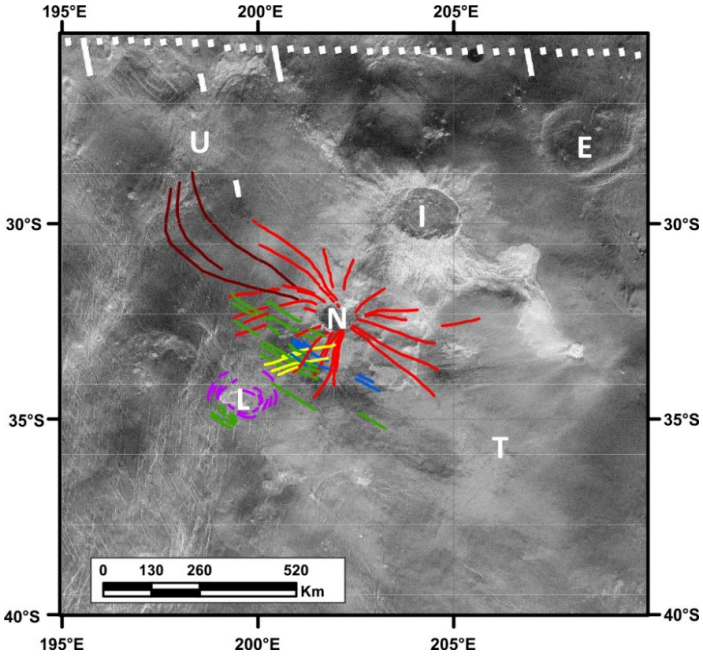


Fig. 2. Generalized trends for some sets of graben-fissure lineaments mapped in Fig. 1. Colours correspond to different generations of interpreted dykes. Labels same as in Fig. 1. Background is Cycle 1 Magellan SAR image. NW-trending narrow white rectangular regions are areas of missing data.

The initial stage of our research (reported in this abstract) is detailed mapping of the radiating graben-fissure systems for the entire region, and grouping of these into different swarms. As seen in Figs. 1 and 2 our preliminary mapping reveals the impressive radiating swarms (red, and dark red) associated with Nott corona (N) and unnamed centre (U), and circumferential swarm (purple) associated with Libby Patera, as well as addition linear swarms (green and yellow) whose source is not yet identified, but could belong to major swarms fed from distal magmatic centres.

Future mapping in this area will focus on detailed mapping (1 : 500 000 scale) of the flows to determine their history, and identify their magmatic sources: fissure-fed from dykes (circumferential or radial) or from shallow collapse features [6], or from circular fractures associated with caldera collapse [7].

REFERENCES:

[1] Bleamaster, L.F. Geologic mapping of Isabella Quadrangle (V50), Venus. // 37th Lunar and Planetary Science Conference, 2006, abstr. No. 2233.

[2] Bleamaster, L.F. Geologic Mapping of Isabella Quadrangle (V-50) and Helen Planitia, Venus. // Abstracts of the Annual Meeting of Planetary Geologic Mappers, Flagstaff, AZ, USA 2008.

[3] Basilevsky, A.T., Raitala, J., Head, J.W. Venus: Estimates of absolute time duration of corona activity. // 40th Lunar and Planetary Science Conference, 2009, Abstr. No. 1827.

[4] Miyamoto, H., Sasaki, S. Two Different Supply Styles of Crater Outflow Materials on Venus Inferred from Numerical Simulations over DEMs. // *Icarus, 2000, V. 145*, P. 533–545.

[5] Buchan, K.L., Ernst, R.E. Plumbing systems of large igneous provinces (LIPs) on Earth and Venus: Investigating the role of giant circumferential and radiating dyke swarms, coronae and novae, and mid-crustal intrusive complexes // Gondwana Research*, 2021* (in press).

[6] MacLellan L.M., Ernst R.E., El Bilali H., Ghail R., Bethell E. Volcanic history of the Derceto large igneous province, Astkhik Planum, Venus // Earth-Science Reviews. 2021. V. 220. No. 103619.

[7] El Bilali, H., Ernst, R.E., Buchan, K.L. Maat Mons, Atla Regio, Venus: magmatic and tectonic history from detailed mapping // Lunar and Planetary Science Conference 52, 2021, abstr. No. 2529.

EVALUATION OF THE CLUSTER OF ANEMONE TYPE VOLCANOES LOCATED SOUTH OF ATLA REGIO, VENUS

F. Najib [1], H. El Bilali [2,3], R.E. Ernst [3], J.W. Head [4], N. Youbi [1]

[1] *Department of Geology, Faculty of Sciences-Semlalia, Cadi Ayyad University, Marrakesh, Morocco; najibfatimaezzahrae@gmail.com;*

[2] *Department of Earth Sciences, Carleton University, Ottawa, Ontario, Canada;hafidaelbilali@cunet.carleton.ca, richard.ernst@ernstgeosciences.com;*

[3] *Faculty of Geology and Geography, Tomsk State University, Tomsk, Russia;*

[4] *Department of Earth, Environmental and Planetary Sciences, Brown University, Providence, RI 02912, U.S.A.*

KEYWORDS:
Volcanic “anemone”, Atla Regio, dyke swarm, Graben-fissure lineaments

INTRODUCTION:

Intermediate volcanoes on Venus are defined as volcanic centres between 20–100 km in diameter [1]. A subclass of these, informally known as the ‘anemone type’, were studied by [1]. They are characterized by petal like lava flows and radiating radar-bright patterns. A total of about 25 anemone have been identified, and they are typically 30 and 40 km diameter [2]. They are unevenly distributed globally and a strong concentration is located in an area south of Atla Regio. An association with fissure eruptions is noted in [1]. Herein we wish to consider in more detail the relationship between anemones and potential feeder dykes.

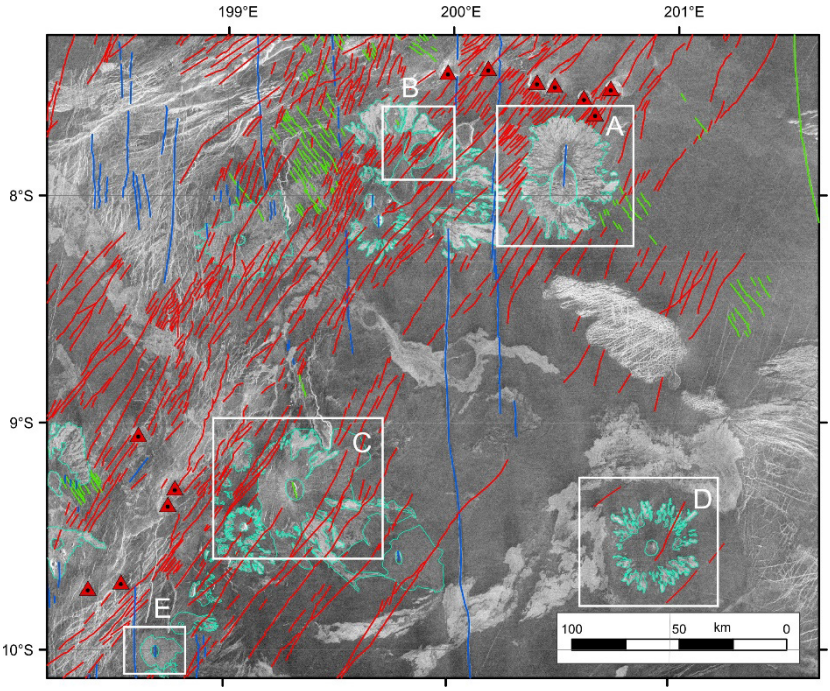


Fig. 1. Region with cluster of Anenomes (with short flows outlined in greenish-blue) and the distribution of the three main graben-fissure systems (N-trending blue, NE-trending red and NW-trending green. Background is Magellan SAR image from Cycle 1.

We focus on the cluster south of Atla Regio (Fig. 1). There are three main trends of graben-fissure systems in the region (N-trending blue set, NE-trending red set, and NW-trending green set). We interpret that each of these sets overlie dyke swarms, as has been suggested for similar graben-fissure systems across Venus (e.g. [3–4]).

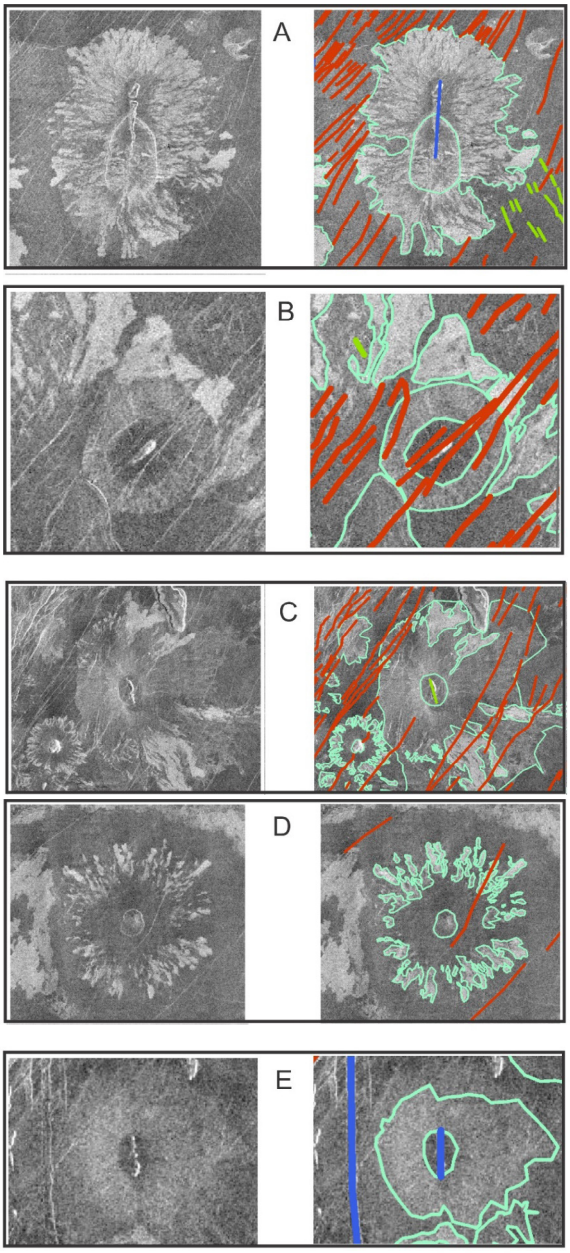


Fig. 2. Examples of anemone-like features located in Figure 1 on Magellan Cycle 1 SAR images. The right side of each pair of images shows the associated outlines of anemone flows (greenish-blue) and three trends of any associated graben (blue, red and/or green).

As shown in Figure 2 it appears that the anemones are associated with all three dyke swarms. In Fig. 2A, the elongate axis of the central trough-like feature is parallel to the N-trending blue swarm. In Fig. 2B, the central trough-like feature is parallel to the NE-trending red swarm. In Fig. 2C the anemone type feature in the lower left of the image is associated with a NE-trending of the red swarm. In the central part of Fig. 2C there is a NNE-trending graben which probably belongs to the NW-trending green swarm. In Fig. 2D the central depression is not elongated, but the only visible graben in the vicinity belong to the NE-trending red swarm. In Fig. 2E the central trough is N-trending and is parallel to the blue swarm. In summary, we have two anemones inferred to belong to the N-trending blue swarm (Figs. 2A and E),

three inferred to belong to the NE-trending red swarm (Figs. 2B, 2C lower left of image and Fig 2D). We have one with a NNE-trend that is most consistent with the NW-trending green swarm (Fig. 2C, centre of image).

IMPLICATIONS

Our analysis supports the suggestion from [1] that anemone are "related to regional patterns of extension and dike emplacement". However, the observation that they are associated with all three trends of regional dyke swarms provides additional constraints on the origin of this anemone cluster. The unusual appearance of the anemone flows, small with a petal-like appearance is very distinctly different from longer and more extensive flows associated with volcanic Mons [5]. A possible interpretation that these anemone type volcanic centres represent a composition different from those associated with Mons which are typically interpreted as basaltic. We consider whether these unusual features could represent alkaline magmatism. Also alkaline magmatism and associated carbonatites are frequently associated with Large Igneous Provinces (LIPs) [6], and can be inferred to reflect an unusual composition in the underlying lithospheric mantle source area (e.g. the Maimecha-Koyui alkaline province of the Siberian Traps LIP). However, the association of this anemone cluster with all three trends of regional dyke swarms would be seem inconsistent with a link to an underlying unusual lithospheric mantle source.

Alternatively, these small edifices and short flow features may be related to low-effusion rate, low-volume, supply-limited flows resulting from pulsation during dike emplacement events [7 - 8].

Regional dyke swarms such as the three identified in Figure 1 are typically part of giant radiating regional dyke swarms fed laterally from a magmatic centre that could be hundreds to more than 1000 km away. Detailed mapping is continuing with the goal of further testing for a genetic link between the anemone and the regional dyke swarms [9 - 10].

REFERENCES:

[1] Head, J.W., Crumpler, L.S., Aubele, J.C., Guest, J.E., Saunders, R.S. Venus volcanism: Classification of volcanic features and structures, associations, and global distribution from Magellan data. // Journal of Geophysical Research, 1992, V. 97, P. 13,153–13,197.

[2] Crumpler, L. S., Aubele, J.C., Senske, D.A., Keddie, S.T., Magee, K.P., Head, J.W. Volcanoes and centers of volcanism on Venus, in *Venus II - Geology, Geophysics, Atmosphere, and Solar Wind Environment*, edited by S. W. Bougher, D. M. Hunten and R. J. Phillips, 1997, pp. 697-756, University of Arizona Press, Tucson, AZ.

[3] Grosfils, E.B., Head, J.W. The global distribution of giant radiating dike swarms on Venus: implications for the global stress state. // Geophysics Research Letters, 1994, V. 21, P. 701 – 704.

[4] Ernst, R.E., Head, J.W., Parfitt, E. Grosfils, E., Wilson, L. Giant radiating dyke swarms on Earth and Venus // Earth Science Reviews, 1995, V. 39, P. 1-58.

[5] El Bilali, H., Ernst, R.E., Buchan, K.L. Maat Mons, Atla Regio, Venus: magmatic and tectonic history from detailed mapping // 52nd Lunar and Planetary Science Conference, 2021, abstr. No. 2529

[6] Ernst, R.E., Bell, K. Large Igneous Provinces (LIPs) and Carbonatites:. // Mineralogy and Petrology, 2010, V. 98, P. 55 – 76.

[7] Head, J. W., Wilson, L. Magma reservoirs and neutral buoyancy zones on Venus: Implications for the formation and evolution of volcanic landforms. //Journal of Geophysical Research, 1992, V. 97, P. 3877 - 3903.

[8] Head, J. W., and L. Wilson: Volcanic processes and landforms on Venus: Theory, predictions, and observations. //, Journal of Geophysical Research, 1986, V. 91, P. 9407 - 9446.

[9] El Bilali, H., Ernst, R.E., Buchan, K.L., Head, J. W. Dyke Swarms of the Alta Regio, The 12th Moscow Solar System Symposium 2021.

[10] El Bilali, H., Ernst, R.E., Buchan, K.L., and Head, J. W. Magmatic and Tectonic History of Atla Regio, Venus: // American Geophysical Union, Fall meeting, 2021.

MAPPING OF GRABEN SYSTEMS ("RIBBON FABRICS") IN WESTERN OVDA TESSERA, VENUS: INTERPRETATION AS DYKE SWARMS

R. Dean [1], R.E. Ernst [1,2], H. El Bilali [1], K.L. Buchan [3]
[1] *Department of Earth Sciences, Carleton University, Ottawa, Ontario, Canada, raidendean@cmail.carleton.ca, richard.ernst@ernstgeosciences.com, hafidaelbilali@cunet.carleton.ca;*
[2] *Faculty of Geology and Geography, Tomsk State University, Tomsk, Russia;*
[3] *273 Fifth Ave., Ottawa, Ontario, Canada, kbuchan33@gmail.com*

KEYWORDS:
Ribbon fabric, tesserae, Ovda Regio, dyke swarms, erosion

INTRODUCTION:
Crustal plateaus on Venus are broad elevated regions with associated tessera terrains. Typically, the tessera terrain comprises an interior basin and dome domain, surrounded by a marginal fold domain. (e.g., Fig. 4 in [1], also [2]. Folds crests tend to parallel the plateau margins, and dense sets of narrow graben (called ribbon fabrics) lie perpendicular to the fold crests and plateau margins [1]. It has been proposed that ribbon fabrics may be underlain by dyke swarms comparable to the dyke swarms observed on Earth and other planets [3]. If so, one might expect to find numerous ribbon "swarms" with a variety of ages, sizes, trends and geometries (linear, radiating, circumferential) as observed, for example, in Precambrian shields on Earth (cf. [4, 5]).

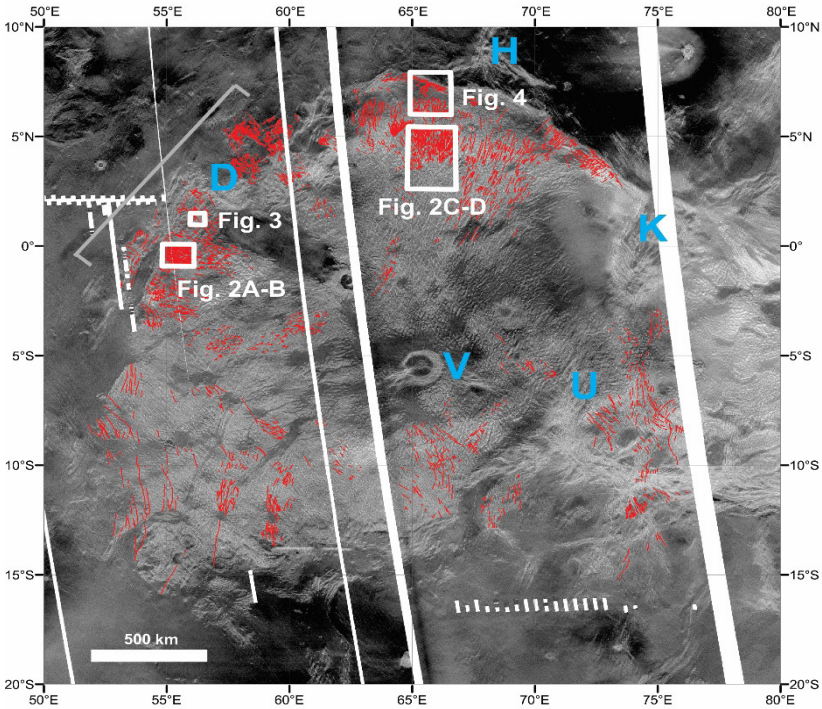


Fig. 1. Selected geological features of western Ovda Regio. Mapped graben, mostly associated with ribbon fabric, are shown in red. Grey bracket locates 1000 km wide linear set. V = Verdandi, D = Disani, H = H'uraru, K = Kaltash, and U = unnamed corona-nova systems. Background image from JMARS. Boxes indicate the locations of Figures 2–4.

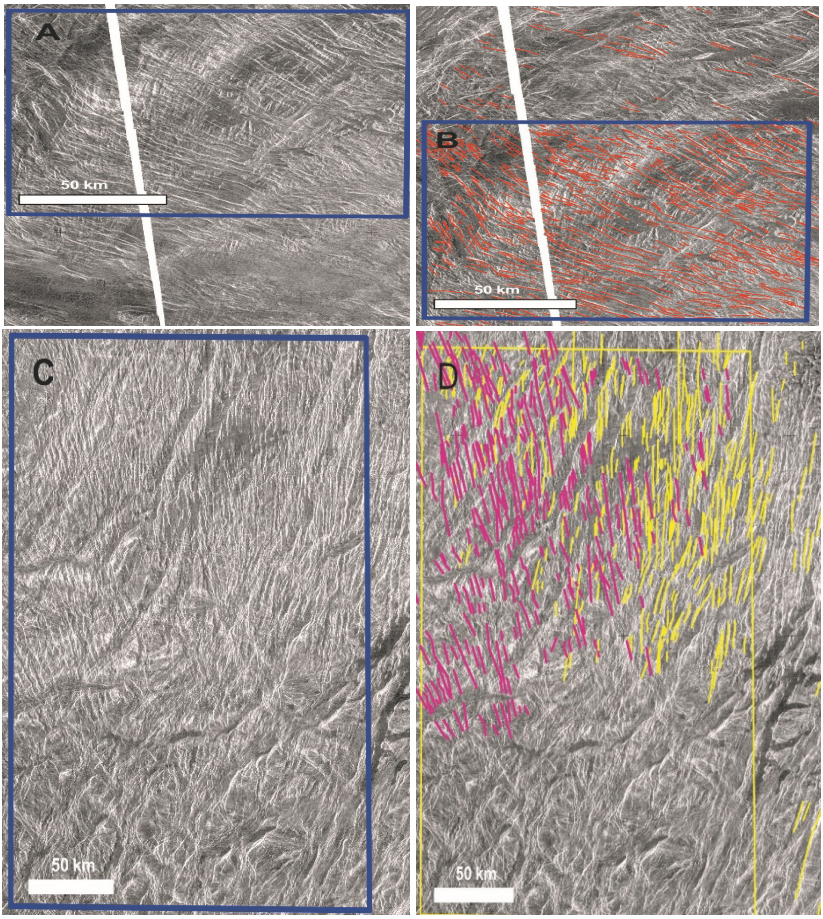


Fig 2. Examples of dense ribbon fabrics in (A, B) the western portion and (C, D) the northern portion of the study area. The mapped graben are superimposed in B and D. Images from JMARS.

The present study focuses on the ribbon fabrics/dyke swarms of the western lobe of Ovda Regio (Fig. 1), a crustal plateau which covers an area a little larger than the Superior craton of the Canadian Precambrian Shield. Here, we present preliminary results of detailed mapping and analysis of the more prominent ribbon fabrics/dyke swarms.

GEOLOGICAL OVERVIEW OF WESTERN OVDA REGIO:

Western Ovda Regio includes a large tessera terrain, with intratessera basins, fracture (shear) zones and fold belts [e.g., 1,6]. Extensional structures, including ribbon fabrics (herein interpreted as dyke swarms, following [3]) are widespread. The Verdandi coupled corona-nova system (V in Fig. 1) and its associated volcanic flows are located near the centre of western Ovda Regio. Several other coronae/novae (Fig. 1) are scattered around the perimeter of western Ovda Regio with graben (dykes) that in some cases can be traced onto the tessera terrain.

***RIBBON FABRIC/DYKE SWARM EXTENT AND GEOMETRY*:**

Dense ribbon fabrics cover large swaths of the tessera of western Ovda Regio, and are particularly prominent in the northern and western regions (Figs. 1, 2). Ribbon fabrics are generally absent in the central region in the vicinity of Verdandi corona. It has been proposed that ribbon fabrics, especially in the outer marginal fold domain of tessera terrains, including that of western Ovda, may form a broad radial pattern (cf. Fig. 1 of [1] and Fig. 4 of [6]).

In the present mapping dense ribbon fabrics in the northern and western portions of western Ovda appear to exhibit a broad radiating geometry (Fig. 1). However, there are instances where “subswarms” clearly intersect

(e.g., Fig. 2d), demonstrating that they are of different age and not part of a single radiating system. The dense ribbons typically extend out to near the edge of the tessera terrain (Fig. 1), but disappear towards the interior of the tessera terrain (Figs. 1, 2d). In the western portion of western Ovda the ribbon fabric (enlarged in Fig. 2a, b) appears to display a very broad (1000 km wide) linear pattern (see bracket in Fig. 1; also see Fig. 3 of [6]).

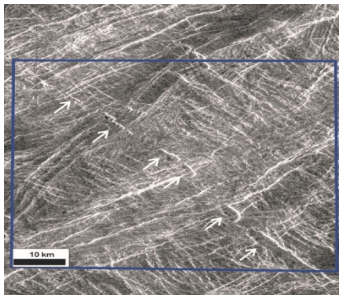


Fig. 3. Example of long linear pit chain (identified by arrows) among the graben of the NW trending ribbon fabric in the western part of the study area. Image from JMARS.

RIBBON FABRIC/DYKE SWARM DESCRIPTION:

The most prominent ribbon fabrics of western Ovda are quite dense (Fig. 2), as has been described for ribbon fabrics in other tesserae terrains in earlier studies (e.g., Hansen et al. 1999). The graben in the densest ribbon fabrics are spaced ~ 500 m apart. This is roughly comparable to the density of dykes in some Proterozoic dyke swarms on Earth, especially within 500 km or less of the swarm focus of giant radiating dyke swarms such as the Mackenzie [7] and Matachewan [8] swarms of the Canadian Shield.

Occasionally, long linear pit chains are observed among and parallel to the ribbons (Fig. 3). Pit chains are seen in association with dykes on Earth (e.g., [9]) and Venus (e.g., [10]).

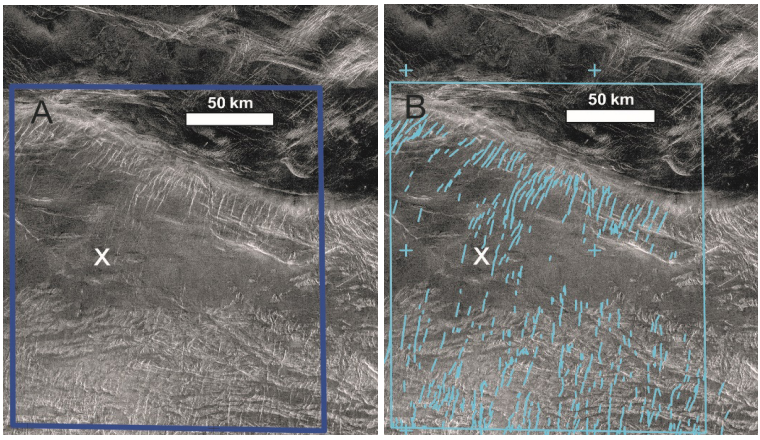


Fig. 4. Example of ribbon fabric that is overlain by volcanic flows of an intratessera basin. (A) JMARS image. (B) Superimposed mapped graben. At the location marked "X" graben and tessera features are visible through very thin volcanic (or sedimentary) cover.

RIBBON FABRIC/DYKE SWARM AGE:

The dense sets of ribbons of western Ovda generally do not extend beyond the tessera into the surrounding volcanic plains (Fig. 1). Nor are they observed in most intratessera basins. For example, in Figure 4, a NNE trending ribbon fabric is observed on either side of a basin but not within the basin (except in one swath, marked by "x" where several dykes and tessera features are visible through very thin cover). This indicates that the ribbons/dykes were emplaced prior to (or at the same time as) the plains and intratessera volcanism.

***LOCATING MAGMATIC SOURCE REGION OF RIBBON FABRICS/DYKE SWARMS*:**

On Earth the focus of a radiating dyke swarm can be used to locate an associated mantle plume centre [11]. On the other hand, a wide linear swarm may represent a portion of a radiating swarm that is distal from the plume centre and has a trend controlled by regional stresses rather than stresses associated with plume uplift. Applying these criteria to the ribbon fabrics (interpreted as dyke swarms) of western Ovda suggests that the centre for the possible radiating swarms of the northern region (Fig. 1) could be in the centre of western Ovda, whereas the centre associated with the possible broad linear swarm of the western region (Fig. 1) could be far to the northwest beneath the younger regional volcanic plains.

REFERENCES

[1] Hansen, V.L., Banks, B.K., Ghent, R.R. Tessera terrain and crustal plateaus, Venus. // Geology, 1999, V. 27, P. 1071–1074.

[2] Gilmore, M. S. & Head, J. W. Morphology and deformational history of Tellus Regio, Venus: evidence for assembly and collision. // Planet. Space Sci., 2018, V. 154, P. 5–20.

[3] Hanmer, S. Tessera terrain ribbon fabrics on Venus reviewed: Could they be dyke swarms? // Earth Science Reviews, 2020, V. 201, N. 103077

[4] Buchan, K.L., Ernst, R.E. Dyke swarms and related units in Canada and adjacent regions. // Geological Survey of Canada Map 2022A (scale 1 : 5 000 000) and accompanying catalogue of dyke swarms, 2004.

[5] Buchan, K.L., Ernst, R.E. Plumbing systems of large igneous provinces (LIPs) on Earth and Venus: Investigating the role of giant circumferential and radiating dyke swarms, coronae and novae, and mid-crustal intrusive complexes // Gondwana Research, 2021 (in press).

[6] Chetty, T.R.K., Venkatrayudu, M., Venkatasivappa, V. 2010. Structural architecture and a new tectonic perspective of Ovda Regio, Venus. // Planetary and Space Science, 2010, V. 58, P. 1286–1297.

[7] Fahrig, W.F. (1987). The tectonic setting of continental mafic dyke swarms: failed arm and early passive margin. // In Halls, H.C. & Fahrig, W.F. (eds.), Mafic Dyke Swarms. Geological Association of Canada, Special Pub. 1987, V. 34, P. 331 – 348.

[8] Bates, M.P., and Halls, H.C. Regional variation in paleomagnetic polarity of the Matachewan dyke swarm related to the Kapuskasing Structural Zone, 0ntario. // Canadian Journal of Earth Sciences, 1990, V. 27, P. 20–211.

[9] Magee, C. Jackson, C.A. Seismic reflection data reveal the 3D structure of the newly discovered Exmouth dyke swarm, offshore NW Australia. // Solid Earth, 2020, V. 11, P. 597 - 600.

[10] Davey, S.C., Ernst, R.E., Samson, C., Grosfils, E.B. (2013). Hierarchical clustering of pit crater chains on Venus. // Canadian Journal of Earth Sciences, 2014, V. 50, P. 109–126

[11] Ernst, R.E., Buchan, K.L. The use of mafic dike swarms in identifying and locating mantle plumes // In: R.E. Ernst, K.L. Buchan (eds.) Mantle Plumes: Their Identification Through Time. Geological Society of America Special Paper, 2001, V. 352, P. 247–265

SESSION 3. EXTRASOLAR PLANETS (EP) ORAL SESSION

ULTRAVIOLET SPECTROGRAPH FOR EXOPLANET (UVSPEX) ONBOARD WSO-UV FOR EARTH-LIKE EXOPLANETS

S. Kameda [1], A. Tavrov [2], G. Murakami [3], A. Nakayama [4], T. Kodama [4], M. Kuwabara [1], M. Ikoma [5], N. Narita [4], N. Terada [6], K. Enya [3], M. Sachkov [7], A. Shugarov [7], O. Korablev [2]

[1] *Rikkyo University, Japan, kameda@rikkyo.ac.jp;*
[2] *Space Research Institute of the Russian Academy of Sciences, Russia;*
[3] *ISAS/JAXA, Japan;*
[4] *The University of Tokyo, Japan;*
[5] *NAOJ, Japan;*
[6] *Tohoku University, Japan;*
[7] *INASAN, Russia*

KEYWORDS:
Exoplanet, exosphere, oxygen, ultraviolet, space telescope.

INTRODUCTION:
Many Earth-sized planets have been discovered, and some of them exist in the habitable zone. However, it is difficult to characterize them as Earth-like one, Venus-like one, or other. Transit spectroscopy observations for the exoplanetary atmosphere have been performed to characterize larger exoplanets however require very high accuracy for small Earth-like exoplanets. A hydrogen exosphere has been detected around a Neptune-sized exoplanet [1], but exospheres of Earth-sized exoplanets have not been detected. Recently, Earth's hydrogen exosphere was re-investigated, and it was revealed that the Earth's exosphere is extended to ~ 38 Earth radii [2]. On the other hand, Venus' and Mars' hydrogen exospheres are not so much extended because of low temperatures of their upper atmosphere. This is caused by the difference in mixing ratio of CO_2 in the upper atmosphere. Venus and Mars have CO_2-rich atmospheres with a lower exospheric temperature. On Earth, CO_2 is removed from its atmosphere by a carbon cycle with its ocean and tectonics. Translating these arguments to exoplanets in a habitable zone presents a possible marker distinguishing Earth-like planets from Mars-like or Venus-like planets. The expanded exospheres can be observed in UV, during the exoplanet transit event in a primary eclipse. It reduces the stellar flux when an exoplanet is orbiting in front of the host star. Low-temperature stars are especially faint in UV. With a large telescope, we would be able to detect the reduction of the intensity of the UV spectral lines in transit.

INSTRUMENTATION:
We need a spectrograph with a very high sensitivity (photon counting) to perform the transit spectroscopy in oxygen lines.

The primary spectrograph WUVS is onboard the future international project WSO – UV (World Space observatory – Ultraviolet); however, its sensitivity is not high enough to observe exoplanet oxygen lines because of the CCD detector noise [3].

A dedicated science instrument UVSPEX (Ultraviolet Spectrograph for Exoplanets) fully optimized for exoplanet atmosphere characterization is being developed in Japan as a Japanese contribution to the WSO – UV mission.

The requirements for UVSPEX are as follows.

- The spectral range from < 120 nm to > 135 nm to detect at least H Lyman alpha (121.6 nm) , O I (130 nm), and C II (133.5 nm).
- The throughput of > 4 %.
- Spectral resolution better than 0.3 nm to separate O I line from other spectral lines.
- Photon counting ability.

A simple spectrograph design is proposed for these requirements, containing the slit, the concave (toroidal) grating as a dispersing element, and the imag-

ing detector. This optical design concept is conventional and used in the other space missions for UV spectroscopy.

Figure 1 shows the optical design of the UVSPEX. The slit is placed in the focus of the WSO-UV telescope. The light passing through the slit is reflected by the toroidal grating, which has spectroscopic and imaging abilities, and then reaches the detector.

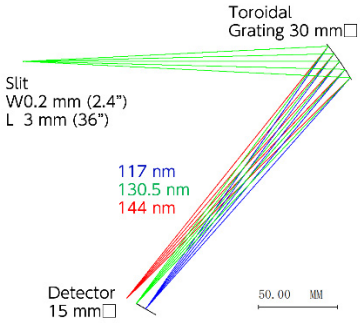


Fig. 1. UVSPEX optical design.

The slit is placed at the primary focus of the telescope from off-axial sub-FoV. The slit width is 0.2 mm, corresponding to 2.4 arcsec. The concave toroidal brazed grating has a groove density of 2400 per mm. The effective area is nearly Ø 30 mm, and the focal length is approximately 200 mm. The surface is coated by Al/MgF2 coating to increase the reflectance, and diffraction efficiency of ~ 29 % can be achieved.

The UVSPEX will be installed on the WSO – UV Field Camera Unit optical bench and will receive the light from the telescope using a pick-up mirror installed at the edge of the telescope focal plane.

In this presentation, we present a preliminary design of the UVSPEX instrument and its science objectives.

REFERENCES:

[1] Ehrenreich, D. et al., A giant comet-like cloud of hydrogen escaping the warm Neptune-mass exoplanet GJ436b. Nature. 2015. V. 522, P. 459–461.
[2] Kameda, S. et al., Ecliptic North-South Symmetry of Hydrogen Geocorona. Geophysical Research Letters. 2015.V. 44, No. 11,P. 706–712.
[3] Shustov B., Sachkov M., Kanev E., Savanov I. et al. The World Space Observatory Ultraviolet (WSO–UV), as a bridge to future UV astronomy. Astrophysics and Space Science, Vol.363, № 4. P. 62, 2018.

PROPERTIES OF RV-EXOPLANETS' DISTRIBUTIONS BY MASSES AND BY ORBITAL PERIODS

V. Ananyeva [1], A. Ivanova [1], I. Litosova [3], A. Tavrov [1], J.-L. Bertaux [2]
[1] *Space Research Institute of the Russian Academy of Sciences; 84/32 Profsoyuznaya Str, Moscow, Russia, 117997;*
[2] *LATMOS/IPSL/CNRS/UVSQ, 78280, Guyancourt, France;*
[3] *Lomonosov State University*

KEYWORDS:
Exoplanets, mass statistics, period statistics, RV exoplanets.

To date, almost 900 exoplanets with a known projective mass have been discovered by the radial velocity (RV-) technique. However, there are strong selection effects that distort the true (original) exoplanets statistics e.g. mass- and period statistics as seen in the observed mass- and period distribution of exoplanets. We have corrected the observed mass- and period distributions by the "detectability window" regularization algorithm. Detailed description of the algorithm is in [1].

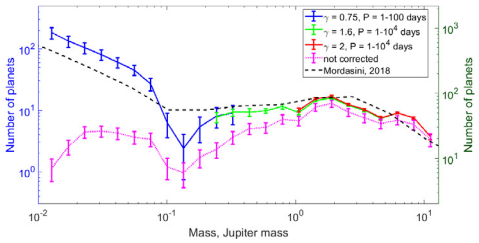


Fig. 1. The complex de-biased projective-mass distribution of RV planets in a domain of (0.011–13) MJ shown by the blue, green and red lines. The magenta dotted line shows the biased (initial from Archive) distribution of RV planets corresponding to the right vertical axis. The dashed black line presents the distribution predicted by the population synthesis theory (Mordasini, 2018).

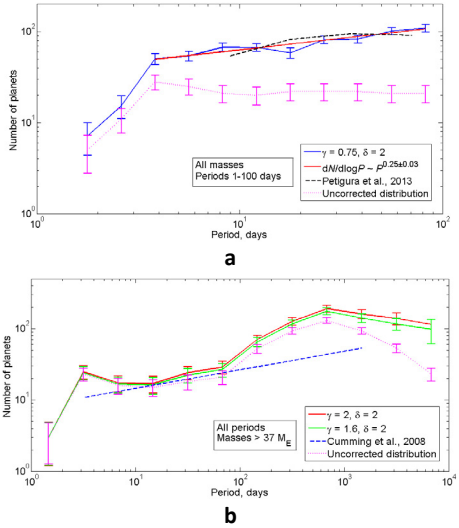


Fig. 2. The orbital-period distribution of RV planets. (**a**) The $N(P)$ de-biased distribution of planets with masses m = (0.011–13) MJ and orbital periods P = 1-100 days; the red and dashed black lines show the power law with an exponent of 0.25, $dN / d\log P \propto P^{0.25}$, and the orbital-period distribution of the transit Kepler planets with radii of (1 - 16) R_E and orbital periods of 6.25–100 days (Petigura et al., 2013), respectively. Initial from Archive (biased) distribution is shown with a dotted magenta line. (**b**) The de-biased $N(P)$ distribution of planets with masses m =(0.116 – 13) MJ and orbital periods P = 1–10^4 days, the dashed blue line show the power law $dN / d\log P \propto P^{0.26}$ proposed by Cumming et al. (2008).

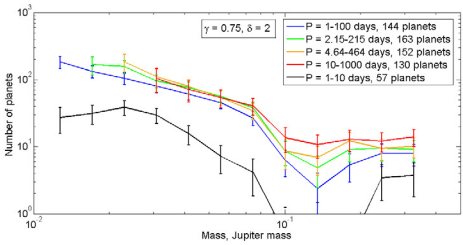


Fig. 3. The de-biased mass distributions of the planets having the orbital periods of 1–100 days (blue line), 2.15–215 days (green line), 4.64–464 days (yellow line), 10–1000 days (red line), and 1–10 days (black line). Therefore we conclude the minimum in the (0.087–0.21) MJ range is caused by planets in tight orbits (hot Neptunes desert).

The complex de-biased projective-mass distribution of RV planets obeys a piecewise power law with two breakpoints at ~ 0.14 MJ and ~ 1.7 MJ (Figure 1).

ACKNOWLEDGEMENTS:
Authors acknowledge the support of Ministry of Science and Higher Education of the Russian Federation under the grant 075-15-2020-780 (N13.1902.21.0039).

REFERENCES:

[1] A.E. Ivanova, O.Ya. Yakovlev, V.I. Ananyeva, I.A. Shashkova, A.V. Tavrov, and J.-L. Bertaux, The Detectability Window" Method to Take into Account Observational Selection in the Statistics of Exoplanets Discovered through Radial Velocity Measurements, ISSN 1063-7737, Astronomy Letters, 2021, V. 47, No. 1, P. 43–49. DOI: 10.1134/S1063773721010059.

[2] V.I. Ananyeva, A.E. Ivanova, A.A. Venkstern, I.A. Shashkova, A.V. Yudaev, A.V. Tavrov, O.I. Korablev, and J.-L. Bertaux, Mass distribution of exoplanets considering some observation selection effects in the transit detection technique, Icarus, V. 346, August 2020, 113773. DOI: 10.1016/j.icarus.2020.113773.

[3] Christoph Mordasini. Planetary Population Synthesis, © Springer International Publishing AG, part of Springer Nature 2018, H.J. Deeg, J.A. Belmonte (eds.), Handbook of Exoplanets, DOI: 10.1007/978-3-319-30648-3_143-1.

COMPARISON OF THE MASS DISTRIBUTIONS OF SHORT-PERIOD EXOPLANETS DETECTED BY TRANSIT AND RV METHODS

O.Ya. Yakovlev [1], V.I. Ananyeva [1], A.V. Tavrov [1]
[1] *Space Research Institute of the Russian Academy of Sciences; 84/32 Profsoyuznaya Str, Moscow, Russia, 117997, yko-v@ya.ru*

KEYWORDS:
Exoplanet, mass distribution, transit method, radial velocity method.

INTRODUCTION:
Mass is a fundamental parameter of a planet, the distribution over which is important for understanding the abundance of planets of different types. In previous works, mass distributions were obtained for two samples (Fig. 1): discovered by the Kepler space telescope by the transit method [1] and by the radial velocity method [2]. The aim of this work is to explain the reasons for the differences in the obtained distributions.

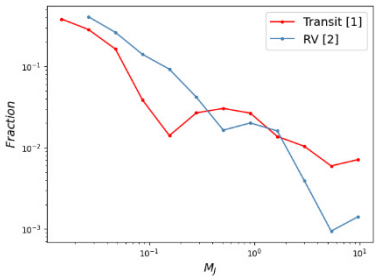


Fig. 1. The distribution of transit exoplanets (by Kepler space telescope) by masses $\frac{\partial N}{\partial M}$ for $M \in [0.12, 13]$ from [1] and the distribution of RV exoplanets by projective masses $\frac{\partial N}{\partial M \times \sin i}$ (the period is $P \in [1{,}100]$ days for $M \times \sin i \in [0.011, 13] M_J$, i is the inclination of the exoplanet's orbit).

METHODS:
To explain the differences in the considered distributions, first of all, the considered ranges of exoplanets were limited by mass $M[0.002, 13] M_J$ (Jupiter masses) and by the period $P = [1, 65]$ days, since in [1] and [2] they were different.

The key reason why the obtained distributions were significantly different was the inclusion of all transit exoplanets, the masses of which were determined by both the TTV method and the RV method. The TTV method determines the nominal mass [3], which may differ significantly from the true one, and in some cases may not be physical. In addition, the mass distribution of such exoplanets is biased due to the selection effect, which differs from the selection effect of the RV distribution, and which must be taken into account separately. Therefore, exoplanets with TTV masses were excluded.

Further, the distributions were corrected to take into account the observational selection effects, following [1] and [2]. For RV exoplanets, only the projective mass is known. To compare the considered mass distributions for transit exoplanets, a transformation was made to the projective mass distribution.

RESULTS:
The obtained distributions are shown in Fig. 2. In the region of medium and large masses, there is a complete correspondence between the distributions. In the region of low masses, the distributions do not coincide, but the slopes of both distributions are close. When determining the mass of transit exoplanets by the RV method, the transit parameters are already

known. While there is no additional information for RV exoplanets. Therefore, more measurements are required, as a result of which there is a lack of them. The transition from true to projective masses changes the distribution only in the region of minima.

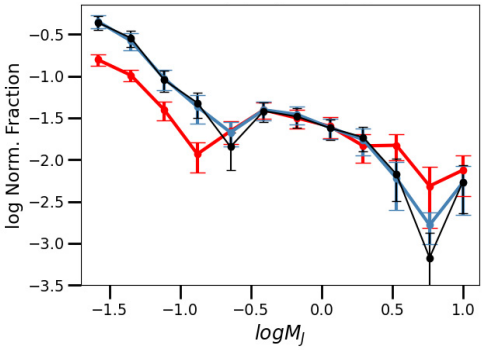


Fig. 2. The distribution of transit exoplanets (by Kepler space telescope, with masses were determined only by the RV method) by masses $\frac{\partial N}{\partial M}$ (black line) and by projective masses $\frac{\partial N}{\partial M \times \sin i}$ (blue); the distribution of RV exoplanets by projective masses $\frac{\partial N}{\partial M \times \sin i}$. The distributions presents after correction due to observational selection effects [1–2]. Only exoplanets with $P \in [1, 65]$ days and $M \in [0.02,13]$ M_J are considered here.

CONCLUSION:

Exclusion of transit exoplanets with masses determined by the TTV method and consideration of both samples in the same intervals in mass and period (taking into account the factors of observational selection) brings into agreement the distributions obtained by independent methods (transit and RV). However, there is a lack of low-mass RV exoplanets, which is explained by the smaller required number of RV measurements for transit exoplanets for determining masses.

ACKNOWLEDGMENTS:

This work was supported by the Government of Russian Federation and Ministry of Education and Science of Russian Federation (grant No. 2020-1902-01-133).

REFERENCES:

[1] Ananyeva V.I., Ivanova A.E., Venkstern A.A., Shashkova I.A., Yudaev A.V., Tavrov A.V., Korablev O.I., Bertaux J.-L.. Mass distribution of exoplanets considering some observation selection effects in the transit detection technique. // Icarus. 2020. V. 346. No. 4. P. 1–18.

[2] A.E. Ivanova, O.Ya. Yakovlev, V.I. Ananyeva, I.A. Shashkova, A.V. Tavrov, J.-L. Bertaux. The ‘‘Detectability Window’’ Method to Take into Account Observational Selection in the Statistics of Exoplanets Discovered through Radial Velocity Measurements // Astronomy Letters. 2021. V. 47, P. 43–49.

[3] S. Hadden, Yo. Lithwick. Densities and Eccentricities of 139 Kepler Planets from Transit Time Variations // The Astrophysical Journal. 2014. V. 787. No. 1. P. 80.

NON-THERMAL ATMOSPHERIC LOSS FOR HOT SUB-NEPTUNE π MEN C

V.I. Shematovich [1], A.A. Avtaeva [1,2]
[1] *Institute of Astronomy of the Russian Academy of Sciences, Moscow, Russia, shematov@inasan.ru;*
[2] *Sternberg Astronomical Institute, Moscow State University, Moscow, Russia*

KEYWORDS:
Hot exoplanets, sporadic stellar activity, atmospheric mass loss, aeronomic model, kinetic Monte Carlo model.

INTRODUCTION:

Exoplanets with substantial hydrogen/helium atmospheres have been discovered in abundance, many residing extremely close to their host stars. Their atmospheres are forced by the extreme irradiation levels resulting in the formation of the extended planetary envelopes due to the thermal and non-thermal atmospheric escape. Ongoing atmospheric escape has been observed to be occurring in a few nearby exoplanet systems through transit spectroscopy both for hot jupiters and for lower-mass sub-neptunes [1, 2].

Modeling of the non-thermal atmospheric loss for the sub-neptune π Men c, the first exoplanet discovered by the TESS space telescope, has been carried out [3, 4]. It orbits a bright nearby star and has a relatively low average density, making this exoplanet an excellent target for atmospheric characterization. Existing models of the upper atmosphere of the planet π Men c predict a significant outflow of atmospheric matter, but in transit observations in the Ly-α line, no atomic hydrogen was found escaping from the planet's atmosphere [3]. The results of calculations of the effect of the extreme ultraviolet (UV) stellar radiation on the production of the suprathermal fraction of atomic hydrogen in the $H_2 \rightarrow H$ transition region in the upper atmosphere of hot sub-neptune π Men c are given in this report.

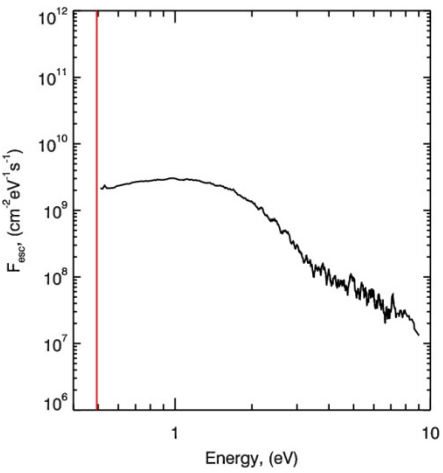


Fig. 1. The energy spectrum of the atomic hydrogen flux escaping from the upper atmosphere of sub-neptune π Men c due to exothermic photochemistry. The vertical red line shows the escape energy of hydrogen atoms at the upper boundary of the model atmosphere at distance of ~ 3 planetary radii.

The formation of the escaping flux of H atoms created by this effect was also studied and the production rate and energy spectrum of the hydrogen atoms with excess kinetic energy due to the exothermic photochemistry were calculated. Using the numerical stochastic model for a hot planetary corona [5], we had investigated the kinetics and transport of suprathermal hydrogen atoms in the upper atmosphere and the flux of atoms escaping from the atmosphere was

calculated (see Figure). The latter is estimated as 4.6×10^9 cm^{-2} s^{-1} for a moderate stellar activity level of UV radiation, which is an indication of the non-thermal atmospheric loss due to the exothermic photochemistry. This estimate is slightly lower but still comparable with estimates [3, 4] of the thermal atmospheric loss calculated with aeronomic models for π Men c.

Additional non-thermal escape processes such as the photoelectron impact and the precipitation of high-energy charged and neutral particles from stellar wind into the extended atmosphere of hot sub-neptune π Men c are also discussed.

ACKNOWLEDGEMENTS:
The study was supported by the Ministry of Science and Higher Education of the Russian Federation (Grant No. 075-15-2020-780 “Theoretical and experimental studies of the formation and evolution of extrasolar planetary systems and characteristics of exoplanets”).

REFERENCES:

[1] Shematovich V.I., Marov M.Ya. Escape of planetary atmospheres: physical processes and numerical models // Physics - Uspekhi. 2018. V. 61. P. 217.
[2] Owen J.E. Atmospheric Escape and the Evolution of Close-In Exoplanets // Annu. Rev. Earth Planet. Sci. 2019. V. 47. P. 67–90.
[3] García Muñoz A., Youngblood A., Fossati L., et al. Is π Men c’s Atmosphere Hydrogen-dominated? Insights from a Non-detection of H I Lyα Absorption // 2020, ApJ, V. 888. L21. P. 15.
[4] Shaikhislamov I.F., Fossati L., Khodachenko M.L., et al. Three-dimensional hydrodynamic simulations of the upper atmosphere of π Men c: comparison with Lyα transit observations // A&A. 2020. V. 639. id.A109. P. 7.
[5] Avtaeva A.A., Shematovich V.I.. Non-thermal atmospheric loss for exoplanet GJ 436b due to the H2 dissociation processes // Sol. Syst. Res. 2021. V. 55. P. 150–58.

LIGHT CURVE ANALYSIS OF TEN EXOPLANETS

Sh. Zamanpour [1], F. Davoudi [1], et al.
[1] *International Occultation Timing Association Middle East Section, info@iota-me.com*

KEYWORDS:
Photometry, Exofast, Hot Jupiter.

INTRODUCTION:
In this study, we have analyzed the light curves of 10 exoplanets and calculated their radii based on small telescopes' observations. The raw data was obtained from the Exoplanet Transit Database (ETD). Ground-based observations have high scientific potential in the discovery of new exoplanets and even have the follow-up potential in providing system parameters as well as mid-transit times [1]. The ETD has been established to collect and classify all available transit data with different quality. The analyzed exoplanets in this study all belong to hot Jupiter type planets with an apparent magnitude between 9.8 and 14.07. They are alone in their planetary system or have distant companions. We first used 14 light curves of 10 exoplanets observed by the Charged Couple Device (CCD) method. The telescopes used in the observations have an average aperture of 350mm. Then we applied Phoebe software to turn Delta Magnitude to normalized flux. After the data reduction, we prepared a file including time in BJDTDB, Flux, and its' Error and then used it as an input for EXOFAST software, which is an IDL library for transit and radial velocity modeling [2]. It can be utilized to find out orbital inclination, planet radius, mass, and average density of the planets [3–6]. EXOFAST has done the best fit on light curves and calculated the parameters of transit based on the given data. The radius of the exoplanet is the most important parameter determined by the transit method. The results show that the radius of exoplanets obtained from ground-based observation with small telescopes in this study is comparable to its value in the NASA Exoplanet Archive (NEA). This is important because it can indicate the role of observations with small telescopes to study more discovered planets. The HR diagram shows that most of the stars in this study are in the middle or second part of their lifetime, and the planets were discovered by primary transit at the time when the star's temperature is cooler than the first part of their lifetime.

REFERENCES:
[1] Davoudi F., Jafarzadeh S.J., Poro A., Basturk O., Mesforoush S., Harandi A.F., Gozarandi M.J., Mehrjardi Z.Z., Maley P.D., Khakpash S., Rokni K. Light curve analysis of ground-based data from exoplanets transit database // New Astronomy. 2020. V. 76. P. 101305.
[2] Eastman J., Gaudi B.S., Agol E. EXOFAST: A fast exoplanetary fitting suite in IDL // Publications of the Astronomical Society of the Pacific. 2013. V. 125. No. 923. P. 83.
[3] Guillot T. The interiors of giant planets: Models and outstanding questions // Annual Review of Earth and Planetary Sciences. 2005. V. 33. P. 493–530.
[4] Sato B.E., Fischer D.A., Henry G.W., Laughlin G., Butler R.P., Marcy G.W., Vogt S.S., Bodenheimer P., Ida S., Toyota E., Wolf A. The N2K consortium. II. A transiting hot Saturn around HD 149026 with a large dense core // The Astrophysical Journal. 2005. V. 633. No. 1. P. 465.
[5] Charbonneau D., Winn J.N., Latham D.W., Bakos G., Falco E.E., Holman M.J., Noyes R.W., Csák B., Esquerdo G.A., Everett M.E., O'donovan F.T. Transit photometry of the core-dominated planet HD 149026b // The Astrophysical Journal. 2006. V. 636. No. 1. P. 445.
[6] Fortney J.J., Saumon D., Marley M.S., Lodders K., Freedman R.S. Atmosphere, interior, and evolution of the metal-rich transiting planet HD 149026b // The Astrophysical Journal. 2006. V. 642. No. 1. P. 495.

MODELING TRANSIT ABSORPTIONS OF HOT JUPITERS IN THE METASTABLE HELIUM LINE

M.S. Rumenskikh [1], A.G. Berezutsky [1], I.B. Miroshnichenko [1], I.F. Shaikhislamov [1]

[1] *Institute of laser physics of Siberian branch of Russian Academy of Sciences, Novosibirsk, Russia, marina_rumenskikh@mail.ru*

KEYWORDS:
Hot Jupiters, HD-189733b, space plasma, transit spectroscopy, star-planetary interactions.

The atmosphere of hot Jupiters is heated by intense radiation of the host star and undergoes an outflow outside the Roche lobe. The transit spectroscopy of hot exoplanets is used to obtain the main characteristics of exoplanetary atmospheres and plasmaspheres, such as composition, temperature, density, as well as to study the effects that occur at interaction of planetary streams with the stellar wind.

Many hot exoplanets consist mostly of hydrogen, and the Ly-a spectral line is valuable for providing evidence of atmospheric escape. However, it is strongly absorbed in interstellar medium and contaminated by geocoronal emission. As it was suggested in [1], the absorption by a metastable helium in the 2^3S state at 10830 Å offers an alternative way to probe the evaporating exoplanetary atmospheres. It is not affected by the interstellar medium and can be observed by ground telescopes with high resolution.

A 3D gas-dynamic model which takes into account the processes of recombination and plasma-photochemistry of plasma components [2, 3] was used in this work to reproduce the transit absorptions in metastable helium 10830 A line of the planet HD-189733b to obtain the best fit to the observational data. For the recently discovered TOI-421b&c system whose spectroscopy is expected in near future we make a prediction of probable absorptions in the metastable helium line. The features of modeling this two-planetary system are considered with varying stellar mass-loss rates and XUV radiation. As a result, the most probable atmospheric parameters for the case of massive (HD-189733b) and relatively low-mass (TOI system) planets have been determined.

ACKNOWLEDGMENTS:
This work was supported by projects of the Russian Science Foundation 18-12-00080, projects of the Ministry of Science and Higher Education of the Russian Federation No. AAAA-A17-117021750017-0, 075-15-2020-780, 121033100062-5 as well as RFBR grants 20-02-00520, 19-02-00993 and 18-29-21018.

REFERENCES:

[1] Oklopčić A., Hirata C.M. A new window into escaping exoplanet atmospheres: 10830 Å line of helium // The Astrophysical Journal Letters. 2018. V. 855. No. 1. P. L11

[2] Shaikhislamov I.F. et al. 3D Aeronomy modelling of close-in exoplanets // Monthly Notices of the Royal Astronomical Society. 2018. V. 481. №. 4. P. 5315.

[3] Shaikhislamov I.F. et al. Global 3D hydrodynamic modelling of absorption in Ly α and He 10830 A lines at transits of GJ3470b // Monthly Notices of the Royal Astronomical Society. 2021. V. 500. №. 1. P. 1404.

REFINED EPHEMERIS FOR THREE HOT JUPITERS USING GROUND-BASED AND TESS OBSERVATIONS

A. Mazidabadi Farahani [1, 2], F. Davoudi [1, 2, 3], et al.
[1] *The International Occultation Timing Association Middle East section, Iran, info@iota-me.com;*
[2] *The Eight IOTA/ME Summer School of Astronomy, Tafresh University, Tafresh, Iran;*
[3] *Astronomy Department of the Raderon Lab., Burnaby, BC, Canada*

KEYWORDS:
Planetary systems, planets, gaseous planets, photometric techniques.

INTRODUCTION:

WASP-33 b, WASP-36 b, and WASP-46 b are three transiting planetary systems on which we studied. These systems' light curves were derived from observations made by the Transiting Light Exoplanet Survey Satellite (TESS) and some ground-based telescopes. We used Exofast — v1 to model these light curves and calculate mid-transit times. Also, we plotted TTV diagrams for them using derived mid-transit times and those available within the literature. Our MCMC analysis of these timings enabled us to refine the linear ephemeris of the three systems. We noticed that the orbital period is increasing in the WASP – 46 b system; probably, its star magnetic activity is a better model for this period variation than orbital decay. WASP – 36 b's TTV diagram shows no apparent quadratic trend, and variations are likely due to incorrect linear ephemeris that has risen over the ten years.

3D MHD MODELING OF HOT JUPIER' MAGNETOSPHERE AND ONSERVATIONAL MANIFASTATIONS

I.F. Shaikhislamov [1], M. Khodachenko [2], I.B. Miroshnichenko [1], M.S. Rumenskikh [1], A.G. Berezutsky [1]

[1] *Institute of Laser Physics SB RAS, Novosibirsk, Russian Federation, ildars@ngs.ru;*

[2] *Space Research Institute, Austrian Academy of Sciences, Graz, Austria*

KEYWORDS:
Hot Jupiter, magnetosphere, transit absorption.

INTRODUCTION:
Using the global 3D multi-fluid MHD model we simulated the magnetosphere of Hot Jupiter HD209458b and calculated synthetic transit absorption depths at the FUV lines, and at the NIR line (10830 Å) of metastable helium HeI (2^3S) triplet. For the first time we studied how the presence of planetary intrinsic magnetic field changes the absorption profiles. MHD simulations have shown that the planetary magnetic dipole moment $\mu_p = 0.6$ of the Jovian value, which produces the magnetic field equatorial surface value of 1 G, profoundly changes the character of the escaping planetary upper atmosphere. The total mass loss rate in this case is reduced by 2 times, as compared to the non-magnetized planet. In particular, we see the formation of the dead- and the wind- zones around the planet with the different character of plasma motion there. The 3D MHD modelling also confirmed the previous 2D MHD simulations result of [1] that the escaping PW forms a thin magnetodisk in the equatorial region around the planet. The significantly reduced velocity of PW at the low altitudes around the planet, and especially at the night side, results in the stronger photo-ionization of species and significantly lower densities of the corresponding absorbing elements. Altogether, the reduced velocities and lower densities result in significant decrease of the absorption at Lyα (HI), OI, and CII lines, though the absorption at HeI (2^3S) line remains nearly the same.

The presented results fitted to the available measurements indicate that the magnetic field of HD209458b should be at least an order of magnitude less than that of the Jupiter. This conclusion agrees with the previous estimates, based on more simplified models and much less observational data, when only Lyα absorption was considered. We believe that the application of 3D MHD models simulating the escape of upper atmospheres of hot exoplanets and the related transits at the available for measurement spectral lines, sensitive to the dynamics of planetary plasma affected by the MF, opens a way for probing and quantifying of exoplanetary magnetic fields and sheds more light on their nature.

ACKNOWLEDGMENTS:
This work was supported by grant № 18-12-00080 of the Russian Science Foundation and grant № 075-15-2020-780 of the Russian Ministry of Education and Science.

REFERENCES:
[1] Khodachenko, M.L., Shaikhislamov, I.F., Lammer, H., et al., 2015, ApJ,V. 813, P. 50.

ACTIVITY OF TWO YOUNG STARS OF SOLAR TYPE WITH PLANETARY SYSTEMS FROM THE URSA MAJOR MOVING GROUP OF STARS AND THE STREAM PSC-ERI

I.S. Savanov [1]
[1] *Institute of Astronomy Russian Academy of Sciences, Moscow, Russia; Pyatnitskaya 48, igs231@mail*

KEYWORDS:
Stars, activity, spots, photometry, variability, planetary systems.

INTRODUCTION:
High precision data from the archive of the TESS space mission are used as the basis of a study of the photometric variability of two young analogs of the Sun with planetary systems: the stars HD 63433 (TOI 1726), a member of the Ursa Major moving group of stars with an age of 414 million years and TOI 451 (CD-38 1467) from the Pisces-Eridani star stream (Psc-Eri) with an age of 120 million years. Manifestations of the activity of these stars with planetary systems are studied. Based on all the available observations we have estimated the rotational periods of the stars and the amplitudes of their brightness variability. The standard method has also been used to estimate the spottedness parameter A in an absolute measure. The areas of the spots on the surfaces of HD 63433 and TOI 451 greatly exceed the area of the spots on the Sun, with 24500 m.s.h. and 12600-33200 m.s.h., respectively. The activity cycles of TOI 451 were estimated using data from the archive of the All Sky Automated Survey and indicated possible activity cycles of 125 and 1280 days. The data for HD 63433 suggest the existence of long-term changes in brightness, but are insufficient for quantitative estimates.

HD 63433 AND CD-38 1467:
This paper presents the results of an analysis of the brightness variability of HD 63433 (TOI 1726, TIC 130181866), a bright young analog of the sun — a member of the Ursa Major moving group with an age of 414 million years [1] and the solar-type dwarf TOI 451 (CD-38 1467) from the star stream Psc-Eri with an age of 120 million years [2]. These results are compared with data on solar-type stars with planetary systems from the young association Tuc-Hor — DS Tuc and AB Pic — which we studied previously.

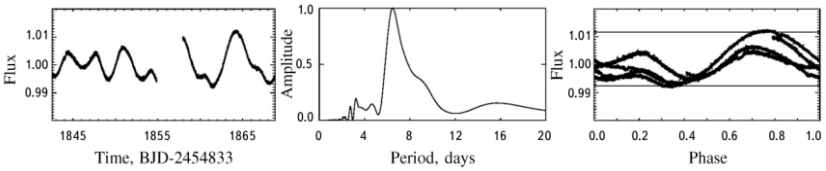


Fig. 1. (Left) a light curve for HD 63433; (center) power of the brightness variation; (right) phase diagram of the brightness variations (the horizontal lines characterize the amplitude of the brightness variation). The data are for observations in sector 20.

Table. 1.

	HD 63433	TOI 451	DS Tuc	AB Pic
T_{eff}, K	5640	5481	5428	5027
P, days	6.47	5.20	2.85	3.86
A, m.s.h.	24500	12600-33200	66700	54000-95000
P cycl., days	-	125, 640, 1280	1610	258, 1120, 2640
Age, million of years	414	120	45	45

REFERENCES:

[1] Mann A.W., Johnson M.C., Vanderburg A., et al. TESS Hunt for Young and Maturing Exoplanets (THYME). III. A Two-planet System in the 400 Myr Ursa Major Group// Astron. J. 2020. V. 160. P. 179–197.
[2] Newton E.R., Mann A.W., Kraus A.R., et al. TESS Hunt for Young and Maturing Exoplanets (THYME). IV. Three Small Planets Orbiting a 120 Myr Old Star in the Pisces-Eridanus Stream // Astron. J. 2021. V. 161. P. 65–85.

SECULAR EVOLUTION OF ORBITAL MOTIONS IN PLANETARY SYSTEM CONSISTING OF A STAR AND TWO PLANETS

V.V. Sidorenko [1], A.V. Ivanova [2]
[1] *Keldysh Institute of Applied Mathematics, 4 Miusskaya sq., 125047 Moscow, Russia, vvsidorenko@list.ru;*
[2] *Moscow Institute of Physics and Technology, 9 Institutskiy per., 141701 Dolgoprudny, Russia*

KEYWORDS:
Exoplanetary systems, three-body problem, apsidal resonances.

An exoplanetary system is considered, in which two planets moves around a central star. The masses of the planets are significantly less than the mass of the star. Within the framework of the double averaged planar unrestricted three-body problem, the evolution of the orbital motion of the planets due to their mutual attraction is studied. Various scenarios of evolution are described in detail, stationary regimes (apsidal resonances) are revealed. The realization of these scenarios in real exoplanetary systems is discussed.

ACKNOWLEDGMENTS:
V.V. Sidorenko acknowledges the support of Ministry of Science and Higher Education of the Russian Federation under the grant 075-15-2020-780 (N13.1902.21.0039).

MIGRATION OF BODIES IN THE PROXIMA CENTAURI PLANETARY SYSTEM

S.I. Ipatov [1]
[1] *V.I. Vernadsky Institute of Geochemistry and Analytical Chemistry of RAS, Moscow, Russia, siipatov@hotmail.com;*

KEYWORDS:
Proxima Centauri planetary system, exoplanets, planetesimals, probabilities of collisions.

INITIAL DATA AND METHODS FOR CALCULATIONS:
Migration of planetesimals was studied in the the Proxima Centauri system during at least $T = 50$ Myr. The mass of the star equaled to 0.122 of the solar mass. Initial bodies-planetesimals were located near the orbit of the exoplanet *c* with a semi-major axis $a_c = 1.489$ AU, eccentricity $e_c = 0.04$, and mass $m_c = 7m_E$ (where m_E is the mass of the Earth). In each calculation variant, initial semi-major axes of planetesimals were in the range from a_{min} to $a_{min} + 0.1$ AU, with a_{min} from 1.2 to 1.7 AU with a step of 0.1 AU. Initial eccentricities e_o of planetesimals equaled to 0.02 or 0.15. Initial inclinations of the planetesimals equaled to $e_o / 2$ rad. 250 planetesimals were considered in each calculation variant. In total 4500 planetesimals with $e_o = 0.02$ and 1500 planetesimals with $e_o = 0.15$ were considered. While studying migration of planetesimals, besides the exoplanet c, the gravitational influence of exoplanet *b* ($a_b = 0.04857$ AU, $e_b = 0.11$, $m_b = 1.17\ m_E$) was also taken into account. Based on the arrays of the orbital elements of migrating planetesimals, the probabilities of collisions of bodies-planetesimals with planets were calculated. The probability p_d of a collision of a planetesimal with the unconfirmed exoplanet *d* ($a_d = 0.02895$ AU, $m_d = 0.29\ m_E$, $e_d = i_d = 0$) was also calculated. The calculations of migration pf planetesimals and of probabilities of collisions with planets were made similar to [1–4], but for another mass of the star.

RESULTS OF INTEGRATIONS:
The probability p_b of a collision of one planetesimal, initially located near the orbit of the exoplanet *c*, with the exoplanet *b* was non-zero in 5 among 18 variants at $e_o = 0.02$ and in 3 among 6 variants at $e_o = 0.15$. In one of 24 variants $p_b = 0.008$, in three variants $p_b = 0.004$, and in other four variants p_b was between to 4×10^{-6} and 3×10^{-4}. Only one of several hundreds of planetesimals reached the orbit of the exoplanet *b*, but the probability p_b of a collision of one planetesimal with this exoplanet (averaged over thousands planetesimals) is greater than the probability of a collision with the Earth of a planetesimal from the zone of the giant planets in the Solar System. The latter probability was less than 10^{-5} per one planetesimal [5]. The probability p_d of a collision of a planetesimal from the zone of the orbit of the exoplanet *c* with the exoplanet *d* was nonzero only for seven variants (among 24). The mean values of p_b and p_d averaged over 6000 planetesimals (with e_o equaled to 0.02 or 0.15) equaled to $8.5 \times \mathrm{m}10^{-4}$ and 7.0×10^{-4}.

The total mass of water delivered to Proxima Centauri *b* can be considered to be equal to $m_{ice} = p_b \cdot k_{\mathrm{ice}} \cdot m_{out}$, where m_{out} is the total mass of the planetesimals beyond the water line that could reach the vicinity of the orbit of Proxima Centauri *c* with time, k_{ice} is the fraction of water ice in planetesimals. As more planetesimals were ejected into hyperbolic orbits than collided with the planet *c*, we can suppose that the value of m_{out} could exceed the mass of the exoplanet *c* by a factor of several, e.g. it could exceed $20\ m_E$. At $p_b \cdot k_{\mathrm{ice}} = 10^{-4}$ and $m_{out} = 20\ m_E$, we have $m_{ice} = 2 \times 10^{-3} m_E$. This value is greater by a factor of 10 than the mass of water in Earth's oceans ($2 \times 10^{-4}\ m_E$). Therefore, a lot of icy material could be delivered to Proxima Centauri *b* and Proxima Centauri *d*.

The probability p_c was about 0.1–0.3, exclusive for a_{min} = 1.4 AU and e_o = 0.02 when p_c was about 0.7–0.8 (and the main growth was before T = 1 Myr). Usually there was a small growth of p_c after 20 Myr. Most of planetesimals were ejected into hyperbolic orbits in 10 Myr. The ratio of the number of planetesimals ejected into hyperbolic orbits to the number of planetesimals collided with the exoplanets usually exceeded 1 if the number of planetesimals decreased by a factor of several. This ratio was less than 1 only at a_{min} = 1.4 AU and e_o = 0.02. In some calculations a few planetesimals could still move in elliptical orbits after 100 Myr. At e_o = 0.02 and T = 50 Myr, three among 4500 planetesimals collided with the star. At e_o=0.15 such collision was for one among 1500 planetesimals.

ESTIMATES OF COLLISIONS AND EJECTION OF BODIES:

In our calculations of migration of planetesimals, planets and planetesimals were considered as material points, and the planetesimals that could collide with exoplanets were not excluded from the integration. If the total calculated probability of planetesimals with all planets is relatively small (e.g. is not more than about 0.3), then such model gives relatively accurate estimates of collided and ejected planetesimals. However, at a_{min} = 1.4 AU and e_o = 0.02 the calculated probability p_c was about 0.7–0.8. In this case, the real number of ejected planetesimals can be smaller than the number of ejected planetesimals obtained at integrations because it is needed to take into account that some planetesimals ejected in our calculations already collided with exoplanets.

At $p_c > 0.3$ in order to estimate the real probability of collisions and ejections, two models were considered. During integration of the motion of planetesimals, the number of planetesimals did not decrease due to collisions of planetesimals with exoplanets. Therefore, the calculated values p_{ej} and p_{st} of the fractions of planetesimals ejected into hyperbolic orbits and collided with the host star are greater than the corresponding values p_{ej}^* and p_{st}^* for the models which delete planetesimals collided with exoplanets. Such difference is small if the fraction $p_{ex} = p_b + p_c + p_d$ of planetesimals that could collide with exoplanets (calculated based on migration of planetesimals) is small.

The below models *A* and *B* exclude planetesimals that collided with exoplanets. For these models, the fraction of planetesimals collided with exoplanets is denoted by $p_{ex}^* = p_b^* + p_c^* + p_d^*$. The ratio of the number of planetesimals moved in elliptical orbits at the considered time to the initial number of planetesimals is denoted by p_{el} for the results of computer simulations of migration of planetesimals. For models *A* and *B,* the similar ratio is denoted by p_{el}^*. At our calculations of migration of planetesimals, collisions of planetesimals with exoplanets were not simulated. Therefore, $p_{st} + p_{ej} + p_{el} = 1$. For models *A* and *B,* it was considered that $p_{ex}^* + p_{st}^* + p_{ej}^* + p_{el}^* = 1$. Let us denote $k = p_{st}^* + p_{ej}^* + p_{el}^* = 1 - p_{ex}^*$ and suppose that $p_{ex}^* = k_2 \cdot p_{ex}$, $p_{st}^* = k \cdot p_{st}$, $p_{ej}^* = k \cdot p_j$, and $p_{el}^* = k \cdot p_{el}$. For the model *A*, we considered $k_2 = k$ and have

$$k = (1 + p_{ex})^{-1},\ p_{ex}^* = p_{ex} / (1+p_{ex}),\ \text{and}\ p_{ej}^* = p_{ej}/(1+p_{ex}). \quad (1)$$

Our calculations of the probability p_{ex} of collisions of a planetesimal with exoplanets take into account the ejection of planetesimals. However, our computer simulations of migration of planetesimals do not take into account collisions of planetesimals with exoplanets. Therefore, k_2 can be greater than k. In models *A* and *B,* the fraction of planetesimals in elliptical orbits is smaller than that in our computer simulations because of collisions of planetesimals with exoplanets, which were not taken into account at the simulations. $k_2 < 1$ because the number of collisions of planetesimals with exoplanets is smaller at a smaller number of planetesimals left in elliptical orbits.. For the model *B*, we consider $k_2 = 1$ and have

$$k = 1 - p_{ex},\ p_{ex}^* = p_{ex},\ \text{and}\ p_{ej} = p_{ej}(1 - p_{ex}). \quad (2)$$

The model B shows the upper limit for values of p_{ex}^* and the lower limit for p_{ej}^*. Using the models *A* and *B*, we can conclude that the values of k can be between $1-p_{ex}$ and $(1 + p_{ex})^{-1}$. For example, at p_{ex} equal to 0.1, 0.2, 0.3, and 0.75,

the values of 1-p_{ex} are equal to 0.9, 0.8, 0.7, and 0.25, and the values of $(1 + p_{ex})^{-1}$ are equal to 0.909, 0.833, 0.769, and 0.57. The values of p_{ex}^{*} are estimated to be in the range between $p_{ex} / (1 + p_{ex})$ and p_{ex}. The values of p_{ej}^{*} are estimated to be between $p_{ej}(1 - p_{ex})$ and $p_{ej} / (1 + p_{ex})$. Based on the values of p_c, p_b, and p_d, and using similar formulas as those for p_{ex}^{*}, we can estimate the values p_c^{*}, p_b^{*} and p_d^{*} of the probabilities of collisions of a planetesimal with exoplanets *c*, *b* and *d*, that take into account the decrease in the number of migrated planetesimals both due to ejections and collisions.

The difference between $p_{ex}^{*} = p_{ex} / (1 + p_{ex})$ and $p_{ex}^{*} = p_{ex}$ and also between $p_{ej}^{*} = p_{ej}(1 - p_{ex})$ and $p_{ej}^{*} = p_{ej} / (1 + p_{ex})$ was valuable only at $a_{min} = 1.4$ AU and $e_o = 0.02$. In this case, $p_{ex} = 0.77$, $(1 + p_{ex})^{-1} \approx 0.56$, $1 - p_{ex} \approx 0.23$, and the ratio of the values p_{ej}^{*} for models *A* and *B* is $(1 + p_{ex})^{-1}(1 - p_{ex})^{-1} = (1 - p_{ex}^{2})^{-1} \approx 2.4$. For other variants of calculations, p_{ex} was usually about 0.1–0.2 and did not exceed 0.33, with the maximum value of $(1 - p_{ex}^{2})^{-1}$ equal to $(1 - 0.33^{2})^{-1} \approx 1.1$.

ACKNOWLEDGMENTS:

For studies of formation of exoplanets, the author acknowledges the support of Ministry of Science and Higher Education of the Russian Federation under the grant 075-15-2020-780 (N13.1902.21.0039) 'Theoretical and experimental studies of the formation and evolution of extrasolar planetary systems and characteristics of exoplanets'. Migration of icy material and volatiles to exoplanets in the habitable zone was carried out as a part of the state assignments of the Vernadsky Institute of RAS № 0137-2019-0004.

REFERENCES:

[1] Ipatov S.I., Mather J.C., Migration of trans-Neptunian objects to the terrestrial planets, Earth, Moon, and Planets. 2003. V. 92. P. 89-98. http://arXiv.org/format/astro-ph/0305519.

[2] Ipatov S.I., Mather J.C. Migration of Jupiter-family comets and resonant asteroids to near-Earth space // Annals of the New York Academy of Sciences. 2004. V. 1017. P. 46–65. http://arXiv.org/format/astro-ph/0308448.

[3] Ipatov S.I., Mather J.C. Comet and asteroid hazard to the terrestrial planets // Advances in Space Research. 2004. V. 33. P. 1524–1533.

[4] Ipatov S.I., Probabilities of collisions of planetesimals from different regions of the feeding zone of the terrestrial planets with the forming planets and the Moon // Solar System Research. 2019. V. 53. No. 5. P. 332–361. http://arxiv.org/abs/2003.11301.

[5] Ipatov S.I.. Migration of planetesimals from beyond Mars' orbit to the Earth. 14th Europlanet Science Congress 2020, https://doi.org/10.5194/epsc2020-71.

SESSION 3. EXTRASOLAR PLANETS (EP) POSTER SESSION

MOTION OF SUPERFAST EXOPLANETS AND SOLAR SYSTEM

V.A. Kotov [1]
[1] *Crimean Astrophysical Observatory, Nauchny, Crimea 298409, Russia, vkotov@craocrimea.ru*

KEYWORDS:
Exoplanets, the Sun, pulsations, Earth, rotation, solar system.

Do exoplanets revolve around their stars at random? It is shown that substantial part of superfast exoplanets moves with periods, near-commensurate with the value P_G and/or $2P_G/\pi$, where the timescale P_G = 9598(60) s coincides within the error limits with both 1/9th of the mean terrestrial day and a period of global pulsations of the Sun, 9600.606(12) s (confidence level of the resonance is nearly 99.9 % for periods P < 2 days).

There is also a noticeable lack of exoplanetary orbits with periods at/near $3\pi P_G \approx 1.05$ days, and the signs of the presence of the P_G timescale in dynamics of the solar system are presented as well.

It is shown the general period distribution of the superfast, $P < 3$ days, exoplanets resembles a diffraction pattern of light passing through a small circular aperture (with a modulus of $2\pi P_G$). The phenomenon might open a new way for an explanation of a remarkable stability and overwhelming planarity of the solar system, its amazing harmony and regularity, and gives perhaps a reasonable explanation of the Earth's spinning rate as observed at the present cosmological epoch.

True physical origin of the "universal" P_G phenomenon, strangely emerging in the solar system and motion of the superfast exoplanets, is however far from clear.

REVEALING EXOPLANET'S ATMOSPHERE COMPOSITION WITH HIGH RESOLUTION SPECTROSCOPY

F. Hasheminasab [1]
[1] *International Occultation Timing Association Middle East Section*

KEYWORDS:
Exoplanets, Exoplanet's atmosphere, Spectroscopy.

INTRODUCTION:
With over and above 4000 extra solar planets that are discovered, our knowledge about many cases can be reduced to their masses and radiuses. Now the exoplanets' characterization and atmosphere is one of the main focus for years ahead. Key elements for trace planetary evolution are planet's atmosphere and their atmospheric composition. The physical, chemical and even biological process can be unveiled with the spectrum of a planet. (Birkby 2018). Diversity in mass and orbits of the confirmed exoplanets leads to more diversity in bulk compositions and atmospheric characterization compare to the solar system. However, it is a great challenge to observe an exoplanet spectrum. The strong glare of the host star may affect the planet spectra greatly.

With the aim of high resolution spectroscopy, isolation of the planet spectra is possible; and molecular features are revealed as a pile of individual lines. Every molecule has a unique pattern, comparing atmospheric modeling codes with the planet's high resolution spectra leads to detection of the lines (Birkby 2018). The Position, depth and shape of spectral lines are affected by the planet's composition, structure and dynamics. High resolution spectroscopy can help us to characterize the exoplanet atmosphere due to sensitivity to mentioned factors.

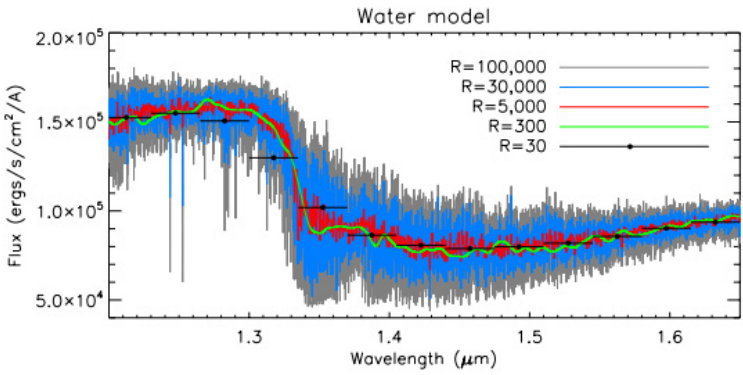


Fig. 1. The difference between low resolution and high resolution spectroscopy in a model Hot Jupiter atmosphere contains water, showed by Birkby (2018).

TECHNIQUE:
Transmission spectroscopy is one of the main used technique to study a planet's atmosphere (Seager & Sasselov 2000). One of the first steps to observe the effects of the faint planet's atmosphere was to measure the slight variation in transit depth with wavelength (Charbonneau et al. 2002). Different atoms and molecules with large opacities in the planet's atmosphere, absorb light in different specific wavelengths and create larger radius compare to the more transparent atmosphere. The transit of a planet is a phenomenon widely used to detect and constrain exoplanet's properties. As the planet passes in front of the star, light passes its atmosphere and we can do a spectroscopic measurement of the transmitted light. The important aspect when it comes to transmission spectroscopy is that the transit is observed at multiple wavelengths. Atoms and molecules in the atmosphere absorbing the stellar light will cause an observable variation of the transit depth

as a function of wavelength. Through the absorption and scattering caused by the atoms and molecules present, transmission spectroscopy reveals the elements present on the planetary atmosphere, its structure, and particles such as haze and clouds (Wakeford & Sing 2015).

REFERENCES:

[1] Birkby, J.L., 2018. Exoplanet atmospheres at high spectral resolution. arXiv preprint arXiv:1806.04617.
[2] Seager, S. and Sasselov, D.D., 2000. Theoretical transmission spectra during extrasolar giant planet transits. The Astrophysical Journal, V. 537(2). P. 916.
[3] Wakeford, H.R. and Sing, D.K., 2015. Transmission spectral properties of clouds for hot Jupiter exoplanets. Astronomy & Astrophysics, V. 573. P. A122.

INVESTIGATION OF THE PERIOD-MASS RELATIONS FOR W UMA-TYPE CONTACT BINARY SYSTEMS BY USING MACHINE LEARNING METHOD

T. Madayaen, A. Poro, et al.
[1] *Astronomy and Astrophysics Department, University of Toronto, Toronto, Ontario, Canada. Tabassom.madayen@mail.utoronto.ca;*
[2] *Astronomy Department of the Raderon Lab., Burnaby, British Columbia, Canada, info@iota-me.com*

KEYWORDS:
Close — binaries, eclipsing — stars, fundamental parameters.

INTRODUCTION:
New period-mass ($P - M$) relations of 122 W UMa systems are presented in this study. To be more precise in the calculations, the parallax values were obtained from Gaia EDR3. The other required parameters including light curve solutions and periods were derived from previous research. As a result, the mass (M) values of each component along with all the other absolute parameters were recalculated for these contact systems. We used a machine learning approach in order to gain the new period-mass relations ($P - M$) per component and added the temperature (T) to the process to acquire the new period-mass-temperature ($P - M - T$) relations. We also investigated the period behavior in terms of $\log(g)$ by new relations for each component.

SIMULATION OF A SYSTEM WITH TWO HOT EXOPLANETS TOI 421

A.G. Berezutsky [1], I.F. Shaikhislamov [1], I.B. Miroshnichenko [1], M.S. Rumenskikh [1]
[1] *Institute of Laser Physics SB RAS, pr. ak. Lavrent'eva 15b, Novosibirsk,630090,Russia*

KEYWORDS:
Numerical simulation, exoplanets, stellar wind.

In the present work, using a three-dimensional self-consistent gas-dynamic model [1–2], we performed a numerical simulation of the exospheres of the Neptune-like planets TOI – 421 b and TOI – 421 c. To understand the processes occurring in the atmosphere, in modeling, for simplicity, we used the solar spectrum and the parameters of the moderate stellar wind. In general, we can say that exoplanets have a rather extensive envelope, with the presence of molecular hydrogen, which does not completely dissociate and is present in a vast area of several dozen radii of the planet. The maximum temperature of the thermosphere reaches approximately 8000 K and 7000 K, and the outflow velocity does not exceed the values V = 30 km/s for TOI – 421b and 25 km/s for TOI – 421 c. The integral mass loss is ~ $5 \cdot 10^9$ g/s. With a change in the XUV flux intensity, the value of the mass loss has an almost linear dependence, at a minimum reaching values of $5 \cdot 10^9$ g/s, as in the case of warm Neptune Gliese 436 b, the maximum is $2.6 \cdot 10^{10}$ g/s. In the presence of a stellar wind, the pressure of planetary matter at a sufficiently large distance is balanced by the thermal pressure of the stellar wind and a shock wave is formed. Modeling the absorption in the Lyα line for two planets showed that the absorption is explained by the presence of ENA, formed due to charge exchange during the interaction of the expanding plasmasphere of the planet with the stellar wind flux, and reaches very high values of ~ 60 % for the near and 80 % of the distant planet, which was predicted in the work [3].

ACKNOWLEDGMENTS:
This work has been performed in the frame of program № 121033100062-5 of Fundamental Studies of ILP (Item 0243-2021-0003), of the Siberian Branch Russian Academy of Science. Parallel computing simulations, key for this study, have been performed at the Computation Center of Novosibirsk State University, the SB RAS Siberian Supercomputer Center, the Joint Supercomputer Center of RAS.

REFERENCES:
[1] I.F. Shaikhislamov et al. Two regimes of interaction of a Hot Jupiter's escaping atmosphere with the stellar wind and generation of energized atomic hydrogen corona // The Astrophysical Journal. 2016. V. 832. №. 2. P. 173.
[2] I.F. Shaikhislamov et al. 3D Aeronomy modelling of close-in exoplanets // Monthly Notices of the Royal Astronomical Society. 2018. V. 481. №. 4. P. 5315–5323.
[3] I. Carleo et al. The Multiplanet System TOI-421: A Warm Neptune and a Super Puffy Mini-Neptune Transiting a G9 V Star in a Visual Binary // The Astronomical Journal. 2020. V. 160. №. 3. P. 114.

REFINED EPHEMERIS FOR HOT JUPITER WASP-12 B USING GROUND-BASED AND TESS OBSERVATIONS

F. Ahangarani Farahani [1,3], F. Davoudi [1,2,3], P.S. Mirshafie Khozani [1,3], E. Paki [1,3], M. Roshana [1,3], F. Hasheminasab[3], A. Mazidabadi Farahani [1,3], T. Farjadnia [3], F. Nasrollahzadeh [1,3], Sh. Rezvanpanah [3], S.M. Mahdi Mousavi [3], R. Foroughi [3], A. Poro [1,2,3], A. Ghalee [3,4]

[1] *The International Occultation Timing Association Middle East section, Iran, info@iota-me.com;*

[2] *Astronomy Department of the Raderon Lab., Burnaby, BC, Canada;*

[3] *The Eight IOTA/ME Summer School of Astronomy, Tafresh University, Tafresh, Iran;*

[4] *Department of Physics, Tafresh University, P.O. Box 39518-79611, Tafresh, Iran*

KEYWORDS:
Planetary systems, planets and satellites, gaseous, planets techniques, photometric.

INTRODUCTION:

The planet WASP – 12 b is a hot Jupiter studied since its discovery in 2008 due to a deviation from a linear ephemeris reported in follow-up observations. Hebb et al. (2009) reported on the planet and its host stars, characteristics obtained from transit light curve and radial velocity. The parameters of WASP – 12 b were refined in 2011, and it was speculated that the TTV signal induces by an additional planet in this system (Maciejewski et al. 2011). Afterward, surveying of the planet's mid-transit times continued and indicated that its orbital period is decreasing. Various scenarios have been proposed to describe this phenomenon; It could be caused by a perturbing planet in the system (Maciejewski et al. 2013) or may be interpreted as the result of orbital decay driven by tidal dissipation in the host star (Maciejewski et al. 2016). Patra et al. (2017) found a rate of $\dot{p} = -29 \mp 3$ ms/yr and they concluded that it is difficult to distinguish that these variations indicate an orbital decay or a portion of a 14-year apsidal precession cycle. The host star's tidal quality factor $Q'_* = (1.82 \pm 0.32) \times 10^5$ is driven (Maciejewski et al. 2018) and Maciejewski et al. (2020) found a 5.8 sigma level for apparent eccentricity of WASP-12 b's orbit, the fact that this value is non-zero is a sign for the presence of the tidal fluid flow. Although, it is also possible that the planet's orbit is slightly eccentric and is undergoing apsidal precession (Yee et al. 2019; they measured $Q'_* = 1.75^{+0.13}_{-0.11} \times 10^5$.

We performed our analysis on the ETD light curve, TESS data, and the previous literature of WASP – 12 b to prepare the WASP – 12 b TTV diagram.

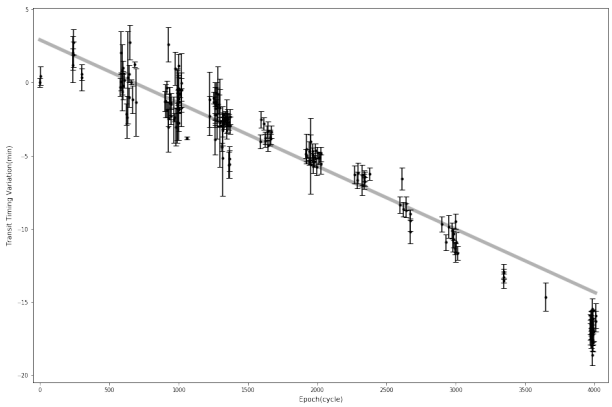


Fig. 1. The TTV Diagram of WASP-12 b with the linear fit on the data points using the MCMC, BIC = 1490.

REFERENCES:

[1] Hebb, L., Collier-Cameron, A., Loeillet, B., et al., 2009. WASP – 12 b: the hottest transiting extrasolar planet yet discovered. // The Astrophysical Journal, V. 693(2), P. 1920.
[2] Maciejewski, G., Dimitrov, D., Fernández, M., et al., 2016. Departure from the constant-period ephemeris for the transiting exoplanet WASP – 12 b. // Astronomy & Astrophysics, V. 588, P. L6.
[3] Maciejewski, G., Dimitrov, D., Seeliger, M., et al., 2013. Multi-site campaign for transit timing variations of WASP – 12 b: possible detection of a long-period signal of planetary origin. // Astronomy & Astrophysics, V. 551, P. .A108.
[4] Maciejewski, G., Errmann, R., Seeliger, M., Spaleniak, I. and Neuhäuser, R., 2011. High-precision photometry of WASP– 12 b transits. // Astronomy & Astrophysics, V. 528, P. A65.
[5] Maciejewski, G., Fernández, M., Aceituno, F., Martín-Ruiz, S., Ohlert, J., Dimitrov, D., Szyszka, K., von Essen, C., Mugrauer, M., Bischoff, R. and Michel, K.U., 2018. Planet-star interactions with precise transit timing. // The refined orbital decay rate for WASP – 12 b and initial constraints for HAT – P – 23 b, KELT – 1 b, KELT – 16 b, WASP – 33 b, and WASP – 103 b. arXiv preprint arXiv:1812.02438.
[6] Maciejewski, G., Niedzielski, A., Villaver, E., Konacki, M. and Pawłaszek, R.K., 2020. An apparently eccentric orbit of the exoplanet WASP – 12 b as a radial velocity signature of planetary-induced tides in the host star. // The Astrophysical Journal, V. 889(1), P. 54.
[7] Patra, K.C., Winn, J.N., Holman, M.J., et al., 2017. The apparently decaying orbit of WASP – 12 b. // The Astronomical Journal. V. 154(1), P. 4.
[8] Yee, S.W., Winn, J.N., Knutson, H.A., et al., 2019. The orbit of WASP – 12 b is decaying. // The Astrophysical Journal Letters, V. 888(1), P. .L5.

CORRECTION OF OBSERVATION SELECTION IN STATISTICS OF RV – EXOPLANETS. FROM THE NUMBER OF DETECTED PLANETS TO OCCURRENCE RATE

A. Ivanova [1], V. Ananyeva [1], I. Litosova [2], A. Tavrov [1]
[1] *Space Research Institute of the Russian Academy of Sciences, 84/32 Profsoyuznaya Str, Moscow, Russia, 117997;*
[2] *Lomonosov State University*

KEYWORDS:
Exoplanets, mass distribution, RV exoplanets, periodogram.

A key problem in studying exoplanet statistics is the heterogeneity of observational data. The main reasons for the heterogeneity of the data are: different sensitivities of spectrographs, different observation periods, different methods of data processing. There are several approaches to solving the problem of data regulation, one of which is the detectability window method.

We have previously demonstrated this technique and its applicability to the data [1, 2]. We are currently working on improving of the method. The basic idea is to use the original radial velocity datasets and analyze them using the Lomb-Scargle periodograms. These datasets contain information about an exoplanet that has characteristics that correspond to the cells of the window of sight. Information about the exoplanet is added to the original datasets, the characteristics (mass, period) correspond to the cell of the detectability window. After that, the data is analyzed using a Lomb-Scargle periodogram and it is possible to conclude whether a planet is observable with the given parameters in such a survey (for a particular star and for a specific spectrograph). This improving could allow us to go from number of detected planets to the occurrence rate.

ACKNOWLEDGMENTS:
Authors acknowledge the support of Ministry of Science and Higher Education of the Russian Federation under the grant 075-15-2020-780 (N13.1902.21.0039).

REFERENCES:
[1] V. Ananyeva et al. Radial velocity- exoplanets distributions by masses and by orbital periods. 11MS3-EP-06. 2020.
[2] A. Ivanova et al. Detectability window regularization algorithm to account for observation selection in statistics of RV- exoplanets. 11MS3-EP-05. 2020.

WAVEFRONT CORRECTION FOR DIRECT IMAGING OF EXOPLANETS. PHASE RETRIEVAL BY LC SLM AS AO TO INTERFERO-CORONAGRAPH

A. Yudaev [1,2], A. Tavrov [1,2]
[1] *Space Research Institute of the Russian Academy of Sciences, 84/32 Profsoyuznaya Str, Moscow, Russia, 117997;*
[2] *Moscow Institute of Physics and Technology, Dolgoprudny, Moscow Region, 141701, Russia, yudaev@phystech.edu*

KEYWORDS:
Exoplanets, direct imaging.

Active adaptive optics (AO) wavefront corrected stellar coronagraph plays a key role for the next generation of high-contrast instruments aiming the direct exoplanet imaging. The current report is devoted to the engineering study where the (phase-only) liquid crystal spatial light modulator (LC SLM) aplied as the pixilated wavefront corrector of AO is functioning with the interfero-coronagraph.

To detect an exoplanet PSF (point spread function) core intensity having the contrast 10^{-9}…10^{-10} relative to the PSF of the host star, an optical quality including telescope and coronagraph are critical. They have the primary mirror — and downstream optics figure error (known as optical aberrations) as well as the surface micro-roughness which remains after polishing. Both factors cause the input wavefront perturbation and critical coronagraphic contrast degradation if the coronagraph aims to achieve the desired image contrast for an exoplanet imaging. Ground-based telescope imaging is perturbed by propagation trough atmosphere. Actually both the space-based and the ground-based exoplanet imaging techniques do require an active and precise wavefront correction. But these corrections have the different scales of aberrations on input: several lambdas — ground based, lambda over 5 — space based, and the different dynamical parameters from quasi-statical regime in space to millisecond scale on ground. The precision of wavefront correction is required at the level of λ/1000 for an hour exposition.

Classical AO techniques are not applicable here because the coronagraphs (of Lyot- or interfero- or appodization- or mixed type) all are very sensitive to downstream (after telescope) optics, which include internal optical elements (lenses, mirrors, apertures) with critical surface errors (at λ/5… λ/20) and aperture edges. Wavefront sensors e.g. Hartmann sensors cannot be applied if it is placed after the coronagraph, because of the dark field regime and the downstream optical plane is located in different position to the secondary pupil plane in which the wavefront corrector is mounted. Later effect is known as the NCPA (non-common-path aberrations). It is difficult to recover the wavefront by the CCD in image plane, because of the unknown phase distribution. Currently, similar techniques (EFC — electric field conjugation, SCC — self coherent camera, etc.) [1] are in focus of intensive studies due to the implementation phase of the WFIRST NASA space telescope (2.4 meter in diameter) within a CGI coronagraph instrument onboard [2]. Here the ground-based facilities are also improving their records, see the instruments ZIMPOL/SPHERE at VLT, SCExAO at Subaru, Gemini Planet Imager at Gemini South Telescope.

Our current study is to develop the telescope-interferometer concept. Its main part consists of the AO (LC SLM) for wavefront correction, the interfero-coronagraph, and the CCD in pupil conjugated plane downstream a coronagraph, this scheme was constructed in lab for experiments. To control the pixilated AO element (phase-only LC SLM wavefront corrector) we retrieve the phase distribution in the secondary pupil plane by the analysis of the field after the interfero-coronagraph in the third pupil.

To do this we send 3 or 4 probe modulation patterns to LC SLM and detect the corresponding intensities by CCD $I_1 \ldots I_4$. By use of $I_1 \ldots I_4$ we precisely recover the wavefront (phase) distribution to control the LC SLM AO. By this procedure we become able to visualize lab modeled planet at $5\lambda/D$ stellarcentric separated on a scattered background of suppressed star. Figure 1 shows a half-field modulation scheme to evaluate pupil phase. Figure 2 shows the residual background (left panel) in which we cannot identify planet (of 10^{-6} PSF core intensity respective the star PSF (10^{0}) intensity). On right panel we show the background is suppressed to identify the paired (interfero-coronagraphic) planet image.

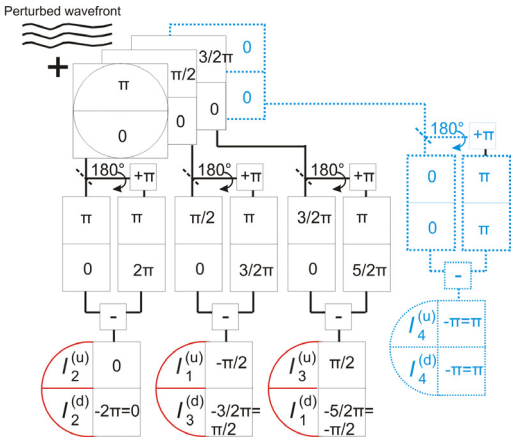


Fig. 1. AO modulation algorithm.

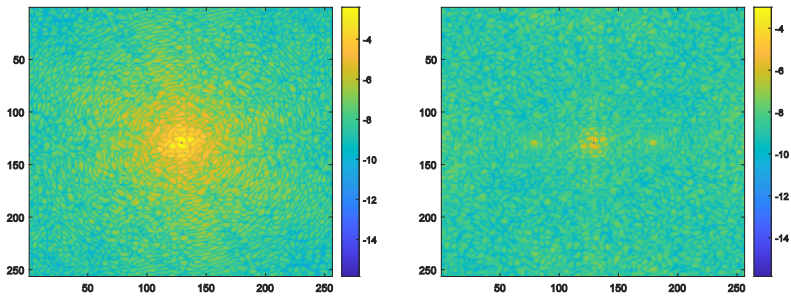


Fig. 2. Star and planet PSFs. Left panel before the wavefront correction, right panel after wavefront correction.

ACKNOWLEDGEMENTS:
Authors acknowledge the support of Ministry of Science and Higher Education of the Russian Federation under the grant 075-15-2020-780 (N13.1902.21.0039).

REFERENCES:

[1] F. Hénault, et all. Phase-shifting coronagraph, arXiv:1709.02672v, 2017.
[2] V.P. Bailey, et all. Lessons for WFIRST CGI from ground-based high-contrast systems, arXiv:1901.04049v1 [astro-ph.IM] 13 Jan 2019, DOI: 10.1117/12.2313820.

ABSORPTION IN THE Hα LINE BY OUTLETING ATMOSPHERES OF HOT JUPITERS

I.B. Miroshnichenko [1,2], I.F. Shaikhislamov [1,2], A.G. Berezutsky [1], E.S. Vetrova [1,2], S.S. Sharipov[1,2], M.S. Rumenskih[1,2]

[1] *Institute of Laser Physics SB RAS, 630132, Russia, Novosibirsk, Acad. Lavrentyeva, 15b;*

[2] *Novosibirsk State Technical University, Russia, Novosibirsk, Prospekt K. Marksa, 20*

KEYWORDS:
Exoplanet, planetary wind, stellar wind, multi-fluid model, Monte Carlo radiation transport.

In this work, the absorption in the Hα line (due to the resonant scattering of Lyα photons) by the outflowing atmospheres of hot Jupiters HD189733b and Wasp – 52b was simulated. The transfer Lyα of photons was calculated by the Monte Carlo method. The problem was solved in the approximation of isotropic partially coherent scattering. The atmosphere was assumed to be spherically symmetric with given profiles of temperature and volumetric density of hydrogen atoms. The bulk density profiles of excited hydrogen atoms were obtained using three-dimensional gas-dynamic modeling [1] at various values of the parameter XUV. The shapes of the emission lines of the stars are taken from [3]. Based on the results of the work, it can be concluded that the transit absorption of hot Jupiters in the Hα line depends significantly on the Lyα radiation of the star, but cannot be fully explained by it. The main contribution is made by intra-atmospheric sources of Lyα photons. Comparison of the results of calculations with observations [4] is shown in Figure 1.

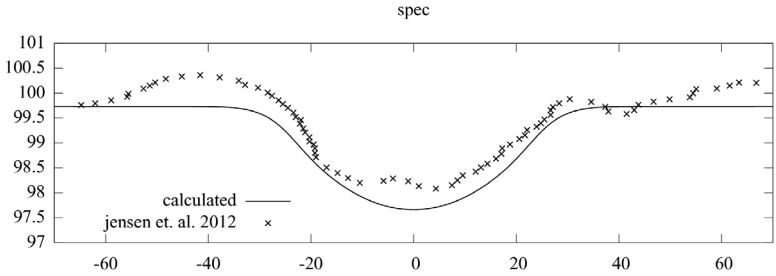


Fig. 1. Comparison of the calculation results with the observed absorption for the planet HD189733b.

ACKNOWLEDGMENTS:
This work was carried out as part of the RSF project No. 18-12-00080, RSF project No. 21-72-00129 and RFBR No. 20-02-00520 and grant of the President of the Russian Federation for state support of young Russian scientists MK-1089.2021.1.2.

REFERENCES:

[1] Shaikhislamov I.F. et al. // Monthly Notices of the Royal Astronomical Society 2019.
[2] Odert P. et al. Modeling the Lyα // arXiv preprint 2019. arXiv:1903.10772.
[3] Bourrier V., des Etangs A. L. // Astronomy & Astrophysics 2013. V. 557. P. A124.
[4] Cauley P.W. et al. // The Astronomical Journal 2016. V. 152(1). P. 20.

SESSION 4. ASTROBIOLOGY (AB)
ORAL SESSION

WHERE WERE THE MOLECULES OF LIFE MADE?

S. Jheeta [1]
[1] *Network of Researchers on the Chemical Evolution of Life (NoRCEL), Leeds, UK*

It is believed that some of the necessary organic molecules may have been formed in the specialised areas of space (namely dark molecular clouds, eg Horsehead nebula) and delivered on to the Earth during the early period of its history, approximately $4.3 – 4.0 \times 10^9$ years ago. These organic molecules may have played a pivotal role in the formation of life on Earth. In addition, it is believed that life on Earth was formed within a very short geological time frame of only 200-300 million years. So, it is not unreasonable to suppose that these molecules were initially made in space as this could be, metaphorically speaking, a huge chemical laboratory.

The research being presented during this oral presentation focuses on the formation of molecules [1–2] under a variety of simulated space conditions (eg different temperatures, levels of radiation energies and different types of impinging radiations). Results pertaining to irradiation of methyl cyanide, mixture of $NH_3 : CO_2$ and $NH_3 : CH_3OH$ ices will be presented.

REFERENCE

[1] Jheeta, S., Ptasinska S., et al. The irradiation of 1:1 mixture of ammonia:carbon dioxide ice at 30 K using 1 kev electrons. Chemical Physics Letters. 2012, V. 543, P. 208–212.
[2] Jheeta, S., Domaracka A., et al. The irradiation of pure CH3OH and 1:1 mixture of NH3:CH3OH ices at 30 K using low energy electrons. Chemical Physics Letters. 2013, V. 556, P. 359–364.

ORIGIN OF LIFE ON A PLANET BY EFFICIENT RESPONSE OF PREBIOTIC SYSTEMS TO HIGH-FREQUENCY OSCILLATIONS IN THE ENVIRONMENT

V.N. Kompanichenko[1]
[1] *Institute for Complex Analysis RAS, Birobidzhan, Russia*

KEYWORDS:
Origin of Life, Astrobiology, Nonequilibrium Thermodynamics, Hydrothermal Systems, Life in Extreme Environment, Laboratory Simulation Experiments.

An essence of the proposed "inversion" approach to the origin of life is described [1]. The approach focuses on the very moment of life emergence. There are its key theses: (1) The transformation of nonliving prebiotic microsystems into a primary living (sub)cells culminates at the moment of thermodynamic inversion, when the contribution of free energy and information to the system begins to prevail over the contribution of entropy; (2) During the transformation, the microsystems are in an oscillatory process of a nonequilibrium transition from the initial (old) equilibrium state to a new equilibrium state; (3) Under such non-equilibrium conditions, thermodynamic inversion occurs through an intensified and purposeful response of the microsystems to high-frequency fluctuations ("pumping") in physicochemical parameters in the environment. Extremely fast chemical reactions, which are investigated by Eigen [2] and other researchers, are also involved into the microsystems' response to the "pumping". The transition of prebiotic microsystems to the living state proceeds through the intermediate state between non-life and life (Figure 1). Hydrothermal systems (including the both subsurface zones and outcrops on continents or oceanic bottom) are the most suitable medium for the origin of life. The proposed mechanism for the emergence of life through thermodynamic inversion can be common for various inhabited planets, since the basic notions used — entropy, free energy and information — are the most fundamental attributes of the Universe.

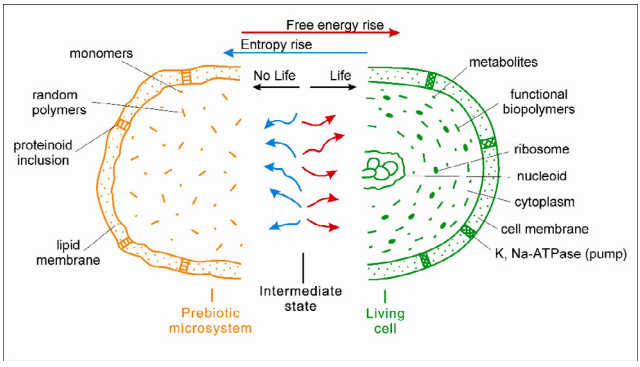


Fig. 1. The intermediate state between non-life and life. On the left, yellow — a non-living prebiotic microsystem (its half) composed of random polymers, monomers, and simple molecules. In the center: thermodynamically intermediate state of the microsystem between non-life and life, relative equality of the contributions of chemical reactions producing free energy (red) and entropy (blue). On the right, green - a primary living microorganism (its half); on the picture its evolutionarily advanced form is shown — a modern prokaryotic cell with basic cellular structures, including a nucleoid (circular DNA), ribosomes and a cell membrane.

To verify this approach, it is proposed scheme of laboratory experiments. It consists in studying the transformations that take place in different types of prebiotic microsystems when they are "pumped" by different-rank oscillations of parameters [3]. In the course of experiments, it is necessary to record the appearance and development of changes in organic microsystems, bringing them closer to a living state (strengthening the role of active transport, increasing the degree of homochirality, etc.).

It follows from this approach that even primary microorganisms and populations could exist in two states:

A) passive (anabiotic), if the "pressure" from the environment (the action of stress factors) exceeds their ability to effectively counteract; such "latent" life can be potentially sustained in spores under unfavorable external conditions for thousands and even million years.

B) active, if their response to environmental stressors is efficient (intensified and purposeful); the ability to the efficient response could provide potential existence of microbial life even in various extreme conditions, like in the Venus' atmosphere or the subsurface zones on Mars.

REFERENCES

[1] Kompanichenko V.N. Thermodynamic Inversion: Origin of Living Systems. Springer: Cham (Switzerland). 2017. P. 75.
[2] Eigen M. Selforganization of matter and the evolution of biological macromolecules. // Naturwissenschaften. 1971. V. 58. P. 465–523.
[3] Kompanichenko V. Rise of Habitable Planet: Four Conditions for the Origin of Life // Geosciences. 2019. V. 9. No. 92.

PROSPECTS FOR THE USE OF LICHENS IN ASTROBIOLOGICAL AND ASTROECOLOGICAL RESEARCH

D.D. Mironov[1,2]
[1] *Institute of Geochemistry and Analytical Chemistry named after V.I. Vernadsky, RAS, Moscow, Russia; 1032193132@rudn.ru;*
[2] *RUDN University, Institute of Environmental Engineering, Moscow, Russia*

KEYWORDS:
Lichens, astrobiology, astroecology, extraterrestial life, Mars, stress physiology.

INTRODUCTION:
With the development of astrobiology, scientists have resorted to using various rganisms in research, but despite this, lichens are rarely considered. The main argument for using them in astrobiology is that the lichens are known as the stress-tolerant organisms [1]. Their high resistance to many extreme factors of environment is explained by morphological features and biochemical relationships between the photobiont and mycobiont. Lichens were able to survive in open space for two weeks [2]. During this time, they were exposed to extreme temperatures and high level of radiation. Lichens were also frozen in liquid nitrogen . Also lichen is called as radioactive contamination indicators.

It has recently been determined that some species of lichens are resistant to a large diurnal temperature variations on the surface of Mars. Using data from Mars climate database v5.3, we were able to repeat the temperature regimes in the Tiu Valley area at Ls 30 °, 0 ° lat. 28 ° W. For several days, lichen species such as Xanthoria parietina, Parmelia sulcata and Hypogimnia physodes existed at this temperature regime. The species Xanthoria parietina proved to be the most resistant to such extreme temperature variations.

Despite the fact that there are not enough data about resistance of lichens to another factors, including high radiation levels, which can be critical for photosynthetic activity for different species (Noetzel et al, 2018), it can be assumed that some species of lichens will be able to exist on the surface of Mars under these conditions.

REFERENCES:
[1] Grime, J.P.: Plant strategies and vegetation processes. John Wiley & Sons, Ltd., Chichester-New York-Brisbane-Toronto, 1979. P. 222.
[2] Young, K.. 2005. Hardy lichen shown to survive in space. New Scientist, November 10th, 2005.
[3] Becket R.P. et al Stress physiology and the symbiosis, Cambridge University Press, 2008. P. 134–151.
[4] De La Torre Noetzel et al : Cellular Responses of the Lichen Circinaria gyrosa in Mars-Like Conditions. Front. Microbiol., 05 March 2018.

UV RADIATION FROM STELLAR FLARES: A CONSTRAINT FOR LIFE?

X.C. Abrevaya[1,2,*], O.J. Oppezzo[3], P. Odert[4], M. Leitzinger[4], M. Patel[5], G.J.M. Luna[6,2], A.F. Forte Giacobone[3,7], E. Guenther[8], A. Hanslmeier[4]

[1] *Instituto de Astronomía y Física del Espacio (IAFE), Universidad de Buenos Aires — CONICET, Ciudad Universitaria, Ciudad Autónoma de Buenos Aires Argentina, abrevaya@iafe.uba.ar;*

[2] *Facultad de Ciencias Exactas y Naturales, Universidad de Buenos Aires, Ciudad Universitaria, Ciudad Autónoma de Buenos Aires, Argentina;*

[3] *Comisión Nacional de Energía Atómica (CNEA), Buenos Aires, Argentina;*

[4] *IGAM / Institut für Physik, University of Graz, Graz, Austria;*

[5] *School of Physical Sciences, The Open University, Milton Keynes, UK;*

[6] *Instituto de Astronomía y Física del Espacio (IAFE), Universidad de Buenos Aires — CONICET, Ciudad Universitaria, Ciudad Autónoma de Buenos Aires Argentina;*

[7] *Departamento de Ingeniería, Universidad Nacional de Tres de Febrero, Buenos Aires, Argentina;*

[8] *Thüringer Landessternwarte Tautenburg (TLS) — Karl-Schwarzschild-Observatorium, Tautenburg, Germany;*

[*] *Invited scientist, IGAM / Institut für Physik, University of Graz, Graz, Austria*

KEYWORDS:
Planetary habitability, exoplanets, stellar radiation, stellar activity, superflares, microorganisms, laboratory simulations, experiments, astrobiology, dM stars.

INTRODUCTION:

Stellar UV radiation (UVR) is in general considered a constraint for life, as UVR wavelengths (200–400 nm) can reach the surface of a planet (depending on the existence of a planetary atmosphere, and its composition and pressure), and have direct and indirect effects on life [1]. It is very well known that UVR can be very harmful and even lethal to living beings, especially shorter UV wavelengths are the most harmful, i.e.: UVB (280–315 nm) and UVC (200–280 nm) regions [2]. UVR is capable to damage DNA (a molecule essential for life "as we know it"), but also is able to damage other cellular components through direct or indirect mechanisms [2]. In fact, exposure to UVC, which is shielded by the ozone layer on the present Earth, could be lethal for most terrestrial organisms.

The determination of the biological impact of UV in extrasolar planets is a very active field of research in the astrobiology area (for reviews on the topic see: [2–3]) and a considerable amount of studies are focused in this wavelength range (see e.g.: [4–6]).

Previous studies, particularly focusing on planets orbiting F, G, K and M – type main-sequence stars, have evaluated the impact of stellar UV radiation on life through theoretical approaches (i.e. modeling) that used empirical data from the literature (e.g.: [7–14]). The fact that previous studies are based on data from the literature poses a problem, partly because most of the currently available knowledge on the effects of UVR on microorganisms is related with the action of sunlight on terrestrial ecosystems, or the use of artificial UV in disinfection processes. In both cases the spectral energy distribution and intensity of the incident radiation is usually very different from those that exoplanets would receive on the surface during stellar flares or superflares. Therefore, the possible biological impact of UV during these astrophysical events cannot be deduced from data reported in the literature. For instance, microorganisms receiving sunlight on terrestrial ecosystems would not be exposed to highly damaging wavelengths from UVC and partially from UVB radiation as these wavelengths do not reach the Earth's surface because they are attenuated by the ozone layer.

Moreover, for studies investigating the impact of UVR on life it is necessary to consider not only the stellar quiescent levels, but also stellar activity, such as sudden energetic events known as flares. These are energetic outbreaks

of radiation commonly observed on magnetically active stars, originating in magnetic processes and affecting all the layers of the stellar atmosphere (photosphere, chromosphere and corona). During flares, stellar radiation, including the UV range, is increased by up to several orders of magnitude and can therefore affect planetary habitability (e.g., [11]). The biological impact of stellar flares and superflares (flares with energies > 1033 erg) has been poorly studied in this context.

In a recent interdisciplinary study, considering the closest potentially habitable planet, Proxima b, we determined, through laboratory experiments and for the first time, the impact that stellar flares and superflares would have on microorganisms on the surface of this exoplanet. We demonstrated that previous studies underestimated the chances of "life as we know it" to thrive under high UVR levels comparable to those from stellar flares and superflares [15]. These efforts are part of the EXO-UV program, an international interdisciplinary collaboration that seeks to contribute to a better characterization of the surface habitability of exoplanets and their potential to host life [16].

In this presentation we will make a general review on the topic, explaining the drawbacks of methodologies used in previous studies in contrast to our first results, and we will present our latest findings about the impact of flares and superflares on potential microbial life in the exoplanetary system orbiting the ultracool dwarf TRAPPIST – 1.

REFERENCES:

[1] Abrevaya X.C. & Thomas B.C. In: Habitability of the Universe before Earth, ed. R. Gordon & A.A. Sharov, (Academic Press) Elsevier, 2018. P. 576.
[2] Kielbassa C., Roza L., Epe B. Wavelength dependence of oxidative DNA damage induced by UV and visible light // Carcinogenesis. 1997. V. 18. No. 4. P. 811–816.
[3] Hanslmeier, A. Planetary Habitability and Stellar Activity. World Scientific Press, Singapore, New York, London, 2018. P. 264.
[4] Talmi, O. & Shaviv, G. 2013, In: Habitability of Other Planets and Satellites. (eds. J : de Vera, P. & Seckbach, J.) Springer, P. 419.
[5] Shields, A.L., Ballard, S., & Johnson, J. A. The habitability of planets orbiting M-dwarf stars // Phys. Rep. 2016. V. 663. P. 1–38.
[6] Segura, A. In: Handbook of exoplanets (ed. H.J. Deeg & J.A. Belmonte), Springer, 2018. P. 3490.
[7] Buccino A.P., Lemarchand G.A., Mauas P.J.D. Ultraviolet radiation constraints around the circumstellar habitable zones // Icarus. 2006. V. 183. No. 2. P. 491–503.
[8] Buccino A.P., Lemarchand G.A., Mauas. UV habitable zones around M stars // Icarus. 2007. V. 192. No. 2. P. 582–587.
[9] Rugheimer, S., A. Segura, L. Kaltenegger, and Sasselov D. UV surface environment of Earth-like planets orbiting FGKM stars through geological evolution // Astrophys. J. 2015. V. 806. No. 1. P. 137.
[10] O'Malley-James J.T. & Kaltenegger L. UV surface habitability of the TRAPPIST – 1 system // MNRAS Lett. 2017. V. 469. No. 1. P. L26–L30.
[11] Howard, W.S., Tilley, M.A., Corbett, H., et al. The first naked-eye superflare detected from Proxima Centauri // ApJ. 2018. V. 860. No. 2. P. L30.
[12] Estrela, R. & Valio, A. Superflare ultraviolet impact on Kepler-96 system: a glimpse of habitability when the ozone layer first formed on Earth // Astrobiology. 2018. V. 8. No. 11. P. 1414–1124.
[13] O'Malley-James J.T. & Kaltenegger L. Lessons from early Earth: UV surface radiation should not limit the habitability of active M star systems // MNRAS Lett. 2019. V. 485. No. 4. P. 5598–5603.
[14] Estrela, R., Palit, S., & Valio, A. Surface and oceanic habitability of Trappist-1 planets under the impact of flares // Astrobiology. 2020. V. 20. No. 12. P. 1465–1475.
[15] Abrevaya X.C., Leitzinger M., Oppezzo O.J., Odert P., Patel M.R., Luna G.J.M., Forte Giacobone A.F., & Hanslmeier A. The UV surface habitability of Proxima b: first experiments revealing probable life survival to stellar flares // MNRAS. 2020. V. 494. No. 1. P. L69–L74.
[16] Abrevaya X.C., Leitzinger, M., Nuñez Pölcher, P.N., Odert, P., Lammer, H., & Hanslmeier, A. The EXO-UV Project: habitable stars // Workshop Star-Planet Interactions and the Habitable Zone. CEA- Irfu, France. 2014. http://irfu.cea.fr.

MICROBIAL FUEL CELLS AS EXTRATERRESTRIAL MICROBIAL LIFE SENSORS

E. Cortón [1], F. Figueredo [1], A. Saavedra-Olaya [1], N. Sacco [1], A. Cauerhff [1]
[1] *University of Buenos Aires and CONICET. Faculty of Ciencias Exactas y Naturales, Ciudad Universitaria, Buenos Aires (1428), Argentina*

KEYWORDS:
Astrobiology, Biosensors, Carbon and non-carbon-based life, Extraterrestrial life detection, Microbial-electrode charge transport, Microbial fuel cells, Metabolism, Redox reactions.

INTRODUCTION:
Microbial fuel cells (MFCs) are bioelectrochemical systems that harvest electrons from redox reactions involved in the metabolism of living microorganisms. Previously, we developed MFC-based sensors for the detection of extraterrestrial life as these redox processes can be coupled to the electric circuit of the MFC and generate an electric current that can be measured and quantified. Using this principle, we demonstrated for the first time that these sensors can detect metabolically active microorganisms in an unequivocal way, clearly distinguishing between those electric parameters that arise from biotic redox reactions and those that arise from abiotic redox reactions [1, 2].

RESULTS AND DISCUSSION:
Our studies up to know have demonstrated that different types of microbial metabolisms presented in Earth can be detected, including heterotrophic (soil microorganism, yeast, among others), photosynthetic microorganism (including bacteria and algae) and autolithotrophic metabolism (that obtains energy from iron/sulfur oxidation activities in the presence of oxygen). Some of our assays were made whit hypersaline and hyperacidophilic microorganisms, using a simple set up that can eventually be miniaturized to be easily transported in planetary space missions, as show in the Figure 1. In this figure is evident the enormous differences in the electrical parameters of the MFCs when metabolic activity is present in the sample allowing the detection of active microbial life.

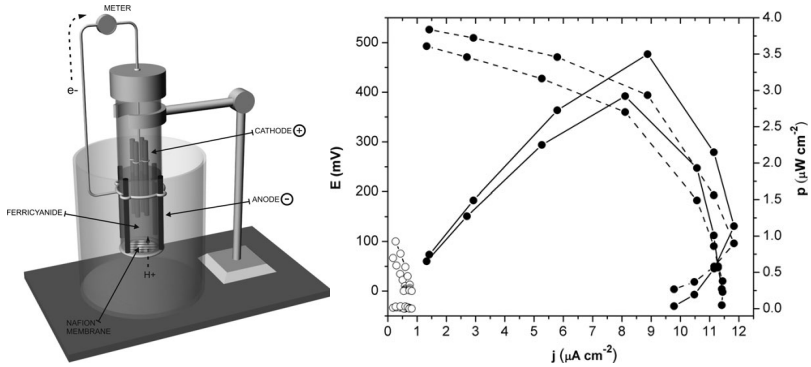


Fig. 1. Set up (left panel) and data obtained (right panel) in MFCs Earth soil experiment. We use sterilized soil (as control, open symbols) and with non-sterilized soil (containing a microbial community, closed symbols) [1].

During this presentation we want to show briefly the work done by our group in this direction during the last 10 years, our goals for future work and our will to participate in future exploration missions. We believe our approach is less "earthcentric", as redox reactions (as the way life have in Earth to obtain energy) would probably also used by non-carbon life forms, if they eventually exist elsewhere. The carbon approach was used by the only missions up to date arriving Mars (the Vikings) to look for metabolic life more than 40 years ago [3], more metabolic experiments able to detect active life would be an interesting addition to relatively complex mission during or before new manned missions to Mars.

REFERENCES:

[1] Abrevaya, X.C., Mauas, P.J.D., Cortón, E. Microbial fuel cells applied to the metabolically based detection of extraterrestrial life // Astrobiology. 2010. V. 10. P. 965–971.
[2] Figueredo, F., Cortón, E., Abrevaya, X.C. In situ search for extraterrestrial life: a microbial fuel cell–based sensor for the detection of photosynthetic metabolism // Astrobiology. 2015. V. 15 P. 717–727.
[3] Levin, G.V., Straat, P.A. Labeled released. An experiment in radiorespirometry // Origin of Life. 1976. V. 7. P. 293–311.

EXTRATERRESTRIAL & INTRATERRESTRIAL DIATOMS & CYANOBACTERIA: IMPLICATIONS TO THE ORIGIN AND DISTRIBUTION OF BIOSPHERES

R.B. Hoover [1,2], M. Karpatov [3], A. Ryumin [3], M.V. Frontasyva [3], N.C. Wilckramasinghe [2], D.H. Wallis [2], A.YU. Rozanov [4]

[1] *NASA-Emeritus, U. S. Space and Rocket Center, One Tranquility Base, Huntsville, AL, USA, RichardBHoover@Icloud.Com;*
[2] *Buckingham Centre for Astrobiology, Univ. of Buckingham, UK;*
[3] *Joint Institute for Nuclear Research, Dubna, Russian Federation;*
[4] *Borissiak Paleontological Institute (RAS) Moscow, Russia*

KEYWORDS:
Meteorites, Diatoms, Cyanobacteria, Deep Crustal Rocks, Heat Producing Elements (HPE's), Extraterrestrial Biospheres, Intraterrestrial Biospheres.

INTRODUCTION:

The origin and distribution of biospheres is one of the great unanswered questions of Science. The widely accepted endogenous origin hypothesis is that the biosphere of planet Earth arose after a long, slow process of the abiotic synthesis of organic carbon compounds and biomolecules in Earth's primordial oceans and atmosphere led to the evolution of the first self-replicating protocells. The endogenous origin hypothesis is challenged by linear regression analysis of the size of functional non-redundant genomes versus the time of origin of major prokaryotic and eukaryotic life forms, which indicates life originated [1] some 9.7 billion years ago - long before the condensation of the proto-Solar nebular and the formation of planet Earth. The exogenous origin (panspermia) hypothesis that life originated elsewhere in the Cosmos and was delivered to Hadean Earth by the influx of comets, asteroids and planetesimals was strengthened by the discovery of the close correspondence between the IR properties of the amorphous silica of diatoms and the observed IR spectrum of Trapezium nebula and galactic center source GC-IRS7 [2]. Recent studies have also found that primordial xenolithic clasts in the ancient Zag (H3-6) chondrite contain organic matter with carbon isotope fractionations (δ 13C = - 28 to - 22 ‰) [3] consistent with the biological fractionations of stable carbon isotopes that have persisted throughout 3.8 Ga of the recorded history of life on Earth. Scanning Electron Microscopy (SEM) investigations carried out during the past 25 years at NASA / MSFC, PIN / RAS and JINR have resulted in the detection of microfossils of cyanobacteria, diatoms and microalgae in the Murchison (CM2), Orgueil (CI1) and Polonnaruwa/Aralaganwila (C - Ung.) meteorites. Mineralogical studies at Cardiff University and Oxygen Isotope analysis in Germany and Japan have shown the low-density (r ~ 0.6 - 0.8) Polonnaruwa/Aralaganwila stones are non-terrestrial (Fig. 1a – c). Recent Epithermal Neutron Activation Analysis (ENAA) at JINR found they are rich in incompatible radiogenic Heat Producing Elements (40K, 235U, 238U, 232Th) as compared with other carbonaceous chondrites [4]. EDS spot data and 2-D x-ray maps have shown the permineralized or carbonized microfossils found embedded in the meteorite rock matrix typically have N < 0.5% and are therefore ancient and indigenous [5]. This meteorite data provides direct observational evidence for the existence of extraterrestrial Biospheres.

The existence of a vast intraterrestrial Biosphere of planet Earth has been revealed by the discovery of viable bacteria, cyanobacteria, diatoms and protists in deep, hot crustal rocks, perennially ice covered lakes, ancient permafrost and deep Vostok ice cores. The discovery of water boiling with hydrogen and hydrogenotrophic cyanobacteria and other prokaryotic and eukaryotic microorganisms thriving in the total darkness of hot, deep crustal granites combined with recent observations of the interstellar comets Oumuamua and 2I Borisov suggests a new paradigm for the exogenous origin lo life on Earth and the possibility of the interstellar transfer of Biospheres.

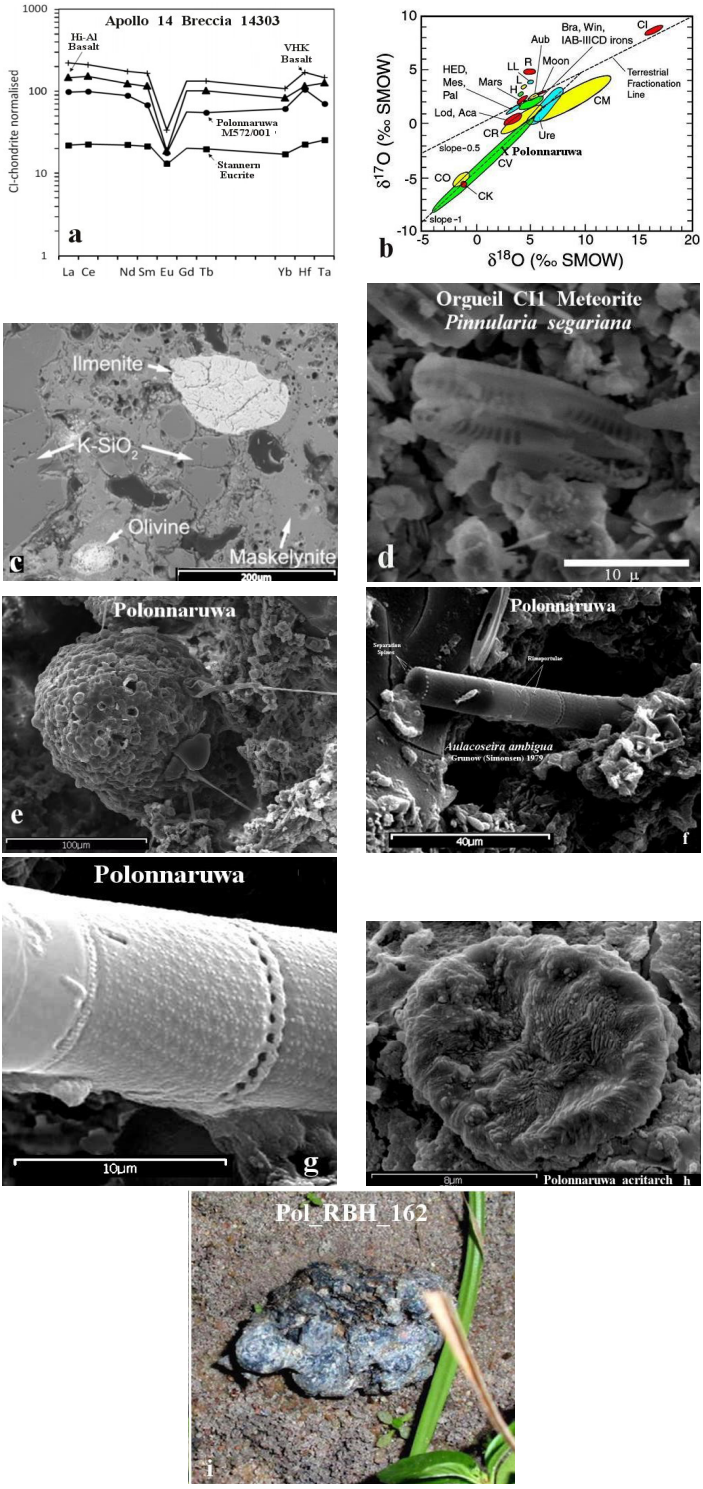


Fig. 1. a. Rare Earth Elements, **b**. Oxygen Isotopes and **c.** K-rich SiO_2 glass, fractured ilmenite & olivine grains & Maskelynite from high velocity asteroidal impacts prove the non-terrestrial nature of the low-density (0.8 g/cm^3) black **g.** Polonnaruwa/Aralaganwila stones that fell in Sri Lanka in 2012. SEM studies show they contain fossils of extinct **e.** hystrichospheres; **h.** acritarchs & **f.g.** diatoms as in **d.** Orgueil. **Images: a&c** J. Wallis & A. Oldroyd**,** *Univ. Cardiff***; b.** A. Pack; *Univ. Grotingen*;**.** M. Kapralov *JINR***; e-i.** J. Wallis, N.C. Wickramasinghe *Univ. Cardiff* and R.B. Hoover, *Univ. Buckingham*.

MATERIALS:

EXTRATERRESTRIAL SAMPLES:

Orgueil (CI1) — MNHN, Paris; Victor Brun Museum, Montauban; PSF, Chicago.

Murchison (CM2) — Field Museum, Chicago; Museum Victoria, Melbourne.

Polonnaruwa/Aralaganwila (C-Ung.) — Hoover Collection, Sri Lanka 1/29/2012.

INTRATERRESTRIAL SAMPLES:

Driefontein Gold Mine, South Africa, Tullis Onstott.

INSTRUMENTS AND METHODS:

NASA/MSFC: FEI Quanta 600; TESCAN MAIA3 Triglev — Uncoated samples.

PIN(RAS) & JINR: TESCAN VEGA 3 SEM - Gold coated samples.

JINR: Epithermal Neutron Activation Analysis (ENAA) study of Rare Earth Elements and radiogenic Heat Producing Elements (^{40}K, ^{235}U, ^{238}U, ^{232}Th).

RESULTS: EXTRATERRESTRIAL BIOSPHERES

SEM studies have revealed indigenous microfossils of diatoms and extinct acritarchs and hystrichospheres in the Orgueil (CI1-Fall, France, 1864) and Polonnaruwa/Aralaganwila (Fall-Sri Lanka, 2012) meteorites (Fig. 1)**.**

The Orgueil CI1 carbonaceous meteorite has been found to contain a great diversity of well-preserved embedded fossils of morphotypes of filamentous cyanobacteria (~ Calothrix sp., Microcoleus sp. Phormidium sp., and the extinct Obruchevella sp.); acritarchs (~ Leiosphaeridia sp.). Diatoms and diatom fragments are extremely rare in the Murchison CM2 and Orgueil CI1 carbonaceous meteorite. Most of diatoms found in Orgueil are fragments of small pennates consistent with morphotypes of Stauroneis sp., Achnanthes sp. and (Fig. 1d) Pinnularia spp. In contrast, the Polonnaruwa/Aralaganwila diatoms, (Fig. 1f,g) acritarchs, (Fig. 1h) and hystrichospheres (Fig. 1e) in the meteorite (Fig. 1i) are astonishingly well-preserved. The long chain of complete intact frustules (Fig. 1f) of the centric diatom Aulacoseira ambigua appears to be covered in an exopolysaccharide sheath (Fig. 1g). The great diversity of indigenous microfossils found in-situ in freshly fractured interior surfaces of the Polonnaruwa/Aralaganwila, Orgueil and Murchison stones provides direct observational evidence of extraterrestrial Biospheres with biology very similar to that of Earth. Some consider it would be impossible for life on icy moons or other planets in the Cosmos to have evolved in the same way as on Earth. However, this ignores the possibility that microbial life may be continually delivered to Earth's oceans via the impacts of planetesimals, Kuiper belt objects, comets, and asteroids an as intact, viable extraterrestrial bio-contaminants. When, where, and how life originated remains unknown.

INTRATERRESTRIAL BIOSPHERES:

The existence of a hydrogen-rich vast deep, hot intraterrestrial Biosphere has recently been discovered. The deep granites of Earth's crust are teeming with microbial life thriving in liquid water boiling with hydrogen and helium.

DRIEFONTEIN GOLD MINE

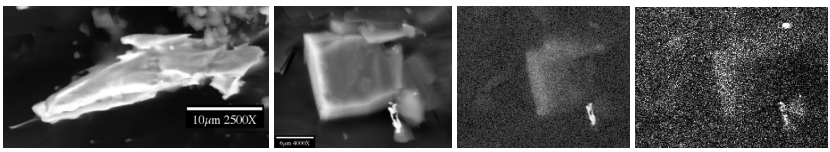


Fig. 2. a. SEM of Eukaryote. **b.** *Caulobacter* sp. **c.** Au Map. **d.** U Map.

Figure 2 shows SEM images of a. large eukaryote and b. Caulobacter sp.that are seen in 2D X-ray maps to have accumulated c. Gold and d. Uranium in the deep, hot rock of the Driefontein Gold Mine of South Africa. Energy for this massive ecosystem is produced by the radioactive decay of the long-lived incompatible radiogenic Heat Producing Elements (^{40}K, ^{235}U, ^{238}U, ^{232}Th) and the exothermal process of serpentinization of ultramafic rocks. Nitrogen fixing heterocystous filamentous cyanobacteria of the genera Calothrix and Nostoc along with Microcoleus and Phormidium are abundant in the of hot, deep biosphere of Earth where they live by metabolizing hydrogen rather than carrying out photosynthesis. The significance of the HPE's in the deep, hot In-

traterrestrial biosphere of Earth is profound. These elements are the primary producers of heat in deep granites of the crust of our planet and they could maintain oceans beneath the icy crusts of interstellar comets or rogue planets in liquid state for billions of years far away from stellar and tidal heating mechanisms. The similarity of the microbial remains in carbonaceous meteorite with the microbiota of the deep Biospheres of Earth provides intriguing insights for a possible mechanism for the origin of life on Earth by interstellar transfer of viable biospheres from ancient star systems.

REFERENCES:

[1] Sharov, A.A. Genome increase as a clock for the origin and evolution of life // Biology Direct 2006, V. 1: P. 1–10.
[2] Hoover R.B., et al. Diatoms on Earth, Comets, Europa and in Interstellar Space // Earth, Moon, and Planets. 1986. V. 35, P. 19-45; Hoyle, F. and Wickramasinghe, N.C. 1982. Evolution fom Space // J. M. Dent, London. P. 1–192.
[3] Kebukawa Y. et al. A novel organic-rich meteoritic clast from the outer solar system // Scientific Reports. 2019. V. 9. P. 1–7.
[4] Hoover, R.B. et al. Epithermal Neutron Activation Analysis of Carbonaceous Chondrites and the Polonnaruwa/Aralaganwila Stones // Aspects in Mining and Mineral Science. 2020. V. 6. No. 1. P. 669-679.
[5] Hoover, R.B. Fossils of Cyanobacteria in CI1 Carbonaceous Meteorites // Journal of Cosmology. 2011. V. 13, P. 1–49.

PHOSPHINE AND OTHER VENUSIAN CLOUD ANOMALIES

J.J. Petkowski [1], W. Bains [1,2], P.B. Rimmer [3,4,5], A. Paschodimas [6,7], S. Seager [1,8,9]

[1] *Department of Earth, Atmospheric, and Planetary Sciences, Massachusetts Institute of Technology, Cambridge, MA 02139, USA;*
[2] *School of Physics & Astronomy, Cardiff University, 4 The Parade, Cardiff CF24 3AA, UK;*
[3] *Department of Earth Sciences, University of Cambridge, Downing St, Cambridge CB2 3EQ, UK;*
[4] *Cavendish Laboratory, University of Cambridge, JJ Thomson Ave, Cambridge CB3 0HE, UK;*
[5] *MRC Laboratory of Molecular Biology, Francis Crick Ave, Cambridge CB2 0QH, UK;*
[6] *Centre for Exoplanet Science, University of St Andrews, St Andrews, UK*
[7] *Earth and Environmental Sciences, University of St Andrews, Irvine Building, North Street, St Andrews, KY16 9AL, UK;*
[8] *Department of Physics, Massachusetts Institute of Technology, Cambridge, MA 02139, USA;*
[9] *Department of Aeronautics and Astronautics, Massachusetts Institute of Technology, Cambridge, MA 02139, USA;*
[*] *Corresponding author: Janusz J. Petkowski, jjpetkow@mit.edu*

KEYWORDS:
Venus, clouds, chemistry, acidity, habitability, phosphine, thermodynamics, photochemistry, biosignature gas, life.

INTRODUCTION:

Scientists have been speculating on Venus as a habitable world for over half a century (e.g. [1]), based on the Earth-like temperature and pressure in Venus' clouds at 48–60 km above the surface. The hypothesis that Venusian clouds are inhabited by an aerial biosphere got recently bolstered by a tentative detection of a biosignature gas phosphine in the atmosphere of Venus [2, 3]. Phosphine however is not the only anomaly that suggests very unusual chemical processes in the clouds, and maybe even life. The presence of such chemical anomalies came to the forefront thanks to the recent efforts to re-analyze and re-interpret the legacy data collected by both the Pioneer 13 and Venera probes [4].

In my talk I will discuss the recent detection of phosphine (PH_3) gas, at ppb levels, in the cloud decks of Venus. I will, discuss the critique and controversies behind the discovery and present most recent re-analysis of the phosphine data. I will summarize our work ruling out all conventional sources of phosphine on Venus (Fig. 1). Therefore, if PH_3's presence in Venus' atmosphere is confirmed, it is highly likely to be the result of a process not previously considered plausible for Venusian conditions. The source of atmospheric phosphine could be unknown geo- or photochemistry—though we have not yet found a process that can reach anywhere near the observed phosphine abundance. An even more extreme possibility is that strictly aerial microbial biosphere produces PH_3.

We have extended our analysis to some other anomalies in the legacy data collected by both Venera and the Pioneer 13 programs. These have been dismissed as artefactual on the grounds that models do not explain them; we argue for a new interpretation, in which it is the model, not the data that is incorrect. We present a new transformative hypothesis for the chemistry of the clouds of Venus, that builds on previous work by Rimmer et al [5]. Our model predicts that the clouds are not entirely made of sulfuric acid, but of ammonium salt slurries, which are the result of biological production of ammonia in cloud droplets. As a result, the clouds are no more acidic than some terrestrial environments that harbor life. Life makes its own environment on Venus. The model's predictions for the abundance of gases in Venus' atmosphere matches observation better than any previous model, and are readily testable.

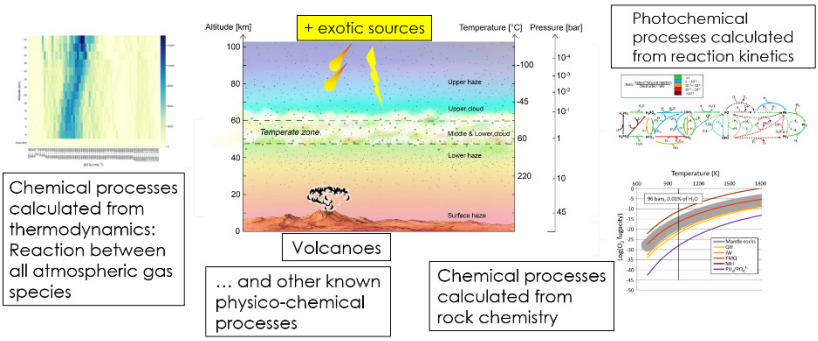


Fig. 1. Phosphine on Venus cannot be explained by conventional processes.

We conclude with a call for more data from the legacy dataset. Regardless of whether our particular model is right, it is clear that there are a lot of unknowns about Venus. New missions to Venus will add data to resolve some of the lingering questions. Even so, we believe that if legacy data were made available, particularly data from the Russian Venera and Vega missions, this data could support or refute current models and predictions, and would provide needed context for future mission results. We ask for this community's help in finding and re-analyzing such data.

REFERENCES:

[1] Seager S., et al. The Venusian Lower Atmosphere Haze as a Depot for Desiccated Microbial Life: A Proposed Life Cycle for Persistence of the Venusian Aerial Biosphere // Astrobiology. 2021. in press.
[2] Greaves J.S., et al. Phosphine gas in the cloud decks of Venus // Nature Astronomy. 2020. P. 1–10.
[3 Bains W., et al. Phosphine on Venus Cannot be Explained by Conventional Processes // Astrobiology. 2021. in press.
[4] Mogul R. et al. Venus' mass spectra show signs of disequilibria in the middle clouds // Geophysical Research Letters. 2021. 48.7. e2020GL091327.
[5] Rimmer P.B., et al. Hydroxide salts in the clouds of Venus: their effect on the sulfur cycle and cloud droplet pH // Planetary Science Journal. 2021. in press.

SESSION 4. ASTROBIOLOGY (AB)
POSTER SESSION

EXTRATERRESTRIAL CYANOBACTERIA AND DIATOMS IN THE ORGUEIL (CI1) AND MURCHISON (CM2) CARBONACEOUS CHONDRITES

R.B. Hoover [1,2], M. Kapralov [3], A. Ryumin [3], A.YU. Rozanov [3,4]
[1] *NASA-Emeritus, U. S. Space and Rocket Center, One Tranquility Base, Huntsville, AL, USA, RichardBHoover@Icloud.Com;*
[2] *Buckingham Centre for Astrobiology, Univ. of Buckingham, Buckingham, UK;*
[3] *Astrobiology Sector, Joint Institute for Nuclear Research, Dubna, Moscow Oblast, Russian Federation;*
[4] *Borissiak Paleontological Institute, Russian Academy of Sciences, Moscow, Russia*

KEYWORDS:
Carbonaceous Chondrites, Orgueil, Murchison, Diatoms, Cyanobacteria Biomolecules, Microfossils.

INTRODUCTION:
Carbonaceous meteorites are messengers from space. The Orgueil (CI1) carbonaceous chondrite fell in France on May 14, 1864 and Murchison (CM2) fell in Australia on September 28, 1969. It is now well established that the CI and CM meteorites contain high percentages of extraterrestrial water (3–20 %) and carbon (2–5 %). The carbon is mainly an insoluble organic matter (IOM) chemically similar to terrestrial kerogen. In 1961, microbiologist George Claus and petroleum geologist Bartholomew Nagy [1, 2] reported *"Microscopic-sized particles resembling fossil algae were found to be present in relatively large quantities in the Orgueil and Ivuna carbonaceous meteorites."* Anders et al. [3] won the ensuing intense scientific debate when they reported finding biogenic protein materials, seeds and coal in Orgueil — explaining the optical activity, kerogen, amino acids, pristine, phytane and all other biomolecules and fossil microalgae previously found as not only contamination — but a hoax possibly perpetrated in 1864. The hint of a possible scientific fraud caused the search for biomarkers and microfossils in meteorites to be abandoned. In 1997 (after the ALH84001 results) Scanning Electron Microscopy studies at NASA/MSFC in the US [4] and at the Borissiak Paleontological Institute (RAS) in Russia [5] resulted in the independent discovery of recognizable fossils of cyanobacteria embedded in freshly fractured interior surfaces of the Murchison meteorite. Subsequent SEM studies in the US, UK and Russia have revealed the remains of a great diversity of microorganisms in many different carbonaceous meteorites. Energy Dispersive X-ray Spectroscopy (EDS) spot analysis and 2D x-ray spectroscopy element maps have shown the recognizable diatoms, cyanobacteria and other clearly biological remains are often permineralized or carbonized sheaths often infilled with magnesium sulfate in Orgueil. The O/C and S/C ratios and nitrogen content below EDS detection limit prove these are ancient, indigenous microfossils rather than post-arrival bio-contaminants.

During the past half century, many researchers, using extremely sensitive instruments and careful methodologies, have established that the Orgueil (CI1) and Murchison (CM2) carbonaceous meteorites contain a vast suite of complex organics and life-critical biomolecules. These include a host of extraterrestrial amino acids (many of which are unknown in terrestrial biology), nucleobases, aliphatic and aromatic hydrocarbons, carboxylic and hydroxyl acids [6]. Only 10 of the 20 proteinogenic amino acids and 3 of the 5 nucleobases essential for life are present in the meteorites [7]. Some of the proteinogenic amino acids in these meteorites are racemic ($D / L = 1$), while others have an excess of the *L*-enantiomer significantly greater than can be obtained by known abiotic production mechanisms. Carbon isotopes have shown the nucleobases in the meteorites are indigenous and extraterrestrial, and indicate the parent body may be a comet [8]. Galimov [9] discovered

clearly extraterrestrial carbon isotopes of protein amino acids in Murchison that exhibited biological fractionation analogous to that of terrestrial microalgae. Some suggest the racemic nature of meteorite amino acid prove they result from abiotic production mechanisms. This argument is invalid, as it is known that the homochirality of different biological amino acids degrades by different racemization rates over geological time periods. This process forms the basis for amino acid geochronometry [10]. The proteinogenic amino acids and the life-critical nucleobases (Cytosine and Thymine) that are missing from the meteorites are also missing from Cretaceous Hadrosaur bones [11]. SEM studies in the US and Russia during the past 25 years have resulted in the discovery of many fossils of cyanobacteria, diatoms and other microalgae in different samples of the Orgueil (CI1) and Murchison (CM2) meteorites [12].

MATERIALS:

Orgueil CI1 (PSF#11) Dr. Paul Sipiera, Planetary Studies Foundation, Chicago.

Orgueil CI1 (Org #9418) Dr. Edmée Ladier, Musée Victor Brun, Montauban.

Orgueil CI1(Org MHNP #2838) Dr. Martine Rossignol-Strick, MNHN, Paris.

Murchison CM2 (#E4806) Dr. William Birch, Museum Victoria, Melbourne.

INSTRUMENTS AND METHODS:

At NASA/MSFC the FEI Quanta 600 FESEM and TESCAN MAIA3 Triglev FESEM instruments were used to examine freshly fractured uncoated meteorite samples. At PIN(RAS) and JINR, the meteorite samples were gold coated prior to study with the thermal emission TESCAN VEGA 3 SEM. A propane torch was used to flame sterilize new preparation trays, mount stubs. tweezers and all tools used to fracture and mount the meteorite fragments on new stubs with the freshly fractured surface exposed for SEM study.

RESULTS:

Well-preserved, recognizable remains of filamentous cyanobacteria, (particularly Oscillatoriales) are relatively abundant in the Murchison (Fig. 1 a,b) and Orgueil (Fig. 1 d,e) meteorites. Many filaments are polarized uniseriate or multiseriate with distinctive morphological features. Diatoms are present but they are extremely rare. After many years of study, only a single fragment (Fig. 1 c) has been found in Murchison. Several fragments and a few complete frustules (Fig. 1 f,g) have been found in the Orgueil CI1 meteorite.

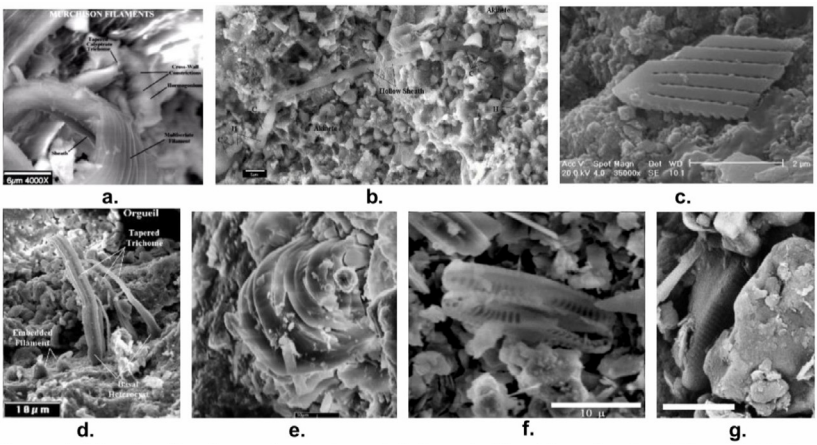


Fig. 1. Microfoddils of cyanobactia and diatoms in Murchison (a – c) and Orgueil (d – g).

Figure 1a shows Murchison filaments with multiple trichomes in a common delaminated sheath (cf. Microcoleus chthonoplastes) near a tapered uniseriate filament with a calyptrate apical cell (cf. Phormidium sp). EDS measurements show the N content of the escaped hormogonium is < 0.5 % atomic, establishing it as an indigenous fossil. Figure 1b shows a Murchison Nostoc sp. filament with a hollow sheath and escaped hormogonium con-

taining three (2.8μ dia.) cells. Figure 1c is an unidentified diatom fragment in Murchison. Figure 1d shows highly differentiated polarized tapered filaments embedded in the Orgueil rock matrix. These filaments exhibit funnel shaped termini and hyaline basal heterocysts consistent with known morphotypes of Calothrix sp. EDS data shows N < 0.5 % and Carbon rich sheaths infilled with the evaporite mineral magnesium sulfate. Fig. 1e is a morphotype of extinct cyanobacterium Obruchavella sp. Fig. 1f shows two complete frustules (after mitosis) of a small form ~ Pinnularia segariana, Foged) discovered in 2015 at JINR in Dubna, Russia [13]. Fig. 1g is an embedded frustule of a minute (14μ × 3.5μ) form interpreted as a morphotype of Stauroneis nana, Hustedt, 1857.

CONCLUSIONS:

The missing life-critical protein amino acids, nucleobases and other unstable biomolecules in the Murchison and Orgueil meteorites clearly establish that the interior regions of these stones are not contaminated by modern biology. PCR amplification studies sensitive enough to detect DNA from a single bacterium have provided additional confirmation [14]. These meteorites do not contain chlorins and chlorophylls but the ancient diagenetic breakdown products (phytane, pristane and porphyrins) of these biomolecules are present [15]. Hence, it is concluded that the well-preserved, recognizable fossils of cyanobacteria. diatoms and other microalgae in the Orgueil CI1 and Murchison CM2 meteorites are indigenous and extraterrestrial and provide evidence for an ancient aquatic biosphere within their parent bodies.

REFERENCES:

[1] Claus, G. and Nagy, B. A Microbiological Examination of Some Carbonaceous Meteorites // Nature. 1961. V. 192. P. 594–596.
[2] Nagy, B. Carbonaceous meteorites. Elsevier Science Publishing, 1975. P. 747.
[3] Anders, et al. Contaminated Meteorite // Science. 1964. V. 146, P. 1157–1161.
[4] Hoover R.B. Meteorites, Microfossils and Exobiology // Proceedings of SPIE. V. 3111, San Diego, California, USA. 1997. P. 115–136.
[5] Zhmur, S.I., Rozanov, A.Yu., et al. Lithified Remnants of Microorganisms in Carbonaceous Chondrites // Geochemistry International. 1997. V. 35, P. 58–60.
[6] Glavin, D. et al. The Origin and Evolution of Organic Matter in Carbonaceous Chondrites and Links to Their Parent Bodies // In Primitive Meteorites and Asteroids. 2018. P. 205–271.
[7] Callahan, M.P. et al. Carbonaceous meteorites contain a wide range of extraterrestrial nucleobases // PNAS. 2011. V. 108. No. 34. P. 13994–13998.
[8] Ehrenfreund, P. et al. Extraterrestrial amino acids in Orgueil and Ivuna: Tracing the parent body of CI type carbonaceous chondrites // PNAS. 2001. V. 98. P. 2138–2141.
[9] Galimov, E.M. The Biological Fractionation of Isotopes. New York, Academic Press, 1985. P. 261.
[10] Bada, J.L. Racemization of Amino Acids in Nature // Interdisciplinary Science Reviews. 1982. V. 7. No. 1. P. 30–46.
[11] Hoover, R.B. Fossils of Cyanobacteria in CI1 Carbonaceous Meteorites // Journal of Cosmology. 2011. V. 13, P. 1–49.
[12] Rozanov, A.Yu., et al. The Orgueil Meteorite (Atlas of Microfossils) // 2020. P. 1–134.
[13] Hoover, R.B. et al. 2018. Diatoms in the Orgueil Meteorite. Paleontological Journal, V. 52, P. 1647–1650.
[14] Aerts, J. et al. A contamination assessment of the CI carbonaceous meteorite Orgueil using a DNA-directed approach // Meteoritics & Planetary Sci. 2016. V. 51. P. 920–931.
[15] Kissin, Y. Hydrocarbon components in carbonaceous meteorites // Geochim. et Cosmochim. Acta. 2003. V. 67, P. 1723–1735.

SUCCESSION OF HYPOTHETICAL MICROBIAL COMMUNITIES ON VENUS DURING PLANETARY CLIMATE CHANGE

O. Kotsyurbenko [1,2], D. Skladnev [2,3], S. Karlov [4], Y. Khrunick [5,6]

[1] *Yugra State University, Khanty-Mansiysk, Moscow, Russia;*
[2] *Network of Researchers on the Chemical Evolution of Life, Leeds, United Kingdom;*
[3] *Research Center of Biotechnology of the Russian Academy of Sciences, Winogradsky Institute of Microbiology, Moscow, Russia;*
[4] *Moscow Polytechnic University, Russia;*
[5] *Department of Heat Treatment and Physics of Metal, Ural Federal University, Ekaterinburg, Russian Federation;*
[6] *M.N. Mikheev Institute of Metal Physics of the Ural Branch of the Russian Academy of Sciences, Ekaterinburg, Russian Federation*

KEYWORDS:
Venusian cloud layer, Life on Venus, Extremophilic microorganisms.

According to the data provided by spacecraft the upper atmospheric layers of Venus are constantly losing water molecules [1, 2]. The extrapolation of this process to the past leads to a hypothesis on the existence of a larger amount of water on Venus during its ancient times, when the conditions were milder and more suitable for Earth-type living organisms. Most likely, surface temperatures on Venus were higher than those on Earth because of the closer proximity of Venus to the Sun. Under such conditions Venus could be dominated by unicellular microbial organisms Climate change and enhanced greenhouse effect followed by temperature rise on the planet forced aboriginal life forms to struggle for survival, at gradual increase of temperature and salinity due to the evaporation of surface water bodies. It resulted in the total domination of prokaryotic microbial community and the selection of polyextremophilic microbial forms.

When the temperature of Venus's surface rose to 100 °C, the water evaporation became of a maximum intensity. It was accompanied by the formation of continuous water cloud masses at the altitudes where water vapors could be cooled down and condensed. Most probably, the layer of the formed clouds was initially less acidic, if not close to neutral. These conditions were favorable for creating proper trophic interactions between different microorganisms and for biogeochemical cycle processes that increased the stability such cloud microbial community. Only later, after Venus's atmosphere had lost the main amount of water, the adaptive selection was directed towards the resistance to extreme acidity and low water activity. Microorganisms thriving such an extreme environment including an increased radiation should have various survival strategies and protection mechanisms.

Terrestrial biogeochemical cycles of elements are the important condition for the stability of an ecological niche where microorganisms can play the key role. Hypothetical microbial community inhabiting Venusian cloud layer can consist of thermo-acidophilic chemolithotrophic and phototrophic anaerobic microorganisms. They consume energy released in red-ox reactions involving sulfur and iron [3]. Microbial sulfate and iron reduction coupled with iron-dependent denitrification is among the simplest biochemical cycles possibly occurring in this ecosystem. Such system can function in the water phase of a foam structure where microorganisms actively interact with solid particles containing different inorganic and organic compounds. Simultaneously, microorganisms can release different stress regulators in order to withstand extreme physical-chemical factors of the environment. These substances can act as surfactants and contribute to the stabilization of the foam structure.

Extremely high temperatures and pressure on Venus's surface exclude the possibility of Earth-type life on its surface. Nevertheless, such conditions allow the chemical reactions resulting in the synthesis of complex polymers [4, 5]. Such polymerization reactions can occur in several stages.

In the presence of iron catalyst and highly accessible atmospheric CO_2 and N_2 these compounds can be further involved in the synthesis of high molecular compounds of g-C_3N_4 formula having graphite structure with triazine as monomers [5]. Such compounds can play a few roles in the cloud layer system. Firstly, they can serve as a nanomatrix for the catalysis of chemical denitrification yielding the generation of gaseous products from nitrite. Secondly, they can contribute to the stabilization of foam structures. Finally, being raised to higher altitudes such compounds may decompose in photocatalytic reactions and serve as an additional carbon source for the cloud microbial system.

REFERENCES:

[1] Donahue T.M., Grinspoon D.H., Hartle R.E., Hodges R.R.. Ion/neutral escape of hydrogen and deuterium: evolution of water. In Venus II Geology. Geophysics, Atmosphere and Solar Wind Environment (S.W. Bougher, D.M. Hunten, and R.J. Phillips, Eds.), 1997, 585–414. Univ. of Arizona Press, Tucson.

[2] Way M.J.; Del Genio A.D. Venusian habitable climate scenarios: modeling Venus through time and applications to slowly rotating Venus-like exoplanets // J. Geophys. Res. Planets 2020, P. 125.

[3] Kotsyurbenko O.R., Cordova Jr.J.A., Belov A.A., Cheptsov V.S., Khrunyk J., Kölbl D., Kryuchkova M.O., Milojevic T., Mogul R., Sasaki S., Słowik G.P., Snytnikov V., Vorobyova E.A.. Exobiology of Venus clouds: new insights into habitability through terrestrial models and methods of detection. Astrobiology 2021, Volume 21, Number 9, 2021.

[4] Ksanfomality L.V., Zelenyi L.M., Parmon V.N., Snytnikov V.N. Hypothetical signs of life on Venus: revising results of 1975–1982 TV experiments // Phys.Uspekhi 2019, V. 62, P. 378–404.

[5] Snytnikov, V.N. Chemical base of hypothetical life on Venus // Venera – D landing sites selection and cloud layer habitability workshop. 2019, 2–5 October, Space Research Institute, Moscow, Russia. http://venera-d.cosmos.ru/uploads/media/7_-_Snytnikov2019-Venera-D.pdf.

AEROSOL OR FOAM - WHICH STRUCTURE OF VENUSIAN CLOUDS IS BETTER FOR SURVIVAL OF HYPOTHETICAL MICROBIAL COMMUNITIES

D.A. Skladnev [1,2], S.P. Karlov [3], Y.Y. Khrunyk [4,5], O.R. Kotsyurbenko [2,6]
[1] *Research Center of Biotechnology of the Russian Academy of Sciences, Winogradsky Institute of Microbiology, Moscow, Russia;*
[2] *Network of Researchers on the Chemical Evolution of Life, Leeds, United Kingdom;*
[3] *Moscow Polytechnic University, Russia;*
[4] *Department of Heat Treatment and Physics of Metal, Ural Federal University, Ekaterinburg, Russian Federation;*
[5] *M.N. Mikheev Institute of Metal Physics of the Ural Branch of the Russian Academy of Sciences, Ekaterinburg, Russian Federation;*
[6] *Yugra State University, Khanty-Mansiysk, Moscow, Russia*

KEYWORDS:
Venusian clouds, water/acid foam structures, microbial community.

It is now considered that the cloud layer at the altitude of 47 to 70 km is the only niche of Venus where the Earth-type extremophiles could survive and where physical-chemical conditions meet the requirements of microbial forms analogous to known terrestrial microorganisms. The literature considers the hypothesis that water/acid of cloud aerosols can serve as an environment for cells allowing the occurrence of microbial processes. Nevertheless, the actual size of droplets can limit the presence of active microbial cells able to develop so that interactions within a microbial community become complicated. The charge on droplets' surface prevents their merging hindering the access of growth substrates necessary for the functioning of living cells and community generally also.

If provided the habitable cloud layer exists as ecological niche, it should contain united liquid media volume, where cells of trophically balanced microbial community could thrive. We hypothesize that such united liquid volume can have foam heterophase structure (gas-solid-liquid) with microbial cells distributed throughout the whole volume of cloud. The structure of this water/acid foam may be stabilized by different compounds including biogenic surfactants — exopolysaccharides and/or other biogenic organics.

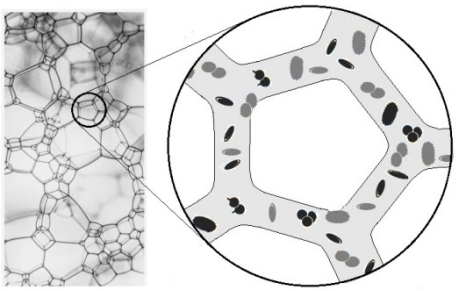


Fig. 1.

Such hypothetical microbial ecosystem existing in foam structures of Venusian clouds could include different species of (poly)extremophilic micro-organisms capable to realize photo- and chemosynthesis using mostly sulfur and iron compounds in their energy metabolism. The whole microbial foam system could maintain its stability by involving in aero-geochemical and matter exchange processes between the cloud layer and the Venus's surface.

RESISTANCE OF DNA (MICROBIAL) TO RADIATION DAMAGE ON THE FROSTY JOVIAN EUROPA SURFACE

S.A. Bulat [1], V.N. Verbenko [1], V.S. Cheptsov [2]
[1] *NRC KI-PNPI, Gatchina, Leningrad region, Russia, bulat@omrb.pnpi.spb.ru;*
[2] *Lomonosov Moscow State University, Soil Science Faculty, Moscow, Russia*

INTRODUCTION:
The dsDNA molecules are relatively stable but could quickly degrade/fragmented by ionization radiation. If we are looking for extraterrestrial life (at least on different bodies — planets and their satellites, of our Solar System), the best place to search for it is icy satellites (e.g., Jovian Europa or Saturn's Enceladus) along with polar ice caps on 'atmosphere-lost' Mars. However, the fluxes of highly energized protons (mostly), electrons (mostly for Europa; the surface 1cm deep irradiation — 30 kGy/year) and heavy ions on these targets from the parent body (e.g., Jupiter) or cosmic radiation can provide a challenge for DNA (microbial) integrity.

OBJECTIVES:
The objective of the study was to estimate the low bound of already-known attenuation effect of ultralow temperature at normal pressure on the efficacy of gamma-radiation in braking/fragmenting dsDNA. The general purpose of the study was to simulate the 'fate' of ocean-below-ice-inhabiting microbes flushed out via cracks on the Jovian Europa — how long their DNA inside the cells could withstand the surface radiation fluxes.

MATERIAL AND METHODS:
As a model, the plasmid vector pCR-4 (~ 4000 bp) for cloning containing the insert of a bacterial rRNA gene (v3 – v4 region — 485 bp) was used in irradiation trials under the liquid nitrogen conditions (- 195.8 ^{o}C). The gamma-induced fragmentation was tested in specific PCR generating the dsDNA band of the expected size (~ 600 bp); in fact, it is disappearing upon complete fragmentation of the insert. As a radiation source, the ^{60}Co-charged device 'Issledovatel' (PNPI) was in use. The tubes with a crude bacterial lysate containing the target (vector with an insert in a cell debris mix) were put at the bottom of a stain steel thermos (with the help of heavy load) filled with the liquid nitrogen. The dose rate was 5 kGy per hour. The down-up of the irradiation camera was taken 18 Gy only. The time series were up to 300 kGy (60 hrs). The detection level of the DNA signal in a gel stained with SYNR Gold was about 10 pg.

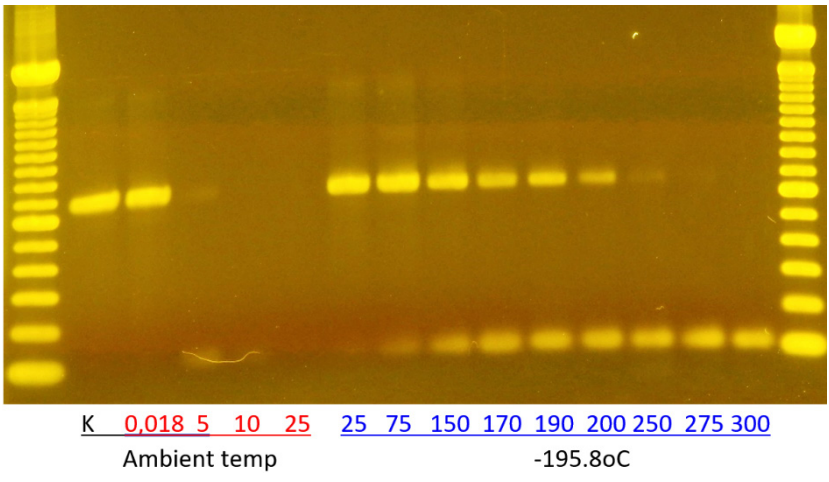


Fig. 1. Agarose gel-electrophoresis loaded with amplicons (~ 600 bp) generated upon gamma-irradiation at ambient and liquid nitrogen temperature. The gel was stained with SYBR Gold. K – non-irradiated control. Doses are shown in kGy.

RESULTS:

At the ambient temperature, the insert entirely disappeared (DNA stained with SYBR Gold) upon the doze ~ 7.5k Gy while under the deep freeze at -195.8 ^{o}C – ~ 270kGy what accounts for ~ 35 difference (Fig. 1). A similar effect was observed at a bit high temperature (- 78.5 ^{o}C — dry ice) (the work in progress).

DISCUSSION AND CONCLUSION:

Such a considerable difference in dsDNA 'survival' may benefit in resisting DNA (microbial) to radiation damage and help in searching freshly deposited from the below (ice crust) extraterrestrial life on icy moons and planets despite their harsh radiation conditions at the surface. It seems there is a chance to pick freshly flushed out microbes/DNA on the Jovian Europa (via tidally driven ice sheet cracks) to verify the extraterrestrial life.

ACKNOWLEDGMENTS:

The reported study was funded by RFBR and DFG according to the research project № 20-55-12006.

THE NECESSITY OF DEVELOPING ML AND AI FOR FUTURE ASTRONOMY

H. Guilani [1], A. Poro [1,2]
[1] *The International Occultation Timing Association Middle East section, Iran, info@iota-me.com;*
[2] *Astronomy Department of the Raderon Lab., Burnaby, BC, Canada*

KEYWORDS:
Machine Learning, Artificial Intelligence, Big Data.

INTRODUCTION:

Novel applications of Machine Learning (ML) and Artificial Intelligence (AI) have contributed to the rapid growth of astronomical data and complexity with the advent of more efficient telescopes and ever-increasing missions into space beyond the capabilities of researchers to process the data and manipulate. ML and AI are adopted for a wide variety of tasks and are becoming increasingly popular with scientists. ML uses various analysis methods under supervised (uses a known training set of input data) and unsupervised (takes only the measured characteristics as input) conditions in order to provide streaming information, such as interpretation, classification, regression, prediction and more, which now have a real impact on all areas of astronomy. Scientists have used ML in various fields of study such as galaxy morphology, exoplanet discovery, transient objects, prediction of solar activities, quasars / AGNs, and more.

One of the most popular supervised ML methods is the Support Vector Machine, which found application in the 2000s and beyond, to detect red variable stars, photometric redshifts, predict solar flares and more. But one of the most dominant ML supervised techniques, the Artificial Neural Network, appeared in the late 1980s and has continued with a wide variety of applications. Thereafter, Deep and Convolutional Neural Networks learning algorithms made a revolution in the computational analysis of image data and classifying images of so many everyday objects (Fluke et al. 2020). Kernel Density Estimation, K-means Clustering and Mixture models are some of unsupervised ML algorithms (Ball et al. 2010).

ML and AI make the classification and regression process, real-time data process, determination of clustering relationships, forecasting of time-based events, and the reconstruction of missing information simpler. As methods become more complex, more training data will be produced and classifications will become more vigorous. ML and AI allow for new objects to be discovered, new predictions to be made, and new scientific insight to be gathered. However main issues of ML in astronomy are on interpreting the results, knowledge transfer and uncertainty treatment. Most algorithms are not developed for astronomical datasets and they subtly assume that all measured aspects are of the same quality, however most of astronomical datasets are noisy. The performance of supervised algorithms strongly depends on signal-to-noise ratio and noise characteristics of the object in the sample and what the algorithm is trained for. while unsupervised algorithms are not trained for a definition of “ground truth” and their results might lead to wrong interpretations patterns and developments in datasets (Baron 2019). Therefore, it is necessary to upgrade existing tools and develop new algorithms for the organization of the immersing flood of data.

REFERENCES:

[1] Fluke, C.J. and Jacobs, C., 2020. Surveying the reach and maturity of machine learning and artificial intelligence in astronomy. Wiley Interdisciplinary Reviews: Data Mining and Knowledge Discovery, V. 10(2), P. e1349.
[2] Ball, N.M. and Brunner, R.J., 2010. Data mining and machine learning in astronomy. International Journal of Modern Physics D, V. 19(07), P. 1049–1106.
[3] Baron, D., 2019. Machine learning in astronomy: A practical overview. arXiv preprint arXiv:1904.07248.

PERCHLORATE TOLERANCE OF SOIL MICROBIAL COMMUNITIES

V.S. Cheptsov [1,2], A.A. Belov [1], O.A. Soloveva [1], E.A. Vorobyova [1], G.A. Osipov [3], N.A. Manucharova [1], M.V. Gorlenko [1]

[1] *Lomonosov Moscow State University, GSP-1, Leninskie Gory 1-12, Moscow, 119991, Russia; cheptcov.vladimir@gmail.com;*

[2] *Space Research Institute of Russian Academy of Sciences, 84/32 Profsoyuznaya Str, Moscow, 117997, Russia;*

[3] *International Analytical Center, Interlab, N.D. Zelinsky Institute of Organic Chemistry of Russian Academy of Sciences, Leninsky Prospekt, 47, Moscow, 119991, Russia*

KEYWORDS:
Astrobiology, Mars, extreme habitats, oxidizers, bacteria.

INTRODUCTION:

Through a number of space missions to Mars, perchlorates were found in the regolith in concentrations of about 0.5–1 %. Due to the high hygroscopicity of perchlorates and the low temperatures of crystallization of their solutions, it is assumed that liquid water can exist in the regolith in the form of brines, which can be a habitat for microorganisms. At the same time, perchlorates in high concentrations can inhibit the growth of microorganisms and lead to their death. To date, it has been established that some prokaryotes are able to survive in environments containing perchlorates in concentrations up to 12 % [1]. Nevertheless, the limits of tolerance of microorganisms to perchlorates have not been determined, and studies of the tolerance of microbial communities to the effects of high concentrations of perchlorates are almost absent [2].

The aim of this work was to study the response of arid soil and ancient permafrost microbial communities to the presence of sodium perchlorate solution *in situ*. Soil and rock samples were moistened with distilled water or with sodium perchlorate solution (the final concentration of perchlorate in the samples was 5 %) and incubated for 10 days at +28 °C. Air-dry samples served as control.

During incubation in the presence of perchlorates, there was an increase in the total number of prokaryotes, determined by epifluorescence microscopy with acridine orange, an increase in the number of metabolically active bacteria and archaea detected by fluorescence *in situ* hybridization, and an increase in the variety of substrates consumed observed by multisubstrate testing method. Using gas chromatography-mass spectrometry of lipids, it was found that in the samples incubated with sodium perchlorate, a high taxonomic diversity of microorganisms was preserved, comparable to the indicators of biodiversity in the control. Thus, it was found that the presence of sodium perchlorate in high concentrations (5 %) does not lead to the death or significant inhibition of microbial communities of soils and rocks *in situ* [2].

REFERENCES:

[1] Heinz J., Krahn T., Schulze-Makuch D. A new record for microbial perchlorate tolerance: fungal growth in NaClO4 brines and its implications for putative life on Mars // Life. 2020. V. 10. No. 5. P. 53.

[2] Cheptsov V., Belov A., Soloveva O., Vorobyova E., Osipov G., Manucharova N., Gorlenko M. Survival and growth of soil microbial communities under influence of sodium perchlorates // International Journal of Astrobiology. 2021. V. 20. No. 1. P. 36–47.

RESISTANCE AND METABOLIC ACTIVITY OF SOIL PROKARYOTIC COMMUNITIES UNDER CONDITIONS OF WATER DEFICIENCY: ASTROBIOLOGICAL IMPLICATIONS

A.A. Belov [1,2], V.S. Cheptsov [1,2,3]
[1] *Soil Science Faculty, Lomonosov Moscow State University, 119234 Moscow, Russia;*
[2] *Network of Researchers on Chemical Evolution of Life (NoR CEL), Leeds 01924, UK;*
[3] *Space Research Institute, Russian Academy of Sciences, 117997 Moscow, Russia*

KEYWORDS:
Desert, permafrost, water activity, CO_2 emission, bacteria culturing.

Extraterrestrial space is characterised by wide range of factors potentially limiting life distribution and functioning such as extremely low and high temperatures, space vacuum, ionizing and ultraviolet irradiation, and water deficiency. Despite the well-known organisms' requirements in water, to date still little is known on microbial communities' reaction on water availability gradient conditions. Arid ecosystems are the most common terrestrial ecosystems, accounting for about 30 % of the land surface, of which 7 % are hyper-arid. The lower limit of water activity (Aw), at which the microorganisms' reproductive activity has been revealed to date, is about 0.605 (microscopic fungi *Xeromyces bisporus* are able to reproduce under these conditions); for soil microbial communities, there is information about metabolic activity at Aw 0.89. However, the activity and taxonomic diversity of soil prokaryotic communities *in situ* under conditions of water activity gradient as well as changes in the structure of bacterial communities with a decrease in the availability of moisture have been little studied.

We assessed the ability of prokaryotic communities to maintain metabolic activity *in situ* in the gradient of Aw from 1 to 0.63. The objects of this study were prokaryotic communities of ancient permafrost (Kolyma basin), sandy sedimentary rocks of the temperate zone (Voronezh region) and arid desert (north of the Sahara Desert). To assess the potential metabolic activity *in situ*, dry glucose and yeast extract (0.1 %) and an antifungal antibiotic (cycloheximide) were added to the studied air-dry samples. Samples in five replicates were incubated in microcosms with constant water vapor pressure and CO_2 emission was estimated after 180 days. Also, the change in the number of cultivated bacteria plated on nutrient media with a gradient of water availability was assessed for samples of the Sahara Desert (similar to those incubated in microcosms) and the soil of the Negev Desert (for which high numbers and biodiversity of extreme tolerant bacteria were previously identified).

It was revealed that *in situ* the community of the surface sedimentary rock of the Sahara Desert was the most tolerant to the low availability of moisture - the respiratory activity was recorded at Aw equal to 0.75 (Figure 1).

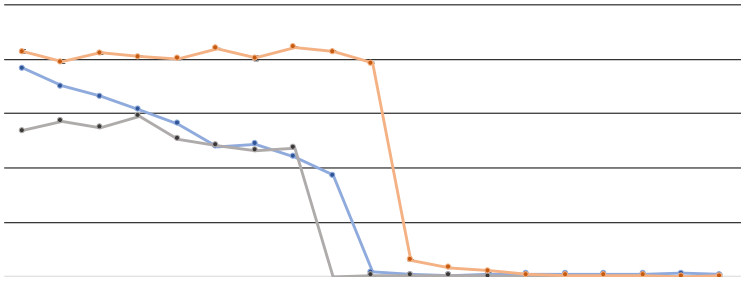


Fig. 1. CO_2 concentration in microcosms after 180 days of incubation under various conditions of moisture availability.

The decrease in CO_2 emission was sharp at Aw 0.8–0.78, which corresponds to the values limiting the metabolic activity of most bacteria. In the range Aw from 1 to 0.8, the respiration rate differed little. The lowest tolerance was shown by the prokaryotic community confined to the non-extreme ecosystem soil (Voronezh region).

During the cultivation of bacteria from desert soil samples, growth was observed down to Aw 0.90 — at this level of moisture availability, bacteria were isolated from a native sample of the surface soil of the Sahara Desert (Figure 2).

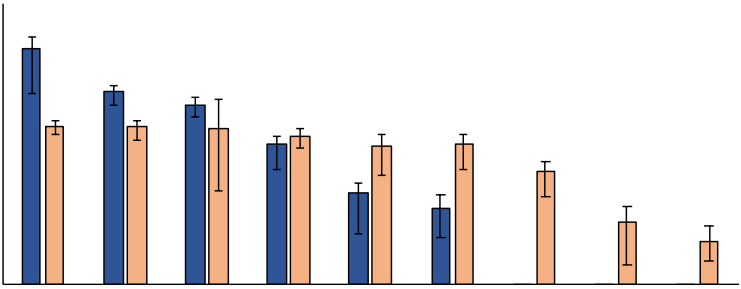


Fig. 2. The number of culturable bacteria on nutrient media with different values of water activity.

Colony formation was not observed at lower water activity values. At present, the identification of the isolated cultures is being carried out.

Estimation of the bacterial communities taxonomic diversity and their functional activity under conditions of moisture deficit can help in refining the criteria for astrobiological search and identifying potentially inhabited space bodies.

ACKNOWLEDGMENTS:
This work was supported by the grant of the President of the Russian Federation No. MK-664.2021.1.4.

SESSION 5. GIANT PLANETS (GP)
ORAL SESSION

JUNO'S EXTENDED MISSION

S. Bolton [1]
[1] *Southwest Research Institute, United States of America*

Juno has transformed our view of Jupiter through major discoveries about its interior structure, origin, and evolution; atmospheric dynamics and composition; magnetic dynamo; and polar magnetosphere. Juno's extended mission began August 1, 2021. During the extended mission (EM), new measurements are enabled by Juno's orbital evolution, addressing discoveries from the prime mission and new objectives that reach beyond the planet itself to the Galilean satellites and Jupiter's enigmatic ring system. The EM science opportunities are intimately associated with the natural evolution of Juno's orbit. Jupiter's northern hemisphere and its satellites and ring systems become high-value targets in a new mission of exploration that includes key high-priority science objectives at Ganymede, Europa, and Io. The close flybys of Ganymede, Europa and Io, Juno's EM measurements will provide important new insights regarding the habitability of Europa, the diversity of these moons and the nature of the ice shell that surrounds them. Juno will literally dissect the Io and Europa tori with a multitude of high-inclination passages throughout the inner magnetosphere. Juno will provide the first detailed exploration of the Jovian ring system, a region draped in mystery and bereft of observations.

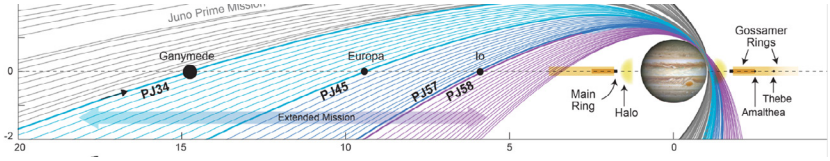


Fig. 1.

TRAPPED GEV HEAVY IONS IN JUPITER'S INNER RADIATION BELTS AT HIGH LATITUDES

H.N. Becker [1], J.W. Alexander [1], J.E.P. Connerney [2,3], M.J. Brennan [1], A. Guillaume [1], V. Adumitroaie [1], M.M. Florence [1], P. Kollmann [4], B.H. Mauk [4], S.J. Bolton [5]

[1] *Jet Propulsion Laboratory, California Institute of Technology, Pasadena, CA, USA, Heidi.N.Becker@jpl.nasa.gov;*
[2] *Space Research Corporation, Annapolis, MD, USA;*
[3] *NASA Goddard Space Flight Center, Greenbelt, MD, USA;*
[4] *Applied Physics Laboratory, The Johns Hopkins University, Laurel, MD, USA;*
[5] *Southwest Research Institute, San Antonio, TX, USA*

KEYWORDS:
Juno, Jupiter, radiation, heavy ion, high energy, ring.

INTRODUCTION:

The unique polar orbit of the Juno spacecraft has enabled unprecedented investigation of Jupiter's radiation belts with full latitudinal and longitudinal coverage. The close periapsis of ~ 1.05 Jovian radii (3 400 km from the 1 bar level) allows Juno to skim the inner edges of Jupiter's relativistic electron belt at high latitudes, encountering a previously unexplored region. A trapped population of > 100 megaelectron volt per nucleon heavy ions has been discovered in this zone (~ 31–46 ° magnetic latitude; radial distances 1.12–1.14 Jovian radii; M — shells 1.5–2.37) with a composition of species as light as helium, but no heavier than sulfur [1]. These are Jupiter's highest energy particles, and are detected as high-signal ionization signatures in images collected by Juno's Radiation Monitoring Investigation [2] using Juno's Stellar Reference Unit (SRU) star camera. The detections occur while the spacecraft is on magnetic field lines that are connected to Jupiter's halo and Amalthea gossamer rings, but not while on field lines magnetically connected to the main ring. Our presentation will discuss this newly revealed feature of Jupiter's extreme radiation environment.

REFERENCES:

[1] Becker H.N., Alexander J.W., Connerney, J.E.P. et al. High latitude zones of GeV heavy ions at the inner edge of Jupiter's relativistic electron belt // Journal of Geophysical Research: Planets. 2021. V. 126, e2020JE006772. https://doi.org/10.1029/2020JE006772.
[2] Becker H.N., Alexander J.W., Adriani A. et al. The Juno Radiation Monitoring (RM) Investigation // Space Sciences Reviews. 2017. V. 213. P. 507–545.

THE NUMBER AND LOCATION OF JUPITER'S CIRCUMPOLAR CYCLONES EXPLAINED BY VORTICITY DYNAMICS

N. Gavriel [1], Y. Kaspi [1]
[1] *Department of Earth and Planetary Sciences, Weizmann Institute of Science, Rehovot Israel*

KEYWORDS:
Jupiter, Vorticity, Polar cyclone, Circumpolar cyclones, Juno, Saturn.

INTRODUCTION:

The Juno mission observed that both poles of Jupiter have polar cyclones that are surrounded by a ring of circumpolar cyclones (CPCs). The north pole holds eight CPCs and the south pole possesses five, with both circumpolar rings positioned along latitude ~ 84 °N/S. Here we explain the location, stability and number of the Jovian CPCs by establishing the primary forces that act on them, which develop because of vorticity gradients in the background of a cyclone. In the meridional direction, the background vorticity varies owing to the planetary sphericity and the presence of the polar cyclone. In the zonal direction, the vorticity varies by the presence of adjacent cyclones in the ring. Our analysis successfully predicts the latitude and number of circumpolar cyclones for both poles, according to the size and spin of the respective polar cyclone. Moreover, the analysis successfully predicts that Jupiter can hold circumpolar cyclones, whereas Saturn currently cannot. The match between the theory and observations implies that vortices in the polar regions of the giant planets are largely governed by barotropic dynamics, and that the movement of other vortices at high latitudes is also driven by interaction with the background vorticity.

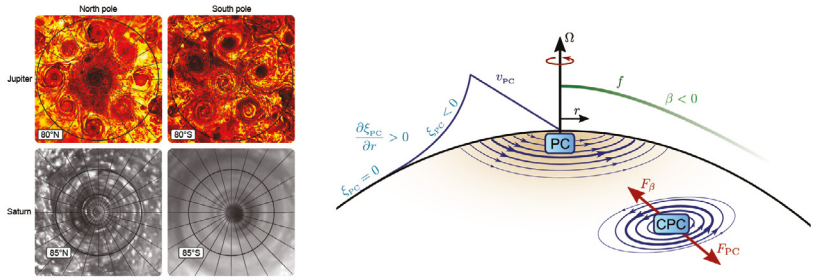


Fig. 1.

INFRARED OBSERVATIONS OF JUPITER'S AURORAE, ATMOSPHERE AND MOONS

A. Mura [1], A. Adriani [1], F. Tosi [1], P. Scarica [1], A. Moirano [1], F. Zambon [1], the JIRAM Team
[1] *INAF-IAPS Rome Italy*

KEYWORDS:
Jupiter, Aurorae, Atmosphere, Moons.

NASA's Juno mission has been observing the Jovian aurorae since 2016 from a polar, highly elliptical orbit [1–3]. From this very favorable position above the poles, Juno obtained unprecedented in-situ measurements of Jupiter magnetosphere, and unique, remote-sensing views of the polar regions, for the investigation of both atmosphere and aurorae. Juno also performed unprecedented observations of the Galilean moons of Jupiter.

Here we present results from the most significant observations performed by Juno's Infrared Imager and Spectrometer JIRAM (Jovian InfraRed Auroral Mapper) [4] during the prime mission, with particular emphasis on the most recent ones, including those acquired during Ganymede flyby.

For the atmosphere, full views of the polar atmospheric structures have been acquired for the first time during orbit 4 [5] by JIRAM. In the north polar region, Juno discovered, in 2017, the presence of an eight-cyclone structure around a single polar cyclone; in the south, a polar cyclone is surrounded by five circumpolar cyclones. The stability of these structures has been monitored for almost 5 years. Recent observations showed that the configurations of the cyclones can temporarily change: in the South the structure moved in a hexagon for a few months, before returning to its original pentagonal shape. In the north, there are significant hints that the octagonal shape may have been lost for a similar period of time. Moreover, the morphology of single cyclones is quite stable over long periods of time, with some noticeable and sudden exceptions. We find that all cyclones show a very slow, westward drift as a rigid ensemble, and, in addition, they oscillate around their rest position with similar timescales. These oscillations seem to propagate from cyclone to cyclone. Here we present the latest observation of these cyclones and we discuss the implications of their secular motion. We also integrate previous studies on the subject with dedicated velocity and vorticity maps, which show an anticyclonic vorticity field surrounding the main cyclones and acting like a stabilizer for the polar structure.

Infrared Aurora comes from electron precipitation, which produces, indirectly, H3+ thermal emission. Images of aurorae in this range are collected by JIRAM at each Juno perijove pass. In the main oval, the field aligned electric currents have very low densities, less than what was previously assumed to explain the intense auroral emissions. Juno observed the high energy (> 100 keV) auroral electron, but also a lower energy component (~ 1 keV), which plays a substantial role. Inside the main oval, persistent upward broadband high-energy (~ 1 MeV) electron are observed. Also, intense auroral emissions are observed in regions where little or no precipitating electron flux is detected, possibly indicating excitation from strong ionospheric electric currents. Juno also revealed a puzzling structure in the electromagnetic interactions between Jupiter and its moons [6], whose signature is the presence of auroral footprints. These are a peculiar series of emission features extending downstream of the leading one and look like a repeating pattern of swirling vortices. These multiple features have a very small scale (~ 100 km), which is not compatible with the simple paradigm of multiple Alfven wave reflections. Other puzzling structures are observed, such as the splitting of Io's footprint tail well downstream of the leading feature, Ganymede's footprints (main and secondary), which appear as a pair of emission features instead of one, and the recent findings of small ring-shaped structures inside the main oval.

Since Juno's orbit insertion at Jupiter until today, the JIRAM spectro-imager observed Io and Ganymede several times and at different distances

and viewing angles, both with its infrared imaging subsystem and with its slit spectrometer sensitive to the 2–5 μm spectral range. In particular, JIRAM observed Ganymede during three dedicated flybys occurred on Dec. 2019, June and July 2021.

Here we discuss the infrared images and spectra that JIRAM was able to acquire during this flyby, with an emphasis on the preliminary spectroscopic results and the distribution of the chemical species detectable in the spectra. We also present recent results from the global campaign of Io observations.

REFERENCES:

[1] Connerney J.E.P. et al., Jupiter's magnetosphere and aurorae observed by the Juno spacecraft during its first polar orbits. Science, DOI: 10.1126/science.aam5928, 2017.
[2] S. Bolton, et al. Jupiter's interior and deep atmosphere: The initial pole-to-pole passes with the Juno spacecraft, Science Vol. 356, Issue 6340, pp. 821-825 (2016).
[3] F. Bagenal et al., Magnetospheric Science Objectives of the Juno Mission, SSR DOI 10.1007 (2017).
[4] Adriani A. et al., JIRAM, the Jovian Infrared Auroral Mapper. Space Sci. Rew., DOI 10.1007/s11214-014-0094-y, 2014.
[5] Adriani, A., et al., Clusters of Cyclones Encircling Jupiter's Poles. Nature, 2018, V. 555, P. 216–219.
[6] Mura et al., Science. 2018 .V. 361, P. 774–777.

THE SEMI-ANALYTICAL FOUR-PLANETARY MOTION THEORY OF THE THIRD ORDER IN MASSES

A.S. Perminov [1], E.D. Kuznetsov [2]
[1] *Ural Federal University, 620000, 51 Lenin Avenue, Ekaterinburg, Russia, perminov12@yandex.ru;*
[2] *Ural Federal University, 620000, 51 Lenin Avenue, Ekaterinburg, Russia, eduard.kuznetsov@urfu.ru*

KEYWORDS:
Semi-analytical motion theory, four-planetary systems, Solar system, giant planets, dynamical evolution, Hori–Deprit method.

INTRODUCTION:
Several dozens of extrasolar planetary systems with three and four planets have been discovered to the present time and require study. Therefore, we constructed the semi-analytical motion theory of the third order in planetary masses to investigate the orbital evolution of non-resonant extrasolar planetary systems with moderate orbital eccentricities and inclinations. Furthermore, the constructed four-planetary motion theory is tested to investigate the orbital evolution of the Solar system's giant planets.

THE HAMILTONIAN SERIES EXPANSION:
The osculating Hamiltonian of the four-planetary problem is written in the Jacobi coordinate system, which is preferable for studying planetary motion. It is a hierarchical coordinate system in which the position of each following body is determined relative to the barycenter of previously included bodies set. Then, it is expanded into the Poisson series in the small parameter and all orbital elements of the second Poincare system. This canonical system has only one angular element – mean longitude, that sufficiently simplifies an angular part of the series expansion. The ratio of the sum of planetary masses to the star mass plays a small parameter.

All orbital elements and mass parameters are conserved symbolically in the series expansion. The series coefficients and degrees of orbital elements are rational numbers with arbitrary precision. It allows eliminating rounding errors in the process of the Hamiltonian construction. The algorithm of the Hamiltonian expansion is described in detail by authors in [1].

THE HORI–DEPRIT METHOD:
The Hamiltonian in averaged orbital elements is constructed by the Hori–Deprit method. The essence of any averaging method is to exclude from the osculating Hamiltonian all short-periodic perturbations, defined by terms with fast variables (mean longitudes in our case). The periods of change of fast variables, contrary to slow variables, are comparable to planets' orbital periods. This approach allows us to sufficiently increase the integration step of the equations of motion in averaged elements.

The equations of motion are constructed as the Poisson brackets of the averaged Hamiltonian with the corresponding orbital elements. The transformation between osculating and averaged orbital elements is performed by the functions for the change of variables. The algorithm of construction of the averaged Hamiltonian and the motion equations in averaged elements is considered by authors in [2, 3].

In the averaged Hamiltonian, the first-order terms in planetary masses save the eccentric and oblique Poincare orbital elements up to the sixth degree, the second-order terms – up to the fourth degree, and the third-order terms to the second degree. In the equation of motion, the first-order terms save the eccentric and oblique orbital elements up to the fifth degree, the second-order terms — up to the third degree, and the third-order terms — up to the first degree.

All analytical manipulations are performed by using a computer algebra system Piranha [4].

THE STUDY OF THE DYNAMICAL EVOLUTION OF SOLAR SYSTEM'S GIANT PLANETS:

An application of the constructed third-order four-planetary motion theory to modeling the orbital evolution of the Solar system's giant planets is considered by authors in [5, 6]. The constructed equations of motion in averaged orbital elements are numerically integrated using different methods over time intervals up to 10 Gyr.

The planetary motion is quasiperiodic, and the short-term perturbations of the orbital elements conserve small values over the whole modeling interval. The comparison of obtained amplitudes and periods of the change of the orbital elements with numerical motion theories shows an excellent agreement with them. For example, the discrepancies between periods of the change of the orbital inclinations obtained by different numerical methods and semi-analytical motion theory do not exceed 0.1 % for all planets. The discrepancies between periods of the change of the orbital eccentricities of Jupiter and Saturn are about 0.01%. For Uranus and Neptune, these discrepancies for the orbital eccentricities are not exceeded 0.3 % and 0.6 % correspondingly.

The constructed motion theory can be used to study the orbital evolution of non-resonant extrasolar planetary systems with moderate values of orbital eccentricities and inclinations.

ACKNOWLEDGMENTS:

This work was supported Ministry of Science and Higher Education of the Russian Federation under the grant 075-15-2020-780 (No. 13.1902.21.0039).

REFERENCES:

[1] Perminov A.S., Kuznetsov E.D. Expansion of the Hamiltonian of the planetary problem into the Poisson series in elements of the second Poincare system // Solar System Research. 2015. V. 49. No. 6. P. 430–441.

[2] Perminov A.S., Kuznetsov E.D. The Hori-Deprit method for averaged motion equations of the planetary problem in elements of the second Poincare system // Solar System Research. 2016. V. 50. No. 6. P. 426–436.

[3] Perminov A.S., Kuznetsov E.D. The implementation of Hori–Deprit method to the construction averaged planetary motion theory by means of computer algebra system Piranha // Mathematics in Computer Science. 2020. V. 14. No. 2. P. 305–316.

[4] F. Biscani. The Piranha computer algebra system.wwwgithub.com/bluescarni/piranha.

[5] Perminov A.S., Kuznetsov E.D. Orbital evolution of the Sun–Jupiter–Saturn–Uranus–Neptune four-planet system on long-time scales // Solar System Research. 2018. V. 52. No. 3. P. 241–259.

[6] Perminov A.S., Kuznetsov E.D. The orbital evolution of the Sun–Jupiter–Saturn–Uranus–Neptune system on long time scales. // Astrophysics and Space Science. 2020. V. 365. P. 144.

MEASUREMENT OF IO'S ATMOSPHERE DURING THE IVO MISSION

P. Wurz [1], A. Vorburger [1], A.S. McEwen [2], K. Mandt [3], A.G. Davis [4], S. Hörst [5], N. Thomas [1]

[1] *Physics Institute, University of Bern, Bern, Switzerland, peter.wurz@space.unibe.ch;*
[2] *Lunar and Planetary Laboratory, Tucson, AZ, USA;*
[3] *Johns Hopkins University-Applied Physics Laboratory, Laurel, MD, USA;*
[4] *Jet Propulsion Laboratory-California Institute of Technology, Pasadena, CA, USA;*
[5] *Johns Hopkins University, Baltimore, MD, USA*

KEYWORDS:
The Io Volcano Observer mission, Io atmosphere, Io atmospheric loss, tidal heating, volcanism, lava lakes.

INTRODUCTION:

The Io Volcano Observer (IVO), a proposed NASA Discovery-class mission (currently in Phase A), with launch in early 2029 and arrival at Jupiter in mid-2033, will perform ten flybys of Io while orbiting Jupiter [1]. IVO's mission motto is to 'follow the heat', reflecting the investigation of tidal heating, which is a fundamental planetary process. Specifically, IVO will determine (I) how and where heat is generated in Io's interior, (II) how heat is transported to the surface, and (III) how Io has evolved with time. The answers to these questions will fill fundamental gaps in the current understanding of the evolution of many worlds across our Solar System and beyond where tidal heating plays a key role, and will give us insight into how early Earth, Moon, and Mars may have worked.

One of the five key science questions IVO will address is the composition of Io's atmosphere and its mass loss via atmospheric escape, the latter of which forms the Io neutral torus. Understanding Io's mass loss today will offer information on the evolution of the chemistry of Io from its initial state and will provide useful clues on how atmospheres on other planetary bodies have evolved over time. IVO plans on measuring Io's atmosphere and mass loss in situ with the Ion and Neutral Mass Spectrometer (INMS), a successor to the instrument that has been built for the JUpiter Icy moons Explorer (JUICE) [2, 3].

THE ION AND NEUTRAL MASS SPECTROMETER (INMS):

INMS is contributed by the University of Bern to the IVO mission. INMS is a time-of-flight (TOF) mass spectrometer that provides high mass resolution, high temporal resolution, and large dynamic range in a small package. The INMS instrument is identical to that flying on JUICE [2], with extensive heritage from earlier designs [10–12]. INMS will measure neutrals and ions in the mass range 1–300 u/e, with a mass resolution (M / ΔM) of 500, a dynamic range of > 10^5, a detection threshold of 100 cm^{-3} for an integration time of 5 s in Io's radiation environment, and a cadence of 0.5–300 s per mass spectrum.

As a TOF mass spectrometer, INMS measures the abundance of ions and neutral species according to their mass [10, 11]. INMS has three operation modes, used to address different measurement objectives. The first two are used for measuring the neutral composition, where neutrals enter the instrument either through the closed source (thermal mode) or the open source (neutral mode). Neutrals are then ionized in the ion source, which produces packets of ions through pulsed extraction with a repetition frequency of 10 kHz. When measuring ions, ambient ions enter through the open source (ion mode) and pass through the ion source, which is not operating because ionization of the target gas is not necessary. Packets of ambient ions or ions produced by electron impact ionization of neutral gas are then guided into the ion optics. All ions in the packet have the same kinetic energy, so their mass-dependent speeds result in different travel times across the TOF section. Separation by species is achieved by measuring the travel times of all ions in the packet and is further enhanced using an ion mirror to lengthen the ion path, which about doubles the mass resolution.

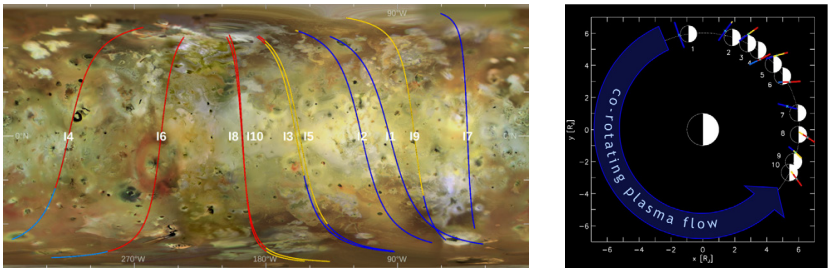


Fig. 1. Left: Projection of the 10 IVO flyby trajectories onto the surface map of Io; Right: Geometry of the 10 IVO trajectories near Io's location in Jupiter's orbit. The colour coding indicates the following conditions: dayside and upstream (red), nightside and upstream (light blue), dayside and downstream (yellow), and nightside and downstream (dark blue).

IO ATMOSPHERE MODELLING:

To fulfil the scientific requirements of IVO ten Io flybys have been foreseen, each with unique flyby conditions, addressing global imaging, selected features of interest on the surface, different illumination conditions, gravity science, tidal forcing, magnetic field and plasma, and atmosphere measurements (see Figure 1). For the formation of the regular atmosphere the solar illumination is important for sublimation of volatiles, as well as the flow of the co-rotating magnetospheric plasma for sputtering of surface material. These external conditions are indicated in Figure 1 by different colours. The co-rotating plasma has a velocity of ~ 74 km/s at Io's orbit, and Io's orbital velocity is 17.35 km/s, thus Io is immersed in a sub-sonic plasma flow, with an upstream and downstream side. Figure 1, right panel, shows the difference scenarios of solar illumination and plasma flow for the 10 planned flybys.

In preparation for the INMS measurements on IVO, we model atmospheric density profiles of species known and expected to be present on Io's surface from both measurements and previous modelling efforts. Based on the IVO mission design, we investigate three different measurement scenarios for the atmosphere we expect to encounter at Io during the flybys: (I) a purely thermal atmosphere from sublimation, (II) the 'hot' atmosphere evaporated from lava fields, and (III) the plume gases resulting from volcanic activity.

SUBLIMATED ATMOSPHERE:

For the sublimated atmosphere (dayside at 130 K, IVO flybys 3–10) we consider SO_2 [4], and the derived species SO, O_2, O_3, and H_2S and H_2O, which might be part of the SO_2 frost on the surface [5]. In addition, there is sputtering from the surface by the co-rotating plasma on Io's upstream side (flybys 4, 6, 8, 10). Sputtering will contribute Na, Cl, and K (from NaCl and KCl) to the atmosphere, with Na already being observed in Io's atmosphere [6].

HOT ATMOSPHERE:

For the species of the hot atmosphere, we consider the species contributed by the lava lakes. IVO flybys 1 and 2 are over extensive lava lakes on Io's night side, thus little interference from the regular atmosphere is expected, IVO flyby 4 is over Loki Patera on the day side where multi-instrument imaging will be available. For lava composition we use a high temperature, low-viscosity silicate lava [7], similar to Hawaiian basalt [8]. Typically, only a small fraction of the lava surface is at ≥ 1350 K, and contributing to the atmosphere. We use the thermodynamic data to calculate evaporation from the hottest surface fractions of the lava lakes. The contributions from the evaporation of a lava lake are KCl, KO, K_2O, FeO, SiO_2, SiO, AlO, MgO, CaO, NaO, Na_2O, and their fragment atoms K, Cl, Fe, Si, Mg, Ca, Al, Na, and O.

PLUME GASES:

We assume that the dominant species in the plume at the altitudes sampled by the spacecraft are volatiles (IVO flyby 6), which were initially dissolved in magma and released when the lava erupts from the volcano. The composition of these volatiles is based on earlier modelling of the volatiles in Pele's plume [9], which are SO_2, S_2, NaCl, KCl, S_2O, SO_3, O_2, and the respective fragments.

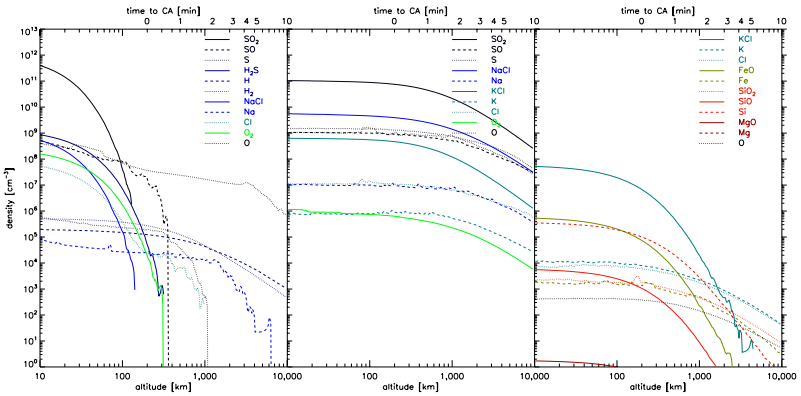


Fig. 2. Density profiles for the sublimated atmosphere (left panel), for the atmospheric contribution from evaporation of lava fields (middle panel), and for the atmospheric contribution from volcanic plumes (right panel).

We calculate atmospheric density profiles, shown in Figure 2, for all known and expected species for these three measurement scenarios, considering the actual IVO observation conditions. From the density profiles we calculate the expected mass spectra to be recorded by INMS during the IVO flybys for the three atmospheric scenarios. In addition to the release of these species into the atmosphere, there are the usual processes of deposition on the surface, re-sublimation, aggregation at cold spots (like the polar areas), chemical processes on the surface, radiolysis, and atmospheric loss via escape or ionization. Io's mass loss is very important for Jupiter's magnetosphere since Io releases about 1100 kg/s of SO and almost 100 kg/s SO_2, forming Io's neutral clouds and ion torus, which serves as a major source of the particle population in Jupiter's magnetosphere.

ACKNOWLEDGMENTS:
This work was supported by the Swiss National Science Foundation.

REFERENCES:

[1] A.S. McEwen, L.P. Keszthelyi, K.E. Mandt, and the IVO Team, 52nd Lunar and Planetary Science Conference, 2021, LPI Contrib. No. 2548. P. 1352.
[2] M. Föhn, et al., IEEE Aerospace proceedings. 2021. In press.
[3] D. Lasi, et al., IEEE Aerospace Proceedings. 2020. 20 pages, DOI: 10.1109/AERO47225.2020. 9172784.
[4] E. Lellouch et al., in Io After Galileo, eds. R. Lopes and J. Spencer, Springer, 2007.
[5] Salama F. et al., Icarus. 1994. V. 107, P. 413.
[6] Burger M.H. et al., Astrophys. J., 2001. V. 563. P. 1063.
[7] A.G. Davis, L.P. Keszthelyi, A.S. McEwen, Geophys. Res. Lett.. 2011. V. 38, P. L21308.
[8] T.L. Wright Geological Professional Paper. 1971. P. 735.
[9] J.I. Moses, M.Y. Zolotov, B. Fegley, Icarus. 2002. V. 76. P. 156. V. 107. P. 156.
[10] S. Scherer et al., Int. Jou. Mass Spectr., V. 73,P. 251 (2006).
[11] Wurz, P. et al., Planet. Sp. Science. 2012. V. 74, P. 264.
[12] Abplanalp, D. et al., Adv. Space Res. 2009. V. 44, P. 870.

SESSION 5. GIANT PLANETS (GP) POSTER SESSION

JUPITER AND LUNAR SEISMOGRAMS

Ş. Tanaka [1], O.B. Khavroshkin [2], V.V. Tsyplakov [2]
[1] *ISAS, Japan;*
[2] *Schmidt Institute of Physics of the Earth of RAS*

Jupiter is so interesting that often the application of many research methods are implemented in parallel in time, and the results are used in several models. Such an extraordinary planet is always capable of manifestations when completely new search methods are effective. Thus, the presented studies of lunar seismicity, as before in the case of gas and dust flows or determining the internal structure of the Moon, have successfully demonstrated the still unaccounted for the role of Jupiter. The fluxes from Jupiter are clearly distinguished in amplitude and permanent existence on lunar seismograms and carry information of interest about the atmosphere of the planet's magnetosphere, as well as about interactions with some satellites. The discovered interaction can also be used in the study of exoplanets, since many of them are similar to or larger than Jupiter. On Earth, research is also underway on cosmic dust, which is collected mainly in the mountains. Until now, a specific source of origin has rarely been identified. Now, within the framework of new information about Jupiter, the problem is changing. In the future, will be use of high-altitude balloons of space technology.

THE FIRST EXPERIENCE OF STUDYING LATITUDINAL VARIATIONS OF A WEAK ABSORPTION BAND NH_3 550nm ON JUPITER

V.D. Vdovichenko[1], A.M. Karimov, G.A. Kirienko, P.G. Lysenko, V.G. Teifel, V.A. Filippov, G.A. Kharitonova, A.P. Khozhenets

[1] *Laboratory of Lunar and Planetary Physics, Fesenkov Astrophysical Institute, Almaty, Kazakhstan, vdv1942@mail.ru*

KEYWORDS:
Jupiter, atmosphere, spectrophotometry, ammonia, molecular absorption bands.

Observations have been carried out and the first results have been obtained for variations in the equivalent widths and equivalent paths along the central meridian of Jupiter for the absorption band of ammonia NH_3 at 550 nm. These variations are compared with those of the 645 nm NH_3 band. The absorption maximum in both bands is observed in the equatorial zone. In the center of the disk, their equivalent widths are: W (550 nm) = 2.58 ± 0.29 Å and W (645 nm) = 6.77 ± 0.25 Å. The NH_3 550 nm band shows a sharper decrease in absorption in the direction of high latitudes in contrast to the NH_3 band at 645 nm.

INTRODUCTION:
Over the past 17 years, we have carried out systematic annual homogeneous studies of the behavior of the absorption bands of methane and ammonia on Jupiter in the range 0.5–0.95 μm. In addition to the ongoing systematic observations of the absorption bands of methane at 619, 702 and 725 nm and ammonia at 645 and 787 nm [1], we undertook the first experiments to study one more, and the weakest, absorption band of ammonia NH_3 at 550 nm. This article presents the preliminary results of the study of this band based on observations made specifically for this purpose in 2019.

OBSERVATIONS:
The observations were made during the 2019 season of Jupiter's visibility. Along with the standard long-term program of spectral observations of Jupiter with the ST-7XE camera, a number of spectrograms of the central meridian of Jupiter with the SBIG STT-3200ME camera were obtained on the RC – 600 telescope. The CCD of this camera has a 2184 × 1472 pixel format. The size of each photosensitive element is 6.8x6.8 microns, the spectral dispersion is 3.24A / pixel. The spatial resolution scale of the spectrogram was 5.4 pxl / arcsec. The Ganymede spectrum was recorded as a comparison spectrum to exclude Fraunhofer lines and telluric bands.

RESULTS:
Both the 550 and 645 nm NH3 bands have relatively low intensities, especially the 550 nm NH3 band. Its equivalent width on average is only about 2.8 Å and the depth at the absorption maximum does not exceed 0.05. The equivalent width of the NH3 645 nm band reaches 6.8 Å and the central depth does not exceed 0.10.

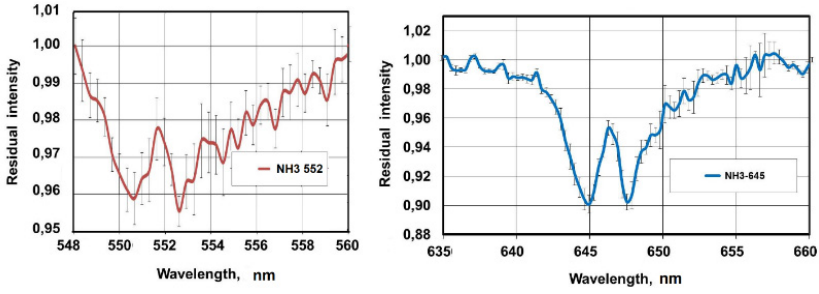


Fig. 1. Profiles of absorption bands NH3 550 and 645 nm in the center of the Jupiter disk.

Using the technique and data of the growth curves in [2], we calculated the equivalent widths W and the equivalent paths CE of absorption for both bands in km-am. For the center of the disk, these values were respectively: W (550) = 2.58 CE (550) = 0.108 km-am W (645) = 6.77 CE (645) = 0.027 km-am. As you can see, the ratio of CE (550) to CE (645) is 4 in the center of the disk.

Figure 2 shows the latitudinal variations of the equivalent widths of both absorption bands normalized to the center of the disk and the ratio of their equivalent paths.

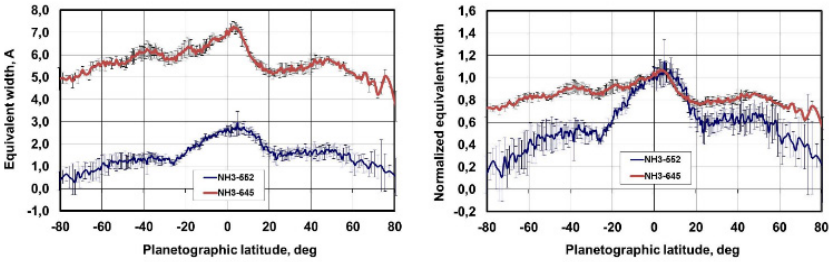


Fig. 2. Latitudinal variations of equivalent widths of absorption bands (left) and their values normalized to the center of the disk (right).

Both absorption bands have a maximum in the region of the equatorial belt and a well-pronounced minimum in the transition zone between the equator and the northern equatorial belt at latitudes of 20–25 degrees. At the same time, in the 550 nm band, this minimum is narrower and slightly shifted to the north by about 5 degrees. Both bands have a pronounced maximum in the region of latitudes 40–60 degrees and a weakly pronounced maximum in the region — (40–60 degrees). Both bands show a decrease in absorption towards high latitudes (60–85 degrees).

The differences lie in the fact that for the 645 nm band, the differences in equivalent widths across the disk range within 15–20 %, while for the 550 nm ammonia band, they reach 40–45%. In the 645 nm band in the northern hemisphere, the integral absorption is less than in the southern one by about 10 %, and in the 550 nm band it is vice versa.

Differences in latitudinal changes in ammonia absorption with an accuracy of a certain factor can be revealed by calculating the ratio of equivalent paths CE (550) / CE (645) over latitudes.

DISCUSSION:

The absorption band NH_3 550 nm in the spectrum of Jupiter has been observed repeatedly (for example 3-7). But the measurements of this band referred only to individual points on the disk of Jupiter. The technique of our observations is that the spectrograph slit intersects the entire image of the planet along the central meridian or along individual latitudinal zones. This makes it possible, even from one spectrogram, to obtain a picture of variations in the intensity of all absorption bands in latitude along the central meridian. A detailed study of the behavior of weak molecular absorption bands in the future is an important way of optical sounding of the clouds and troposphere of Jupiter. The comparative data described above for two absorption bands of ammonia, as well as the results of previous studies, show that these bands are formed at significantly different effective optical depths. We would like to draw your attention to the need for further research of this kind. In combination with observations of thermal radiation of Jupiter in the infrared and microwave regions of the spectrum, they can be very useful in studying the structure of the Jupiterian troposphere.

ACKNOWLEDGMENTS:

The work was carried out within the framework of grant funding MES RK 0073/GF4 AP05131266 and also as a basis for further study of the atmosphere of Jupiter on the behavior of weak molecular absorption bands.

REFERENCES:

[1] Tejfel' V.G., Vdovichenko V.D., Lysenko P.G., Karimov A.M., Kirienko G.A., Bondarenko N.N., Filippov V.A.,Kharitonova G.A., Khozhenets A.P.. 2018. Ammonia in Jupiter' s atmosphere: spatial and temporal variations of the NH3 absorption ands at 645 and 787 nm, Solar System Research, V. 52. P. 480–-494.

[2] Lutz B.L., and Owen T.. 1980. The visible bands of Ammonia: Band strengths, curves of growth, and the spatial distribution of Ammonia on Jupiter, Astrophysic. Journal, 235:285–293, DOI: 10.1086/157632.

[3] Woodman J.H., Trafton L., Owen T. 1977. The abundances of ammonia in the atmospheres of Jupiter, Saturn and Titan. Icarus, V. 32(3). P. 314–320. doi: 10.1016/0019-1035(77)90004-5 (in Eng.).

[4] Woodman J.H., Cochran W.D., Slavsky D.B.. 1979. Spatially resolved reflectivities of Jupiter during the 1976 opposition. Icarus. V. 37(1). P. 73–83. doi:10.1016/0019-1035(79)90116-7.

[5] Moreno F., Molina A. and Lara L.M. Charge-Coupled Device Spectral Images of Spatially Resolved Regions of Jupiteirn the 6190-and 8900-A Methanae nd6 450-A Ammonia Bands During the 1989 Opposition.(1991) Journal of Geophysical Research, V. 96, No. A8, P. 14,119-14,127, August 1, 1991 **.**NB-Moreno1991.pdf.

[6] Moreno F. and Molina A. 1989. Spatially resolved spectroscopic observations of the Jupiter during the 1987 opposition. Earth, Moon, and Planets V. 46, P. 207–219 1989EM+P___46__207M.pdf.

[7] Moreno F. and Molina A. (1991) Jupiter's atmospheric parameters derived from cpectroscopic observations in the red region during the 1988 opposition. Astron. Astrophys, V. 241, P. 243-250. 1991A+A___241__243M.pdf.

ESTIMATES OF THE POSSIBLE DEHYDRATION OF HYDRATED SILICATES IN THE CORES OF LARGE ICY SATELLITES

Kronrod E.V. [1], **Kronrod V.A.** [1], **Kuskov O.L.** [1]
[1] *Vernadsky Institute of Geochemistry and Analytical Chemistry RAS, Moscow, Russia, e.kronrod@gmail.com*

KEYWORDS:
Primordial rocky core, temperature, convection, chondrites, hydrated silicates, dehydration.

INTRODUCTION:
On the basis of the geophysical and geochemical data (obtained during space missions “Galileo”, “Cassini-Huygens”), models of the internal structure of the icy satellites of the giant planets were constructed. The models include the water-ice shell, the iron-rocky core (± internal Fe – FeS core) [1] and located between them the mantle, represented either by an undifferentiated rock-ice mixture [2–4], or by a layer of hydrated silicates [5, 6]. A special place in the study of icy giant satellites is occupied by the problem of studying the central region (core). Models of the internal structure of large icy satellites impose restrictions on the size and composition of satellite cores. On the other hand, temperature distributions in the cores of satellites largely determine the degree of hydration of their silicate component. This paper presents the results of calculations of nonstationary temperature regimes in the cores of icy satellites depending on the composition and size of the core, taking into account convective heat transfer and possible dehydration.

MODEL DESCRIPTION:
The thermal evolution of the core is determined by its size, as well as physical properties — density, thermal conductivity, heat capacity, and radiogenic heat release. Two geochemical models of the composition of the core and their combinations that are most different in physical properties were considered. In the first model, silicate (Sil), the composition of the iron-rocky material corresponds to the bulk composition of the matter of ordinary (L / LL) chondrites [1, 4]. The second type of models (hydrated silicate, HSil) is used in models of the internal structure of fully differentiated satellites; the iron-rocky core can be composed of a hydrated mineral material of low density, close in composition to the substance of carbonaceous CI chondrites [5].

Physical properties of iron-stone matter of the core (density (ρ), thermal conductivity coefficient (k), heat capacity (C_p), heat release per unit mass of the core at time t - $Q(t)$, volume expansion coefficient (α), thermal diffusivity (k)) calculated for a homogeneous mixture of silicates and hydrated silicates. To calculate the pressure, the satellite radius is to be calculated: $R_{sat} = ((\rho_{core} - \rho_{wis}) / (\rho_{mid} - \rho_{wis}))^{1/3} R_{core}$, where R_{core} is the core radius, ρ_{core} is the core density, ρ_{wis} is the average density of the water-ice shell, and the core density is $\rho_{core} = \rho_{Sil} \cdot C_{Sil} + \rho_{HSil} \cdot (1 - C_{Sil})$, C_{Sil} is the concentration of silicates, ρ_{Sil}, ρ_{HSil} is the density of silicates and hydrated silicates, respectively, ρ_{mid} is the average density of the satellite. The radius of the core R_{core} was set in the range from 500 to 2100 km.

The heating of the primordial core formed over a time of about 500 million years [5, 7] (the time during which the ice melting point (≈ 500 K) is reached) occurs due to the decay energy of long-lived radioactive isotopes. When the primordial core is heated to a temperature of $T_{ph} = 873$ K [8], the reaction of dehydration of hydrated silicates occurs. The dehydration reaction is endothermic with energy consumption: $Q_{ph} = 4.17 \cdot 10^5$ Jkg^{-1} [8]. As a first approximation, it is believed that the water released as a result of dehydration processes does not significantly affect the physical properties of the rock and its chemical composition. The change in volume due to a decrease in density during dehydration is also not taken into account. The vis-

cosity of silicates is determined, depending on temperature and pressure, similarly to [9], the viscosity of hydrated silicates is assumed to be constant ($4 \cdot 10^{19}$ Pa·s) in the whole range of temperatures and pressures [9]. The viscosity of the silicate + hydrated silicates mixture (η_{HSil}) was calculated using the isostress model for the composite [10].

Two mechanisms of heat transfer in the core were considered: conductive and convective. The transition to convection is estimated by the Rayleigh number [7]. Heat transfer in the convection zone is modeled by multiplying the thermal conductivity coefficient by a dimensionless coefficient (Nusselt number – Nu): $K_{ef} = Nu \cdot k_{cond}$, $Nu = 1.04\,(Ra_0 / Ra_{crit})^{1/3}$, $Ra_{crit} \approx 1000$, where Ra_{crit} is the critical Rayleigh number, k_{cond} is the coefficient thermal conductivity.

RESULTS:

As a result of calculations, it was found that the initial concentration of hydrated silicates (C_{HSil}) and the radius of the core (R_{core}) significantly affect the thermal evolution and dehydration of the core. The higher the content of hydrated silicates in the core, the faster convection occurs. For concentrations $C_{HSi} \geq 0.85$, weak convection ($Nu > 1$) arises very quickly, the convective zone occupies almost the entire region of the core, with the exception of the boundary layer. A phase transition (dehydration) occurs when the temperature reaches 873 K at times from ≈1 billion years (at a low initial content of hydrated silicates – 10–15 %) to ≈ 1.5 billion years (at a high content of hydrated silicates) and continues up to ≈ 2.5 billion years. Fig. 1 shows the size of the region that was subjected to phase transition processes (dehydration radius). Fig. 2 shows the change in the bulk concentration of hydrated silicates in the interval of 500 million years – 4.5 billion years from CAI. Fig. 1 and 2 show that dehydration is possible only at the initial $C_{Sil} \geq 0.85$. At $R_{core} < 600$ km, dehydration is not possible for any initial C_{Sil}.

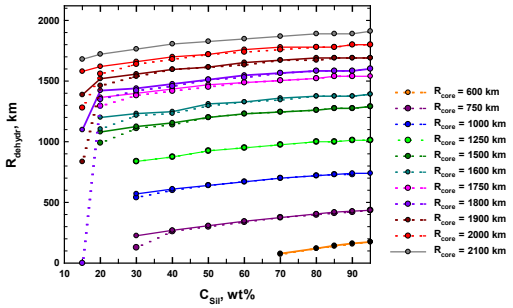


Fig. 1. The radius at which dehydration of hydrated silicates occurs, depending on the radius of the core and the initial concentration of silicates in the core. Solid lines are the radius at which dehydration was complete (final $C_{Sil} = 100$ wt%). Dotted lines - partial dehydration (final $C_{Sil} < 100$ wt %).

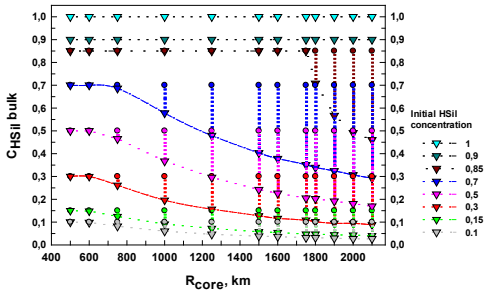


Fig. 2. The bulk concentration of hydrated silicates in the cores of satellites ($C_{HSil\ bulk}$) depending on the radii of the cores (R_{core}). Circles - t = 500 million years from CAI: triangles - t = 4.5 billion years from CAI. The color indicates the initial concentration of hydrated silicates in the core.

CONCLUSION:

According to the calculation results, it can be concluded that in the presence of convection, the initial concentration of hydrated silicates in the core mainly determines the thermal evolution of the core. At $C_{HSil} \geq 0.9$, dehydration processes do not occur for all core sizes.

ACKNOWLEDGMENTS:

The work was performed as part of the state assignment of Vernadsky Institute of Geochemistry and Analytical Chemistry № 0137-2019-0004.

REFERENCES:

[1] Kuskov O.L., Kronrod V.A. Core sizes and internal structure of Earth's and Jupiter's satellites // Icarus. 2001. V. 151. P. 204–227.

[2] Dunaeva A.N., Kronrod V.A., Kuskov O.L. Physico-chemical models of the internal structure of partially differentiated Titan // Geochemistry International. 2016. V. 54. No. 1. P. 27–47.

[3] Kronrod V.A., Dunaeva A.N., Gudkova T.V., Kuskov O.L. Matching of Models of the Internal Structure and Thermal Regime of Partially Differentiated Titan with Gravity Field // Solar System Research. 2020. V. 54, No. 5, P. 405–419.

[4] Kuskov O.L., Kronrod V.A. Internal structure of Europa and Callisto // Icarus. 2005. V. 177. P. 550–569.

[5] Castillo-Rogez J.C., Lunine J.I. Evolution of Titan's rocky core constrained by Cassini observations // Geophys. Res. Lett. 2010. V. 37. P. L20205.

[6] Dunaeva A.N., Kronrod V.A., Kuskov O.L. Physico-chemical models of the internal structure of partially differentiated Titan. // Geochemistry International. 2016. V. 54. No 1. P. 27–47.

[7] Grasset O., Sotin C., Deschamps F. On the internal structure and dynamics of Titan // Planet. Space Sci. 2000. V. 48. P. 617-636. doi 10.1016/S0032-0633(00)00039-8.

[8] Wakita S., Sekiya M. Thermal evolution of icy planetesimals in the solar nebula // Earth Planets Space. 2011. V. 63. P. 1193–1206.

[9] Kimura J., Nakagawa T., Kurita K. Size and compositional constraints of Ganymede's metallic core for driving an active dynamo // Icarus. 2009. V. 202. P. 216–224.

[10] Ji S. and Zhao P. 1993. Flow laws of multiphase rocks calculated from experimental data on the constituent phases // Earth and Planetary Science Letters. V. 117. P. 181–187.

SOME DATA CONFIRMING THE HYPOTHESES OF THE FORMATION OF SILICATE AND IRON-HYDROCARBON-CONTAINING SHELLS OF GIANT PLANETS

A.L. Kharitonov [1]
[1] *Pushkov Institute of Terrestrial Magnetism, Ionosphere and Radio Wave Propagation of the Russian Academy of Science, 108840, Moscow,Troitsk, Kaluzhskoe Highway, 4, IZMIRAN Russia, ahariton@izmiran.ru*

KEYWORDS:
Giant planets, pressure of gas-fluid shells of planets, stratification of the bowels of planets, silicate and iron-hydrocarbon-containing shells of planets

INTRODUCTION:
According to the hypothesis of T. Gold and A. A. Marakushev [1], the giant planets of the proto-Solar system were formed together with the solar mass from icy planetary mirrors as a result of condensation and solidification of the substrate of the primary gas cloud that arose as a result of the explosion of a giant star, the proto-Sun. In modern conditions, the substrate of the primary gas cloud has been preserved only on the periphery of the Solar System (the Oort cloud and the Koiper belt). The high concentration of hydrogen in the core of many planets of the Solar System is a direct consequence of the stratification of the bowels of the giant proto-planets of the Solar system into silicate mantle shells and iron-hydrocarbon- containing core, occurring under conditions of enormous fluid pressure. In the modern Solar system, such conditions can be achieved only in the depths of the giant planets Saturn and Jupiter. We assume that in the deep layers of these planets, the physical and chemical processes of delamination of matter into silicate shells and iron-hydrocarbon-containing nuclei are currently continuing, which occur under the influence of the enormous pressure of their external fluid (mainly hydrogen) shells. As a result of this stratification of the matter of the giant planets, the magnetic fields of these planets were formed, similar in nature to the magnetic field of the Earth. This is confirmed by the presence in the bowels of many planets of the Solar system of radioactive chemical elements inherent only in giant stars [2]. Judging by the data of this hypothesis, the planets of the Earth group (Mercury, Venus, Earth, Mars) at the early stages of their development were similar to the currently existing giant planets (Saturn, Jupiter, Uranus, Neptune).

REFERENCES:
[1] Marakushev A.A. Origin and evolution of the Earth and other planets of the Solar system. Moscow, Nauka, 1992. P. 207.
[2] Tayler R.J. The origin of chemical elements. Moscow, Mir, 1975. P. 232.

THE CONTENT OF HYDRATED SILICATES IN THE PRIMORDIAL ROCKY CORE OF GANYMEDE

V.A. Kronrod [1], E.V. Kronrod [1], O.L. Kuskov [1]
[1] *Vernadsky Institute of Geochemistry and Analytical Chemistry RAS, Moscow, Russia, va_kronrod@mail.ru*

KEYWORDS:
Ganymede, primordial rocky core, core, composition, temperature, convection, chondrites, hydrated silicates.

INTRODUCTION:
As a result of research missions to Jupiter and Saturn (Galileo, Cassini-Huygens), fundamentally new information about the icy giant satellites Ganymede, Callisto and Titan was obtained, which made it possible to build models of the internal structure of the satellites [1–6]. A comparison of probable element ratios and geochemical parameters of the Galilean satellites with the corresponding characteristics of chondrites led to the conclusion that the bulk composition of Io and the compositions of the rock-iron cores of Io, Europa and Ganymede are similar to the compositions of L / LL chondrites but very different from the geochemical characteristics of H ordinary chondrites and carbonaceous chondrites [2–4]. The small value of the moment of inertia factor and the strong intrinsic magnetic field observed for Ganymede are consistent with a strongly differentiated interior with a conductive core [1–4]. The dimensions of the iron-stone core of Ganymede are estimated at 1734 km, the inner Fe — 10 % S core – 695 km [4]. Temperature distributions in the iron-rocky core of Ganymede determine the degree of dehydration of hydrated silicates, the possibility of the formation of a metal core. Thus, the existence of a core in Ganymede does not allow us to speak unambiguously about the presence or absence of hydrated silicates in the primordial rocky core. In this work, the thermal evolution of the iron-rocky primordial core of Ganymede is considered and probable restrictions on its initial composition were estimated.

MODEL DESCRIPTION:
The process of heating the primordial core by the energy of radioactive decay to a temperature exceeding the melting point of ice (~ 500 K), redistribution of ice, water and stone with the formation of a homogeneous rocky core takes about 500 million years [7, 8]. Subsequently, the thermal evolution of the core arises due to radioactive energy sources. Two geochemical models of the composition of the primordial core and their combinations that are maximally different in physical properties were considered: silicate (with the concentration of C_{Sil}) is established by analogy with the material of the bulk composition of the substance of ordinary (L / LL) chondrites [2–4] and hydrated silicates, with a concentration of $C_{HSil} = 1 - C_{Sil}$. The hydrated silicates model assumes a low-density hydrated mineral material such as serpentine (antigorite), which is close in composition to that of carbonaceous CI chondrites. The hydrated silicates model is popular in the construction of Titan models [5]. It is assumed that at a temperature of $T_{ph} = 873$ K [9], the reaction of dehydration of hydrated silicates occurs. Anhydrous olivine and water are formed from serpentine and talc. The dehydration reaction is endothermic, the energy consumption is: $Q_{ph} = 4.17 \cdot 10^5$ Jkg^{-1} [9]. As a first approximation, we assume that the water released as a result of dehydration processes does not significantly affect the physical properties of the rock and its chemical composition. The change in the volume of the composite due to the increase in density during dehydration was also not taken into account.

We performed numerical simulations for the internal thermal evolution using a spherically symmetric model for the convective and conductive heat transfer with radial dependence of viscosity, heat source distribution and taking into account the energy of dehydration. The heat transport in the convec-

tion zone is modeled simply by multiplying the coefficient of the heat conduction in the convective zone: $K = Nu \cdot k_{conduct}$, [10]. Here Nu is dimensionless Nusselt number; $Nu = 1.04\,(Ra / Ra_{crit})^{1/3}$, $Ra_{crit} \approx 1000$. The transition to convection is estimated by the Rayleigh number (Ra) [8, 10]. The viscosity of silicates is determined, depending on temperature and pressure, similarly to [11], the viscosity of hydrated silicates is assumed to be constant $4 \cdot 10^{19}$ Pa s in the entire range of temperatures and pressures [12]. The viscosity of the silicates + hydrated silicates composite is calculated using the isostress model for the composite [13]. The thickness of the thermal boundary layer is determined from the conditions [14].

RESULTS AND DISCUSSION:

The temperature distributions in the primordial core of Ganymede were calculated. The dimensions of the primordial core and the thickness of the water envelope were set from probable estimates [2, 4], then the pressure distribution in the satellite was calculated. The initial composition of the primordial core (C_{Sil}) varied from 0 to 1. The physical properties of the composite (density, heat capacity, thermal conductivity, viscosity) were determined at each time step. To calculate the Rayleigh number, the temperature was averaged over the volume in each calculation zone.

Calculations have shown that the initial concentration of hydrated silicates (C_{HSil}) and the radius of the iron-rocky core (R_{core}) determine the nature of thermal evolution and the possibility of the formation of an inner metallic core. The higher the content of hydrated silicates in the core, the faster convection occurs. For the concentrations of hydrated silicates $C_{HSil} \geq 0.85$, weak convection (Nu > 1) occurs very quickly, the convective zone occupies almost the entire region of the core, with the exception of the boundary layer. At core sizes $R_{core} > 700$ km and $C_{HSil} < 0.85$, the temperature at the center of the core reaches 873 K, and the process of phase transition of hydrated silicates to silicates begins.

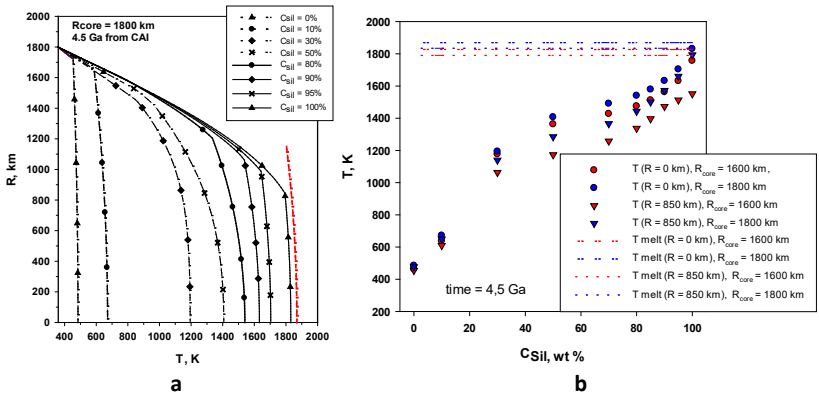


Fig. 1. Temperature distribution in the core of Ganymede for time = 4.5 Ga from CAI depending on the initial concentration of silicates (C_{Sil}) in the core. The dotted lines show the melting point of silicates according to [15] (expression (3)) at T_0 = 1650 K. (**a**) - radial temperature distribution; (**b**) - temperature in the center (circles) and at a radius of R = 850 km (triangles).

The possibility of the formation of a metal core is estimated from the highest temperature in the central region. It is believed that when the melting point of silicates is reached, the metal core can be formed as a result of the migration of the molten substance of the future core (Fe – FeS) to the center [15]. Otherwise, the metal core is not formed and the iron-rocky core remains nondifferentiated. The melting point of silicates is approximately determined by expression (3) from [15]. The melting point of silicates at zero pressure (T_0) was taken as 1650 K as the average estimated value for silicates. The existence of a magnetic field predetermines the presence of a conductive liquid layer in the core. Therefore, an additional constraint on the temperature in the central region is the condition for the existence of a liquid

melt layer in the Fe–FeS system. In accordance with the phase diagram given in [11], for probable sulfur concentrations of ≈ 10 % S in the Fe – FeS core [4], the temperature of the existence of a liquid layer in the central region should approximately correspond to the constraints T > 1800 K. The temperature distributions in Fig. 1 show that the formation of the Fe – FeS core in Ganymede is possible, but only at the initial concentration of hydrated silicates in the primordial core $C_{HSil} \approx < 5$ wt% (Fig. 1a). In this case, the temperature in the central region of the core is sufficient for the formation of a liquid conducting layer (Fig. 1b).

ACKNOWLEDGMENTS:
The work was performed as part of the state assignment of Vernadsky Institute of Geochemistry and Analytical Chemistry № 0137-2019-0004.

REFERENCES:

[1] Anderson J.D. et al. Gravitational constraints on the internal structure of Ganymede // Nature. 1996. V. 384. P. 541–543.
[2] Kuskov O.L., Kronrod V.A. Core sizes and internal structure of Earth's and Jupiter's satellites // Icarus. 2001. V. 151. P. 204–227.
[3] Kuskov O.L., Kronrod V.A. Internal structure of Europa and Callisto. Icarus. 2005. V. 177. P. 550–569.
[4] Kronrod V.A., Kuskov O.L. Chemical differentiation of the Galilean satellites of Jupiter: 4. Isochemical models for the compositions of Io, Europa, and Ganymede // Geochem. Int. 2006. V. 44. P. 529-546. doi 10.1134/S0016702906060012.
[5] Dunaeva A.N., Kronrod V.A., Kuskov O.L. Physico-chemical models of the internal structure of partially differentiated Titan // Geochemistry International. 2016. V. 54. No. 1. P. 27–47.
[6] Kronrod V. A., Dunaeva A.N., Gudkova T.V., Kuskov O.L. Matching of Models of the Internal Structure and Thermal Regime of Partially Differentiated Titan with Gravity Field // Solar System Research. 2020. V. 54, No. 5, P. 405–419.
[7] Castillo-Rogez J.C., Lunine J.I. Evolution of Titan's rocky core constrained by Cassini observations // Geophys. Res. Lett. 2010. V. 37. L20205.
[8] Grasset O., Sotin C., Deschamps F. On the internal structure and dynamics of Titan // Planet. Space Sci. 2000. V. 48. P. 617–636. doi 10.1016/S0032-0633(00)00039-8.
[9] Wakita S., Sekiya M. Thermal evolution of icy planetesimals in the solar nebula // Earth Planets Space. 2011. V. 63. P. 1193–1206.
[10] Czechowski L., Witek, P., Comparison of early evolutions of Mimas and Enceladus // Acta Geophys. 2015, V. 63. No. 3. P. 900–921.
[11] Kimura J., Nakagawa T., Kurita K. Size and compositional constraints of Ganymede's metallic core for driving an active dynamo // Icarus. 2009. V. 202. P. 216–224.
[12] Hilairet N., Reynard B., Wang Y., Daniel I., Merkel S., Nishiyama N., Petitgirard S. High-Pressure Creep of Serpentine, Interseismic Deformation, and Initiation of Subduction // SCIENCE. 2007. V. 318. P. 1910–1913.
[13] Ji S., Zhao P. Flow laws of multiphase rocks calculated from experimental data on the constituent phases // Earth and Planetary Science Letters. 1993. V. 117. P. 181–187.
[14] Sotin C., Labrosse S. Three dimensional thermal convection in an isoviscous, infnite Prandtl number fluid heated from within and from below: applications to the transfer of heat through planetary mantles // Phys. Earth Planet. Int. 1999. V. 112. No. 34. P. 171–190.
[15] Bhatia G.K., Sahipal S. The early thermal evolution of Mars // Meteoritics & Planetary Science. 2016. V. 51, No. 1. P. 138–154.doi: 10.1111/maps.12573

CONDENSED PHASES OF CARBON DIOXIDE IN TITAN'S ICY CRUST: INFLUENCE ON RHEOLOGICAL PROPERTIES

A.N. Dunaeva [1], V.A. Kronrod [1], O.L. Kuskov [1]
[1] *V.I. Vernadsky Institute of Geochemistry and Analytical Chemistry RAS, Moscow, dunaeva.an@gmail.com*

KEYWORDS:
Titan, carbon dioxide clathrates, CO_2-ice, elastic moduli, Love numbers.

INTRODUCTION:
Carbon dioxide CO_2 is the most abundant (after H_2O) component of cometary and planetesimal ices involved in the formation of numerous icy satellites of the giant planets of the Solar System. According to theoretical and experimental data, the content of CO_2 in the ice component of planetesimals is 11-13.5 mol% [1], in cometary ices — 2-30 mol% relative to H_2O [2]. The results of space observations indicate a wide distribution of CO_2 in the icy satellites of the giant planets (Europa, Ganymede, Callisto, Enceladus, and many others).

On Titan, the largest icy satellite of Saturn, carbon dioxide is contained in small amounts ($n \cdot 10^{-6}$ %) in the atmosphere and qualitatively determined in the gas phase emitted from the satellite surface, where the Huygens Probe landed [3]. Although the available data are insufficient to estimate the content of CO_2 on Titan, we can assume the presence of this component in the water-ice depths of the satellite.

This paper discusses the main forms of CO_2 in Titan and their influence on the physical and rheological properties of the satellite's icy crust. Models of Titan's water-ice shell, including CO_2-containing ice or clathrates in equilibrium with the internal ocean, were constructed. For each model, tidal Love numbers, k_2, were calculated and compared with the Cassini spacecraft data.

CO_2-PHASES AND THEIR PHYSICAL PROPERTIES UNDER CONDITIONS OF THE WATER-ICE SHELL OF TITAN:
CO_2 compounds enter Titan in the form of dry (solid CO_2) ice, as the main condensed phase of carbon at temperatures and pressures of the Saturnian gas-dust disk [4]. At the late stages of Titan's accretion, owing to the large mass of rock-ice impactors and high temperatures of impact events, the outer regions of the satellite melt and the surface ocean is formed. In this case, the volatile components of planetesimal/cometary ices are distributed between the ocean and the primary atmosphere according to thermodynamic equilibrium. In particular, carbon dioxide will partially remain dissolved in the ocean and partially gasify into the near-surface atmosphere. As the satellite cools, the outer icy crust crystallizes, with the formation of Ih ice and CO_2-clathrates (condensed phases of other volatile components are not discussed). Within the first 20-30 km of the ice crust, where Titan's surface temperature is low enough (less than the temperature of the lowest quadrupole point of ~ 121 K) CO_2-clathrates become unstable and dissociate into CO_2-ice and water ice [5]. In addition, CO_2-ice can form a regolith layer on Titan's surface, as redeposited ice precipitated from the atmosphere during its cooling. Both ice phases of carbon dioxide, CO_2-clathrate and CO_2-ice, differ in their properties from water ice and can significantly change the physical and rheological properties of the satellite's icy crust.

In Fig. 1 (a-c), the values of density and elastic moduli of CO_2-clathrate and CO_2-ice in T-P conditions of Titan's icy crust and internal ocean are shown in comparison with those for Ih ice. For ice Ih, the density (ρ) and bulk modulus (K_T) were obtained using the model [6]; the shear modulus (μ) was calculated by equation [7]. For CO_2-clathrate the density value is taken from [8], K_T and μ – from [5]. For CO_2-ice ρ and K_T values were calculated according to the method [9]. To calculate the shear modulus of CO_2-ice the standard isotropic elasticity relations were used:

$\mu = \frac{3K_T(1-2\eta)}{2(1+\eta)}$, where η is Poisson's ratio, which was calculated from experimental data [10] by the formula:

$\eta = \frac{\vartheta_{lg}^2 - 2\vartheta_{ts}^2}{2(\vartheta_{lg}^2 - 2\vartheta_{ts}^2)}$, where ϑ_{lg}^2 and ϑ_{ts}^2 — longitudinal and transverse sound velocities of solid carbon dioxide.

Along the T-P profile of Titan's ice crust η is assumed to be 0.27.

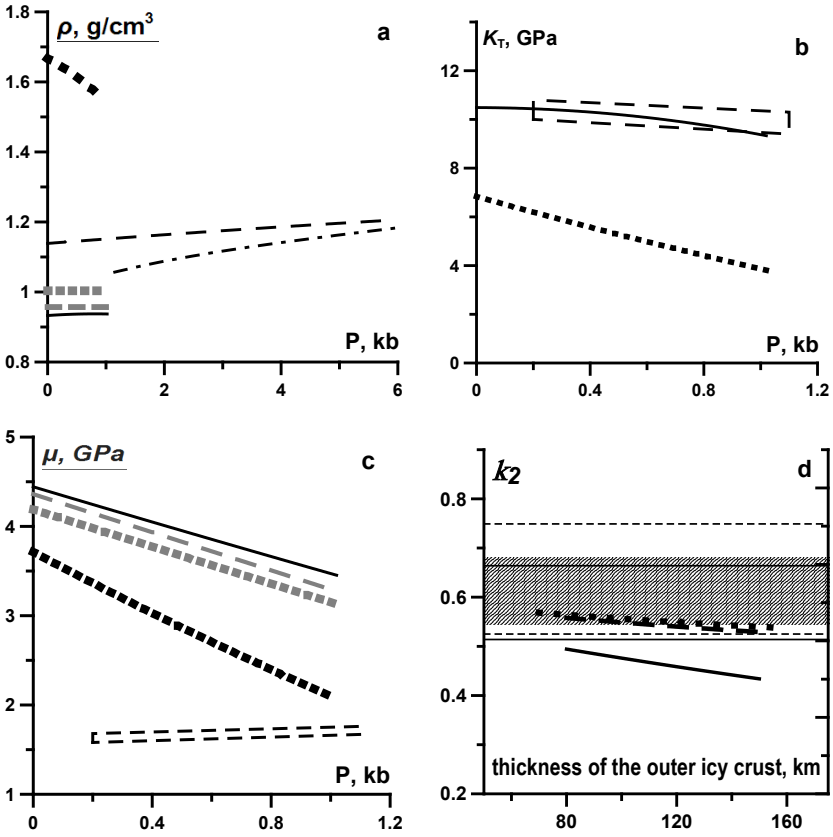


Fig. 1. Physical properties of condensed phases in the water-ice shell of Titan and the tidal Love numbers k_2 of the satellite.
(**a**-**c**) Solid lines — ice I_h, broken lines — CO_2-clathrate, dotted lines — CO_2-ice, dash-dotted line — density of the internal ocean in equilibrium with CO_2-clathrate. Gray dashed and dotted lines refer to the properties of the Ih-icy crust with 10 % admixture of CO_2-clathrate or CO_2-ice, respectively.
Titan Love numbers k_2 (**d**) are shown for the following icy crust compositions: pure Ih (heavy solid curve), Ih + 10 % CO_2-clathrate (heavy broken curve), Ih + 10% CO_2-ice (dotted curve). Shaded area is the region of experimental k_2 values [11]. Thin solid and dashed lines are $k_2 \pm 1\sigma$: 0.589 ± 0.075 and 0.637 ± 0.112 [12].

Comparison of the physical characteristics of different icy phases shows that CO_2-clathrate and CO_2-ice are much denser than water ice, but are rheologically markedly weaker compared to it.

MODEL PARAMETERS AND RESULTS:

The main parameters affecting the tidal characteristics of Titan (tidal Love numbers, k_2) are the thickness, density and elastic moduli of the icy crust, as well as the density of the internal ocean. The thickness of the icy crust depends on the heat flux of the satellite and serves as a parameter in further calculations. The densities for the two compositions of icy crust (Ih + 10 % CO_2-clathrate and Ih + 10 % CO_2-ice) are shown in Fig. 1(a). The density

of the ocean with dissolved CO_2 was calculated using models [8, 13]. To estimate the k_2 values, the approximation [14] was used. Comparison of the calculated k_2 values with the results of space experiments [11–12] is shown in Fig. 1 (d). It follows from the figure that the tidal Love numbers of Titan with an ice crust including CO_2 — ice or hydrate phases display better agreement with experimental observations compared to a pure water system.

REFERENCES:

[1] Marboeuf U., Thiabaud A., Alibert Y., Cabral N., Benz W. From stellar nebula to planetesimals // Astronomy & Astrophysics. 2014. V. 570. P. A35.
[2] Mumma M.J., Charnley S.B. The chemical composition of comets—emerging taxonomies and natal heritage // Annual Review of Astronomy and Astrophysics. 2011. P. 49.
[3] Niemann H.B. et al. Composition of Titan's lower atmosphere and simple surface volatiles as measured by the Cassini-Huygens probe gas chromatograph mass spectrometer experiment // Journal of Geophysical Research: Planets. 2010. V. 115(E12.).
[4] Makalkin A.B., Dorofeeva V.A. Accretion disks around Jupiter and Saturn at the stage of regular satellite formation // Solar System Research. 2014. V. 48. P. 62–78.
[5] Jia J., Liang Y., Tsuji T., Murata S., Matsuoka T. Elasticity and stability of clathrate hydrate: role of guest molecule motions // Scientific reports. 2017. V. 7(1). P. 1–11.
[6] Feistel R., Wagner W. A new equation of state for H_2O ice Ih // Journal of Physical and Chemical Reference Data. 2006. V. 35(2). P. 1021–1047.
[7] Journaux B. et al. Holistic approach for studying planetary hydrospheres: Gibbs representation of ices thermodynamics, elasticity, and the water phase diagram to 2,300 MPa // Journal of Geophysical Research: Planets. 2020. V. 125(1). P. e2019JE006176.
[8] Levi A., Sasselov D., Podolak M. The abundance of atmospheric CO_2 in ocean exoplanets: a novel CO_2 deposition mechanism // The Astrophysical Journal. 2017. V. 838(1). P. 24.
[9] Jäger A., Span R. Equation of state for solid carbon dioxide based on the Gibbs free energy // Journal of Chemical & Engineering Data. 2012. V. 57(2). P. 590–597.
[10] Yamashita Y., Kato M. Viscoelastic properties of polycrystalline solid methane and carbon dioxide // Geophysical research letters. 1997. V. 24(11). P. 1327–1330.
[11] Iess L. et al. The tides of Titan // Science. 2012. V. 337(6093). P. 457–459.
[12] Durante D. et al. Titan's gravity field and interior structure after Cassini // Icarus. 2019. V. 326. P. 123–132.
[13] Teng H. et al. Solubility of liquid CO2 in water at temperatures from 278 K to 293 K and pressures from 6.44 MPa to 29.49 MPa and densities of the corresponding aqueous solutions // The Journal of Chemical Thermodynamics. 1997. V. 29(11). P. 1301–1310.
[14] Baland R.M. et al. Titan's internal structure inferred from its gravity field, shape, and rotation state // Icarus. 2014. V. 237. P. 29–41.

REPEATABILITY OF A GIVEN CONFIGURATION OF PLANETS

A. Sukhanov [1]
[1] *Department of Space Dynamics and Mathematical Information Processing, Space Research Institute of the Russian Academy of Sciences (IKI), 84/32 Profsoyuznaya Str, Moscow, 117997, Russia*

KEYWORDS:
Planet, periodicity, continued fraction, planet parade.

The implementation of space flights with a flyby of several planets is possible only with an appropriate mutual position (configuration) of these planets. This raises the question of how often the configuration favorable for a particular flight is repeated. The presentation is devoted to determining the periodicity of a given configuration of planets, i.e. finding the time interval after which this configuration is repeated. It is shown that this time interval may be determined with any given accuracy using continued fractions. A brief description of continued fractions is given. Examples of both accomplished and possible future space missions are given. The periodicity of the so-called planet parades, when several planets line up near a straight line emanating from the Sun, is also considered.

SESSION 6. SMALL BODIEIS (INCLUDING COSMIC DUST) (SB) ORAL SESSION

NEGATIVE POLARIZATION OF DISTANT COMET C/2017 K2 (PANSTARRS)

E. Zubko [1], A. Kochergin [2], E. Chornaya [3,2], M. Zheltobryukhov [2], G. Videen [1,4], G. Kornienko [2], I. Luk'yanyk [5], S.S. Kim [1,6]

[1] *Humanitas College, Kyung Hee University, 1732 Deogyeong-daero, Yongin-si, Gyeonggi-do 17104, Republic of Korea, evgenij.s.zubko@gmail.com;*

[2] *Institute of Applied Astronomy of RAS, 10 Kutuzova Emb., Saint-Petersburg, 191187, Russia;*

[3] *Far Eastern Federal University, 8 Sukhanova St., Vladivostok 690950, Russia;*

[4] *Space Science Institute, 4750 Walnut Street, Boulder Suite 205, CO 80301, USA;*

[5] *Astronomical Observatory, Taras Shevchenko National University of Kyiv, 3 Observatorna St., Kyiv, 04053, Ukraine;*

[6] *Department of Astronomy and Space Science, Kyung Hee University, 1732 Deogyeong-daero, Yongin-si, Gyeonggi-do 17104, Republic of Korea*

KEYWORDS:
Comet C/2017 K2 (PANSTARRS), observations, polarimetry, dust, modeling, agglomerated debris particles.

INTRODUCTION:
Comet C/2017 K2 (PANSTARRS), hereafter K2, was discovered on May 21, 2017 at an extremely long heliocentric distance $r_h = 16.09$ au. Analysis of the pre-discovery images suggests its activity started at $r_h > 23.7$ au (e.g., [1]). While the comet approaches its perihelion passage on December 20, 2022, it will be the target of numerous studies. We conducted presumably the first polarimetric observations of Comet C/2017 K2 (PANSTARRS) in February – March, 2021, when its heliocentric distances decreased from 7.135 au to 6.801 au.

OBSERVATIONS:
During 10 nights between February 8 and March 23, 2021, we observed Comet K2 using the *RC500* telescope ($D = 0.5$ m; $F = 4$ m) of the Ussuriysk Astrophysical Observatory, a division of the Institute of Applied Astronomy of Russian Academy of Science (code C15). The telescope is equipped with CMOS detector *ZWO ASI 6200 pro* (resolution — 9576 × 6388, size of pixel — 3.76 μm) exploited in the 2 × 2 binning mode. In addition, we used two filters: (1) the broadband *R* filter of the *Bessell photometric system* ($\lambda_{eff} = 0.64$ μm, FWHM = 0.16 μm) and (2) a dichroic polarization filter (analyzer). The analyzer was rotated around the optical axis at three discrete orientations, 0 °, 60 °, and 120 °. At each analyzer position, we captured an image of the comet that was processed later on with the *Image Reduction and Analysis Facility* (IRAF) software, including bias subtraction, removal of cosmic-ray events, and flat-field correction.

Using a set of measurements at three different orientations of the analyzer, one can compute the total linear polarization *P* and position angle of its plane with regard to the first orientation of the analyzer θ (e.g., [2]). The latter is aligned with regard to the scattering plane, binding three points: Sun, nucleus of comet, and observer. It is important that, within the error bars, the plane of linear polarization in comets appears either parallel or perpendicular to the scattering plane (e.g., [3]). This feature makes it possible to consider a sign-dependent definition of the degree of linear polarization $P_Q = -P\cos(\theta) = (F_\perp - F_{||}) / (F_\perp + F_{||})$, where $F_\perp$ and $F_{||}$ are the fluxes of the scattered light whose electric fields vibrate perpendicular and within the scattering plane, respectively. P_Q is typically measured in percent. It is significant that at small phase angles, $\alpha < 30$ °, comets often reveal the phenomenon of negative polarization that simply implies $F_\perp < F_{||}$ (e.g., [4] for review). We have found the negative polarization in Comet K2 in our measurements with the circular-aperture radius of 10 000 km.

RESULTS AND DISCUSSION:

In Fig. 1, we plot the degree of linear polarization P_Q as a function of phase angle α in Comet K2 with that of two other comets observed in red light at long heliocentric distance, Comet 29P / Schwassmann – Wachmann measured in the same aperture at $r_h \approx 5.9$ au [5], and Comet C/1995 O1 (Hale-Bopp) measured in a circular aperture having radius ~ 26 000 km at $r_h \approx 2.6$ au [6]. As one can see, the aperture-averaged negative polarization of Comet K2 resembles that of the other two comets. It is worth noting, however, that the negative polarization is somewhat stronger in distant comets as compared to comets at $r_h < 1.5$ au typically measured in ground-based observations (cf. with the data compilation in [4]).

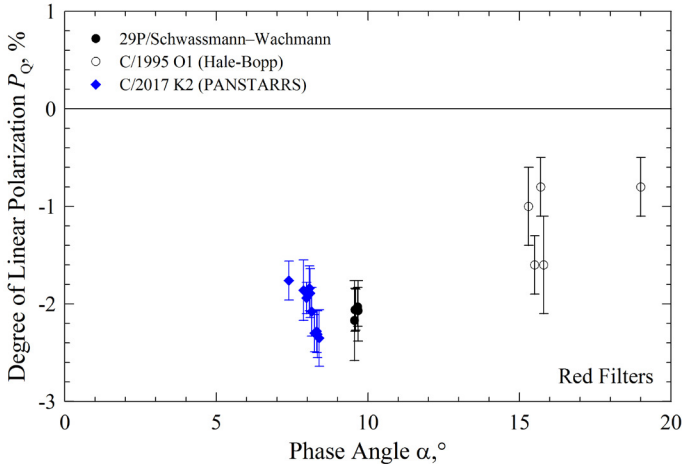


Fig. 1. Aperture-averaged degree of linear polarization P_Q as a function of the phase angle α of three distant comets. Blue diamonds show results of our observations of Comet K2 with an aperture of 10,000 km, black points to Comet 29P/Schwassmann–Wachmann [5], and open symbols to Comet C/1995 O1 (Hale-Bopp) [6].

During our observations, the amplitude of the negative polarization in Comet K2 slowly increased from $P_Q = -(1.76 \pm 0.20)$ % on February 8, 2021, to $P_Q = -(2.35 \pm 0.29)$ % on March 22, 2021. This change exceeds the uncertainty in our measurements and, therefore, it could reflect a real change in the dust population.

The bottom panel of Fig. 2 provides clues for better understanding the microphysical properties of dust particles governing the negative polarization observed in Comet K2. It shows P_Q at $\alpha = 8°$ as a function of the index n of the power-law size distribution of agglomerated debris particles r^{-n} at seven different refractive indices m (see six examples on top in Fig. 2). The m solid red line corresponds to the median value of the negative polarization of Comet K2, $P_Q = -2.1$ %. It is worth noting that the irregular morphology of the agglomerated debris particles mimics what was found in cometary dust *in situ* [2, 4]. Moreover, agglomerated debris particles have proven capable of fitting the polarization and photometric color measured in comets (e.g., [2–5]).

Fig. 2 reveals that the agglomerated debris particles with $I_m(m) > 0.04$ produce insufficiently strong negative polarization to meet observations of Comet K2. For instance, amorphous-carbon particles with $m = 2.43 + 0.59i$ produce exclusively positive polarization over the entire range of phase angle α [4]. This suggests that the K2 coma is unlikely dominated by particles with high carbon content, such as organic matter or amorphous carbon. It seemingly consists of either water-ice particles with $m = 1.313 + 0\,i$ or Mg-rich silicate particles with $\mathrm{Re}(m) = 1.5$ and $\mathrm{Im}(m) = 0$–2.

We note that increasing the power index n dampens the negative polarization. The water-ice particles with $m = 1.313 + 0\,i$ and Mg-rich silicate particles with $m = 1.5 + 0\,i$ fit the median polarization in Comet K2 at $n \approx 3.9$ and 3.8,

respectively. However, both these materials reveal a blue photometric color [3]. To ensure red color of dust particles, the index of their power-law size distribution should be constrained to $n < 3$ [3]. This can be achieved with $m = 1.5 + 0.03\,i$ ($n \approx 2.7$). While we have not measured the color of Comet K2, such measurements could help to further constrain chemical composition and size distribution of its dust.

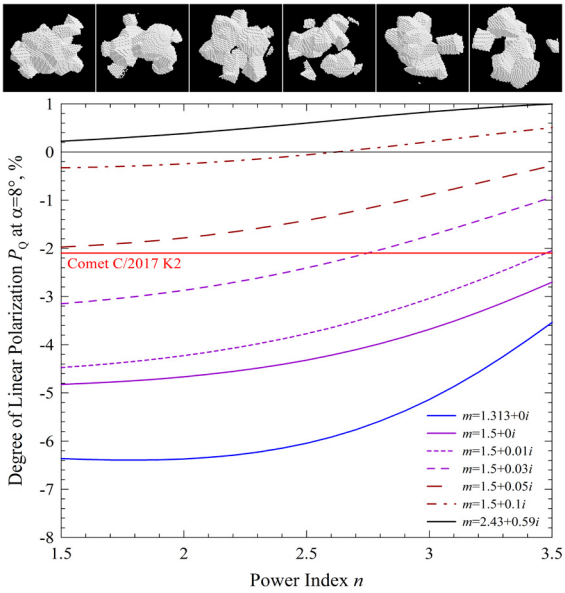


Fig. 2. Six samples of agglomerated debris particles (top) and their degree of linear polarization P_Q at phase angle $\alpha = 8°$ as a function of power-law index n (bottom). Solid and dashed curves show results obtained at various refractive indices m (see legend). The solid red line corresponds to the median value of negative polarization in the inner coma of Comet C/2017 K2 (PANSTARRS).

REFERENCES:

[1] Jewitt D., Hui M.-T., Mutchler M., et al. A comet active beyond the crystallization zone // Astroph. J. Lett. 2017. V. 847, Article ID: L19.
[2] Chornaya E., Zubko E., Luk'yanyk I., et al. Imaging polarimetry and photometry of comet 21P/Giacobini Zinner // Icarus. 2020. V. 337. Article ID: 113471.
[3] Zubko E., Videen G., Hines D.C., et al. Comet C/2012 S1 (ISON) coma composition at ~ 4 au from HST observations // Planet. Space Sci. 2015. V. 118. P. 138–163.
[4] Zubko E., Videen G., Hines D.C. and Shkuratov Yu. The positive-polarization of cometary comae // Planet. Space Sci. 2016. V. 123. P. 63–76.
[5] Kochergin A., Zubko E., Chornaya E., et al. Monitoring the negative polarization in Comet 29P/Schwassmann–Wachmann during quiescence // Icarus. 2021. V. 366. Article ID: 114536.
[6] Kikuchi S. Linear polarimetry of five comets // J. Quant. Spectrosc. Radiat. Transfer. 2006. V. 100. P. 179–186.

FAST VARIATIONS OF POLARIZATION MAXIMUM IN COMET C/2020 S3 (ERASMUS)

E. Chornaya [1,2], E. Zubko [3], A. Kochergin [1], M. Zheltobryukhov [1], G. Videen [3,4], G. Kornienko [1], and S.S. Kim [3,5]

[1] *Institute of Applied Astronomy of RAS, 10 Kutuzova Emb., Saint-Petersburg 191187, Russia;*

[2] *Far Eastern Federal University, 8 Sukhanova St., Vladivostok 690950, Russia;*

[3] *Humanitas College, Kyung Hee University, 1732, Deogyeong-daero, Giheung-gu, Yongin-si, Gyeonggi-do 17104, South Korea;*

[4] *Space Science Institute, 4750 Walnut Street, Boulder Suite 205, CO 80301, USA;*

[5] *Department of Astronomy and Space Science, Kyung Hee University, 1732, Deogyeong-daero, Giheung-gu, Yongin-si, Gyeonggi-do 17104, South Korea*

KEYWORDS:
Comet C/2020 S3 (Erasmus); polarization maximum; modeling; agglomerated debris particles.

INTRODUCTION:
Comet C/2020 S3 (Erasmus) is a long-period comet having an orbital period of ~ 2,600 years. In ground-based observations, this comet appeared at relatively large phase angles, $\alpha > 60°$. This made it possible to constrain its positive-polarization amplitude, P_{max}.

OBSERVATION AND DATA REDUCTION:
We conducted polarimetric measurements of Comet Erasmus on November 13, 20, 22, and 23 of 2020, using the 0.22-m telescope ($F = 0.503$ m) of the Ussuriysk Astrophysical Observatory (code C15), that is a division of Institute of Applied Astronomy of Russian Academy of Sciences. The telescope was equipped with a commercially available CMOS camera *ZWO ASI1600MM pro*, having resolution of 4656 × 3520 pixels and pixel size of 3.8 μm. The field of view of the detector is 1.55 × 1.17 degrees with angular resolution of 2.39 × 2.39 arcsec per pixel. The comet was imaged through the broadband *R* filter of the *Bessell photometric system* [1] through a dichroic polarization filter (analyzer) that was rotating through three fixed position angles 0 °, + 60 °, and + 120 °. The obtained images were processed using the *Image Reduction and Analysis Facility* (IRAF) [2, 3]. These three measurements fully characterize the linear polarization of the scattered light. In our analysis, we consider the degree of linear polarization $P_Q = (F_\perp - F_{||}) / (F_\perp + F_{||})$, where $F_\perp$ and $F_{||}$ are the fluxes of the scattered light whose electric fields vibrate perpendicular and within the scattering plane, respectively. The degree of linear polarization is often measured in percent. The log of the polarimetric observations is given in Table 1.

RESULTS AND DISCUSSION:
On all epochs, we have found qualitatively the same spatial distribution of the polarization in the Erasmus coma. Namely, the inner part of the coma systematically produced lower positive polarization compared to the outer coma (Fig. 1). A similar spatial distribution of polarization has been observed in other comets, like, for instance, the short-period comets 1P / Halley [3], 46P/Wirtanen [4] and 2P/Encke [5]. A heterogeneous distribution of polarization in comets suggests the presence of at least two types of dust particles, for instance, Mg-rich silicate particles producing the low positive polarization and carbonaceous particles producing high positive polarization [6].

On the bottom in Fig. 2 we plot the aperture-averaged values of the degree of linear polarization P_Q as a function of the phase angle α in four different comets: C/1989 X1 (Austin), C/1995 O1 (Hale-Bopp), C/1996 B2 (Hyakutake), and C/2020 S3 (Erasmus). Observations of the first three comets are adapted from [7].

Table 1. Log of observations of Comet C/2020 S3 (Erasmus) in November of 2020 with the aperture radius 5000 km.

Date, UT	Exp, sec	*F*	r_h, au	Δ, au	α, °	*m*	P_Q, %
13.87	30	*R*	0.820	1.048	62.6	10.45 ± 0.04	13.35 ± 0.33
20.88	30	*R*	0.686	1.040	66.2	9.86 ± 0.03	15.07 ± 0.56
22.86	30	*R*	0.648	1.047	66.5	9.71 ± 0.04	15.70 ± 0.81
23.86	30	*R*	0.629	1.051	66.6	9.20 ± 0.02	18.41± 0.38

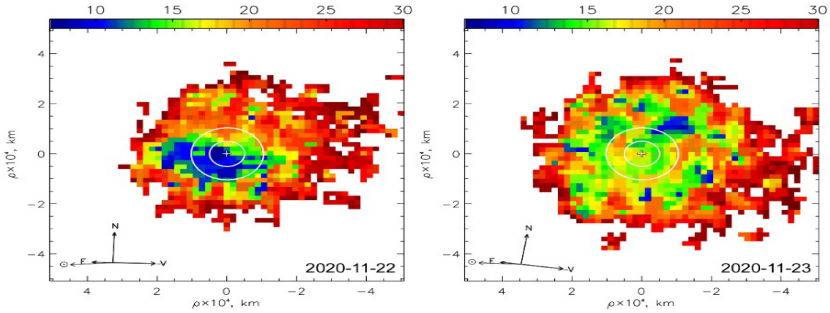


Fig. 1. Spatial distribution of the degree of linear polarization *P* in Comet Erasmus in November 22 and 23, 2020. The white cross denotes the photometric center and two circles correspond to apertures of integration with radii of 5 000 km and 10 000 km.

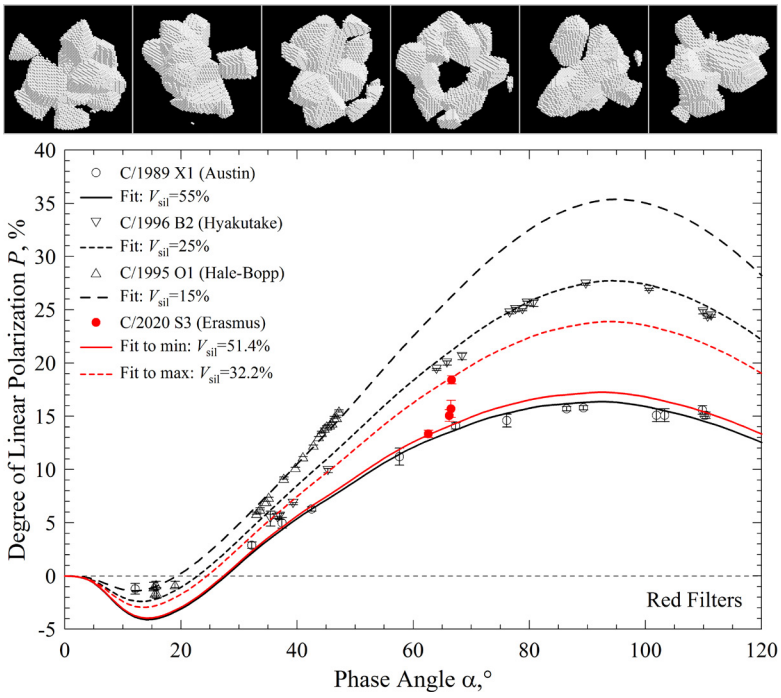


Fig. 2. Aperture-averaged degree of linear polarization as a function of the phase angle α in four different comets. Red dots show results of our observations of Comet Erasmus with the aperture of 5000 km; other symbols correspond to data adapted from the literature (see legend).

Interestingly, while on the first epoch (α = 62.6 °), the polarization of Comet Erasmus nearly matches that of the low-P_{max} Comet C/1989 X1 (Austin); whereas, on the latest epoch (α = 66.6 °), it appears consistent with the high-P_{max} Comet C/1996 B2 (Hyakutake). In other words, the population of dust

in the inner coma of Comet Erasmus has been replaced from what is typical of low-P_{max} comets to that of high-P_{max} comets within only several days. It also is worth noting that such a significant change in dust populations has not been accompanied with a dramatic change in brightness of Comet Erasmus (see Table 1).

It is important that the dispersion of the polarization maximum in comets has been quantitatively reproduced with a realistic model of the *agglomerated debris particles* in [6]; see six examples of these particles on top in Fig. 2 and discussion of their morphology in [2] and [6]. A mixture of these particles having two different chemical compositions, Mg-rich silicates and organics / amorphous carbon, is capable of fitting the degree of linear polarization in various comets [6]. Within this approach, the polarization maximum P_{max} is governed by the volume ratio of silicates V_{sil} and carbonaceous materials $V_{car} = 1 - V_{sil}$. Black lines in Fig. 2 demonstrate fits to polarization in Comets C / 1989 X1 (Austin), C / 1995 O1 (Hale-Bopp), and C/1996 B2 (Hyakutake); whereas, red lines here correspond to a fit to Comet Erasmus on the first epoch (solid line) and on the latest epoch (dashed line). Values of V_{sil} providing the best fits are given in the legend to Fig. 2. As one can see, the increase of polarization in Comet Erasmus can be explained with a decrease of relative abundance of Mg-rich silicates in its coma, from $V_{sil} = 51.4$ % to 32.2 %. This change presumably results from emanation of large amount of carbonaceous particles.

REFERENCES:

[1] Bessell M.S. UBVRI passbands // Publications of the Astronomical Society of the Pacific. 1990. V. 102. P. 1181–1199.
[2] Chornaya E., Zubko E., Luk'yanyk I. et al. Imaging polarimetry and photometry of comet 21P/Giacobini Zinner // Icarus. 2020. V. 337. P. 113471.
[3] Dollfus A., Suchail J.-L. Polarimetry of grains in the coma of P/Halley. I – Observations // Astron. Astrophys. 1987. V. 187. P. 669–688.
[4] Zheltobryukhov M., Zubko E., Chornaya E. et al. Monitoring polarization in comet 46P/Wirtanen // Mon. Not. Roy. Astron. Soc. 2020. V. 498. P. 1814–1825.
[5] Jewitt D. Looking through the HIPPO: Nucleus and Dust in Comet 2P/Encke // Astron. J. 2004. V. 128. P. 3061–3069.
[6] Zubko E., Videen G., Hines D.C. and Shkuratov Yu. The positive-polarization of cometary comae // Planet. Space Sci. 2016. V. 123. P. 63–76.
[7] Kikuchi S. Linear polarimetry of five comets // J. Quant. Spectrosc. Radiat. Transfer. 2006. V. 100. P. 179–186.

REFLECTANCE SPECTRA OF ASTEROIDS WITH SIMULTANEOUS SUBLIMATION ACTIVITY: REGISTRATION AND MODELS

V.V. Busarev [1, 2], E.V. Petrova [3], M.P. Shcherbina [1], S.I. Barabanov [2]

[1] *Lomonosov Moscow State University, Sternberg Astronomical Institute (SAI MSU), University Av., 13, Moscow, 119992, Russian Federation (RF), busarev@sai.msu.ru;*

[2] *Institute of Astronomy, Russian Academy of Sciences (IA RAS), Pyatnitskaya Str., 48, Moscow, 119017, RF;*

[3] *Space Research Institute, Russian Academy of Sciences (IKI RAS), Profsoyuznaya 84/32, Moscow, 117997, RF, epetrova@iki.rssi.ru*

KEYWORDS:
Main-belt asteroids, reflectance spectra, low-temperature mineralogy, ice sublimation near perihelion, radiative transfer models, solar activity influence.

INTRODUCTION:
To date, it has been found that about 30 objects of the Main asteroid belt show some signs of activity (e.g., [1] and references therein). A thorough analysis of the phenomenon suggested that activity of main-belt asteroids (MBAs) may be induced, in addition to dust production and sublimation of ices excavated at collisions, by some other factors, such as dehydration stresses, thermal fracture, disintegration at fast rotation, electrostatic repulsion, and radiation pressure sweeping, or their combinations [2]. Thus, activity of asteroids is a complex phenomenon, the sources of which are not yet fully understood. Here, on the basis of low-resolution spectrophotometric ($R \equiv \lambda / \Delta\lambda \sim 100$) and multiband (*UBVRI*) observations of asteroids and numerical simulations of the reflectance spectra (RS), we analyze the events of simultaneous sublimation activity observed on three primitive MBAs (145, 704, 779) and one Mars-crosser (1474) in 2012 [3, 4] and on three primitive-type MBAs (24, 449, 704) in 2019 [5] near their perihelia. Activity of 24 and 449 was detected for the first time.

RESULTS OF OBSERVATIONS:
According to the common classifications by Tholen [6] and SMASSII [7], 145 Adeona (D = 127.8 km) is an asteroid of C or Ch type, 704 Interamnia (D = 306.3 km) — of F or B type, 779 Nina — of M or X type, and 1474 Beira — of FX or B type. The values of the geometric V – band albedo of Adeona, Interamnia, and Nina are 0.06, 0.08, and 0.16, respectively [8]. Taking into account the B classification of Beira [7], we conditionally adopted its geometric albedo (still unknown) as ~ 0.08 [4]. Asteroids of these types (except Nina) are supposed to be primitive, including low-temperature compounds (hydrated silicates, oxides, organics, etc.) (e.g., [9, 10]). Despite the previously debated high-temperature mineralogy of Nina, radar observations showed that the asteroid may also be primitive but heterogeneous in composition [11]. Close in time spectrophotometric observations of Adeona, Interamnia, Nina, and Beira, being near their perihelia on 13–19 September 2012 [3, 4], showed unusual maxima (at ~ 0.35–0.60 μm for Adeona, Interamnia, and Nina and ~ 0.55–0.75 μm for Beira) in their RS, which do not correspond to a solid silicate surface. These RS of the asteroids are shown in Fig. 1 together with their typical ones from the SMASSII database. We supposed that the detected features may be signs of a dust/ice exosphere induced by sublimation of ices (predominately H_2O) around an asteroid at a high subsolar temperature near perihelium [3, 4]. Despite of unstable state of H_2O ice at the surface temperatures of MBAs (e.g., [12]), water ice may survive in the shallow subsurface of these bodies due to a very low thermal conductivity of the surface layers of primitive-type asteroids, the microporosity of which reaches ~ 50 % [13, 14]. Assuming frequent meteoroid impacts on MBAs (since their number is large and continuously grows), one may expect that water ice on primitive MBAs is regularly excavated, which results in sublimation activity becoming more intense near perihelion.

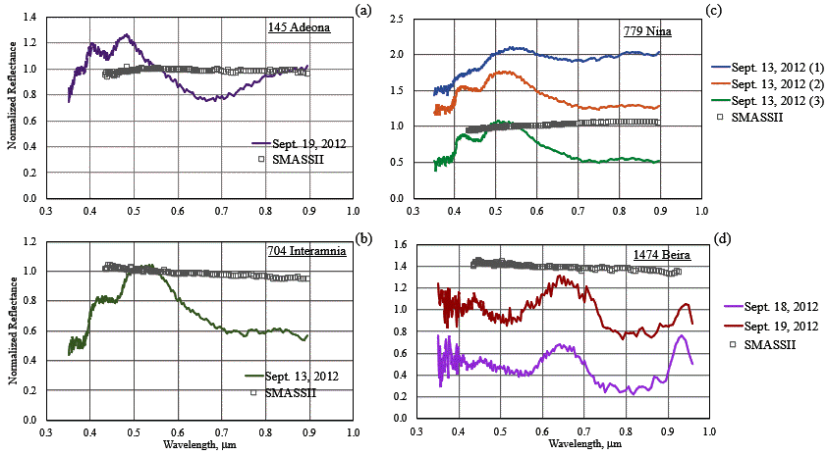


Fig. 1.

One more considerable factor apparently participated in creating particular conditions for the considered asteroids in September 2012. It was strong, close to maximum, solar activity events. As follows from the GOES-15 X-ray satellite data, our observations in 2012 were performed after a two-week period of frequent solar flares and the accompanying coronal mass ejections (CMEs), the intensity of which varied from weak to medium nearly every day (https://tesis.lebedev.ru/en/sun_flares.html?m=9&d=6&y=2012). As a result, the elevated and changing electromagnetic pressure of the solar wind possibly inflated asteroid exospheres and made them more extended (e.g., from several dozen to several hundred kilometers in height), which in turn intensified the light-scattering maxima in the RS of asteroids.

These results and our suppositions were confirmed by our next observations of simultaneous sublimation activity of three primitive MBAs, 24 Themis, 449 Hamburga, and 704 Interamnia, being near perihelion in March 2019 [5]. Themis (D = 198 km) is an asteroid of C [6] or B [7] type, while Hamburga (D = 85.6 km) is the C-type asteroid (EAR-A-5-DDR-TAXONOMY-V4.0). The values of geometric albedo of Themis and Hamburga are 0.067 and 0.04, respectively (https://ssd.jpl.nasa.gov/sbdb.cgi#top). The UBVRI-observations of Themis, Hamburga, and Interamnia along with a non-variable solar analog star, HIP 29759, were performed with the 0.6-m telescope at the Crimean observatory of the SAI MSU [5]. The approximate RS of Themis, Hamburga and Interamnia (Fig. 2) were obtained from the UBVRI data (at corresponding effective wavelengths of the bands) of the asteroids and those of the analog star [5]; here we only conditionally call the reflectance curves of the asteroids as “spectra”.

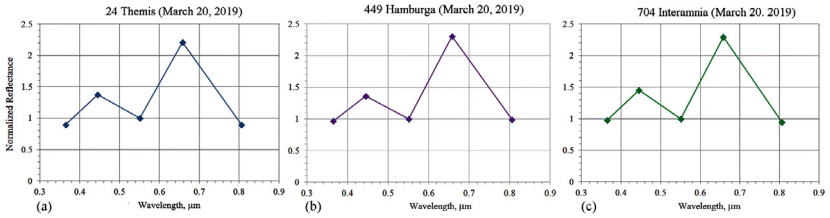


Fig. 2.

As seen from the Fig. 2, the RS of Themis, Hamburga and Interamnia include unusual maxima at 0.44 and 0.66 μm instead of a smooth spectrum like SMASSII one of Interamnia shown in Fig. 1b. Amazing resemblance of the curves could be explained by the close-in-time action of several factors rather than only by the same widely spaced in wavelength filters. The main factors may be (1) the presence of a tenuous dust/ice exosphere formed due

to sublimation of water ice at perihelion, (2) the similarity in the composition and structure of dust particles caused by similar composition of the asteroids themselves, and (3) the influence of the solar wind with similar parameters on the asteroids, which were at close heliocentric distances and elongation angles from the Sun. In contrast to high solar activity in 2012, rare solar flares and the accompanying CMEs in 2019 could also significantly change the solar wind parameters. Two weak solar flares spaced by the 32-hour interval and accompanied by CMEs occurred ~ 11 days before (https://tesis.lebedev.ru/en/sun_flares.html?m=3&d=9&y=2019) observations of active asteroids in March 2019 and, according to our estimation, influenced the parameters of their exospheres.

MODELS:

To verify our assumptions about the nature of unusual maxima in RS of considered asteroids, we modeled the RS using the light-scattering and radiative-transfer theories for a conditional asteroid (with a mean surface spectral characteristics) enveloped by an exosphere (the optical thickness is 0.5). The latter is assumed to contain aggregate particles of submicron constituents with different composition (water ice, tholins, and olivine), the formation mechanism of which is presumably similar to that for cometary coma particles ([15] and references therein). Taking into account spectral dependences of the refractive index of compounds, we calculated RS of a model asteroid at a phase angle of 20 ° typical of observations. The model RS are given for different radii of spherical monomers (0.0955, 0.1150, and 0.1300 μm) composing aggregates in an asteroid's exosphere (Figs. 3a-3c), for two cases of size deviations of the polydisperse constituents (Figs. 3d and 3e), and for two porosities of dust aggregates (see inserts) (Fig. 3f). One can see that the RS of Adeona (Fig. 1a), Interamnia (Fig. 1b), and Nina (Fig. 1c) obtained in 2012 well agree with the models in Figs. 3a and 3d. As for the RS of Beira (Fig. 1d), they are probably consistent with combinations of models in Figs. 3b, 3e, and 3f. Finally, the RS of Themis, Hamburga, and Interamnia of March 2019 resemble the models in Fig. 3c or may agree with combinations of those in Figs. 3a and 3e.

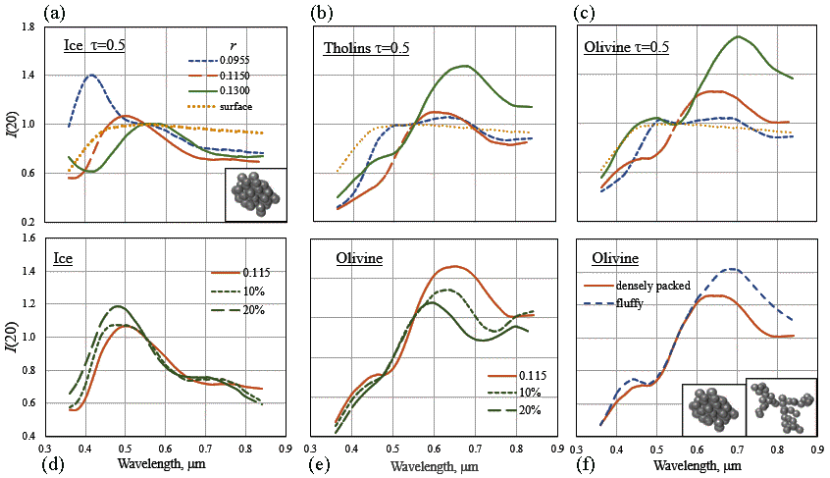


Fig. 3.

CONCLUSIONS:

(1) A phenomenon of simultaneous sublimation activity near perihelion was observed for the first time in September 2012 on three main-belt primitive asteroids, 145 Adeona, 704 Interamnia, 779 Nina, and Mars-crosser 1474 Beira [3, 4]. Our observations in March 2019 of 704 Interamnia, 24 Themis, and 449 Hamburga confirmed the reality of this effect and revealed it for the first time on the latter two asteroids [5]. This fact apparently points to a widespread phenomenon, which is strengthened by high solar activity or close-in-time CMEs.

(2) A necessary condition for the sublimation-induced mass loss by primitive MBAs is a considerable content of water ice in their matter, sufficient to support sublimation activity for several billions of years. It means that this phenomenon is an indication of the origin of primitive MBAs (or their majority) beyond the snow-line.

(3) Results of our numerical simulations demonstrate that the light-scattering maxima in the measured RS of active asteroids may be produced by tenuous exospheres of aggregate particles (composed of ice, silicates, and organics) enveloping these asteroids.

REFERENCES:

[1] Chandler C.O., Curtis A.M., Mommert M. et al. // PASP. 2018. V.130. 114502.
[2] Jewitt D. // Astron. J. 2012. V. 143. No. 66. P. 14.
[3] Busarev V.V., Barabanov S.I., Rusakov V.S. et al. // Icarus. 2015. V. 262. P. 44.
[4] Busarev V.V., Barabanov S.I., Puzin V.B. et al. // Solar Syst. Res. 2016. V. 50. P. 281.
[5] Busarev V.V., Scherbina M.P., Irsmambetova T.R. et al. // 10th Moscow Solar System Symposium (11M-S3). 2019. Space Research Inst., Abstract 10MS3-SW-07.
[6] Tholen D.J. // In: Asteroids II (Binzel R.P. et al., eds.), Univ. of Arizona Press, 1989. P. 1139.
[7] Bus S.J., Binzel R.P. // Icarus. 2002. V. 158. P. 146–177.
[8] Masiero J.R., Grav T., Mainzer A.K. et al. // Astroph. J. 2014. V. 791. P. 121.
[9] Gaffey M.J., Bell J.F., Cruikshank D.P. // In: Asteroids II (Binzel R.P. et al., eds.), Univ. of Arizona Press, 1989. P. 98.
[10] Gaffey M.J., Cloutis E.A., Kelley M.S., Reed K.L. // In: Asteroids III (Bottke W.F. et al., eds.), Univ. of Arizona Press. 2002. P. 183.
[11] Shepard M.K., Clark B.E., Ockert-Bell M. et al. // Icarus. 2010. V. 208. P. 221.
[12] Busarev V.V., Makalkin A.B., Vilas F. et al. // Icarus. 2018. V. 304, P. 83.
[13] Schorghofer N. // Astroph. J. 2008. V. 682. P. 697.
[14] Grott M., Biele J., Michel P. et al. // JGR: Planets. 2020. V. 125, e2020JE006519.
[15] Busarev V.V., Petrova E.V., Shcherbina M.P. et al. // MNRAS. 2021. V. 502. P. 1882.

NEAR EARTH ASTEROIDS: DEPLETION TIME SCALES, ESCAPE ROUTS AND ESTIMATE OF SHARE OF INTERSTELLAR BODIES

B.M. Shustov [1], R.V. Zolotarev [2]
[1] *Institute of Astronomy, Russian Academy of Sciences, 48 Pyatnitskaya str., Moscow, 119017, Russia, shustov@mail.ru;*
[2] *Southern Federal University, 105/42 Bolshaya Sadovaya str., Rostov-on-Don, 344006, Russia,*

KEYWORDS:
Near Earth Objects, dynamics of asteroids

In [1] we considered some aspects of the dynamic evolution of the population of near-Earth asteroids (NEAs): the change of the rate of NEA depletion with time, including the dependence of the rate on the initial parameters of the NEA orbits, the efficiency of various channels of NEA depletion, and diffusion of NEA orbits. We studied both real asteroids and a simulated population. For the study, 3024 real asteroids larger than 1 km with a perihelion distance $q < 1.6q < 1.6$ A.U. were selected, of which 833 NEAs had $q < 1.3q < 1.3$, i.e., we took into account almost all large NEAs (see Fig. 1). For some purposes the population of NEAs was also modeled using NEOPOP (ESA) code. The orbits were integrated for 10 Myr using the REBOUND [2] numerical complex. The solar gravitational field and field of planets, as well as the possibility of collisions, were considered.

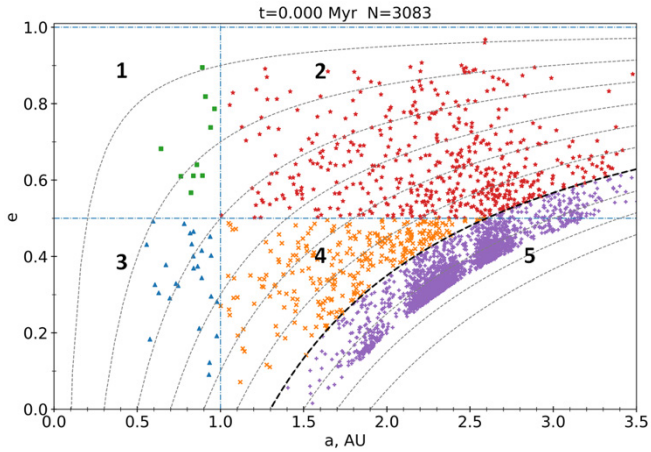


Fig. 1. NEAs distribution at *a*-*e* plane. The dashed bold line marks the boundary of $q = 1.3$, i. e. it separates the regions of NEAs and non-NEAs.

It is shown that the total population of NEAs has the median time of depletion $t_{NEA} \simeq 3.5$ Myr; this rectifies the estimates of other authors. The main advantage of the this study is that, for the first time, the dependence on the initial values of the orbital parameters: semi-major axis a of the orbit and eccentricity e was investigated. It is shown that this dependence is very strong: for the subset of asteroids with large a and a, t_{NEA} is dozens of times lower than for the subset with small a and a (see Fig. 2).

Obtained qualitative estimates of the dependence $t_{NEA}(a, e)$ are important for the quantitative analysis regarding the various model of mechanisms of replenishing the population of NEAs.

The details of the diffusion (mixing of parameters) of the asteroid orbits in the plane "*a*–*e*" in the process of evolution have been studied. During the time t_{NEA}, ~ 10 % of the NEAs were ejected from the Solar System, ~ 1.5 % fell onto the planets (including 0.2% onto the Earth), ~ 27 % fell onto the Sun, and ~ 11.5 % left the NEAs zone.

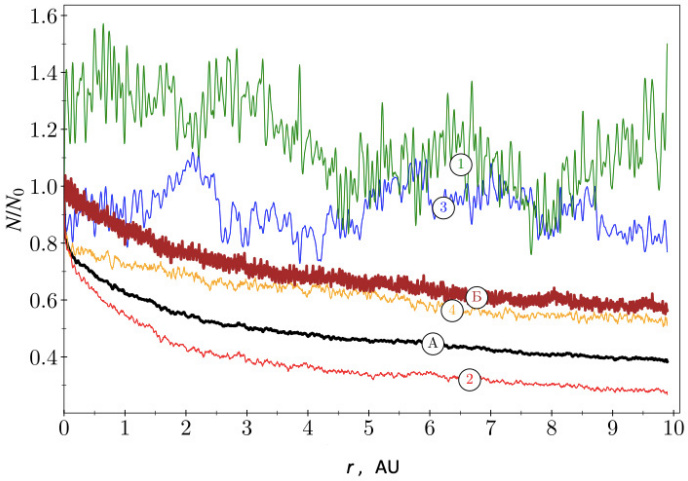


Fig. 2. The change of relative number of NEAs in the process of denamic evolution. The colors of the lines and symbols correspond to Fig. 1. The line "**А**"shows the change in the relative number of asteroids in the model containing only the NEAs, the line "**Б**" — in the model containing the entire initial sample.

Asteroids and meteoroids leaved the Solar system and replenish population of interstellar minor bodies. We brief review observations of interstellar dust, meteoroids and larger bodies, and on the basis of models describing the spectra of the masses of these bodies, we mark a huge spread (about 8 orders of magnitude!) in estimates of the ratio η of the flow of interstellar particles to the total particle flux near the Earth and in the whole Solar system. These differences mean that modern capabilities do not allow us to definitely answer how many interstellar objects are in the Solar System. When analyzing the results of observations, it is necessary to take into account the nature of the dependence of the ratio η on the particle size r, i. e. $\eta(r)$. This dependence is determined by the processes of generation and dynamic evolution of the population of small bodies in the Solar system and beyond.

REFERENCES:

[1] Zolotarev R. V., Shustov B.M. On the Dynamic Evolution of the Population of Near-Earth Asteroids // Astronomy Reports. 2021. V. 65. Issue 6. P. 518–527.
[2] Rein H, Hernandez, D.M., Tamayo D., et al. Hybrid symplectic integrators for planetary dynamics // Monthly Not. Roy. Astron. Soc. 2019. V. 85. P. 5490–5497.
[3] Borisov G.V., Shustov, B.M. Discovery of the First Interstellar Comet and the Spatial Density of Interstellar Objects in the Solar Neighborhood // Solar System Research. 2021. V. 55, Issue 2. P. 124–131

RECENT PROGRESS IN STUDYING POLARIZATION OF THE JUPITER'S AND SATURN'S SATELLITES AND NEAS IN THE CRIMEAN ASTROPHYSICAL OBSERVATORY AND THE PEAK TERSKOL OBSERVATORY

N. Kiselev [1], V. Rosenbush [2,3], A. Savushkin [1], E. Zhuzhulina [1], N. Karpov [4]

[1] *Crimean Astrophysical Observatory, Russian Academy of Sciences, Nauchny, Crimea, Russia;*

[2] *Main Astronomical Observatory of the National Academy of Sciences of Ukraine, Kyiv, Ukraine;*

[3] *Astronomical Observatory of Taras Shevchenko National University of Kyiv, Kyiv, Ukraine;*

[4] *ICAMER, Peak Terskol Observatory, Ukraine*

KEYWORDS:
Polarimetry, ground-based observations, planetary satellites, NEAs.

INTRODUCTION:
Polarimetry is a powerful technique to study surfaces of airless solar-system objects, especially at small phase angles were so called negative branch of polarization (NBP) is observed. NBP can have different shape and polarization values for different composition of the surfaces. Recently we have been able to accurately determine the NBP of Jovian and Saturn's satellites and selected NEAs at different phase angles.

Observations and results

To measure the polarization of satellites of Jupiter and Saturn, and NEAs we use the 2.6-m (f/16) Shain telescopes of the Crimean Astrophysical Observatory and the 2-m (f/8) telescope of the Peak Terskol Observatory (North Caucasus, Russia). The telescopes are equipped with the same design dual channel photoelectric polarimeters "POLSHAKH". The red channels were used for observations of the program objects in the *RI* bands. The blue channels provide observations in the *UBV* bands. We received new data on the shape and parameters of the negative branch of polarization of Jupiter's satellites (Io, Europa, Calisto, Ganymede) and Saturn's moons (Enseladus, Tethys, Rhea, Dione, Iapetus).

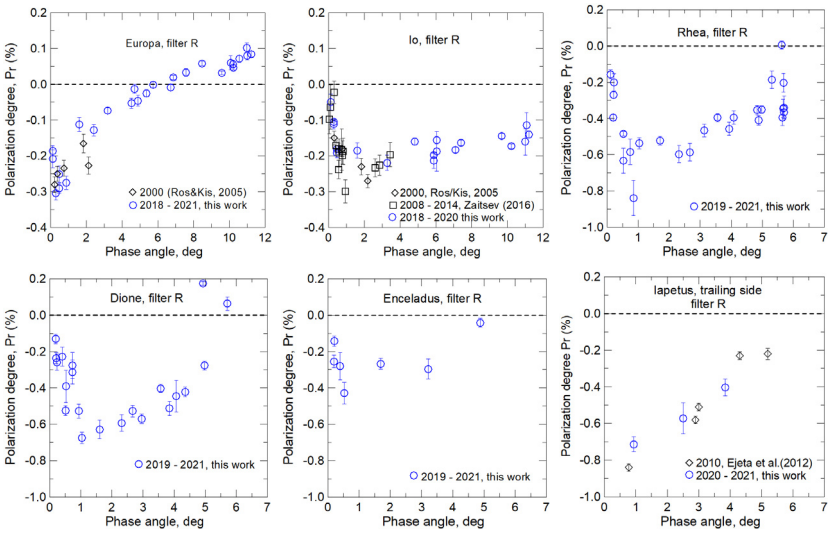


Fig. 1. The phase polarization dependences of Europa, Io, Rhea, Dione, Enceladus and Iapetus in the R bands.

As an example, we present the phase-angle polarization dependences of Europa, Io, Rhea, Dione, Enceladus and Iapetus in the R bands are showed in the Figure 1. As you can see, the negative branch of the polarization of each satellite has its own shape and individual parameters. They will be interpreted in terms of existing light scattering mechanisms and the properties of regolithic surfaces.

We also conducted polarimetric observations of selected near-Earth asteroids. They are 163373, 52768, 159402, 162082. Additionally, we presented data for NEAs (3200) Phaethon, 2014 JQ25 and 33342 that were observed at the Shain telescope earlier. Polarization and physical parameters of the NEAs are presented in Table, where we listed the range of observed phase angle $\Delta\alpha$, the degree of minimal polarization P_{min}, the polarimetrical slope h, the degree of maximal polarization P_{max}, the geometric albedo ρ, diameter asteroids D, the taxonomical class and reference. We found the geometric albedo ρ of NEAs from the relations ρ_v vs P_{max} [3] and ρ_v vs P_{min} [4]. The mean diameters of the NEAs were estimated using the expression $2\log D = 6.259 - \log p_v - 0.4V(1,1,0)$ [5].

Table. 1. Polarization and physical parameters of some NEAs.

NEAs	Δα deg	P_{min} %	h %/deg	P_{max} %	ρ	D km	Taxon Class	Ref
163373	69– 109			3.76	0.15	0.95	S?E	This work
52768	70– 75						S?C	This work
159402	32– 66		0.18		0.112	2.38	S?C	This work
162082	3.5– 27	-0.48 ±0.06			0.35 ± 0.05	0.33	S	This work
3200	19– 135		0.30 ± 0.02		0.057 ±0.002	6.6	B	This work
2014 JQ25	55.6				0.2		S	[1]
33342	12– 83			1.68	0.43	0.420.33	E	[2]

REFERENCES:

[1] Rumyantsev V.V., Kiselev N.N., and Ivanova A.V. CCD Polarimetry of Near-Earth Asteroid 2014 JO25 and Comet 41P/Tuttle–Giacobini–Kresák at the Prime Focus of the 2.6-m Shain Telescope of the Crimean Astrophysical Observatory. Solar System Research, 2019. V. 53. P. 91–97.

[2] Kiselev N., Rosenbush V., Jockers K. Polarimetry of near-Earth asteroid 33342 (1998 WT24). Synthetic phase angle dependence of polarization for the E-type asteroids. 2002. ESA SP-500. P. 887–890.

[3] Zheltobryukhov M., Chornaya E., Kochergin A., et al. Umov effect in asteroid (3200) Phaethon. Astron. Astrophys. 2018. V. 620. A179.

[4] Lupishko, D.F. (2018) Generalized Calibration of the Polarimetric Albedo Scale of Asteroids.Solar System Research. 2018. V. 52. P. 98–114.

[5] Bowell E., Hapke B., Domingue D., et al. Application of photometric models to asteroids. In Asteroids II, (ed. R. Binzel, T. Gehrels, M. Matthews) 1989. P. 524–556.

STUDY OF THE NONLINEARITY PROBLEM FOR THE NEAR-SUN ASTEROIDS

T.Yu. Galushina [1], O.N. Letner [2], S.A. Guryanov [3]
[1] *Tomsk state university, 36, Lenin Ave, Tomsk, Russian Federation, +73822-52-97-76, tanastra@nxt.ru;*
[2] *Tomsk State University, 36, Lenin Ave, Tomsk, Russian Federation, +73822-52-97-76, oksana.letner@gmail.com;*
[3] *the Ministry of Internal Affairs of Russia for the Tomsk region, 18, Krasnoarmeiskaya St, Tomsk, Russian Federation, +79234281761, sgurianov7@mvd.ru.*

KEYWORDS:
Near-Sun asteroids, confidence region, nonlinearity indicators, 2007 GT3, 2015 KO120.

INTRODUCTION:
The study of the probabilistic orbital evolution of asteroids consists of two stages: construction of an initial confidence region and tracing of its evolution. The initial confidence region may be built by linear or nonlinear methods in depending on nonlinearity of the estimation problem. The main purpose of this paper is to obtain the nonlinearity coefficients for all Near-Sun asteroids and to study the orbital evolution of confidence regions built by linear and nonlinear methods for some asteroids.

NONLINEARITY COEFFICIENTS FOR ALL NEAR-SUN ASTEROIDS:
The objects of our study are asteroids with perihelion distance less than 0.15 AU. There are 51 such celestial bodies according to data from minor planet center site on June 2021. Nonlinearity was estimated on the base of parameter χ, that has been described in [1, 2]. This parameter shows deviation the level surface from ellipsoid. If $\chi < 0.01$ the problem is weak nonlinear and confidence region may be constructed as ellipsoid in six-dimension space of coordinates and velocity components. If $0.01 \le \chi < 0.1$ we can say about medium nonlinearity and if $\chi \ge 0.1$ than nonlinearity is powerful.

Table 1. The values of nonlinearity coefficients and data about observations for some asteroids.

Asteroid	χ	N	Δt, days
394130 2006 HY51	1.9	300	4784
2007 GT3	2.4	31	13
3200 Phaethon	3.4	5781	13454
137924 2000 BD19	1.1	779	8772
2007 PR10	1.1	54	4020
2017 TC1	4.5	54	22
2015 HG	8.7	27	7
2020 HE	1.1	41	6
2011 BT59	1.1	13	8
2019 VE3	2.2	20	3
2020 HY2	2.4	24	3
2015 EV	3.1	52	4
2013 HK11	5.1	22	6
2015 KO120	1.8	15	3

We estimated the parameter χ for all asteroid under consideration. Table 1 shows results for some asteroids: the nonlinearity parameter χ, number of observations N and arc length Δt. Our study shown that for the only asteroid 2015 KO120 the problem is powerful nonlinear, for six objects (from 2020 HE to 2013 HK11 in table 1) nonlinearity is medium, the other objects are characterized by weak nonlinearity. Nonlinearity coefficient depends on arc

length and number of observations. Usually, if asteroid was observed less than 10 days that nonlinearity is moderate or strong.

PROBABILISTIC ORBITAL EVOLUTION OF SOME ASTEROIDS:

To illustrate the differences between linear and nonlinear methods we studied the probabilistic orbital evolution of following asteroids with different values of the nonlinearity parameter: 2007 GT3, 2017 TC1, 2015 HG, and 2015 KO120. Table 2 contains information about orbit fitting process: number of observations N under use, the mean square error σ and the mean square error of the LSM (least square method) estimate $\sigma(x_0)$ and $\sigma(v_0)$ of the asteroid position vector and velocity respectively. We see that orbits of all asteroids under consideration are not reliably determined.

Table 2. The results of orbit fitting for some asteroids.

Asteroid	N	σ, ”	$\sigma(x_0)$, AU	$\sigma(v_0)$, AU
2007 GT3	31	0.548	2.3	1.5
2017 TC1	52	0.244	7.5	4.6
2015 HG	27	0.252	8.8	6.3
2015 KO120	15	0.449	8.4	1.8

For example, Fig. 1 presents the graphs of evolution for asteroid 2007 GT3: approaches to the Earth (a1, a2), the evolution of the eccentricity (b1, b2), and inclination to ecliptic plane (c1, c2). The nominal orbit is marked by black color, the confidence domains constructed by linear (a1, b1, c1) and nonlinear (a2, b2, c2) methods are shown by grey color. It should be noted that in linear method confidence domain is built as ellipsoid in six-dimension space of coordinates and velocity components, and we used the method of perturbed observations as nonlinear one [3]. We see that the confidence domain created by the nonlinear method is slightly bigger in the ends of interval under study, but difference is insignificant.

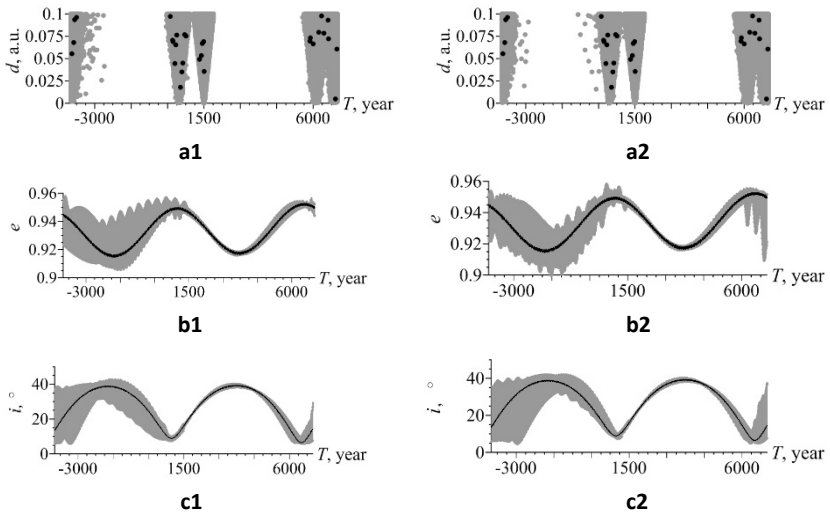


Fig. 1. 2007 GT3: approaches to the Earth (**a1**, **a2**), the evolution of the eccentricity (**b1**, **b2**), and the inclination to ecliptic plane (**c1**, **c2**).

CONCLUSION:

We estimated the nonlinearity for all asteroids with small perihelion distances. Our study shown that problem for almost all these objects is weak nonlinear, only six asteroids are characterized by medium nonlinearity, and for one asteroid nonlinearity is powerful.

The probabilistic orbital evolution demonstrated that for asteroids with moderate and strong nonlinearity we should use nonlinear methods. Even if nonlinearity is weak but initial confidence region is large than the nonlinear methods give more reliable prediction.

AKNOWLEDGMENTS:
The research was carried out within the state assignment of Ministry of Science and Higher Education of the Russian Federation (theme No. 0721-2020-0049)

REFERENCES:

[1] Syusina O.M., Chernitsov A.M., Tamarov V.A. Construction of confidence regions in problem on probabilistic study into motion of minor bodies of the solar system // Sol. Syst. Res. 2012. V. 46, I. 3. P. 195–207.
[2] Draper N.R., Smith H. Applied Regression Analysis. John Wiley & Sons, Inc. 1998. P. 706.
[3] Avdyushev V.A. Nonlinear methods of statistic simulation of virtual parameter values for investigating uncertainties in orbits determined from observations // Celest. Mech. 2011. V. 110(4). P. 369–388.

THE UMOV EFFECT IN THE NEAR-EARTH ASTEROIDS

M. Zheltobryukhov [1], E. Zubko [2], E. Chornaya [1,3], A. Kochergin [1], G. Kornienko [1], G. Videen [2,4]

[1] *Institute of Applied Astronomy of RAS, 10 Kutuzova Emb., Saint-Petersburg 191187, Russia, maxim.s.zheltobryukhov@gmail.com;*

[2] *Humanitas College, Kyung Hee University, 1732, Deogyeong-daero, Giheung-gu, Yongin-do 17104, South Korea;*

[3] *School of Natural Sciences, Far Eastern Federal University, 8 Sukhanova St., Vladivostok 690950, Russia;*

[4] *Space Science Institute, 4750 Walnut Street, Boulder Suite 205, CO 80301, USA*

KEYWORDS:
Observation, polarimetry, the Umov effect, asteroid (52768) 1998 OR2.

INTRODUCTION:
The Umov effect manifests itself as an inverse correlation between the linear polarization maximum of an object's scattered light P_{max} and its geometric albedo A. The Umov effect was demonstrated to hold in the lunar regolith [1]. As such, it presumably is applicable to regolith in asteroids. Thus, the Umov effect could help constrain the reflectivity of asteroids and, hence, determine their size from their apparent brightness. In this work, we infer the Umov-effect diagram of the near-Earth asteroids based on our previous results on asteroid (3200) Phaethon [2] and new polarimetric observations of asteroid (52768) 1998 OR2.

OBSERVATION:
Between April 10 and 28, 2020, We observed asteroid (52768) 1998 OR2 using the 0.5 m telescope (F = 1.62 m) located at the Ussuriysk Astrophysical Observatory, a division of the Institute of Applied Astronomy of RAS (code C15, Russia). We used the CCD detector *SBIG STX–16803* (resolution — 4096 × 4096, size of pixel - 9 μm), the *V* filter of the *Johnson photometric system* (efficient wavelength λ_{eff} = 0.551 μm and bandpass $\Delta\lambda$ = 0.088 μm), and a dichroic polarization filter (analyzer). The analyzer was rotated through three fixed position angles 0 °, + 60 °, and + 120 °, which allows a complete characterization of the degree of linear polarization as described in [3]. The obtained images have been processed using the *Image Reduction and Analysis Facility* (IRAF) software system for reduction and analysis of astronomical data. The data reduction includes dark frame subtraction, removal of cosmic ray events, flat field correction, and compensation of instrumental polarization.

The largest phase angle achieved in our polarimetric observations of the asteroid 1998 OR2 was as high as α = 77.4 ° where we detected polarization P = (14.42 ± 1.16) %. It is worth noting that, although α = 77.4 ° does not necessarily corresponds to the phase angle of polarization maximum α_{max}, the polarization of asteroids slightly varies at such large phase angles (e.g., [1]) and, hence, we consider P = (14.42 ± 1.16) % as a reasonably good constraint for P_{max} in the asteroid 1998 OR2. In what follows, we, therefore, set P_{max} = (14.42 ± 1.16) %.

RESULT AND DISCUSSION:
Fig. 1 demonstrates the Umov diagram obtained for 21 sites on the lunar surface measured at two wavelength, 0.65 μm and 0.42 μm (data adapted from [3]). As one can see here, all the data points merge in a single straight line. It is worth noting that a similar linear correlation between log(P_{max}) and log(A) was found in laboratory optical measurements of powder-like surfaces ([3, 4]), which are good structural analogs for planetary regolith. Moreover, the same linear correlation holds also for single-scattering cosmic dust particles [5].

It seems reasonable, therefore, to assume also a linear trend in the case of asteroids. Thus, the Umov diagram in asteroids could be constrained using two data points. One of them, corresponding to asteroids (3200) Phaethon

is shown with the red symbol in Fig. 1; whereas, the data point obtained from polarimetric observations of asteroid (52768) 1998 OR2 is shown here with the blue symbol. We note that in the case of asteroid (52768) 1998 OR2, the geometric albedo was computed using the Arecibo radar measurements of its geometric cross section [6] and absolute magnitude at $\alpha = 0$ ° reported in [7]. One needs to note, however, that the accuracy of the absolute magnitude could be further improved in future observations.

It is important to stress the Umov diagram inferred from the observations of two asteroids (black line in Fig. 1) appears remarkably parallel to the Umov diagram in the lunar regolith. However, the Umov diagram of asteroids requires further investigation via involving into consideration more asteroids of different taxonomic types. This is a goal for our future research.

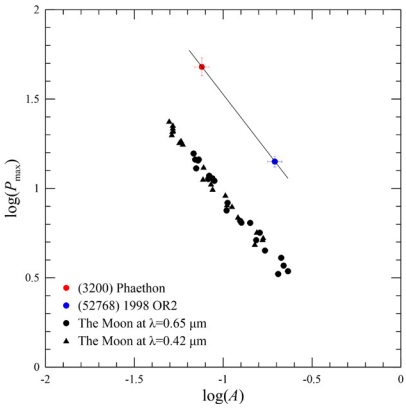


Fig. 1. The Umov effect inferred for two asteroids (red and blue symbols) versus that in the lunar regolith (black symbols).

REFERENCES:

[1] Shkuratov Yu., Opanasenko N. Polarimetric and photometric properties of the moon: Telescope observation and laboratory simulation 2. The positive polarization // Icarus. 1992. V. 99. P. 468–484.
[2] Zheltobryukhov M., Chornaya E., Kochergin A. et al. Umov effect in asteroid (3200) Phaethon // Astron. & Astrophys. 2018. V. 620. Art. ID: A179.
[3] Chornaya E., Zubko E., Luk'yanyk I. et al. Imaging polarimetry and photometry of comet 21P/Giacobini Zinner // Icarus. 2020. V. 337. Art. ID: 113471.
[4] Zubko N., Gritsevich M., Zubko E. et al. Optical measurements of chemically heterogeneous particulate surfaces // J. Quant. Spectrosc. Radiat. Transfer. 2016. V. 178. P. 422–431.
[5] Zubko E., Videen G., Zubko N., Shkuratov Yu. The Umov effect in application to an optically thin two-component cloud of cosmic dust // Mon. Not. Roy. Astron. Soc. 2018. V. 477. P. 4866–4873.
[6] http://www.naic.edu/~pradar/press/1998OR2.php.
[7] Devogèle M., Virkki A., Marshall S.E. et al. Heterogeneous surface of 1998 OR2 // Bull. Am. Astron. Soc. 2020. V. 52. I. 6. Abstract #415.04.

THE CASLEO POLARIMERIC SURVEY OF THE MAIN ASTEROID BELT

R. Gil-Hutton [1]
[1] *Planetary Science Group, San Juan National University and CONICET, Av. J. I. De la Roza oeste 590, J5402DCS, San Juan, Argentina, icardo.gil-hutton@conicet.gov.ar*

KEYWORDS:
Solar system, minor bodies, asteroids, main belt, polarimetry.

INTRODUCTION:
The radiation that we receive from any asteroid at visible wavelengths consists of partial polarized light produced by the scattering of the sunlight on the solid surface of the body. The polarization is usually found to be linear with its azimuth either normal or parallel to the scattering plane, which in the olar system is the plane containing the asteroid, the Sun, and the Earth at the epoch of observation.

For all the asteroids measured so far the linear polarization is more significant than the circular and the state of linear polarization varies owing to a complex interplay of surface properties like the composition, roughness, and other physical properties of the target and also depends on the illumination conditions. In general, the linear polarization is found with its azimuth either normal or parallel to the scattering plane, which in the solar system is the plane containing the asteroid, the Sun, and the Earth at the epoch of observation.

The variation of the degree of linear polarization as a function of the phase angle, which is the angle between the directions to the Sun and to the observer as seen from the object, produces the so-called phase-polarization curve (see Fig. 1). This curve is described by some polarimetric parameters that provide information about the properties of the surface [1–5].

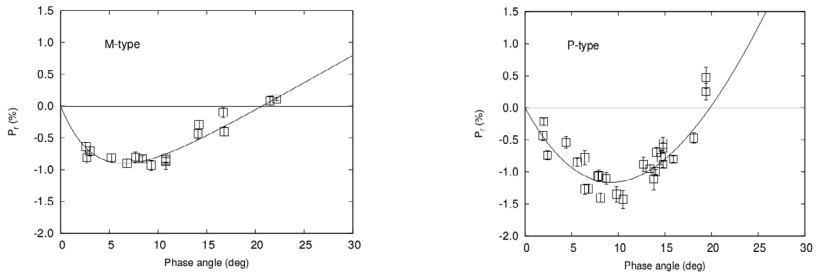


Fig. 1. Polarimetric observations of M- and P-type asteroids [6]. In both cases the best fit found for the polarization curve is also shown.

Polarimetry is one of several observational techniques used to obtain information about the light scattering phenomena and the rough surfaces of asteroids, but it was also used to study the albedo heterogeneity]of asteroid surfaces [7], active main-belt asteroids [8], and targets of space missions [9] among other cases.

Although polarimetry provides useful information about the physical properties of the asteroid surface, polarimetric observations of these objects are not easy to obtain. As a consequence, the database of asteroid polarimetric measurements was very small until about 1990 and very few objects had their polarimetric parameters well determined. Since 2003 we have made an extensive effort to conduct polarimetric observations at Complejo Astronómico El Leoncito (CASLEO), Argentina; the main objective has been to increase the available polarimetric database of main-belt asteroids. The first epoch of this survey ended in 2012 and a second epoch started in 2013 using new and more sensitive equipment.

This survey provided more than 4000 polarimetric measurements of main-belt asteroids, including objects not observed before, and has the advantage of being a homogeneous dataset that has always been observed and reduced following the same procedures. These data, combined with results previously published, were used to obtain phase-polarization curves and polarimetric parameters of good quality for more than 140 main-belt asteroids [10]

In this talk I will present some recent achievements in asteroid polarimetry obtained with the survey data and the role of this technique in the overall scenario of asteroid science.

REFERENCES:

[1] Dollfus A., Wolff M., Geake J.E., Dougherty L.M., Lupishko D.F. 1989, in Asteroids II, ed. R.P. Binzel, T. Gehrels, M.S. Matthews. University of Arizona Press. P. 594–616.
[2] Muinonen K., Piironen J., Shkuratov Y.G., Ovcharenko A., Clark B.E. 2002a, in Asteroids III, ed. W.F. Bottke, Jr., A. Cellino, P. Paolicchi, R.P. Binzel, University of Arizona Press. P. 123–138.
[3] Kaasalainen S., Piironen J., Kaasalainen M., et al. 2003, Icarus V. 161. P. 34.
[4] Penttilä A., Lumme K., Hadamcik E., Levasseur-Regourd A.-C. 2005. A&A. V. 432. P. 1081.
[5] Gil-Hutton R.. 2007. A&A. V. 464,P. 1127.
[6] Cañada-Assandri M., Gil-Hutton R., & Benavidez P. 2012. A&A. P. 542. V. a11.
[7] Masiero, J. 2010, Icarus. V. 207. P. 795.
[8] Bagnulo S., Tozzi G.P., Boehnhardt H., Vincent J.-B., Muinonen K. 2010, A&A. 514. A99.
[9] Belskaya I., Fornasier S., Krugly Yu.N., et al. 2010, A&A. 515. A29.
[10] Gil-Hutton R., García-Migani E. 2017. A&A. V. 607. P. A103.

USING OPTIMAL NUMBER OF ASTEROIDS ON THE RESONANCE ORBITS TO CONSTRUCT THE PLANETARY DEFENSE SHIELD

V.A. Zubko [1], D.W. Dunham [2], N.A. Eismont [1], K.S. Fedyaev [1], A.A. Belyaev [1]
[1] *Space Research Institute of Russian Academy of Science, 84/32 Profsoyuznaya Str., 117997, Moscow, Russia;*
[2] *KinetX, Inc., 7913 Kara Ct, Greenbelt, MD 20770, USA*

Keywords:
Planetary defense shield, resonant orbits, asteroids, asteroid impact, optimization.

The current research focuses on the methods allowing use of small asteroids targeted to dangerous celestial objects in order to deflect them from collision with the Earth. This approach as a level of concept was proposed about ten years ago. As a tool for directing a projectile asteroid to the approaching hazardous one, a gravity assist maneuver was proposed. Unanswered questions include the one related to the possibilities to use a minimum number of asteroids intended to be applied as projectiles for any coming hazardous celestial body. In an ideal case one can expect only one projectile asteroid as a sufficient number required for the task solution. Also, an important point is estimation of the minimum allowed time interval between detection and cataloging/characterizing the target asteroid and hitting it. In the earlier published papers, it was proposed to use the Earth resonance orbit with 1 : 1 orbital period ratio as a parking trajectory for the projectile asteroid.

So, we have on hand an asteroid in a resonance orbit waiting for the moment when it would be commanded to start operations to send it to intercept an approaching dangerous celestial body. These operations consist of one or more gravity assist maneuvers near Earth, intended to transfer finally the projectile asteroid to a trajectory hitting the target asteroid. With enough free parameters, that is our case, one can state that it is possible to reach any direction of hyperbolic velocity vector with respect to Earth. With the mentioned required duration of fulfillment of the commanded maneuver sequence, possible scenarios of events were explored on the basis that a celestial body coming from any direction is intercepted well before it might hit the Earth. The surface of interception points are positions that the projectile asteroid can reach after the last gravity assist maneuver sending it to the target. It changes with time, expanding till an inevitable meeting with the target. In the paper the results of modeling the scenario with real asteroids and virtual hazardous objects are presented. It is explained in the paper how to build the mentioned surface as a defense shield in such a way that avoids holes that would permit bypassing it to impact the Earth. In addition, it is estimated how, by increasing the number of asteroids in the defense shield, that influences the characteristics of the surface of interception. Also, possibilities were explored to increase the number of maneuvers versus the cost of decreasing the number of projectile asteroids or broadening the time interval needed for the defense operations.

CALCULATING PERIOD AND THE ROTATION SPEED OF THE ASTEROIDS BY USING OBSERVATIONAL DATA COLLECTION

M. Hadizadeh [1], A. Poro [1], E. Paki [1], et al.
[1] *International Occultation Timing Association Middle East section, Iran, info@iota-me.com*

KEYWORDS:
Asteroid, period, rotation, diameter.

INTRODUCTION:
We studied 12 asteroids, (3285) Ruth Wolfe, (1035) Amata, (505) Cava, (1320) Impala, (1148) Rarahu, (176) Iduna, (1494) Savo, (2709) Sagan, (164) Eva, (4606) Saheki, (122) Gerda, and (48) Doris. The data selected from the ALCDEF database based on the short period asteroids. We calculate the orbital rotation speed, and rotation period, and also analysis of 33 light curves with Period4 software. Therefore, we show the place of each asteroid on the frequency-diameter diagram, and all asteroids are below the limit line.

COLLISIONS OF PLANETESIMALS WITH THE EARTH AND THE MOON

S.I. Ipatov [1], M.Ya. Marov [1]
[1] *Vernadsky Institute of Geochemistry and Analytical Chemistry of Russian Academy of Sciences, Moscow, Russia, siipatov@hotmail.com, marovmail@yandex.ru*

KEYWORDS:
Planetesimals, migration, velocities of collisions, Earth, Moon, giant planets.

INTRODUCTION:
The problem of migration of celestial bodies in the Solar System is important for understanding of the formation and evolution of the Solar System [1]. Earlier in our studies of migration of bodies to the Earth and the Moon we paid the main attention to the probabilities of collisions of bodies with these celestial objects. The considered bodies migrated from different distances from the Sun. In this presentation we discuss the times elapsed before collisions of bodies-planetesimals with the Earth and the characteristic velocities of their collisions with the Earth and the Moon.

PROBABILITIES OF COLLISIONS OF PLANETESIMALS WITH THE EARTH:
The average probability of collisions of planetesimals with the Earth was estimated to be $p_E = 2 \times 10^{-6}$ for planetesimals from the Jupiter and Saturn zones [2]. For bodies that initially had orbits of Jupiter-family comets p_E was higher than 4×10^{-6} [3–6]. The p_E values were, on average, smaller for greater initial values of the semi-major axes a_o of orbits at $5 \le a_o \le 40$ AU [7–8].

At $p_E = 2 \times 10^{-6}$ and with the assumption that the total mass of planetesimals in the Jupiter and Saturn feeding zone was $100m_E$ (where m_E is the Earth's mass) [9–10], we found out that the total mass of planetesimals that have fallen onto the Earth was $2 \times 10^{-4} m_E$. About the same amount of bodies could collide with the Earth from the outer asteroid belt and from behind the Saturn's orbit. If the ice made up a half of the mass of this material, then the total ice mass delivered to the Earth from behind the snowline was equal to the total mass of the Earth's oceans ($\sim 2 \times 10^{-4} m_E$). Similar conclusion was made in 2001 in [11–12], based on the studies of migration of Jupiter-crossing objects presented in [13]. Estimated ice amounts in comets are no higher than 33 %. However, some authors believe that the primary planetesimals may have contained more ice than it is now found in comets. Some fraction of water was lost at collisions, especially with the Moon. Therefore, the amount of water accumulated by the terrestrial planets and the Moon may have been lower than the water amount delivered to these celestial objects.

TIMES ELAPSED BEFORE COLLISIONS OF BODIES WITH THE EARTH:
Bodies initially located at different distances from the Sun reached the Earth at different times. Former Jupiter-crossing bodies could become Earth-crossers within the first million years. The migration time of bodies from the feeding zone of Uranus and Neptune depends on when large embryos of these planets appeared in this zone. The main changes in elements of the orbits of the embryos of the giant planets took place within no more than 10 million years [9–10]. At present orbits and masses of the planets, some bodies from the Uranus and Neptune zone may have fallen onto the Earth in more than 20 million years. At an initial value a_o of the semi-major axis of the body's orbit within the range of 4 to 5 AU, most bodies fell onto the Earth within 10 million years. Some bodies with $3 \le a_o \le 3.7$ AU could fall onto the Earth in billions of years, and such bodies could be involved in the late heavy bombardment (LHB) of the Earth and the Moon.

PROBABILITIES OF COLLISIONS OF BODIES WITH THE MOON:
For planetesimals in the feeding zone of the terrestrial planets [14] the ratio r_{EM} of the number of planetesimals colliding with the Earth to that with the Moon mostly varied from 20 to 40. Planetesimals initially more distant from the Earth's orbit came to it from more eccentric orbits, and their

r_{EM} ratio was smaller than that for more close orbits with small eccentricities. Our recent calculations of the migration of the bodies from $3 \le a_o \le 5$ AU may lead to the conclusions that $16.4 \le r_{EM} \le 17.4$ in approximately 80 % of the calculation variants. In other calculation variants, the r_{EM} ratio could be equal to 14.56 and 17.89. The r_{EM} ratio averaged over 2000–2500 bodies varied mainly from 16.47 to 16.72 in each calculation set for planetesimals with $5 \le a_o \le 12$ AU. The actual ratio of the Earth's and Moon's radii is 3.667, and the squared ratio is 13.45. Because the Earth's gravitational influence is greater than that of the Moon, the obtained r_{EM} value is greater than 13.45.

VELOCITIES OF COLLISIONS OF BODIES WITH THE EARTH AND THE MOON:

Based on the r_{EM} ratio of the number of planetesimals colliding with the Earth and the Moon, it is possible to estimate the characteristic velocities v_{relE} (relative to the Earth) of planetesimals when they enter the Earth's sphere of action. In [15] we obtained

$(v_{relE} / v_{parE})^2 = [r_{EM} (v_{parM} / v_{parE})^2 (r_M / r_E)^2 - 1] / [1 - r_{EM} (r_M / r_E)^2]$, where r_M and r_E are the Earth's and Moon's radii, and v_{parM} and v_{parE} are the parabolic velocities at the Earth's and Moon's surface, respectively.

Using the r_{EM} values presented in [15], we estimated the characteristic collision velocities of bodies with the Earth and the Moon for some cases. For planetesimals with $0.9 \le a_o \le 1.1$ AU and with relatively small initial eccentricities (at $30 \le r_{EM} \le 40$), the characteristic velocities of their collisions with the Earth lied mostly within the range of 13 to 15 km/s, and the collision velocities with the Moon were 8 to 10 km/s. For planetesimals coming from other parts of the feeding zone of the terrestrial planets (at $20 \le r_{EM} \le 40$), the scatter of the characteristic velocities of collisions of the planetesimals with the Earth was mostly within the range of 13 to 19 km/s, and that with the Moon was 8 to 16 km/s. For most bodies with $a_o \ge 3$ AU (at $16.4 \le r_{EM} \le 17.4$), the analogous scatter of the collision velocities was 23 to 26 km/s for the Earth and 20 to 23 km/s for the Moon. However, the range of velocities of all bodies from this zone (at $14.56 \le r_{EM} \le 17.89$) was wider: 22 to 39 km/s for the Earth and 19 to 38 km/s for the Moon.

The characteristic collision velocities of planetesimals that initially located relatively close to the orbit of the Earth's embryo, with the Earth's and Moon's embryos, which masses were tenfold smaller than the present masses of these celestial objects, were generally within the range of 7 to 8 km/s for the Earth's embryo and 5 to 6 km/s for the Moon's embryo. For planetesimals coming from more distant (relative to the Earth's orbit) regions of the feeding zone of the terrestrial planets, the characteristic velocities ranged from 9 to 11 km/s for collisions with the Earth's embryo and from 7 to 10 km/s for collisions with the Moon's embryo.

ACKNOWLEDGEMENTS:

The studies of collisions of bodies with the Earth were carried out as a part of the state assignments of the Vernadsky Institute of RAS № 0137-2019-0004. The studies of collisions of bodies with the Moon were supported by the Russian Science Foundation, project 21-17-00120, https://rscf.ru/project/21-17-00120/.

REFERENCES:

[1] Marov M. The Formation and Evolution of the Solar System. Oxford Research Encyclopedia of Planetary Science (Eds. P Read et al.). 2018. Oxford: Oxford University Press, id.2.

[2] Marov M.Ya., Ipatov S.I. Delivery of water and volatiles to the terrestrial planets and the Moon // Solar System Research. 2018. V. 52. No. 5. P. 392–400. https://arxiv.org/ftp/arxiv/papers/2003/2003.09982.pdf.

[3] Ipatov S.I., Mather J.C., Migration of trans-Neptunian objects to the terrestrial planets // Earth, Moon, and Planets. 2003. V. 92. P. 89–98. http://arXiv.org/format/astro-ph/0305519.

[4] Ipatov S.I., Mather J.C. Migration of Jupiter-family comets and resonant asteroids to near-Earth space // Annals of the New York Academy of Sciences. 2004. V. 1017. P. 46–65. http://arXiv.org/format/astro-ph/0308448.

[5] Ipatov S.I., Mather J.C. Comet and asteroid hazard to the terrestrial planets // Advances in Space Research. 2004. V. 33. P. 1524–1533. http://arXiv.org/format/astro-ph/0212177.
[6] Ipatov S.I., Mather J.C. Migration of small bodies and dust to near-Earth space // Adv. Space Research. 2006. V. 37. No. 1. P. 126–137. http://arXiv.org/format/astro-ph/0411004.
[7] Marov M.Ya., Ipatov S.I. Water inventory from beyond the Jupiter orbit to the terrestrial planets and the Moon // Proc. IAU Symp. No. 345 "Origins: from the Protosun to the First Steps of Life", ed. by Bruce G. Elmegreen, L. Viktor Tóth, Manuel Gudel, Proc. IAU. Vol. 14. Symp. S345, Cambridge University Press. 2020. P. 164–167. doi:10.1017/S1743921319001479.
[8] Ipatov S.I. Migration of planetesimals from beyond Mars' orbit to the Earth. 14th Europlanet Science Congress 2020, https://doi.org/10.5194/epsc2020-71.
[9] Ipatov S.I. Migration of bodies in the accretion of planets // Solar System Research. 1993. V. 27. No. 1. P. 65–79. https://www.academia.edu/44448077/Migration_of_bodies_in_the_accretion_of_planets.
[10] Ipatov S.I. Migration of celestial bodies in the Solar system. Moscow. URSS. 2000, 2021. P. 320. In Russian. https://doi.org/10.17513/np.451.
[11] Marov M.Ya., Ipatov S.I. Volatile inventory and early evolution of planetary atmospheres // Collisional processes in the solar system, eds. M.Ya. Marov and H. Rickman, Astrophysics and space science library. 2001. V. 261, Dordrecht: Kluwer Academic Publishers, P. 223–247.
[12] Ipatov S.I. Comet hazard to the Earth // Advances in Space Research, 2001. V. 28, No. 8. P. 1107–1116. http://arXiv.org/format/astro-ph/0108187.
[13] Ipatov S.I., Hahn G.J. Orbital evolution of the P/1996 R2 and P/1996 N2 objects // Solar System Research. 1999. V. 33. No. 6. P. 487–500.
[14] Ipatov S.I. Probabilities of collisions of planetesimals from different regions of the feeding zone of the terrestrial planets with the forming planets and the Moon // Solar System Research. 2019. V. 53. No. 5. P. 332–361. http://arxiv.org/abs/2003.11301.
[15] Marov M.Ya., Ipatov S.I. Formation of the Earth and the Moon: Influence of small bodies // Geochem. Int. 2021. V. 66. No. 11. P. 1–8.

HOW THE THIRD FORCE OF DIAMAGNETIC EXPULSION AND THE MECHANISM OF MAGNETIC ANISOTROPIC ACCRETION ALLOWED SATURN TO CREATE RINGS BY ITSELF

V.V. Tchernyi [1], S.V. Kapranov [2]
[1] *Modern Science Institute, SAIBR. Moscow, Russia, chernyv@mail.ru;*
[2] *A.O. Kovalevsky Institute of Biology of the Southern Seas, RAS, Moscow, Russia, sergey.v.kapranov@yandex.ru*

KEYWORDS:
Saturn rings origin, space magnetism, space diamagnetism, magnetic anisotropic accretion, ice of rings, space ice.

For the first time we propose a new physical mechanism of how Saturn could create rings on its own without external action using its own magnetic field that once appeared. There is a reason for this. After four NASA missions to Saturn: Pioneer-11 (1979), Voyager-1 (1980), Voyager – 2 (1981), and the outstanding Cassini probe (2004–2017), there is no definitive consensus on the origin, evolution, and age of Saturn's rings since G. Galilei first saw them in 1610. J.K. Maxwell proved that rings consist of particles (1856), G.P. Kuiper predicted that particles are made up of ice (1947), and the Cassini mission (2004–2017) confirmed that ring particles are 93 % ice. The well-known explanations of the emergence of particles in Saturn's rings are based on the ideas of a gravitational defragmentation of a massive body that approached Saturn, tidal disruption of a comet, etc, followed by the collision-induced collapse of the spinning particle cloud. If we observe these theories from the scenario which is following from classical V. Safronov theory of the evolution of protoplanetary cloud we can see they missing how the sombrero disk of rings is so perfectly made up of separate particles, with the fine ring structure and extraordinary flatness. Also, if we compare the thickness-to-length ratio of a sheet of A4 paper with that of Saturn's ring system, then the relative thickness of the rings will be a thousand times smaller. It is amazing how such a thin icy disk of huge diameter hangs in outer space. The questions arise as to whether all possible Saturn's ice particles interactions in the planetary cloud have been taken into account in the previous theories and whether a possible role of other interactions in the existence of the rings has not been overlooked. Based on Cassini data it was found the deuterium to hydrogen isotopic ratio for the ice of Saturn's rings is the same as for the ice on Earth. Studying type of ice on the Earth we found Ice of the XI type has stable parameters at the temperature of the rings and it is diamagnetic. We assert that the angular momentum conservation within gravitational interaction is not the only reason for the collision-induced flattening of the spinning cloud of particles around Saturn. That's why we try to understand how the diamagnetism of ice particles of the protoplanetary cloud can affected the origin of rings. A new mechanism of the rings origin includes the appearance of an additional third force — the force of diamagnetic expulsion of a diamagnetic ice particle after the emergence of the magnetic field of Saturn and the scenario of magnetic anisotropic accretion. After the emergence of Saturn's magnetic field and diamagnetic expulsion of ice particles, all the chaotic orbits of the particles inside the planetary nebula shifted to the plane of the magnetic equator, where the minimum of magnetic energy of the particles is observed. The equation for the polar angle of a particle with a constant orbit radius in the superposition of the spherically symmetric (gravitational) and axisymmetric (magnetic) fields has a singular solution at $\pi/2$, which explains the extraordinary flatness of the rings. As result, the cloud of particles surrounding Saturn ended up by collapsing into a disk with the particles orbiting in the planet's magnetic equator plane. The solution of the equations of motion of particle in the gravitational field only yielded the angular velocity components whose ratio, under an assumption of particle collisions occasionally happening, turned out to be extremely

unlikely, which spoke against the purely gravitational approach to Saturn's rings. Thus, a host of particles formed the disk-shaped system of rings. The gravitational force in the orbit of the particle is balanced by the centrifugal force and the force of diamagnetic expulsion. Every particle on the magnetic equator comes to a stable position, and it prevents its horizontal and vertical shift. Magnetic field density gradient repels particles from each other; it also makes the gaps between rings and forms the rigid thin structure of separated rings. The particles are trapped within three-dimensional magnetic well. We started with solving the problem of magnetization and, consequently, the potential energy of a spherical ice particle in the magnetic field of Saturn, which solution was later used to describe the dynamics of a particle in the superposition of the gravitational and magnetic fields of the planet. As it follows from modeling the ring system as a disk-like structure, an important role in the genesis and stability of the ring system is due to the axisymmetric magnetic field and its role increases as the particle size decreases. The other theories of the rings origin are considered earlier by other authors may contribute some features to the final picture of the rings. In the proposed theory, the famous knowledge about their contribution to the origin of rings of Saturn is not denied, but complemented by the fundamental role of the Saturn's magnetic field with appearance of the third force of diamagnetic expulsion and additional mechanism of magnetic anisotropic accretion.

REFERENCES:

[1] V.V. Tchernyi, S.V. Kapranov. The third force of diamagnetic expulsion and the mechanism of the magnetic anisotropic accretion of the origin of Saturn's rings. https://arxiv.org/abs/2104.03967. 17 May, 2021.

[2] V.V. Tchernyi, S.V. Kapranov. To the problem of the properties of Ice of the Saturn's rings particles. 238 Annual Meeting of the American Astronomical Society. 7–9 June 2021. Session: Circumstellar Disks and The Solar System. 316.

STUDY OF PLUTO'S ATMOSPHERE BASED ON 2020 STELLAR OCCULTATION LIGHT CURVE RESULTS

F. Najafi Kodini [1], A. Poro [1], F. Ahangarani Farahani [1], M. Bahraminasr [1], M. Hadizadeh [1], M. Rezaee [1], M. Seifi Gargari [1]
[1] *The International Occultation Timing Association Middle East section, Iran, info@iota-me.com*

KEYWORDS:
Occultations, planets and satellites, atmospheres, Kuiper belt objects, individual, Pluto.

INTRODUCTION:
On 6 Jun 2020, Pluto's stellar occultation was successfully observed at a ground-based observatory and Pluto's atmospheric parameters were investigated. We used an atmospheric model of Pluto (DO15), assuming a spherical and transparent pure N2 atmosphere. Using ray-tracing code the stellar occultation light curve was satisfactorily fitted to this model. We found that Pluto's atmospheric pressure at the reference radius of 1215 km is µbar. Our estimated pressure shows a continuation of the increasing pressure studied in 2016 consistent with a seasonal volatile transport model. We concluded that the N2 condensation processes in the Sputnik Planitia glacier are increasing due to the heating of the N2 ice in this basin. This study's result was shown on the diagram of the annual evolution of atmospheric pressure.

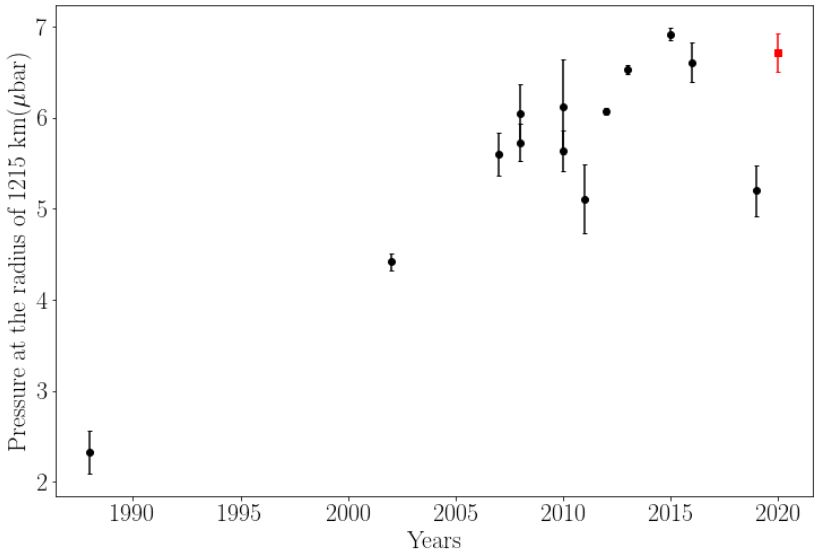


Fig. 1. Pluto's atmospheric pressure at the reference radius of R = 1215 as a function of time. The red square dot is for this study. Black dots show the other atmospheric pressure obtained from 1988–2019 stellar occultation measurements with their error bars.

DUST DYNAMICS AT THE MOON: LEVITATION OR LOFTING

S.I. Popel [1], A.P. Golub' [1], A.I. Kassem [2,3], L.M. Zelenyi [1]

[1] *Space Research Institute of the Russian Academy of Sciences (IKI), 84/32 Profsoyuznaya Str, Moscow 117997, Russia;*

[2] *Moscow Institute of Physics and Technology (State University), Institutskiy per. 9, Dolgoprudnyi, Moscow region 141700, Russia;*

[3] *Faculty of Science, Mansoura University, 60 Elgomhoria str., Mansoura 35516, Egypt*

KEYWORDS:
Dust and dusty plasmas, lunar missions, dust dynamics, dust levitation, dust lofting, nonstationary processes, dust particle charging, damping of oscillations.

INTRODUCTION:

Dust and dusty plasmas at the Moon are actively studied now [1, 2]. The Luna – 25, Luna – 26, Luna – 27, etc., missions are under preparation in Russia. The landers of the Luna – 25 and Luna – 27 spacecrafts will assumingly be equipped with instruments for the study of the properties of dust and dusty plasma at the surface of the Moon. The NASA mission LADEE (Lunar Atmosphere and Dust Environment Explorer) [3] launched in 2013 studied the dusty plasma in a wide range of altitudes above the Moon by means of observations from orbit.

In this context, the study of the dusty plasma near the surface of the Moon becomes important. The dusty plasma system in the surface layer over the illuminated part of the Moon was described in [4] within a self-consistent model. The model proposed in [4] was not used to describe nonstationary processes occurring, e.g., because of the time finiteness of the daytime on the Moon. In this work, we attempt to determine the consequences of the time finiteness of the daytime on the Moon, which is estimated as half the period of its revolution about the axis, i.e., of the order of 10^6 s, for the description of the dusty plasma near the surface of the Moon. In addition, it is well known [5–7] that processes associated with the variation of charges of dust particles in the dusty plasma are often significantly nonequilibrium, and the role of anomalous dissipation, which is caused by processes associated with variation of charges of dust particles, is often decisive. One of the aims of this work is to analyze the role of variation of the charges of dust particles in the processes of formation of the dusty plasma near the surface of the Moon.

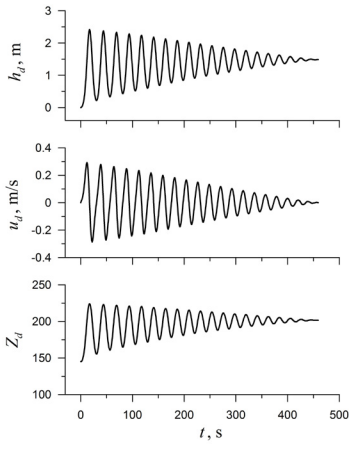


Fig. 1. Parameters characterizing the trajectory of the dust particle with the radius $a = 105$ nm and with a variable charge over the surface of the Moon at $\Theta = 87$ °: rising altitude h_d, velocity u_d, and charge number Z_d.

DUST PARTICLE DYNAMICS:

The behavior of dust particles in the near-surface layer is described by the equations for their dynamics and charging. Calculations allow, in particular, determining the parameters of the trajectories of dust particles. Figure 1 shows the parameters characterizing the motion of a dust particle with the radius $a = 105$ nm and the charge $q_d = Z_d e$ (where e is the elementary charge) for the subsolar angle $\Theta = 87$ °. One can see a significant damping of oscillations about the equilibrium position $h_{d0} = 148$ cm, $u_{d0} = 0$, $Z_{d0} = 202$. Here, h_d and u_d are the rising altitude and velocity, respectively. The period of oscillations is 26.8 s. Figure 2 shows the same parameters as in Fig. 1, but they were obtained under the assumption of the constant charge number $Z_d = Z_{d0} = 202$. It is seen that oscilla-

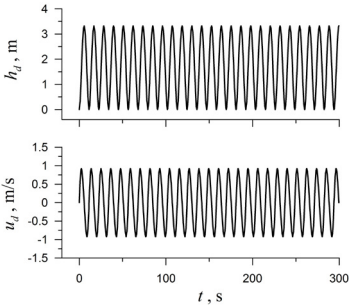


Fig. 2. Same as in Fig. 2, but for the dust particle with the radius a = 105 nm and with a constant charge.

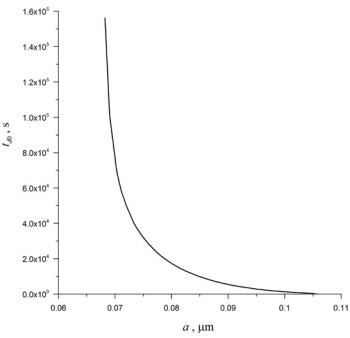


Fig. 3. Characteristic damping time t_{d0} of oscillations of the dust particle versus its radius at Θ = 87 °.

tions about the equilibrium position are undamped. Thus, the damping of oscillations of the dust particle over the surface of the Moon is related to variations of its charge in agreement with concepts of anomalous dissipation caused by processes associated with the variations of the charges of dust particles [5–7].

The characteristic damping time t_{d0} of oscillations of the dust particle can be defined as the time beginning with which all subsequent oscillations of $h_d(t)$ have the maximum rising altitude of the dust particle over the surface of the Moon below h^* determined from the relation

$$\ln\left(\frac{h_{d,max}-d_{d0}}{h^*-h_{d0}}\right)=1$$

where $h_{d'}$ max is the maximum of the function $h_d(t)$ for the first oscillation. The dependence of the characteristic damping time t_{d0} of oscillations of the dust particle on its radius is shown in Fig. 3.

It is noteworthy that $t_{d0} < 10^6$ s for a wide range of radii of dust particles (from 68 to 105 nm). This means that the damping time of oscillations for most (~ 83 %) of the dust particles with radii larger than 68 nm rising over the surface of the Moon because of the photoelectric and electrostatic processes is shorter than the daytime; i.e., most of the dust particles above the lunar surface can be considered as "levitated" those. For the dust particles with the sizes smaller than 68 nm the nonstationarity is manifested during almost entire day on the Moon. Thus such small particles can be treated as "lofted" those. The formation of the dusty plasma caused by photoelectric and electrostatic processes in the near-surface layer over the illuminated part of the Moon occurs, as in the stationary case [4], when the subsolar angle is larger than about 76° because, for a particle to rise, the electrostatic force repulsing the particle from the surface of the Moon should exceed the gravitational force. The levitated dust particles can move toward the smaller subsolar angles. This effect is caused by the action of the magnetic field and is significant when the Moon is inside the magnetotail of the Earth.

SUMMARY:

To summarize, we have shown that the formation of the dusty plasma system in the near-surface layer over the illuminated part of the Moon has a nonstationary character. Variations of the charges of dust particles result in the damping of their oscillations above the surface of the Moon. This allows us to consider larger dust particles with the sizes from 68 to 105 nm as "levitated" those, and smaller dusts (with the sizes < 68 nm) as "lofted" those. The effect of transport of the levitated dust particles toward equator is possible due to the action of the magnetic field when the Moon is inside the magnetotail of the Earth.

ACKNOWLEDGMENTS:

This work was supported in part by Theoretical Physics and Mathematics Advancement Foundation "BASIS" (grant "Leader").

REFERENCES:

[1] Popel S.I., Golub' A.P., Zelenyi L.M., Dubinskii A.Yu. Lunar dust and dusty plasmas: Recent developments, advances, and unsolved problems // Planet. Space Sci. 2018. V. 156. P. 71–84.

[2] Zelenyi L.M., Popel S.I., Zakharov A.V. Dusty plasma at the Moon. Challenges of modeling and measurements // Plasma Phys. Rep. 2020. V. 46. No. 5. P. 527–540.
[3] Popel S.I., Golub' A.P., Zelenyi L.M., Horányi M. Impacts of fast meteoroids and a plasma-dust cloud over the lunar surface // JETP Lett. 2017. V. 105. No. 10. P. 635–640.
[4] Popel S.I., Kopnin S.I., Golub' A.P., et al. Dusty plasma at the surface of the Moon // Solar Syst. Res. 2013. V. 47. No. 6. P. 419–429.
[5] Popel S.I., Golub' A.P., Losseva T.V. Dust Ion-Acoustic Shock-Wave Structures: Theory and Laboratory Experiments // JETP Lett. 2001. V. 74. No. 7. P. 362–366.
[6] Popel S.I., Andreev S.N., Gisko A.A., et al. Dissipative Processes during the Propagation of Nonlinear Dust Ion-Acoustic Perturbations // Plasma Phys. Rep. 2004. V. 30. No. 4. P. 284–298.
[7] Popel S.I., Losseva T.V., Golub' A.P., et al. Dust Ion-Acoustic Shocks in a Q Machine Device // Contrib. Plasma Phys. 2005. V. 45. No. 7. P. 461–475.

IONIZATION PROPERTIES OF DUSTY MARTIAN IONOSPHERE

Yu.S. Reznichenko [1, 2], A.Yu. Dubinskii [1], S.I. Popel [1]
[1] *Space Research Institute, Russian Academy of Sciences, Moscow 117997, Russia, nfkpb@bk.ru;*
[2] *Moscow Institute of Physics and Technology, Institutskiy Pereulok 9, Dolgoprudny, Moscow Region 141701, Russia, dvju@yandex.ru.*

KEYWORDS:
Dusty plasmas, dust clouds, dust particles, electrons, ions, Mars, ionosphere.

The planetary ionosphere dusty plasmas have been intensively exploring since 1990s [1–4]. Nowadays there is also a high interest in Mars exploration. For example, the spacecraft Mars Science Laboratory Curiosity has recently taken photos of dust clouds (these clouds, presumably, consist of solid carbon dioxide), located at altitudes more than 60 km in Martian ionosphere. Previously in [5, 6] we have presented a theoretical description of possible formation mechanism of such dust structures. In this paper we calculate the typical values of dust particle sizes and charges in such clouds. Also we study ionization properties of dusty Martian ionosphere and explore how dust particles influence the number densities of electrons and ions.

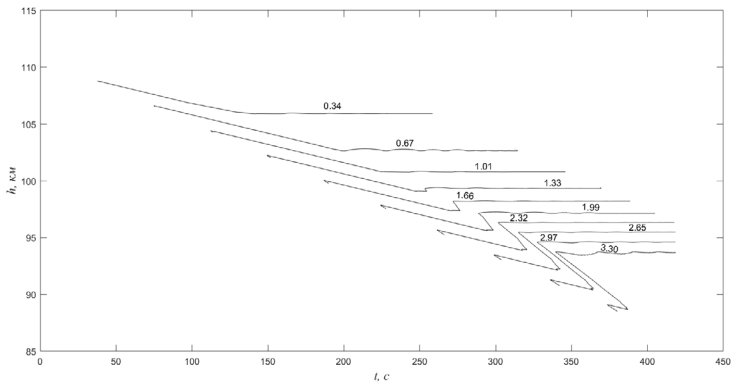


Fig. 1. Sedimentation of a dust cloud initially constituting the model rectangular profile at altitudes of 110–120 km. The initial size of the dust particles in the cloud is 10 nm. The particle sizes expressed in μm are presented above the curves.

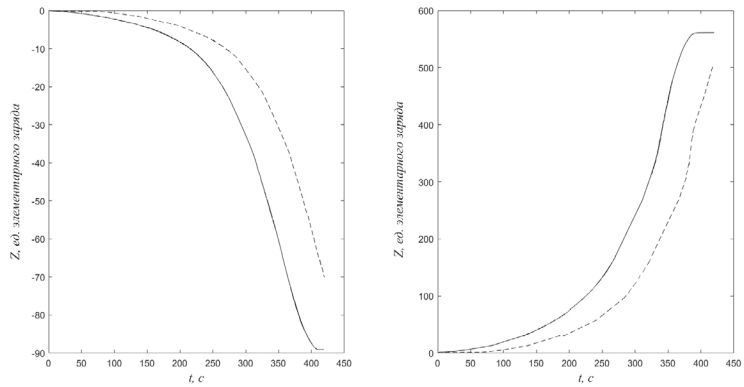


Fig. 2. Time dependence of the dust particle charge. The left panel corresponds to the absence of the photoelectric effect, while the right one to its presence.

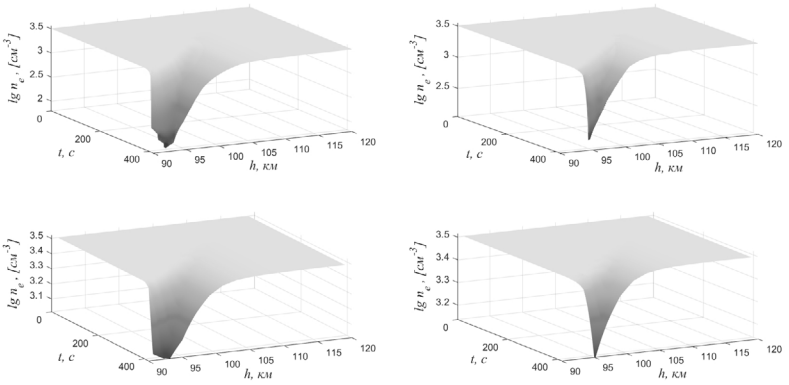


Fig. 3. The electron number density versus time and height for the nighttime conditions in the process of sedimentation of the dust layer.

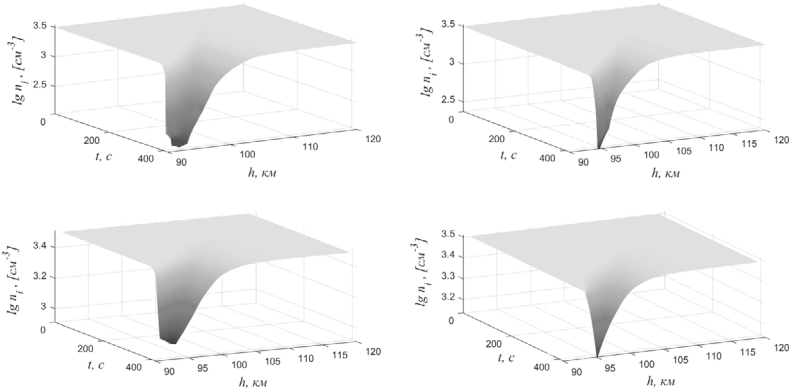


Fig. 4. The ion number density versus time and height for the nighttime conditions in the process of sedimentation of the dust layer.

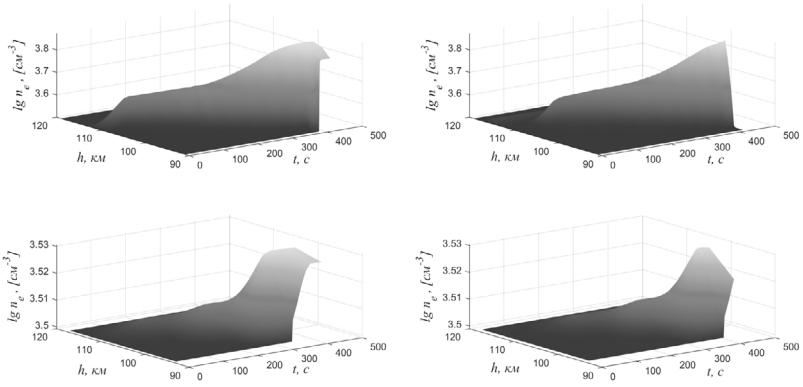


Fig. 5. The electron number density versus time and height for the daytime conditions in the process of sedimentation of the dust layer.

We find that all dust particles in the cloud reach sizes of about 0.3–3.5 μm. Under night conditions (the absence of the photoelectric effect) dust grains acquire negative charges ($|Z_d| \sim 10$) because of the influence of fluxes

of electrons and ions on dust particles. The number densities of electrons and ions in this case decrease because of extra recombination on dust particle surfaces. Under day conditions (the presence of the photoelectric effect) dust grains acquire positive charges ($|Z_d| \sim 100$). The electron number density in this case increases because of the appearance of photoelectric current, the ion number density (as before) decreasing. Under the day conditions we consider the case of metal impurities in dust particles, so that the work function is 4 eV. The results are presented in Figures 1–6. In Figures 3–6 the top panel corresponds to the dust particle number density $n_d = 100$ cm^{-3}, while the lower panel to the $n_d = 1$ cm^{-3}. The left panels of Figures 3–6 correspond to the case when initially the dust layer is located at an altitude of 112 km, while the right panels to the case of altitude of 115 km.

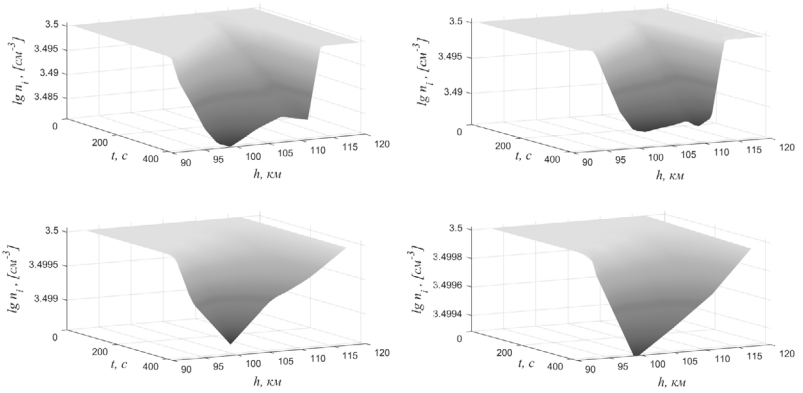


Fig. 6. The ion number density versus time and height for the daytime conditions in the process of sedimentation of the dust layer.

ACKNOWLEDGEMENTS:
This work was supported in part by the Theoretical Physics and Mathematics Advancement Foundation «BASIS» (Grant «Leader»).

REFERENCES:

[1] Shukla P. K., Mamun A. A. // Introduction to Dusty Plasmas Physics. Bristol/Philadelphia: Institute of Physics Publishing, 2002.
[2] Tsytovich V. N., Morll G. E., Vladimirov S. V., Thomas H. // Elementary Physics of Complex Plasmas. Berlin; Heidelberg: Springer, 2008.
[3] Fortov V. E., Ivlev A. V., Khrapak S. A., Khrapak A. G., Morll G. E. // Phys. Reports. 2005. V. 421. P. 1.
[4] Popel S. I., Kopnin S. I., Yu M. Y., Ma J. X., Huang F. // J. Phys. D: Applied Phys. 2011. V. 44. Art. 174036.
[5] Yu.S. Reznichenko, A.Yu. Dubinskii, and S.I. Popel // Plasma Physics Reports. 2019. V. 45. P. 913.
[6] Yu.S. Reznichenko, A.Yu. Dubinskii, and S.I. Popel // Journal of Physics: Conference Series. 2020. V. 1556. Art. 012072.
[7] B.A. Klumov, S.I. Popel, and R.Bingham // JETP Letters. 2000. V. 72. P. 364.
[8] B.A. Klumov, G.E. Morfill, snd S.I. Popel // JETP. 2005. V. 100. P. 152.

THE RAMAN SPECTROMETER RAX AS AN ANALYTICAL INSTRUMENT FOR THE JAXA MMX SAMPLE RETURN MISSION

U. Böttger [1], Y. Cho [2], F. Rull [3], H.-W. Hübers [1], T. Belenguer [4], A. Börner [1], M. Buder [1], Y. Bunduki [1], E. Dietz [1], T. Hagelschuer [1], S. Kameda [5], E. Kopp [1], A.G. Moral [4], S. Mori [2], C. Perez Canora [4], M. Pertenais [1], G. Peter [1], O. Prieto-Ballesteros [6], S. Rockstein [1], S. Rodd-Routley [1], P. Rodriguez Perez [4], C. Ryan [1], P. Santamaria [4], Th. Säuberlich [1], F. Schrandt [1], S. Schröder [1], S. Ulamec [7], T. Usui [8], I. Weber [9], K. Westerdorff [1]

[1] *Institute of Optical Sensor Systems, German Aerospace Center, 12489 Berlin, Gemany, Ute.Boettger@dlr.de;*

[2] *Department of Earth and Planetary Science, The University of Tokyo, Tokyo 113-0033, Japan;*

[3] *Universidad de Valladolid – GIR ERICA, E-47151 Boecillo, Valladolid, Spain*

[4] *Instituto Nacional de Técnica Aerospacial (INTA), 28850 Torrejón de Ardoz, Spain;*

[5] *Department of Physics, College of Science, Rikkyo University, Tokyo 171-8501, Japan;*

[6] *Centro de Astrobiología (CAB-INTA-CSIC), 28850 Torrejón de Ardoz, Spain;*

[7] *Deutsches Zentrum für Luft- und Raumfahrt e.V. (DLR), Cologne, 51147, Germany;*

[8] *Japan Aerospace Exploration Agency (JAXA), Institute of Space and Astronautical Science, Department of Solar System Sciences, Sagamihara, Kanagawa, 252-5210, Japan;*

[9] *Institut für Planetologie, Westfälische Wilhelms-Universität Münster, 48149 Münster, Germany;*

KEYWORDS:
Raman spectroscopy, space technology, mineralogy, in-situ exploration, Phobos, MMX, RAX.

The Martian Moons eXploration (MMX) mission will be launched in 2024 by the Japan Aerospace Exploration Agency (JAXA). During this mission the two Mars moons, Phobos and Deimos, will be observed remotely and in-situ investigation will be performed on the surface of Phobos and samples from Phobos will be collected and returned to Earth [1–2]. Several scientific instruments will conduct measurements on the surface of Phobos onboard a rover developed by DLR and CNES [3]. Part of this rover payload is a DLR/INTA/JAXA Raman spectrometer.

Phobos is a low-gravity object inside the gravity well of Mars. Scientifically, the origins of Phobos as well as of Deimos are uncertain. The answer to the question of their origin provides insights into the formation of the inner Solar System, which includes the terrestrial planets [4–5]. Therefore, the main motivation for the MMX mission and the accompanying Rover mission is to obtain the mineralogical, elemental, and isotopic composition of Phobos to improve the understanding of the origin, evolution, and formation of the Solar System bodies. Furthermore, investigation of returned sample in a terrestrial laboratory allows more detailed analyses, and compared with the in-situ and orbiter measurements a comprehensive data base and knowledge is available to evaluate the origin hypotheses.

RAX (Raman spectrometer for MMX) (Fig. 1) is a Raman instrument with a volume of approximately 82x98x125 mm^3 and a mass of less than 1.4 kg developed together by DLR, INTA/UVA, and JAXA/UTo: RAX a small and lightweight instrument which is designed to withstand the harsh environment on Phobos, which is characterized by strong temperature variations in a dusty surrounding with strong space exposure.

Onboard the MMX-Rover (Fig. 2) RAX will perform Raman spectroscopic measurements on the Phobos surface. This will be done with assistance of the rover, which brings RAX in the right distance to the Phobos surface

to achieve a rough focused position of about 10 cm over Phobos soil that can be finetuned with the autofocus system developed by JAXA/UTo. The laser for excitation of the sample for Raman scattering is developed by INTA/UVA and has its heritage from the laser of the RLS instrument of the ExoMars 2022 mission [6].

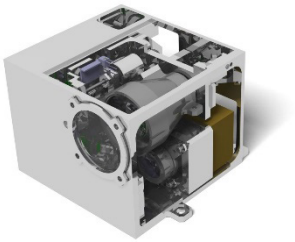


Fig. 1. CAD design of the Raman spectrometer part of RAX

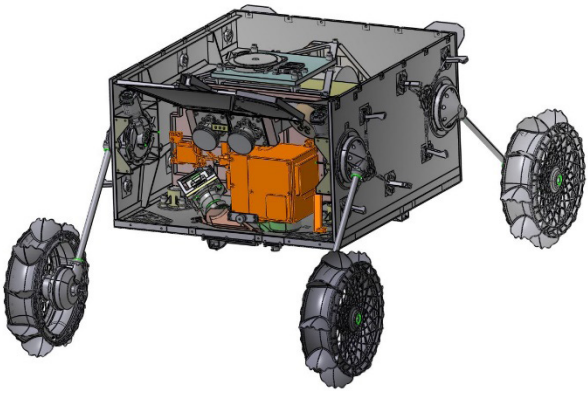


Fig. 2. CAD design of the MMX rover with RAX (in orange).

The Raman spectra measured by RAX will be used to identify the mineralogy of the Phobos surface. Moreover, the RAX data will support the characterization of a potential landing site and the selection of samples to be returned to Earth. Furthermore, the RAX measurements will be compared directly with Raman measurements obtained from the RLS instrument, on board the Rosalind Franklin rover during the ExoMars 2022 mission, to have an obvious proof for the Martian or non-Martian origin of the surface minerals on Phobos.

REFERENCES:

[1] Kuramoto K., Kawakatsu Y., Fujimoto M., Genda H, Imamura T., Kameda S., Matsumoto K., Miyamoto H., Morota T., Nagaoka H., Nakamura T., Ogawa K., Otake H., Ozaki M., Sasaki S., Senshu H., Tachibana S., Terada N., Usui T., Wada K., Watanabe S., and MMX study team, MARTIAN MOONS EXPLORATION (MMX) CONCEPTUAL STUDY UPDATE. Lunar Planet. Sci 49, 2018, abstract #?.

[2] Usui T, Bajo Ki, Fujiya W. Furukawa Y., Koike M., Miura YN., Sugahara H., Tachibana S., Takano Y., Kuramoto K. (2020) The Importance of Phobos Sample Return for Understanding the Mars-Moon System. Space Sci Rev 216:49. doi:10.1007/s11214-020-00668-9.

[3] Michel et al., (2021) The MMX rover: performing in-situ surface investigations on Phobos. Earth, Planets and Space (2021, in print).

[4] Pieters CM., Murchie S., Thomas N., Britt D. (2014) Composition of Surface Materials on the Moons of Mars. Planetary and Space Science 102:144-151. doi: http://dx.doi.org/10.1016/j.pss.2014.02.008.

[5] Murchie, S., Eng, D., Chabot, N., Guo, Y., Arvidson, R., Trebi-Ollennu, A., Seelos, F., Adams, E., Fountain, G., (2012). MERLIN: Mars–Moon exploration, reconnaissance and landed investigation. Acta Astronaut., http://dx.doi.org/10.1016/j.actaastro. 2012.10.014.

[6] Rull F. et al (2017) The Raman Laser Spectrometer for the ExoMars. Rover Mission to Mars, Astrobiology 17; DOI: 10.1089/ast.2016.1567

TIDAL DEFORMATION MODELING AS A POTENTIAL MEANS OF CONSTRAINING THE INTERIOR STRUCTURE OF PHOBOS

A.A. Dmitrovskii [1], A. Khan [1,2], C. Boehm [1], A. Bagheri [1], M. Van Driel [1]
[1] *Institute of Geophysics, ETH Zürich, Zürich, Switzerland;*
[2] *Physik-Institut, University of Zürich, Zürich, Switzerland*

KEYWORDS:
Phobos, interior structure, tidal deformations.

INTRODUCTION:
Phobos is one of the two moons of Mars, the only other terrestrial planet to have companions. In spite of decades of Earth- and Space-based observations of Phobos and Deimos, the origin of the Martian moons remains to be understood. This unsettled state of affairs reflects a dearth of data related to its interior structure and bulk composition, both of which hold the key to solving the question of the provenance of the satellites.

In this project, we constructed a series of models of the interior of Phobos in accordance with current observations and determine their tidal deformation. The models include a homogeneous body, ice-rock mixtures, models with positive and negative density gradients, and layered models. To compute the deformation of Phobos precisely, we solve the three-dimensional elastostatic problem to obtain the full displacement field. For this, we rely on a higher-order spectral-element method [1] and to account for a correct representation of shape and resulting displacement field, we accurately mesh the figure of Phobos by employing the digital terrain model of [2]. To enable us to further distinguish between models, we also rely on currently available geophysical data [2–10] (e.g., magnitude of libration in longitude, mean density, gravity field, and moments of inertia). Our results show that the homogeneous (Fig.1), ice-rock mixture, and negative density gradient models are largely degenerate and therefore difficult to separate, but that models with a density increase with depth (Fig.2) can be differentiated from the former model families. These observations will be of considerable interest for the future exploration of Phobos as envisaged with the Martian Moons Exploration mission.

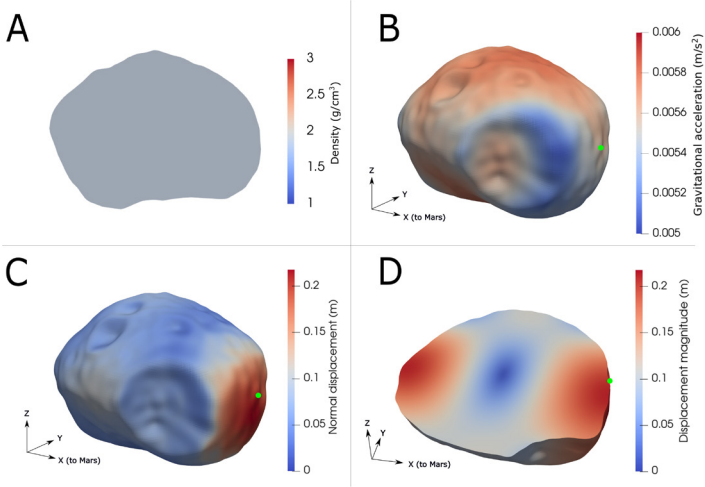


Fig. 1. Three-dimensional modeling results for a homogeneous Phobos (A). (B) Surface gravity; (C) normal component of surface tidal displacement field; (D) magnitude of interior tidal displacement field. The coloured dot indicates the location of the sub-Mars point. For the case studied here, shear modulus is 0.01 GPa.

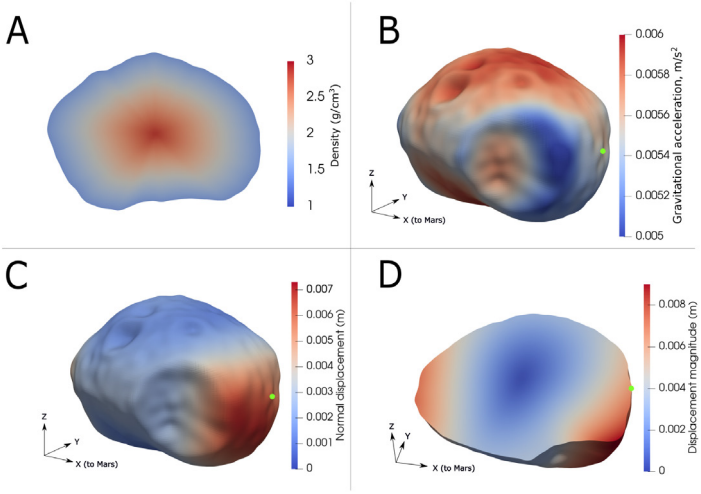


Fig. 2. Three-dimensional modeling results for a model of Phobos with linearly increasing density toward the center of the body (A). (B) Surface gravity; (C) normal component of surface tidal displacement field; (D) magnitude of interior tidal displacement field. The coloured dot indicates the location of the sub-Mars point. For the case studied here, shear modulus is 0.179 GPa and surface density is 1.5 g/cm3

REFERENCES:

[1] Afanasiev, M., Boehm, C., van Driel, M., Krischer, L., Rietmann, M., May, D.A., Knepley, M.G., Fichtner, A. Modular and flexible spectral-element waveform modelling in two and three dimensions. // Geophysical Journal International. 2019. V. 216, P. 1675–1692.
[2] Willner, K., Shi, X., Oberst, J., Phobos' shape and topography models. // Planetary and Space Science. 2014. V. 102, P. 51–59.
[3] Pätzold, M., Andert, T.P., Tyler, G.L., Asmar, S.W., Häusler, B., Tellmann, S. // Phobos mass determination from the very close flyby of Mars Express in 2010. // Icarus. 2014b. V. 229. P. 92–98.
[4] Willner, K., Oberst, J., Hussmann, H., Giese, B., Hoffmann, H., Matz, K.D., Roatsch, T., Duxbury, T. Phobos control point network, rotation, and shape. // Earth and Planetary Science Letters. 2010. V. 294, P. 541–546.
[5] Oberst, J., Zubarev, A., Nadezhdina, I., Shishkina, L., Rambaux, N.,The Phobos geodetic control point network and rotation model. // Planetary and Space Science. 2014. V. 102. P. 45–50.
[6] Burmeister, S., Willner, K., Schmidt, V., Oberst, J., Determination of Phobos' rotational parameters by an inertial frame bundle block adjustment. // Journal of Geodesy. 2018. V. 92. P. 963–973.
[7] Jacobson, R.A., The orbits and masses of the Martian satellites and the libration of Phobos. // The Astronomical Journal. 2010. V. 139. P. 668–679.
[8] Lainey, V., Pasewaldt, A., Robert, V., Rosenblatt, P., Jaumann, R., Oberst, J., Roatsch, T., Willner, K., Ziese, R., Thuillot, W., Mars moon ephemerides after 14 years of Mars Express data // Astronomy & Astrophysics. 2021. V. 650. P. A64.
[9] Jacobson, R.A., Lainey, V., Martian satellite orbits and ephemerides. // Planetary and Space Science. 2014. V. 102. P. 35–44.
[10] Yang, Y., Yan, J., Guo, X., He, Q., Barriot, J.P., An elastic model of Phobos' libration. // Astronomy & Astrophysics. 2020. V. 636. P. A27.

MONITORING OF SPACE PRECIPITATION AT THE VOSTOK ANTARCTIC STATION USING THE EXAMPLE OF COLLECTING MAGNETITE MICROPARTICLES FROM MAY TO SEPTEMBER 2017

Yu.O. Chetverikov [1], M.S. Glukhov [2], E. M. Ivankova [3], V.D. Kalganov [4], A.S. Loshachenko [4], O.V. Yakubovich [5]

[1] *NRCKI PNPI, Russia, Gatchina, Orlova roscha st. 1. chetverikov_yo@pnpi.nrcki.ru;*

[2] *Kazan Federal University, Institute of Geology and Petroleum Technologies, Russia, Kazan, Kremlyevskaya st., 18, gluhov.mixail2015@yandex.ru;*

[3] *Institute of Macromolecular Compounds RAS, Russia, St.Petersburg, V.O., Bolshoy pr. 31.ivelen@mail.ru;*

[4] *IRC «Nanotechnology», Research park, St Petersburg University, Russia, St.Petersburg, Universitetskaya emb. 7/9. a.loshachenko@spbu.ru;*

[5] *Saint-Petersburg State University, Russia, St. Petersburg, Universitetskaya emb. 7/9; IPGG RAS, Russia, St. Petersburg, Makarova emb. 2. Olya.v.yakubovich@gmail.com*

KEYWORDS:
Meteor showers; Space precipitation; Antarctic station Vostok

Dust particles obtained as a result of filtering fresh snow collected from May to September 2017 near the Vostok Antarctic station were studied using a scanning electron microscope. The collection of the dust contains about 200 magnetite spheres with a diameter of 2 to 70 μm (Fig. 1.). The statistics of the particle size distribution show an increase in the population with decreasing size and a dramatic drop in the population of particles with a size less than 3 μm.

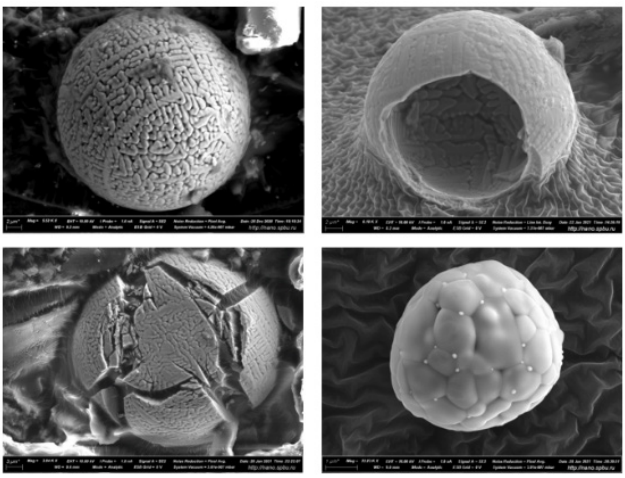


Fig. 1. Examples of SEM images of typical magnetite particles

The collected particles have an uneven time distribution with a short-term and intense peak of collection in the period from 27 to 28 July. Analysis of the collected material, meteorological data [1–3], anthropogenic and natural sources [4, 5] allows us to make a conclusion about the probable meteoric origin of magnetite particles and their belonging to the Southern Delta Aquarids meteor shower (Fig. 2.).

The dispersion of short-term precipitated particles in size allows us to make an assumption about the accelerated precipitation of particles in the form of condensation nuclei of ice crystals of stratospheric clouds.

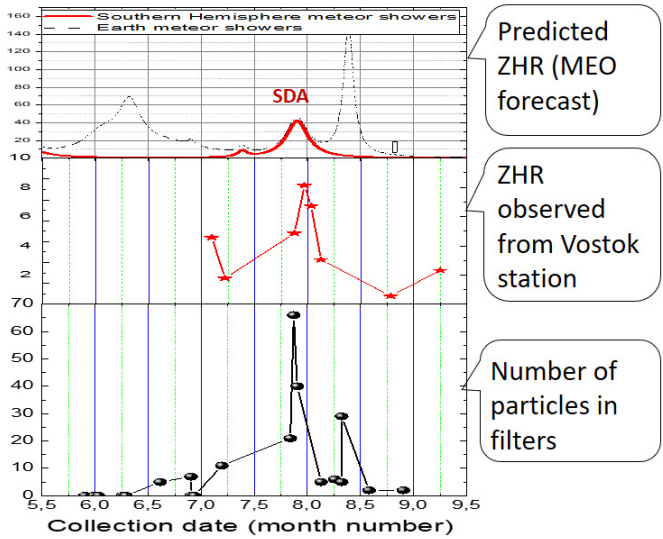


Fig. 2. Demonstration of correlation magnetite particles histogram and meteor showers intensity [6].

REFERENCES:

[1] URL: http://www.ready.noaa.gov/HYSPLIT.php;
[2] Snels M. et al. Quasi-coincident observations of polar stratospheric clouds by ground-based lidar and CALIOP at Concordia (Dome C, Antarctica) from 2014 to 2018 // Atmospheric Chemistry and Physics. 2021. V. 21. No. 3. P. 2165–2178;
[3] https://www-calipso.larc.nasa.gov/tools/data_avail/index.php?d=2017;
[4] Mather T.A., Pyle D.M., Oppenheimer C. Tropospheric volcanic aerosol // Geophysical Monograph-American Geophysical Union. 2003. V. 139. P. 189–212;
[5] https://www.celestrak.com/;
[6] Moorhead A., Cooke B., Moser D. The 2017 meteor shower activity forecast for Earth orbit //NASA technical report. 2017. P. 4.

RECONCILING ESTIMATES OF ENDOGENIC POWER EMITTED FROM THE SOUTHERN POLAR REGION OF ENCELADUS

A. Pankine [1]
[1] *Space Science Institute, Boulder, CO, USA, apankine@spacescience.org*

KEYWORDS:
Enceladus, 'tiger stripes', plumes, sub-ice ocean, endogenic heat.

INTRODUCTION:

In 2005 data returned by the Cassini's Composite Infrared Spectrometer (CIRS) revealed anomalously warm region surrounding "tiger stripes" (TS) fractures at the southern polar region (SPR) of Enceladus. Subsequently data from Cassini revealed the TS fractures as the source of the Enceladus' plumes of water vapor and ice particles. Several theories were put forward to explain the origin of the plumes and high thermal emission in the SPR. The emerging view is that water from the global sub-ice ocean partially fills ice fractures at the SPR and the plumes are formed by evaporation from the ocean water exposed to near-vacuum inside fractures. Results of numerical modeling [1, 2] suggest that latent heat of the vapor condensing on ice fractures' walls and conducted to the surface is the main source of the heat observed by the CIRS in the SPR.

Estimates of the endogenic heat emitted from the SPR of Enceladus range from ~ 4.2 GW [3] to ~ 15.8 GW [4]. These estimates rely on observations with different sensors on CIRS and cover different spatial and spectral regions: the lower one is from high spatial resolution observations by CIRS FP3 and FP1 detectors observing the vicinity of TSs [3], while the higher one is from low spatial resolution observations by CIRS FP1 detector observing large fraction of the SPR south of the latitudes 60 °–70 °S including TSs [4]. The FP3 detector is sensitive to thermal emission from surfaces with temperatures ~ 100 K and higher, while FP1 detector is sensitive to lower temperatures.

The large difference in the estimates of the emitted endogenic heat is puzzling. Numerical modeling of the heat exchange in the fractures and accounting for the heat conducted from the sub-ice ocean allows reconciling these estimates. Vapor condensing in ice fractures produces heat flux of ~ 2.7 GW, heat conducted from the water-filled portion of the fractures produces another ~ 1.5 GW of power, and the heat conducted from the sub-ice ocean results in another ~ 11.6 GW for the entire SPR. The relatively large power conducted from the ocean corresponds to the relatively thin (~ 2 – 4 km) ice shell over the SPR, consistent with the recent estimates of ice thickness based on topography and gravity data [5]. The existing endogenic heat estimates [3, 4] are thus interpreted as FP3 detection of ~ 2.7 GW heat flux from vapor condensing in the fractures and FP1 detection of ~ 1.5 GW heat flux conducted from water-filled portion of the fracture, for a total of ~ 4.2 GW [3]. The low-resolution FP1 observations also register heat flux from these sources (~ 4.2 GW) and the broader distributed heat flux conducted from the sub-ice ocean (~ 11.6 GW), for a total of ~ 15.8 GW. The details of the analysis are presented below.

VAPOR FLOW AND HEAT EXCHANGE IN FRACTURES:

To estimate power generated by various processes within ice fractures at Enceladus' SPR the updated numerical model [1, 2] was used. Straight ice fractures penetrate through the ice shell and connect to the sub-ice ocean. Water fills ~ 92 % of the fractures' height due to isostasy. Water-filled portions of the fractures are cooled by conduction through ice (next section). Cooled water inside a fracture sinks down and is replaced by upwelling warmer water from the ocean, preventing freezing and closing of the fractures. At the water surface within fracture evaporation and controlled boiling [2] create a vapor plume that accelerates upward towards the surface. The vapor plume ascending through fracture partially condenses on fracture walls, transferring latent heat to ice. This heat is conducted to the surface and is emitted to space.

Numerical model describing vapor flow and heat exchange in the vapor-filled portion of the fracture [1, 2] was updated to include sublimation of ice near the fracture outlet at the surface, effects of snow layer on the surface, higher spatial resolution near surface where most of the vapor condensation takes place and temperature dependent ice thermal conductivity. Accounting for surface ice sublimation limits maximum surface temperatures to ~ 216 K, consistent with observations [6]. A surface snow layer ~ 2 m thick reduces surface temperatures near fractures' outlets by ~ 20 – 50 K. The model was applied to ice shells with thicknesses 2–12 km in accordance with the recent estimates of ice thickness at the SPR [5]. The resultant estimated heat output per fracture (without snow on the surface) is ~ 1.8 – 2.4 GW (assuming 500-km-long fracture) depending on fracture width (0.05 – 0.1 m) and depth to water table. A surface snow layer ~ 2 – 10 m thick reduces heat output by a factor 2–3.

These model estimates of the heat flux correspond to the observed 'high temperature' component (surface temperatures ~ 120 – 165 K) of the emission from the SPR registered by the CIRS FP3 detector near TSs [3], but they are lower than the observed flux of ~ 2.7 GW, especially if a snow layer is present on the surface. Modeling and observations can be reconciled if multiple closely-spaced fractures exist within TSs. Indeed, some high-resolution CIRS observations hint at two fractures separated by ~ 100 m distances within a TS (e.g. Plate 9(c) in [7]). Doubling the number of fractures does not increase the heat output by a factor of 2. For fractures separated by distances ~ 100 m heat conduction is affected by the presence of a fracture nearby and the resultant heat output increase is less than 100% per added identical fracture. Therefore, groups of 2 or 3 fractures per TS are responsible for generating the ~ 2.7 GW emission from the 'high temperature' component observed by FP3 [3].

HEAT CONDUCTION FROM WATER-FILLED FRACTURE:

To calculate the heat conducted from the water-filled portion of the fracture, an analytical solution for heat flux from a thin vertical plate at constant temperature buried in a semi-infinite media was used [1, 2]. The total flux is the sum of fluxes into the ice walls from the base of the ice shell up to the water table level. After integration over water-filled portion the expression for total conducted heat flux $F_{c\ total}$ is:

$$F_{c\ total} = \frac{4k(T_2 - T_1)}{\pi} \ln\left(\frac{d_2}{d_1}\right) \times L$$

where T_2 = 273 K is temperature inside water-filled fracture, $T_1 = T_e$ =53 K is surface temperature in equilibrium with annual insolation at SPR, k = 4.5 W/m/K is effective thermal conductivity of ice, d_2 is depth to the ocean, d_1 is depth to the water table inside fracture, L is total horizontal length of fractures (~ 500 km). d_2 / d_1 = 1/0.08 = 12.5 (from isostasy) and it follows that $F_{c\ total}$ estimate is independent of the fracture depth d_2. Substituting the above values into the expression for total flux, $F_{c\ total}$ ~ 1.5 GW. Close-spaced groupings of fractures produce the same output, because temperature inside water-filled portion of the fracture cannot be higher than 273 K. Heat conducted from the water-filled portion of the fracture increases surface temperatures on both sides of a fracture over distances comparable to fracture depth (~ 1 – 10 km). Because flux is spread out over larger area, the surface temperature increase is relatively small. This emission corresponds to the 'low temperature' ~ 1.5 GW component of the heat flux observed by high spatial resolution CIRS FP1 observations near TSs [3]. The presence of a snow layer on the surface does not significantly affect this estimate.

HEAT CONDUCTION FROM THE OCEAN UNDER SPR:

Heat conducted from the ocean underneath the SPR was calculated by solving the non-linear equation balancing radiative heat loss from the surface with conduction through ice:

$$\sigma\left(T_s^4 - T_e^4\right) = \frac{k(T_b - T_s)}{h}$$

where σ is Stefan-Boltzmann constant, T_s is surface temperature, T_b = 273 K is the temperature at the base of the ice shell, h is the thickness of the ice shell.

Two sets of calculations were carried out for a range of ice shell thicknesses, one without snow on the surface, and the other with a 10-m layer of snow. Total heat flux calculated for areas of two CIRS FP1 observations analyzed in [4] (26619 km^2 for revolution (rev) 61 and 47199 km^2 for rev 91) are shown in Figure 1.

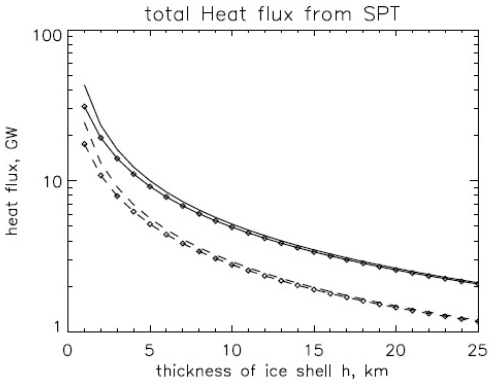


Fig. 1. Heat flux from subsurface ocean for SPR areas observed on FP1 rev 61 (dashed) and rev 91 (solid) as a function of ice shell depth without (lines) and with snow on the surface (lines with symbols).

The endogenic heat flux from SPR measured by CIRS FP1 detector on rev 61 (12.9–15.5 GW) and rev 91 (15.0–17.2 GW) includes emission from all sources. Subtracting 4.2 GW that are due to condensing vapor and conduction from water-filled fracture from these estimates leaves 8.7–11.3 GW (rev 61) and 10.8–13.0 GW (rev 91) for the heat conducted from the ocean. From Figure 1 these ranges are consistent with the heat conducted from the sub-ice ocean through ~ 2–4 km ice shell in the SPR, consistent with the ice thickness estimates in [5]. The difference in rev 61 and rev 91 flux estimates is mostly due to difference in surface area of SPR within FP1 field-of-view. The average FP1 estimate of ~ 15.8 GW for endogenic heat [3] corresponds to ~ 11.6 GW conducted from the ocean and ~ 4.2 GW from condensing vapor and conduction from water-filled fracture.

ACKNOWLEDGMENT:
This research was funded by NASA Grant NNX16AI48G.

REFERENCES:

[1] Ingersoll A.P. and Pankine A.A. (2010) Icarus, V. 206(2), P. 594–607.
[2] Nakajima M. and Ingersoll A. P. (2016) Icarus, V. 272, P. 309–318.
[3] Spencer J.R. et al. (2013) EPSC Abstracts, V. 8, P. 840–841.
[4] Howett C.J.A. et al. (2011) J. Geophys. Res: Planets, V. 116(E3).
[5] Čadek O. et al. (2016) Geophys. Res. Lett., V. 43(11),P. 5653–5660.
[6] Goguen J.D. et al. (2013) Icarus, V. 226(1), P. 1128–1137.
[7] Spencer J.R. et al. (2018) Plume Origins and Plumbing: From Ocean to Surface. Enceladus and the Icy Moons of Saturn, V. 163.

SESSION 6. SMALL BODIES (INCLUDING COSMIC DUST) (SB) POSTER SESSION

POSSIBLE SPACE MISSION TO SEDNA AT LAUNCH IN 2029-2037

V.A. Zubko [1,2], A.A. Sukhanov [1], K.S. Fedyaev [1], V.V. Koryanov [2], A.A. Belyaev [1,2]

[1] *Department of Space Dynamics and Mathematical Information Processing, Space Research Institute of the Russian Academy of Sciences (IKI), 84/32 Profsoyuznaya Str, Moscow, 117997, Russia;*

[2] *Department of Dynamics and flight vehicles control, Bauman Moscow State Technical University, 10 Gospitalnyi side street, Moscow, 105005, Russia*

KEYWORDS:
Space mission, gravity assist maneuver, Sedna, trans-Neptunian objects, Oort Cloud.

INTRODUCTION:

One of the most intriguing trans-Neptunian objects (90377) Sedna is a celestial body with a diameter of about 1000 km. According to existing data it is considered as a typical representative of a separate group of objects with the orbit located in the Kuiper belt and in the scattered disk. Some estimates of the surface composition of Sedna show that it may be covered by a layer of hydrocarbon sediment (tholin), which is formed as a result of methane irradiation. This surface composition is typical for Kuiper Belt objects, but the orbit of Sedna is significantly different. Currently Sedna is at the distance of about 80 AU from the Sun and expected to pass the orbital perihelion in 2075–2076. Because of its orbital period which is more than 11 000 years, now we may have a unique opportunity to send a spacecraft to study this remote object from a close distance.

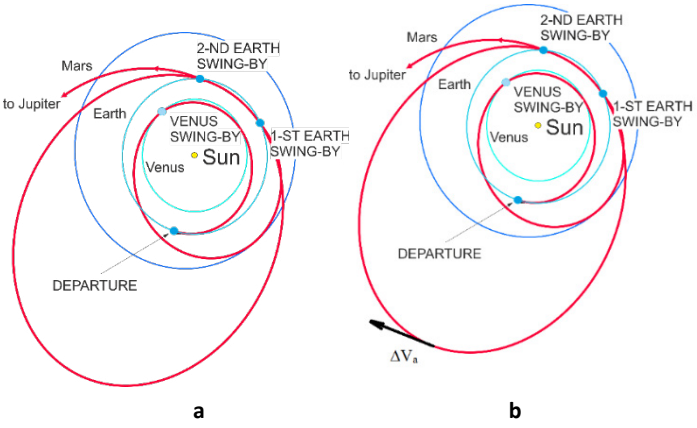


Fig. 1. A sequence of gravity assist maneuvers: (**a**) Earth-Venus-Earth-Earth; (**b**) Earth-Venus-Earth-ΔV_a-Earth.

The results of the analysis of possible trajectories of the flight to Sedna at launch in 2029–2037 are presented. The flight schemes using gravity assist maneuvers near some planets including Venus and Jupiter are considered. A direct Earth-Sedna flight has been also analyzed, and its inefficiency at any launch date is shown. Most of the considered flight schemes use the Earth-Venus-Earth-Earth sequence of gravity assists, as well as its modification with a small ΔV in the aphelion (ΔV_a) of the Earth-Earth section (Fig. 1). Such assists sequences allow reaching Jupiter with the value of ΔV_Σ equal to the value of ΔV_0 impulse necessary only for reaching Venus from a low Earth orbit. In addition, all considered schemes of flight to Sedna (except the direct flight) include a gravity assist maneuver near Jupiter. Also some flight schemes with gravity assist maneuvers near Saturn and Neptune were considered.

For all analyzed flight schemes, the optimal (in terms of the minimum $\Delta V\Sigma$ value) trajectories are determined under restrictions on the flight duration of 20, 25, 30, 40 and 50 years. The type of the optimal flight scheme depends on the launch date: for 2029 and 2031 the best scheme is the Earth-Earth-Earth-Jupiter-Sedna (Fig. 2), for 2034 the best one is the Earth-Earth-Earth-Earth-Jupiter-Neptune-Sedna.

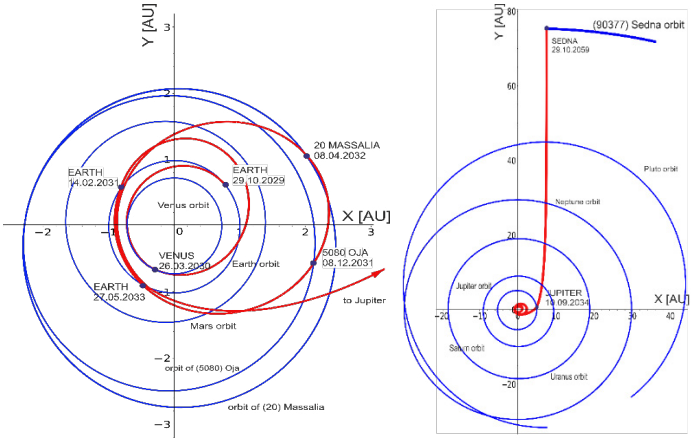


Fig. 2. Mission to Sedna with encounters of the main belt asteroids.

In some of the considered flight schemes the spacecraft approaches Jupiter at a relatively close distance. For example, in the Earth-Venus-Earth-Earth-Earth-Jupiter-Sedna scheme at launch in 2034 and duration of 30 years the spacecraft approaches Jupiter at a height of 3.6 thousand km. Such as close flyby could cause the radiation damage of the onboard equipment. The current research presents the results of the analysis of the radiation dose absorbed by the spacecraft during the Jupiter flyby.

For some of the considered optimal flight trajectories to Sedna the possibility of a close approach one or more asteroids of the main belt with small additional active maneuvers is also shown (see Fig. 2) [1, 2].

REFERENCES:

[1] Zubko V.A. et al Analysis of optimal transfer trajectories to the trans-Neptunian object (90377) Sedna // Astron. Lett. Pleades Publishing, 2021. V. 47. P. 188–195.
[2] V.A. Zubko, A.A. Sukhanov, K.S. Fedyaev et al., Analysis of mission opportunities to Sedna in 2029–2034, Advances in Space Research, https://doi.org/10.1016/j.asr.2021.05.035

PRELIMINARY TESTS WITH A 3D THERMOPROBE FOR MEASURING THE THERMOPHYSICAL PROPERTIES OF REGOLITH

M. Dominguez-Pumar [*], C. Rosero-Pozo [1], J. Ramos-Castro [1], N. Sola-Peñafiel [1], X. Manyosa [1], , V. Jimenez [1], S. Bermejo [1], J. Pons-Nin [1]
[1] *Institut d'Estudis Espacials de Catalunya - Universitat Politecnica de Catalunya,Barcelona, Spain, manuel.dominguez@upc.edu*

KEYWORDS:
Regolith, asteroids, thermophysical properties.

Introduction:

Accurate in situ measurement of the thermophysical properties of the regolith is very important in order provide ground-truth for remote measurements of thermal inertia, [1, 2]. Large variations in thermal inertia are typically linked to different granularities in the regolith. Particle size can vary from the nanometer scale, as in the upper layers of the lunar regolith, to centimeter scale, as in the case of Bennu, or even larger.

The two thermophysical properties that determine the temperature distribution and thermal emission of airless planetary bodies are: thermal inertia and surface roughness, [3]. Therefore, it is important that landers bring instruments and sensors for the in situ characterization of the regolith.

In this abstract, we will present an extension on our previous work in a 3D heat flux sensor, [1, 2], focused on analyzing the capability of the sensor in characterizing the thermophysical properties of granular materials. The sensor is a metallic sphere divided in four sectors. Six silicon dice, with embedded Pt resistors on them, provide independent temperature/power control to the sectors and two inner core additional dice.

A photograph of the sensor can be seen in Figure 1.

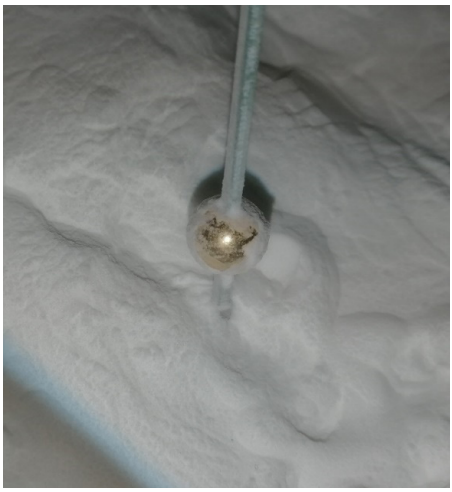


Fig. 1. Spherical 3D thermoprobe being inserted in regolith simulant made of glass microbeads. The sphere is divided in four sectors, which can be controlled independently. Six silicon dice, fabricated at the IEEC-UPC clean room, have been placed inside the sphere, containing Pt resistors.

EXPERIMENTAL RESULTS

Experimental results have been obtained using the 3D thermoprobe with different types of regolith simulants made of glass microbeads. The range of thermal conductivities tests is 46–100 mW/(mK). The objective of the measurement is to obtain the thermal impedance of the sphere in the frequency domain.

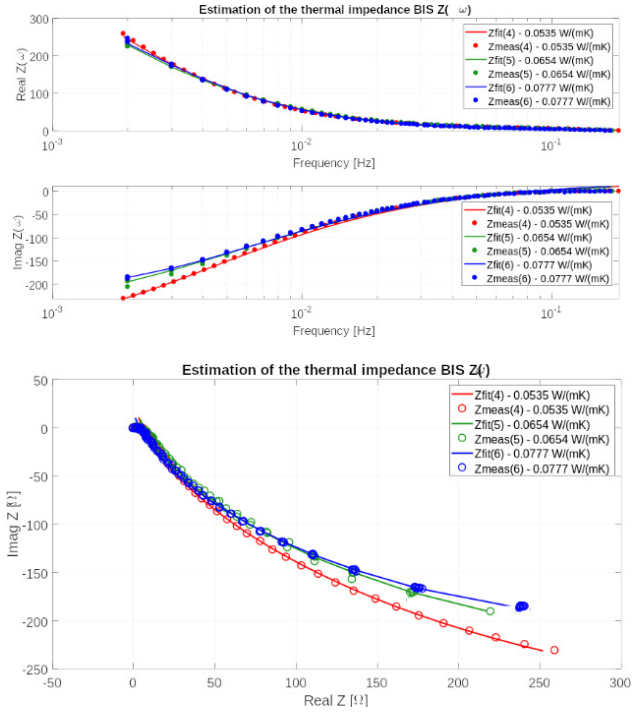


Fig. 2. Thermal impedance from the 3D spherical thermoprobe to the environment, for three different regoliths (numbered 4 to 6). (Top) Real and Imaginary parts of the thermal impedance. (Bottom) Nyquist plots associated. Superimposed can be found the fittings with analytical expressions (1).

Figure 2 shows the thermal impedance measured from the 3D spherical thermoprobe to the environment for a regolith of conductivity 0.0990 W/(mK). The fitting is made against the thermal impedance, in the Laplace domain, of a perfect sphere:

$$Z_{th}(S)=\frac{1}{4\pi r_0 k_r}\frac{1}{1+r_0\sqrt{\frac{S}{D}}}$$

The frequency response is then: (1)

$$Z_{th}(\omega)=\frac{1}{4\pi r_0 k_r}\frac{1}{1+r_0\sqrt{\frac{j\omega}{D}}}$$

Where r_0 is the radius of the sphere, k_r is the thermal conductivity of the regolith and D is its diffusivity. The *fractional* nature of the impedance reflects the fact that the regolith is not considered a lumped circuit element, but a *distributed model*. With this approach it is possible to obtain estimations of the thermal conductivity and diffusivity of the regolith.

Extensive measurements have been made with nine regolith simulants made of glass microbeads. The errors in the estimation of the thermal conductivity have been below 7 %, and below 4 % in the case of having conductivities larger than 50 mW/(mK).

REFERENCES:

[1] Domínguez-Pumar, Manuel, et al. “A Miniaturized 3D Heat Flux Sensor to Characterize Heat Transfer in Regolith of Planets and Small Bodies.” Sensors, V. 20, No. 15, 25 July 2020, p. 4135, doi:10.3390/s20154135.

[2] Domínguez-Pumar, Manuel, et al. “ First Experiments with a Miniaturized 3D Heat Flux Sensor for Planetary Regolith”, The Eleventh Moscow Solar System Symposium 11M-S3, 387-389, 2020.

[3] Rozitis, B., et al. “Asteroid (101955) Bennu’s weak boulders and thermally anomalous equator.” Sci. Adv., vol. 6, no. 41, 1 Oct. 2020, p. eabc3699, doi:10.1126/sciadv.abc3699.

TRANSPORT CHARACTERISTICS OF THE NEAR-SURFACE LAYER OF THE NUCLEUS OF COMET 67P

Yu. Skorov [1,2] , V. Reshetnyk [3,4]
[1] *Max Planck Institute for Solar System Research, Göttingen, Germany;*
[2] *Institute for Geophysics and Extraterrestrial Physics, Technical University of Braunschweig, Braunschweig, German;*
[3] *Taras Shevchenko National University of Kyiv, Kyiv, Ukraine;*
[4] *Main Astronomical Observatory, National Academy of Sciences of Ukraine, Kyiv, Ukraine*

KEYWORDS:
Comet, comet dust, coma simulation.

INTRODUCTION:
The Rosetta space mission to comet 67P/Churyumov–Gerasimenko ushered in a new era in the study of short-period comets. Various scientific instruments aboard the orbital and landing modules performed comprehensive studies of physical processes both in the comet nucleus and the surrounding gas-dust coma. Several review articles summarizing the present state of affairs were published in Space Science Reviews [1–4]. It has been convincingly shown that the surface of the comet nucleus is covered with a nonvolatile material, which we will call comet dust. It should be noted that the size of the dust particles, their composition, and their physical properties are very diverse. The core as a whole has a very high porosity of ~ 65–85 %. Dust particles captured by the COSIMA, GIADA, and MIDAS instruments on the orbital module also have a complex porous structure. Gas activity is observed almost ubiquitously and follows sunlight that allows us to conclude that ice is located close to the surface.

These results indicate that the study of gas activity requires an accurate study of the transport properties of the screening porous layer of dust on the surface. A consistent model of energy and mass transfer in the near-surface layer includes consideration of the absorption of direct solar radiation in the layer, thermal emission of heated dust particles, diffusion of vapour through the porous layer, and an estimate of the effective sublimation rate taking into account the gas-dynamic impedance of the layer. Consideration of each of these processes is directly related to the transport properties of the near-surface layer, such as (a) permeability of the layer for the gas flow; (b) effective pore size; (c) average vertical displacement between collisions in the layer; and (d) distribution of depths for the first and last collisions in the layer. The first characteristic influences the effective rate of sublimation; the second one affects the radiative thermal conductivity; the third one is a measure of pore tortuosity; the distribution of the depths of the first and last collisions is used to estimate the volumetric absorption of solar radiation in the layer and the effective temperature of emitted molecules upon passing through the nonisothermal layer. Hereafter, we propose a consistent approach for their quantitative assessment based on the analysis of the microstructure of a model porous layer.

MODEL LAYERS:
We consider various model porous layers with both homogeneous and heterogeneous structures. The layers consist of spherical nonintersecting particles of either one size (monodisperse layers) or two sizes (bidisperse layers). In addition, the layer may contain cavities (gaps with a size much larger than the particle size) or slits (a model analogue of microscopic cracks, the width of which also exceeds the size of model particles). For the first time, we present simulation results for layers built from complex porous aggregates, i.e. layers with a hierarchical structure. Examples of model layers are shown in Figure 1.

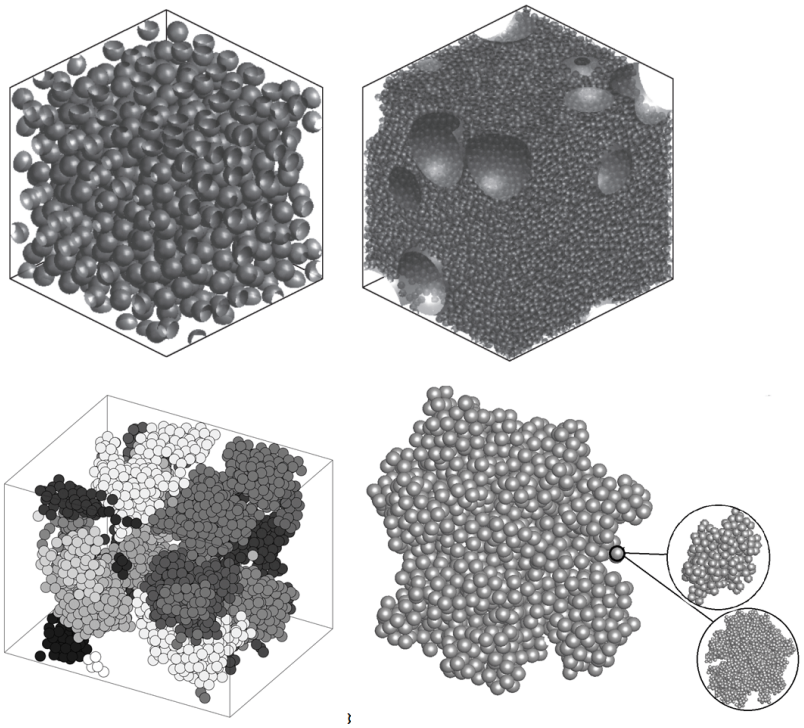


Fig. 1. Examples of model layers. TOP: part of a layer composed of spheres of the same size. The porosity of the layer is 65% (left panel); part of a layer containing spheres of the same size and cavities ten times the size of a small sphere (right panel). The effective porosity of the layer is 50%. BOTTOM: a part of a layer consisting of different variants of the ballistic aggregate (coloured in different colours), consisting of 256 spheres of one size (left panel). A ballistic aggregate composed of pseudo-monomers, where each pseudo-monomer is an aggregate containing spheres of the same size (shown in the sidebars).

EFFECT OF LAYER TRANSPORT CHARACTERISTICS ON GAS PRODUCTION RATE:

Based on the modelling results, we quantitatively estimate the uncertainty introduced by insufficient knowledge of the microstructure of the porous surface layer of dust into all theoretical models of the gas activity of comets. We consider a two-layer model of a thermophysical model of a porous surface layer, which explicitly includes the effective thermal conductivity including the radiation term and gas resistance of the porous dust layer. A detailed description of the model, as well as the simplifications and the corresponding limitations arising, can be found, for example, in [5]. Figure 11 shows the illustrative results obtained for the hierarchical layers, calculated for a solar flux corresponding to the perihelion of comet 67P. The aggregate sizes are 5, 10 and 20 microns (rows from top to bottom). The porosity values are shown on the curves (from 70 % to 85 %). Near perihelion, for all considered cases, changes in gas production are small and remain less than the expected uncertainty due to statistical scatter of layer structure and uncertainty of the scattering model. At large distances, changes in gas production due to porosity are more noticeable, but in this case, they have the same magnitude as changes due to the listed uncertainties. Thus, we formulate the general conclusion: quantitative estimates of the resulting gas productivity depend on the mean void size, which in turn is a function of effective porosity. However, in the expected range of porosity for the considered values of aggregate sizes and layer thicknesses, it is unlikely that an inhomogeneous gas flow will occur due to micro-variations in aggregate sizes, layer structure, and changes in local porosity.

Modelling of hierarchical layers as well as of heterogeneous layers containing cavities and cracks showed that the mean free path length is still well described by the theoretical dependence obtained for a random homogeneous porous layer. This means that the presence of micro-inhomogeneities and a hierarchical structure does not change to any appreciable extent the resulting sublimation concerning the corresponding homogeneous layer. It should be remembered that adding complicating elements to the model introduces an unavoidable statistical scatter (the model ceases to be completely deterministic as in the case of a homogeneous layer of monomers) and that the magnitude of the resulting uncertainty is tens of per cent.

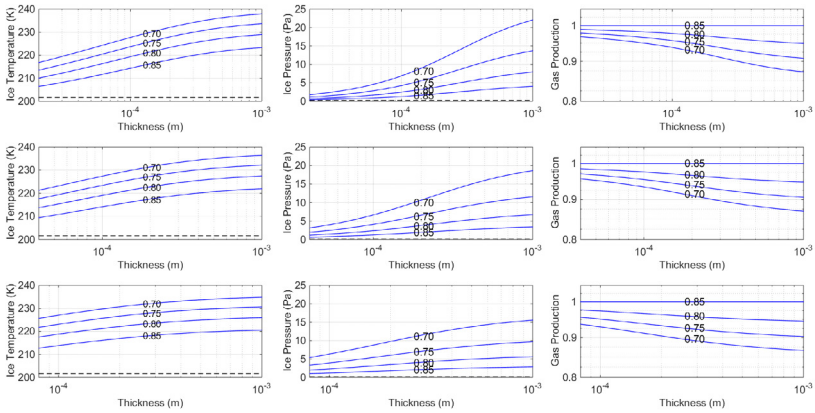


Fig. 2. The sublimating ice temperature (left column), the corresponding water vapour pressure under the dust layer (middle column) and the dimensionless gas production rate (right column), calculated for a solar flux corresponding to the perihelion of comet 67P (R_H = 1.243 au) as a function of the layer thickness. The aggregate sizes are 5, 10 and 20 microns (rows from top to bottom). The porosity of the dust layer is shown on the curves.

REFERENCES:

[1] El-Maarry et al. 2019, Space Sci. Rev., V. 36. P. 215..
[2] Choukroun et al. 2020, Space Science Rev., V. 27. P. 216.
[3] Vincent *и др.* 2019, Space Science Rev.,V. 30. V. 215.
[4] Groussin et al. 2019, Space Sci. Rev., V. 29. P.215.
[5] Skorov et al. 2021, MNRAS, V. 501, V. 2635.

SYSTEM OF OBSERVATION OF DAY-TIME ASTEROIDS (SODA)

A.S. Shugarov [1], B.M. Shustov[1], V.E. Shmagin[1], A.I. Buslaeva[1]
[1] *Institute of Astronomy, Russian Academy of Sciences, 119017, Pyatnitskaya str, 48, Moscow, Russia, shugarov@inasan.ru*

KEYWORDS:
Near Earth Objects, asteroid hazard problem, day-time asteroids, survey space telescope, slewing mirror.

INTRODUCTION:
It is known that the Chelyabinsk meteoroid that collided with the Earth on 15 February 2013 was detected by neither ground-based nor near-Earth space telescopes before it entered the Earth atmosphere [1]. One of the major lessons of the Chelyabinsk event is obvious: to detect a NEO coming from the day sky and to properly calculate its orbit we need a space-born telescope located far away from the Earth.

In [2, 3] we proposed the System of Observation of Daytime Asteroids (SODA). The main SODA project goals are:

- to detect almost all bodies larger than 10 m entering the near-Earth space (i.e. approaching the Earth at a distance of less than 10^6 km) from the Sun direction;
- to quickly identify a body of special interest (e.g. an asteroid at collisional orbit) and to characterize it, i.e. perform an accurate orbit determination and body mass estimation;
- in the case of a collisional orbit, the system should ensure a warning time of about 10 hours and determine coordinates of the atmospheric entry point with the best possible accuracy.

The concept of the SODA system consists of one or two (in optimal configuration) spacecraft (SC) placed into orbits in the vicinity of the Lagrange point L1 of the Sun-Earth system. The SC is equipped with one to three small aperture (25−30 cm) telescopes to observe near Space in a conical region around the Earth. SODA telescopes should provide two modes of operation:

- discovery mode: to discover nearly all new asteroids coming from the solar celestial hemisphere using the barrier technique of detection;
- target mode: to accurately define the orbits of dangerous asteroids.

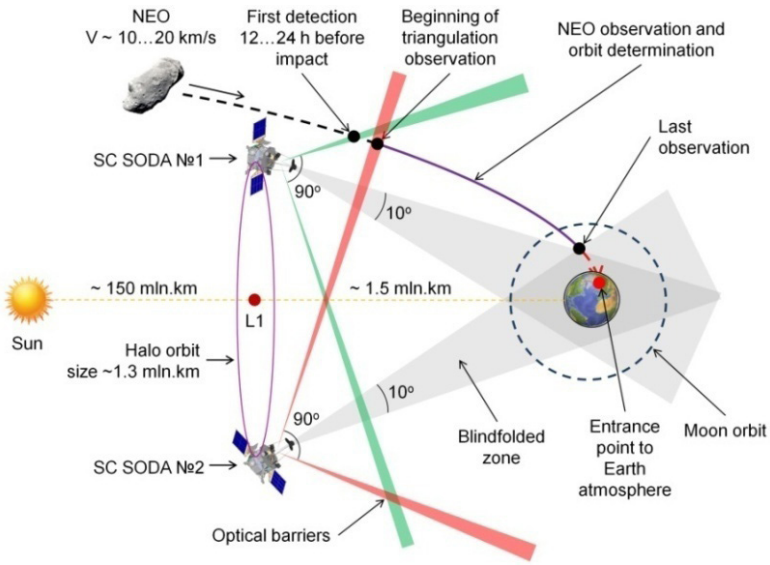


Fig. 1. Scheme of observation by SODA project, ecliptic planeprojection.

A NEO approaching the Earth from the Sun crosses the optical barrier approximately one day before its closest approach to the Earth. A typical NEO will be observed 6 times while crossing the barrier. This is not sufficient for an accurate orbit determination, but quite sufficient to classify an object as dangerous or not. The data is transmitted to the ground center where a preliminary orbit will be calculated. If the NEO is classified as an object of special interest, the ground center will send a command to SODA to observe this object in a target mode, for example, every 3.5 minutes.

It is expected that SODA will be able to detect all decameter-sized (and larger) bodies coming towards the Earth from the Sun (day-time celestial hemisphere). For objects on collisional orbits SODA will ensure a warning time of up to 10 hours and the accuracy of coordinates of the atmospheric entry point up to ~ 10 × 100 km.

According to the simulation we performed, the number of decameter size bodies to be detected per year is about 600, more numerous smaller meteoroids can be detected with lower completeness. This makes it possible to test current statistical models of the minor body population in the Solar system.

For the last two years additional research was carried out to make the SODA concept more mature.

Recent progress in manufacturing of CMOS detectors with a small pixel size makes it possible to design a more compact optical system without impacting the efficiency. The new optical system (30 cm aperture, F : 1.5, 3.75 deg field of view) based on the Sonnefeld camera optical design has been proposed. In combination with the pre-aperture slewing mirror (480 × 340 mm) it provides a possibility to observe with a single telescope in a 50 × 120 degree sky area.

The proposed trajectory design for the SODA mission allows the insertion of 2 SC (~ 500 kg each) into orbit around the L1 point with a required phase delayby a medium-class launcher Souz-2 with a Fregat-SB upper stage. It is also possible to launch one SC based on a space bus Navigator with a total mass of up to 1800 kg (Figure 2).

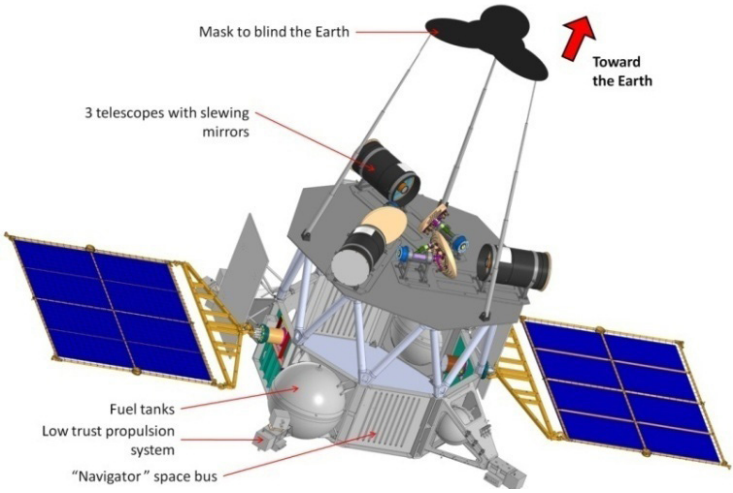


Fig. 2. SODA spacecraft concept with Navigator space bus.

The scientific potential of the mission can be enhanced by including instruments for monitoring the activity of the Sun (similar to the DSCOVR space mission) and for the Earth observation.

The characteristics of the SODA system can be improved by using a modern off-axis TMA optical design in combination with a small pixel size CMOS detector with enhanced NIR sensitivity. Due to the absence of vignetting and wider spectral range, this option will potentially reduce the telescope aperture down to 20-25 cm without impacting the system efficiency.

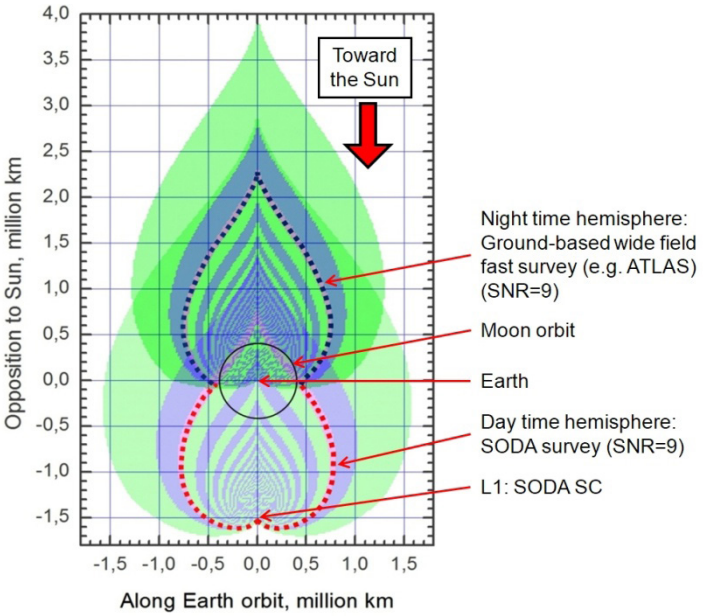


Fig. 3. Combined visibility zone of 10 m NEOs for a ground-based telescope (19^m) and space-based SODA project (in projection on the ecliptic plane).

Another idea to improve the key SODA mission parameter, the waring time, is to use a forced stationary position in the Sun-Earth line at a given distance from Earth which islarger than the L1 point, e.g. to put SC closer to the Sun. The SC would use a solar sail as the main tool to resist the gravity force from the Sun and an additional high efficiency low-thrust propulsion engine. This approach can double the warning time, up to one day, without serious impact on the size and complexity of the scientific payload.

We believe that the most efficient approach is to combine SODA and ground-based NEO detection systems (e.g. ATLAS). Another argument for closer international collaboration is the necessity of construction of a global network of data receiving stations. These stations can be equipped with low-cost 6 m antennas. International cooperation is highly welcome.

REFERENCES:

[1] Asteroid-comet danger: a counteraction strategy, Under. total. Edited by V.A. Puchkov // M.: FSBI VNII GOChS(FC). 2015. P. 272.
[2] Shagarov, A., Shustov, B., Naroenkov, S.. System of observation of day-time asteroids (SODA). // Open astronomy. 2018. V. 27, No. 1, P. 132–138.
[3] Shugarov A.S., Shustov B.M., Naroenkov S.A., Zvereva M. A. Space system for detecting dangerous celestial bodies approaching the Earth from the daytime sky ("SODA") // Space Research. 2018. V. 56 No. 4. P. 300–310.

ON THE POSSIBILITY TO STUDY THE SURFACE MATTER COMPOSITION OF PRIMITIVE MAIN BELT ASTEROIDS NEAR PERIHELION

A.A. Savelova [1], V.V. Busarev [1,2], M.P. Shcherbina [1], S.I. Barabanov [2]
[1] *Lomonosov Moscow State University, Sternberg Astronomical Institute (SAI MSU);*
[2] *Institute of Astronomy, Russian Academy of Sciences*

KEYWORDS:
Asteroid, main belt, mineral, meteorite, composition, reflectance spectra, modeling.

INTRODUCTION:
Earlier [1] we introduced our program OSVAS that can make an estimation of surface matter mineral composition of an asteroid and find its proper meteorite analogues. This program uses reflectance spectra of meteorites or minerals from open databases [2, 3]. Also we introduced another program we wrote that helps to determine a taxonomic class of an asteroid using the spectral reflectivity and visible-range geometric albedo bounds of taxonomic classes [4]. We calculated spectral reflectivity bounds using SMASSII database [5] and albedo bounds using JPL small-body database [6].

In December of 2020 our group collected new reflectance spectra of some main belt primitive asteroids being near perihelion. Our programs were applied to clarify the possibility of their matter composition study.

RESULTS AND CONCLUSIONS:
We used our programs to study asteroids 102 Miriam (SMASSII type C) and 266 Alina (SMASSII type Ch) and found meteorite analogues for them that are in agreement with their taxonomic types. However, our attempts to find meteorite analogs for other eight asteroids of predominately primitive types (19, 52, 177, 200, 203, 250, 379, and 383), which were observed in December of 2020, were not so successful. We suppose that presence of a dust exosphere on these asteroids near perihelion (due to sublimation of ices) and solar activity influence to it (shock-waves in the solar wind) changed reflectance spectra of these asteroids too much. Thus, the main conclusion is that the mentioned effects preclude correct determination of taxonomic types of considered asteroids in the period of their perihelion passage.

REFERENCES:
[1] Rezaeva A.A., Shcherbina M.P., Busarev V.V. Modeling of asteroid reflectance with laboratory databases of analog sample // Abstracts of the Tenth Moscow Solar System Symposium (10M-S3). Space Research Institute. Moscow. Russia. 2019. P. 439–440.
[2] NASA REFLECTANCE EXPERIMENT LABORATORY. Available at: http://www.planetary.brown.edu/relabdocs/relab_disclaimer.htm (accessed 10 August 2021).
[3] CENTER FOR TERRESTRIAL AND PLANETARY EXPLORATION. Available at: https://ctape.uwinnipeg.ca/ (accessed 10 August 2021).
[4] The "template" metod: determing the spectral types of asteroids // Abstracts of all-russian conference «Ground-based astronomy in Russia. XXI century". Special Astrophysical Observatory of the RAS. Nizhny Arkhyz. Russia. 2020. P. 196–197.
[5] Bus S.J., Binzel R.P. Phase II of the Small Main-Belt Asteroid Spectroscopic Survey. A Feature-Based Taxonomy // Icarus. 2002. V. 158. P. 146–177.
[6] JPL Small-Body Database Search Engine. Available at: https://ssd.jpl.nasa.gov/sbdb_query.cgi (accessed 10 August 2021).

INVESTIGATION OF (159402) 1999 AP10 ASTEROID WITH OBSERVATIONS AND SIMULATION DATA

A. Kartashova [1], V. Emel'yanenko [1], M. Husárik [2], N. Kiselev [3], E. Bakanas [1], K. Antoniuk [3], A. Savushkin [3], N. Karpov [4]

[1] *Institute of Astronomy Russian Academy of Sciences, Moscow, Russia, akartashova@inasan.ru;*

[2] *Astronomical Institute, Slovak Academy of Sciences, SK- 05960, Tatranská Lomnica, Slovak Republic;*

[3] *Crimean Astrophysical Observatory, Russian Academy of Sciences, Nauchny, Crimea, Russia;*

[4] *Terskol Branch, Institute of Astronomy Russian Academy of Sciences, Tyrnyauz, Russia*

KEYWORDS:
Asteroids, photometry, polarimetry, ground-based observations, long-term evolution.

INTRODUCTION:
1999 AP10 was discovered on January 14, 1999 by LINEAR. This asteroid has an absolute magnitude of 16.1 and period of rotation of 7.9 hours.

On October 19, 2020 asteroid approached the Earth within 0.0807 au, what is the closest distance until the year 2500.

OBSERVATIONS AND RESULTS
We acquired observations from September to November 2020 which allow us to estimate the physical characteristics of the asteroid (color indices, effective diameter and rotational period etc.).

We performed different observing runs with telescopes, ranging from 0.61-m to 2-m in imaging mode in the optical range. The photometric data were obtained using the B, V, and R broadband filters. The mean color index and diameter of the asteroid were measured. Our observation suggested an S -type classification for this object and the size is 1.38 ± 0.04 km.

Also we derived a convex 3D shape model based on lightcurves from our photometric data (Fig. 1).

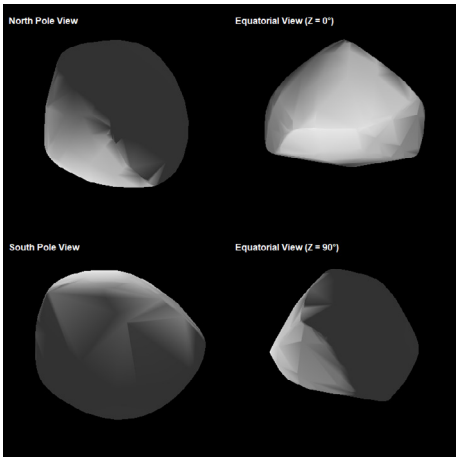


Fig. 1. The shape of the 1999 AP10.

Polarimetric observations of the 159402 (1999 AP10) were carried out during 10 nights from October 6 to 9 November 9, 2020 at the 2.6 (f/16) Shain telescope of the Crimean Astrophysical Observatory (Nauchnij, Crimea) and the 2.0 (f/8) RCC telescope of the Terskol branch of INASAN (Nord Caucasus, Russia) equipped with the identical two-channel aperture polarimeters

"POLSHAKH". The observations covered a range of phase angles from 32.1 ˚ to 71.4˚. The broadband V, R, I filters closed to the Johnson-Cousins system were used in our observations.

The phase angle α, the position angle of the scattering plane φ, the filter, the degree of linear polarization P, and the position angle Θ of the polarization plane with their mean square errors σ_P and σ_Θ, respectively, the difference Θ_r between the polarization plane and the normal to the scattering plane, the degree of polarization P_r with respect to the scattering plane and the telescopes were estimated.

The phase dependence of the polarization of NEA 1999 AP10 in the R filter is shown in the Figure 2.

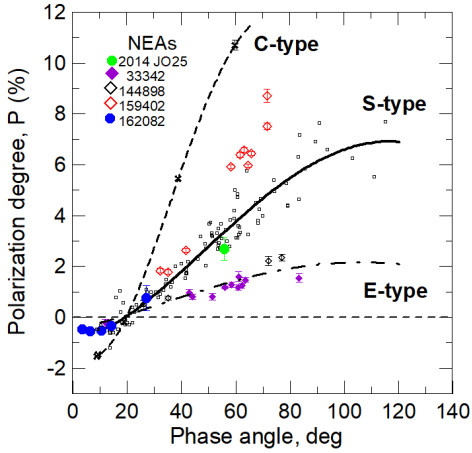


Fig. 2. The phase dependence of the polarization of NEA 159402 (red diamonds) in comparison with the PDP of the main (C, S, E) classes of asteroids and other NEAs.

The data for asteroid 1999 AP10 are close to the upper data limit for S-type asteroids. Therefore, it can be expected that the geometric albedo of this asteroid will be lower than the average albedo of 0.2 for in S-asteroids [1].

The evolution of the orbit of the asteroid 1999 AP10 was studied. The investigation was based on using the symplectic integrator [2]. The perihelion distance change in the past for the nominal orbit is shown in Fig. 3. The dynamical behavior of this asteroid has cometary features. In particular, this object comes to the near-Earth region after approaching Jupiter.

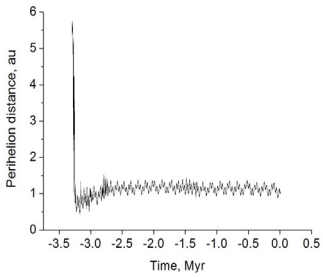


Fig. 3. The perihelion distance change in the past for the nominal orbit of NEA 1999 AP10.

ACKNOWLEDGMENTS:
The work by MH was supported by the Slovak Grant Agency for Science VEGA (Grant No. 2/0023/18) and by the Slovak Research and Development Agency under the Contract No. APVV-19-0072.

REFERENCES:

[1] Shevchenko, V.G., Lupishko, D.F. 1998. Optical properties of asteroids from photometric data. Solar System Research, V. 32. No. 3. P. 220–232.
[2] Emel'Yanenko V.V. 2007. Celestial Mechanics and Dynamical Astronomy. V. 98. No. 3. P. 191–202.

FEATURES OF THE PHASE DEPENDENCE OF THE DEGREE OF LINEAR POLARIZATION OF SUNGRAZING COMET C/1965 S1

D.V. Petrov [1], E.A. Zhuzhulina [1]
[1] *Crimean Astrophysical Observatory (CrAO RAS), Nauchnyj, 298409, Crimea*

KEYWORDS:
Comets, phase dependence, polarization, light scattering, computer simulation.

INTRODUCTION:
Comet Ikeya-Seki (C/1965 S1) is a long-period comet with an orbital period of 880 years, belonging to the family of near-solar comets. Observations of the Ikeya-Seki tail polarization at λ = 0.53 μm show both positive and negative polarization [1]. The phase dependence of the linear polarization degree significantly differs from other comets [2] in green filters (see fig. 1).

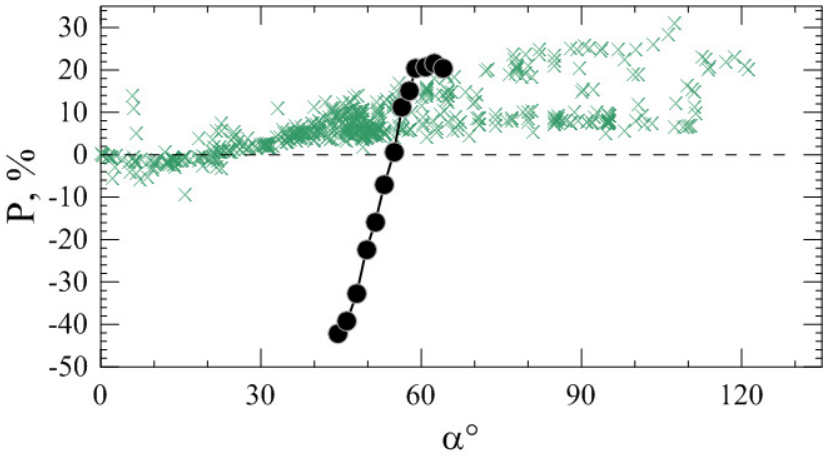


Fig. 1. Phase dependence of linear polarization of comet Ikeya-Seki (circles) and synthetic data of 14 other comets in green filters from database [2] (crosses).

COMPUTER SIMULATION:
We used the computer simulation of light scattering by silicate-carbon mixture of very irregular conjugated Random Gaussian Particles, which were used for interpretation of cometary observations [3]. But it turned out that there are no such parameters of irregular particles that would provide similar steep course of the phase dependence. This can be explained in the only possible way - the presence of regular particles, for example, spheres, formed due to the strong heating of the comet by the Sun.

REFERENCES:
[1] Weinberg J.L., Beeson, D.E. Polarization reversal in the tail of comet Ikeya-Seki (1965 VIII) // Astronomy and Astrophysics. 1976. V. 48. P. 151–153.
[2] Kiselev, N., Velichko, S., Jockers, K., Rosenbush, V., and Kikuchi, S., Eds., Database of Comet Polarimetry. NASA Planetary Data System, 2006.
[3] Petrov D.V., Kiselev N.N. Conjugated Gaussian Random Particle Model and Its Applications for Interpreting Cometary Polarimetric Observations // Solar System Research. 2019. V. 53. P. 294–305.

APPLICATION OF SMALL METEOR ABLATION MODEL TO PERSEID OBSERVATIONS

V. Efremov [1,2], O. Popova [2], D. Glazachev [2], A. Margonis [3], J. Oberst [3, 4], A. Kartashova [5]

[1] *Moscow Institute of Physics and Technology, Moscow, Russia;*
[2] *A.Sadovsky Institute of Geosphere Dynamics RAS, Moscow, Russia;*
[3] *Technische Universität Berlin, Institute of Geodesy and Geoinformation Science, Berlin, Germany;*
[4] *German Aerospace Center (DLR), Institute of Planetary Research, Berlin, Germany;*
[5] *Institute of Astronomy RAS, Moscow, Russia*

KEYWORDS:
Meteors, meteoroids, ablation, Perseids shower

INTRODUCTION:
Meteoroid bodies, along with asteroids and comets, are a source of information about our Solar system, since the material of which they are composed indicates the composition of matter in the early stages evolution of the Solar system. One of the ways to obtain information about the properties of a meteoroid is to study the process of its interaction with the atmosphere (meteorite event). Despite extensive research of meteor phenomena in previous years, the task of accurate determination of parameters such as mass, density and material properties is still relevant.

DESCRIPTIONS OF MODEL:
A model describing the interaction of small meteoroids with the Earth's atmosphere is presented. In this model, the mass loss of a meteoroid is determined using the saturated vapor pressure of the assumed meteoroid's substance. Dependencies of the saturated vapor pressure on the temperature vary from author to author for the same substance. This affects the determination of the parameters (density, size/mass) of meteoroids. An automated method to estimate the physical parameters of a meteoroid by comparing observational and model derived data with known parameters was suggested.

OBSERVATIONS:
For testing of the model, the optical meteor observations of SPOSH cameras in 2016 were used [1]. Meteor particles of Perseid meteor shower were chosen for our calculations. The range of absolute magnitudes of meteors was - 6^m - +2^m. The meteors selected for the study were less bright than - 2^m.

DISCUSSION:
Light and deceleration of a number of meteor events were reproduced. Corresponding meteor particles parameters (density, size/mass) were determined. The effects of the saturated vapor pressure dependence and solution methods on meteoroid parameters were analyzed. Obtained Perseid meteoroids density is compared with independent estimates (~ 400 - 800 kg/m^3 [2]).

REFERENCES:
[1] Margonis, A., Christou, A., Oberst, J. Characterisation of the Perseid meteoroid stream through SPOSH observations between 2010-2016 // Astronomy and Astrophysics. 2019. 626, A25.
[2] Kikwaya, J.B., Campbell-Brown, M. & Brown, P.G. Bulk density of small meteoroids // Astronomy and Astrophysics. 2011. 530, A113.

DUST ACOUSTIC WAVES IN MARTIAN ATMOSPHERE

Yu.N. Izvekova [1], Yu.S. Reznichenko [1], S.I.Popel [1]
[1] *Space Research Institute, Russian Academy of Sciences, Moscow, 117997 Russia*

KEYWORDS:
Dusty plasma, Martian ionosphere, dust acoustic waves, kinetic instability.

INTRODUCTION:
It is shown that the horizontal winds in Martian ionosphere, at the initial stage of their interaction with dusty plasma clouds at altitudes of about 100 km, can cause conditions for the excitation of dust acoustic waves due to the development of kinetic instability. The dispersion relationship of the dust acoustic waves is determined as well as their growth rate in the conditions under study. It is noted that the generation time of the dust acoustic wave is substantially long to allow the formation of nonlinear plasma wave structures, e.g., solitons. The possibility of generation of dust acoustic perturbations in Martian ionosphere should be taken into account during processing and interpretation of observation data. Thus, the altitude region of about 100 km in Martian atmosphere is of a substantial interest from the viewpoint of the studies of dusty plasma processes. In this region, the main parameters of the dusty ionosphere are determined by night-time conditions. The objective of this work is to estimate the possibilities of the excitation of waves in the plasma of the night-time Martian ionosphere at altitudes ~ 100 km.

CONDITIONS IN NIGHT-TIME IONOSPHERE OF MARS:
It is understood that, as a result of the heating by Solar radiation and the rotation of Mars, asymmetrical circulation takes place, leading to an appearance of horizontal winds, which propagate at velocities u of about 100 m/s above extended surface areas. Due to the contrast of day–night temperatures, the horizontal winds can move through the terminator near the poles at altitudes of about 100 km. Thus, a situation is possible when the dusty plasma clouds end up in the regions with horizontal homogenous winds. The dust grains, whose masses appreciably exceed the ion and electron mass, are dragged into the wind motion much slower. Therefore, until stationary motion is established, there exists a relative velocity between the ions and dust grains, whose value is of the same order of magnitude as that of the neutral wind. This effect can lead to the development of a plasma instability similarly to, e.g., the situation in which the dusty plasma near lunar surface interacts with the plasma of the tail of Earth's magnetosphere [1].

The ion composition of Martian ionosphere near the altitude of 100 km consists mainly, of positive ions, with the major deposition of ions. The ion temperature is $T \geq 90$ K [2]. Thus, the thermal ion velocity v_{Ti} is no lower than 150 m/s. This means that under these conditions, the Bunemantype hydrodynamic instability, which can develop at $\omega >> kv_{Ti}$, is impossible. Here, k is the wave vector, $k=|k|$, and ω is the wave frequency.

KINETIC DUST ACOUSTIC INSTABILITY:
The kinetic dust acoustic instability is realized at $kv_{Td} \ll \omega \ll kv_{Ti}$, where v_{Ti} is the thermal velocity of dust grains. In this case, the dispersion equation has the form

$$1+\frac{1}{k^2\lambda_{De}^2}+\frac{1}{k^2\lambda_{Di}^2}\left(1+i\sqrt{\frac{\pi}{2}}\frac{\omega-ku}{kv_{Ti}}\right)-\frac{\omega_{pd}^2}{\omega^2}=0$$

Here, $\lambda_{De(i)}$ is the electron (ion) Debye length and ω_{pd} is the plasma frequency of dust grains. In this case, the linear dispersion is that for dust acoustic waves and has the form

$$\omega_k=\frac{\omega_{pd}k\lambda_d}{\sqrt{1+k^2\lambda_d^2}},$$

where

$$\frac{1}{\lambda_D^2}=\frac{1}{\lambda_{De}^2}+\frac{1}{\lambda_{Di}^2}\ .$$

The instability growth rate is determined by the expression

$$\gamma_k=\frac{\omega_k^3}{k^2\lambda_{Di}^2\omega_{pd}^2}\sqrt{\frac{\pi}{8}}\frac{ku-\omega}{kv_{Ti}}\ .$$

The instability characteristic growth rate has the form

$$\gamma\sim\omega_{pd}\frac{u}{v_{Ti}}$$

The condition for the instability development

$$u>\omega_{pd}\lambda_D$$

is realized under the plasma conditions in the region of dusty plasma clouds at altitudes of about 100 km. For the plasma parameters T = 90 K, $n_n = 10^{12}$ cm^{-3}, $m_n = 7\times10^{-23}$ g, u = 100 m/s, n_d = 1 cm^{-3}, and a ~ 100 nm, we have γ ~ 0.1 s^{-1} and v_{dn} ~ 10^{-2} s^{-1}. Thus, the condition τ^{-1} ~ γ >> n_{dn} is satisfied, dust acoustic waves are excited, and generation of nonlinear waves is possible. Nonlinear waves in the form of solitons are studied in details in [3].

ACKNOWLEDGEMENTS:
This work was supported in part by Theoretical Physics and Mathematics Advancement Foundation “BASIS”.

REFERENCES:

[1] Popel S.I., Morozova T.I. Wave processes during the interaction of the Earth’s magnetotail with dusty plasma near the lunar surface // Plasma Physics Reports. 2017. V. 43, P. 566.
[2] Forget F., Montmessin F., Bertaux J.L., Gonzalez-Galindo F., Lebonnois S., Quemerais E., Reberac A., Dimarellis E., Lopez-Valverde M.A. Density and temperatures of the upper Martian atmosphere measured by stellar occultations with Mars Express SPICAM // J. Geophys.Res. 2009. V. 114. E01004.
[3] Izvekova Yu.N., Reznichenko Yu.S., Popel S.I. On the Possibility of Dust Acoustic Perturbations in Martian Ionosphere // Plasma Physics Reports. 2020. V. 46. No. 12. P. 1205–1209.

DWARF PLANET CERES RESONANCE PERTURBATIONS

A.E. Rosaev [1]
[1] *GAUK YO Center named after V.V. Tereshkova, 150000, Yaroslavl, Chaikovskogo, 3, hegem@mail.ru*

KEYWORDS:
Dwarf planet, resonance, orbital element evolution, perturbations, asteroids.

INTRODUCTION:
As it is known, Ceres can be a source of global chaos in asteroid belt and in whole Solar system [1]. Moreover, Ceres can strongly perturb orbits of asteroids in the Main belt [2]. By these reasons, the study of Ceres dynamic is very important.

RESULT OF RESONANCE SEARCH FOR:
In our numeric integrations we have found periodic variations of Ceres semimajor axis (Fig. 1). We suppose that it is effect of resonance and provide search for nearest resonance by our method [3] and by data of Smirnov & Schevchenko paper [4]. We have obtained that 1 : 4 : 4MJ three body resonance at 2.767605 AU (2.767668 AU by [4]) is nearest for the Ceres orbit (distance about 0.00055 AU). This resonance may be a reason of observed Ceres semimajor axis periodic variations.

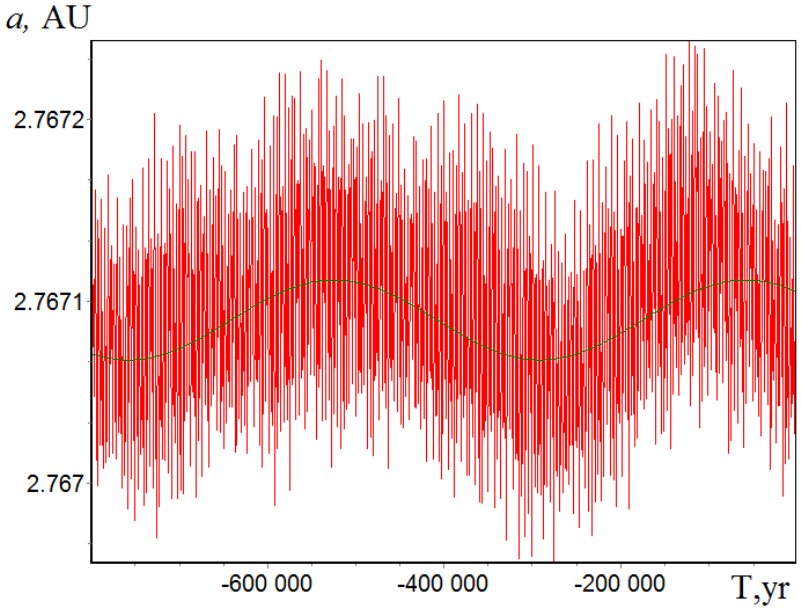


Fig. 1. Ceres semimajor axis evolution and their approximation.

ORBITAL ELEMENTS EVOLUTION APPROXIMATION:
After that, we have done the approximations of all orbital elements of Ceres by method described in [5]. We have found some periodic component in orbital elements perturbations. In particular, we have found perturbations with period of node precession (in inclination) and perihelion precession in eccentricity. We note that our approximation of orbital elements:

$$E_i = E_{i00} + E_{i0} t + \sum_k^N \left(c_{ik} \cos\left(\omega_{ik} t + \varphi_{ik} \right) \right)$$

is better (has smaller error) than Fourier approximation and allow to obtain values of frequencies with better precision.

Below we give a picture of Ceres eccentricity evolution as an example of our approximation (Fig. 2).

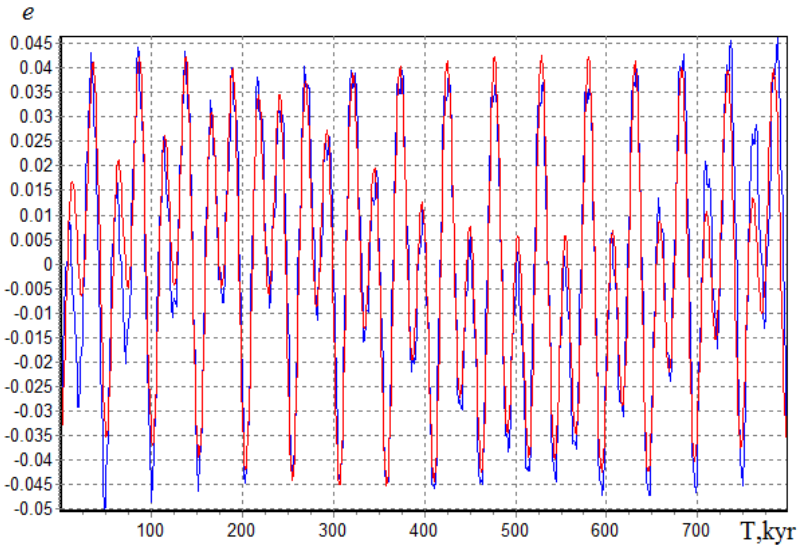


Fig. 2 Ceres eccentricity evolution (blue) and their approximation (red).

Our approximation is (t in kyr):

e = 0.118 + 0.0288cos(0.243t+2.87) - 0.005cos(0.008t+4) + 0.02cos(0.126t+4).

The Fourier coefficients are:

0.117966	W= 0.007869 1/kyr
0.0015246 COS(1 Wt)	0.0028232 SIN(1 Wt)
- 0.0000671 COS(2 Wt)	- 0.0018333 SIN(2 Wt)
- 0.0076992 COS(16 Wt)	- 0.0051326 SIN(16 Wt)
0.0011605 COS(28 Wt)	- 0.0004822 SIN(28 Wt)
0.0017523 COS(29 Wt)	- 0.0008386 SIN(29 Wt)
0.0038548 COS(30 Wt)	- 0.0007285 SIN(30 Wt)
- 0.0129049 COS(31 Wt)	0.0029412 SIN(31 Wt)
- 0.0024957 COS(32 Wt)	0.0009228 SIN(32 Wt)
- 0.0012777 COS(33 Wt)	0.0004308 SIN(33 Wt)
- 0.0012350 COS(47 Wt)	- 0.0003642 SIN(47 Wt)
0.0013832 COS(140 Wt)	- 0.0000785 SIN(140 Wt)

REFERENCES:

[1] Laskar J.,et al. : Strong chaos induced by close encounters with Ceres and Vesta., A&A. 2011. P. 532, V. L4.
[2] Novakovic B., Maurel C., Tsirvoulis G., Knezevich Z.. Asteroid secular dynamics: Ceres' fingerprint identified., arXiv:1506.01586v1 [astro-ph.EP] 4 Jun 2015.
[3] Rosaev et al 2020 List of the Close Asteroid Pairs Strongly Perturbed by Three-body Resonances Res. Notes AAS 4 239
[4] Smirnov E.A., Shevchenko I.I. Massive identification of asteroids in three-body resonances., Icarus. 2013. V. 222(1). P. 220–228.
[5] Rosaev A., Plavalova E.: The Fourier approximation for orbital elements for the members of very young asteroid families, Planetary and Space Science, 2021, V.202, 105233

MODULATIONAL INTERACTIONS IN THE DUSTY PLASMAS OF METEOROID TAILS

T.I. Morozova [1], S.I. Popel [1]
[1] *Space Research Institute, Russian Academy of Sciences, Moscow, 117997 Russia*

KEYWORDS:
Meteoroids, dusty plasmas, meteoroid tail, modulational interaction, electrophonic sounds, low-frequency perturbations, dust acoustic waves.

INTRODUCTION:
The possibility of the occurrence of modulational instability [1] of electromagnetic waves in the tails of meteoroids, associated with a dust acoustic mode at altitudes of 80–120 km is investigated. The parameters of the tails of meteoroids at different altitudes in the Earth's ionosphere are considered. The mechanism of formation of dusty plasmas in the tails of meteoroids is described. It is shown that the highest concentration of particles in meteoroid tails can be achieved as a result of the crushing of the meteor body and the outbursts. It is shown that the charging of dust particles of meteoric matter leads to the conditions in dusty plasmas of meteoroid tails when dust acoustic waves can exist. Dust acoustic disturbances are excited as a result of the development of modulational instability of electromagnetic waves from a meteor body, which emits in the optical and radio ranges [2]. The influence of neutrals on the development of modulational interaction is taken into account. It is noted that the concentration of neutrals in meteor tails is higher than the concentration of neutrals in the Earth's ionosphere. It was found that at altitudes of 100–120 km for the typical parameters of the dusty plasmas of meteoroid tails, the condition for the excitation of dust acoustic waves is satisfied. It is shown that due to collisions of dust and neutrals the development of modulational instability is suppressed at altitudes of 80–90 km, while inelastic collisions of neutrals with electrons and ions do not affect the development of modulational instability.

DISCUSSION:
The modulational instability of electromagnetic waves associated with dust acoustic waves can explain the occurrence of low-frequency noise during the passage of meteor bodies in the frequency range characteristic for dust acoustic waves. In particular, the connection between the occurrence of electrophonic noises during the passage of meteor bodies and the development of modulational instability in the tails of meteoroids is noted. It is assumed that electromagnetic waves modulated by low-frequency dust acoustic waves reach the Earth's surface and can be converted into sound waves by means of receivers [3–5]. It is shown that time of the development of modulational instability much less than lifetime of meteoroid tail for characteristic temperatures and particle concentrations in the tails of meteoroids. The equations of the charging of dust particles in the tails of meteoroids are given. It is calculated that due to intense emission currents from the surface of dust particles, the dust is positively charged both in the daytime and at night. The characteristic charges of nanoscale dust particles in the tails of meteoroids are estimated. It is noted that modulational instability at 80 km will be suppressed due to collisions of dust with neutrals.

REFERENCES:
[1] S.V. Vladimirov, V.N. Tsytovich, S.I. Popel, and F.Kh. Khakimov, "Modulational Interactions in Plasmas", Kluwer Academic Publishers, Dordrecht-Boston-London (1995), P. 539.
[2] Filonenko A.D. High-frequency radio emission from meteors // Geomagnetism and Aeronomy. V. 58. No. 5. S. P. 720–727. 2018.
[3] Spalding R., Tencer J., Sweatt W., Conley B., Hogan R., Boslough M., Gonzales G., Spurný P. // Sci. Reps. 2017. V. 7. P. 41251. doi: 10.1038/srep41251.
[4] Verveer P., Bland A., Bevan A.W.R. // 63rd Ann. Meteoritical Soc. Meeting. 2000. Publisher: Meteoritical Society, Pages: A163–A164.
[5] Zgrablić G., Vinković D., Gradečak S., Kovačić D., Biliskov N., Grbac N., Andreić Ž., Garaj S. // J. Geophys. Res. 2002. V. 107. P. SIA11-1. doi: 10.1029/2001JA000310.

ESTIMATION OF THE AGE OF YOUNG ASTEROID PAIR (21436) CHAOYICHI — (334916) 2003 YK39

V.S. Safronova [1], E.D. Kuznetsov [1]
[1] *Ural Federal University, Lenina Avenue, 51, Yekaterinburg, 620000, Russia, v.s.safronova@urfu.ru, eduard.kuznetsov@urfu.ru*

KEYWORDS:
Asteroids, individual (21436) Chaoyichi, (334916) 2003 YK39, asteroid pair, numerical simulation, probabilistic evolution.

INTRODUCTION:
Among the asteroids of the Main Belt, there are pairs of objects in close orbits whose members, as a rule, have a common origin, and the dynamic evolution of their orbits has common laws [1]. In [2], we identified candidates for young pairs by calculating the Kholshevnikov metrics [3] and studying their dynamic evolution using nominal orbits. In this paper, we will estimate the age of young asteroid pair (21436) Chaoyichi – (334916) 2003 YK39. In [4] estimated the age of the pair from 10 to 140 kyr, with the most probable value of 31 kyr. Analysis of the dynamic evolution of the pair (21436) Chaoyichi — (334916) 2003 YK39 in [5] showed that the age of the pair does not exceed 150 kyr and ranges from 37 to 68 kyr. In this paper, we will study the probabilistic evolution of the pair (21436) Chaoyichi — (334916) 2003 YK39.

METHOD:
To study probabilistic evolution for each asteroid, we generated 1000 trajectories with initial data from the confidence region, which corresponds to 1 million variants of the dynamic evolution of pair. The simulation was carried out in the Orbit9 program (http://adams.dm.unipi.it/orbfit/), which is part of the OrbFit software package. The equations of motion of eight major planets, the dwarf planet Pluto and the asteroid, were integrated consistently, considering the influence of the Yarkovsky effect, the oblateness of the Sun, and relativistic effects. We have studied the orbital evolution of asteroids over 100 kyr

To estimate the drift rate of the semimajor axis, we used the approach proposed in [6, 7]. Estimates of the maximum modulus of the drift rate of the semimajor axis $|da/dt|_{max}$ were obtained based on the relations between the parameters of the studied asteroid and asteroid (101955) Bennu. In contrast to the traditional approach, considering the Yarkovsky effect, we obtained age estimates for several fixed values of the semimajor axis drift velocities corresponding to different positions of the asteroid's rotation axis to the orbital plane. For each asteroid five variants of evolution were considered at the values of the drift rate corresponding to different orientations of the asteroid's axis of rotation relative to the plane of its orbit: $da/dt = 0$ at $\varphi = 90°$ or 270 °; $da/dt = \pm 1/2\ |da/dt|_{max}$ at $\cos(\varphi) = \pm 1/2$, respectively; $da/dt = \pm\ |da/dt|_{max}$ at $\varphi = 0°$ and 180 °, respectively.

We used two techniques to estimate the age of a pair of asteroids. The first is based on an analysis of low relative-velocity close encounters. The second is based on the search for the minimum distance between the orbits using the Kholshevnikov metrics [3].

We analyzed the conditions of low relative-velocity close encounters: $\Delta r < 10\ R_H$ and $\Delta V < 4V_{esc}$, where R_H is the radius of the Hill sphere of the more massive asteroid in the pair, V_{esc} is the escape velocity relative to the more massive asteroid, Δr is the relative distance between asteroids, and ΔV is the relative velocity of the asteroids.

RESULTS:
We present estimates of the age of the pair (21436) Chaoyichi — (334916) 2003 YK39 for two values of the semi-major axis drift rate for each of the asteroids: $(da/dt)_{21436} = 0.7 \times 10^{-4}$ and 1.4×10^{-4} au/Myr, $(da/dt)_{334916} = 2.25 \times 10^{-4}$

and 4.5×10^{-4} au/Myr. Table 1 gives the estimates of the age of the pair (21436) Chaoyichi — (334916) 2003 YK39 from the analysis of low relative-velocity close encounters. Table 2 shows the estimates of the age of the pair from the analysis of minimum distances between orbits.

Table 1. Estimates of the age of the pair (21436) Chaoyichi — (334916) 2003 YK39 in years from the analysis of low relative-velocity close encounters.

$(da/dt)_{21436}$ [au/Myr]	$(da/dt)_{334916}$ [au/Myr]	
	2.25×10^{-4}	4.5×10^{-4}
0.7×10^{-4}	94 530 ± 830	45 200 ± 200
1.4×10^{-4}	Orbits diverge	53 110 ± 250

Table 2. Estimates of the age of the pair (21436) Chaoyichi — (334916) 2003 YK39 in years from the analysis of minimum distances between orbits

$(da/dt)_{21436}$ [au/Myr]	$(da/dt)_{334916}$ [au/Myr]	
	2.25×10^{-4}	4.5×10^{-4}
0.7×10^{-4}	93 600 ± 8 100	46 900 ± 1 700
1.4×10^{-4}	Orbits diverge	51 510 ± 290

DISCUSSION

The age estimate of the pair (21436) Chaoyichi — (334916) 2003 YK39 depends on the semi-major axis drift rate significantly. The age estimates obtained are consistent with the results obtained in [4, 5]. Nevertheless, the age estimates obtained based on the analysis of low relative-velocity close encounters and the search for the minimum distance between the orbits are consistent with each other. The differences in the age estimates based on low relative-velocity close encounters and Kholshevnikov metrics are because the proximity of orbits does not yet guarantee the approach of asteroids but is only a necessary condition.

CONCLUSIONS

We are continuing our exploration of the pair (21436) Chaoyichi — (334916) 2003 YK39. In the future, it is planned to carry out a study of the probabilistic evolution and obtain the age estimates for the following values of the semi-major axis drift rates $(da/dt)_{21436} = 0, -0.7 \times 10^{-4}$ and -1.4×10^{-4} au/Myr, $(da/dt)_{334916} = 0, -2.25 \times 10^{-4}$ and -4.5×10^{-4} au/Myr. The significant dependence of the age estimate on the values of the drift velocities used indicates that it will be possible to obtain reliable age estimates only after the drift velocities of the semi-major axes of the asteroid's orbits are determined due to the Yarkovsky effect. At present, having only estimates of the maximum modulus of the drift rate of the semi-major axes of asteroid's orbits, one can only indicate the possible age range of the studied pair of asteroids (21436) Chaoyichi — (334916) 2003 YK39.

ACKNOWLEDGMENTS:

The work was supported by the Ministry of Science and Higher Education of the Russian Federation via the State Assignment Projects FEUZ-2020-0030 (EDK) and FEUZ-2020-0038 (VSS).

REFERENCES:

[1] Vokrouhlický D., Nesvorný D. Pairs of asteroids probably of a common origin // Astronomical Journal. 2008. V. 136. P. 280–290.

[2] Kuznetsov E.D., Rosaev A.E., Plavalova E., Safronova V.S., Vasileva M.A. A Search for Young Asteroid Pairs with Close Orbits // Solar System Research. 2020. V. 54. No. 3. P. 236–252.

[3] Kholshevnikov K.V., Kokhirova G.I., Babadzhanov P.B., Khamroev U.H. Metrics in the space of orbits and their application to searching for celestial objects of common origin // Mon. Not. R. Astron. Soc. 2016. V. 462. P. 2275–2283.

[4] Pravec P., Fatka P., Vokrouhlický D., Scheirich P., Ďurech J., Scheeres D.J., Kušnirak P., Hornoch K., Galad A., Pray D.P., Krugly Yu.N., Burkhonov O., Ehgamberdiev Sh.A., Pollock J., Moskovitz N., Thirouin A., Ortiz J.L., Morales N., Husarik M.,

Inasaridze R.Ya., Oey J., Polishook D., Hanuš J., Kučakova H., Vraštil J., Vilagi J., Gajdoš Š., Kornoš L., Vereš P., Gaftonyuk N.M., Hromakina T., Sergeyev A.V., Slyusarev I.G., Ayvazian V.R., Cooney W.R., Gross J., Terrell D., Colas F., Vachier F., Slivan S., Skiff B., Marchis F., Ergashev K.E., Kim D.-H., Aznar A., Serra-Ricart M., Behrend R., Roy R., Manzini F., Molotov I.E. Asteroid pairs: a complex picture // Icarus. 2019. V. 333. P. 429–463.

[5] Kuznetsov E.D., Rosaev A.E., Plavalova E., Safronova V.S. Age estimation of asteroid pair with close orbits (21436) Chaoyichi — (334916) 2003 YK39 // INASAN Science Reports. V. 5(2). M.: Janus-K, 2020. P. 52–55.

[6] Spoto F., Milani A., Knezevic Z. Asteroid family ages // Icarus. 2015. V. 257. P. 275–289.

[7] Del Vigna A., Faggioli L., Milani A., Spoto F., Farnocchia D., Carry B. Detecting the Yarkovsky effect among near-Earth asteroids from astrometric data // Astron and Astrophys. 2018. V. 617. Id. A61. P. 16.

DUST ACOUSTIC SOLITONS IN THE MAGNETOSPHERE OF SATURN

S.I. Kopnin [1], D.V. Shokhrin [2], S.I. Popel [1]
[1] *Space Research Institute of the Russian Academy of Sciences (IKI), 84/32 Profsoyuznaya Str, Moscow 117997, Russia, serg_kopnin@mail.ru;*
[2] *National Research University Higher School of Economics, Myasnitskaya 20, Moscow 101000, Russia*

KEYWORDS:
Dusty plasmas, dust acoustic solitons, kappa distribution, magnetosphere of Saturn.

INTRODUCTION:
An important object from the viewpoint of studying dusty plasmas is the magnetosphere of Saturn [1, 2]. Plasma parameters in the magnetosphere of Saturn were measured within the Voyager 1 and 2 missions [3] in the 1980s. The existence of waves in the plasma of Saturnian magnetosphere was proved on the basis of the data obtained by the Voyager 1 spacecraft [4]. Theoretical studies of ion-acoustic waves in the magnetosphere of Saturn were carried out in [5]. Dusty plasma in the vicinity of Saturn's moon Enceladus was discovered by the Cassini mission [1, 2].

Plasmas in the magnetosphere of Saturn have some features in comparison with other space systems, which are under consideration now (for the Moon, see, e.g., [6]). For example, measurements of the parameters of electrons of Saturnian magnetosphere, obtained in the framework of the Voyager [3, 4] and Cassini [7] missions, showed the coexistence of two types (hot and cold) of electrons. It turned out [7] that the velocities of electron populations obey the so-called κ-distribution with independent low values of κ.

Thus the problem of studying nonlinear wave structures in dusty plasmas under conditions typical for the Saturnian magnetosphere is urgent. Solitons are an important type of nonlinear structures observed in space [8, 9]. In this paper, we consider nonlinear wave structures in the dusty magnetosphere of Saturn, which are typical for dusty plasmas, namely, dust acoustic solitons. We take into account the fact that two types of electrons (hot and cold) coexist in the magnetosphere of Saturn, obeying two different κ-distributions.

SOLITON SOLUTIONS:
To describe dust acoustic solitons, one can use the set of equations, which includes the continuity equation and the Euler equation for dust particles, the Poisson equation for the self-consistent electrostatic potential in the dusty plasma of Saturnian magnetosphere, the expressions for distributions of ions and electrons valid on dust acoustic time scales. Furthermore, due to the fact that dust acoustic waves are slow enough so that the time scales characterizing them exceed significantly the characteristic times of dust particle charge variations, the charges of dust particles can be determined from the steady-state charging equation.

This set of equations can be solved by the Sagdeev potential method. For a localized wave solution propagating with a certain constant velocity M, we can move to new coordinate system $\xi = x - Mt$. In this case, all the parameters of the problem depend only on the new variable ξ. We use the dimensionless variables $\frac{e\varphi}{T_i} \to \varphi$, $\frac{M}{C_{Sd}} \to M$, $\frac{\zeta}{\lambda_{Di}} \to \zeta$, where $-e$ is the electron charge, φ is the electrostatic potential, T_i is the ion temperature, $C_{Sd} = \sqrt{\frac{T_i}{m_d}}$, m_d is the dust particle mass, $\lambda_{Di} = \sqrt{\frac{T_i}{4\pi n_{i0} e^2}}$, and n_{i0} is the unperturbed number density of ions. Below the results are given of calculations that were carried out for the following plasma parameters of Saturnian magnetosphere (see [3, 5, 7]): $n_{i0} = 10\ \mathrm{cm}^{-3}$, $T_i = 100$ K, $T_{ec} = 10$ eV, $T_{he} = 700$ eV, $\alpha = 0.5$,

$\kappa_c = \kappa_h = 2$, where the subscripts "c" and "h" characterize cold and hot electrons, respectively, T_e is the electron temperature, α is the ratio coefficient between the number densities of cold and hot electrons, κ is the parameter of the electron distribution.

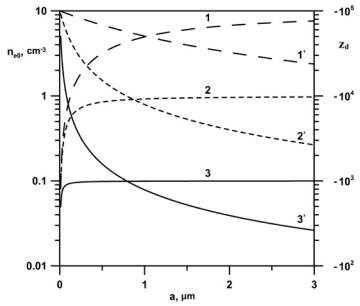


Fig. 1. Dependences of the charge numbers Z_d of dust particles (curves 1–3), as well as the total electron number densities (curves 1'–3') on the size of dusts for various number densities of dust particles: $n_{d0} = 10^{-4}$ cm^{-3} (curves 1, 1'), $n_{d0} = 10^{-3}$ cm^{-3} (curves 2, 2'), $n_{d0} = 10^{-2}$ cm^{-3} (curves 3, 3').

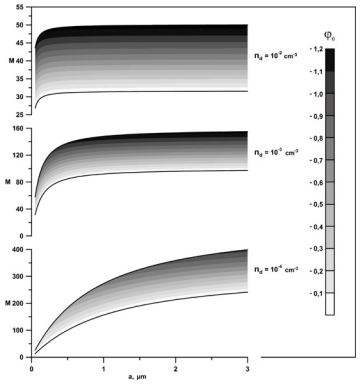


Fig. 2. Amplitudes φ_0 of dust acoustic solitons depending on the size of dust particles and on the dimensionless velocity of the soliton for $n_{d0} = 10^{-4}$ cm^{-3}, $n_{d0} = 10^{-3}$ cm^{-3}, and $n_{d0}=10^{-2}$ cm^{-3}. The bold lines correspond to the boundaries of the function domain of M.

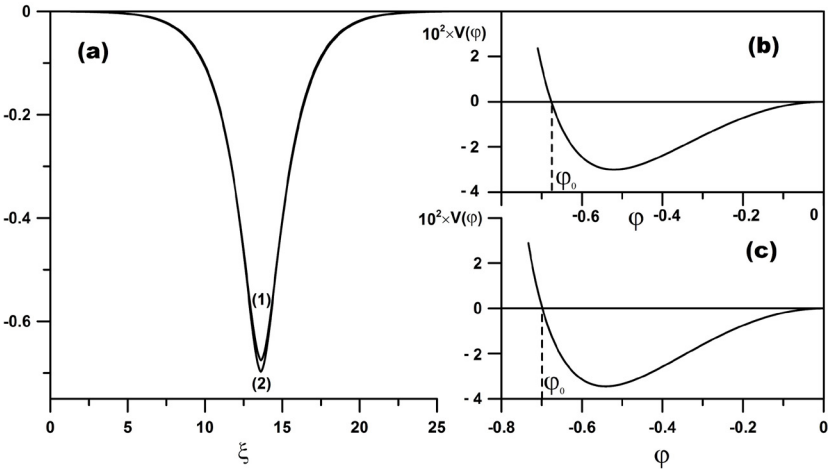


Fig. 3. Dust acoustic solitons (**a**) and the corresponding Sagdeev potentials (**b**) and (**c**) for the case when $n_{d0} = 10^{-2}$ cm^{-3} and $M = 40$. Soliton (**1**) and Sagdeev potential (**b**) correspond to the dust particle size $a = 2$ μm. Soliton (**2**) and Sagdeev potential (**c**) correspond to the dust particle size $a = 0.2$ μm.

Figure 1 shows the dependences of the charge numbers Z_d of dust particles and the total number density of electrons (including cold and hot those) on the size of the dusts for various number densities of dust particles. Figure 2 presents the amplitudes of dust acoustic solitons depending on the size of dusts for the entire possible range of dimensionless velocities at different dust particle number densities. Figure 3 shows typical types of solitons and the corresponding Sagdeev potentials for different sizes of dust particles. It can be seen that over the entire domain of definition, the amplitudes of dust acoustic solitons φ_0 are negative, and their absolute values are rather large (of the order of T_i/e).

SUMMARY:

To summarize, we have shown a possibility of propagation of localized wave structures such as dust acoustic solitons in dusty plasmas of Saturnian magnetosphere, which includes electrons of two types (hot and cold), magnetospheric ions, as well as charged dust particles. The regions of possible velocities and amplitudes of solitons are determined. Soliton solutions are found for various sizes and number densities of dust particles in the magnetosphere of Saturn. The amplitudes of the electrostatic potential of dust acoustic solitons are shown to be negative over the entire range of definition. Moreover, their absolute values can be quite large (of the order of Ti/e), which indicates the possibility of observing dust acoustic solitons in the magnetosphere of Saturn in future space missions.

ACKNOWLEDGMENTS:

This work was supported in part by Theoretical Physics and Mathematics Advancement Foundation “BASIS”.

REFERENCES:

[1] Wahlund J.-E., André M., Eriksson A.I.E., et al. Detection of dusty plasma near the E-ring of Saturn // Planet. Space Sci. 2009. V. 57. P. 1795–1807.
[2] Yaroshenko V.V., Ratynskaia S., Olson J., et al. Characteristics of charged dust inferred from the Cassini RPWS measurements in the vicinity of Enceladus // Planet. Space Sci. 2009. V. 57. P. 1807-1812.
[3] Sittler, Jr. E.C., Ogilvie K.W., Scudde J.D. Survey of Low-Energy Plasma Electrons in Saturn’s Magnetosphere: Voyagers 1 and 2 / J. Geophys. Res. 1983. V. 88. No. A11. P. 8847–8870.
[4] Barbosa D.D., Kurth W.S. On the Generation of Plasma Waves in Saturn’s Inner Magnetosphere // J. Geophys. Res. 1993. V. 98. No. A6. P. 9351-9356.
[5] Koen E.J., Collier A.B., Maharaj S.K., Hellberg M.A. Particle-in-cell simulations of ion-acoustic waves with application to Saturn’s magnetosphere // Phys. Plasmas. 2014. V. 21. No. 7. P. 072122.
[6] Popel S.I., Golub’ A.P., Zelenyi L.M., Dubinskii A.Yu. Lunar dust and dusty plasmas: Recent developments, advances, and unsolved problems // Planet. Space Sci. 2018. V. 156. P. 71-84.
[7] Schippers P., Blanc M., Andre N., et al. Multi-instrument analysis of electron populations in Saturn’s magnetosphere // J. Geophys. Res. 2008. V. 113. P. A07208.
[8] Pécseli H.L., Lybekk B., Trulsen J., Eriksson A. Lower-hybrid wave cavities detected by instrumented spacecrafts // Plasma Phys. Controlled Fusion. 1997. V. 39. No. 5A. P. A227–A236.
[9] Popel S.I. Threshold Energy Density of Lower Hybrid Waves in the Freja Experiment // Plasma Phys. Rep. 2001. V. 27. No. 5. P. 448–450.

INVESTIGATION OF THE DUST PARTICLES DYNAMICS UNDER THE AIRLESS BODIES' CONDITIONS: EXPERIMENTAL SET-UP

I.A. Shashkova [1], A.Yu. Poroikov [2], A.V. Zakharov [1], I.A. Kuznetsov [1], S.A. Bednyakov [1], G.G. Dolnikov [1], A.N. Lyash [1], A.A. Kartasheva [1], A.S. Bychkova [1], A.V. Shekhovtsova [1], M. Essam [1]

[1] *Space Research Institute of the RAS, Moscow, Russia, kia@iki.rssi.ru;*
[2] *National Research University "Moscow Power Engineering Institute", Moscow, Russia*

KEYWORDS:
Dusty plasma, dust,. dust dynamics, atmosphereless body, Moon, Experimental set-up

INTRODUCTION:

One of the complicating factors of the future robotic and human lunar landing missions is the influence of the dust. Meteorites bombardment has accompanied by shock-explosive phenomena, disintegration and mix of the lunar soil in depth and on area simultaneously. Therefore, the lunar soil has undergone melting, physical and chemical transformations.

Studying the properties of lunar dust is important both for scientific purposes to investigation the lunar exosphere component and for the technical safety of lunar robotic and manned missions.

The absence of an atmosphere on the Moon's surface is leading to greater compaction and sintering. Properties of regolith and dust particles (density, temperature, composition, etc.) as well as near-surface lunar exosphere depend on solar activity, lunar local time and position of the Moon relative to the Earth's magnetotail. Upper layers of regolith are an insulator, which is charging as a result of solar UV radiation and the constant bombardment of charged particles, creates a charge distribution on the surface of the moon: positive on the illuminated side and negative on the night side. Charge distribution depends on the local lunar time, latitude and the electrical properties of the regolith (the presence of water in the regolith can influence the local distribution of charge).

On the day side of Moon near surface layer there exists possibility formation dusty plasma system. Altitude of levitation is depending from size of dust particle and Moon latitude. The distribution dust particle by size and altitude has estimated with considering photoelectrons, electrons and ions of solar wind, solar emission.

Moreover, most of these processes take please on most body in the space without the atmosphere.

Experimental investigation of the dust dynamics near the atmospereless bodies are quite challenging. Experimental set-up should include the sources of electrons, UV, ions (solar interaction), special materials. It also should be accurate registration system, see Fig. 1 [1].

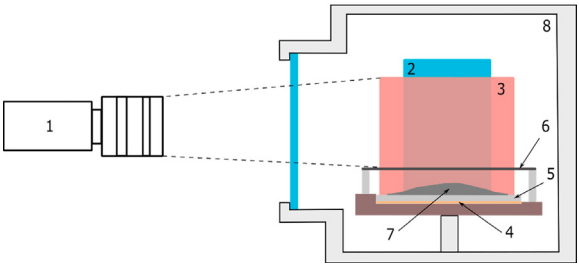


Fig. 1. Scheme (side view) of the experimental setup for investigating dust particle trajectories (**1** – CMOS cameras, **2** – mirror, **3** – expanded laser beam, **4** –conductive substrate, **5** – nonconductive substrate, **6** – steel mesh, **7** – dust particles, **8** – vacuum chamber) [2].

This study demonstrates the visualization and recovery of the 3D dynamic trajectories of charged microparticles in electric field conditions. The main aim of this work is to simulate plasma-dust processes above the surfaces of the Moon and other Solar system bodies without atmospheres. The experimental setup includes two parts: a vacuum chamber, in which microparticles imitate lunar dust dynamics under electrostatic field conditions (Fig. 2), and a stereo camera system for image registration combined with laser and optics for illuminating the investigation volume. Image processing techniques for estimating the 3D particle trajectory were developed. Examples of processing results and their prospective application are discussed. [2]

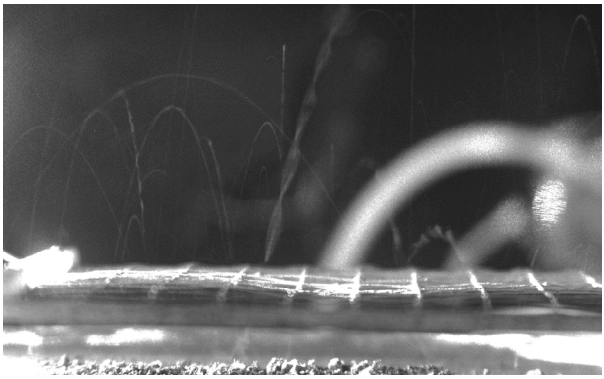


Fig. 2. Direct visualization of the levitation of SiO2 particles (the thin parabolic lines in the photograph) with noticeable steel mesh and particles on the substrate [2].

REFERENCES:

[1] A.Yu. Poroykov, S.A. Bednyakov, A.V. Zaharov, G.G. Dolnikov, A.N. Lyash, I.A. Shashkova and I.A. Kuznetsov, Application of the particle trajectory imaging for modelling dusty plasma levitation on the Moon // J. Phys.: Conf. Ser., 2019, 1421 012037, https://iopscience.iop.org/article/10.1088/1742-6596/1421/1/012037, doi:10.1088/1742-6596/1421/1/012037.

[2] A.V. Zakharov, A.Yu. Poroykov, S.A. Bednyakov, A.N. Lyash, I.A. Shashkova, I.A. Kuznetsov, G.G. Dolnikov, Recovery of dust particles trajectories in modeling physical processes in the near-surface exosphere of the moon // Measurement, Volume 171, 2021, 108831, ISSN 0263-2241, https://doi.org/10.1016/j.measurement.2020.108831.

INVESTIGATION OF THE LUNAR NEAR-SURFACE DUSTY PLASMA EXOSPHERE INTERACTION WITH PIC METHOD SIMULATION

I.A. Kuznetsov, A.V. Zakharov, G.G. Dolnikov, S.A. Bednyakov, A.S. Bychkova, A.E. Dubov, A.A. Kartasheva, A.N. Lyash, I.A. Shashkova, A.V. Shekhovtsova
[1] *Space Research Institute of the RAS (IKI RAN), 84/32 Profsoyuznaya Str, Moscow, Russia, 117997, kia@iki.rssi.ru*

KEYWORDS:
Dust, lunar dust, dusty plasma, lunar lander, Luna-25, Moon, numerical modelling, Particle-In-Cell.

INTRODUCTION:
One of the complicating factors of the future robotic and human lunar landing missions is the influence of the dust. The upper insulating regolith layer is electrically charged by the solar ultraviolet radiation and the flow of solar wind particles. Resulted electric charge and thus surface potential depend on the lunar local time, latitude and the electrical properties of the regolith.

Understanding of mechanisms of the dust electric charging, dust levitation and electric charging of a lander on the lunar surface is the essential for interpretation of measurements of the instruments of the Luna – 25 lander payload, e.g. the Dust Impact sensor and the Langmuir Probe (Electric Field Sensor) [1].

One of the tools, which allows simulating the electric charging of the regolith and lander and the transport and deposition of the dust particles on the lander surface, is the Spacecraft Plasma Interaction Software toolkit, called the SPIS-DUST [2].

This work describes the SPIS-DUST numerical simulation of the interaction between the solar wind plasma, ultraviolet radiation, regolith and a lander and presents as result qualitative and quantitative data of charging the surfaces, plasma sheath and its influence on spacecraft sensors as well as nearby dust dynamics. The model considers the geometry of the Luna – 25 lander, the electric properties of materials used on the lander surface, as well as Luna – 25 landing place solar irradiation conditions. Initial conditions are chosen using current theoretical models of formation of dusty plasma exosphere and levitating charged dust particles. [3]

Simulation for the three cases (local lunar noon, evening and sunset) showed us the surrounding plasma sheath around the spacecraft which gives a significant potential bias in the spacecraft vicinity (Fig. 1).

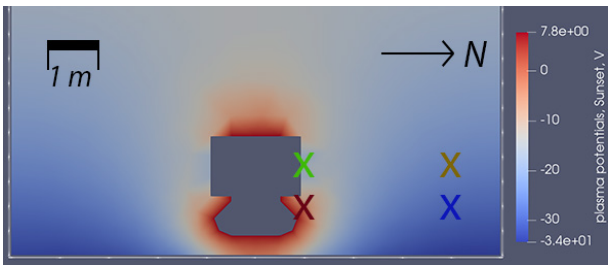


Fig. 1. Plasma potentials at the steady state of simulation in “Sunset” conditions. Sun is behind the spacecraft and with 1° zenith angle above the horizon.[3]

This bias influences on the spacecraft sensors but with SPIS software we can estimate the potential of uninfluenced plasma with the data from the plasma sensors (Langmuir probes). SPIS-DUST modification allows us to get the dust dynamics properties (Fig. 2).

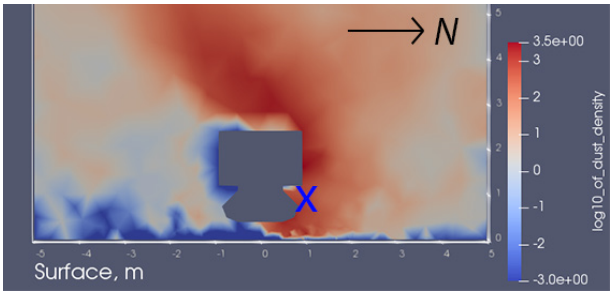


Fig. 2. Common logarithm of the dust density in particle per cubic meter at the local lunar evening. The sun is on the right, with 11° zenith angle above the horizon. Dust Impact Sensor from the PmL instrument location marked by "X" sign.[3]

For our three cases we've obtained the dust densities around the spacecraft and near the surface of the Moon. As another practical result of this work we can count a suggestion of improving of dusty plasma instrument for the next mission: it must be valuable to relocate the plasma sensors to a distant boom at some distance from the spacecraft.

REFERENCES:

[1] Kuznetsov I.A., Zakharov A.V., Dolnikov G.G., Lyash A.N., Afonin V.V., Popel S.I., Shashkova I.A., Borisov N.D. // Solar System Research. 2017. V. 51. № 7. P. 611–622.

[2] Hess S.L.G., P. Sarrailh, J.-C. Matéo-Vélez, B. Jeanty-Ruard, F. Cipriani, J. Forest, A. Hilgers, F. Honary, B. Thiébault, S.R. Marple and D. Rodgers, New SPIS capabilities to simulate dust electrostatic charging, transport and contamination of lunar probes. // IEEE Transactions on Plasma Science, 2015, V. 43, No. 9, P. 2799 – 2807

[3] Kuznetsov I.A., Hess S.L.G., Zakharov A.V., Cipriani F., Seran E., Popel S.I., Lisin E.A., Petrov O.F., Dolnikov G.G., Lyash A.N., Kopnin S.I. Numerical modelling of the Luna-Glob lander electric charging on the lunar surface with SPIS–DUST. // Planetary and Space Science. 2018. V. 156. P. 62–70.

COLLISIONAL COOLING OF ELECTRONS AT COMET 67P/CHURYUMOV–GERASIMENKO AS VIEWED FROM 3D PARTICLE-IN-CELL SIMULATIONS

A.V. Divin [1], J. Deca [2], P. Henri [3], A. Eriksson [4], V. Olshevsky [5], S. Markidis [6]
[1] *St. Petersburg State University, St. Petersburg, Russia, a.divin@spbu.ru;*
[2] *Laboratory for Atmospheric and Space Physics (LASP), University of Colorado Boulder, 80303, USA;*
[3] *LPC2E, CNRS, Orléans, 45071, France;*
[4] *Swedish Institute of Space Physics, Uppsala, Sweden;*
[5] *Main Astronomical Observatory (MAO NASU) Kiev, Ukraine;*
[6] *KTH Royal Institute of Technology, SE-100 44, Stockholm, Sweden*

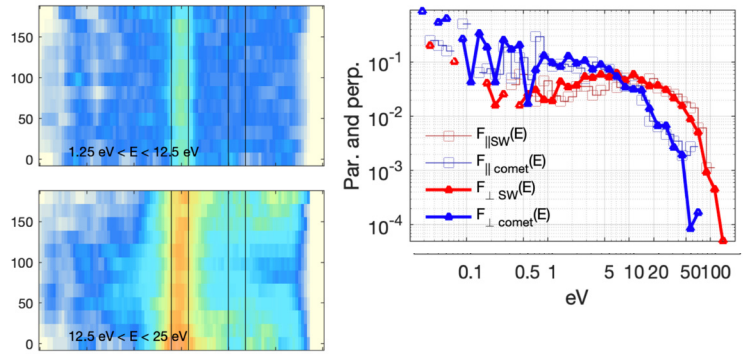
KEYWORDS:
Particle-in-Cell (PIC) simulations; electron acceleration; ambipolar electric field; collisional kinetics; high-performance computing.

INTRODUCTION:
Cometary atmosphere is formed when the cometary nucleus gets close to the Sun and solar radiation evaporates the volatile material and gases. Neutral particles are slowly ionized (by photoionization or charge exchange with solar wind ions) and interact with the magnetic and electric fields of the solar wind. Cometary activity is measured by the total outgassing rate Q (the number of new particles implanted into solar wind each second). A weakly outgassing comet ($Q < 10^{26}$ s^{-1}) introduces relatively weak perturbations into the solar wind and plasma is nearly collisionless, but the interaction should be treated using kinetic approach.

RESULTS:
In our previous study [1, 2] we conducted numerical 3D Particle-in-Cell (PIC) simulations of solar wind–comet interaction for a weak outgassing regime ($Q = 10^{25}$ s^{-1}). We use plasma simulation code iPIC3D, which is a high-performance PIC code suitable for modern supercomputers. Our main finding was the discovery of a hot population of passing electrons with energies up to 50–70 eV, that is several times the average energy of the ambient cometary electrons. Particles are accelerated by the electrostatic ambipolar potential which is supported the electron pressure gradient. Our past simulations didn't take into account electron–neutral collisions, which are important close to nucleus and which provide efficient electron cooling [3]. In the present study we combine a MCC (Monte-Carlo Collisions) method [4], and the article mover to add collisionality to iPIC3D code. Electron–water collision cross sections are tabulated from [5]. The effect of electron-neutral collisions becomes clearly visible in the distribution functions:

- The distribution function of electrons of both solar and cometary origin become nearly isotropic in the vicinity of the cometary nucleus in a wide range of energies (see Figure 1a). The change in the total energetic electron flux is insignificant, i.e. the presence of inelastic collisions does not lead to the suppression of energetic electrons. Far from the nucleus, where collisions can be neglected, e.g. at a distance of ~ $0.5d_i$ = 100 km in the solar and anti-solar directions, the parallel anisotropy remains (here d_i is ion inertial length).
- A population of cold electrons with energies $E < 0.1$ eV is formed, which persists within ~ 10–30 km to the nucleus. Cooling is mainly due to the excitation of vibrational states of water molecules. Notably, the cold population is formed by cometary electrons (Figure 1b, blue lines), while electrons with $E > 10$ eV are mostly of solar wind origin (Figure 1b, red lines), which is similar to the collisionless kinetic simulation results.

Our study indicates the electron-neutral collisions are important even in a weak outgassing regime and that it affects electron dynamics strongly.



a **b**

Fig. 1. Electron thermal population pitch-angle distributions from 3D PIC simulation (**a**). Electron energy spectra for cometary electrons shown by blue lines, and solar wind electrons shown by red lines (**b**).

ACNOWLEDDGMENTS:
This work was supported by grant #20-1-2-18-1 by “Basis” Foundation.

REFERENCES:

[1] J. Deca, J. Henri, A. Divin, A. Eriksson, M. Galand, A. Beth, K. Ostaszewski, and Horányi, M., 2019. Building a weakly outgassing comet from a generalized Ohm’s law // Phys. Rev. Let., V. 123. No. 5, P. 055101.
[2] A. Divin, J. Deca, A. Eriksson, P. Henri, G. Lapenta, V. Olshevsky, and S. Markidis. “A fully kinetic perspective of electron acceleration around a weakly outgassing comet.” // ApJL 889. 2020. V. 2. No. L33.
[3] A.I. Eriksson, I.A. Engelhardt, M. André, R. Boström, N.J. Edberg, F.L. Johansson, C. Norberg, et al.. 2017. Cold and warm electrons at comet 67P/Churyumov-Gerasimenko. // Astronomy & Astrophysics, P. 605, No. A15.
[4] V. Vahedi, & M. Surendra. 1995. A Monte Carlo collision model for the particle-in-cell method: applications to argon and oxygen discharges. // Computer Physics Communications, V. 87.No. 1–2, P. 179–198.
[5] Itikawa, Yukikazu, and Nigel Mason. Cross sections for electron collisions with water molecules. // Journal of Physical and Chemical reference data 34.1 2005. P. 1–22.

SIMULATING THE REFLECTANCE OBSERVED ON MACROSCOPIC SCALE PLANETARY SURFACES BY A GPU RAY-TRACING TECHNIQUE

T. Drozhzhova [1], A. Gracia [1], A. Pommerol [1], N. Thomas [1]
[1] *Space Research & Planetary Sciences Division, Physikalisches Institut, University of Bern, Sidlerstrasse 5, CH-3012 Bern, Switzerland*

KEYWORDS:
Simulation, reflectance, Unity, ray-tracing technique, comet, planetary surface.

INTRODUCTION:
The reflectance observed by a camera onboard spacecraft during space exploration missions is extremely useful to draw important conclusions about the properties and composition of planetary surfaces. In addition to this, important information about the possible large-scale roughness on the planetary surface can be also obtained.

In this work we present the multi-boundaries scattering method using

GPU-accelerated technique with Unity engine [1]. The reflectance from fractal surfaces is calculated, aiming to simulate the imaging of macroscopic scale planetary surfaces.

On the first stage in the laboratory, we measured reflectance factor for different types of surfaces (white matt, grey matt and meteorite one).

Then GPU ray-tracing method uses these measurements to calculate the variations in the reflectance when introducing a large-scale roughness parameter on the fractal surface, by simulating the interaction of a light beam when it is cast onto a 3D fractal mesh.

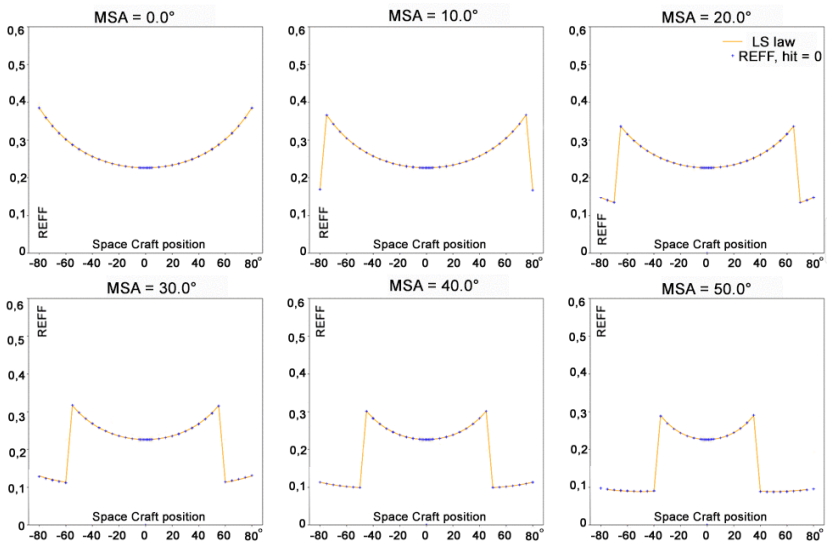


Fig. 1. Lommel-Seeliger law comparison with simulation geometry reflection technic for different MSA (mean slope angle) sample V-shape surface for sun elevation = 90 °.

Simulation geometry reflection technique received a good agreement with Lommel-Seeliger law [2] for single scattering on simple V-shape planes [Fig. 1]. Then fractal surface single and multi-boundaries scattering reflectance were compared for simulation technique, Hapke interpolation [3] and laboratory measurements for different types and roughness of surfaces [Fig. 2].

By implementing this technique for 3D shape model that can represent any real planetary surface, we can calculate the reflectance on the macroscopic scale surface.

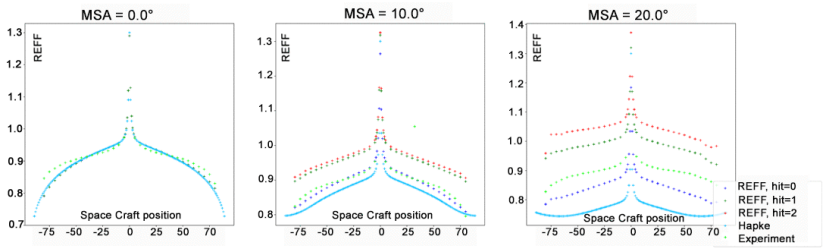


Fig. 2. Fractal surface multi-boundaries scattering reflection for different MSA (mean slope angle) in comparison with Hapke interpolation and experimental measurements. Single scattering (hit=0), one and two extra hit for photon (hit = 1, hit = 2) for sun elevation = 90 °.

REFERENCES:

[1] A. Gracia-Berná, A. Pommerol, N. Thomas, R. Marschall, Z. Yoldi, B. Jost, O. Poch, Photometry of fractal meshes for applications to large-scale rough planetary surfaces, in GPU Technology Conference.2016..
[2] Xiang-Jie Huang et al. 2017. Res. Astron. Astrophys. V. 17. P. 106.
[3] B. Hapke, Theory of Reflectance and Emittance Spectroscopy: Topics in Remote Sensing. Cambridge University Press, 1993. Cambridge Books Online.

ON THE NATURE OF OBSERVED COMETS AND THE MECHANISM OF THEIR FORMATION

A.A. Barenbaum [1]
[1] *Oil and Gas Research Institute RAS, Gubkin str. 3, Moscow, 119333, Russia, azary@mail.ru;*

KEYWORDS:
Galactic comets, asteroid belt, long-period and short-period comets.

INTRODUCTION:
Comets are observed by humans for many thousands of years. These are large cosmic bodies composed of frozen masses of ice, dust, gas and rocky material that revolve around the Sun in orbits more diverse and distant from the Sun than planets and asteroids. There are two main groups of comets: long-period comets with a rotation period T > 200 years around the Sun and short-period comets with T < 200 years. The properties of both groups of comets are well studied and explained. However, the question of the origin of the comets themselves remains open and replete with conflicting, often mutually exclusive judgments.

HYPOTHESES OF COMETS ORIGIN:
In accordance with two comet groups, all hypotheses of origin of observed comets are divided into two types: hypotheses of the "capture", which allow capture of comets of the galactic origin by the Sun, and the "eruptive" hypotheses, offering comets formation in the Solar system (table 1).

Table. 1. Types of known hypotheses of comets origin and author's concept.

Hypotheses of "capture"	"Eruptive" hypotheses
Laplace (1796)	Lagrange (1812)
Svedstrup (1883)	Proctor (1881)
Oppenheim (1924),	Orlov (1936, 1960)
Bobrovnikoff (1929)	Oort (1950, 1951)
Lyttleton (1948)	Kuiper (1951)
McCrea (1953)	Whipple (1964)
Vitkovskiy (1971)	Vsekhsvyatskiy (1967)
Radziyevskiy, Tomanov (1973, 1991)	Safronov (1972)
Kazimirchak-Polonskaya (1978)	Öpik (1975)
Yabusita, Hasegawa (1978)	Koval (1976)
Shorma, Khonna (1988)	Van Flandern (1977)
Van den Bergh (1982)	Drobyshevsky (1978)
Bailey (1986)	Hills (1982)
Dolgopolova, Marochnik (1987)	Tsitsin F.A. et al. (1985)
Chepurova, Shershkina (1989)	Guliev (1992)
Barenbaum (1990, 2002, 2010)	

In connection with the recent discovery in astronomy of the phenomenon of jet outflow of matter from center of our Galaxy and other spiral galaxies [1], the author proposed a new hypothesis for the origin of comets in the Solar System [2, 3]. He expressed this hypothesis at the "2-th Vsesvyatskikh Readings on Physics and Dynamics of Comets" (Kiev, 1990), and later theoretically substantiated it in books [1, 4] in the form of a "cometoasteroid" concept of comets formation in the Solar System. This concept proposes the physical mechanism for formation of observed comets, that not contradictory explains the main properties of long-period and short-period comets, opening the true nature of these cosmic objects.

AUTHOR'S CONCEPT:

This concept of comets origin in the Solar System is based on the representations of Galactocentric paradigm [4], which takes into account phenomenon of jet outflow of gas-dust matter from Galaxy center [1]. According to the new concept, both long-period and short-period comets of the Solar System are "daughter" products of galactic comets collisions with asteroid belt bodies, captured by Sun gravitational attraction into elliptical circumsolar orbits, which are more distant from Sun than bodies in the belt. Daughter comets are composed of condensed gas-dust matter of galactic comets mixed with asteroid debris. Therefore the Solar System comets cannot be regarded as objects of only eruptive or galactic origin, and should be considered as special category bodies of dual genesis — "cometoasteroids".

Most cometoasteroids were formed in the time interval from 5 to 0.7 million years ago during the period when Sun was in the Orion-Cygnus jet stream [1]. Depending on size of the orbits that were obtained by these objects when ejection of asteroid belt, they are classified as long-period or short-period comets. The former have aphelion of ~ $10^4 – 10^5$ AU, as a result of which they are returning back to Sun for the first time since their ejection from asteroid belt. The substance of these bodies contains a large proportion of galactic comets ice. When approaching the Sun, ice intensively evaporates and the outflow of gas and dust from them increases sharply. When approaching the Sun, ice intensively evaporates and the outflow of gas and dust from them increases sharply. This gives reason to consider long-period cometoasteroids as very young objects that have survived since the Solar System formation.

Unlike long-period daughter objects, short-period cometoasteroids revolve around the Sun with much shorter periods. They never left the planetary system of Sun, completed tens of thousands of revolutions around it, today they gravitate towards the ecliptic plane and were able to survive only in outer space behind the giant planets and between them. When they accidentally approach these planets, they are thrown towards the Sun, and then they are referred to the family of short-period comets of corresponding giant planet. As result of multiple flights near Sun, such cometoasteroids lose frozen gas-dust matter, and their glow decreases. After its complete disappearance, meteor showers and small asteroids, which differ little from ordinary bodies of asteroid belt, are found in place of "dead" cometoasteroid.

This concept postulates a close relationship of observed comets with other small bodies of the Solar System, primarily asteroids and interplanetary dust. There is no fundamental difference between comets of the solar system and bodies of the asteroid belt. The differences between these two groups of bodies are determined by the parameters of their orbits. The overwhelming majority of asteroids move within the asteroid belt, which is located from Sun at distances, where ice melts under the influence of solar radiation. Whereas cometoasteroids outside this zone keep these ice for much longer.

Author's concept also attaches great importance to the connection of comets with many other processes in the Solar System and on its planets, which are considered as a complex of interrelated residual phenomena caused by the recent presence of the Sun in the stream of galactic comets. These include: the "peculiar" state of the Sun (Glushneva, 1994), increased Earth geological activity (Artyushkov, 1994), strong turbulence of giant planets atmospheres (Marov, 1981), excited state of asteroid belt bodies (Ruskol, 1986), strong "dusting" interplanetary space (Brownlee, 1984) and presence in it of large quantities of comets, meteorites and asteroids with a dynamically short lifetime (Simonenko, 1985).

CONCLUSION:

- Long-period and short-period comets are secondary objects captured by the Sun gravity – the cometoasteroids, which have arisen as a result of collisions of Galaxy comets – the primary comets, with bodies of the asteroid belt.
- Substance of the Solar System comets represented by conglomerates formed at chemical and mechanical mixing of ice of frozen gases and dust of galactic origin with clastic (solid) and diffuses (evaporated) material of asteroids.

- Short-period comets have never left planetary system of the Sun. As a result of multiple flights near the Sun, they have lost a significant part of their ice component. Whereas, a long-period comets, on the contrary, spent almost their entire life far from the Sun and preserved this component.
- High concentration of aphelions of long-period comets orbits at a distance of 10^4–10^5 AU from the Sun is a direct physical consequence of their formation and ejection from asteroid belt during last bombardment by galactic comets, which took place from 5.0 to ≈ 0.7 million years ago, when the Sun was in the Orion-Cygnus jet stream.

Also note that author's concept combines the best aspects of other known hypotheses of observed comets origin, without repeating their shortcomings. This concept differs from "interstellar" hypotheses in that it has no difficulty in explaining origin cometary families of the giant planets. And from "eruptive" hypotheses it differs in that easily explains the orbits of long-period comets.

The concept preserves also ideas about presence near Sun of a "comets cloud". However, unlike hypotheses of Oort (1950), Kuiper (1951), Whipple (1964), Hills (1982), Tsitsin et al. (1985), this "cloud" is an extremely non-stationary formation and contains not only comets, but also a huge amount of gas and dust. Moreover it such cloud appears only during epochs of Sun being in streams of galactic comets and exists for ~ 10^6–10^7 years. The total number of cometoasteroids in it, according to our estimate, is ~ 10^7.

And, finally, no less advantage of the outlined concept is that it is part of the general system of representations – Galactocentric paradigm that connects observed phenomena in the Solar System and on its planets with space processes in the Galaxy [4].

REFERENCES:

[1] A.A. Barenbaum Galaxy, Solar System, Earth. Subordinate processes and evolution. (Moscow. Publishing house GEOS). 2002. P 393.
[2] Barenbaum A.A. New ideas about the origin of comets and their interactions with the objects of Solar System // Kometnyy circular. 1990, No. 418 (Kiev), P. 11–12.
[3] Barenbaum A.A. On the nature of C-asteroids and carbonaceous chondrites // Kometnyy circular. 1990, No. 419 (Kiev), P. 9–10.
[4] Barenbaum A.A. Galactocentric paradigm in geology and astronomy. (Moscow. Publishing House LIBROKOM). 2010. P. 546.

SESSION 7. MOON AND MERCURY (MN) ORAL

BEPICOLOMBO EN ROUTE TO MERCURY – RESULTS FROM SOME INVESTIGATIONS DURING CRUISE

J. Benkhoff, J. Zender[1], G.D. Murakami[2]
[1] *European Space Research and Technology Centre, Keplerlaan 1, 2200AG Noordwijk ZH, Netherlands, Johannes.Benkhoff@esa.int and Joe.Zender@esa.int;*
[2] *Department of Solar System Science, Institute of Space and Astronautical Science (ISAS), Japan Aerospace Exploration Agency (JAXA), 3-1-1 Yoshinodai, Chuo, Sagamihara, Kanagawa 252–5210, Japan, go@stp.isas.jaxa.*

KEYWORDS:
BepiColombo, Mercury, Planetary Orbiter, Magnetospheric Environment

ABSTRACT:
BepiColombo is a joint project between the European Space Agency (ESA) and the Japanese Aerospace Exploration Agency (JAXA). The Mission consists of two orbiters, the Mercury Planetary Orbiter (MPO) and the Mercury Magnetospheric Orbiter (MIO). Both spacecraft has been launched with an ARIANE V in October 2018 for an arrival at Mercury in late 2025. From their dedicated orbits the two spacecraft will be studying the planet and its environment.

On its route BepiColombo will pass by Earth, two times Venus, and six times Mercury before jettisoning its orbiters and putting them into orbit around the innermost planet.

Instrumentation on the two orbiters will study and understand the composition, geophysics, atmosphere, magnetosphere and history of Mercury, the least explored planet in the inner Solar System. In addition, the two satellites will provide a rare opportunity to collect multi-point measurements in a planetary environment. This will be particularly important at Mercury because of short temporal and spatial scales in the Mercury's environment. The foreseen orbits of the MPO and MIO will allow close encounters of the two spacecrafts throughout the mission.

Already during its cruise into the inner solar system scientific and engineering operations has been scheduled, especially during the swing-by's. The magnetometer, the accelerometer, the environmental sensor, the gamma-ray and neutron spectrometer, the solar intensity x-ray and particle spectrometer, the radio science experiment, the thermal infrared spectrometer, the UV-spectrometer and some sensors of the SERENA suite has been operated. Also, instruments or some parts of the instruments of the Japanese Mio spacecraft like the dust monitor, the plasma wave instrument, the particle and plasma experiment and the magnetometer were already successfully operated in their science modes. In addition, BepiColombo also took regular "selfie" images with their three monitoring cameras on the MTM. All the other instruments such as cameras and NIR spectrometer, the laser altimeter, the x-ray spectrometer, etc. are operational but cannot used in their scientific modes until the Mercury in-orbit commissioning in early 2026 because their field of view is blocked by the underlying Transfer Module or sunshield, respectively.

A status of the mission and instruments and a summary of first results from measurements taken during the first three years en route to Mercury will be given.

MGNS FLIGHT TO MERCURY: STATUS REPOT

A.S. Kozyrev[1], I. Mitrofanov[1], M. Mokrousov[1], A. Sanin[1], S. Nikiforov[1] and D. Golovin[1]
[1] *IKI RAS, Moscow, Russia*

KEYWORDS:
Mercury, space background, gamma-ray bursts, solar flares

The Russian Space Research Institute has developed the Mercury Gamma-ray and Neutron Spectrometer (MGNS) for remote sensing observations of the Mercury from the Mercury Polar Orbiter (MPO), which is the part of ESA's BepiColombo mission. The BepiColombo mission was launched on Oct. 20, 2018, is currently in the cruise phase and is expected to arrive at Mercury in March 2026.

During the BepiColombo long cruise to Mercury, the MGNS instrument operates practically continuously to perform measurements of neutrons and gamma-ray fluxes. This report will present the results of measurements performed during the first three years of the cruise, which include monitoring of the local radiation background of the prompt spacecraft emission due to bombardment by energetic particles of Galactic Cosmic Rays, registration and localization of cosmic gamma-ray bursts, and registration of solar flares. Moreover, the results obtained during special sessions of measurements during flybys of Earth and Venus will be presented.

GEOLOGIC CONTEXT FOR LUNAR SOUTH CIRCUMPOLAR REGION EXPLORATION: IMPLICATIONS FOR GOALS, SITE SELECTION AND OPERATIONS STRATEGY

J. Head[1], C. Pieters[1], D. Scott[1], M. Ivanov[2], S. Krasilnikov[2], A. Krasilnikov[2], A. Basilevsky[2], H. Hiesinger[3], C. van der Bogert[3], B. Jolliff [4], N. Petro[5], D. Moriarty[5], P. Lucey[6]

[1] *Brown Univ., USA, james_head@brown.edu;*
[2] *Vernadsky Inst., Russia;*
[3] *Westfälische Wilhelms-Univ., Germany;*
[4] *Washington Univ., USA;*
[5] *NASA GSFC, USA;*
[6] *Univ. Hawaii-Manoa, USA.*

KEYWORDS:
South pole, geology, site selection, science, operations

INTRODUCTION:
National and international exploration of the Moon has become focused on the South Circumpolar Region (SCR) due to: 1) the scientific desire to explore outside the northern nearside Apollo-Luna-Chang'e 3/5 region, 2) the "Transformative Lunar Science" questions that can be addressed in the SCR (e.g., crust-mantle structure/composition, absolute chronology, water cycle record/resources, role of South Pole-Aitken (SPA) basin, etc.) and 3) the need for solar illumination/power to survive lunar night [1-2]. We focus here on the basic background geologic setting ("bedrock" geology) of the SCR in order to 1) identify the major sequence of events, 2) assess what this means for addressing the primary (non-volatile) scientific questions, and 3) assess how these influence human/robotic exploration strategy. SCR polar volatile history exploration strategy are treated separately [3].

GLOBAL CONTEXT:
The SCR is a fundamentally unexplored region, outside the Apollo-Luna-CE3/5 zone, providing access to the farside and two major relatively unexplored lunar crustal terranes (FHT and potentially SPA [5]), enhancing the likelihood of understanding crustal stratigraphy, magma ocean lateral heterogeneity, potentially providing access to mantle samples, and providing major insight into lunar chronology and Solar System impact flux (e.g., SPA and dozens of craters and basins).

SEQUENCE OF EVENTS:
Following magma ocean formation and solidification [6] (the FHT), the ~2500 km SPA basin formed [7-11], creating the largest and oldest known lunar multi-ring basin; subsequent impact events dominate the region at all scales (Schrodinger, Orientale, Mendel-Rydberg, and subsequent craters, e.g., Shackleton, Cabeus, Haworth, Faustini, Shoemaker, etc.) [12-13].

SOUTH POLE LOCATION:
The center of the SCR is located within the SPA outer ring, equivalent to the Orientale Cordillera outer ring (Fig. 1-3), and similar in setting to the A-15 site at Imbrium, but due to the multitude of subsequent impact events and their ancient ages [11-14], SCR is more similar to the A-16 central highlands (complex impact polymict breccia-dominated geology [15-16]). On the basis of A-16 experience, the deconvolution of the complex SCR history represents a formidable challenge, one requiring an integrated strategy for site selection, traverse planning, sample assessment/documentation and acquisition, and analysis upon return.

CONCLUSIONS: SOME GUIDELINES FOR ADDRESSING SCIENTIFIC GOALS (NON-VOLATILE-RELATED) IN THE SCR:
1. Geologic/Stratigraphic Framework: The SCR topography is dominated by the SPA basin outer ring [17], (Fig. 3) but obscured and complicated by multiple subsequent overlapping impact events and ejecta deposits (Fig. 2).

The geologic framework is most like the Apollo 16/Descartes Highlands (Fig. 1); detailed local geomorphology provides minimal clues to multiple polymict breccia provenance. At SCR, 20+ km diameter craters/interleaved ejecta deposits dominate (Fig. 2). The largest craters (Haworth, Shoemaker, and Faustini; Nectarian in age [13]) and Shackleton (Late Imbrian in age [18]) dominate the region and individual crater deposits at all scales will dominate walking traverse sampling [19].

2. The SPA Basin Ejecta/Mantle Sampling Paradox: The SCR lies on the SE outer topographic ring of the ancient ~2500 km SPA basin (~4.2 Ga? [20]), considered by some [9] to have excavated mantle material. However, SPA is interpreted by most [7-11] to have formed from an oblique impact (SSW-NNE); most of the ejecta, including the most deeply excavated (mantle?) material, is likely to have been deposited *away* from the SCR. The SPA-B topographic rim in the SCR (e.g., Mons Malapert) [17; Fig. 3] may consist of pre-SPA–B highland crust overlain by SPA–B ejecta, and is very unlikely to contain deep-crustal or mantle material sampled by SPA–B. Emphasis needs to be placed on sampling exotics/xenoliths as well as polymict breccias. The most likely place to sample SPA-B material is the steep-sloped Mons Malapart [17] (Fig. 3). If SPA-B mantle samples exist, remote sensing data [4] suggest that it will occur at the hand-sample scale as small breccia fragments, admixed further by subsequent impacts.

3. Determining Basin/Crater Absolute Chronology: Due to the difficulty in determining polymict breccia provenance, dating specific SCR crater/basin chronology will be largely statistical, putting focus on obtaining a regional sample that is both representative of SCR and collects any "exotics", and also samples specific secondary crater sites where provenance is known [11-12, 21].

4. Importance of Secondary Craters in Establishing Absolute Chronology: Shocked samples at secondaries from distant basins (Mendel-Rydberg, Schroedinger, Orientale, etc.) and craters (e.g., Tycho) will be important to sample in detail to date the source craters.

5. Landing Site Selection: Pinpoint landing is necessary to ensure access to specific targets of crater/basin ejecta, secondaries, SPA–B mountains. Returning to the same site multiple times works against scientific diversity in a complex terrain. In all cases, ranging far from the landing sites is essential, as amply demonstrated by Apollo. For example, the scientific knowledge delta from six consecutive missions to the Apollo 16 site is clearly much less than that represented by the six Apollo 11-17 missions. Therefore, significant sortie mobility (>10s of km) is required.

6. Traverse Design/Mobility: Two major requirements derive from SCR geology: 1) Due to the complexity of the geology and samples, time at individual sampling stations will be long and learning/discovery-intensive relative to Apollo; 2) Mobility in excess of Apollo 15-17 is required to obtain the necessary representative and diverse samples. A DRM-CONOPS would feature long, radially oriented traverses with multiple, widely spaced, long-duration stations, at which large quantities of carefully selected samples would be collected. As in Apollo, driving first to the consumable constraint radius and working backward provides geologic reconnaissance and optimizes sampling success. Fresh blocky craters are attractive stations, and rover design should exceed design/performance of Apollo and Lunokhod rovers in order to ascend SPA–B massifs (e.g., Mons Malapert [17]).

7. Sampling Procedures: Triaging polymict breccias on the lunar surface is not a productive option. Required are: 1) Real-time, hand-held, helmet-displayed remote sensing capability to identify key "fingerprints" (e.g., mafic/ultramafic, KREEP-rich), 2) tools ensuring diverse and representative samples (e.g., lunar rake [22]), 3) large sample-return mass to ensure valid petrogenetic and chronologic statistics, and 4) mobility (>10s of km) to determine the regional petrologic variability of 20+ km diameter craters, underlying SPA basin regional ejecta deposits, and basin/crater secondaries.

8. Astronaut Training: Successful exploration of complex brecciated terrains requires a balance of specialized field, lab and classroom training, and use of hand-held, real-time remote sensing tools.

9. Mission Operations and Science Support: Very steep on-site learning curve; respect situational awareness, develop ground advisor/consultant psychology [23], practice inter-EVA debriefings/briefings/updates to develop techniques for Mars surface exploration.

10. Human-Robotic Partnerships: Due to complex geology, robotic missions necessary at all stages/scales: *precursor scouting*, *human exploration area interpolation*, and *extrapolation 100s of km beyond*.

11. Programmatics, International Coordination-Cooperation: To optimize science return, programs such as Artemis require complex systems engineering [24] and constant international coordination and cooperation.

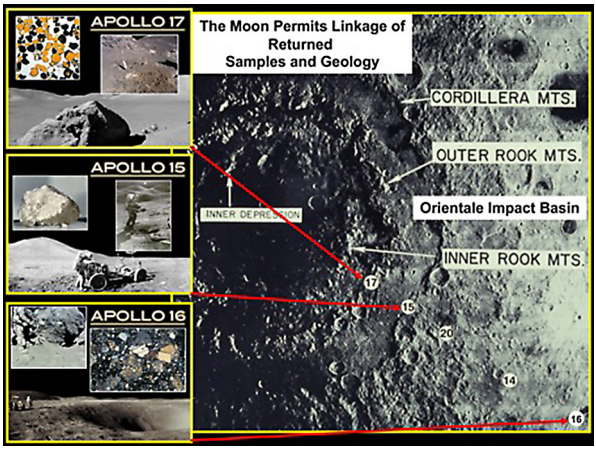


Fig. 1. Context of Apollo Sites and Orientale Basin.

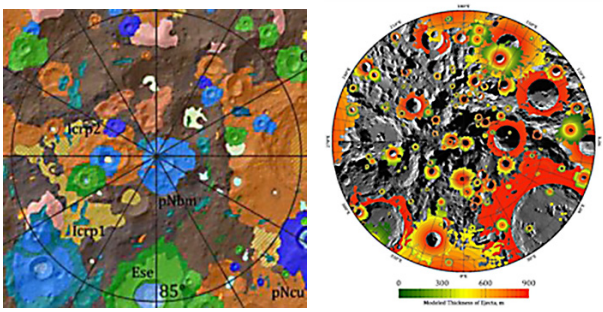


Fig. 2. a. SCR Geologic Map [12]. **b.** Crater/basin ejecta thickness decay [14].

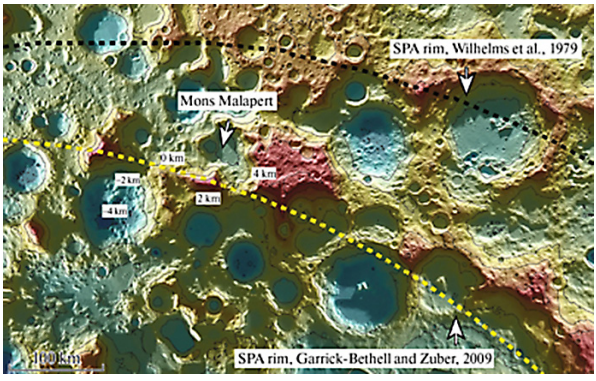


Fig. 3. SPA–B outer ring (Cordillera equivalent; Fig. 1) & Mons Malapert. [17].

REFERENCES:

[1] Pieters et al. (2018) https://sservi.nasa.gov/articles/transformative-lunar-science/;
[2] Weber et al. (2020) https://www.nasa.gov/sites/default/files/atoms/files/artemis-iii-science-definition-report-12042020c.pdf;
[3] Lucey et al. (2021) LPSC52 #1764;
[4] Pieters & Lucey (2020) IAWG SP Reference Mission;
[5] Jolliff et al. (2000) JGR105, E2;
[6] Shearer et al. (2006) RMG60, 365;
[7] Garrick-Bethell & Zuber (2009) Icarus204, 399;
[8] Potter et al. (2012) Icarus220, 2;
[9] Melosh et al. (2017) Geology45;
[10] Moriarty & Pieters (2018) JGR123, 3;
[11] Poehler et al. (2021) LPSC52 #1915;
[12] Krasilnikov et al. (2021) LPSC52 #1428;
[13] Tye et al. (2015) Icarus255, 70;
[14] Krasilnikov et al. (2021) LPSC52 #1459;
[15] Hodges & Muehlberger (1981) USGSPP 1048;
[16] Kortotev (1997) MAPS32, 447;
[17] Basilevsky et al. (2019) SSR53, 383;
[18] Zuber et al. (2012) Nature486, 378;
[19] Ivanov et al. (2018) PSS162, 190;
[20] Garrick-Bethell & Miljković (2018) LPSC49 #2633;
[21] Guo et al. (2018) JGR123, 1344.
[22] https://www.hou.usra.edu/meetings/lunarsurface2020/;
[23] Krikalev et al. (2010) ActaAstron66, 70;
[24] Cappellarri, ed. (1972) BSTJ 51, 5.

GEOLOGICAL EXPLORATION OF THE MOON: REGOLITH, VOLATILE AND RARE ELEMENTS

A. Gusev[1a,b], R. Khasanov[1c], A. Kosov[2], Zh. Meng[3], J-S. Ping[4]
[1a] *Geophysics&IT,*
[1b] *MathMethods in Geology,*
[1c] *Regional Geology and Mineral Resources Depts, Kazan Federal University, Kazan, Russia;*
[2] *IKI RAS, Moscow, Russia;*
[3] *College of Geoexploration Science and Technology, Jilin University, Changchun, China;*
[4] *National Astronomical Observatory of China CAS, Beijing, China, agusev33@gmail.com.*

KEYWORDS:
Moon, regolith, volatile & rare elements, production & investigation of lunar simulants on Earth

INTRODUCTION

The review will consider 1) the geological substantiation for a detailed study of mineral resources in surface layer (regolith) on the Moon in the framework of future Russian and international lunar missions, 2) the concept of extended field geology and geophysics for planetary analogs "AGPA", 3) combining training programs and analog field geological procedures with geophysical methods on the Moon and remote sensing of the Moon, 4) goals, objectives, methods of studying the lunar regolith and production of lunar simulants for investigation at Kazan federal university(KFU).

The increasing availability of the Moon for spacecraft sharply raises the question of searching for and extracting mineral raw materials on a natural satellite of the Earth. The Moon is associated with significant resources of important minerals, which in lunar rocks can be found in concentrations greater than in their terrestrial counterparts. [1-13]. In the geological structure of the lunar surface, the most important are gabbro-anorthosite rocks, marine basalts, as well as the outcrops of rocks between the mantle and crust of the KREEP-rocks layer [2, 3]. The joint presence of a wide range of valuable metals in lunar rocks is an important quality that can increase the value of raw materials due to their complexity. The discovery of hematite in lunar rocks [4], the formation of which is associated with oxidation processes, allows us to reconsider the views on geochemistry and the peculiarities of mineral formation under conditions of the lunar airless surface and with its constant bombardment by meteorites.

The main targets for geo-exploration on the Moon are rocket fuel (propellant), water, hydrogen, oxygen, life support consumables, and minerals, including volatiles, rare and rare earth elements. Rocket fuel can be produced from local ice (water ice at the moon's poles), hydrogen and oxygen – from water and lunar minerals. Building materials can be produced from regolith and rocks found on the lunar surface. Metals and materials can be obtained from metal oxides and silicates found in lunar rocks. The main components of the life and energy supply of the lunar stations are oxygen, hydrogen, water, and methane. However, they are volatile and have not been established on the Moon in a free state. The discovery of the listed chemical components may be associated with the lunar regolith and bedrock complexes of the lunar crust. The study of the ultrafine component of the regolith [5] showed the presence of oxygen-containing compounds (metal oxides, sulfates, sulfites), mineral phases with hydroxyl groups, as well as high-carbon oxygen-containing films, which suggests the theoretical possibility of extracting such elements as O_2, H_2, CH_4. Their industrial production on the lunar surface is the extremely low content of these components in the regolith material, as well as the low thickness of the regolith layer itself (from several cm to 10–15 meters). Thus, the industrial extraction of vital components (O_2, H_2, C), which can be used for the production of water and methane, should be associated with the bedrock

rocks of the lunar crust, which consists of rocks of 3 types [2,3] – olivine basalts, gabbro-anorthosites and KREEP-rocks. Prospects for the discovery of oxygen and hydrogen compounds should be associated with olivine-containing complexes, in which autometamorphic processes could occur during the crystallization of magmatic melt under the influence of intrinsic magmatogenic fluids. Under terrestrial conditions, the autometamorphism of olivine-bearing rocks is accompanied by hydration of mineral phases with the formation of hydroxyl groups.

The main direction of the study of the Moon should be associated with the study of bedrocks and the forms of oxygen, hydrogen and carbon in them, as potential components for production of vital O_2, H_2O, CH_4. The Institute of Geology & Oil/Gas Technologies of the Kazan Federal University has highly qualified personnel and modern laboratory equipment for this. The foregoing makes it possible to significantly expand the estimated mineral resource base on the Moon at the expense of oxygen- and hydrogen-containing minerals. Volatile components of the lunar crust, giant volcanic intrusions, a globally distributed layer of the purest anorthosite, and the discovery of a new type of rocks (Mg-spinel anorthosite) represent only a small fragment of completely new perspectives obtained in lunar research over the past decade [6].

REGOLITH IS ONE OF THE PROMISING MATERIALS FOR 3D PRINTING ON THE MOON

It is readily available and widespread on the Moon in several forms and states. The study of the lunar regolith is based on educational practices that can be tested by lunar simulants on Earth [7,12]. Teaching the basics of geosciences and using special geophysical equipment has been successful for NASA's Apollo program [8]. The recent expansion of the ESA PANGEA-X cosmonaut training campaign has allowed the use and validation of several geological and geophysical experiments and protocols in volcanic regions of the Earth, similar in composition to the territories of the Moon [8, 11, 12]. The concept of extended field geology and geophysics for planetary analogs "AGPA" [9] includes a flexible set of experiment methods used during the ESA PANGEA-X field campaign. The work performed included remote sensing (stereo-grammetry, lidar) and geophysical (geoelectrics, active and passive seismic) studies [10, 11, 12, 13].



Goals, objectives, methods, technologies for the development of lunar regolith and bedrock of the lunar crust in KFU and the Republic of Tatarstan: 1) Search and study of the primary matter of the solar system in the lunar regolith; 2) Search and study of traces of the impact of cosmic matter, meteorites and comets on the surface of the Moon. Cosmic dust, balls and conglomerates in the lunar regolith; 3) Search and study of geological forms of finding volatile elements and rare metals in the regolith in the polar and equatorial regions on the visible and far sides of the Moon; 4) Search, study and creation in lunar conditions of technologies for producing hydrogen, oxygen and other volatile elements from lunar rocks a) for the creation of rocket fuel and b) means of long-term safe life support for astronauts, including energy supply, food and intellectual activity; 5) Search and creation of technologies for using local raw materials and natural shelters to protect astronauts on the Moon from various space threats: lunar lava caves and artificial security structures; 6) Search and study of the possibilities of organizing the manufacture of building materials on the Moon for protection from cosmic radiation. 3D printing technologies for construction and other useful materials from lunar raw materials in lunar conditions [12]; 7) Search and creation of modern technologies for the manufacture of terrestrial analogs

of the lunar regolith for carrying out numerous scientific, technical, technological and industrial experiments on Earth for their further use in the scientific, industrial and commercial development of the useful resources of the Moon for earthlings. The research of rotation, internal structure and geological exploration of the Moon, KFU have a long-term fruitful experience of cooperation with key laboratories of astronomical observatories of the Academy of Sciences and universities of China (Beijing, Shanghai, Jilin Univ.) and Japan (Tokyo, Mizusawa, Iwate Univ.) [1-3, 11].

REFERENCES:

[1] Gusev A., Hanada H., Petrova N., Kosov A., Kuskov O., Kronrod V., Kronrod E., Rotation, physical librations and interior structure of the active and multi-layer Moon, 2015, Monograph, Kazan University Publishing Co., Kazan, 328pp. (Russian+English).
[2] Xiao et al., A young multilayered terrane of the northern Mare Imbrium revealed by Chang'E-3 mission. // Science, 2015, v. 347, Issue 6227, pp. 1226-1229.
[3] Li J, Meng Z, Gusev A., Recent Advances in Lunar Exploration Using Radar and Microwave Techniques" "Advances in Astronomy", v.2019, 2 Art. № 479425816.
[4] Li S., Lucey P.G., et. al., Widespread hematite at high latitudes of the Moon // Science Advances, 2020, v. 6, DOI: 10.1126/sciadv.aba1940.
[5] Mokhov A.V. New ultradispersed mineral phases of the lunar regolith according to analytical electron microscopy // Abstract of thesis for the degree of Doctor of Geological and Mineralogical Sciences, Institute of Geology of Ore Deposits, Petrography, Mineralogy and Geochemistry of the RAS, Moscow, 2009, P. 1-47.
[6] Dhingra D., The New Moon: Major Advances in Lunar Science Enabled by Compositional Remote Sensing from Recent Missions. // Geosciences 2018, 8(12), 498; https://doi.org/10.3390/geosciences8120498.
[7] Garry, W., Bleacher, J., eds. Analogs for Planetary Exploration // 2011. No. 483 in GSA Special Paper, The Geological Society of America, Boulder, USA, P. 1-567.
[8] AGPA Team: http://www.agpa-project.eu, January 2018.
[9] ESA, 2019, https://exploration.esa.int/web/moon/-/61369-esa-space-resources-strategy.
[10] Gusev A.V., Bakhtin A.I., Kosov A.S., Hanada H., Meng Zh, Ping Z., Sungatullin R. Kh, Khasanov R.R. Scientific, geological and commercial exploration of the Moon, 2021, Transactions of LV Scientific Readings in memory of K.E. Tsiolkovsky, Section "Problems of rocket and space technology", Kaluga, September 15-17, 2020, KFU edition, Kazan, P. 161-176.
[11] Liu C., Mei L., Meng Zh., Wang Y., Zhu K., Cheng W., Cai Zh., Ping J-S, Gusev A., 2021, Special Thermophysical Features of Floor Materials in Mare Smythii Indicated by CE-2 CELMS Data // IEEE Journal of Selected Topics in Applied Earth Observations and Remote Sensing, 2021, v.14, P. 8135-8143.
[12] Isachenkov M., Chugunov S., Akhatov I., Shishkovsky I., Regolith-based additive manufacturing for sustainable development of lunar infrastructure – An overview // Acta Astronautica, 2021, v.180, P. 650-678.
[13] Foster & Partners design for the ESA's concept of 3d-printed shielding for lunar habitat. https://www.fosterandpartners.com/projects/lunar-habitation, 2012. (Accessed 9 August 2021, Credit: Foster & Partners).

IMPACT-CAUSED REGOLITH REWORKING WITHIN THE POLAR REGIONS OF THE MOON

A.T. Basilevsky[1], M.A. Kreslavsky[2], V.A. Dorofeeva[1], Yuan Li[3], LiGang Fang[3]
[1] *Vernadsky Institute of Geochemistry @ Analytical Chemistry, RAS, Kosygin str., 19, 119991, Moscow, Russia, atbas@geokhi.ru;*
[2] *University of California – Santa Cruz, Santa Cruz, CA, 95064, USA;*
[3] *Suzhou vocational University, SuZhou, 215009, China.*

KEYWORDS:
The Moon, polar, regolith, impact reworking, water ice, volatiles, differentiation.

INTRODUCTION:
Regolith in polar areas of the Moon containing water ice and other frozen volatiles is a subject of interest both for fundamental lunar science and for practical needs. Under discussion are the timing of water delivery to the polar cold traps [e.g.,1-4] and evolution of the ice-bearing deposits with time [e.g., 5,6]. In this work we consider part of the second issue, namely, question of impact-caused reworking of polar regolith and its effect on water ice and other ices in it. Cratering rate in lunar polar areas of the Moon comparing to that in equatorial areas is lower only by ~20% [7] so for this work it is considered the same as for all lunar surface. The question of impact-caused reworking of lunar regolith was considered long time ago [e.g., 8-10] and it looks like that those considerations are still valid. Recently a number of researches revisited regolith gardening with more sophisticated models [e.g., 11,12] and applied them to analysis of water ice in the lunar polar areas [e.g., 13-15]. In this paper we apply simple analytical approach of [10] to the issue of polar regolith by considering characteristics of population of small (D <1-2 km) lunar craters.

THE APPROACH:
Here we present simple estimates of regolith reworking by small impacts following [10]. The population of small craters can be divided into two parts: equilibrium sub-population of smaller craters and non-equilibrium (accumulating) sub-population of relatively larger craters with boundary between them at the "critical" crater diameter D_{cr} (Fig. 1).

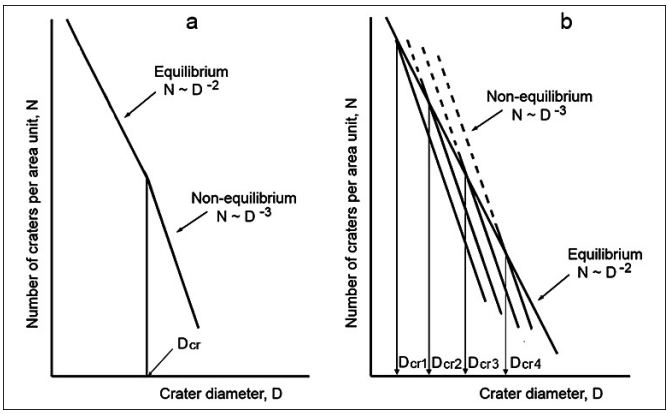


Fig.1. a) Schematic plot of number of craters (N) with diameter greater than D per unit area as a function of D; logarithmic scale on both axes; D_{cr} is a boundary diameter between the equilibrium and non-equilibrium subpopulations; **b)** The same plot showing increase of D_{cr} with time.

Random character of spatial distribution of craters along the area leads to variations of the reworking depth from pace to place. These variations can be presented as minimum, median and maximum thicknesses: 1) Minimum thickness of regolith $H_{\min}$ is the thickness in the place where the reworking was on minimal for this area depth; calculated from [10] for the case n = 1. 2)

Median thickness of regolith represents the median (50% frequency) in the distribution of thicknesses in the area. 3) Maximum thickness of regolith H_{max} is the depth of the largest and completely eroded and buried crater in the given area, that is depth of the crater with diameter equal D_{cr}. It can be shown that: $H_{min} = D_{cr}/50$, $H_{med} = D_{cr}/25$, $H_{max} = D_{cr}/5$. We compared our shown below crude results with more sophisticated model used by [12] and found remarkable similarity of our and their results.

CALCULATION RESULTS:

Below we show calculated minimum, median and maximum thickness of regolith on the floors of craters Shoemaker (D = 52 km, T = 4.16 Ga), Sverdrup (D = 33 km, T = 3.8 Ga), and Shackleton (D = 21 km, T = 3.15 Ga) and for comparison show estimates for the Luna-16, 17 and 24 landing sites which were partly given by [10]. Also for these areas we calculated numbers (n) of the reworking acts down to the depths 2, 1.5, 1, 0.5, 0.2 and 0.05 m as well as average numbers (n_{av}) of the reworking acts down to these depths (see Table).

Parameter	Luna-24	Luna-16, 17	Shackleton	Sverdrup	Shoemaker
D_{cr}, *m*	80	100	~80	~350	~1000
Max. cratering intensity*	2,5	6	2,5	200	1000
H_{min}, *m*	1,6	2	1,6	7	20
H_{med}, *m*	3,2	4	3,2	14	40
H_{max}, *m*	16	20	16	70	200
n for H = 2 *m*	1,6	2	1,6	7	20
n_{av} for H = 2 *m*	16	20	16	69	198
n for H = 1,5 *m*	~2	~3	~2	9	27
n_{av} for H = 1,5 *m*	19	29	19	87	260
n for H = 1 *m*	~3	4	~3	14	40
n_{av} for H = 1 *m*	28	37	28	129	368
n for H = 0,5 *m*	6	8	6	28	80
n_{av} for H = 0,5 *m*	51	68	51	238	681
n for H = 0,2 *m*	16	20	16	70	200
n_{av} for H = 0,2 *m*	121	150	121	531	1518
n for H = 0,05 *m*	64	80	64	280	800
n_{av} for H = 0,05 *m*	397	500	397	1739	4968

**cratering intensity in Eratosthenian-Copernican periods is assumed to be 1.*

It is seen from the Table 1 that calculated by us median regolith thickness in the landing sites of Luna-16, 17 and 24 is between 3.2 and 4 m, that agrees with estimations of the average thickness and its standard deviations of regolith in lunar maria based on the Arecibo radar data [16]. Median thickness of regolith on the floor of relatively young (3.15 Ga) crater Shackleton was found to be 3.2 m that looks reasonable. Median thickness of regolith on the floor of the older crater Sverdrup (3.8 Ga) was found to be 14 m, that agrees well with the results of [16] – their Fig. 11. These agreements suggest that our approach to estimate thickness of lunar regolith using value D_{cr} is valid and consider as acceptable our estimate of the 40 m median thickness of regolith on the floor of the oldest among the considered crater Shoemaker (4.16 Ga).

DISCUSSION AND CONCLUSIONS:

Regolith in polar areas of the Moon accumulated and reworked like in other lunar areas. Estimated content of water ice in it – from a few tenths of weight percent to a few percent [17-20], – probably do not influence significantly on this process. It is important to note that in this process some portion of the regolith material at each given impact passes through the stage of compression. If compression is low that is typical at relatively large distances from the impact point, it should lead to grain-to-grain friction resulted in moderate heating with melting and vaporization of the water ice and other ices.

Closer to the impact point the heating is much more effective. Impactors bombarding lunar surface have velocities from ~2,5 to ~70 km/s with average ~17 km/s [7,21,22]. Impacts with such velocities should lead to very high heating especially if target is porous that is the case for regolith. The earth-based observations at the National Observatory of Athens led to finding 112 light flashes on the lunar surface that allowed to estimate masses of the impactors and temperatures of those flashes. It was found that the impactors are of centimeter-decimeter in diameters and the temperatures are within 1000 to 7000 K with average ~2700 K [23]. Impact heating of polar regolith should lead to vaporization and partial decomposition of at least part of the frozen volatiles. The vaporized volatiles partly escape to the open space but some part of them meet the local cold materials and condense on them that should lead to physico-chemical differentiation of the volatiles. So, impact reworking of polar regolith should lead not only to its mixing but to physico-chemical differentiation of volatiles too.

ACKNOWLEDGEMENTS:
The work is supported by the Russian Science Foundation grant № 21-17-00035. We are grateful to Anton Sanin and Boris Ivanov for help.

REFERENCES:
[1] Deutsch A.N. et al. Icarus. 2020. V. 336. 113455.
[2] Deutsch A.N. et al. Geophys. Res. Lett. 2020. V. 47, is. 15, e2020GL087782.
[3] Lawrence D.J.J. Geophys. Res.; Planets. 2017. V. 122, 21–52.
[4] Siegler M.A. et al. Nature. 2016. V. 531(7595). 480–484.
[5] Li S. et al. PNAS. 2018. 115(36). 8907–8912.
[6] Farrell W.M. et al. Geophys. Res. Lett. 2019. V. 46. 8680–8688.
[7] Le Feuvre M., Wieczorek M.A. Icarus. 2008. V. 197. 291–306.
[8] Shoemaker E.M. et al. J. Geophys. Res. 1969. V. 74(25), 6081–6119.
[9] Gault D. et al. Proc. 5th Lunar Conf, Suppl., Geochim. Cosmochim. Acta 3, 1974. 2365–2386.
[10] Basilevsky A.T. Kosmicheskie Issledovaniya. 1974. V. XII. Is. 4. 606-609 (in Russian).
[11] Costello E.S. et al. Icarus. 2018. V. 314. 327–344.
[12] Hirabayashi M. et al. J. Geophys. Res.; Planets. 2018. 123, 527–543.
[13] Hurley D.M. et al. Geophys. Res. Lett. 2012. V. 39, L09203.
[14] Cannon K.M., and Britt D.T. Icarus. 2020. V. 347. 113778.
[15] Costello E.S J. Geophys. Res.: Planets. 2020. V. 125(3), e06172.
[16] Shkuratov.Y., Bondarenko N. Icarus, 2001. V. 149(2), 329–338.
[17] Feldman W.C.J. Geophys. Res. 2000.V. 105, No. E2. 4175–4195.
[18] Colaprete A. et al., Science, 2010. V. 330, 463-468.
[19] Mitrofanov I.G. et al. Science. 2010. V. 330, 483-486.
[20] Sanin A.B. et al. Icarus. 2017. V. 283. 20–30.
[21] Melosh H.J. Planetary Surface Processes. 2011. Camb. Univ. Press. 500 p.
[22] Werner S.C., Ivanov B.A. Treatise on Geophysics. 2015. 327-365.
[23] Avdellidou C.et al. Pl. Space Sci. 2021. V. 200. 105201.

TRANSIENT VOLCANICALLY-INDUCED LUNAR ATMOSPHERE: BASIC PROPERTIES AND EFFECT ON VOLATILE TRANSPORT

I. Aleinov[1,2], G. Gronoff[3,4], C.W. Hamilton[5], C. Harman[6], J.W. Head[7], K. Tsigaridis[1,2], M.J. Way[2,8], E.T. Wolf[9]

[1] *Columbia University, 2880 Broadway, New York, NY, 10025, USA, igor.aleinov@columbia.edu;*
[2] *NASA Goddard Institute for Space Studies, 2880 Broadway, New York, NY, 10025, USA;*
[3] *Science Directorate, Chemistry and Dynamics Branch, NASA Langley Research Center, Hampton, VA, USA;*
[4] *SSAI, Hampton, VA, USA;*
[5] *Lunar and Planetary Laboratory, University of Arizona, Tucson, AZ, USA*
[6] *Space Sciences Division, NASA Ames Research Center, Moffett Field, CA, USA;*
[7] *Brown University, Providence, RI, USA;*
[8] *Theoretical Astrophysics, Department of Physics & Astronomy, Uppsala University, Uppsala SE-75120, Sweden;*
[9] *University of Colorado, Boulder, USA.*

KEYWORDS:
Lunar atmosphere, 3-D modeling, volcanism, volatiles, poles

INTRODUCTION:

The possibility that the Moon developed a tenuous transient atmosphere due to volcanic outgassing has been discussed for decades [1]. The discovery of lunar polar volatiles, and recent conjecture [2] that during the peak of volcanic activity such an atmosphere could accumulate to pressures up to 10 mb, has raised the question of the possible effect of such an atmosphere on transport of volcanically-produced volatiles and their deposition in polar regions where they could have been preserved in cold traps until modern times. While a more recent study by Head et al. [3] concludes that accumulation of such an atmosphere to substantial pressures is unlikely due to sparsity of volcanic events, even a single major volcanic event could produce an atmosphere ~1 microbar thick, which would survive for at least a few thousand years. This would be a collisional atmosphere, and its effect on volatile transport cannot be neglected. In this work we study such volcanically induced atmospheres for the range from 10 mb to 0.1 mb. While current limitations of our model prevent us from looking at atmospheres thinner than 0.1 mb, we hope that our results can be extrapolated, and one can make conjectures concerning thinner atmospheres.

METHODS:

To study the volcanically-outgassed lunar atmosphere we use the ROCKE-3D [4] planetary 3-D General Circulation Model. In our experiments the model was set to 4^{o} x 5^{o} horizontal resolution and 40 vertical layers of the atmosphere with the upper layer at ~10^{-4} of the surface pressure. To represent the conditions at 3.5 Ga (peak of lunar volcanic activity), we set the solar constant to 0.75 of the modern value and set the lunar rotational period to 17.7 modern Earth days (which corresponds to the distance from Earth 0.75 of the modern value). We assumed that the Moon's surface has not changed significantly since the era of the Late Heavy Bombardment, and so we used modern observations for the topography, the albedo and the distribution of permanently shadowed regions. Based on [2], we assumed that main outgassed species contributing to the atmosphere were CO and H_2O, with the possibility of CO converting to CO_2 in the presence of H_2O at sufficiently high temperatures.

EXPERIMENTS:

To understand the basic properties of volcanically-induced lunar atmospheres, we conducted a series of experiments for CO and CO_2-dominated atmospheres with atmospheric pressures from 0.1 mb to 10 mb and

obliquities from 0° to 40°. We present some of these results here. In addition, we performed a series of major volcanic outgassing experiments. For the Moon with a CO_2-dominated atmosphere in an equilibrium state, we set up a major volcanic event according to [5]. In particular, we assumed that the site of eruption was in the middle of Mare Imbrium, its duration was 100 days, and the H_2O outgassing rate was 3 x 10^4 kg/s (which assumes 1000 ppmw H_2O in lava). We followed the fate of the outgassed water. In the majority of our experiments most of the outgassed water was quickly delivered to the polar regions and was deposited there in the form of snow or frost. Figure 1 shows the amount of water that was deposited in polar regions 3 years after the onset of the eruption. One can see that in the 0-obliquity case, thin atmospheres can efficiently deliver water to the poles, and the efficiency of this process actually, increases as the atmosphere gets thinner. This is probably a result of the fact that for the same amount of outgassed water, thin atmospheres become more saturated, and, hence, are more likely to get rid of water in the form of precipitation.

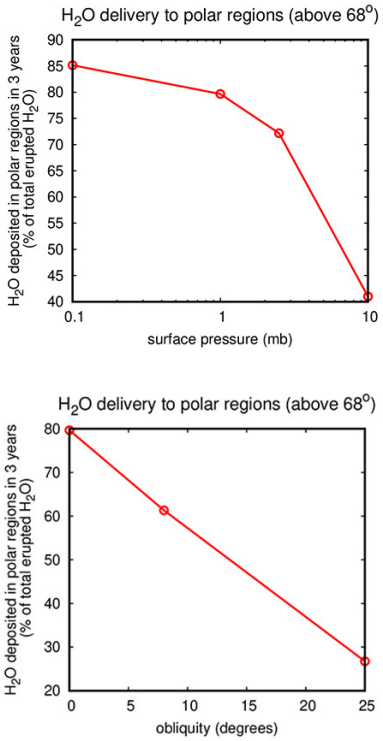


Fig 1. The amount of H_2O delivered to the polar regions (above 68° N or below 68° S) in 3 years after the onset of the eruption as a percentage of the total erupted amount. Left: dependence on surface pressure (0-obliquity case). Right: dependence on obliquity (1 mb surface pressure case).

For non-zero obliquity the efficiency of water delivery decreases with increasing obliquity, since poles become warmer. At obliquities >8°, poles start to lose water due to seasonal sublimation, and the entire process collapses at ~25° obliquity.

CONCLUSIONS:

During the peak of volcanic activity at ~3.5 Ga, the Moon could have had transient volcanically-induced atmospheres. Such atmospheres could efficiently transport volatiles from the outgassing regions to the polar cold traps. In our experiments the efficiency of volatile delivery increases as the atmosphere gets thinner. This allows us to conjecture that even microbar-scale atmospheres resulting from a single major eruption can efficiently deliver volatiles to the poles.

ACKNOWLEDGMENTS:
This research was supported by NASA Solar System Workings program award 80NSSC21K0163 and by NASA Nexus for Exoplanet System Science. We acknowledge support from the GSFC Sellers Exoplanet Environments Collaboration (SEEC), which is funded by the NASA Planetary Science Division's Internal Scientist Funding Model. Resources supporting this work were provided by the NASA High-End Computing (HEC) Program through the NASA Center for Climate Simulation (NCCS) at Goddard Space Flight Center.

REFERENCES:
[1] Stern S.A. The lunar atmosphere: History, status, current problems, and context // Rev. of Geophysics. 1999. V. 37. P. 453-492.
[2] Needham D.H., Kring D.A. Lunar volcanism produced a transient atmosphere around the ancient Moon // Earth and Planetary Sci. Lett. 2017. V. 478. P. 175-178.
[3] Head J.W. et al. Volcanically Induced Transient Atmospheres on the Moon: Assessment of Duration, Significance, and Contributions to Polar Volatile Traps // GRL. 2020. V. 47. e2020GL089509.
[4] Way M.J. et al. Resolving Orbital and Climate Keys of Earth and Extraterrestrial Environments with Dynamics (ROCKE-3D) 1.0: A General Circulation Model for Simulating the Climates of Rocky Planets // ApJS. 2017. V. 231. 12.
[5] Wilson L., Head J.W. Controls on Lunar Basaltic Volcanic Eruption Structure and Morphology: Gas Release Patterns in Sequential Eruption Phases // GRL. 2018. V. 45. P. 5852-5859.

IN SITU DETERMINATION OF MULTIPLE PHYSICAL PROPERTIES OF PLANETARY SURFACE ROCKS AND SOILS THROUGH A SINGLE MEASUREMENT OF THEIR COMPLEX SUSCEPTIBILITY

J.L. Mesa[1], C. Aroca Hernandez-Ros[2], M.D. Michelena[1]
[1] *Instituto Nacional de Técnica Aeroespacial, Payloads and Space Science Department, Torrejón de Ardoz, Madrid, Spain;*
[2] *ISOM, Universidad Politécnica de Madrid, Madrid, Spain.*

KEYWORDS:
Magnetic Sensor, Magnetic Susceptibility, Magnetometer, Susceptometer, Inductive Device.

INTRODUCTION:
The characterization of the magnetic field and the magnetic properties are powerful tools to understand the composition, structure and geological history of the surface rocks. These characteristics have important implications on the determination of magnetic fields present in the early history of the planets.

Determining the complex magnetic susceptibility (both real and imaginary parts) of rocks complements their magnetic characterization and can improve the understanding of their evolution along the planetary history [1].

Real and imaginary magnetic susceptibility provide information, such as: how much magnetization can acquire a rock in the presence of an external field, how this magnetization behaves under alternating current (AC) or the magnetic energy losses during the magnetization by different mechanisms (induced currents, hysteresis, etc.) which helps the identification of minerals, their magnetic carriers and the phases. For instance, the imaginary component of the susceptibility of magnetite and hematite is related not only to their volume percentage but also to their distribution in the rock (layered, interstitial, etc) and the overall texture. This component is also sensitive to the crystal system, the characteristics of the grains and their boundaries and to the development of silicates and carbonates in the rock [2], which could be key information and a potential selection criteria for sample return missions or as in-situ scientific study of the magnetic properties during planetary missions.

Recently, we have developed a novel compact and robust instrument to measure the complex susceptibility of rocks in the planetary exploration. We had reported the calibration of the real part of the susceptibility and establish a method for the calibration of the imaginary component [3]. In this work, we present the full calibration of the instrument, an overview of its performance as well as the demonstration of its capabilities during terrestrial analogues campaigns.

The calibration process for the susceptometer casted very good results. For the real component, the calibration was carried out by means of relating the results obtained with the susceptometer with those from reference equipment. A batch of ad-hoc reference samples made of magnetic material diluted in a non-magnetic epoxy matrix were manufactured for the calibration of the real component measurement procedure. The samples were measured with the susceptometer and related with the results from a Vibrating Sample Magnetometer (VSM) for the calibration of the sensor response.

The calibration of the imaginary component of the magnetic susceptibility was made by comparison with an ad-hoc developed magnetometer for the determination of the AC magnetic moment. For these purpose, a series of samples made of steel spheres (2.5 mm diameter) distributed in a body center cubic geometry within an epoxy matrix was manufactured to ensure orientation and magnitude controlled values of the real and imaginary magnetic susceptibility.

The calibration was completed by obtaining the same results for the complex susceptibility with both susceptometer and reference equipment.

The instrument reached a resolution of about $\chi = 10^{-4}$ (S.I. Vol. Susceptibility) and a dynamic range from $\chi' = 10^{-4}$ S.I. and $\chi' = 10^{1}$ S.I. for the real susceptibility, which are values that are representative of the Earth, lunar and Martian rocks [4, 5, 6]. The imaginary susceptibility measurement has a resolution in the order of $\chi'' = 10^{-6}$. Such resolution is adequate for most natural rocks characterization and competitive with that of larger and widely proved laboratory instruments (Vibrating Sample Magnetometer – VSM) or instrumentation currently used in field campaigns based on electromagnetic induction, capacitive coupling resistivity, and galvanic contact resistivity methods.

Table 1. Susceptometer range.

Range	Minimum (S.I.)	Maximum (S.I.)
Real Volume Susceptibility	10^{-4}	10^{1}
Imaginary Volume Susceptibility	10^{-6}	N.A.*

This sensor provides a great advantage compared to available commercial susceptometers, given that it does not require sample preparation or loading, but only the approach of its head to a minimum sample size of 50 × 20 × 20 mm approximately.

Its size, power consumption and portability make it suitable to be placed on board rovers, or to be used as a portable device during field campaigns or astronauts in manned space missions. Its robustness has been demonstrated through testing of the most critical parts i.e. vibration and thermo-vacuum tests with levels representative of Mars and Moon missions.

The validation of the instrument is in course. In particular, it has been used in several scientific campaigns in terrestrial analogs to characterize in situ the real part of the susceptibility like in the studies developed in Barda Negra crater [7] and in Cerro Gordo volcano [8], showing a good correlation between the susceptibility values and the different geological structures, with the capability to identify between the different deposits by means of the real component of the magnetic susceptibility. The instrument showed a good performance during the fieldwork and proved its suitability for in situ operation.

REFERENCES:

[1] Kuipers B.W. M., Bakelaar I.A., Klokkenburg M., and Erné B.H.. Complex magnetic susceptibility setup for spectroscopy in the extremely low-frequency range. 2008. Review of Scientific Instruments. 79, 013901. https://doi.org/10.1063/1.2827450

[2] Lisa Vella & Don Emerson. Electrical Properties of Magnetiteand Hematite-Rich Rocks and Ores. 2012. ASEG Extended Abstracts. DOI: 10.1071/ASEG2012ab232.

[3] Díaz Michelena M., Mesa J.L., Pérez M., Maicas M.C., Cobos P., Aroca C., A novel induction-based device for the measurement of the complex magnetic susceptibility. 2017. Sensor Actuat A-Phys, 263: 471-479.

[4] Rochette, P., Gattaccea, J., Chevrier, V., Hoffmann. V., Lorand, J.-P., Funaki, M. & Hochgleitner, R.. Matching Martian crustal magnetization and magnetic properties of Martian meteorites. 2005. Meteoritic and Planetary Science, 40 (4): 529–540.

[5] Rochette, P. Magnetic properties of lunar materials: Meteorites, Luna and Apollo returned samples. 2010. Earth and Planetary Science Letters. 292: 383–391.

[6] Hunt, C.P., Moskowitz B.M. & Banerjee S.K.. Magnetic Properties of Rocks and Minerals, Wiley. 2013. Online Library. DOI: 10.1029/RF003p0189.

[7] Díaz Michelena M., Kilian R., Baeza O., Rios F., Rivero M.A., Mesa J.L., González V., Arlensiú Ordoñez A., Langlais B., Rocca M.C.L., Acevedo R.D. The formation of a giant collapse caprock sinkhole on the Barda Negra plateau basalts (Argentina): Magnetic, mineralogical and morphostructural evidences. 2020. Geomorphology. 367.107297.

[8] Monasterio O.G., Oliveira J.S., Romero S.F., García Bueno J.L. and Diaz Michelena M. Cerro Gordo, an analog of a Martian composite volcano. 2021. Terrestrial Analogs 2021 (LPI Contrib. No. 2595).

PROVENANCE OF MATERIALS AT THE CHANG'E-5 LANDING SITE

Yuqi Qian[1,2], Long Xiao[1], James W. Head[2], Carolyn H. van der Bogert[3], Harald Hiesinger[3], Lionel Wilson[4]

[1] *Planetary Science Institute, China University of Geosciences, Wuhan, China, yuqii.qian@gmail.com;*

[2] *Department of Earth, Environmental and Planetary Sciences, Brown University, Providence, USA;*

[3] *Institut für Planetologie, Westfälische Wilhelms-Universität Münster, Münster, Germany;*

[4] *Lancaster Environment Centre, Lancaster University, Lancaster, UK.*

KEYWORDS:
Chang'e-5; Lunar Sample Return; Northern Oceanus Procellarum; Lunar Regolith; Young Mare Basalts

INTRODUCTION:
The Chang'e-5 (CE-5) mission is China's first lunar sample return mission. CE-5 landed in Northern Oceanus Procellarum (43.06°N, 51.92°W) on December 1, 2020, collected 1731 g of lunar samples, and returned to the Earth on December 17, 2020. The CE-5 landing site is ~170 km ENE of Mons Rümker, on one of the youngest mare basalts (Em4/P58) on the Moon [1,2], which were not sampled by the Apollo or Luna missions. The CE-5 returned samples are currently being analyzed by Chinese scientists, and the relevant basic information can be found in the Lunar Sample Information Database (https://moon.bao.ac.cn/moonSampleMode/index.html). This study describes the provenance of lunar regolith at the CE-5 landing site in order to provide context for the ongoing sample analysis.

EXOTIC MATERIALS:
The returned CE-5 samples consist of two types of materials based on remote sensing analysis, i.e., local mare basalts and distal ejecta [3-5]. Local materials dominate the overall regolith composition (~90%) of the CE-5 landing site [3,4]. An ~4-7 m thick regolith layer [6], developed by post-mare impact bombardment, overlies the CE-5 basalts. The regolith layer was admixed with impact ejecta from distant sources. We have used multiple-source remote sensing data [4], including TiO_2 abundance, FeO abundance and albedo maps to trace the ejecta source craters (Figure 1), and find NE-SW ejecta/rays from Harpalus are the main ejecta overlaying the CE-5 mare basalts. Further, a power law model was used to calculate the abundance of distal materials, and we find Harpalus (~6%), Copernicus (~2%), and Aristarchus (~1%) are the dominant sources.

LOCAL MARE BASALTS:
In addition to exotic materials delivered by the distal impacts, the overall composition of the lunar soils is controlled by the local (~91%) mare basalts erupted by Rima Sharp [7]. CE-5 mare basalts have intermediate-Ti, relatively high-olivine and high-Th abundances, while clinopyroxene is the most abundant mineral type [8]. CE-5 mare basalts cover an area of ~37,000 km^2, with a mean thickness of ~51 m and volume of ~1450–2350 km^3 [8]. No specific source vents (e.g., fissures, cones, domes) were found within the unit, and Rima Sharp is the most likely source region for the CE-5 mare basalts.

According to our analysis, we found that Rima Sharp, previously thought to be the longest lunar sinuous rille, is instead characterized by source vents at its beginning and end and is composed of two main rilles. The North Vent feeds several rilles, and the largest one, Rima Sharp, flows south into, and feeds the CE-5 mare unit. The South Vent begins at what was previously thought to be the rille terminus, and flows northward into the CE-5 mare unit. Neither source appears to have substantial associated pyroclastic deposits. Rima Mairan postdates Rima Sharp and flows into its southern end. Both source vents and rilles appear to be traversing and emptying into the CE-5 mare unit and are thus likely to be its source. The composition of the basaltic lavas

transported in both rilles appears very similar, despite their sources separation of ~350 km. Models for rille formation should account for these characteristics and relationships, and the nature of topography at the time of emplacement and produced subsequently.

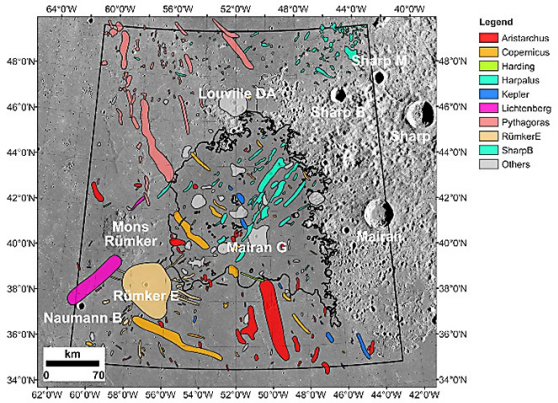


Fig. 1. Ejecta distribution of major source craters in Northern Oceanus Procellarum [4]

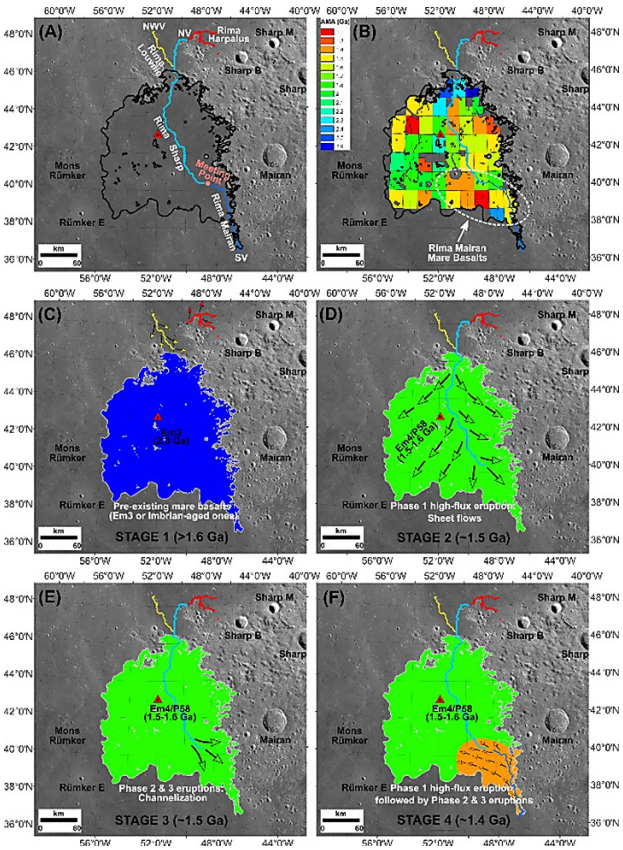


Fig. 2. Volcanic evolution of the CE-5 young mare unit in Northern Oceanus Procellarum [6]

In summary, the CE-5 samples are predicted to have two different ages, potentially separated by several hundred million years, representing lavas from the two different rille sources, predominated lava from Rima Sharp, but with contributions from the younger Rima Mairan. Together these will form an unprecedented window into the petrogenesis of young mare basalts.

REFERENCES:

[1] Hiesinger H., Head J.W., Wolf U. et al. Ages and stratigraphy of lunar mare basalts: A synthesis // Special Paper of the Geological Society of America. 2011. No. 477. P. 1–51.
[2] Qian Y., Xiao L., Zhao S., et al. Geology and Scientific Significance of the Rümker Region in Northern Oceanus Procellarum: China's Chang'E-5 Landing Region // JGR: Planets. 2018. V. 123, P. 1407–1430.
[3] Xie M., Xiao Z., Zhang X., et al. The Provenance of Regolith at the Chang'e-5 Candidate Landing Region // JGR: Planets. 2020. V. 125. P. e2019JE006112.
[4] Qian Y., Xiao L., Wang Q., et al. China's Chang'e-5 landing site: Geology, stratigraphy, and provenance of materials // EPSL. 2021. V. 561. P. 116855.
[5] Liu T., Michael G., Zhu M., et al. Predicted Sources of Samples Returned From Chang'e−5 Landing Region // GRL. 2021. V. 48. P. e2021GL092434.
[6] Qian Y., Xiao L., Yin S., et al. The regolith properties of the Chang'e-5 landing region and the ground drilling experiments using lunar regolith simulants // Icarus. 2020. V. 337. P. 113508.
[7] Qian Y., Xiao L., Head J.W. et al. The Long Sinuous Rille System in Northern Oceanus Procellarum and Its Relation to the Chang'e-5 Returned Samples // GRL. 2021. V. 48. P. e2021GL092663.
[8] Qian Y., Xiao L., Head J.W., et al. Young lunar mare basalts in the Chang'e-5 sample return region, northern Oceanus Procellarum // EPSL. 2021. V. 555. P. 116702.

SCIENCE PROGRAM OF LUNA-25 AND LUNA-27 MISSIONS

V. Tretyakov[1], L.M. Zelenyi[1] and I. Mitrofanov[1]
[1] *Space Research Institute, Moscow, Russian Federation, vladtr@mx.iki.rssi.ru.*

KEYWORDS:
Moon, polar regions, landers, spacecraft, robotic missions.

Scientific goals, current status and nearest plans for Russian Landers missions with Luna-25 (project Luna-Glob) and Luna-27 (project Luna-Resource) will be presented. Both projects aimed on search for volatiles and water ice in upper layer of regolith, study structure and content of regolith and investigate of moon's near-surface dust and plasma exosphere at lunar polar regions. Luna-25 and Luna-27 missions are developing with international participation shell provide the necessary scientific and technological experience for future long life-time Landers at the polar regions and for future exploration of Moon.

The scientific experiments which were selected in accordance with the main goals of these missions, will be shortly described. Main and spare landing sites for Luna-25 will be presented selected on the base both of engineering suitability (flatness and roughness of surface, radio visibility, solar irradiation and so on) and of scientific motivation. Criteria for landing sites selection for Luna-27 will be presented too as well as preliminary areas are suitable for landing and operation. The detailed science program for the first lunar days of Luna-25 and preliminary plans of surface operations for Luna-27 will be presented and discussed.

TESTS OF LUNAR ROBOTIC ARM WITH LUNAR POLAR REGOLITH SIMULANT

M. Litvak[1], T. Kozlova[1], A. Iliin[1], A. Kiselev[1], A. Kozyrev[1], I. Mitrofanov[1], V. Tretyakov[1], V. Yakovlev[1]
[1] *IKI RAS, Moscow, Russia.*

KEYWORDS:
Moon, polar, Luna-25, robotic arm, water ice

INTRODUCTION:
In 2022 it is planned to launch first Russian lunar landing mission “Luna-25”. It shall study mineralogical, chemical, and isotopic composition of the lunar regolith, as well as to search for volatile compounds (including water ice) in the top regolith layer at the high-latitude regions of the Moon [1]. The landing site was selected at the near polar area with coordinates of 43.544 degrees east longitude and 69.545 degrees south latitude [2].

To conduct contact investigations of the lunar regolith properties during “Luna-25” surface operations it was proposed to use a compact, lightweight and multifunctional robotic arm. Robotic arm shall excavate and take samples of lunar soil from different depths (down to 25 cm) at the selected location, deliver these collected samples to the laser ionization mass spectrometer for elemental and isotope analysis [3], see Figure 1.

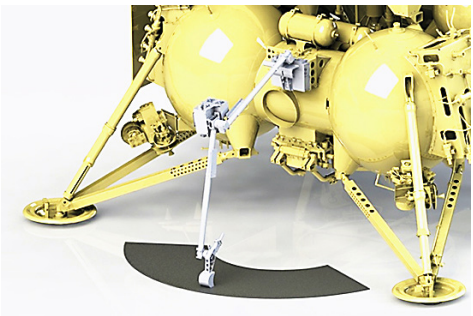


Fig. 1. The illustration of robotic arm operations onboard “Luna-25” lander.

In this study we presented a brief overview of the ground-based functional tests that were conducted with the robotic arm to verify that all these requirements were met, including interaction with an analog of lunar soil

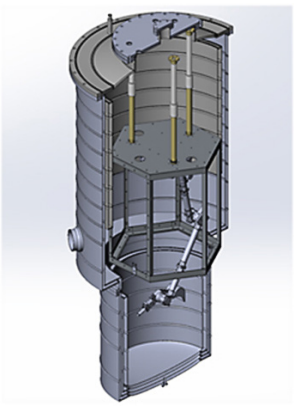


Fig. 2a. The concept of cryogenic vacuum chamber used for the robotic arm tests.

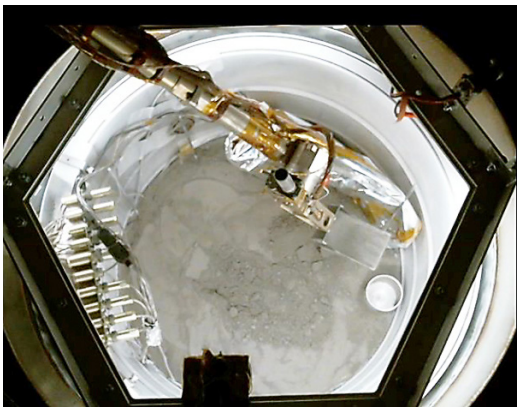


Fig. 2b. The photo of robotic arm operations in cryogenic vacuum chamber: excavation, sample acquisition and delivery to the special container.

enriched with water ice under low pressure and cryogenic temperatures (operations in lunar like conditions), see [4].

To conduct such tests, a special cryogenic vacuum chamber was developed, which allows to allocate inside a robotic arm, as well as a container with an analog of lunar soil that could be frozen to the temperatures ~ -150°C at low pressure (~10^{-2} Torr), see Figure 2.

Analog of compacted lunar regolith for these tests was specially developed at Vernadsky institute imitating physical and mechanical properties of lunar regolith which most important for the robotic arm operations [5].

During ground experiment several tests were conducted with analog of the lunar regolith with different water content (0.1–1.5% by mass fraction) and temperature as low as -100°C at the robotic arm excavation zone.

It was shown that robotic arm actuators are sufficiently powerful enough to excavate frozen soil and take its samples (and to repeat it several times) if water ice content achieved 1.5% by mass fraction.

REFERENCES:

[1] Mitrofanov et al., (2021), Solar System Research, in Press.
[2] Dyachkova et al (2017), Solar System Research, 54, 275-287.
[3] Козлова и др. (2021) Вестник НПО им. С.А. Лавочкина. 2021, подано в журнал.
[4] Litvak et al., (2021), Solar System Research, in Press.
[5] Slyuta et al., (2021), Acta Astronautica, 180, 447-457.

LUNAR NEAR-SURFACE DUSTY PLASMA INVESTIGATIONS WITH PML INSTRUMENT

I.A. Kuznetsov[1], A.V. Zakharov[1], G.G. Dolnikov[1], S.A. Bednyakov[1], A.S. Bychkova[1], A.E. Dubov[1], A.A. Kartasheva[1], A.N. Lyash[1], I.A. Shashkova[1], A.V. Shekhovtsova[1]

[1] *Space Research Institute of the RAS (IKI RAN), 84/32 Profsoyuznaya Str, Moscow, Russia, 117997, kia@iki.rssi.ru.*

KEYWORDS:
Dust, lunar dust, dusty plasma, lunar lander, Luna-25, Moon

INTRODUCTION:

One of the complicating factors of the future robotic and human lunar landing missions is the influence of the dust. The upper insulating regolith layer is electrically charged by the solar ultraviolet radiation and the flow of solar wind particles. Resulted electric charge and thus surface potential depend on the lunar local time, latitude and the electrical properties of the regolith.

Recently we have some reemergence of the interest of Moon investigation. Number of governments, space agencies and collaborations declared their intentions to build manned orbit stations or surface bases in next decades. In Russian space program developing the polar lunar base is also stated.

In the following years several missions are also under development, including "Luna-25" lunar lander project (to be launched in 2022) and "Luna-27" lunar lander (2024).

LUNAR DUST PROBLEMATIC:

Studying the properties of lunar dust is important both for scientific purposes for the lunar dusty-plasma exosphere investigation and for the technical safety of lunar robotic and manned missions. Properties of regolith and dust particles (density, temperature, composition, etc.) as well as near-surface lunar exosphere depend on solar activity, lunar local time and position of the Moon relative to the Earth's magnetospheric tail. Upper layers of regolith are an insulator, which is charging as a result of solar UV radiation and the constant bombardment of charged particles, creates a charge distribution on the surface of the moon: positive on the illuminated side and negative on the night side. Charge distribution depends on the local lunar time, latitude and the electrical properties of the regolith (the presence of water in the regolith can influence the local distribution of charge).

On the sunlit side of the Moon the possibility of the dusty plasma dynamics formation exists near the lunar surface. Altitude of dust levitation depends from size of dust particle and Moon latitude. The distribution of the dust particles by size and altitude has been estimated considering photoelectrons, electrons and ions of solar wind, solar emission in numerous papers [e.g. 1-5].

DUST MONITORING INSTRUMENT:

Dust analyzer instrument PmL for future Russian lander missions intends for investigation the dynamics of dusty plasma near lunar surface. PmL consists of three parts: Impact Sensor and two Electric Field Sensors.

Impact sensor

Impact sensor (Fig. 1) purpose is to investigate the dynamics of dust particles near the lunar surface (speed, charge, mass, vectors of a fluxes).

Possible detectable events may occur with:

a) high speed micrometeorites

b) secondary particles after micrometeorites soil bombardment

c) levitating dust particles due to electrostatic fields.

PmL instrument will measure dust particle mechanical momentum. Also Impact Sensor will measure the electrical charges of dust particles. In case the charge and impulse of a dust particle are measured with properly time-stamps of events, we can calculate the velocity and mass of the particles (Fig. 2).

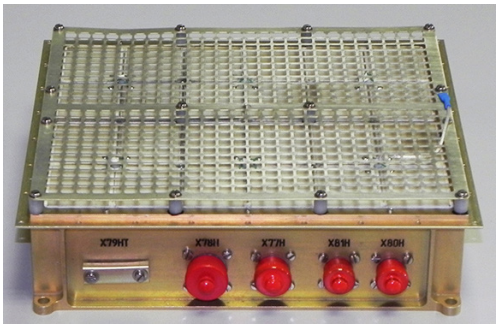


Fig. 1. The Impact Sensor.

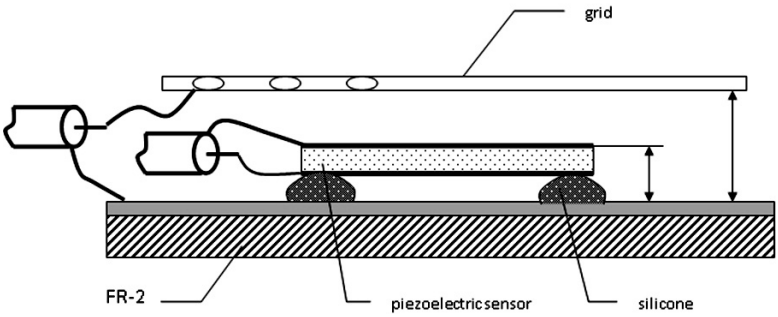


Fig. 2. Impact Sensor measurement technique schematics.

Electric Field Sensor

Electric field Sensor (Fig. 3) will measure the value and dynamics of the electric fields near the lunar surface. The measurement technique is based on classic Langmuir probe plasma investigation method. Two Electric Field Sensors allow to measure the concentration and temperature of charged particles (electrons, ions, dust particles). Using Langmuir probes near the surface through the lunar day and night, we can obtain the energy spectra photoelectrons in various periods of time.

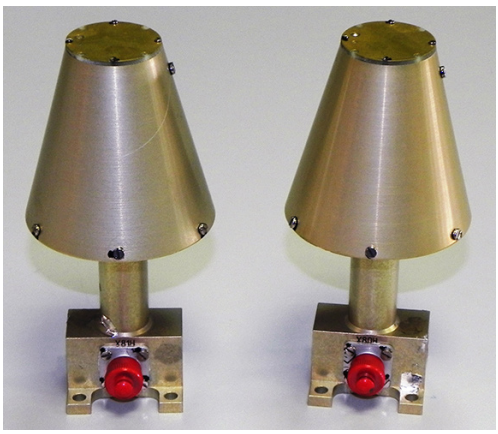


Fig. 3. Electric Field Sensor.

STATUS:

PmL instrument is developing and manufacturing in IKI.

The flight sample of the instrument is finished, tested and mounted onboard the spacecraft. A numerous amount of calibration results from the simulating chambers with dust particles injectors and plasma inside has been collected. All the important achievements are presented in this report.

REFERENCES:

[1] Popel S.I., Golub' A.P., Izvekova Yu.N., Afonin V.V., Dolnikov G.G., Zakharov A.V., Zelenyi L.M., Petrov O.F., Fortov V.E. (2014). On the distributions of photoelectrons over the illuminated part of the Moon // JETP Letters, Volume 99, Issue 3, pp. 115-120.

[2] Colwell J.E., Batiste S., Horanyi M., Robertsson S., Sture S. (2007). Lunar surface: Dust dynamics and regolith mechanics. // Rev. of Geophys.45, p. 1-26.

[3] Stubbs T.J., Vondrak R.R., Farrell W.M. (2007b). Impact of dust on lunar exploration. NASA Goddard Spaceflight Center, http://helf.jsc.nasa.gov/files/StubbsImpactOn Exploration.4075.pdf.

[4] Vaverka J., Richterová I., Pavlu J., Šafránková J., and Němeček Z., LUNAR SURFACE AND DUST GRAIN POTENTIALS DURING THE EARTH'S MAGNETOSPHERE CROSSING // The Astrophysical Journal, 825:133 (10pp), 2016 July 10.

[5] Kuznetsov I.A., Hess S.L.G., Zakharov A.V., Cipriani F., Seran E., Popel S.I., Lisin E.A., Petrov O.F., Dolnikov G.G., Lyash A.N., Kopnin S.I. Numerical modelling of the Luna-Glob lander electric charging on the lunar surface with SPIS–DUST. // Planetary and Space Science. 2018. V. 156. P. 62-70.

INSTRUMENTS ARIES-L AND LINA-R FOR INVESTIGATION OF SPACE PLASMA INTERACTION WITH THE LUNAR REGOLITH

O.L. Vaisberg[1], R.N. Zhuravlev[1], D.A. Moiseenko[1], A.Yu. Shestakov[1], S.D. Shuvalov[1], P.P. Moiseev[2], M.V. Mitjurin[2], I.I. Nechushkin[2], A.D. Vasilyev[2], E.I. Rodkin[2], V.V. Letunovsky[2]

[1] *Space Research Institute of the Russian Academy of Sciences (IKI), 84/32 Profsoyuznaya Str, Moscow, Russia, 117997, olegv@iki.rssi.ru;*

[2] *Astron Electronics LLC, Russia, 302019, Oryol, 2 Vesyaolaya Str, astronel-moiseev-pp@yandex.ru.*

KEYWORDS:
Solar wind, secondary ion mass spectrometry, ion energy-mass analyzers, neutral atoms.

INTRODUCTION:

The study of the solar wind interaction with regolith the lunar surface, as well as the characteristics of secondary and reflected ions and neutral particles is an actual scientific problem in development of the lunar space program. The main sources of neutral atoms on the Moon are solar photon-stimulated desorption of regolith [8], micrometeorite activity [2] and the scattering of solar wind protons [3; 4]. The ARIES-L neutral particles converter operation principle is based on the effect of surface ionization as a result of interaction at small angles with a tungsten plate [6], which will allow registering neutral atoms with energies above 10 eV, originating from of the processes of solar wind to surface interaction.

ARIES-L and LINA-R instruments are ion energy-mass analyzers with a wide field of view (FOV) that measure ion parameters in the energy range from 10 eV to 5000 eV, with an option of registering fluxes of neutral atoms from the lunar surface. The key feature of the instruments is simultaneous registration of ions of the selected energy in a FOV close to 2π [1]. The main goals of ARIES-L instrument onboard Luna-25 mission are to study the processes of solar wind interaction with regolith, regolith composition analysis via secondary ion mass spectrometry, and analysis of the neutral exospheric populations. LINA-R instrument onboard Luna-26 mission will measure space plasma and neutral atom fluxes from lunar orbit. Large FOV close to 2π allows the simultaneous registration of solar wind and secondary particles from regolith, which makes possible the study of interaction of charged particles with regolith depending on the variety of different incidence angles during the lunar day. The instrument will also perform measurements within magnetotail during certain mission period.

Instruments optics is a combination of electrostatic and time-of-flight (TOF) elements, which perform ion analysis by energy per charge ratio E/Q, and mass analysis. The structure of the ARIES-L instrument is shown in Figure 1.

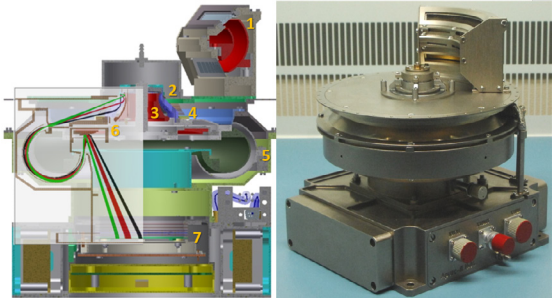


Fig. 1. The structure and general view of the ARIES-L instrument.
1 – neutral particle converter; 2 – electronic optics entrance aperture; 3 – M1 mirror; 4 – time of flight gate; 5 – electrostatic analyzer; 6 – M2 mirror; 7 – microchannel plate position-sensitive detector.

The analysis scheme operation principle is: ions passing through the circular diaphragm (2), are reflected by the mirror M1 (3) and focused to the entrance of the toroidal electrostatic analyzer (5). The M1 mirror has a specific geometry which allows transformation of 2π ion fluxes into a single focal point [7]. The toroidal electrostatic analyzer selects ions of a narrow energy range. Its inner plate is grounded, and the deflection potential is applied to the outer plate. After passing the electrostatic analyzer the particles of the selected energy range are reflected by the mirror M2 (6). M2 has a conical shape, it redirects the ions onto the position-sensitive detector. The position of the particle on detector surface allows the determination of the direction from which the particle came to the instrument's aperture. The position-sensitive detectors of ARIES-L and LINA-R are based on microchannel plate (MCP) assembly with a wedge and strip type anode.

The LINA-R instrument has a separate neutral particle detector. Its operation principle is also based on the of neutral atoms surface ionization an a flat tungsten electrode with subsequent acceleration of ionized neutral atoms to the known energy and following mass analysis of particles by M/Q ratio in the gap of two magnets [7]. The structure of the sensor is shown in Figure 2. The entrance aperture of the neutral particle sensor is equipped with a mesh assembly (1), which prevents charged particles from entering the aperture. The ionized atoms (2) are accelerated by electrical field towards the exit window and then enter the magnetic analyzing system. Depending on the mass, the ions move along different trajectories in the magnetic field, and only certain mass passes the diaphragms (4) and reach the detector (5) based on channel electron multiplier.

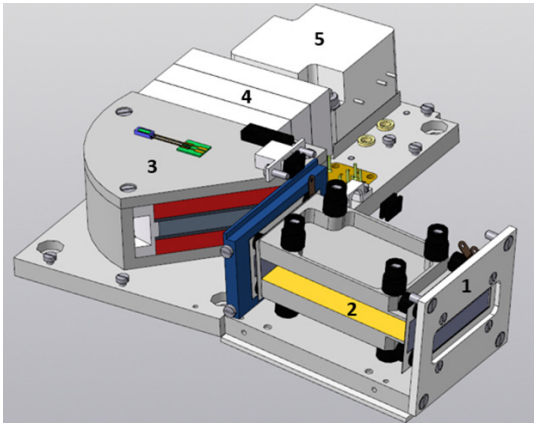


Fig. 2. Structure of the LINA-R neutral particle converter.
1 – entrance aperture with mesh assembly that cuts off charged particles; 2 – ionizer tungsten electrode; 3 – magnetic analyzing system; 4 – a system of diaphragms, 5 – channel electron multiplier based detector.

Table 1. Instrument performance

Instrument performance		
Parameter	**ARIES-L (laboratory test results)**	**LINA-R (target model parameters)**
Polar angles, deg	0-80	0-85
Azimuthal angles, deg	360	360
Resolution of polar angles, deg.	30	30
Resolution of azimuth angles, deg.	40	40
Energy resolution, ΔE/E	3% … 13%	15% or better
Mass resolution, M/ΔM	> 30	> 30
Energy range	10–5000 eV	10–5000 eV
Registration of neutral particles	Efficiency ~$2 \cdot 10^{-6}$	Efficiency ~$2 \cdot 10^{-4}$

Technical details		
Dimensions, mm	190x186x165	231x178x152
Mass, kg	2.5	3.3
Power consumption, W	2.5–7	2.5–6

REFERENCES:

[1] Vaisberg O., Berthellier J.J., Moore T., Avanov L., Leblanc F., Leblanc F., Moiseev P., Moiseenko D., Becker J., M. Collier, G. Laky, J. Keller, G. Koynash, H. Lichtenneger, Leibov A. et al. The 2π charged particles analyzer: All-sky camera concept and development for space missions // J. Geophys. Res. Space Physics. 2016. V. 121. P.11750–11765. doi:10.1002/2016JA022568.

[2] Colaprete, A., Sarantos, M., Wooden, D.H., Stubbs, T.J., Cook, A.M., & Shirley, M. How surface composition and meteoroid impacts mediate sodium and potassium in the lunar exosphere// Science. 2015. V. 351(6270). P.249–252. doi:10.1126/science.aad2380.

[3] Dukes C.A., & Johnson R.E. Contribution of Surface Processes to the Lunar Exosphere // Encyclopedia of Lunar Science. 2017. P.1-7. doi:10.1007/978-3-319-05546-6_96-1.

[4] Futaana Y., Barabash S., Holmström M., & Bhardwaj A. Low energy neutral atoms imaging of the Moon // Planetary and Space Science. 2006. V. 54(2). P. 132–143. doi: 10.1016/j.pss.2005.10.010.

[5] Los J., & Geerlings J.J. Charge exchange in atom-surface collisions // Physics Reports. 1990. V. 190(3). P. 133–190. doi: 10.1016/0370-1573(90)90104-a.

[6] Sigmund P. Theory of Sputtering. I. Sputtering Yield of Amorphous and Polycrystalline Targets // Physical Review. 1969. V.184. P.383. doi:10.1103/PhysRev. 187.768.

[7] Wurz, P., Scheer, J., & Wieser, M. Particle Scattering off Surfaces: Application in Space Science // e-Journal of Surface Science and Nanotechnology. 2006. V. 4. P. 394–400. doi: 10.1380/ejssnt.2006.394

[8] Yakshinskiy B.V., Madey T.E. Photon-stimulated desorption as a substantial source of sodium in the lunar atmosphere // Nature. 1999. V. 400(6745). P. 642–644. doi: 10.1038/23204.

THE ESA PROSPECT PAYLOAD FOR LUNA-27: DEVELOPMENT STATUS AND SCIENCE ACTIVITIES

D.J. Heather[1], R. Fisackerly[1], R. Trautner[1], P. Reiss[1], B. Houdou[1], E. Sefton-Nash[1], S. Barber[2], the PROSPECT Science Team[*] and the PROSPECT Industrial Team

[*] The PROSPECT Science Team: Feargus Abernethy, Mahesh Anand, Simeon Barber, Sebastien Besse, Neil Bowles, John Brucato, Abigail Calzada-Diaz, James Carpenter, Luke Chipperfield, Barbara Cohen, Aidan Cowley, Ian Crawford, Gabriele Cremonese, Maria Cristina De Sanctis, Simone Di Angelis, Kerri Donaldson-Hanna, Carlos Espejel, Marco Ferrari, Richard Fisackerly, Michelangelo Formisano, Teresa Fornaro, Evelyn Fueri, Mikhail Gerasimov, Fred Goesmann, Laura Grill, Christian Gscheidle, Christophe Hissler, Hung Q. Hoang, Katherine Joy, Akos Kereszturi, Julian Klaus, Julian-Alexandre Lamamy, Michèle Lavagna, Mark Leese, Maxim Litvak, Veneranda Lopez-Diaz, Paolo Lunghi, Dayl Martin, Francesca McDonald, Jeffrey McDonnell, Andrea Meneghin, Giada Meogrossi, Igor Mitrofanov, Andrew Morse, James Mortimer, Laurent Pfister, Jacopo Prinetto, Andrea Rusconi, Guido Sangiovanni, Hannah Sargeant, Nicole Schmitz, James Schwanethal, Christian Schwartz, Simon Sheridan, Romain Tartèse, Vlad Tretyakov, Sasha Verchovsky, Ulrich Walter, Tristram Warren, Kris Zacny

[1] *ESTEC, European Space Agency, Noordwijk, The Netherlands, David.Heather@esa.int;*

[2] *The Open University, Milton Keynes, UK.*

KEYWORDS:
Moon, volatiles, polar, Luna-Resurs 1, PROSPECT

INTRODUCTION:

The Package for Resource Observation and in-Situ Prospecting for Exploration, Commercial exploitation and Transportation (PROSPECT) is a payload in development by ESA for use at the lunar surface. Current development is for flight on the Russian-led 'Luna-Resurs 1' Lander (Luna 27) mission, and PROSPECT has also recently been 'pre-manifested' on a NASA CLPS mission in 2024. Both missions will target the south polar region of the Moon.

PROSPECT will perform an assessment of the volatile inventory in the near surface lunar regolith (down to ~ 1m), and complete elemental and isotopic analyses to determine the abundance and origin of any volatiles discovered. PROSPECT also has ISRU capabilities, and will aim to complete in-situ extraction of oxygen (and solar wind implanted volatiles) from lunar minerals, which will constitute potential science return from anywhere on the Moon.

PROSPECT OVERVIEW:

PROSPECT is comprised of the ProSEED drill element and the ProSPA analytical laboratory [1]. The ProSEED drill module will enable the acquisition of samples from depths of up to 1 m and deliver them to ProSPA via its Solid Inlet System (SIS) (Figure 1). In ensemble, PROSPECT has a number of sensors and instruments (including ion-trap and magnetic sector mass spectrometers, imagers, and sensors for temperature, pressure, and permittivity) that form the basis for a range of science investigations [2] that are (almost all) led by the PROSPECT Science Team.

The drill is capable of collecting two icy samples of different sizes and mechanical properties in a single sampling operation, one of up to 45 mm^3 and a second up to 8 cm^3, with the smaller sample delivered to ProSPA. The drill rod also has integrated temperature sensors and a sensor to measure the electrical permittivity of the lunar soil along the borehole.

The ProSPA laboratory will receive samples from the drill, seal them in miniaturized ovens, and process them via ramped (EGA), stepped (isotopic) or single step (ISRU) heating up to 1000°C, completing physical and chemical processing of released volatiles, and analysing of the obtained constituents via mass spectroscopy (ProSPA contains both an Ion Trap Mass Spectrometer and a Magnetic Sector Mass Spectrometer).

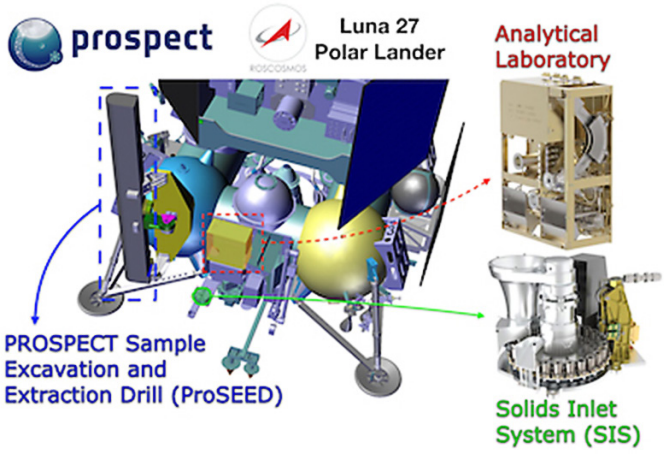


Fig. 1. Renderings – Left: PROSPECT mounted on Luna 27, including ProSEED drill element (left), Solids Inlet System [SIS] (green circle), and analytical laboratory drawer (yellow box) containing ProSPA gas processing system and instruments.
Upper right: ProSPA analysis package containing magnetic sector and ion-trap mass spectrometers.
Lower right: Solids Inlet System to receive samples from the drill, with sample camera assembly (Sam-Cam) and a carousel of ovens for volatile extraction from regolith samples.

ProSEED and ProSPA will also each carry small cameras. The ProSEED Camera has multispectral capabilities via 6 LEDs, which can illuminate the surface with wavelengths ranging from 451 to 970 nm. This will provide images of the drill working area to monitor activities and deliver contextual scientific information. ProSPA's Sample Camera (SamCam) has its own specific illumination unit (with similar capabilities to the ProSEED Camera), and will provide images of the samples in the ovens, providing information on their morphology, grain size, volume and mineralogy.

DEVELOPMENT STATUS AND CURRENT ACTIVITIES:

PROSPECT Phase C, 'detailed definition', began in December 2019. A plan of research activities is in progress to gain from and guide on-going development, build strategic scientific knowledge, and to prepare for operation of the payload.

Recent developments include the construction of an EM of the p-sensor and of the ProSEED Imaging System, and their successful testing in representative environments. Details of further activities are described below.

Drill Testing. Testing of the ProSEED Development Model was carried out in December 2019 as part of the final Phase B activities. Test procedures were formulated to demonstrate drilling and sampling functionality in ambient, cold and thermal vacuum (TV) laboratory conditions (at CISAS, University of Padova). Tests included drilling into, and sampling from, well-characterized NU-LHT-2M simulant mixed with anorthosite inclusions of various sizes [3] covering a plausible range of lunar regolith characteristics [e.g. [4]]. The main functionalities of the drill system were successfully demonstrated and required performances were achieved in these tests.

ProSPA Bench Development Model (BDM). The BDM of the ProSPA analytical lab at the Open University has been tested to demonstrate science performance against measurement requirements. Instrument level EGA verification has been completed using Allende and Murchison meteorite standards, ensuring the capability of the instrument to measure the required species. Dedicated efforts recently focused on verification of evolved gas analysis (EGA) and demonstration of ISRU capabilities using lunar simulants [5, 6]. As well as demonstrating ProSPA's ability to perform ISRU, these efforts are helping to improve our understanding of ProSPA's sensitivity to volatile abundance and possible contamination [7].

Volatile preservation. Efforts continue on understanding the capability of PROSPECT to sufficiently preserve the volatile content in regolith throughout the sampling-analysis chain for the range of expected volatile contents, e.g. [8]. Detailed modelling and experimental work is ongoing to better understand water sublimation rates in realistic lunar surface operational environments, regolith structures, and geometries [9], and to better constrain the potential effect on measured D/H of sublimation of lunar water ice (for example, elaborating from [10]). Results from this work will help ensure that even in a 'hot operational case', the original volatile inventory can be determined with sufficiently small uncertainties.

ProSEED Imaging System Testing: In June/July 2021, members of the Science team at IAPS in Italy have successfully tested the Engineering Model of the ProSEED Imaging System. Testing included measuring the spectral profile of each of the LEDs, characterizing the geometric, radiometric and spectral response of the camera, and assessing the impact that dust deposition may have on the camera sensitivity.

Sample analysis. In 2020, PROSPECT Science Team members successfully requested two samples of lunar regolith (2 g each) from the Apollo collections. The proposed experiments will investigate loss of water ice through sublimation and the effects that the bulk properties and the ice-regolith coupling have on the sublimation process.

ACKNOWLEDGEMENTS:
The PROSPECT Industrial Consortium and development of ProSEED is led by Leonardo (Italy). The development of ProSPA is led by The Open University (UK).

REFERENCES:
[1] Trautner, R. et al., (2018) in *Proc. Int. Astronaut. Congr. IAC*, Vol. 2018-October.
[2] Murray, N.J. et al. (2020) in *Lunar Planet. Sci. Conf.,* LPI, Abs #. 1918.
[3] Martin, D.J. P. and Duvet, L., (2019) in *Lunar Planet. Sci. Conf.*, LPI, Abs #. 2663.
[4] Hayne, P.O. et al., (2017) *J. Geophys. Res. Planets 122* (12), 2371–2400.
[5] Sargeant, H.M. et al., (2020) *Planet. Space Sci. 180* (104751).
[6] Sargeant, H.M. et al., (2020) in *Lunar Planet. Sci. Conf.* LPI, Abs #. 2058.
[7] Abernethy, F.A. J. et al., (2020) *Planet. Space Sci. 180* (104784).
[8] King, O. et al., (2019) *Planet. Space Sci.* 104790.
[9] Formisano, M. et al., (2019) *Planet. Space Sci. 169*.
[10] Mortimer, J. et al., (2018) *Planet. Space Sci. 158*, 25–33.

EXTRACTION OF SOIL SAMPLES FROM SUBSURFACE: INSTRUMENT GZU FOR LUNAR ROBOTIC LANDERS

T. Kozlova[1], M. Litvak[1], M. Mokrousov[1]

[1] *IKI RAS, Moscow, Russia*

KEYWORDS:
Moon, polar, cryogenic drill, water ice

INTRODUCTION:

The next lunar landing missions will explore lunar polar regions to search for volatiles and water ice, delivered to Moon by comets and asteroids, and preserved in the polar lunar regolith for a long time. The most attractive locations are found inside permanently shadowed regions, but they are very hard for lander/rover operations due to extremely cold temperatures, absence of solar illumination and radio link with Earth. Nevertheless, lunar studies have shown that water ice and volatiles could survive at some depth at polar partially sunlit areas accessible for the landing.

It means that successful implementation of these missions requires excavation, drilling of lunar regolith to the different depths and extraction of soil samples for the farther analysis. It could be in situ analysis (by lander science instruments) or sample return to Earth. The drill shall be designed to avoid overheating of regolith during drilling operations and sample acquisition to exclude evaporation of volatiles (so called cryogenic drilling).

The Russian Luna-27 and Luna-28 polar landers are developed to perform sample analysis and are specially equipped with drill systems capable to drill lunar regolith enriched with water ice down to 1-2 m. In case of Luna-27 (in situ analysis of regolith samples) such a drill system is being contributed by ESA (PROSPECT instrument suite). The spare option of drill system (GZU) for Luna-27 and primary option for Luna-28 (in situ analysis and sample return) is being developed by Space Research Institute (Russia).

In this study we present and discuss the concept of the Russian drill system which already passed through design review and its laboratory prototype participated in ground functional tests to verify its drilling capabilities (see Figure 1). It was shown that this prototype could drill lunar regolith to the depths 1-1.5 m, allowing to take probes with necessary volume from different depths.



Fig. 1. The laboratory prototype of GZU.

FUTURE LUNAR SAMPLE RETURN MISSION

M. Litvak[1], I. Mitrofanov[1], V. Tretyakov[1], L. Zelenyi[1]

[1] *IKI RAS, Moscow, Russia*

KEYWORDS:
Moon, polar, sample return, Luna-28, water ice.

INTRODUCTION:

The Moon's south pole and its surrounding high-latitude regions are now considered as the most perspective landing sites for the upcoming robotic and manned missions. This area could be enriched with deposits of different volatiles (including water ice) and is established as an ideal storehouse preserving records of the Solar system evolution by the trapping of water ice and other volatiles deposits (including organics) brought by comets and asteroids for the billions of years. The access to these deposits could provide very important science data and shed light to the evolution of Solar system. It could also break through with human space expansion and select perspective locations for the long-term presence and survival of cosmonauts on the Moon.

Russian lunar program includes several near polar landing missions (Luna-25, Luna-27, Luna-28) which should be implemented to explore mineralogical, chemical, and isotopic compositions of the lunar regolith, to study ambient lunar environment.

In this study we discuss perspectives and capabilities of lunar polar sample return mission Luna-28. It will be landed at the south polar area previously selected and investigated by Luna-27. It should deliver to the Moon cryogenic drilling system (2 m) to take and encapsulate samples of lunar soil taken from different depths which will be delivered to Earth. This mission also shall deliver first Russian lunokhod to perform geological survey (1 year of surface operations) and autonomous stations to study and monitor local environment (temperature, dust, plasma, radiation, seismic activity). It is planned that during surface operations we could test some critical technologies such as oxygen production, 3-D laser printing from lunar regolith.

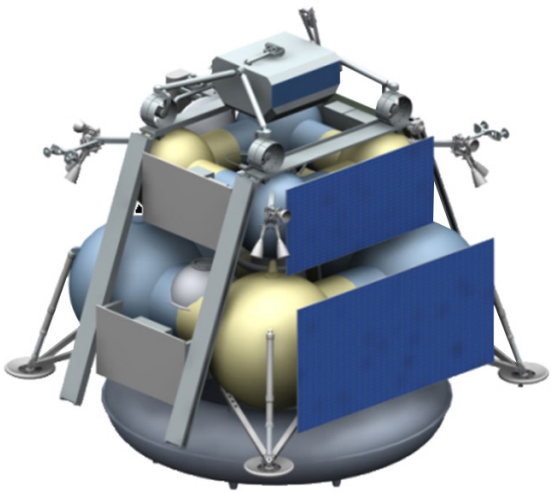


Fig. 1. The illustration of concept of "Luna-28" lander.

DATA IMPROVEMENT OF GEOLOGICAL AND MORPHOLOGICAL STRUCTURE OF THE LUNA-25 LANDING SITES

S.S. Krasilnikov[1], A.S. Krasilnikov[1], M.A. Ivanov[1]
[1] *Vernadsky Institute of Geochemistry and Analytical Chemistry RAS, Moscow, Russia, krasilnikovruss@gmail.com.*

KEYWORDS:
Moon, Luna-25, Luna-Glob, geology.

INTRODUCTION:
The size for Luna-25 landing sites ellipses is 15x30 km. Three of them have a high-priority status [1]. Better shuttle-checking mechanisms allow chousing a smaller area with the surface's better scientific and engineering properties. Analysis of engineering properties includes inclination of the surface, solar illumination, and radio communication with the surface. At the same time, accurate geological analysis on a larger scale allow supposing the type and origin of material on the surface. For the studied ellipses, the geological maps were finalized, geologic sections were produced, and the area with better engineering properties was chosen in the ellipses.

For analysis of the surface, LROC WAC mosaic with 100 m/pixel and LOLA-based DTM with 60 m/pixel resolution were used. LROC NAC images with ~0.5 m/pixel resolution were used on a local scale. LEND data used for the analysis of water equivalent hydrogen (WEH) concentration [2]. The DIviner data [3] operated for analysis of boulder concentration.

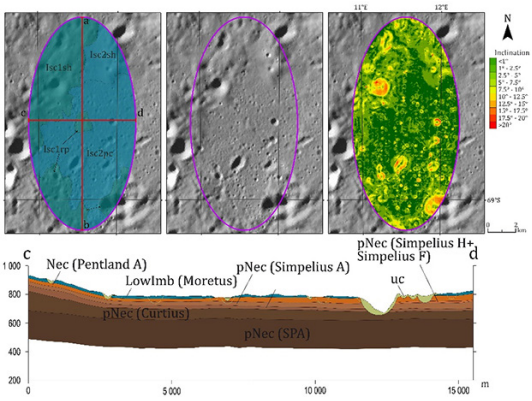


Fig. 1. Example of maps for Ellipse-4 with geological and geomorphological information. Bellow – geological section of the ellipse.

RESULTS:
The new geological map, with the 1:300 000 scale, on the studied area, was made. This map is the part of the polar map shown in work [4]. On the lower scale, detailed geologic and geomorphologic maps for each ellipsis were produced. Cross the ellipses, we made geological sections (fig. 1). These sections allow us to understand the interior structure of the area, type and approximate age of the material that can be found on the surface.

The distribution of WEH in studied ellipses is uneven. The highest concentration of WEH can be found at the northeast part 1 and 6 ellipses, and on the southwest part of ellipse 4. The median concentration WEH: ellipse-1 (0.13 ± 0.01 wt %, hereinafter 1σ) and ellipse-4, 6 (0.12 ± 0.01 wt %).

Engineering analysis of the surface, geological and geomorphological analysis, adding information of WEH concentration, allow us to understand preferred landing sites in the ellipses. As a result, we produced a map with a preferred location of the landing site in the ellipses. Prioritization of zones was divided into three types: high, medium, and low. In low priority zone,

the landing will be dangerous because of engineering limits. The medium priority zone is not perfect enough because of some different reasons. High priority zone is many suits for landing sites because of low rate of other zones inside and high concentration of hydrogen.

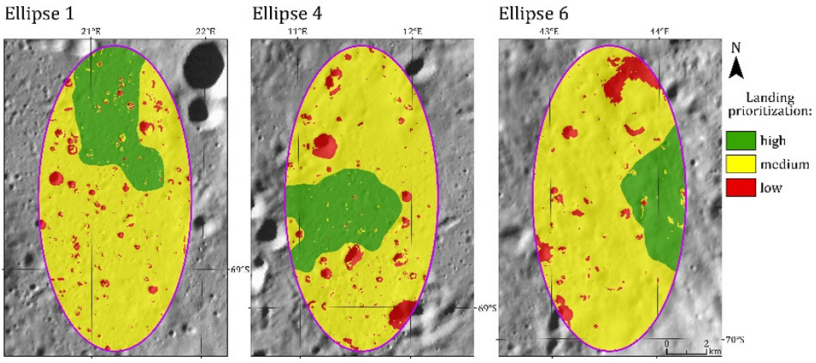


Fig. 2. Prioritization of landing zones for Ellipse 1, 4, and 6.

In **ellipse 1**, a high potential landing zone located on the north of the ellipse and occupy ~21.86 km^2 (3.5x7 km) in relatively flat Low-Imbrian cratered (Isc1pc) surface (~3.82 ± .02 Ga). Inside of it, low and medium zones occupy 4.4% of the area. WEH values slowly rise to the north and have a mean of 0.13 ± 0.001 wt %.

The high potential landing zone for **ellipse 4** located on the west and in the middle of the ellipse, occupy around 20 km^2 (6x4 km). This is the part of relatively flat Upper-Imbrian cratered (Isc2pc) surface (~3.69±0.03 Ga). The mean WEH value is around 0.13 ± 0.009 wt %.

The area of the high potential landing zone in **ellipse 6** is located on the east and occupies ~14.87 km^2 (3.3x7.4 km) of area. As a surrounding surface (pNserp), the landing area is located in a gently undulating Pre-Nectarian cratered plain (~4.04 ± 0.03 Ga). The mean WEH value is around 0.13±0.002 wt %.

ACKNOWLEDGMENTS:
This work is partly supported by the Russian Science Foundation grant № 21-17-00035: Estimates of the rate of exogenous resurfacing on the Moon.

REFERENCES:
[1] Djachkova, M. V, Litvak, M.L., Mitrofanov, I.G., Sanin, A.B., Selection of Luna-25 Landing Sites in the South Polar Region of the Moon. // Sol. Syst. Res. 2017. 51, 185–195.
[2] Sanin, A.B., Mitrofanov, I.G., Litvak, M.L., et al. Hydrogen distribution in the lunar polar regions // Icarus. 2017. 283, 20–30.
[3] Paige, D.A., Foote, M.C., Greenhagen, et al., The lunar reconnaissance orbiter diviner lunar radiometer experiment. // Space Sci. Rev. 2010. 150, 125–160.
[4] Krasilnikov S.S., Ivanov M.A., Head J.W. Geological investigation of the South pole of Moon // 12MS3. 2021. 3 p.

LASER EXPERIMENTAL MODELING OF THE FORMATION OF NANOPHASE IRON (NP-FE^0)

E.M. Sorokin[1], O.I. Yakovlev[1], E.N. Slyuta[1], M.V. Gerasimov[2], M.A. Zaitsev[2], V.D. Shcherbakov[3], K.M. Ryazantsev[1], S.P. Krasheninnikov[1], V.Y. Shklover[4]

[1] *Vernadsky Institute RAS, 119991 st. Kosygin 19, Moscow, Russia, egorgeohim@ya.ru;*

[2] *Institute of Space Research RAS, 117997, st. Profsoyuznaya 84/32, Moscow, Russia;*

[3] *Moscow State University, Geological Faculty, 119991 Lenin Hills Moscow, Russia;*

[4] *"Systems for Microscopy and Analysis" (SMA), 121353 Skolkovskoe highway 45, Moscow, Russia.*

KEYWORDS:
Micrometeorite bombardment, nanophase iron, np-Fe^0, space weathering, experiment, laser.

INTRODUCTION:
One of the signs of "space weathering" on the Moon is the formation of nanophase metallic iron (np-Fe^0) in the regolith of the Moon, observed in condensate films on the surface of regolith mineral grains and in the agglutinates glass. Np-Fe^0 is ubiquitous in samples of lunar regolith in the form of globules ~ 5–20 nm in size [1-3]. During micrometeorite bombardment, it is formed as a result of condensation of vapor arising from the shock evaporation of lunar rocks. The presence of nanophase metallic iron is subdued characteristic absorption features in reflected spectrum from airless bodies, reduces reflection in the visible region and increases in the red and infrared regions (the so-called redness) [4-7].

EXPERIMENTAL METHODS AND TECHNIQUE:
For the experiment a pulsed neodymium glass laser was used. The laser radiation wavelength was 1.06 μm, the pulse duration was 10^{-3} s, and the pulse energy was ~600–700 J. The energy flux density was ~10^6–10^7 W/cm^2. The temperature at the "impact" point was of the order of 4000–5000 K [8]

There were three types of targets: 1) crystalline basalt (without glass), 2) basalt glass, and 3) peridotite.

RESULTS AND DISCUSSION
When examining the crater from the experiment with basalt glass (it was obtained by melting and rapid quenching of crystalline basalt), placers (trains) of nanophase iron are clearly manifested (Fig. 1). In this case, two fronts of chains of such iron are distinguished. The first front is on the edge of the crater, that is, almost at the air-glass boundary. The second one borders the bright region, which is enriched with aluminum and calcium oxides (respectively, depleted in silicon oxide). Moreover, the second front partially outlines the contours of such an area. Particle sizes approximately vary from tens to hundreds of nanometers. It is assumed that the particle size can be related to the thermal history of the particle so that the formation of large particles (hundreds of nm) can be associated with coalescence effects when large particles are assembled from smaller ones [6].

According to preliminary data from a transmission electron microscope, these are alpha-iron single crystals. They contain minor nickel impurities, sulfur and phosphorus. It should be noted that phosphorus gravitates to the periphery of the particle, as if bordering it.

It should be emphasized that in this case, the formation of spherules occurs exclusively by thermal means in the thickness of the melt. Based on the experimental conditions, there are no reducing agents, and the arrangement (glass-matrix relationship) of the spherules themselves suggests their formation in the melt without an evaporation-condensation mechanism.

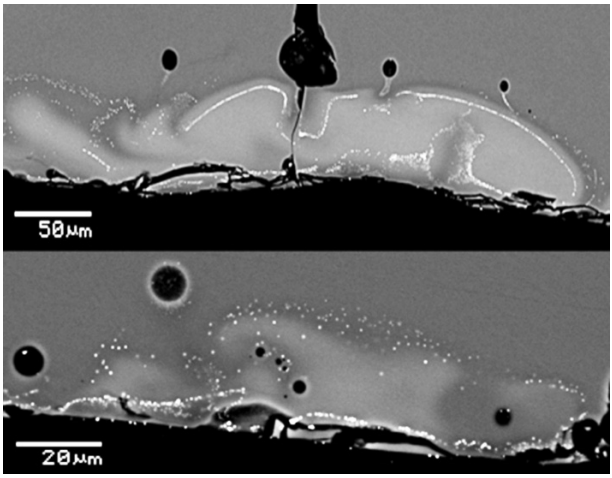


Fig. 1. Crater zones in a basalt glass target where nanophase iron placers were detected – SEM.

CONCLUSION:

Thus, a new way for the formation of nanophase iron is shown – in the bulk of the melt without a reducing agent by thermal means. Similar views were expressed earlier in some publications [9]. In addition, we assume that the arrangement of such particles is due to the passage of the shock wave.

REFERENCES:

[1] Runcorn S.K. Collinson D.W., O'Reilly W., Battey M.H., Stephenson A., Jones J.M., Manson A.J., and Readman P.W. Magnetic properties of Apollo 11 lunar samples // Proc. Apollo 11 Lunar Sci. Conf., Geochim. Cosmochim. Acta. 1970. Suppl. 1, V. 3, pp. 2369-2387

[2] Housley R.M. Grant R.W., Muir A.H. Jr., Blander M., and Abdel-Gawad M. Mossbauer studies of Apollo 12 Samples // Proc. Apollo 11 Lunar Set Conf, Geochim. Cosmochim Acta. 1971. Suppl. 1, V. 3, pp. 2125-2136.

[3] Tsay F., Chan S.I ., Manatt S.L. Ferromagnetic resonance of lunar samples // Geochimica at Cosmochimica Acta,1971, V. 35. pp. 865-875.

[4] Hapke, B. Space Weathering from Mercury to the asteroid belt // J. Geophys. Res. 2001. V.106. pp. 10039-10073

[5] Pieters, C.M., Fischer, E.M., Rode, O. and Basu, A. Optical Effects of Space Weathering: The Role of the Finest Fraction // J. Geophys. Res. 1993. V.98. pp 20817-20824

[6] Pieters C.M. and Noble S.K. Space weathering on airless bodies // J. Geophys. Res. Planets. 2016. V.10, P. 121.

[7] Moroz, L.V. Starukhina L.V., Rout S.S., Sasaki S., Helbert J., Baither D., Bischoff A., Hiesinger H. Space weathering of silicate regoliths with various FeO contents: New insights from laser irradiation experiments and theoretical spectral simulations // Icarus. 2014. V. 235. pp. 187–206.

[8] Gerasimov M. V, Ivanov B.A., Yakovlev O.I., Dikov Yu. P. Physics and Chemistry of Impacts // Laboratory Astrophysics and Space Research. Astrophys. Space Sci. 1999. V.236. pp. 279-330

[9] Li Y., Li S.J., Xie Z.D., Li X.Y. Laser irradiated impact experiments show that nanophase iron particles formed by shock-induced melting rather than vapor deposition // Proc. 79th Annual Meeting of the Meteoritical Society. 2016, #6338.

THE CONCEPT OF LUNAR PRINTER FOR FUTURE ROBOTIC MISSIONS

A.A. Kim[1], A.M. Lysenko[1], S.N. Ponomareva[1] and T.M. Tomilina[1]

[1] *A.A. Blagonravov Mechanical Engineering Research Institute of the Russian Academy of Science, kim@imash.ac.ru.*

KEYWORDS:
Moon, 3D printing, regolith, robotic missions.

Currently, after a long pause, the process of studying and exploration of the Moon on the basis of new technologies has been re-launched. The issue of creating a lunar infrastructure for conducting experiments directly on the lunar surface is being actively discussed, including using natural material – lunar soil for construction, which will make it possible to abandon the delivery of massive cargo from Earth. Now the cost of delivering one kilogram by a heavy rocket is $50,000–$70,000.

By now, there are already a number of works dedicated to creating samples of various shapes from a lunar regolith simulator using additive technologies in ground conditions. However, the feasibility of this approach has not yet been proven.

In this report, the concept of experiment with Lunar Printer is presented, which objective is producing of testing mechanical details from lunar regolith in situ. The proposed manufacturing method, as based on the Selective Laser Melting, is considered. The advancing laboratory experiments with lunar regolith simulants are discussed, which are necessary to perform before development of space instrument with Lunar Printer for future robotic mission for lunar samples return. Parts made from lunar regolith will also be returned by this mission to study their mechanical properties on Earth.

THE CONCEPT OF LUNAR-BASED UV-OPTICAL-IR TELESCOPE FOR ILRS

Andrey Shugarov[1], Mikhail Sachkov[1], Huijuan Wang[2], Subo Dong[3], Xiaojun Jiang[2], Vladimir Shmagin[1], Sergey Sichevskij[1], Anna Buslaeva[1], Igor Savanov[1], Jianfeng Wang[2], Xiaoming Zhang[2], Ping Chen[3], Jiaqi Wang[2]

[1] *Institute of Astronomy, Russian Academy of Sciences, 119017 Pyatnitskaya str, 48, Moscow, Russia, shugarov@inasan.ru;*

[2] *National Astronomical Observatory, Chinese Academy of Sciences (NAOC), 20A Datun Road, Chaoyang District, Beijing 100101, China, wanghj@nao.cas.cn;*

[3] *Kavli Institute for Astronomy and Astrophysics, Peking University, Yi He Yuan Road 5, Hai Dian District, Beijing 100871, China, dongsubo@pku.edu.cn.*

KEYWORDS:
UV astronomy, Moon based telescope, slewing mirror, ILRS.

INTRODUCTION:

Since observations in Ultraviolet (UV) using ground-based telescopes are not possible, observations in infrared (IR) are seriously affected by the atmosphere, and the amount of observation time on large space telescopes, such as the Hubble Space Telescope, are very limited, the presence of a small UV-optical-IR telescope on the Moon surface will make a significant contribution to the operational observation of various astrophysical objects.

UV, optical and IR observations from the Moon surface give us a unique opportunity to conduct research from a stable platform outside the Earth atmosphere. The main advantages of placing a telescope on the Moon are as follows:

- stable position of the telescope from the micro-disturbances point of view (some spacecraft may have problems with stability during long exposures);
- absence of the atmosphere;
- longer duration of uninterrupted observations (the rotation of the Moon is much slower than the Earth);
- being above the geocorona main layers (the glow of the geocorona in UV affects observations from the low Earth orbit).

The International Lunar Research Station (ILRS) on the Moon surface gives us a unique opportunity to install a set of telescopes, maintain them for a long time and upgrade instruments in future.

SCIENTIFIC OBJECTIVES

A Moon based UV-Optical-IR telescope will be an important research tool for astronomers to perform an all sky survey in UV, to study the origin of the Universe, dark matter and dark energy, evolution of stars and galaxies, to explore of Earth like planets, to search and to characterize comets, asteroids and near-Earth objects (NEA) in the Solar system.

At the moment, the GALEX catalog is the only more or less complete homogeneous catalog of UV sources on the sky. One of the important tasks of modern UV astronomy is to fill in the gaps in the GALEX catalog, which covers about 77% of the celestial sphere in various modes, on the remaining part of the celestial sphere in a compatible photometric system. The part of the celestial sphere that is not covered by the GALEX project mainly contains bright sources, which can be observed with a relatively small telescope. The Moon is a convenient place for such telescope [1].

Today we have a lot of ground based wide filed telescopes of different apertures aimed to search and characterize asteroids, comets and NEAs. However, all on-ground survey systems are unable to observe objects inside the Earth orbit (e.g. on the day time sky) and have limited efficiency of observation along the Earth orbit (e.g. at sunset and sunrise, close to the horizon). Having only one moderate aperture wide filed telescope at ILRS, we can significantly expand the NEAs accessible area of observation inside the Earth orbit.

Moon-based telescopes are suitable for early warning and monitoring of NEAs. Long-term continuous observation and wide band coverage can obtain important parameters such as the composition of small celestial bodies, rotation characteristics and more accurate orbital elements.

CONCEPTUAL DESIGN OF THE LUNAR BASED UV-OPTICAL-IR TELESCOPE

For the ILRS we propose a full reflective telescope with a relatively large focal plane to accommodate two detectors optimized for UV and IR regions. The main parameters of the telescope are:

- Aperture 300 mm
- Optical scheme TMA (full reflective)
- Focal length 1800 mm
- Field of view 2.4×1.2 deg
- Spectral range 115-900 nm
- D80 9 μm @ 900 nm, 3 μm @ 115 nm
- Central obstruction 30%
- Detectors 2x, 4×4 k, 37×37 mm
- Pixel size 9 μm
- Pixel scale 1 arcsec/pixel
- Typical exposure up to 1000 s
- Limiting magnitude 20^m

To repoint the telescope, we suggest using a pre aperture mirror. A good example of this technology is a two-coordinate optomechanical scanning device BSKR-T of the multi-zone scanning instrument onboard the meteorological satellite Electro-L. BSKR-T has worked in continuous mode for 10 years together with a 220 mm aperture IR telescope. A two-dimensional gimbal with a flat mirror to track the objects was successfully used in the Moon-based Ultraviolet Telescope (MUVT) on the Chang'e-3 lunar lander [2].

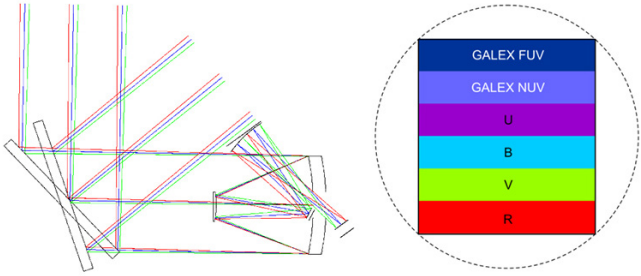


Fig. 1. Telescope with a slewing mirror optical design, proposed layout of the UV channel detector with filters on its surface.

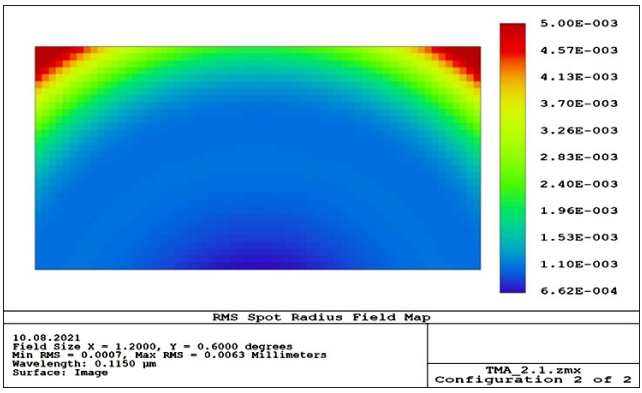


Fig. 2. Optical quality of the telescope.

The main parameters of the telescope repointing system are:

- Repointing mirror size 480×340 mm
- Slewing angle Pitch +0° …+50°, Roll –60° …+60°
- Area of observation 50°×120°
- Time of repointing 3 s
- Overall system length 1100 mm

It is planned to use a modern CMOS detector from the Chinese company GPEXEL with a special treatment of the back side of the silicon wafer to increase sensitivity in the UV range.

One of the main problems of using CCD or CMOS detectors for observations in the UV range is the long-wave transmission of light filters. For the near-UV range it is possible to build a multilayer filter with an acceptable suppression of the optical component. For the far-UV range the photometric correction of the observed data is required. Therefore, in addition to the FUV and NUV bands, we propose to observe each object in 3-4 standard bands U, B, V, R.

The technological progress in the CMOS detectors manufacturing with small pixels (about 5 μm) would enable to improve the angular resolution of the proposed telescope without impacting the size and mass of the system.

The proposed telescope is considered as a first step to begin astronomical observations from the ILRS. In future a lunar-based network of telescopes of different apertures, including ultra-wide field array, can be implemented.

Another type of UV telescope for the ILRS under consideration is a set of small extra wide field lens UV telescopes, which will be capable of imaging a significant fraction of the visible sky with combined field of view of ~10000 deg^2 at a high cadence of ~10 minutes. This moon-based network can obtain the valuable high-quality data for the nearby transients, which are the best objects to be studied by multi-wavelength and multi-messenger probes.

REFERENCES:

[1] Sachkov M.E., Shugarov A.S., et al., The concept of the Moon-based astrophysical UV telescope (The Luna-UV project), INASAN proceedings, 2020, 5(5): P. 368-373.

[2] W.-B.Wen, et. all, Data preprocessing and preliminary results of the moon based ultraviolet telescope on the CE-3 lander, Research in Astronomy and 580 Astrophysics 14 (12) (2014) 1674–1681.

DIRECTIONS OF RESEARCH AND ACHIEVEMENTS OF THE SCHOOL FOR THE CREATION OF LOCOMOTION SYSTEMS OF PLANETARY ROVERS. TO THE 100th FROM THE BIRTH OF A.L. KEMURDJIAN

M.I. Malenkov[1], A.N. Bogachev[1], N.K. Guseva[1], E.A. Lazarev[1], V.A. Volov[1]
[1] *J.S.Co. Scientific and Technical Center "ROCAD",*
11 Lomanaya str., 196006, St. Petersburg, Russia, m.i.malenkov@gmail.com

KEYWORDS:
Locomotion system, planetary rovers (planetokhody), wheeled, tracked and wheeled – walking propellers, self-propelled chassis, cross-country ability, travers ability (over loose soil), PrOP – pribor ozenki prokhodimosti (passability estimator)

INTRODUCTION:
The result of the activities of Alexander Kemurdjian (1921–2003) is not only the creation of the self-propelled automatic chassis of the Lunokhod-1 (fig. 1) [1,2]. He contributed to the formation of a talented team, all-Union cooperation of specialists and scientists for the development of a new direction – mobile spacecraft. The report examines the topics and achievements of this professional school. Some ideas have been implemented in modern space expeditions [3].



Fig. 1. Alexander Kemurdjian in 1945 and 2001. In the center are the obverse and reverse of the medal of the Russia Cosmonautics Federation

BEGINNING OF ENGINEERING ACTIVITY:
A.L. Kemurdjian (A.L.K.) was born in Vladikavkaz on October 4, 1921. In 1939, he graduated with honors from the 26th secondary school in Baku. In 1940, he entered the tank faculty of the Moscow Higher Technical School (MVTU) named after N.E. Bauman. He was able to finish his studies at this university with honors only in 1951, being a Stalin scholar who received practical research skills in the student scientific society.

Since 1942 he has been in military service as a cadet at the Artillery School, and since 1943 – in the active army. Together with his 162-th rifle division, he celebrated Victory Day in Pomerania. In 1946 he was demobilized with the rank of senior lieutenant, holder of military orders and medals. Frontline hardening, personal participation in victorious battles – all this contributed to the formation of a strong, strong-willed character.

In 1951–1958 A.L.K. worked in the departments of engine building and then in the transmission of tanks VNII-100 (now J.S. Co VNIITransmash), defended his Ph.D. Here he received the first experience of the head of a scientific topic on the smooth regulation of the speed of movement of tanks. Then the director of VNII-100 P.K. Voroshilov instructed him to study the possibility of creating a heavy military vehicle for movement in unprepared terrain. A.L.K was able to attract the best scientific forces to this research and worthily complete a large complex topic. Therefore, the next director of VNII-100

V.S. Starovoitov in 1963 appointed A.L.K. the head of a new fantastic theme. At the request of S.P. Korolev, it was necessary to investigate the possibility of creating a "lunar self-propelled apparatus".

THE MAIN WORK OF HIS LIFE:

Starting a new job, A.L. Kemurdjian managed to see in it not a temporary task, but a strategic task of creating a new direction. This is a space transport technology. He foresaw that the beginning process of studying celestial bodies by contact methods would be replaced by the era of the development of new extraterrestrial territories by man. The demand for various mobile space robots and manned spacecraft will continue to grow.

He believed that the main task of the new school is to master a systematic approach, to thoroughly study each component of the "terrain – planetokhod – remote driver" system in order to choose optimal solutions at all stages of design and ground testing of a self-propelled chassis. However, he was not limited only to the Moon [4,5]. Under his leadership (1963–1991), the following were created: a walking micro marsokhod PrOP-M (installed at the Mars-2 station); mobile device PrOP-F for jumping over the Phobos surface (installed at the Phobos-2 station); space instruments PrOP-V (installed at Venera-13, 14, Vega-1, 2) and venerokhod ground models to assess the possibility of movement on the surface of Venus. Reviews of the scientific data available at that time were carried out to assess the conditions for the movement of scientific equipment on the surface of all planets of the solar system and their satellites. The scientific and technical report on this topic also included an assessment of possible way of movement on the surface of these celestial bodies. Several promising mock-ups of planetary rovers (planetokhody) with wheeled, tracked, walking and wheeled-walking propellers were manufactured and tested at natural testing grounds.

The synthesis of new technical solutions for rover locomotion systems for increase cross-country ability, travers ability, reliability of remote and autonomous control is the main direction of research of the Kemurdjian school.

All other lines of research arose as components of this main task. This applies, for example, to studies of the relief and physical and mechanical properties of the soil of the Moon and Mars as a support surface for motion; ensuring the operability and resource of friction pairs during the operation in vacuum, in the atmosphere of Mars and Venus; creation of bench equipment for simulating gravitation, temperature conditions and environmental; physical modeling of the interaction of various propellers with models of the lunar and Martian soils; mathematical modeling of the movement of rovers on difficult terrain; search and creation of new structural and lubricants for self-propelled chassis mechanisms and others.

In the afterword to the monograph [6], the creator of the team himself named his closest associates in the development of these areas at the stage of creating the self-propelled chassis of Lunokhod-1. This is P.S. Sologub, A.F. Solovyov, V.I. Komissarov, V.K. Mishkinuk, G.N. Korepanov, A.V. Mitskevich, I.I. Rosenzweig, A.P. Sofiyan, V.V. Gromov, P.N. Brodsky. 14 employees of the institute are co-authors of articles on the structure and results of research of Lunokhod-1, published hot on the heels of its historical journey on the Moon [7]. True, all of them (except for V.V. Gromov), as well as the Lavochkin Association employees, appear there under pseudonyms. For example: A.L. Kemurdjian – A.K. Leonovich and A.K. Alexandrov, G.N. Babakin – G.N. Nikolaev, etc. A complete decoding of the pseudonyms of the VNII-100 employees is given in [8].

A.L.K. attaches great importance to the patent purity of technical solutions. In total, over the period from 1963 to 1991, its team, the number of engineers and scientists of which did not exceed 150 people, received more than 500 USSR patents. Including this is a patent for a self-propelled automatic chassis of Lunokhod-1, the authors of which are 21 employees of J.S. Co. VNIITransmash and 9 employees of Lavochkin Association.

SOME RESULTS:

The above areas of research, which developed in cooperation with specialists from the Lavochkin Association, remain relevant today. All new specialists from different countries who are involved in the problem of contact studies of the surface of celestial bodies along the paths of rover movement, study and use the experience of the Kemurdjian school.

And this applies not only to the calculation justification and design of the Lunokhod-1 self-propelled chassis, which have become classic prototypes for designers. For example, V.V. Gromov (1940–2007) proved the possibility of creating so-called mobile penetrometers – "moles". These are cylindrical shells capable of moving in the soil due to its compaction into the inner walls of the well. A patent for such a projectile was awarded a gold medal at the 44th World Salon of Inventions (Brussels, 1995). This idea was used in the development of new scientific equipment for the failed expedition "Phobos Grunt" and the Martian automatic station InSight. I.F. Kazhukalo (1938–2016) proved the possibility of a qualitative increase in the permeability of rovers on very loose soils by using a wheel-walking method of movement [6]. This idea found a kind of development in the design of the self-propelled chassis of the Chinese Zhurong Mars rover and in the design of the European rover of the ExoMars program planned for launch in 2022.

Later, with the participation of A.L.K. to the listed areas, the creation of onboard manipulators of planetary rovers with a set of instruments and scientific equipment, made in the form of a rotary end link, was added. This pioneering solution, which has become firmly established, for example, in the modern practice of designing American Mars rovers, was worked out in cooperation with the IKI RAS. In this cooperation, with the participation of American, French, Hungarian scientists and specialists, tests of an articulated wheel-walking model of a Mars rover with remote and partially autonomous control systems were carried out at natural ranges in California and Kamchatka.

A.L.K. was the initiator of the first domestic reports on the locomotion systems of Lunar rovers and Mars rovers in conjunction with the properties of the surface of celestial bodies at international conferences. He headed the authors' teams and was the editor of a number of monographs on the design and development of planetary rovers. About 20 dissertations were defended on the subject of planetary rovers directly in the space research team of VNII-100. More than 20 dissertations were defended in research teams of enterprises and universities of Leningrad, Moscow, Kiev and Kharkov based on the results of research carried out according to the technical specifications of VNII-100. Unfortunately, many of them, for various reasons, are still inaccessible to a wide range of historians and specialists.

In their totality, published materials on self-propelled automatic chassis, which were largely initiated by A.L. Kemurdjian, represent the basics of design and ground testing of the planetary rovers locomotion system. It is clear that the further development of this direction in Russia, for example, in terms of generalization and implementation of the accumulated scientific and technical groundwork in new objects, largely depends on the implementation of domestic space programs. Unfortunately, today there is a danger of breaking the living connection between generations of specialists in this profile.

However, the Kemurdjian school did not close with the death of the teacher, because he had, is and, we hope, will have students – people who recognize his creative heritage and continue the development of space transport engineering.

REFERENCES:

[1] A.L. Kemurdjian – ucheny, grazhdanin, chelovek. Compiled by V.A. Kemurdjian. MVTU named after N.E. Bauman. Moscow. 2013. 189 p. (In Rus.)

[2] Malenkov M.I. Creation of Lunokhod-1 as an Outstanding Scientific and Technological Achievement of the XX Century // Solar System Research. 2013. V. 47. No. 7. P. 610–617.

[3] Friedman L.D. The solar couple is the technology of the future // Cosmonautics News. 2010. No. 9. P. 70-72. (In Rus.)
[4] Alexander Kemurdjian. From the Moon Rover to the Mars Rover // The Planetary Report. Vol. 10. Number 4. July/August 1990. P.4-11.
[5] Kemurdjian, A.L., Gromov, V.V. Malenkov M.I. et. al. Soviet Development of Planet Rovers in Period 1964–1990. // Proc. of the Meeting «Planet Rovers: Purpose Technology and Design» Toulouse 1992 r.
[6] Kemurdjian, A.L., Gromov, V.V., Kazhukalo I.F. et. al. Planetokhody. Ed. Kemurdjian, A.L. Moscow. Mash. 2nd edition, revised and enlarged. 1982. (In Rus.)
[7] Peredvizhnaya Laboratoriya na Lune Lunokhod-1. Ed. A.P. Vinogradov. Moscow. Nauka. 1971. Vol. 1. 127 p. and Moon panorams. (In Rus.)
[8] Mikhail Malenkov. Self-propelled automatic chassis of Lunokhod-1: History of creation in episodes // Frontiers of Mechanical Engineering. 2016. # 11(1). P. 60-86.

SESSION 7. MOON AND MERCURY (MN) POSTER SESSION

A MISSION SUGGESTION: DYNAMICS OF LUNAR ROTATION & FRAME TIE OF ASTRONOMY FOR ILRS

J.S. Ping[1], D. Marshalov[2], A.S. Kosov[3], A.V. Gusev[4], J. Sun[5], M.Y. Wang[6]
[1] *National Astronomical Observatory, CAS, Datun Rd. 20A, Beijing, 100101, China, jsping@bao.ac.cn;*
[2] *Institute of Applied Astronomy, RAS, Kutuzova Quay 10, St. Petersburg, 191187, Russia, marshalov@iaaras.ru;*
[3] *Space Research Institute, RAS, Profsoyuznaya 84/32, Moscow, 117810, Russia, akosov@iki.rssi.ru;*
[4] *Kazan Federal University, 18 Kremlyovskaya street Kazan, 420008, Russia, agusev33@gmail.com;*
[5] *National Astronomical Observatory of CAS, Datun Rd. 20A, Beijing, 100101, China, sunjing@bao.ac.cn;*
[6] *National Astronomical Observatory of CAS, Datun Rd. 20A, Beijing, 100101, China, wangmy@bao.ac.cn.*

KEYWORDS:
Dynamics; Lunar Rotation; Frame Tie; ILRS; Lunar Ranging; VLBI; GNSS;

INTRODUCTION:
The China and Russia space agencies are jointly promoting a plan of International Lunar Research Station, the ILRS. Astronomical study is a key part for this joint station project. Based on a collaborating Chinese and Russian scientific expert team is arranged in the joint construction of the ILRS, with the team direction or name of the Dynamics of Lunar Rotation & Frame Tie of Astronomy. The team likes to suggest a mission by means of sitting the lunar surface radio beacons, new lunar laser retro-reflectors, and GNSS receiving systems on the Moon, to strength the observation studies for the lunar dynamics, and for linking the celestial reference frames of VLBI radio sources, GNSS and Earth-Moon ephemeris.

CURRENT STATUS OF SCIENTIFIC KNOWLEDGE AND OUTSTANDING PROBLEMS:
The knowledge of the internal structure of the Moon is a key to understand the origin and the evolution of our nearest celestial body, in particular from the dynamical, rotational and internal structure. A characterization of the inner core of the Moon would bring key answers to these questions. In the past 50 years, the lunar laser ranging (LLR) method is the important one on study the LPhL and interior structure of the Moon. Large progress has been made on finding two and multi-layer Moon. LLR also contributes the main parts on estimating the lunar orbit and test the general relativity in the Earth-Moon space. A high accuracy lunar dynamical frame has been constructed. However, the multi-layered Moon has not been clearly modelled, which is blocking the study of lunar evolution study. The currently lunar surface LLR network has poor geometric distribution of five retro-reflectors, with maximum baseline about 1kkm only, at the center of the near side. Polar area retro-reflectors and radio beacons will be more sensitive to LPhL components.

Recent years, the Chang'E-3 lander radio tracking link has been used as a new kind of space tool to test the observation of the lunar and geo-dynamics. The joint SINO-RUSSA 2018–2022 space cooperation frame program also set a project No. 1.5, to support this bi-lateral pre-research for this kind of space technology. A mixed lunar geophysical next work is suggested which will combine the laser retro-reflectors, radio beacons, seismometers and thermometers, to improve the interior structure and evolution study of the Moon, especially at the polar and/or rim area.

In addition, the lunar dynamical reference frame or ephemeris is also very important for studying the lunar and planetary evolution. This frame also has not been closely tied to the ITRF and ICRF, even has been dramatically developed by global scientists and engineers after dozens of years. Although the LLR, VLBI and GNSS have realized different types of celestial frames,

however the links between these frames are relatively loose. A space collocated site even on the Moon can contribute more on solving this problem.

REQUIREMENTS TO PAYLOAD OF ILRS:

The new prospects for establishment of a liquid/rigid core model and for studying its contribution in physical librations of the full Moon for direct studies of tidal and non-tidal "breath" of the Moon with new multi-parametric rheological interior will be viewed and investigated. A new big size corner cubes reflectors (CCR) and a stable long-lived radio beacons would be desirable experiments on future lunar landers. An ILRS composing laser reflector or transmitter, radio beacon and GNSS multi-satellite receivers, with atomic clock as time and frequency standard are required to improve dozens times better than current situation. Four kinds of payloads are suggested:

1) Radio beacon and transponder/transmitter

   A newly designed and developed radio beacon is suggested for Luna and Chang'E mission(s). Main features of the beacon are: X band Up-link channel and two Down-link channels – X and Ka bands. PN Ranging code will be used, it should be according to the CCSDS standard (T4B PN Ranging code). The VLBI delay should be with mm accuracy. The Doppler measurements should be with 0.1 mm/s accuracy.

2) GNSS multi-satellite receiver

   Like Chang'E-5 lunar test and lander missions, we suggest to use a GNSS receiver onboard S/C for navigation and POD. The GNSS receiver and antenna can catch the L-Band dual frequency navigation signal of GPS, Beidou, GLONASS, Galileo satellites. A high gain antenna (HGA) about 1 meter in diameter will be used. Similar payload has been suggested and will be used by NASA team in their missions.

3) New type of SLR/LLR laser retro-reflector

   In the Chinese lander(s) of CE-/6/7/8, both new types of SLR/LLR laser retro-reflectors from Italia and China have been suggested and considered. Setting these newly large unit laser retro-reflectors at ILRS, collocated with radio beacon and GNSS receiver, will dramatically improve the study of lunar dynamics and frame tie work. There is not additionally SLR/LLR laser retro-reflector payload suggested, beyond the suggestions from Italia and China. Team will arrange the China, Russia and global distributed ground SLR/LLR stations to do new observation for more LLR data, especially at NIR bands (1064 nm).

ACKNOWLEDGEMENT:

The Chinese authors of this paper are supported by China MOST international collaboration project No. 2016YFE0120000, by the Chinese Academy of Sciences key international collaboration project between Chinese Academy of Sciences and Russia for lunar reference frame study (2018–2020), Strategic leading science and technology project for space No. XDA15020303, and the Chang'E-6 lunar mission. The Russian authors of this paper have been supported by Luna missions.

REFERENCES:

[1] Программа российско-китайского сотрудничества в космической области на 2018–2022 годы.

[2] Rambaux, N., Williams J.G., "The Moon's physical librations and determination of their free modes", 2011, Celest. Mech. Dyn. Astron., v. 109, p. 85–100.

[3] Gusev A., Hanada H., Petrova N., Kosov A., Kuskov O., Kronrod V., Kronrod E., "Rotation, physical librations, internal structure of the active and multi – layer Moon", 2015, Collective monography, Publishing house of Kazan federal University, Kazan, 323pp., (English + Russian).

[4] Weber, R.C., P.-Y. Lin, E.J. Garnero, Q. Williams, and P. Lognonne "Seismic detection of the lunar core", 2011, Science, v. 331, p. 309–312

[5] Gusev A.V., Petrova N.K., "Rotation, physical librations and internal structure of Moon"., 2008, Monography, Publishing house of Kazan federal University, Kazan, 208 pp., (Russian).

[6] Marshalov D. , Ping J., Li W. et al., 3-Way Lunar Radio Ranging Experiment on RT-32 Radio Telescopes, Latvian Journal of Physics and Technical Sciences, 2020, N 1-2, PP22-27.

[7] Ping, J., Meng, Q., Wang, M., Tang, G., Jian, N., Wang, Z., … & Cao, J. (2014). First 3-Way Lunar Radio Phase Ranging and Doppler Experiment in Chang'E-3 Lander Mission. In European Planetary Science Congress 2014, EPSC Abstracts, 9, EPSC2014- 226-1. 5.
[8] Vasilyev, M.V., Shuygina, N.V., & Yagudina, E.I. (2017). Expected impact of the Lunar Lander VLBI Observations on the Lunar Ephemeris Accuracy. IAA RAS Transections,40, 16–21.
[9] Khan, A. & Mosegaard, K. Further constraints on the deep lunar interior. Geophys. Res. Lett. 32, L22203 (2005).
[10] Williams, J.G., Boggs, D.H., Yoder, C.F., Ratcliff, J.T. & Dickey, J.O. Lunar rotational dissipation in solid body and molten core. J. Geophys. Res. 106, 27933–27968 (2001).
[11] Van Kan Parker, M. et al. Neutral buoyancy of titanium-rich melts in the deep lunar interior. Nature Geoscience. 5, 186–189 (2012).
[12] Garcia, R.F., Gagnepain-Beyneix, J., Chevrot, S. & Lognonné, P. Very preliminary reference Moon model. Phys. Earth Planet. Inter 188, 96–113 (2011).
[13] Harada Y., Goossens S., Matsumoto K., Yan J., Ping J., Noda H. and Haruyama J., Strong tidal heating in an ultralow-viscosity zone at the core–mantle boundary of the Moon, Nature Geoscience, 2014, Vol. 7, PP569-572.
[14] Kosov A., Ping J., A. Gusev A., et al., Main features of Moon's radio beacon and orbiter Ka-Band Receiver, Inlcuded into "Luna-Resource-1", in THE ELEVENTH MOSCOW SOLAR SYSTEM SYMPOSIUM 2020.

GEOLOGICAL INVESTIGATION OF THE SOUTH POLE OF THE MOON

S.S. Krasilnikov[1], M.A. Ivanov[1], J.W. Head[2]
[1] *Vernadsky Institute of Geochemistry and Analytical Chemistry RAS, Moscow, Russia, krasilnikovruss@gmail.com;*
[2] *Department of Earth, Environmental & Planetary Sciences, Brown University, Providence, RI, USA.*

KEYWORDS:
Moon, geology, South Pole, geological map

INTRODUCTION:
A significant part of Moon's missions relates to the southern polar region. This interests mainly depend on few things: 1) the increased concentration of hydrogen in the regolith [1], and its possible correlation with the presence of ground ice [2], and 2) the unquestionable presence of ejecta from a few vast basins, like South Pole-Aitken basin (SPA), Orientale and Pre-Nectarian basin materials.

GEOLOGICAL MAPPING:
The ambitious investigation program of the South pole needs an accurate scientific analysis of the surface. One of the components of it is a geological and geomorphological analysis of the studied area. Now, only three geological maps of the southern polar region of the Moon were available: the global map of the Moon compiled in 1979 at 1:5 000 000 scale [3], the new remastered global map 1:5 000 000 scale by [4], and the map of the SPA basin at 1:500 000 scale [5]. Our analysis is based on LROC WAC mosaic with 100 m/pixel and LOLA-based DTM with 20–80 m/pixel resolution. At a local level, LROC NAC images with ~0.5 m/pixel resolution were used. And we can suggest a map of the geological and geomorphological structure of the pole region on a better scale (1:300 000). For the detailed analysis of stratigraphy, more than 200 measurements of the crater size-frequency distribution were made.

Geomorphological units were subdivided into two main groups: impact-related geological units (basins and craters material) and modified surfaces (plains and landslides).

Impact processes have a primary influence on surface formation. As a result of this, crater holes from microns to hundreds of kilometers can be formed, and ejecta material overlaps a significant area. Also, during the impact processes, central uplift/peak rim, secondary craters (single craters or group of its with an elongated shape radial direction) can be formed.

The impact process serves as a cause of the dark planes, formed by melted rocks on the bottom of the craters, and light plains, formed by the deposit of ejecta material formation. After the impact and formation of the crater hole with the deposition of ejecta, subsequent processes start to modify the surface. This group of processes can be subdivided into gravitational and hypogene processes (magmatism and tectonic).

THE RESULTS AND FUTURE RESEARCH:
As a result of our research, the new geologic map with a 1:300 000 scale was made (fig. 1). The publication with an accurate description of it is coming soon and will be included an online version of the map in GIS format. Our project has additional material, like crater catalog, modeled estimation of the ejecta thickness etc., which already enrolled in some other projects (etc. [6]).

ACKNOWLEDGMENTS:
Input of KSS and MAI is partly supported by the Russian Science Foundation grant № 21-17-00035: Estimates of the rate of exogenous resurfacing on the Moon.

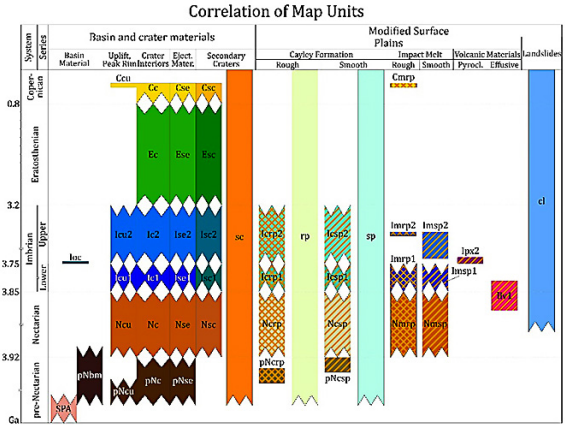


Fig. 1.

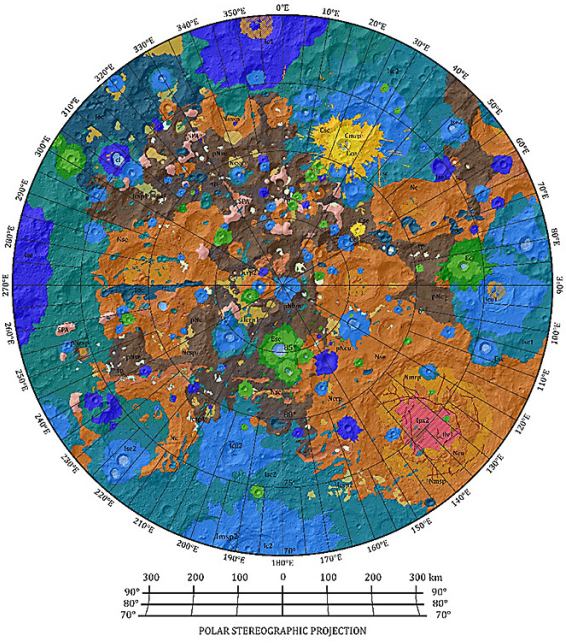


Fig. 2. Geological map of South pole of the Moon.

REFERENCES:

[1] Mitrofanov, I., Litvak, M., Sanin, A., et al. Testing polar spots of water-rich permafrost on the Moon: LEND observations onboard LRO. // J. Geophys. Res. Planets. 2012. 117.

[2] Sanin, A.B., Mitrofanov, I.G., Litvak, M.L., et al. Hydrogen distribution in the lunar polar regions // Icarus. 2017. 283, 20-30.

[3] Wilhelms, D.E., Geologic mapping of the second planet. US Geol. Surv. Interag. Report, Astrogeology 55, 1–36.

[4] Fortezzo C.M., Spudis P.D., Harrel S.L. Release of the digital unified global geologic map of the Moon at 1:5,000,000-scale // 51st Lunar Planet. Sci. Conf. 2020. 2760.

[5] Poehler, C.M., Ivanov, M.A., Bogert, C.H. Van Der, Hiesinger, H., Pasckert, J.H., Wright, J., Head, J.W. The Lunar South Pole-Aitken Basin Region : A New Geological Map // EPSC2020. 2020. 14, 19921.

[6] Krasilnikov A.S., Krasilnikov S.S., Ivanov M.A. The model esimates of the craters ejecta thickness in the southern polar regon of the Moon // 52st Lunar Planet. Sci. Conf., 2021. 2548.

STUDY THE TRAJECTORY OF DUST PARTICLES BY SIMULATING THE PLASMA ENVIRONMENT ON THE MOON'S SURFACE

M.E. Abdelaal[1], I.A. Shashkova[2], A.Y. Poroykov[3], I.A. Kuznetsov[2], G.G. Dolnikov[2], A.A. Kartasheva[2], A. Shekhovtsova[2], A.S. Bychkova[2], A.N. Lyash[2], A.E. Dubov[2] and A.V. Zakharov[2]

[1] *Moscow Institute of Physics and Technolog, Institutskiy Pereulok, 9, Dolgoprudny, Moscow Oblast, 141701;*

[2] *Space Research Institute of the Russian Academy of Sciences, Profsoyuznaya 84/32, Moscow 117997, Russia;*

[3] *National Research University "Moscow Power Engineering Institute", Krasnokazarmennaya 14, Moscow 111250, Russia.*

KEYWORDS:
Dust particles, regolith, trajectory measurements, charged micro-particles, digital image processing, cameras stereo system, lunar exosphere.

INTRODUCTION:

The Moon is one of our solar system's most significant airless bodies since it reflects the Earth's closest natural plasma climate. The lunar surface is still dense with interactions between plasma and regolith due to the effects of micrometeorites, solar radiation, and solar wind. According to these activities, a near-surface double layer is created from the photoelectrons and the charged regolith surface. This study demonstrates the 3D dynamic trajectories of charged micro-particles under the influence of an external electric field and a plasma source, which will aid in demonstrating the plasma-dust process on the lunar surface. The experimental setup for the physical modeling of dusty plasma levitation using a vacuum chamber is defined. A stereo system of two cameras with a laser as a source of illumination is used to visualize the dust particle trajectory. Image processing techniques and examples of processing results are provided for estimating the particle trajectory in three-dimensional coordinates.

DIGITAL FORMATS FOR FIGURES:

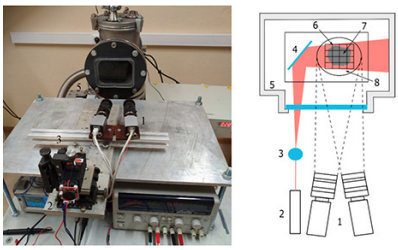


Fig. 1. Picture and scheme (top view) of the experimental setup for investigating the dust particles trajectories (1 – CMOS cameras, 2 – laser, 3 – beam expander, 4 – mirror, 5 – vacuum chamber, 6 – steel mesh, 7 – dust particles, 8 – conductive substrate).

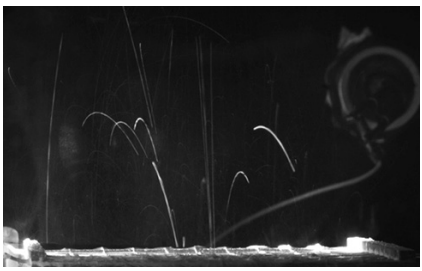


Fig. 2. Visualization of the levitation of Mica particles (the thin parabolic lines in the photograph) with noticeable steel mesh and particles on the substrate.

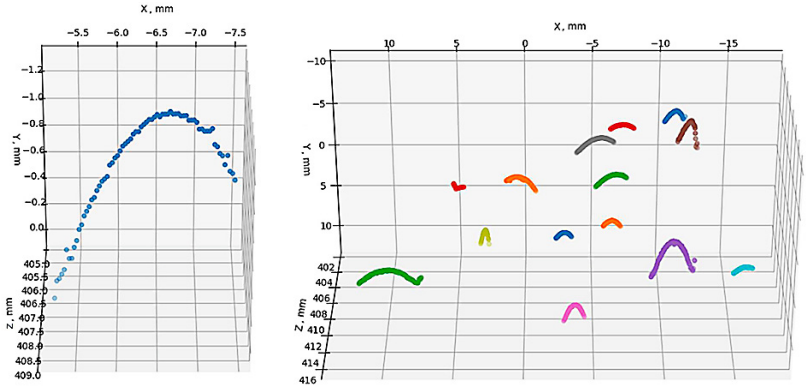


Fig. 3. Particle trajectory obtained after the image processing.

Table 1. Experimental parameters.

Experiment#	Material	Particle size (μm)	Voltage (KV)	Exposure time (ms)	Gain
1	SiO_2	90–100	2.5	50	10
2	Mica	90–100	8.0	60	7
3	Andesite	90–100	8.0	70	5
4	Sand	90–100	10.0	80	15

EXPERIMENTAL SETUP

Using different materials with different size particles, the experiment was conducted. The experimental parameters are listed in Table 1. In the first experiment, Silicon dioxide (SiO_2) spheres with smooth surfaces and diameters of 90–100 μm were used. We choose this size because the spheres of comparable sizes were found in the lunar regolith [24]. Besides silicon dioxide, particles from Andesite, sand, and Mica were sieved with an analytical sieve shaker (Retsch AS200) to obtain 90–100 μm samples. The composition of Mica was SiO_2 54.78%, Al_2O_3 28.23%, Fe_2O_3 5.72%, and K_2O 10.59%, and for Andesite, it was SiO_2 content ranging between 57 and 63 wt. %, and Na_2O + K_2O contents around 5 wt. %, while for sand, it was SiO_2. The sued particles simulate conductive particles of lunar regolith based on the lunar surface chemical composition.

Particles were poured onto the substrate with a thin layer of 0.3–0.7 mm. Subsequently, the vacuum chamber was depressurized to 3×10^{-3} Tor. The voltage from the power source was gradually increased until particle levitation occurred in sufficient numbers to be observed with video cameras. The voltage value ranged from 2.5 to 10.0 kV. We believe that particles are set in motion due to their polarization in the field created in the gap between the lower electrode and the metal mesh. Once the particles detached from each other, they can exchange their charges

RESULTS

The proposed approach and image processing technique allow not only visualizing and obtaining the quantitative values of dust particles levitation parameters. These parameters make a valuable contribution to physical experiments on modeling the dusty plasma levitation and increase the likelihood of success of future lunar landing missions.

CONCLUSION

The aim of this research was to investigate and improve the measurement technique for determining the trajectory parameters of dust particles. One of the benefits of this technique is that it can accommodate limited optical access to the investigation volume by using low-speed cameras and lasers with limited power. The developed technique was used to visualize dust particle levitation with particles of various sizes and materials. The ability to measure

particle velocities and charges was facilitated by the ability to determine 3D trajectories of levitated particles. These parameters will be useful in future experiments involving the modeling of dust plasma levitation. The previous experiments in the same area and the numerical findings from these experiments agree well. The use of a stereo camera device, on the other hand, represents a significant advancement in assessing 3D particle levitation trajectories. This method increases the measurement precision of quantitative values, allowing the theoretical models of the near-surface dynamics of atmosphereless bodies to be refined. Our method will be used to analyze data collected during future lunar missions, such as the Luna-Glob (set to launch in 2021) and Luna-Resource (launch planned in 2023).

REFERENCES:

[1] A.V. Zakharov, L.M. Zelenyi, and S.I. Popel', 'Lunar Dust: Properties and Potential Hazards', *Sol. Syst. Res.*, vol. 54, no. 6, pp. 455-476, 2020, doi: 10.1134/s0038094620060076.

[2] G.H. Heiken, D.T. Vaniman, and B.M. French, *Lunar Sourcebook, a user's guide to the Moon*. 1991.

[3] J.S. Levine, 'Lunar Dust and Its Impact on Human Exploration: Identifying the Problems', *LPICo*, vol. 2141, p. 5007, 2020.

[4] T.J. Stubbs, R.R. Vondrak, and W.M. Farrell, 'Impact of dust on lunar exploration', *URL: https://www.nasa.gov/centers/johnson/pdf/486014main_StubbsImpactOnExploration.4075.pdf*, 2007.

[5] W.M. Farrell, T.J. Stubbs, R.R. Vondrak, G.T. Delory, and J.S. Halekas, 'Complex electric fields near the lunar terminator: The near-surface wake and accelerated dust', *Geophys. Res. Lett.*, vol. 34, no. 14, 2007.

[6] T.L. Jackson, W.M. Farrell, R.M. Killen, G.T. Delory, J.S. Halekas, and T.J. Stubbs, 'Discharging of roving objects in the lunar polar regions', *J. Spacecr. Rockets*, vol. 48, no. 4, pp. 700–704, 2011.

SENSOR DLS-L OF THE GC-L INSTRUMENT OF THE "LUNA-RESOURCE" MISSION: CALIBRATION RESULTS AND PERSPECTIVE DISCUSSION

I.I. Vinogradov[1], V.A. Kazakov[1], A.A. Koposov[3,1], Yu.V. Lebedev[1], V.V. Meshcherinov[2,1], A.V. Nosov[1], M.V. Spiridonov[1], A.A. Venkstern[1]

[1] *Space Research Institute IKI of the Russian Academy of Sciences, Moscow, Russia, imant@iki.rssi.ru;*

[2] *Moscow Institute of Physics and Technology MIPT, Moscow Region, Russia*

[3] *Lomonosov Moscow State University, Faculty of Space Research, Moscow, Russia*

KEYWORDS:
Luna-Resource; Lunar soil; chemical composition; isotopic ratios; tunable diode laser absorption spectroscopy.

INTRODUCTION:
Studies of lunar soil are planned on-board of the Luna-27 polar landing probe of the coming soon Luna-Resource mission. A sensor, called DLS-L, was integrated, as an additional analytical unit, inside a Gas Chromatography (GC-L) instrument of a Gas Analytical Package, which is targeted for studying evolved products of the Moon soil samples. The soil will be sampled from a close location of the Lunar probe landing point. The DLS-L will measure pyrolytical output dynamics and integral content of H_2O, CO_2, and will retrieve isotopic ratios D/H, $^{18}O/^{17}O/^{16}O$, $^{13}C/^{12}C$ for isotopologues of H_2O and CO_2.

METHOD OF MEASUREMENT AND ON-GROUND RESULTS:
Advantages of tunable diode laser absorption spectroscopy (TDLAS) will provide for fine and rapid measurement of target molecules of evolved gas, delivered by carrier gas He from a miniature pyrolytical cell of the GC-L instrument into the DLS-L analytical volume – a small capillary tube with edge optical windows. Gas sample will be sounded by a set of monochromatic distributed feed-back (DFB) lasers, operated sequentially.

On-ground calibration of the DLS-L have been carried out for IR regions of 2.64 μm (for H_2O isotopologue absorption lines), 2.68 μm (H_2O and CO_2 main molecules), 2.78 μm (CO_2 isotopologues), using pure H_2O and CO_2 under low pressure of 10–20 mbar. Actual molecular content values and isotopic ratios were retrieved from the raw recorded analytical optical cell transmission spectral data and confirmed sub-percent accuracy of the DLS-L operation.

The DLS-L output data will be sent back to Earth as series of instant high-resolution optical transmission spectra of the sampled gas, to be regularly measured during lifetime of the Lunar lander and being completely processed on ground. The DLS-L sensor data would help for further understanding of physics and chemistry of the Lunar body, as original data of polar Lunar soil first-ever direct study.

FUTURE PERSPECTIVES:
Further improvement of the DLS-L sensor is planned by extending of the molecular targets list, for carrying out additional measurements at the near-IR range of 1.53 μm for H_2C_2, NH_3, HCN main molecules and of 2.44 μm for OCS molecule. DFB-laser modules, which are available for these ranges, completely match current configuration of the DLS-L sensor. Molecular isotopic ratios could be also measured at wavelengths beyond 3 μm, where molecular absorption becomes much stronger. DFB-lasers, emitting at those longer wavelengths, are known as inter-band cascade lasers (ICL) or quantum cascade lasers (QCL), and are noticeably more demanding sources of monochromatic light. A multichannel laser absorption spectrometer, efficiently operating at longer wavelengths, both in the near-IR and the medium-IR ranges, could become an instrument of the next generation scientific payload on-board a future interplanetary landing probe.

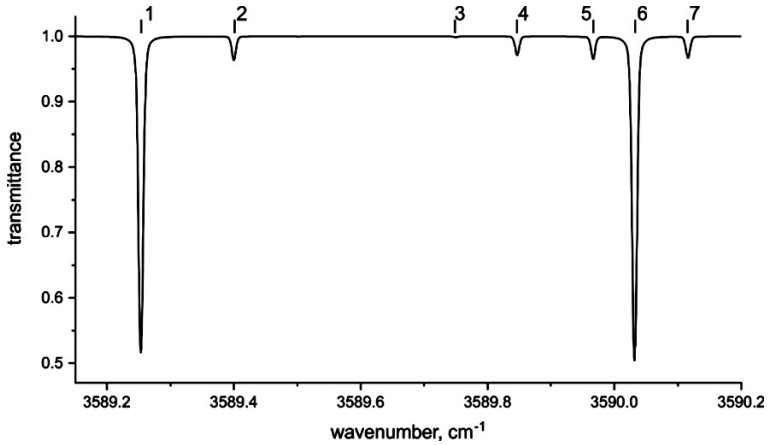


Fig. 1. An example of CO_2 data processing in the 2785 nm spectral region.

Table 1. Brief parameters of absorption lines, shown in Figure 1.

N	Wavenumber, cm^{-1}	Isotopologue	Intensity, cm^{-1} / (molecule cm^{-2})	Energy, cm^{-1}
1	3589.253315	CO_2	1.330e-21	718.94190
2	3589.399934	$C^{18}OO$	7.013e-23	278.27970
3	3589.749561	$C^{17}OO$	3.152e-24	2.27170
4	3589.846641	$^{13}CO_2$	5.520e-23	843.07010
5	3589.966458	$C^{18}OO$	6.582e-23	298.88760
6	3590.031647	CO_2	1.379e-21	728.41230
7	3590.115999	CO_2	6.429e-23	1648.42100

REFERENCES:

[1] Vinogradov I., Barke V., Gazizov I., Kazakov V., Kozlova T., Lebedev Yu., Meshcherinov V., Nosov A., Rodin A., Roste O., Spiridonov M., Stepanov A., Tepteeva E., Venkstern A., Zenevich S., Ghysels-Dubois M., Durry G., Bizien L. Diode laser spectroscopy sensor DLS-L of the GC-L instrument for the Luna-Resource (Luna-27) mission: scientific targets, design options and future perspectives // The eleventh Moscow Solar System symposium (11M-S^3), October 05-09 2020, Moscow, IKI RAS. Presentation 11MS3-MN-PS-17, Abstract Book P. 235-236. ISBN- 978-5-00015-050-4. DOI: 0.21046/11MS3-2020.

[2] Meshcherinov V.V., Vinogradov I.I., Kazakov V.A., Spiridonov M.V., Venkstern A.A., Kozlova T.O., Lebedev Yu.V., Nosov A.V., Ghysels-Dubois M., Durry G. Lunar multichannel diode laser spectrometer DLS-L for in-situ study of samples pyrolytically evolved from regolith onboard “Luna-27” mission // XXVII International Symposium “Atmospheric and Ocean Optics. Atmospheric Physics”, July 05-09, 2021, Moscow. Proceedings (in Russian) P. C-504 – C-507. ISBN 978-5-94458-187-7.

LUNAR TERRITORIES WITH DIRECT VISIBILITY OF THE EARTH

B.A. Epishin[1], M.I. Shpekin[1]
[1] *Kazan Federal University, Kremlyovskaya 18. Kazan, Tatarstan 420008, Russia, epishin.boris@yandex.ru , MichaelS1@yandex.ru*

KEYWORDS:
Earth visibility map, Earth ephemeris, Earth direct visibility, coordinates on the lunar sky, computer program, physical libration, optical libration, south pole, Schrödinger crater

We studied the nature of the Earth's movement in the lunar sky earlier. These results are presented in our papers 2017–2019 [1, 2, 3]. In connection with the beginning of active exploration of the far side of the Moon [4], it is interesting to see what part of the far side hemisphere of the Moon is available for direct radio visibility from the Earth. It is known that almost 60% of the Moon's surface area is visible from the Earth due to the optical and physical libration of the Moon. This includes the entire hemisphere facing the Earth, as well as areas visible due to libration, which are called the "marginal zone of the Moon". The surface of the marginal zone for optical observations from the Earth is not of particular interest. However, these territories can be useful for long-term expeditions, lunar bases and observatories. The first condition, which is of fundamental importance, will be the presence of the Earth direct visibility to ensure reliable radio communications.

To assess line-of-sight conditions, we performed calculations over an interval of 18 years. The calculations were carried out on the basis of the barycentric coordinates of celestial objects of the DE 430 JPL theory [5]. The physical libration of the Moon was also taken into account when calculating the topocentric coordinates of celestial objects according to the algorithm for accounting for physical libration in the Almanac [6].

It is important to note that on the territory of the visible hemisphere of the Moon, the direction of the Earth's motion across the lunar sky occurs along an ellipse in one direction for three years and in the opposite direction for three years also. The visibility of the Earth from different places on the lunar surface is very different: as the observer moves away from the center to the edges of the visible hemisphere of the Moon, this ellipse of the Earth's motion will shift across the sky from the zenith to the horizon. If in the center of the visible hemisphere of the Moon the Earth moves near the zenith, then at the edges of the visible hemisphere of the Moon the Earth rises and sets on the horizon.

Using the Lunar QuickMap technology [7], we plotted the results of our calculations on a map of the lunar surface. Only part of the entire map is shown here, namely the South Pole area (Fig. 1). In this picture, the top half of the circle is the hemisphere facing the Earth. On the far side (lower half of the figure) four lines are shown - these are the boundaries of the Earth's visibility, taking into account its dimensions visible from the Moon. From the territory shown in Fig. 1 below line No. 3, the Earth is never visible at all. On the territory of the visible hemisphere (upper half of the figure), the boundary line (without a number) is shown of the constant visibility of the full disk of the Earth in the lunar sky. That is, for an observer located north of this line, the Earth is always visible in the lunar sky above the horizon or touches the horizon line. The regions from the upper line of the visible hemisphere to the lower line No. 3 of the far hemisphere are the territories where the Earth rises above the horizon and sets over the horizon at different times.

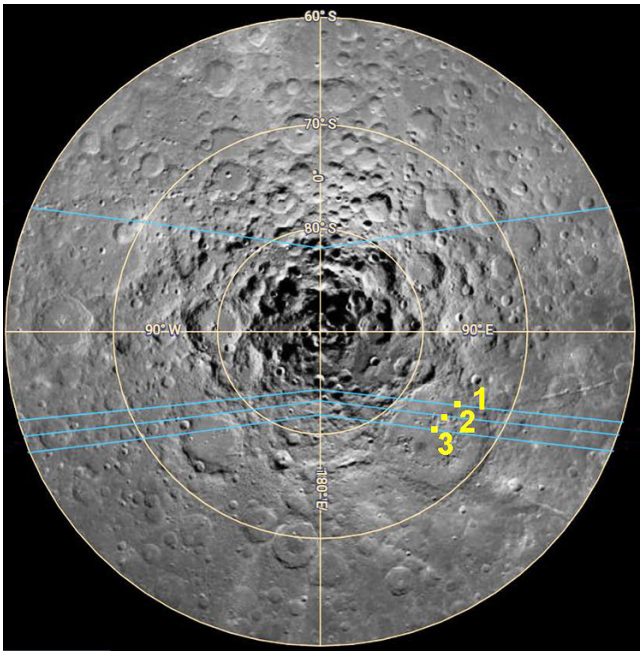


Fig 1. The image of the south pole of the Moon and its surroundings on the Lunar QuickMap [7]. The blue lines in the figure show the four boundaries of the line of the Earth direct visibility. The description of each line by its number (yellow) is given in the text.

Table 1. The boundary of the Earth's visibility is the touch of the upper edge of the Earth's disk to the lunar horizon for the topocenter on line No. 3 for a period of 18 years (2018–2036).

Dates	Maximum height of the Earth
20 July, 17 August 2018	The top edge of the Earth touches the horizon
November 2021	–3°.8
25 Sept, 23 October 2024	The top edge of the Earth touches the horizon
June 2027	–3°.8
1 December 2030	The top edge of the Earth touches the horizon
31 July, 27 August 2036	The top edge of the Earth touches the horizon

It is curious to note that some interesting elements of the lunar relief fall on the territory of the lunar marginal zone, although they belong to the far side of the Moon. So, for example, the large Schrödinger crater (75 S, 134 E), as can be seen from Fig. 1, falls into the area of our calculations. Three blue lines run through its territory. This means that the expedition, having reached the northern part of the crater, enters the territory where the Earth is not constantly visible, but appears above the local horizon at certain periods of time. See, for example, Table 1.

Unfortunately, in short theses it is not possible to consider the issues of direct visibility of the Earth in more detail. The authors intend to do this in separate article.

The work is performed according to the Russian Government Program of Competitive Growth of Kazan Federal University.

We acknowledge the use of imagery from Lunar QuickMap (https://quickmap.lroc.asu.edu), a collaboration between NASA, Arizona State University and Applied Coherent Technology Corp.

REFERENCES:

[1] Shpekin M.I., Epishin B.A. Analysis of apparent motion of Sun, Earth and stars on the lunar sky, The Eighth Moscow Solar System Symposium, 2017, p. 380-382.
[2] Shpekin M.I., Epishin B.A. Analysis of occultations of stars by the Earth on the lunar sky, The Ninth Moscow Solar System Symposium, 2018, p. 381-383.
[3] Shpekin M.I., Epishin B.A. Occultations of Stars by the Earth on the Lunar Sky // Тезисы докл. межд. Конф. ФизикА.СПб 22–24 октября 2019 года, Санкт-Петербург 2019, —576 с., стр. 22-23. ISBN 978-5-7422-6681-5. http://physica.spb.ru/data/uploads/physica2019/Tesises2019.pdf
[4] Шпекин М.И. Бассейн «Южный Полюс – Эйткен» от первых измерений («Зонд-6», 1968) до первой посадки Лунохода («Чанъ'э-4», 2019) // Научные труды Института астрономии РАН. Том 5, вып.3, стр. 157-162— М.: Изд-во Янус-К, 2020. ISSN 2658-5669. DOI: 10.26087/INASAN.2020.5.3.014.
[5] JPL planetary and lunar ephemerides. ftp://ssd.jpl.nasa.gov/pub/eph/planets/
[6] Taylor D.B., Bell S.A., Hilton J.L. Computation of the Quantities Describing the Lunar Librations in The Astronomical Almanac.
[7] Lunar Quick Map *ACT/NASA/ASU/LRO,* https://quickmap.lroc.asu.edu.

THE SETUP FOR STUDYING THE SUBLIMATION OF WATER ICE ON THE MINERAL COMPOSITION AT LUNAR CONDITIONS

A.P. Krivenko[1], V.S. Sevastianov[1], S.A. Voropaev[1]
[1] *Vernadsky Institute of Geochemistry and Analytical Chemistry of Russian Academy of Sciences.*

KEYWORDS:
Moon, regolith, adsorption, desorption, sublimation, water ice.

INTRODUCTION:
In the last decade, there has been renewed interest in the study of the content of volatile compounds on the lunar surface. The existence of the water on the Moon was established by the detection of hydrogen deposits at the lunar poles through the neutron spectrometry by the Lunar Prospector spacecraft [1]. The adsorption features of a small amount of H_2O on the surface of a mineral composition similar to lunar regolith indicate that the water probably was not confined to the polar regions. The water in the regolith in the form of ice undergoes sublimation and evaporation under the influence of sunlight [2]. As a result, the isotopic composition of hydrogen and oxygen in water ice changes [3], [4]. The European Space Agency (ESA) developed the PROSPECT program to estimate the amount of gases and water in the regolith that will be sampled by the Luna 27 spacecraft and return to Earth.

Moreover, it is known that the roughness of the lunar surface has a strong effect on the adsorption and desorption of lunar water [5]. Therefore, it is extremely important to consider surface roughness in order to get an accurate picture of the amount of adsorbed water on the surface of the Moon and in its exosphere. The calculations have shown that water ice is present on most of the lunar surface, even from the dawn to noon. Surface frost can accumulate in cold, dark areas and, under the influence of sunlight, cyclically move into the lunar exosphere. Then the molecules condense on the surface as frost in other cold, dark places. Experimental studies are necessary to confirm the calculated data. For this, an installation will be created to perform investigation of sublimation and sorption processes on an analogue of the lunar regolith and up to 10% water ice and allowing the creation of the required temperatures and pressures inside the vacuum chamber.

SETUP:
The developed setup (Fig. 1) has a compact size but extended functionality. The working chamber has the thermostatic surface at the bottom and the optical window at the top. This surface is connected to a copper rod, which is connected through a copper bus bar to the copper “hot” core of the heating furnace. The free end of this rod is connected through a second copper bus bar to the “cold” copper core, which is lowered into the Dewar vessel with liquid nitrogen. A temperature sensor is located at the base of the thermostatted surface. The microcontroller controls the power of the heating element of the furnace, according to the readings of temperature sensor. Thereby microcomputer changes the heat flow to the copper core. The working chamber has inlets in the upper part. The first one is connected to a vacuum sensor and a forevacuum pump. The second one is connected to water coldtraps. All surfaces of pipelines, as well as the collector, are heated to exclude the possibility of gas sorption on internal surfaces.

OPERATION:
An experiment on the sublimation of water ice from the surface of a mineral composition involves the following stages:

- placement of the mineral composition on a thermostatted surface;
- desorption of volatile components from the surface of the mineral composition by heating the thermostatted surface to 200°C;
- reaching a vacuum of the order of $1x10^{-3}$ mbar;

- cooling the mineral composition to a temperature at which water from a heated pre-weighed coldtrap with the source water will condense on the surface mineral composition;
- accumulation of sublimated water in a pre-weighed coldtrap due to its freezing;
- accumulation of residual water in a pre-weighed coldtrap due to its freezing;
- weighing sublimated water and residual water, measuring its isotopic composition;

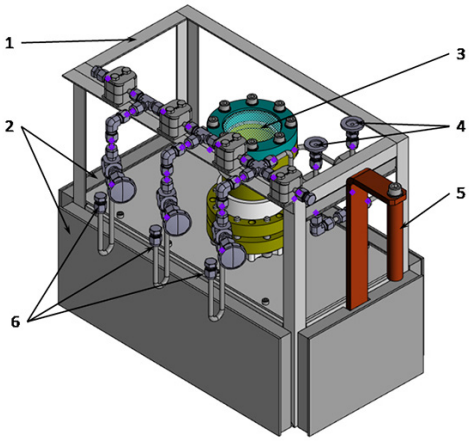


Fig. 1. Installation: 1 – the frame, 2 – the heat shields, 3 – the working chamber with the optical window at the top, 4 – the connection to a vacuum sensor and a forevacuum pump, 5 – the "cold" copper core, 6 – the water coldtraps.

DISCUSSION:

The sublimation and sorption processes of water vapor on the surface of a mineral composition (analog of regolith) at lunar condition has significant implications for understanding the presence and evolution of water on the lunar surface. Isotope effects accompanying the processes of sorption and desorption of water lead to a change in its physicochemical properties. The possibility of UV and IR irradiation of the regolith surface with lamps through an optical window allow us to simulate the presence of darkened and irradiated areas on the mineral composition surface. Thereby, the estimation the changes in the ice sublimation rate in the presence of darkened areas is possible.

The carried out research will help to understand the role of shadows, sublimation and sorption processes in the accumulation of water ice and gas molecules on the Moon and beyond, for example, on Mars or on particles in the rings of Saturn.

ACKNOWLEDGMENTS:

This work was supported by the Russian Science Foundation, project no. 21-17-00120:

REFERENCES:

[1] Feldman W.C., Maurice S., Binder A.B., et. al., Fluxes of Fast and Epithermal Neutrons from Lunar Prospector: Evidence for Water Ice at the Lunar Poles// Science. 2016. V. 281. I. 5382. P. 1496-1500.

[2] Brown R.H., Lauretta D.S., Schmidt B., et. al., Experimental and theoretical simulations of ice sublimation with implications for the chemical, isotopic, and physical evolution of icy objects// Planetary and Space Science. 2012 V. 60 P. 166-180.

[3] Moores J.E., Brown R.H., Dante S., et. al., Experimental and theoretical simulation of sublimating dusty water ice with implications for D/H ratios of water ice on Comets and Mars // Planetary Science. 2012 V. 1:2. P. 1-30.

[4] Mortimer J., Lecuyer C., Fourel F., et. al., D/H fractionation during sublimation of water ice at low temperatures into a vacuum // Planetary and Space Science. 2018 V. 158 P. 25- 33

[5] Davidsson B.J.R., Hosseini S., Implications of surface roughness in models of water desorption on the Moon // MNRAS. 2021 V. 506 P. 3421-3429.

RESULTS OF SPECTRAL ANALYSIS OF THE MAGNETIC AND GRAVITATIONAL FIELDS OF THE MOON ACCORDING TO THE DATA OF THE APOLLO SPACECRAFT

A.L. Kharitonov[1]
[1] *Pushkov Institute of Terrestrial Magnetism, Ionosphere and Radio Wave Propagation of the Russian Academy of Science, 108840, Moscow, Troitsk, Kaluzhskoe Highway, 4, IZMIRAN Russia, ahariton@izmiran.ru.*

KEYWORDS:
Moon, spectrum of gravity field, spectrum of magnetic field, depth nhomogeneities of lunar crust.

INTRODUCTION:
Recently, great importance has been attached to various studies of the Moon, as the closest space neighbor of the planet Earth, in connection with the preparation for the upcoming launches of American, European and Russian spacecraft with astronauts on board to the Moon. Apparently, in the near future, the range of issues related to the inhomogeneities of the internal structure of the Moon may become especially interesting, if it is possible to find large accumulations of those chemical elements whose reserves are limited on Earth. Also interesting is the question of the similarity or difference of the deep internal structure of the Earth and the Moon, which allows us to shed some light on the solution of the question of the origin of the Moon (the hypothesis of the capture of an alien body or the formation of a single gas-dust cloud). It is possible to solve this issue correctly, without excessive costs for launching different measured fields in the shape of the satellite's orbit and its height, which are not coordinated according to the programs, on uninhabited spacecraft preceding the launch of astronauts to the Moon, if, according to the available satellite information, it is possible to analyze several different fields simultaneously, at different heights of shooting above the surface of the Moon (20–300 kilometers).

INITIAL SATELLITE GRAVITY AND MAGNETIC DATA:
In order to study the deep structure of the Moon, experimental data were analyzed, measured at different heights of the radial component of the magnetic field (Z_R) of the Moon (Fig. 1), as well as the gravitational field (dg) of the Moon (Fig. 2), in its equatorial part [1, 2].

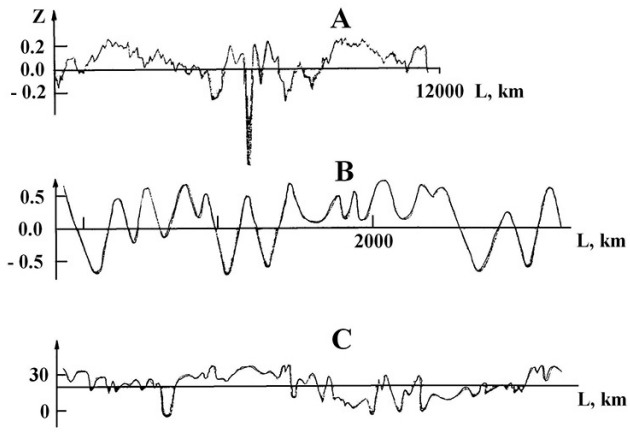


Fig. 1. Values of the radial component of the anomalous magnetic field of the Moon, measured at different altitudes (A=100, B=30, C=0 kilometers). The values of the magnetic field are given in nanotesles.

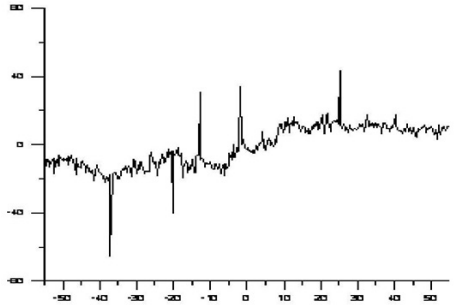


Fig. 2. The gravitational field of the Moon – (dg). The values of the gravitational field in milligalls are shown along the vertical axis of the graph. The values of the northern (+) and southern (–) latitudes of the lunar surface are shown along the horizontal axis of the graph.

These data were obtained as a result of the launch of the artificial satellites of the Moon (ISL) – Apollo-15 and Apollo-16 (USA), as well as the Russian Lunokhod spacecraft [3]. The authors used the data of the Moon's magnetic field at an altitude of 160, 100, 75 and 30 kilometers. In particular, all 48 orbits of the Apollo-15 satellite at an altitude of 160 to 75 kilometers were performed near the equator, in the sublatitudinal direction around the Moon, in a band about 250 km wide, in the latitude range from 15 degrees north latitude to 15 degrees south latitude. To calculate the statistical parameters of the Moon's magnetic field, the data of the maximum high (h=160 km), average orbit height (h=100 km), minimum orbit height (h=75 km) orbits of the Apollo-15 satellite were used. The length of the orbit of the Apollo-15 satellite at an altitude of 100 kilometers was 12000 km, with a sampling interval of 55 km of measured data. Data on the magnetic field of the Moon at an altitude of 30 km were presented by a single profile of Apollo-16 with a length of 3090 kilometers. The sampling interval of the measured magnetic field in this case was 20 km for a more reliable data sample.

An important property of the magnetic field measured on artificial satellites of the Moon is the complete absence on the Moon of the main magnetic field associated with the dynamo effect in the liquid cores of planets. The absence of the main magnetic field on the Moon allows us to observe in a natural form (without preliminary calculations) its anomalous magnetic field, mainly associated with various anomalously magnetized inhomogeneities located in the mantle layer inside the Moon.

METHODS OF PROCESSING SATELLITE GRAVITATIONAL AND MAGNETIC DATA:

Using the capabilities of spectral and autocorrelation analysis, the normalized spectra and autocorrelation functions were calculated from the values of the gravitational field (g g) and the radial component of the magnetic field (ZR) measured on artificial satellites of the Moon. The parameters of the first four statistical moments (mathematical expectation – M, variance – S, asymmetry coefficient – A, kurtosis coefficient – E) and the values of the correlation radius (r03) within a sliding window moving along a series of measured values of the gravitational (Fig. 3) and magnetic fields (Fig. 4) were calculated using autocorrelation functions.

The results of this multi-altitude analysis of the magnetic and gravitational fields of the Moon show that using the values of the coefficients of asymmetry (A) and kurtosis (E) of the correlation radius (r_{03}), it is possible to determine the optimal heights of joint gravitational-magnetic surveys from an artificial satellite around any space objects (planets, asteroids, comets, and others) to obtain consistent results about deep inhomogeneities manifested in several main physical fields simultaneously.

The authors ' Fourier spectral analysis of the gravitational and magnetic fields of the Moon shows that the Moon has 3 main density boundaries and 7 magnetic ones.

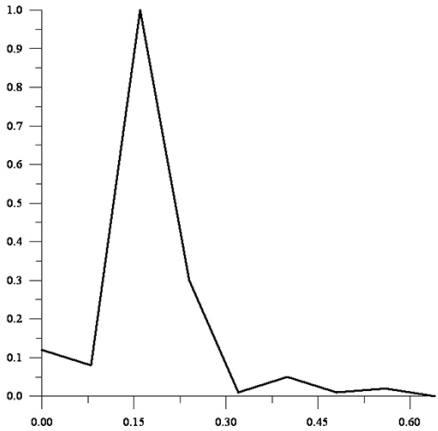


Fig. 3. The Fourier spectrum of the gravitational field of the Moon at an altitude of 100 km.

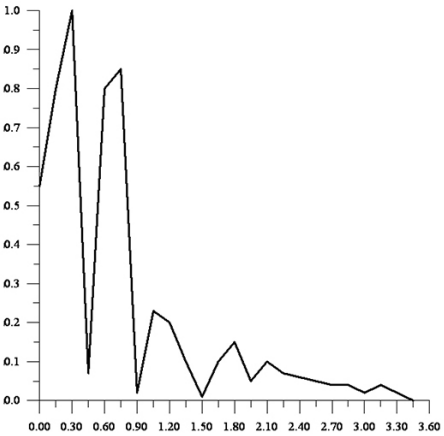


Fig. 4. The Fourier spectrum of the anomalous magnetic field of the Moon at an altitude of 100 km.

CONCLUSIONS:

1. The optimal height of a complex gravitational-magnetic survey above the surface of the Moon is approximately 75 km.
2. The moon has 3 main density boundaries and 7 magnetic ones, unlike the Earth.

REFERENCES:

[1] Russell C.T., Coleman P.J., Fleming B.K., Hilburn L., Ianidis G., Lichtenstein B.R. and Schubert G. // Proc. Lunar Sci. Conf. 6-th. 1975. 2955 p.

[2] Vanyan L.L., Yeroshenko Ye.G., Lugovenko V.N., Okulesskii B.A., Popov A.G. and Kharitonov A.L. A comparison of the magnetic field anomalies for the Moon and Earth // The Moon. 1997. No. 16. P. 289-294.

[3] Gorshkov E.S. Investigation of the magnetic properties of lunar samples. Abstract of the dissertation for the degree of Candidate of Physical and Mathematical Sciences. Moscow: IZMIRAN, 1976. 25 p.

OPTIMAL SYSTEMS OF RECORDING ACOUSTIC SIGNALS ON SPACECRAFT OF THE CYLINDRICAL FORM

V.Yu. Burmin[1]
[1] *Schmidt Institute of Physics of the Earth, Russian Academy of Sciences (vburmin@yandex.ru)*

ABSTRACT:
For manned spacecraft, a great danger is the destruction of the shell of the modules as a result of collisions with micrometeors and space debris. In this regard, the problem arises of placing sensors for detecting shocks in such a way that the errors in determining the locations and times of breakdowns are minimal.

We write the equations connecting the coordinates of sources and coordinates of oscillation detectors. Place *n* detectors on the lateral surface of a cylinder. Then, let the cylinder axis be in the origin of the Cartesian coordinate system. The 0*Z* axis lies perpendicularly to the cylinder axis; the 0*X* axis goes along the cylinder axis; and the 0*Y* axis is perpendicular to the *XZ* plane (Fig. 1). Presented is the system of nonlinear equations

$$(X_0-x_i)^2+(Y_0-y_i)^2+(Z_0-z_i)^2=r_i^2. \quad (1)$$

where X_0, Y_0, Z_0 are the coordinates of the oscillation source; x_i, y_i, z_i are the coordinates of detectors; and;

$r_i=R_i-R_0$; $|R_i|=R_i=\sqrt{x_i^2+y_i^2+z_i^2}$; $|R_0|=R_0=\sqrt{X_0^2+Y_0^2+Z_0^2}$, i=1, 2, ..., n.

We expand the brackets in Eq. (1) and use the relations for R_i and R_0. Then, we have

$$X_0x_i+Y_0y_i+Z_0z_i=0.5(R_0^2+R_i^2+r_i^2). \quad (2)$$

The values r_i^2 will take the form

$$r_i^2=c_i^2(\tau_i-\tau_0)^2=c_i^2\tau_i^2-2c_i^2\tau_i\tau_0+c_i^2\tau_0^2,$$

where τ_i is the time when oscillations arrive at the station; τ_0 is the time of onset of oscillation excitation (the time in the source); c_i are the effective velocities of propagation of oscillations (an acoustic or seismic wave) that are numerically equal to the ratio of the distance along the straight line between the *i*-th station and the source of oscillations to the time of wave travel in the beam.

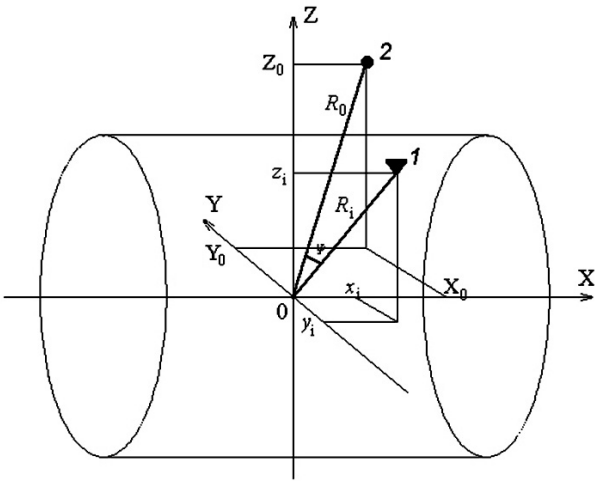


Fig.1. The Cartesian coordinate system and the cylindrical surface *1* is an oscillation detector; *2* is an oscillation source.

We substitute the obtained equation for r_i^2 to the right part of Eq. (2) and group the members. As a result we have

$$X_0x_i + Y_0y_i + Z_0z_i + T_0q_i = f_i, \quad (3)$$

where $q_i = -t_i c_i^2$, $f_i = 0.5[R_0^2 + R_i^2 - c_i^2(\tau_i^2 + \tau_0^2)]$.

We consider the estimates of errors in determining the unknown parameters and questions of stability of solving the systems of linear algebraic equations (3).

We present system (3) in the matrix form (Burmin, 1994, 1995)

$\mathbf{Kp}=\mathbf{f}$,

where $\mathbf{p}^{\mathbf{T}}=\{p_j\}$ is the required parameters (j=1, 2, 3, 4); $\mathbf{K}$ is the matrices of the systems; and $\mathbf{f}^{\mathbf{T}}=\{f_j\}$ is the observed values (i = 1, …, n).

For the error of the vector p, the following equation takes place [Burmin, 1995]

$\Delta\mathbf{p}=\tilde{\mathbf{K}}^{+}(\Delta\mathbf{f}-\Delta\mathbf{K}\mathbf{p})$.

The estimate of error $\Delta\mathbf{p}$ of vector $\mathbf{p}$ takes the respective form

$$\|\Delta\mathbf{p}\| \le \|\tilde{\mathbf{K}}^{+}\| \|\Delta\mathbf{f} - \Delta\mathbf{K}\mathbf{p}\|.$$

We assume that the errors both in the elements of matrix $\mathbf{K}$ and in the right parts of the equations are due to only the errors of the arrival time of τ_i, whose absolute values may be accepted equal to $|\delta\tau_i| = \rho_i|\Delta\tau|$. Then, for the norm of the full vector of error $\Delta\mathbf{p}$, the following estimate is valid (Burmin, 1986, 1995)

$$\|\Delta\mathbf{p}\| = \left\{\sum_{i=1}^{n} |\Delta p_i|^2\right\}^{1/2} \le \|\tilde{\mathbf{K}}^{+}\| \|R\nu\rho\| |\Delta\tau|, \quad (4)$$

where $\|R\nu\rho\| = \left\{\sum_{i=1}^{n} |R_i\nu_i\rho_i|^2\right\}^{1/2}$.

The weight factors ρ_i indicate that the measured values at the observation points are not equally accurate and the systematic errors appear in determining τ_i because of the deviation of actual velocities from the accepted model.

The majorant estimate (4) guarantees accuracy in determining coordinates of oscillation sources. If the coordinates of observation points are varied, their position may be selected so that the estimate (4) would take the minimum value. Since the right part of inequality (4) presents the estimate of the maximum error in determining the hypocenter parameters, we come to a minimax problem to obtain the optimal placement of seismic stations. Thus, the problem for determining the optimum geometry for the observation system can be considered as a problem of minimization of the objective function $J = \|\tilde{\mathbf{K}}^{+}\| \|R\nu\rho\|$ that has a sense of maximum error in calculating the estimated parameters at a maximum error in assigning a time of arrival of oscillations to receivers.

The optimality criterion for observation systems connected with minimizing a norm of the matrix $\mathbf{K}$ – $\|\mathbf{K}^{+}\|$ or $\|\mathbf{K}\|\|\mathbf{K}^{+}\|$ is called a *C*-optimality criterion (Burmin, 1976).

The set of points *xi* where the observations are carried out and the respective values r_i of the number of observations at these points $\sum_{i=1}^{n} r_i = N$ are called an experimental design (Burmin, 1995).

As is shown in (Burmin, 1976), the matrix $\mathbf{K}$ of the system of linear algebraic equations corresponds to the optimal design with respect to the *C*-optimality criterion. The matrix columns are mutually orthogonal and the norms are mutually equal. Moreover, the maximum value of the matrix determinant of the normal system of equations corresponds to the optimal design with respect to the *C*-optimality criterion. In this case, we obtain a socalled *D*-optimality criterion (Burmin, 1976).

We turn now to the system (3). The matrix of normal equations for it is written as follows:

$$B=K^TK=\begin{pmatrix} \sum_{i=1}^{n} x_i^2 & \sum_{i=1}^{n} x_i y_i & \sum_{i=1}^{n} x_i z_i & \sum_{i=1}^{n} x_i q_i \\ \sum_{i=1}^{n} x_i y_i & \sum_{i=1}^{n} y_i^2 & \sum_{i=1}^{n} y_i z_i & \sum_{i=1}^{n} y_i q_i \\ \sum_{i=1}^{n} x_i z_i & \sum_{i=1}^{n} y_i z_i & \sum_{i=1}^{n} z_i^2 & \sum_{i=1}^{n} z_i q_i \\ \sum_{i=1}^{n} x_i q_i & \sum_{i=1}^{n} y_i q_i & \sum_{i=1}^{n} z_i q_i & \sum_{i=1}^{n} q_i^2 \end{pmatrix}.$$

According to the Cauchy–Binet formula, the determinant of the matrix **B** equals (Gantmacher, 1968)

$$\det(B)=\sum_{i_1<i_2<i_3<i_4}^{n}\begin{vmatrix} x_{i_1} & y_{i_1} & z_{i_1} & q_{i_1} \\ x_{i_2} & y_{i_2} & z_{i_2} & q_{i_2} \\ x_{i_3} & y_{i_3} & z_{i_3} & q_{i_3} \\ x_{i_4} & y_{i_4} & z_{i_4} & q_{i_4} \end{vmatrix}^2. \quad (5)$$

We decompose the determinants in Eq. (5) by the last column. Then, we have

$$\det(B)=\sum_{i_1<i_2<i_3<i_4}^{n}\left\{q_{i_1}\begin{vmatrix} x_{i_2} & y_{i_2} & z_{i_2} \\ x_{i_3} & y_{i_3} & z_{i_3} \\ x_{i_4} & y_{i_4} & z_{i_4} \end{vmatrix}-q_{i_2}\begin{vmatrix} x_{i_1} & y_{i_1} & z_{i_1} \\ x_{i_3} & y_{i_3} & z_{i_3} \\ x_{i_4} & y_{i_4} & z_{i_4} \end{vmatrix}+\right. \quad (6)$$

$$\left.+q_{i_3}\begin{vmatrix} x_{i_1} & y_{i_1} & z_{i_1} \\ x_{i_2} & y_{i_2} & z_{i_2} \\ x_{i_4} & y_{i_4} & z_{i_4} \end{vmatrix}-q_{i_4}\begin{vmatrix} x_{i_1} & y_{i_1} & z_{i_1} \\ x_{i_2} & y_{i_2} & z_{i_2} \\ x_{i_3} & y_{i_3} & z_{i_3} \end{vmatrix}\right\}^2.$$

It is easy to believe that all determinants in the brackets are equal to a sextuple value of volumes of tetrahedrons with summits (Pogorelov, 1983):

$M_{i_2}(x_{i_2}, y_{i_2}, z_{i_2})$, $M_{i_3}(x_{i_3}, y_{i_3}, z_{i_3})$, $M_{i_4}(x_{i_4}, y_{i_4}, z_{i_4})$, $M_0(0,0,0)$;
$M_{i_1}(x_{i_1}, y_{i_1}, z_{i_1})$, $M_{i_3}(x_{i_3}, y_{i_3}, z_{i_3})$, $M_{i_4}(x_{i_4}, y_{i_4}, z_{i_4})$, $M_0(0,0,0)$;
$M_{i_1}(x_{i_1}, y_{i_1}, z_{i_1})$, $M_{i_2}(x_{i_2}, y_{i_2}, z_{i_2})$, $M_{i_4}(x_{i_4}, y_{i_4}, z_{i_4})$, $M_0(0,0,0)$;
$M_{i_1}(x_{i_1}, y_{i_1}, z_{i_1})$, $M_{i_2}(x_{i_2}, y_{i_2}, z_{i_2})$, $M_{i_3}(x_{i_3}, y_{i_3}, z_{i_3})$, $M_0(0,0,0)$

and do not depend on the position of sources, while the value of the determinant of the matrix **B** depends on the position of the source. Nevertheless, we may show that for all possible positions of the hypocenters, the greater the volume of a polyhedron with summits at the points of observations, i.e., the greater the amount of volumes of all tetrahedrons with the common summit M_0, the greater the value of a determinant of the matrix **B** of the-normal system of linear equations. Thus, the optimal placement of sensors weakly depends on the position of oscillation sources and is determined mainly by the internal geometrical network of observations.

It is clear that if all summits of the tetrahedrons, except for the one that coincides with the coordinate center, lie on one arc of a big circle, the volumes of the respective tetrahedrons equal zero. This means that if all points of observation lie on one arc of a big circle, the determinant of the system of normal equations equals zero, and the system itself is degenerate.

To calculate numerical values for coordinates of points of observation corresponding to polyhedrons with maximum volumes, it is required to differentiate the determinant of a normal system of equations by respective coordinates, to equate the derivatives to zero, and to solve the obtained system of equations.

At the same time, determinant (5) takes the maximum value only when the sum of squares of values of volumes of all tetrahedrons inscribed in the cylinder will be maximal. On the other side, each set of points on the cylinder is a set of summits of a certain polyhedron, whose volume equals the sum of volumes of respective tetrahedrons with one common summit at the origin of coordinates. It is known that the polyhedron that has the greatest volume among all polyhedrons with a given number of summits inscribed in any fixed smooth concave surface is definitely a true polyhedron with triangular faces (Tot, 1958), i.e., a polyhedron, all of whose faces are triangular and lie in different planes.

There are three such polyhedrons: tetrahedron, octahedron, and icosahedron. If the signal detector can be placed only on the lateral surface of a cylinder, only a tetrahedron will be a solution to the problem (Fig. 2). It is easy to determine that the length of the generatrix of the cylinder, in which a tetrahedron is inscribed, equals the cylinder diameter divided by a square root of two, i.e., $L_{optim}=D/\sqrt{2}$.

We apply this problem to manned space stations. In this case, sensitive microphones serve as sensors to record acoustic waves that propagate inside the station from the breakdown spots. For technological reasons there should be a minimal number of microphones. They may be placed only on the lateral internal surface of the station. The numerical solution to this problem as applied to the International Space Station (ISS) was obtained in [8], [7]. Here, the individual modules of the station body (Fig. 3), the modules *A* and *B* were approximated by the cylinders.

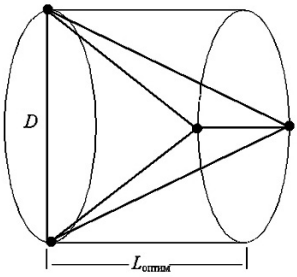


Fig. 2. The optimum system of observations on the cylinder surface.

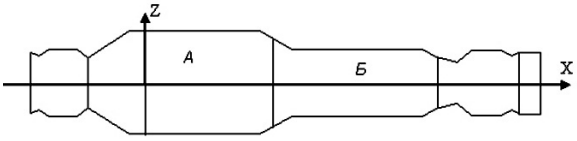


Fig. 3. The sectional plane of the international space station.

Figure 4 shows the positions of the sensors 1–6 obtained in [7] as a result of solving the problem numerically in accordance with the *D*- and *C*-optimality criteria. Author used the Monte Carlo method in the algorithm of the search for the optimal arrangement of the sensors.

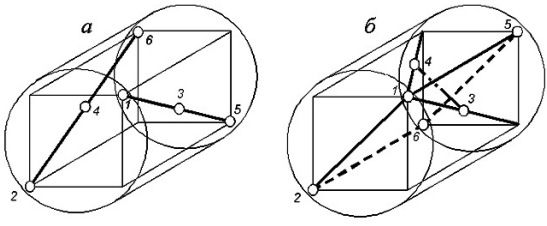


Fig. 4. The optimal observation systems established for the sensors *1–6* on the basis of *D*-optimality (*a*) and *C*-optimality (*b*) criteria by the Monte Carlo method.

Figure 5 presents the system composed of six microphones that should be considered the optimum system for recording breakdowns for the modules *A* and *B* (Fig. 3) in accordance with the above results and taking into account that the ratio of modules *A* and *B's* length to diameters is 1.25. The height of the cylinder in Fig. 5 is $L=2L_{optim}=D\sqrt{2}$. It is evident that the optimal arrangement of the sensors on the cylinder surface is calculated with accuracy to the arbitrary turn of the observation system relative to the cylinder axis.

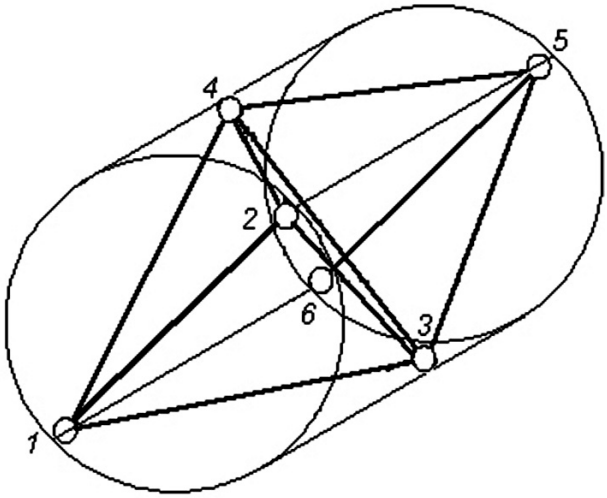


Fig. 5. The optimal observation systems we obtained for the sensors *1–6* in this work on the basis of *C*-optimality criterion.

The results of the comparison in Figs. 5 and 4 show that the solutions obtained by the numerical methods are close to an accurate solution, but are different from it. Besides, the solutions in Figs. 4a and 4b differ from each other, though according to the system, they should coincide.

REFERENCES

[1] Burmin, V.Yu., The Problem of Experimental Planning and Condition of Systems of Linear Algebraic Equations, Izv. Akad. Nauk SSSR, Tekh. Kibern., 1976, no. 2, pp. 195–200.
[2] Burmin, V.Yu., Optimal Arrangement of Seismic Stations when Recording of Near Earthquakes, Izv. Akad. Nauk SSSR, Fiz. Zemli, 1986, no. 5, pp. 34–42.
[3] Burmin, V.Yu., Optimal Arrangement of Seismic Stations on the Surface of the Globe, Izv. Ross. Akad. Nauk, Fiz. Zemli, 1994, no. 12, pp. 1–9.
[4] Burmin, V.Yu. Nekotoryye obratnyye zadachi seysmologii. Teoriya, eksperimenty, rezul'taty.- Moskva. «Nauka». 2019. 276 p. (Some inverse problems of seismology. Theory, experiments, results. – Moscow. "The science". 2019.276 p.
[5] Gantmakher, F.R., Teoriya matrits (Theory of matrices), Moscow: Nauka, 1968.
[6] Pogorelov, A.V., Geometriya (Geometry), Moscow: Nauka, 1983.
[7] Polovnev, A.L., Optimization of Experimental Plan in the Problem Concerning Determination of Coordinates of Breakdown Spot in Containment of a Manned Space Vehicle, Extended Abstract of Cand. (Phys._Math.) Sci. Dissertation, Moscow, 2011.
[8] Polovnev, A.L., Determination of Coordinates for a Breakdown Spot Made in Containment of the ISS Modulus by a High_Speed Particle, Nauch. Vestn. MGTU GA, 2009, no. 56, pp. 198–203.
[9] Toth, F.L., Lagerungen in der Ebene, auf der Kugel und im Raum, Berlin: Springer, 1953.

EXCESS OF SODIUM IONS DENSITY REQUIRED TO CREATE A WIDE CURRENT AT THE HERMEAN MAGNETOPAUSE

E.S. Belenkaya[1], I.A. Pensionerov[1], I.I. Alexeev[1], D.A. Parunakian[1]
[1] *Federal State Budget Educational Institution of Higher Education M.V.Lomonosov Moscow State University, Skobeltsyn Institute of Nuclear Physics (SINP MSU), 1(2), Leninskie gory, GSP-1, Moscow 119991, Russian Federation, elena.belenkaya.msu@gmail.com.*

KEYWORDS:
Mercury, magnetopause, diamagnetic current, sodium ions, solar wind magnetic field

INTRODUCTION:
We consider a structure observed at the Mercury's magnetopause during the first two MESSENGER flights and called the "Double Magnetopause" [1]. We suppose that it is associated with a current carried by the Na^+ ions. Two cases are considered, when sodium ions prevail outside the Hermean magnetosphere, and when they predominate inside it. These ions have been observed in the magnetosphere and beyond. We study what Na^+ density excess can be enough to create a wide magnitization magnetopause current and on which side of the magnetopause this current is located. For each case the influence of northward and southward solar wind magnetic field is analyzed.

REFERENCES:
[1] Slavin J.A., Acuña, M.H., Anderson B.J, Baker, D.N., Benna M., Gloeckler G., Gold R.E., Ho G.C., KillenR.M., Korth H., Krimigis S.M., McNutt Jr. R.L., Nittler L.R., Raines J.M., Schriver D., Solomon S.C., Starr R.D., Trávníček P., Zurbuchen T.H. Mercury's Magnetosphere After MESSENGER's First Flyby // Science 2008. V. 321, 85-89; DOI: 10.1126/science.1159040.

THE ORIGIN OF THE LUNAR PROCELLARUM KREEP TERRANE (PKT): STRATIGRAPHIC EVIDENCE AND IMPLICATIONS FOR LUNAR GEOLOGICAL AND THERMAL EVOLUTION

Jingyi Zhang[1,2], James W. Head[2], Jianzhong Liu[1], Ross W. K. Potter[1,2,3]
[1] *Center for Lunar and Planetary Science, Institute of Geochemistry, Chinese Academy of Sciences, Guiyang 550081, China, zhangjiangyi@mail.gyig.ac.cn.*
[2] *Department of Earth, Environmental and Planetary Sciences, Brown University, Providence, RI 02912 USA.*
[3] *Clarivate Analytics, London, UK.*

KEYWORDS:
KREEP, Procellarum KREEP Terrane, Thorium.

INTRODUCTION:
The Luna 3 mission launched by the Soviet Union in 1959 provided the first view of the lunar far side, reveaing significant differences between the nearside and the farside in crustal thickness, composition and distribution of maria. Most lunar evolution models predict that fractional crystallization of a lunar magma ocean produced a layer of melt enriched in incompatible elements such as K, REE, and P (i.e., KREEP) [1]. On the basis of results from the 1998 Lunar Prospector mission [2] and the 1994 Clementine mission [3], Jolliff et al. proposed that the surficial distribution of Th, which was measured on a global-scale [4,5,6], can be used as a proxy for determining the global distribution of KREEP; they used the Th and FeO distribution to divide the lunar surface into three main terranes: Procellarum KREEP Terrane (PKT), Feldspathic Highland Terrane (FHT) and South Pole-Aitken Terrane (SPAT) [3]. We use the PKT boundary of Haskin et al. [7].

The most significant characteristic of the PKT is the high-abundance of incompatible elements (such as Thorium) (Figure 1). The lateral extent and vertical distribution of this "KREEP" layer is still a matter of debate, and there are many models for the origin and evolution of the radioactive elements in PKT. On the basis of the asymmetry of Th distribution, some workers suggested that the Procellarum region is the oldest lunar impact basin, the formation of which may have caused the accumulation of KREEP-rich residual liquid on the nearside; in contrast, the lunar far side generally lacks the same high abundances of Th and other KREEPy elements [8,9]. Other mechanisms have been proposed to explain the asymmetry of KREEP materials, including inhomogeneous differentiation of the magma ocean [10], and antipodal effects of impact [11].

In this analysis, we use impact craters and basins superposed on the ancient lunar crust to document the 3–D (lateral and vertical) extent of Th in PKT in order to establish the geometry and potential evolution of the KREEP layer. We use the relations between transient cavity depth or diameter and crater excavation depth given by Potter [12] and Melsoh [13] to obtain sampling depth estimates. We then assess the three-dimensional geometry of Th concentrations in the PKT and compare the relations between PKT and SPA as a basis for a hypothesis to explain Th distribution and its characteristics.

RESULTS AND DISCUSSIONS:
The Th abundance map shows that the high-Th areas are 1) mainly related to Imbrium ejecta (Fra Mauro Formation-FMF) and/or post-Imbrium KREEP volcanism in the PKT, and 2) concentrated at the location of young impact craters in mare and highlands regions (Figure 1) [16]. We studied several such craters located on highlands and mare regions (Figure 1; Table 1), including Mairan, Kepler, Aristarchus, Aristillus, Copernicus and Plato. In particular, the high-Th concentration regions are near Mairan, Kepler, Aristarchus, and Aristillus. However, not all craters on Imbrium ejecta show high-Th concentrations. Copernicus and Plato, which are located on the FMF and the Imbri-

um rim respectively, show relatively low Th values, suggesting that the high-Th terrain does not exist below the surficial FMF in these areas. Craters within Mare Imbrium generally show lower Th abundance than those on the highlands (suggesting that they are excavating maria, not Th-rich FMF or crust). A second concentration of Th is within Mare Ingenii area in SPA (Figure 2a). This concentration shows peaks at two impact craters, Birkeland (81.4 km diameter) and Oresme V (56.1 km diameter) (Figure 2b, Table 2).

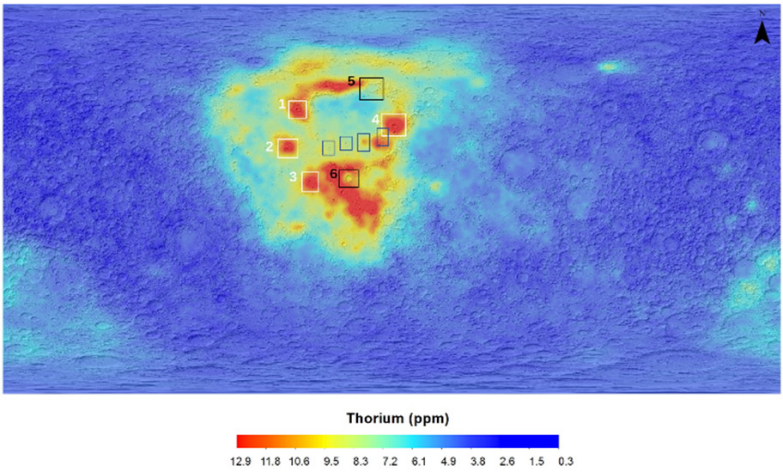


Fig. 1. Global thorium abundance from LP gamma-ray spectrometer overlain on LOLA hillshade map [14][15]. White and black square boxes show high-Th and low-Th concentrations, respectively. 1 – Mairan; 2 – Aristarchus; 3 – Kepler; 4 – Aristillus; 5 – Plato; 6 – Copernicus. Blue square boxes are some small craters in Imbrium basin, representing Euler, Lambert, Ti-mocharis and Archimedes, from left to right respectively.

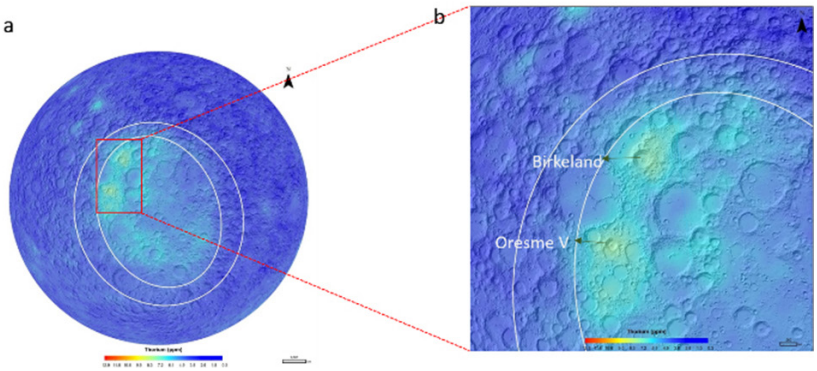


Fig. 2. Thorium abundance from LP gamma-ray spectrometer overlain on LOLA hillshade map[14][15]. a) White oval represents SPA area. Red dashed rectangle represents the highest Th value region in SPA, centered on two impact craters. b) Birkeland and Oresme V craters in SPA with peak Th abundances.

Table 1

Name	Diameter (km)	Transient cavity diameter c (km)	Transient cavity depth c (km)	Excavation depth a (km)	Excavation depth b (km)
Euler	26.03	23.96	7.99	2.88	2.66
Kepler	31	26.65	8.88	3.19	2.96
Lambert	30.12	27.13	9.04	3.26	3.01
Timocharis	34.14	30.18	10.06	3.62	3.53

Name	Diameter (km)	Transient cavity diameter c (km)	Transient cavity depth c (km)	Excavation depth a (km)	Excavation depth b (km)
Aristarchus	42	34.52	11.51	4.14	3.84
Marian	34.49	34.15	11.83	4.09	3.94
Aristillus	54.37	44.82	14.94	5.38	4.98
Archimedes	81.04	62.92	20.97	7.55	6.99
Copernicus	96	72.71	24.24	8.73	8.08
Plato	100.68	75.67	25.22	9.08	8.41

Table 2

Name	Diameter (km)	Transient cavity diameter c (km)	Transient cavity depth c (km)	Excavation depth a (km)	Excavation depth b (km)
Birkeland	81.64	63.32	21.11	7.59	7.04
Oresme V	56.1	46.03	15.34	5.52	5.11

a, Potter et al. (2015);
b, Melosh (1989);
c, 2015 LPI Impact Crater Database (Croft 1985; Stöffler et al. (2006).
Red craters in Table 1 represent those craters with relatively high Th content in PKT.

INTERPRETATIONS:

On the basis of these stratigraphic and geometric relationships, we interpret the high Th distribution in PKT to be related to sequential oblique and near-vertical impacts. First, an oblique impact formed a Procellarum basin, removing much of the upper and middle crust in the area and bringing the residual KREEP-rich layer close to the surface. This was followed by formation of the SPA basin by oblique impact [17], similarly removing much of the upper and middle crust and exposing the KREEP-rich lower crust covered by SPA impact melt. Subsequently, the more vertical Imbrium basin impact penetrated into the shallow KREEP layer, ejecting it to form the FMF and related Th-rich ejecta and impact melt deposits. Later mare volcanism buried the KREEP-rich deposits under hundreds of m to km of lava. In the SPA basin, similar vertical impacts Birkeland and Oresme V excavated Th-rich material from below the melt sheet to create the locally high Th anomalies.

In summary, this interpretive scenario attributes the origin of the PKT and Th anomalies to sequential impact processes, requiring no additional processes to concentrate KREEP in the PKT terrain at depth, in agreement with [18]. We interpret the Th anomaly in SPA to be due to formation of SPA by oblique impact, similarly removing much of the upper and middle crust and exposing the KREEP-rich lower crust covered by SPA impact melt. Then, vertical impacts Birkeland and Oresme V excavated Th-rich material from below the melt sheet to create the locally high Th anomalies.

Analysis of the young Procellarum mare basalt samples returned by Chang'E 5 [19] will provide a test of this hypothesis. If the mare basalts show high Th concentrations, then this suggests that the PKT anomaly is extensive and significantly influenced the petrogenesis of the mare basalts, perhaps explaining their youth [20]. It the Chang'e 5 mare basalts are low in Th, then this supports our model of a more typical KREEP layer at depth in this region, with the PKT anomaly formed by sequential oblique and vertical impact excavation and redistribution.

REFERENCES:

[1] Warren and Wasson, The Origin of KREEP. RGSP, 1979, 17, 73-88.
[2] Binder, A., Lunar Prospector: Overview. Science, 1998, 281, 1475-1476.
[3] Nozette S., et al., The Clementine mission to the Moon: Scientific overview. Science, 1994, 266, 1835-1839.
[4] Lawrence et al. Global Elemental Maps of the Moon: The Lunar Prospector Gamma-Ray Spectrometer, 1998, Science 281, 1484.
[5] Lawrence et al. Small-area thorium features on the lunar surface, 2003, JGR 108, 5102.
[6] Lawrence et al. Global spatial deconvolution of Lunar Prospector Th abundances, 2007, GRL, 34(L03201).
[7] Haskin et al. The materials of the lunar Procellarum KREEP Terrane: A synthesis of data from geomorphological mapping, remote sensing, and sample analyses, 2000, JGR 105, 20403-20415.
[8] Warren & Kallemeyn (1998) LPI 6048.
[9] Zhu et al. Are the Moon's Nearside-Farside Asymmetries the Result of a Giant Impact? 2019, JGR 124, 2117-2140.
[10] Loper et al. On lunar asymmetries 1. Tilted convection and crustal asymmetry, 2002, JGR 107, 5046.
[11] Schultz et al. Origin of nearside structural and geochemical anomalies on the Moon, 2011, GSA SP 477, 141-159.
[12] Potter et al. Scaling of basin-sized impacts and the influence of target temperature, 2015, GSA SP 518, 99.
[13] Melosh, Impact Cratering – A Geologic Process, 1989, 74.
[14] Alan B. Binder, Lunar Prospector Overview, 1998, Science 281, 5382.
[15] Smith David E et al. Initial observations from the Lunar Orbiter Laser Altimeter (LOLA) 2010, Space Sci Rev, 150, 209.
[16] Lawrence et al. Thorium abundances on the lunar surface, 2000, JGR 105, 20307.
[17] Schultz et al., (2011) GSA SP 477.
[18] Alexander J. Evans, The Lunar Geochemical Asymmetry Implications for KREEP and Magma Ocean Crystallization, 2019, LPSC 50 #2733.
[19] Qian et al., China's Chang'e-5 landing site: Geology, stratigraphy, and provenance of materials, Earth and Planetary Science, 561, 116855, doi: 10.1016/j.epsl.2021.116855.
[20] Wieczorek and Phillips, 2000, Jour. Geophys. Res. 105, 20417.
[21] http://www.lpi.usra.edu/lunar/surface/.

MORPHOLOGICAL AND MORPHOMETRIC FEATURES OF MERCURIAN CRATERS

E.A. Feoktistova[1], Zh.F. Rodionova[1], A.Yu. Zharkova[1,2], A.A. Kokhanov[2], I.Yu. Zavyalov[2]

[1] *Sternberg Astronomical Institute, Universiteytskiy pr. 13, Moscow, Russia, 119234, jeanna@sai.msu.ru;*

[2] *Moscow State University of Geodesy and Cartography, Gorokhovskiy per. 4, Moscow, Russia, 105064.*

KEYWORDS:
Mercury, catalog, craters, morphology, morphometric parameters, statistical analysis.

INTRODUCTION:
Impact craters are one of the main landforms of atmosphereless bodies in the solar system. The new global catalog of craters for Mercury includes information on the morphological and morphometric features of about 23,000 craters of Mercury with a diameter of more than 10 km. This catalog was compiled by the Sternberg Astronomical Institute (GAI MGU) and MIIGAiK. To create the catalog, the latest global DEM with a resolution of 665 m / pixel, obtained as a result of the MESSENGER mission, was used.

DATA AND METHODS:
To compile the catalog, we used the global mosaic of Mercury MESSENGER MDIS with a resolution of ~ 166 m / pixel and several MESSENGER DEMs – the first global DEM of Mercury with a resolution of 665 m / pixel [1], and at the same time four DEMs in the quadrants of Mercury with a resolution of ~ 222 m / pixel [2]. Morphological features can be identified and described using visual image analysis. Morphometric parameters can be measured using the DEM processing method.

The morphological description of craters was developed at the SAI MSU and was used to compile catalogs of craters on the Moon, Mars and Mercury. Morphological features include: degradation of the rim, terrace or slope collapse, faults, central uplifts (hills, peaks or ridges), crater chains at the bottom, cracks, bottom character, presence of lava at the bottom of the crater, presence of a ray system, underlying terrain: highlands, plains, transition zone [3, 4].

The global catalog includes such morphometric characteristics of craters as: 1) the diameter of the inner element (flat floor, central apex or inner ring); 2) depth and relative depth of each crater; 3) maximum and minimum slopes; 4) the average level of the slope of the outer surface; 5) inner slopes of the crater; 6) the ratio of the volume of the crater to the volume of the bowl.

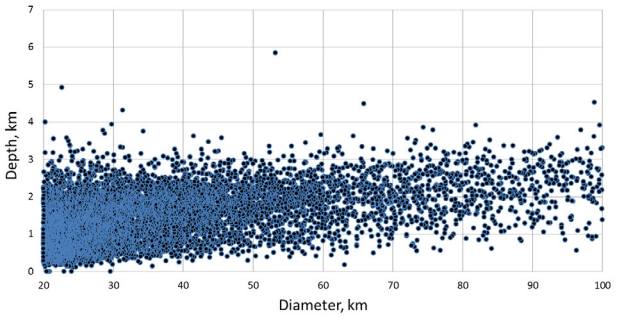
Currently, a morphological and morphometric description has been made for 7950 craters with diameters of more than 20 km. According to our data, most of these craters (30.6 and 35.5%, respectively) belong to the 3rd and 4th stages of preservation according to the SAI MSU classification, that is, they have a smoothed or destroyed walls, rim faults. Ruins (5th degree of preservation according to the SAI MSU classification) include 18.6 % of the craters of Mercury with a diameter of ≥ 20 km. Percentage of fresh craters (1 and 2 preservation classes is 2.5 and 12.8 % of the total number of craters with a diameter of ≥ 20 km). The rim is absent in 5.6 % of the craters. A significant proportion (16.5 %) of well-preserved craters have a powerful outer ridge. Only 0.6 % of craters have a ray system. 1.1 % of craters have an inner ring ridge. One of the features of the craters of Mercury is the presence of a fossa in the region of the central rise of the crater. Presumably, such formations can be associated with volcanic activity. About 0.3 % of Mercury's craters have such pits. Several investigated craters have a dark halo around the rim (0.3 %). 1.4 % of craters with a diameter ≥ 20 km are crossed by scarps.

There are three types of underlying surface on Mercury: plain, highland, and the transition zone between highland and plain. The transition zone is widespread on Mercury, in contrast to the Moon. According to our data, 12.4 % of craters with diameters ≥ 20 km are located on plains, 41.9 % – on highland, and 45.7 % – in the transition zone.

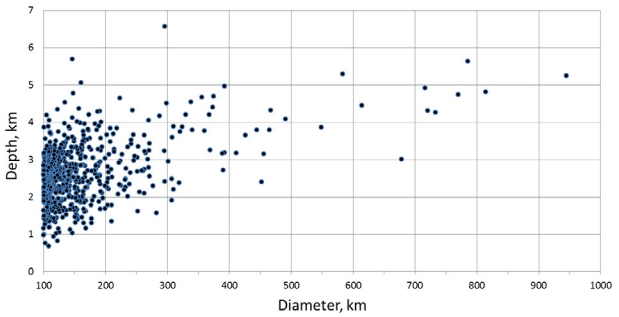
We used MLA altimetry profiles to assess the morphometric parameters of craters. The depths, bottom dimensions, and wall slopes were estimated for craters with a diameter of ≥ 20 km.

Figure 1 shows the distribution of craters by depth depending on the diameter: for diameters from 20 to 100 km (Fig. 1a) and for diameters from 100 km and more (Fig. 1b). The maximum depth of the craters of Mercury exceeds 6.5 km (Fig. 1b).

In fig. 2 shows the ratio of the depth of craters (h) to their diameter (D). It can be seen that large basins in D>300–400 km have h/D from 0.004 to 0.01. Earlier [5] it was suggested that such a ratio is typical for basins that were formed as a result of collisions with the planet's surface of low-density projectiles, for example, large comets.



a)



b)

Fig. 1. Distribution of Mercury craters with D> 20 km in depth.

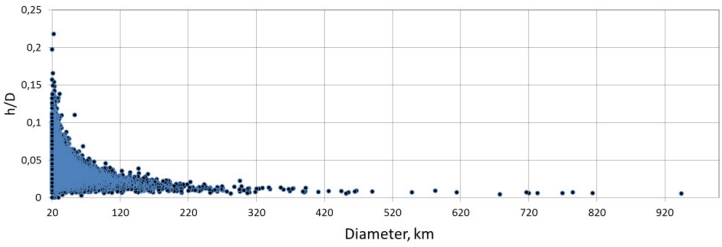


Fig. 2. The ratio of the crater's depth to diameter in dependence of D.

AKNOWLEDGMENTS:
E.A. Feoktistova, A.Yu. Zharkova, I.Yu. Zavyalov, A.A. Kokhanov and Zh.F. Rodionova were supported by Russian Foundation for Basic Research (RFBR), project No 20–35–70019.

REFERENCES:

[1] Zharkova A. Yu., Karachevtseva I. P., Zubarev A. E., Brusnikin E. S., Kokhanov A. A., Kreslavsky M. A., Issledovanie poverkhnosty Merkuriya kartograficheskimi metodami s ispolzovaniem noveyshikh topographicheskikh dannykh, poluchennykh na osnove obrabotki izobrazheniy KA MESSENGER. // Sovremennye problemy distantsionnogo zondirovaniya Zemli iz kosmosa, 2016, Vol. 13, No 5, pp. 265-274.
[2] Johnson, C. L., and S. A. Hauck. A whole new Mercury: MESSENGER reveals a dynamic planet at the last frontier of the inner solar system. 2016. J. Geophys. Res. Planets, Vol. 121, P. 2349-2362.
[3] Feoktistova E. A., Zharkova A.Yu., Kokhanov A. A.,Rodionova Zh.F., Rotaru V. A. Compilation of a new global catalog of Mercury's craters. 2020. Abstracts of the eleventh Moscow Solar System Symposium.
[4] Kozlova E. A., Sitnikov B. D., Rodionova J. F., Shevchenko V. V. Analysis of Mercurian Craters by Means of Cartographic Method // Proceedings of the 22d International Cartographic Conference (ICC) A Coruña, Spain, 9–16 July, 2005, "Mapping Approaches into a Changing World".
[5] Rodionova Zh. F., Zharkova A. Yu., Grishakina E. A., Shevchenko V. V. Topographic Features of the Lunar Maria and Basins // Solar System Research, 2021, Vol. 55, No. 3, pp. 183-199.

O-C ANALYSIS OF 545 LUNAR OCCULTATIONS

N. Mahdavi[1], A. Poro[1], et al.
[1] *The International Occultation Timing Association Middle East Section, info@iota-me.com*

KEYWORDS:
Moon, Lunar Occultation, Occult 4, O-C

INTRODUCTION:
In this study, we have studied the reports of lunar occultations by this project observation's teams (named APTO) in comparison with other observations of the objects. Thirteen binary stars were selected for this study. All the previous observations of these stars were also collected. Finally, an analysis of O-C of all reports was performed.

THE MODEL ESTIMATES OF THE CRATERS EJECTA THICKNESS IN THE SOUTHERN POLAR REGION OF THE MOON

A. S. Krasilnikov[1], S. S. Krasilnikov[1], M. A. Ivanov[1], J. W. Head[2]
[1] *Vernadsky Institute of Geochemistry and Analytical Chemistry RAS, Moscow, Russia, grossular13@gmail.com;*
[2] *Department of Earth, Environmental & Planetary Sciences, Brown University, Providence, RI, USA.*

KEYWORDS:
Moon, South Pole, ejecta thickness, secondary craters, ejecta.

INTRODUCTION:
The Roscosmos corporation considers the South polar region of the Moon as the primary target for the Russian lunar program. Significant interest in this region is linked with the enhanced concentration of hydrogen in the regolith and various geological processes associated with the possible presence of ground ice. The largest and oldest known lunar impact basin is South Pole – Aitken (SPA). The present relief and geological structure of the studied region are associated with the SPA impact. The SPA remnants have a high scientific capability because of the ancient material of lunar crust and the possible availability of ancient mantle material. The ejecta of younger craters is also interesting as they contain ancient material excavated from beneath the SPA blanket.

The impact process is the primary agent of the re-distributor of material on the Moon. As a result, contiguous ejecta, rays, satellite, and secondary craters around the primary craters can be formed. Here we present the model estimates of the ejecta thickness in the pole region (upper 65°S) for Nectarian, Imbrian, Eratosthenian and Copernican craters. Our estimates are based on the new geological map of the southern polar region of the Moon compiled at 1:300,000 scale [1]. Pre-Nectarian craters did not consider our research because of the poor preservation state and overlapping ejecta by younger deposits.

ESTIMATION OF CRATER EJECTA THICKNESSES:
The geological map based on the LOLA DTMs (20–60 m/px resolution) and the LROC WAC images (100 m/px). The map allows identification of impact craters and their ejecta, which belong to different epochs of the geological history of the Moon. Along with the geological map, we used the catalog of lunar craters with a diameter > 20 km [2]. The diameters of smaller craters were determined directly from the geological map.

In the past, five models have been developed to estimate the thicknesses of craters ejecta [3–7].

The McGetchin et al. model [3] was based on ejecta thickness's statistics for small-scale impact craters and craters, formed by nuclear tests. The results of these measurements were extrapolated for the impact structures of the larger diameter. McGetchin et al. have proposed the following formula for the ejecta thickness (T): $T=0.14\cdot R\cdot 0.74\cdot(r/R)^{-3}$. Here and thereafter, R is the crater radius, r is the distance from the crater center, all values are in meters. In his paper, Pike [4] severely critiqued McGetchin's approach and proposed an alternative formula is $T=0.033\cdot R\cdot(r/R)^{-3}$. The Housen et al. model [5] was developed based on theoretical modeling of a projectile's impact with specific velocity, diameter, and density. Their resulting formula is: $T=0.0078\cdot R\cdot(r/R)^{-2.61}$. Using new topographic data collected by the LOLA instrument [8], Fassett et al. [6] developed a model that describes the variation of the ejecta thicknesses for the Orientale basin. Their formula is $T=2900(\pm300)\cdot(r/R)^{-2.8(\pm0.5)}$, where R is the radius of the Cordillera rim. Finally, in the work of Sharpton [7], the new topographic data to describe the topology of relatively small craters (2–45 km diameter) were used. The formula proposed by Sharpton is $T=3.95(\pm1.19)\cdot R^{0.399}\cdot(r/R)^{-3}$.

ESTIMATES OF THE EJECTA THICKNESSES IN THE SOUTH POLAR REGION OF THE MOON:

In order to estimate the thickness of the recognizable ejecta in the study region, we have selected the models of Hausen et al. [5] and Sharpton [7], because the formulae of McGutchin [3] and Pike [4] may either underestimate or overestimate the thickness estimates. The formula by Fassett et al. [6] is likely applicable for the largest impact structures such as basins (>300 km diameter). We applied the Housen et al. formula to the craters larger than 45 km. For the smaller craters, we used the formula by Sharpton.

The resulting map (Fig. 1) shows the ejecta thickness estimates. For each studied crater, the ejecta thicknesses in the form of diverging annular zones. The zone width depends upon the crater rim diameter and increases for the larger craters. The width is 2.5 km for craters <25 km dimeter, 5 km for craters 26–80 km diameter, 10 km for craters 81–130 km diameter, and 20 km for the larger craters.

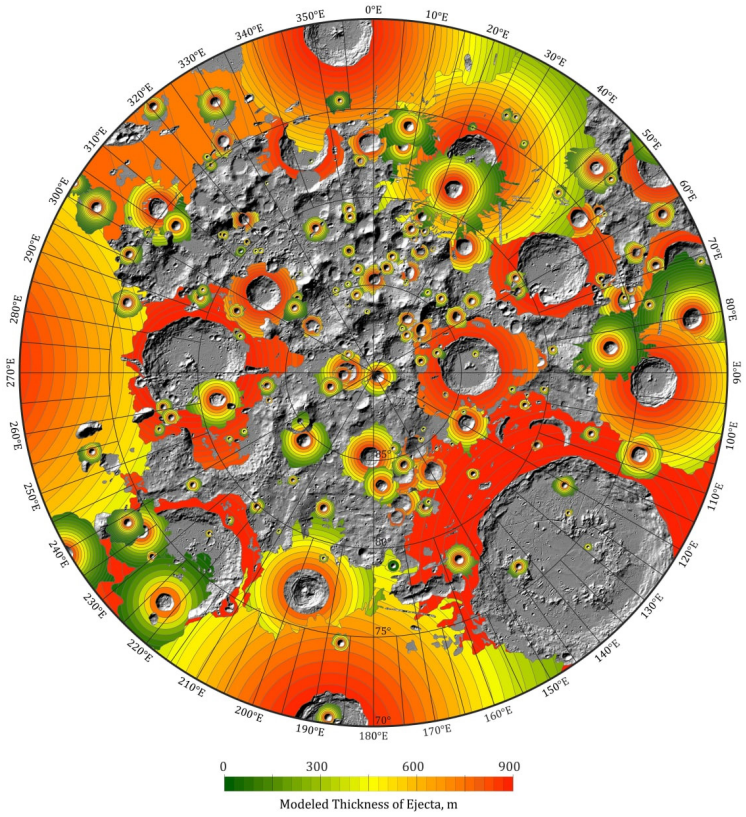


Fig. 1. The model thickness of ejecta blankets for craters of the Nectarian – Copernican ages in the South polar region of the Moon

The map of the model ejecta thickness provides the possibility to quantitatively estimate the contribution of impact events of different ages to the formation of the polar regolith, identify the sources of the material, the depth of its excavation, and its proportion in the regolith. This information is important for the selecting of a landing site and interpretation of the results of the future lunar missions.

ACKNOWLEDGEMENTS:

Input of KAS, KSS and MAI is partly supported by the Russian Science Foundation grant № 21–17–00035: Estimates of the rate of exogenous resurfacing on the Moon.

REFERENCES:

[1] Krasilnikov S. S., Ivanov M. A., Head J. W. Geological map of the south pole of Moon // 52nd LPSC. Houston. 2011. 2548.
[2] Head J. W., Fassett C. I., Kadish S. J., et al. Global distribution of large lunar craters: Implications for resurfacing and impactor populations // Science. 2010. V. 329 (5998). P. 1504–1507.
[3] McGetchin T. R., Settle M., Head J. W. Radial thickness variation in impact crater ejecta: implications for lunar basin deposits // Earth and Planetary Science Letters. 1973. V. 20 (2). P. 226–236.
[4] Pike R. J. Ejecta from large craters on the Moon: Comments on the geometric model of McGetchin et al. // Earth and Planetary Science Letters. 1974. vol: 23 (3). pp: 265–271.
[5] Fassett C. I., Head J. W., Smith D. E., et al. Thickness of proximal ejecta from the Orientale Basin from Lunar Orbiter Laser Altimeter (LOLA) data: Implications for multi-ring basin formation // Geophysical Research Letters. 2011. V. 38(17). L17201.
[6] Housen K. R., Schmidt R. E., Holsapple K. A. Crater ejecta scaling laws: fundamental forms based on dimensional analysis // Journal of Geophysical Research. 1983. V. 88 (B3). P. 2485–2499.
[7] Sharpton V. L. Outcrops on lunar crater rims: Implications for rim construction mechanisms, ejecta volumes and excavation depths // Journal of Geophysical Research: Planets. 2014. V. 119 (1). P. 154–168.
[8] Smith D. E., Zuber M. T., Jackson G. B., et al. The lunar orbiter laser altimeter investigation on the lunar reconnaissance orbiter mission // Space Science Reviews. 2010. V. 150 (1–4). P. 209–241.

ON ORIGIN AND AGE OF MARE ORIENTALE ON MOON

A.A. Barenbaum[1], M.I. Shpekin[2]
[1] *Oil and Gas Research Institute RAS, Gubkin str. 3, Moscow, 119333, Russia, azary@mail.ru;*
[2] *Kazan Federal University, Kremlyovskaya 18. Kazan, Tatarstan 420008, Russia, michaels1@yandex.ru.*

KEYWORDS:
Orientale basin, Mare Orientale, galactic comets.

ANNOTATION:
It is concluded that Mare Orientale was formed ~1 Ma at last bombing of Moon by galactic comets of Orion-Cygnus jet stream. To substantiate this conclusion, we used measurements of flux density comets in this jet stream, new explaining of giant South Pole-Aitken basin origin, as well as size-distribution of large craters in the Mare Orientale.

INTRODUCTION:
Mare Orientale is the central part of large multi-ring shock basin (figure 1) with coordinates of the center – 19°54′ S and 94°42′ W.

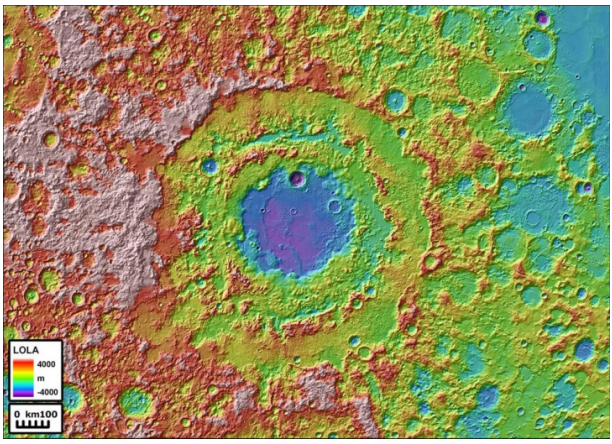


Fig. 1. Mare Orientale basin

In structure of Orientale Basin, three displaced rings can be distinguished, each of which has its own level of surface height: one outer – Montes Cordillera with diameter of 930 km and two inner – Montes Rook. The height of Montes Rook is about +6 km above the surrounding terrain, and diameter of their outer ring is 650 km. The central part of basin with diameter of 320 km has average elevation heights of –4.0 km. The sections between outer and inner rings of Montes Rook are at elevations from –2.0 to –2.5 km.

The thickness of lava in Mare Orientale is small, probably less ≈1 km, which is less than that of other seas in visible Moon hemisphere.

It is believed [1] that Orientale basin originated about 3800 Ma when Moon collided with a large asteroid. Modeling has shown [y] that the asteroid had a diameter of about 64 km and fly at a speed of about 14 km/s. The volume of ejected rocks was no less than $(3.4\pm0.2)\times10^6$ km^3 [2].

A NEW APPROACH TO SOLVING THE PROBLEM:
In the works [3–8] we showed that large craters and sea basins on Moon, as well as on Mars and Mercury, were created did not by falls of interplanetary asteroids, as today is believed [9], but at result of bombardments by high-speed comets of Galaxy origin. The bombardments are in nature of intense cometary showers lasting of 1–5 mln years, which occur during the periods of Sun's stay in jet streams and spiral arms of Galaxy and are repeated after

20–37 mln years. Wherein, after 150 mln years, galactic comets alternately bombard southern and northern hemispheres of planets [3].

As a result, most craters 10–180 km in diameter and basins larger than 180 km in size on Moon, Mars and Mercury arose during the last one and to a lesser number during the two–three previous cometary bombardments, when comets mostly fell in the southern hemisphere of planets.

The last bombardment occurred in period T from 5 to 0.7 Ma, when Sun was in the nearest to it jet stream of galactic comets – in Orion-Cygnus branch. Comets consisted mainly of water ice with density of ≈1 g/cm^3, had diameter of ~0.1÷3.5 km, mass ~10^{12}÷10^{17} g and energy ~10^{20}÷10^{25} J. They had exponential distribution in diameters, moved relative to Sun at speed of 450 km/s and bombarded mainly southern hemisphere of planets. According to our estimates [7], comets flux density was $\Phi \approx 5\times10^{-10}$ (year km^2)$^{-1}$, and their falls density on Moon, Earth and other planets was ≈2×10^{-3} km^{-2}.

Given the high density of falls of galactic comets, their craters can overlap each other, which increase the final size and depth of the impact structure. We called this mechanism of formation of the largest craters and sea basins by comets "cumulative" [5]. In [8], we explained by this mechanism origin of the South Pole -Aitken basin on Moon, and in this work we explain to them later formation of the Orientale Basin.

MARE ORIENTALE BASIN AGE:

When determining Mare Orientale basin age, we must take into account three circumstances:

1) The Orientale basin is located in zone of rock ejection during the South Pole -Aitken basin origin, which, according to our data, was finally formed as a result of last cometary bombardment in the period T from 5.0 to 0.7 Ma. Consequently, the Mare Orientale basin age cannot exceed 5 mln years.
2) With basin diameter D = 930 km, bombardment duration T = 4.3 mln years, and comet falls density of $\Phi = 5\times10^{-10}$ (year km^2)$^{-1}$, $N = \pi D^2 \Phi T/4 = 1.5\times10^3$ comets could have fallen on basin area. This is more than enough to create it.
3) However, Mare Orientale basin could arise both at the beginning of last cometary bombardment and at its end. To clarify this time, consider density of cometary craters in Mare Orientale. In figure 2 [10] shows R-distribution of craters in several basalt seas, as well as measured by Zond-8 on continents.

The cometary craters in figure 2 occupy the region D>7 km. The density of such craters in all sea basins is lower than on continents, and in Mare Orientale this difference is ~15 times. If we assume that during bombardment the frequency of galactic comets falling was constant, all cometary craters in Mare Orientale could have formed during time $\Delta t \approx T/15$ ~0.3 mln years before of bombardment end. Thus, the solidification time of basalts in Mare Orientale has only ~1 mln years.

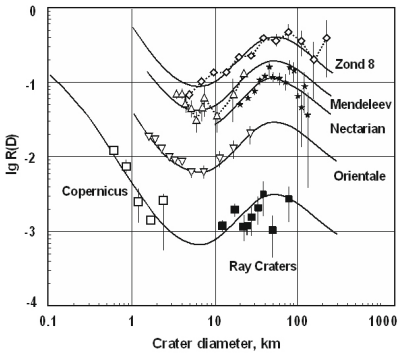


Fig. 2. R-distribution of craters with diameter of 0.01 to 200 km in the seas of Moon as well as measured by automatic station Zond-8. Solid curves is approximation of crater distributions [10]

CONCLUSION

1. The Mare Orientale basin was not formed as a result of the impact of a single cosmic body 3.8 billion years ago [1], but last bombardment of Solar System by galactic comets of Orion-Cygnus jet stream.
2. Localization of Mare Orientale at the edge of zone of rock ejection from South Pole -Aitken basin; multi-ring structure of Mare Orientale basin with misaligned position of centers of rings; low thickness of basaltic lavas, as well as reduced density of cometary craters in basin central region, we explain by emergence of basin not at beginning of cometary bombardment, but closer to its end. Thus, we believe that Mare Orientale Basin was finally formed ~1 Ma and is therefore one of youngest large impact structures on Moon.

REFERENCES:

[1] Zuber M.T. et al. Gravity field of the Orientale basin from the Gravity Recovery and Interior Laboratory Mission // Science. 2016, Vol. 354, Is. 6311, pp. 438-441.
[2] Johnson B.C. et al. Formation of the Orientale lunar multiring basin // Science. 2016. Vol. 354, Is. 6311, pp. 441-444.
[3] Barenbaum A.A. Galaxycentric Paradigm in Geology and Astronomy, 2010, (PH: Librokom, Moscow).
[4] Barenbaum A.A., Shpekin M.I. Problem of lunar mascons: an alternative approach // J. of Physics: Conf. Ser. 2018. 946. 012079.
[5] Barenbaum A.A., Shpekin M.I. Cumulative formation of mares and mascons on Moon by galactic comets // Night Moscow Solar System Symp., 2018, 9MS3-PS-81.
[6] Barenbaum A.A., Shpekin M.I. Origin and formation mechanism of craters, seas and mascons on the Moon // J. of Physics: Conf. Ser. 1147, 2019, 012057. Barenbaum A.A., Shpekin M.I. Problems of interpretation crater data in the Solar System // Tenth Moscow Solar System Symp., 2019, 10MS3-PS-50.
[7] Barenbaum A.A., Shpekin M.I. Estimation of the flux density of galactic comets in the Orion-Cygnus branch based on number of shield volcanoes on Venus, craters on Mars and marine basins on the Moon // J. of Physics: Conf. Ser. 2021. 1787. 012021.
[8] Barenbaum A.A., Shpekin M.I. The problem of the «South Pole-Aitken» basin formation // Eleventh Moscow Solar System Symp. 2020. 11MS3-MN-PS-12.
[9] Melosh H.J., Freed A.M., et al. The origin of lunar mascon basins // Science. 2013, Vol. 340, Is. 6140, pp. 1552-1555.
[10] Neukum G., Ivanov B.A., Hartmann W.K. Cratering records in the inner Solar System in relation to the lunar reference system // Space Science Reviews, 2001. Vol. 96 (1-4), pp. 55-86.

A STUDY ON THE VISIBILITY LIMIT OF STELLAR OCCULTATIONS WITH THE MOON AT SUNSET AND SUNRISE

M. Madani[1], A. Poro[1], et al.
[1] *The International Occultation Timing Association Middle East Section, info@iota-me.com.*

KEYWORDS:
Observation, Timing, Occultation, Moon

INTRODUCTION:

In this study, we tried to find new criteria for both the degree of visibility and timing of the occultation of stars by the Moon at sunset and sunrise in the presence of the sky backlight. To do so, distinct moon phases were observed in different weather conditions and locations, always taking into account important parameters such as the apparent magnitude of the star, the altitude of the sun below the horizon, as well as the angular separation between the sun and the moon. We made program observations that proved that the previous criteria defined could be improved. Following, additional observations were performed to determine the new visibility limit of the stellar occultation by the Moon at a specific time.

ANALYSIS OF TOPOGRAPHIC ROUGHNESS VS WEH CONCENTRATION IN THE REGOLITH OF THE LUNAR SOUTH POLAR AREA

Yuan Li[1], A.T. Basilevsky[2], M.A. Kreslavsky[3], A.B. Sanin[4], I.G. Mitrofanov[4], M.L. Litvak[4], LiGang Fang[1]

[1] *Suzhou vocational University, SuZhou, 215009, China;*
[2] *Vernadsky Institute of Geochemistry and Analytical Chemistry, RAN, 119991, Moscow, Russia;*
[3] *Earth and Planetary Sciences, University of California Santa Cruz, Santa Cruz, CA, 95064, USA;*
[4] *Institute for Space Research, RAN, Moscow 117997, Russia.*

KEYWORDS:
Moon, PSRs, WEH, Roughness, Slope

1. INTRODUCTION

Permanently shadowed regions (PSRs, Fig.1) in the lunar polar regions have potential ability to retain water ice as low temperature (< 110 K). Several instruments on board the lunar spacecrafts have shown that a small amount of hydrogen components exist in the PSRs. Because of the scientific interests and the future construction of lunar base, Russia,China and USA planed their lunar polar mission in the near future. During the rover landing, the surface geographic situation is important for the mission success. Here we analysis whether and how the surface morphologic roughness in the lunar south pole area correlates with concentration of water equivalent hydrogen (WEH, Fig.2).

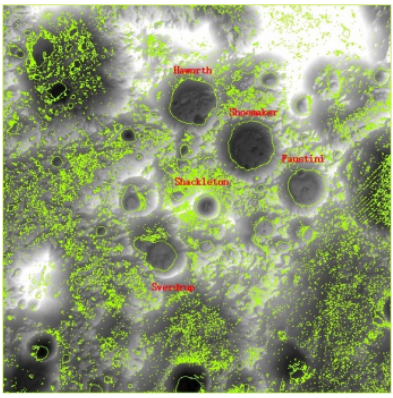


Fig. 1. Digital terrain model of five study craters with the boundaries of permanently shaded regions (light green lines) overlaid.

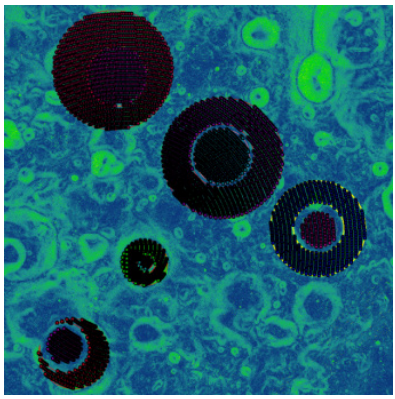


Fig. 2. WEH estimation data points at the five study crater walls and floors that we use for the following analysis and comparison, are shown on the slope map.

2. DATA ANALYSIS

We consider floors and walls of 5 large (D>20 km) and topographically prominent craters (Fig. 1 and Table 1). LOLA data with resolution of 10 /pixel is used to estimate the surface roughness and slope. Roughness map is calculated by interquartile range of curvature with circle sliding window 320 m, surface curvature is estimated by Laplacian of the elevation with baseline 20 m. Slope map is estimated in software Arcgis. The WEH concentration in the regolith top ~ 1 m with standard resolution of 10 km/pixel (Fig. 2) for five study craters come from measurements by LEND onboard LRO [2]. The median values of the surface roughness and slope, mean values of WEH at study crater floors and walls are summarized in Table 1.

Table 1

Crater name	Mean WEH at the crater wall/floor (wt%)	Median roughness at the crater wall/ floor	Median slope at the crater wall/ floor (degree)
Haworth	0.29/0.36	0.79/0.44	15/5.4
Shoemaker	0.35/0.46	0.56/0.29	15.4/3.9
Faustini	0.27/0.25	0.40/0.28	15.5/3.2
Shackleton	0.24/0.23	1.70/0.55	30.9/7.2
Sverdrup	0.27/0.29	0.65/0.27	16.8/3.2

3. RESULTS

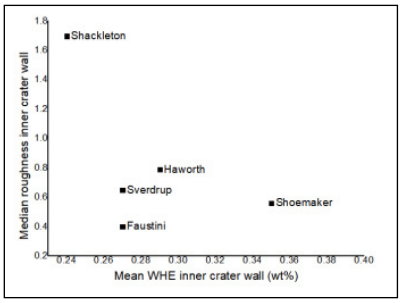


Fig. 3. Roughness vs slope at crater wall

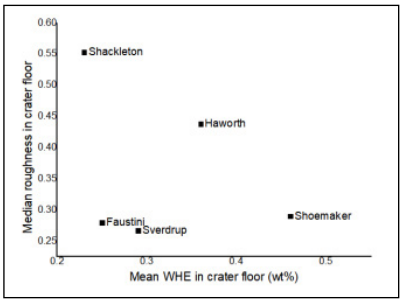


Fig. 4. Roughness vs WEH at crater floor

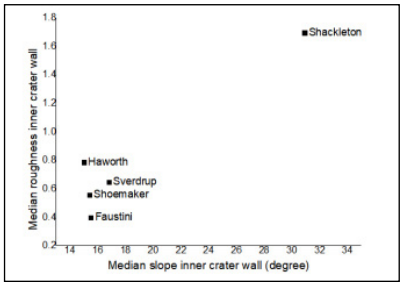


Fig. 5. Roughness vs slope at crater wall

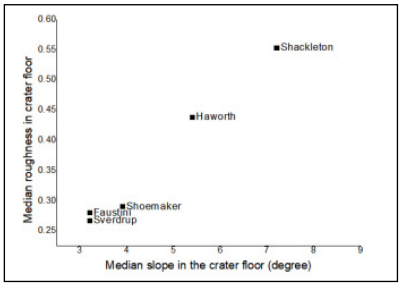


Fig. 6. Roughness vs slope at crater floor

4. DISCUSSION

There is no obvious correlation between surface roughness and WEH in Fig. 3 and Fig. 4. Especially, crater Haworh (4.18±0.02), Shoemaker (4.15±0.02) and Faustini (4.10±0.03) have similar formation age, if WEH influence the surface roughness performance, their roughness values should give an trend when their WEH change at crater wall and crater floor. However, it is not.

Formally, Fig. 5 seems to show an increase trend. If we ignore Shackleton, the situation will change. Generally, the slope of crater wall represents the tilt degree of crater wall, it usually correlates with crater degradation processes and formation age. Roughness values with 20 m baseline usually represent the surface regolith movements [3]. Therefore, we consider the roughness value depend on the tilt degree of crater wall. The larger slope value at the crater wall result in more violent regolith movements. Therefore, the crater Shackleton with obviously more tilted wall have a higher roughness value. The rest craters have the similar tilted wall in a narrow range of roughness value. Over time, most of fine regolith material on the crater wall surface move down, waiting for the next violent locally shock by subsequently geological events. This probably is the potential reason for the relatively old craters with various roughness values. In the future, more local geological analyses are needed.

Fig. 6 presents an obvious increase trend between surface roughness and slope. The change of roughness at crater floor (or at the surface horizontally) can be considered as a measurement of surface slope. This indicate that for lower down to several degree, the surface regolith movements are slow in time scale.

5. CONCLUSION

(1) WEH or WEH with lower content of < 0.5 wt% do not show any significant influence in the surface roughness performance.

(2) Surface morphology and activities at the baseline of 20 m seems mostly influence by surface slope but not WEH.

(3) More deeply studies on the effects of WEH in the regolith movements are needed in the future.

ACKNOWLEDGEMENTS:

This work was supported by the JiangSu education department of China under Grant 20KJD160001. A.T. Basilevsky was supported by the Russian Science Foundation grant № 21-17-00035: Estimates of the rate of exogenous resurfacing on the Moon.

REFERENCE:

[1] K. Watson et al. (1961) J. Geophys. Res. 66 (9), 3033-3045.
[2] I. G. Mitrofanov et al. (2010a), Space Sci. Rev. 150, 183-207.
[3] M. A. Kreslavsky et al. (2013), Icarus, 226(1), 52-66.

MORPHOMETRIC PARAMETERS FOR THE NEW CATALOG OF MERCURY CRATERS

V.A. Rotaru[1], I.Yu. Zavyalov[1], A.Yu. Zharkova[1, 2], M.M. Kolenkina[1], N.A. Kozlova[1], E.A. Feoktistova[2], Zh.F. Rodionova[2], A.A. Kokhanov[1]

[1] *Moscow State University of Geodesy and Cartography, Gorokhovskiy per. 4, Moscow, Russia, 105064, vladimrotaru@yandex.ru.*

[2] *Sternberg Astronomical Institute Moscow University, Universiteytskiy pr. 13, Moscow, Russia, 119234, a_zharkova@miigaik.ru.*

KEYWORDS:
Mercury, craters, morphometric parameters, algorithms of automation, planetary relief, planetary cartography

INTRODUCTION:
The main goal of our work is to improve our new catalog of Mercury craters – to supplement it with new morphometric parameters (crater depths and slopes) using special automated algorithms, as well as to create maps for visualization and spatial analysis of the obtained data.

DATA:
The new catalog of Mercury craters [1], created by Extraterrestrial Laboratory of Moscow State University of Geodesy and Cartography (MExLab) and Sternberg Astronomical Institute Moscow University (SAI), contains a morphological descriptions for 16599 craters more than 10 km in diameter and values of morphometric parameters of 22831 craters less than 10 km. Thus, it improves previously created catalogs, including the catalog of Mercury craters of Brown University, USA [2]. The new catalog includes more than 39000 craters with diameters from 4–5 km, as well as a few craters that are smaller. Morphological descriptions will only be added for craters larger than 10 km in diameter.

For morphometric calculations we used: the global digital elevation model (DEM) of Mercury with a resolution of 665 m/pixels [3], DEM for the quadrants H-3, H-5, H-6, H-7 – 222 m/pixels [4] and additional DEM for the north pole of Mercury H-1–250 m/pixels.

DEFINING MORPHOMETRY AND CREATING MAPS:
The values of the crater slopes allow us to approximately calculate the age of the crater which used for scientific analysis of the processes that form the Mercury surface, as well as for solving engineering problems related to the study of Mercury in the future (for example, spacecraft landings). In this abstract, the calculation of crater slopes was performed in the ArcGIS program using DEM for the entire surface of Mercury. In this case, the maximum slope within the crater under consideration is determined.

The measurement of crater depths, as in the case of crater slopes, helps us to understand the age of the crater and gives an idea of the nature of the underlying surface and its features. To automate the measurement of crater depths, a special program was created in the Python programming language using the GDAL library. For successful processing the following data are required: 1) Four relief profiles of crater with a length of 1.5 of this crater diameter. 2) Points of rim's inflection or boundaries of the rim (Fig. 1). 3) Slopes of crater after their correction if it's needed (inflection points must be on the same height).

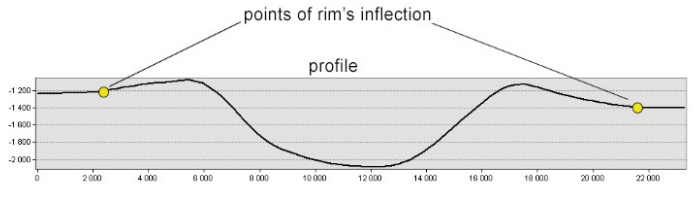


Fig. 1

The depth calculation is performed after the crater alignment: the crater depth in our case is defined as a perpendicular from the level of the underlying surface to the deepest point of the crater. The crater depth is calculated as the average value of the obtained profile depths. The search for the central peak is also performed after the crater is leveled: firstly the search for the points of inflection of the rim is carried out, and then, if such points are located, parameters of central peak (its diameter/height) are also can be calculated (Fig. 2).

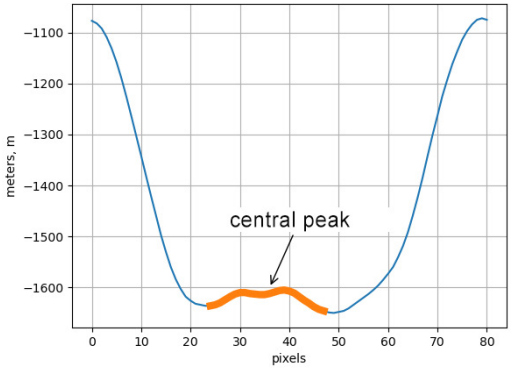


Fig.2

Maps based on new data were created in the ArcGIS software. For maps of slopes and crater depths, an equidistant cylindrical projection was chosen, because it has small distortions at the equator and in its middle latitudes, where high-resolution DEMs are mainly located.

Crater density maps are created to display the average number of craters per 10,000 km^2 by high-resolution DEMs (222 m/pixels). To create a raster layer by craters' centroids and buffers, the Point Density tool was used (https://desktop.arcgis.com/en/arcmap/10.3/tools/spatial-analyst-toolbox/how-point-density-works.html).

MAIN RESULTS:

24 maps were created, including maps that show the density, depth and slopes of craters in the H-3, H-5, H-6, H-7 quadrants. These maps clearly demonstrate the relationship between the relief of the surface of Mercury, visible on the images, and values of calculated morphometric parameters, which cannot be estimated by human eye.

The greatest slopes of craters are found in relatively small craters located near large craters. This may be due to emissions and further distribution of debris during the impact formation of the large crater. Small fragments and avalanche-like granular flows fell out and settled near the large central crater, forming an "uneven" shaft with small craters around it [5]. A similar relationship can be traced in the depths of craters. Than larger the crater, than deeper it is. This is also can be due to the peculiarities of the impact formation of the crater and its further geological development. Studying the relief of the surface of Mercury we can rely on similar studies of the Moon, since these two celestial bodies have similar surface structure and conditions of their formation and development [6].

FINANCING:

E.A. Feoktistova, I.Yu. Zavyalov, A.Yu. Zharkova, A.A. Kokhanov, M.M. Kolenkina, N.A. Kozlova, Zh.F. Rodionova were supported by Russian Foundation for Basic Research (RFBR), project No 20-35-70019.

REFERENCES:

[1] Feoktistova E.A., Zharkova A.Yu., Kokhanov A.A., Rodionova Zh.F., Rotaru V.A. Compilation of a new global catalog of Mercury's craters // The 11th Moscow Solar System symposium (11MS-3), Space Research Institute, Moscow, Russia, October 5–9, 2020.

[2] Fassett C.I., Kadish S.J., Head J.W., Solomon S.C., Strom R.G. The global population of large craters on Mercury and comparison with the Moon. Geophys. Res. Lett., 2011. 38, L10202, doi: 10.1029/2011GL047294.
[3] Becker K.J., Robinson M.S., Becker T.L., Weller L.A., Edmundson K.L. Neumann G.A., Perry M.E., Solomon S.C. First Global Digital Elevation Model of Mercury // 47th Lunar and Planetary conference, The Woodlands, Texas, March 21–25, 2016, Abstract # 1903.
[4] Preusker F., Oberst J., Stark A., Matz K–D., Gwinner K., Roatsch T. HighResolution Topography from MESSENGER Orbital Stereo Imaging – The Southern hemisphere // EPSC Abstracts, 2017, Vol. 11, EPSC2017–591.
[5] Xiao Z., Komatsu G. Impact craters with ejecta flows and central pits on Mercury // Planetary and Space Science. 2013. 82–83:62–78, doi: 10.1016/j.pss.2013.03.015.
[6] Karachevtseva I., Kreslavsky M., Basilevsky A., Gusakova E. Morphometry of Small Impact Craters in the Lunokhod 1 Study Area // Planetary and Space Science. 2013. 92:1174, doi: 10.1016/j.pss.2013.12.016.

GEOLOGICAL ANALYSIS OF THE LUNAR CRATER PLASKETT

E. A. Grishakina[1], M. A. Ivanov[1]
[1] *Vernadsky Institute of Geochemistry and Analytical Chemistry, RAS, 119991, Kosygin St. 19, Moscow, Russia, grishakina@geokhi.ru*

KEYWORDS:
Moon, Plaskett crater, geological map, North Pole, boulders, impact crater, central peak.

The north polar region of the Moon is of special interest because of significant abundance of hydrogen-containing compounds which may include water ice in permanently shadowed areas [1]. The North Pole region does not have the very rugged terrain seen at the South Pole. This provides a number of advantages when planning a lunar base. According to rough estimates of water ice deposits based on Chandrayan data, the most significant reserves are found in the Plaskett crater [2]. Besides, location of the crater (81.63° N, 176.71° E) is within the libration zone. This makes the crater to be an important site for an autonomous manned extraterrestrial base that in future will be established also on Mars.

The Plaskett is an impact crater 114.34 km across, it has steep inner walls, a relatively flat bottom, and a central peak. In order to refine a synoptic geological map of the North Pole in the Plaskett crater area, we use the high-resolution data from the LRO narrow-angle camera (NAC) to compile a mosaic of images. In this mosaiced dataset, we have defined several geomorphological units by their morphology, abundance of boulders, and degree of cratering. Within these units, we have counted boulders that can be recognized in the NAC images in order to assess their size-frequency distribution (SFD) and quantify the meter-scale roughness of the mapped units and estimate effect of the slope processes acting in the region of investigation.

The normal distribution of boulders in the study areas is an indicator of the predominance of one random process that causes the current state of the rockiness, – it is the impact re-working of surface material. The different shape of the curves of the SFD of boulders, shown in the graphs (fig. 1), demonstrates the distinct influence of slope processes on the surface rockiness depending upon varying degrees of the surface slopes on the inner walls and the central peak of the crater [3].

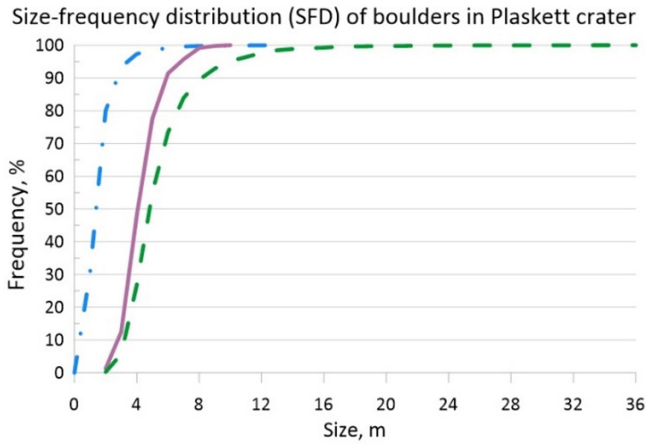


Fig. 1. Size-frequency distribution (SFD) of boulders in Plaskett crater: blue – inner walls, purple – floor, green – central peak

ACKNOWLEDGEMENTS:
The work is supported by the Russian Science Foundation grant № 21-17-00035: Estimates of the rate of exogenous resurfacing on the Moon.

REFERENCES:

[1] Sanin A.B., Mitrofanov I.G., Litvak M.L. et al. Hydrogen distribution in the lunar polar regions // Icarus. 2017. V. 283. P. 20-30.
[2] Grishakina E.A., Slyuta E.N. Probable Reserves of Water Ice in the Lunar Polar Regions // 52nd Lunar and Planetary Science Conference. 2021. Abs. 1882.
[3] Grishakina E.A., Ivanov M.A. Rock abundance in the Plaskett lunar crater // Proc. 11th Moscow Solar System Symposium, Moscow: IKI RAS. 2020. 11MS3-MN-PS-8.

ANALYSES OF OBSERVATIONAL PARAMETERS IN THE TIMING ACCURACY OF LUNAR OCCULTIATION

E. Bozorgzadeh[1], A. Poro[1], et al.
[1] *The International Occultation Timing Association Middle East Section, info@iota-me.com.*

KEYWORDS:
Observation, Timing, Occultation, Moon

INTRODUCTION:

In this observation project named APTO, teams participating, observed the lunar occultations. A total of 9 stars were observed and 20 were reported. The Occult 4 software was used to predict these observations. And we designed SkyTiming 2 application for this project for android smartphones based on GPS. Also, ten of the observational parameters in the project report series were examined. This indicates that, in most cases, the expected results are obtained.

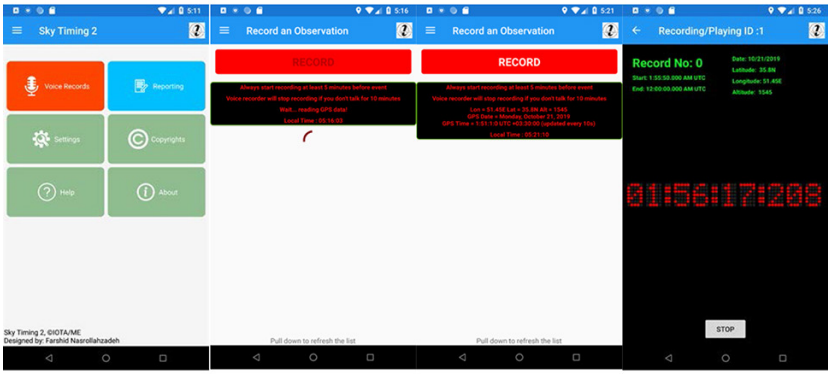


Fig. 1. Left to right: Main screen, recording screen waiting for GPS data, recording screen after received GPS data, recording screen in action

COMPARISON OF THE CRATERING OF THE NORTH AND SOUTH POLAR REGIONS OF THE MOON

N.A. Slodarzh[1], Zh.F. Rodionova[2]
[1] *Ural Federal University, Mira street 19, Ekaterinburg, Russia, nikolai.slodarzh@yandex.ru;*
[2] *Sternberg Astronomical Institute Moscow State University, Universitetskiy pr. 13, Moscow, Russia, jeanna@sai.msu.ru*

KEYWORDS:
Moon, craters, morphometry, measurements, coordinates, diameters, angles of inclinations, statistical analysis, DEM.

INTRODUCTION:
Morphometric catalogs of craters with diameters of 10 km and more have been created for the northern and southern polar regions limited by latitudes +/– 60° [1, 2]. Input data from a digital model of relief was Lunar Orbiter Laser Altimeter (LOLA) of Lunar Reconnaissance Orbiter (LRO) [3]. The catalogs define: coordinates of craters, diameters, angles of inclinations of inner and outer slopes, maximum and minimum heights of the bottom and crests of ramparts, depth and depth-to-diameter ratios. Using the ArcGIS Desktop and the CraterTools add-on module, 1 320 craters for the South Polar region and 2 302 craters for the North Polar region were digitized and measured.

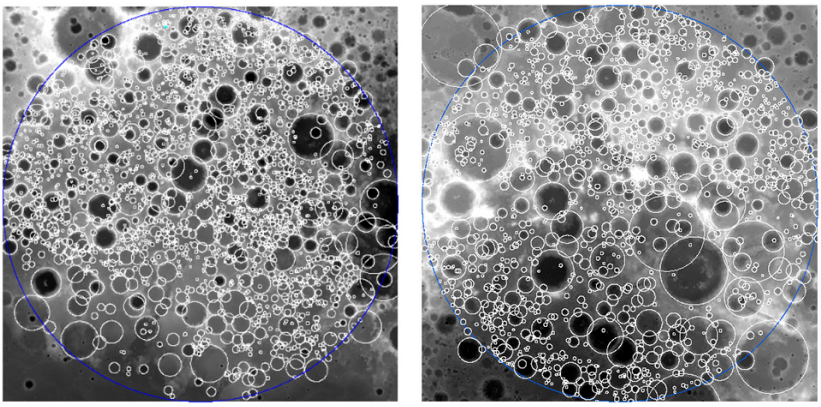


Fig. 1. DEM of the North and South polar regions and digitized craters.

RESULTS:
Figure 2 shows the graphs of the cumulative distribution of craters in the southern and northern polar regions of the Moon. The approximate age of the surfaces was determined from them - in both cases it was (4.30 ± 0.02) billion years.

The Figures 3, 4 show graph of crater depth to diameter ratio (d/D). The graph adds lines corresponding to d/D = 0.1, d/D = 0.2 and third order polynomial trend line.

CONCLUSION:
A technique has been developed for the automated creation of morphometric catalogs of lunar craters on the basis of a digital elevation model constructed from altimetry data from the Lunar Reconnaissance Orbiter spacecraft.

Morphometric catalogs of craters with a diameter of 10 km and more have been created for the northern and southern polar regions, limited by latitudes +/- 60°. The catalogs define: coordinates of craters, diameters, angles of inclination of inner and outer slopes, maximum and minimum heights of the bottom and crests of ramparts, depths and depth-to-diameter ratios.

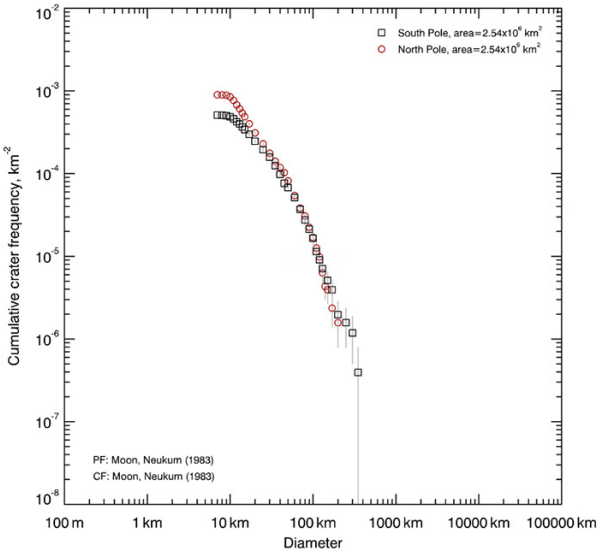


Fig. 2. Distribution of the craters and surface age determination using Craterstats 2.

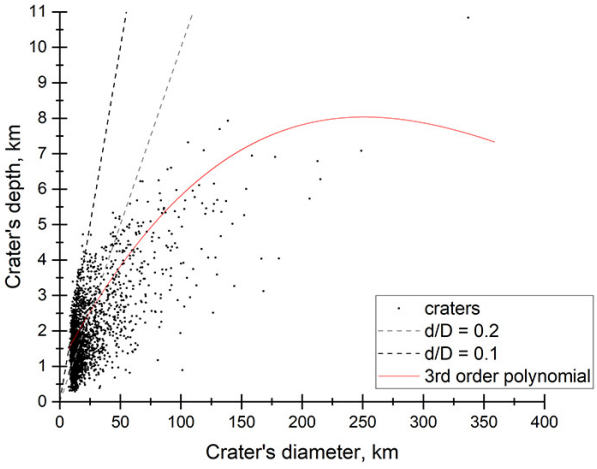


Fig. 3. Graph of crater depth to diameter ratio (d/D) for northern polar region.

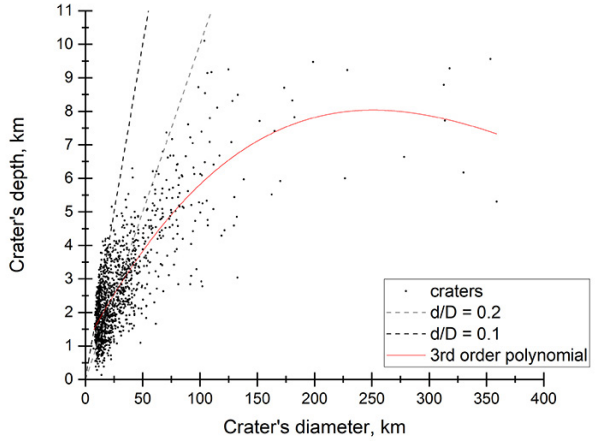


Fig. 4. Graph of crater depth to diameter ratio (d/D) for southern polar region.

In the northern polar region, 2,302 craters were found, in the southern one, 1,323 craters, and in the northern hemisphere there were more craters with a diameter of 10 to 30 km (almost twice).

In the southern polar region, on average, the inner slopes turned out to be steeper than in the northern region.

The age of the surfaces of the northern and southern polar regions, formed 4.3 billion years ago, was determined.

The height differences of the crests of the crater ramparts increase with the increase in the crater diameters.

REFERENCES:

[1] Slodarzh N.A., Rodionova Zh.F.Morfometricheskiy Katalog Kraterov Severnoy Polyarnoy Oblasty Luny. 2021,78 p. //Site otdela issledovaniy Luny I planet SAI MSU.
[2] Slodarzh N.A., Rodionova Zh.F., Levitskaya T.I. Morfometricheskiy Katalog Kraterov Yuzhnoy Polyarnoy Oblasti Luny 2020. 46 p.// http://selena.sai.msu.ru/Rod/Publications/morph-catalog-craters-moon/morph-catalog-craters-moon.htm.
[3] LOLA PDS Data Node .– URL: http://imbrium.mit.edu/.

EARTH AND MOON: DIFFERENT AGES OF SIMILAR WAVE TECTONICS REFLECTING THEIR UNEQUAL MASSES

G.G. Kochemasov[1]
[1] *IGEM RAS, Moscow, Staromonetny 35, kochem.36@mail.ru.*

KEYWORDS:
Earth, Moon, wave structures, similar tectonics, different masses, plate tectonics, impacts

ABSTRACT:
"Orbits make structures"-main point of the wave planetology. Earth and Moon share the same heliocentric orbit. As a result, they are similarly structured. This is substantiated by various structures: 2πR, πR, and πR/2

The Earth and Moon's tectonics are usually discerned separately. However, the wave planetology allows considering them together [1, 2]. The key point of the wave planetology is following: "Orbits make structures". The planet and its satellite share the same circumsolar orbit. That is why their structures are analogous. Wave structures are schematically presented in Fig.1-9. Actually, caused by the fundamental wave dichotomous structure of planets and satellites is long ago established: two different hemispheres-segments (Fig.1-4).Proceeding the harmonic line, take in the account the first overtone forming tectonic sectors comparable in the both bodies (Fig. 1-4).Further, the smaller structures (granules) appear. In the fig. 9 the rows of lunar ring structures are shown traditionally considered as impacts (hits). The crater chains, not obeying to random hits, are placed in the both hemispheres [2]. In addition to asymmetry of Polar regions and hemispheres (repetition of the Earth's tectonics) we give attention to the middle latitudes of the southern hemisphere where there is a repetition of uplifts and subsidences of relief. This is, most probably, due to a wave process (fig. 9, [2]).This lunar wave chain is inclined to the equator as black thick line in the north. Such wave repetition in the lithosphere is comparable to alternation of ancient cratons and oceans in the northern hemisphere of Earth [1, 2].

Conclusion: Instead of two pseudo tectonics (Earth-plates, Moon-giant impacts) we consider one common for the both bodies wave tectonics. It embraces harmonic structures of various scales- from the fundamental one to tectonic granules. New Earth-Moon wave tectonics denies terrestrial plate tectonics and lunar earlier giant impacts. School and university programmers must consider corrections.

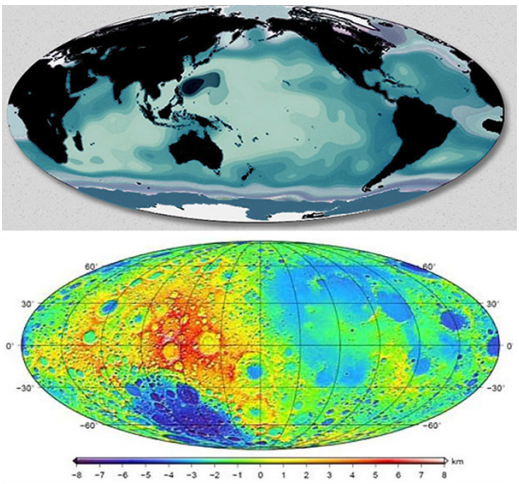


Fig. 1, 2. Dichotomy and tectonic triads of Earth (up) and Moon. Pacific-Indonesia-Indian Ocean. Oceanus Procellarum-Mare Orientale-Basin South pole-Aitken [2].

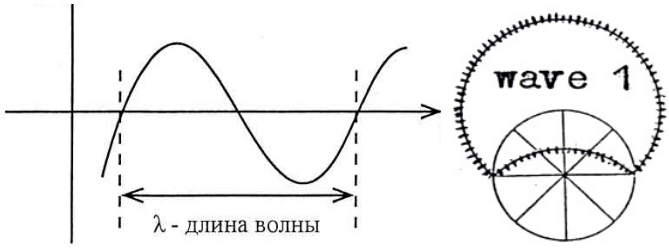


Fig. 3, 4. Fundamental wave in line and circle.

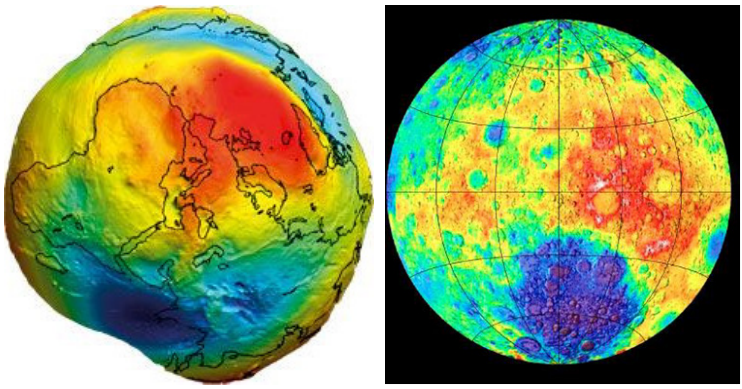


Fig. 5, 6. Geoid miima in Earth (left) and Moon.

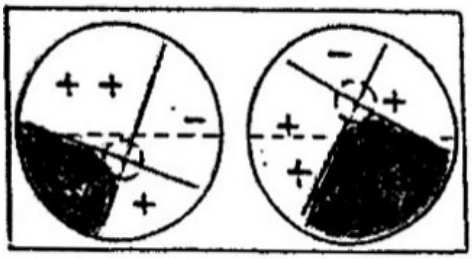


Fig. 7. Sectors in Earth (right) and Moon Black sectors-Indian geoid minimum and South pole Aitken minimu

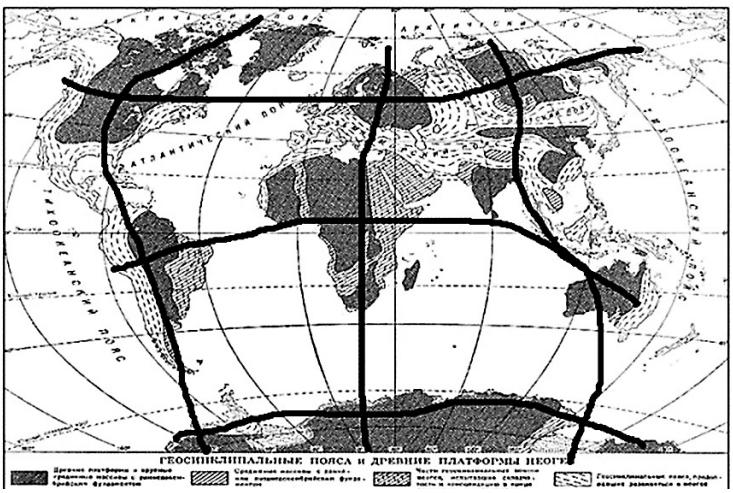


Fig. 8. Achaean cratons of Earth (granules) in net

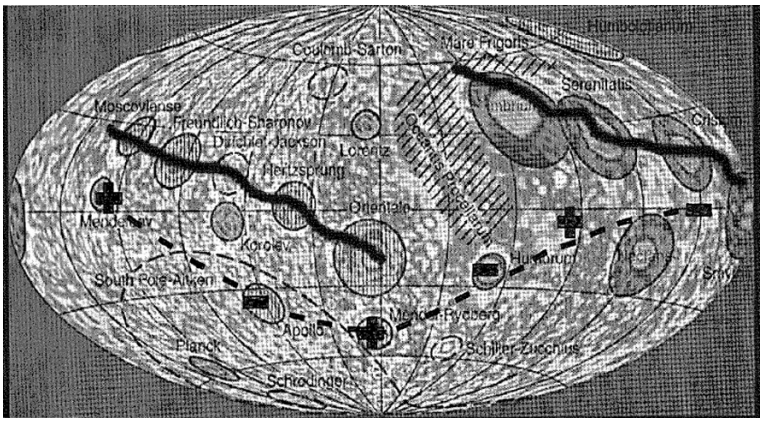


Fig.9. (below0 Lunar tectonics. Gravity map of the Moon. LPOD-Sept6-09 (www2.lpod.com)+ uplift, – subsidence in lunar relief. Mare Fecundidatis(-) – in center between Marea Crisium,Smithii, Nectaris) – Crater Ptolemaeus-Ruper Altai (+)-Mare Humorium (-) – crater Mendal-Rydberg (+) – crater Apollo (-) – Crater Mendeleev(+).

REFERENCES:

[1] Kochemasov G.G.(2014) Earth and Moon: similar structures – common origin// NCGTJournal,2014, v.2,#2, 28-38.
[2] Kochemasov G.G. (2018) Regular wave tectonics of the Moon// B.Cudnic (ed.) Encyclopedia of Lunar Science, Springer International Publishing AG, part of Springer Nature 2018. https://doi.org/10.1007.978-3-319-05546-6_121-1.

CHANG'E-5 CONFIRMS GLOBE-WIDE DISTRIBUTION OF THE CENTIMETER-SCALE RIPPLING CAUSED BY COUPLING TWO LUNAR FREQUENCIES (NEAR EARTH AND IN GALAXY)

G.G. Kochemasov[1]

[1] *IGEM of the Russian Academy of Sciences, 119017 Moscow, Staromonetny 35, kochem.36@mail.ru.*

KEYWORDS:
Chang'E-5, Moon's globe, fine rippling, lunar frequencies coupling

ABSTRACT:
Orbits make structures -a main point of the new comparative wave planetology. However, any body moves in several orbits with various frequencies simultaneously. Thus, coupling orbits is a fundamental action in nature where exist together main and side frequencies and corresponding them structures. Moon has globe wide fine (centimeter size) microwave structures and undulations as well as much larger 2πR, πR and πR/2 harmonic main structures. Galaxy rotation leaves its trace in lunar structures coupling with lunar rotations around Earth and Sun.

There are rare chances to observe fine lunar surface structures on landing sites of several probes. Among them the first was Apollo11, and then in recent years Chang'E 3&4 and now Chang'E 5 (Fig. 1–8). Landing surfaces possibly cleaned by thruster jets of landing device revealed clear crossing lineation of a few centimeters spacing and produced them granules. This very fine granulation fortunately can be calculated comparing it with a track of the Yutu' rover wheel. (~10 cm wide) or the boot imprint of N. Armstrong (~20–25 cm long) and now with the drill or leg of the Chang'e-5 . 'Orbits make structures"- a main point of the wave planetology [1–3]. Earth, as a scale, has 1-year orbiting period and corresponding granule size πR/4. Earth and its satellite both move in Galaxy with ~1/200 000 000 y. frequency. Calculations for the Moon: (1y. : 200 000 000y)πR = (1 : 200 000 000) 3.14 x 1738 km = =5.46 cm wave length for the circumsolar orbiting (or 0.46 cm wavelength for the around Earth orbiting). These waves as crosscutting centimeters long ripples one observes on the above-mentioned surfaces and, as a conclusion, on the whole Moon – far and near, south and north sides.

CONCLUSION:
Several lunar landing points, including Chang'e-5, have detailed surface images showing centimeter-size intercrossing ripples. They are results of coupling two lunar frequencies: around Earth and in Galaxy. This frequency modulation process is most common in Universe as all celestial bodies move simultaneously in several orbits with various orbital frequencies. This process [1–3] might explain various wave emissions in Universe.

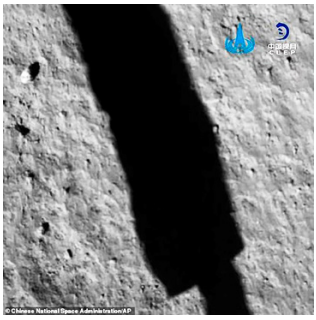


Fig. 1. 36346652-9013549-images_released_by the Chnese_guvernment_show_a_barren_scene_at-a-5_1606992823491

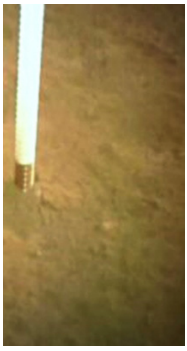


Fig. 2. A portion of and-2-2-350x 256.



Fig. 3. A portion of Rock near Foot pad



Fig. 4. A portion of lunar-surface-change-5-100-percent-1536x806-1-900x472.

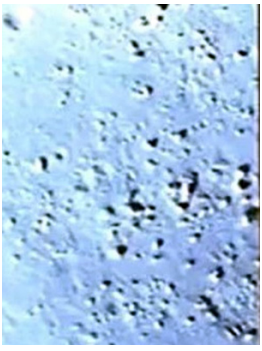


Fig. 5. A portion of land-2-2-350x256. Equal diam. “craters” mark subsiding parts of crossing ripples.



Fig. 6. Apollo 11, footprint of N. Armstrong

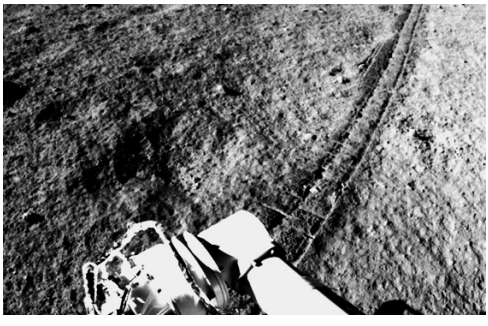


Fig. 7. Fine rippling near the Chang’e-3.



Fig. 8. Fine rippling near the Chang'e-4.

©Fig. 1–5 3634 Chang'e-5 images

REFERENCES:

[1] Kochemasov G.G. (2016) Gamma-ray emission in the Universe – a possible explanation by the wave modulation // Gamma-Ray Burst Symposium (2016), 4107.pdf.
[2] Kochemasov G.G. (2018) Modulated wave frequencies in the Solar system and Universe // Journal of Physics and Application 12(4): 68-75, 2018. Doi:10.13189/ujpa.2018.120402.
[3] Kochemasov G.G. (2019) Modulated lunar orbiting frequencies and corresponding them structures (Chang'E 3 & 4 discoveries) // The 4th LDSE2019, China, Abstract Volume, 100-102.

LASER IONIZATION MASS SPECTROMETER LASMA-LR ONBOARD LUNA-25 AND LUNA-27 SPACECRAFT

V.S. Cheptsov[1], A.E. Chumikov[1], P. Wurz[2], N.G. Managadze[1], G.G. Managadze[1]

[1] *Space Research Institute of Russian Academy of Sciences, Profsoyuznaya str. 84/32, Moscow, 117997, Russia, cheptcov.vladimir@gmail.com;*
[2] *Physics Institute, University of Bern, Sidlerstrasse 5, 3012, Bern, Switzerland.*

KEYWORDS:
LASMA; element composition; isotope composition; time-of-flight mass spectrometry; Lunar regolith.

LASMA-LR is laser ionization time of flight mass spectrometer able to perform analysis of elemental and isotopic composition of solid samples (regolith and dust) with high accuracy and high spatial resolution. Its predecessor, the LASMA instrument, was onboard Phobos-Grunt spacecraft [1]. The measurement technique by LASMA-LR is based on the sample atomization and ionization by a laser pulse of 7 ns duration and with a power density of ~10^9 W/cm^2 provided by a Nd:YAG laser operating at 1.064 μm wavelength. The ions are formed in the plasma plume induced by the laser pulse. The free spatial expansion of the plume allows the ions to enter into the time-of-flight mass analyzer, where they are mass-per-charge separated by their time of flight. The ions separated in time, after their reflection in the retarding field of the electrostatic reflector, are registered by a secondary electron multiplier. The recorded the signal is processed by an analog-to-digital converter and is stored in the device's memory as a single spectrum for each laser shot. By the time of flight of ions and signal intensity, it is possible to determine ions masses and relative concentrations [1,2].

The instrument is accepted for Luna-Resource-1 (Luna-27) and Luna-Glob (Luna-25) missions [3], and its' main goal is to provide characteristic of the regolith's element composition and to identify rock types in the landing sites located in poorly studied areas of the lunar South pole region. LASMA-LR allows the analysis of ions in a wide range of masses – 1–250 a.m.u. Mass resolution (M/ΔM) is at least 300, absolute mass detection limit at analysis of one spectrum is better than 5×10^{-14} g, dynamic range of one spectrum is not less 10^4. The limits of detection for element analysis are at least 50 ppmA (ppm atomic fraction) in one mass spectrum and 5 ppmA at analysis of an accumulation of 100 mass spectra. Preliminary calibrations have shown that the relative error for the concentration of matrix elements measurements does not exceed 10% at analysis of ~100 mass spectra [4,5].

LASMA-LR has compact dimensions (130×206×254 mm), low weight (2.8 kg) and low mean operating power consumption (≤ 8 W). Structurally, the instrument is in the form of a single unit, which includes an electronics module, a mass analyzer, a laser emitter module with laser focusing system (laser optical module), and a sample receiving device. It is able to operate in a wide temperature range from –50˚C to +50˚C. Service life of the instrument is limited by the laser service life and is at least 100,000 shots.

The data which will be obtained by LASMA-LR through Luna-25 and Luna-27 missions will contribute to the study of fundamental issues related to the conditions of the Moon formation and its evolution, as well as to the solution of a number of applied problems of the Moon exploration.

REFERENCES:

[1] Managadze G.G. et al. Study of the main geochemical characteristics of Phobos' regolith using laser time-of-flight mass spectrometry // Solar System Research. 2010. V. 44. № 5. P. 376–384.

[2] Managadze G.G. et al. A new method and mass-spectrometric instrument for extraterrestrial microbial life detection using the elemental composition analyses of Martian regolith and permafrost/ice // Astrobiology. 2017. V. 17. № 5. P. 448-458.
[3] Mitrofanov I.G. et al. Science program of Lunar Landers of “Luna-Glob” and “Luna-Resource” missions // Lunar and Planetary Science Conference. 2011. V. 42. P. 1798.
[4] Chumikov A.E. et al. Accuracy of analysis of the elemental and isotopic composition of regolith by laser time-of-flight mass spectrometry in the future Luna-Glob and Luna-Resurs-1 missions // Solar System Research. 2020. V 54. № 4. P. 288-294.
[5] Chumikov A.E. et al. Design, characteristics and scientific tasks of the LASMA-LR laser ionization mass spectrometer onboard Luna-25 and Luna-27 space missions // International Journal of Mass Spectrometry. 2021. DOI: 10.1016/j.ijms.2021.116676.

ON THE CAPTURE OF PROTOPLANETARY BODIES DURING THE FORMATION OF THE EARTH-MOON SYSTEM

V.N. Afanasyev[1, 2], G.V. Pechernikova[1]
[1] *Institute for Dynamics of Geospheres, Russian Academy of Science, Leninsky Prospect 38-1, Moscow, Russia, 119334;*
[2] *Moscow Institute of Physics and Technology, Dolgoprudniy, Russia, vladimir.afanasev@phystech.edu.*

KEYWORDS:
Moon, protoplanetary bodies, protolunar disk, accretion, evolution, formation, origin, capture probability, planetesimals, collisions

INTRODUCTION:
The co-accretion hypothesis of the origin of the Moon [1,2] assumes the joint formation of the Moon and Earth. Such scenario of the Moon formation is the natural consequence of the widely recognized Safronov's theory of the Solar system's formation from protoplanetary accretion disks [3]. As Earth accreted mass, the potential well and the Hill's sphere of Earth grew. Planetesimals from Earth's feeding zone constantly collided in the Hill's sphere of early Earth. Some of the fragments as a result of collisions were captured in the near-Earth orbit, which ultimately led to the formation of the protolunar disk. Subsequent accretion of particles in this disk gradually formed the Moon. One of the key issues of the co-accretion hypothesis is the quiet rough estimation of the capture probability [4]. The aim of our study is to calculate the fraction of the captured mass in paired collisions of planetesimals.

MODELS AND METHODS:
In our model, the collision model and the capture criterion completely determined the fraction of captured matter, i.e., the probability of capture. Both components may differ depending on the approach. The collision model approximates the outcome of the collision. We assumed that after collision of two bodies cloud of debris was formed. We considered the cloud of debris as a material dot, moving with velocity of the center mass of colliding bodies. The capture criterion is a set of conditions which determine whether a fragment will be captured. There are three major conditions. The first is the energy condition: the total energy of the fragment must be less than zero. The second condition is that debris must not fall on the surface of Earth. The last is spatial condition: the collision occurred inside the Hill's sphere. These conditions we derived from laws of conservation of energy and angular momentum in two-body problem:

$$\begin{cases} \dfrac{1}{r(r+1)} < v^2 < \dfrac{1}{r} \\ \sin\varphi > \sin\varphi_{cr} = \dfrac{1}{r}\sqrt{1+\dfrac{1-\dfrac{1}{r}}{v^2}}\,. \\ r < r_h \approx 235 \end{cases} \quad (1)$$

For calculation of the averaged capture probability the frequency of collisions is required. Distribution on angles between velocities of colliding bodies we considered uniform, while distribution on velocities of colliding bodies we considered Maxwell's according to Safronov [3]. We consider distribution of protoplanetary bodies in close proximity from Earth and because of that it deviates from classic Maxwell's distribution.

RESULTS:
Applying three conditions of the capture criterion and the simplest model of collision we obtained formula for capture probability averaged on angle φ between the direction of center mass velocity and direction to the center of Earth from the point of the collision.

$$\bar{p}(v_1,v_2,\alpha,k,r)_\phi=\Theta(r_h-r)\Theta\left(\frac{1}{r}-V_{cm}^2\right)\Theta\left(V_{cm}^2-\frac{1}{r(r+1)}\right)\sqrt{1-\frac{1}{r^2}\left(1+\frac{1-\frac{1}{r}}{V_{cm}^2}\right)}. \quad (2)$$

Where V_{cm} is the center mass velocity, which is expressed by the formula:

$$V_{cm}^2=\frac{v_1^2+k^2v_2^2+2kv_1v_2\cos\alpha}{(1+k)^2}. \quad (3)$$

The obtained formula (2) for the capture probability allows to calculate numerically the average fraction of the captured matter at the given mass ratio k, the velocities v_1 and v_2 in dimensionless units $v_{1,2}=V_{1,2}/\sqrt{2GM_\oplus/R_\oplus}$ ($V_{1,2}$ – velocities in meters per second), the angle between the velocities of colliding bodies α and the distance between the center of Earth and the point of collision r in dimensionless units $r=R/R_\oplus$ (R – distance in meters).

Capture probability averaged on angle α and velocities v_1 and v_2 for free-free collisions (the case when both planetesimals are from the Earth's feeding zone) was obtained through averaging on frequency of collisions.

$$\bar{p}(k,r)=\frac{\int_0^{2\pi}\int_{\frac{1}{\sqrt{r}}}^{\infty}\int_{\frac{1}{\sqrt{r}}}^{\infty}\bar{p}(v_1,v_2,\alpha,k,r)_\phi v_0(v_1,v_2,\alpha,r)dv_1dv_2d\alpha}{\int_0^{2\pi}\int_{\frac{1}{\sqrt{r}}}^{\infty}\int_{\frac{1}{\sqrt{r}}}^{\infty}v_0(v_1,v_2,\alpha,r)dv_1dv_2d\alpha}. \quad (4)$$

Where $\bar{p}(v_1,v_2,\alpha,k,r)_\phi$ is expressed according to (2) and $v_0(v_1,v_2,\alpha,r)$ is the frequency of collisions which we obtained as the following:

$$v_0(v_1,v_2,\alpha,r)=Cv_1v_2\sqrt{\left(v_1^2-\frac{1}{r}\right)\left(v_2^2-\frac{1}{r}\right)(v_1^2+v_2^2-2v_1v_2\cos\alpha)}e^{-3\theta(v_1^2+v_2^2)}. \quad (5)$$

Here C is a constant and θ is Safronov's parameter [3], which can be taken approximately equal to 3.

For the averaged capture probability we have built graph presented below:

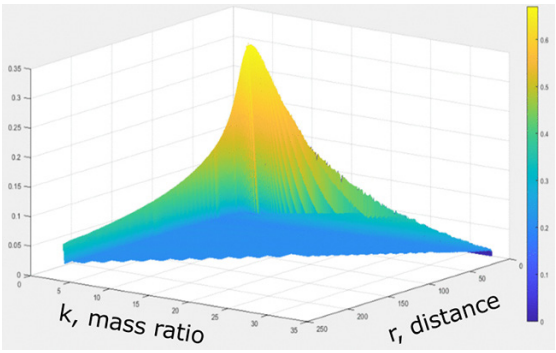


Fig. 1. Graph for the averaged capture probability $p=\bar{p}(k,r)$ (4) depending on mass ratio k of colliding planetesimals and the distance r from the point of collision to the center of Earth in dimensionless units $r=R/R_\oplus$.

DISCUSSION:

As a result of the conducted research, we obtained formulae for calculating the capture probability of protoplanetary bodies during paired collisions in the Hill's sphere of Earth. Despite some approximations, significant progress has been made compared to the estimations of Ruskol [4]. In contrast to the Ruskol's formula, the formulae (2, 4) give the dependence of the capture probability not only on the distance to the center of Earth, but also on the masses and velocities of colliding bodies, as well as on the angle between the velocities. In addition, there is no restriction on the ratio of the masses of colliding bodies, as it was the case of the Ruskol's estimation. We found that taking into account the possibility of a collision of fragments with Earth

turns to zero the capture probability at the Earth's surface. In the calculations of Ruskol, it was assumed that the capture probability in the protolunar swarm is the maximum at the Earth's surface. According to the graph of the averaged capture probability (Fig. 1) we found that the greatest contribution to the capture probability in most cases comes from the energy condition of capture. At distances less than 5–10 Earth's radii, proximity to the Earth affects, and here the condition of non-falling of fragments to Earth is essential, which closely to the surface of Earth becomes the main factor affecting the capture probability. The consequence of the presence of two main capture conditions is the presence of a maximum in the capture probability function at a distance of approximately 2.9 Earth's radii and mass ratio 2.1. At the maximum, the capture probability reaches approximately 0.3. The spatial capture condition is also significant, since outside the Hill's sphere it turns the capture probability into zero, which would be non-zero in the absence of this condition. For great distances and mass ratios beyond observed maximum, decrease of escape velocity causes a decrease of capture probability and larger values of mass ratio are linked with less capture probability as well.

CONCLUSION:

Capture probability is the crucial parameter in the co-accretion hypothesis of the origin of the Moon. This research is the first, which is devoted to calculation of the capture probability after the Ruskol's study done almost half a century years ago. Formulae (2) and (4) obtained in the study for the capture probability will later be used to calculate the total mass and angular momentum of the protolunar swarm, which may allow us to confirm the co-accretion hypothesis of the origin of the Moon.

REFERENCES:

[1] Ruskol E.L. On the past history of the Earth-Moon system // Icarus. 1966. V. 5. I. 1-6. P. 221-227.
[2] Harris A.W., Kaula W.M. A co-accretional model of satellite formation // Icarus. 1975. V. 24. I. 4. P. 516-524.
[3] Safronov V.S. Evolutsia doplanetnogo oblaka i obrazovanie Zemli i planet. Nauka, 1969. 244 p.
[4] Ruskol E.L. Proishozhdenie Luny. Nauka, 1975. 188 p.

DENSITY, SRESS, AND GRAVITATIONAL FIELD ANOMALIES INSIDE THE MOON, MARS, AND EARTH: A COMPARATIVE ANALYSIS

N.A. Chujkova[1], L.P. Nasonova[2] , T.G. Maksimova[2]
[1] *Государственный астрономический институт им. П.К. Штернберга, МГУ, Москва, Россия, chujkova@sai.msu.ru;*
[2] *Государственный астрономический институт им. П.К. Штернберга, МГУ, Москва, Россия, nason@sai.msu.ru.*

KEYWORDS:
Moon, Mars, Earth, internal structure, internal gravity field, isostatic compensation, comparative analysis

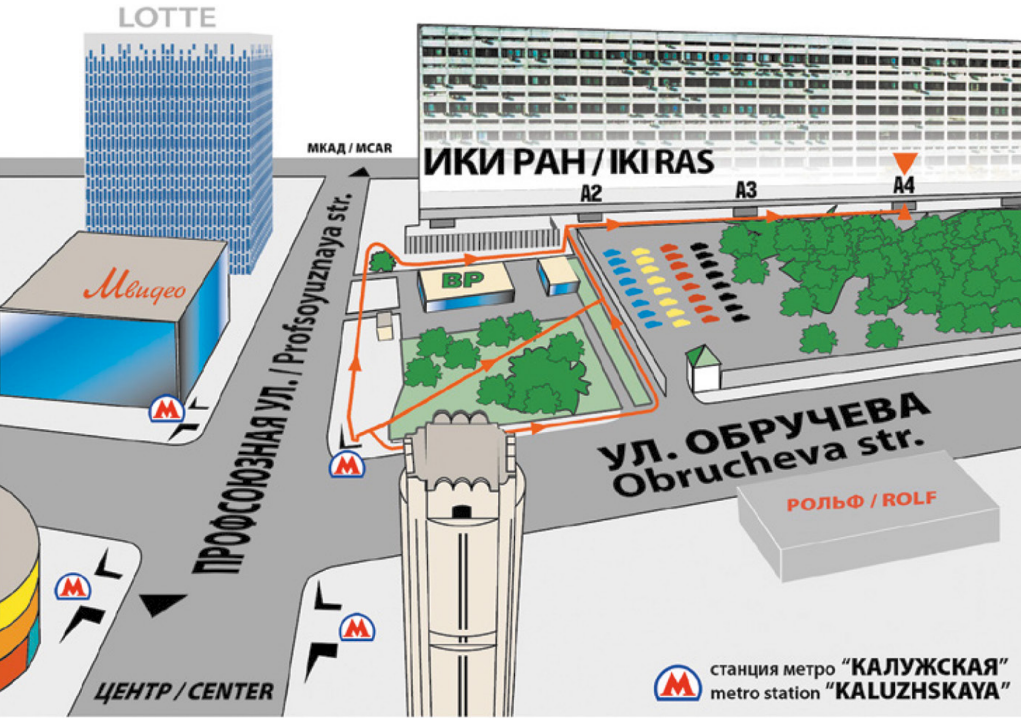
INTRODUCTION:
The method we developed for searching for water and other minerals on the Moon was previously tested on the example of Earth and Mars (Chuikova et al., 2014, 2019, 2020). The essence of the technique is that, based only on space data on the gravitational field and the relief of the planet, the most likely depths of isostatic compensation of the relief masses are uniquely determined, and the distribution of compensating masses at these depts is constructed. It is particularly important to apply this technique to the far side of the Moon, where possible places of deposits of water and other volatile elements (for example, helium-3) under lowlands and deposits of dense rocks under highlands are found. For the purpose of verification, the locations of maskons on the Earth were determined using a similar method and the possible locations of volatile and other mineral reserves were found to correspond to previously explored deposits.

REFERENCES:
[1] Chuikova N.A., Nasonova L.P.,Maksimova T.G. Density, stress, and gravity anomalies in the interiors of the Earth and Mars and the probable geodynamical implications: comparative analysis // *Izvestiya. Physics of the Solid Earth*. 2014. V. 50, No. 3. P. 427-443.
[2] Chuikova N.A., Nasonova L.P.,Maksimova T.G. The new method to found the anomalous internal structute of terrestrial planets and its test on the Earth. IAG Symp. Ser., 2014b, vol.144, no. 195. pp. 209-219 . https://doi.org / 10.1007/978-3-319-39820-4.
[3] Chuikova N.A., Nasonova L.P.,Maksimova T.G. A new solution to the inverse gravimetry problem for terrestrial planets and its verification for the Earth, in Astronomiya, geodeziya I geofizika (Astronomy, Geodesy, and Geophysics),-Moscow: Tsentr Geodez., Kartogr. Infrastr. Prostranstvennykh Dannykh, 2018, pp. 90-113.
[4] Chuikova N.A., Rodionova Zh.F., Maksimova T.G. and Grishakina E.A. Analysis of Lunar Terrain Altitudes and Correlation Links between the Terrain and Gravitational Field; Preliminary Conclusions on the Global Density Inhomogeneities of the Lunar Crust. // Solar System Research, 2019, Vol. 53, No. 3. P. 161–171.
[5] Chuikova N.A., Nasonova L.P.,Maksimova T.G. Determination of Global Density Inhomogeneities Inside the Moon // Sol. Syst. Res. 2020. V. 54. No 4. P. 1–12).

INFORMATION

address:
Space Researh Institute (IKI)
Profsoyuznaya street 84/32
post code 117997
metro station: Kaluzhskaya
Moscow, Russia





ИКИ РАН

площадь академика Келдыша
метро «Калужская», первый вагон из центра, по тоннелю – прямо,
по второму поперечному тоннелю – направо, выход на площадь,
далее по стрелкам на схеме

IKI RAS

You should get off at “Kalyzhskaya” metro station using the southern exit.
After leaving a station lobby through glass doors you should go straight
to the end of the tunnel, then take right and use the stairs to get to the surface.
From this point you may follow either arrow on this map

MOSCOW METRO SCHEME



СХЕМА МОСКОВСКОГО МЕТРОПОЛИТЕНА



REGISTRATION AND INFORMATION DESK
location: IKI, entrance A-4
time:
11 october, 9:30–18:00
12 -15 october, 9.30-18.00

ORAL SESSIONS
location: IKI conference hall, second floor

POSTER SESSIONS
online discussion

COFFEE BREAKS, WELCOME PARTY, RECEPTION
location: IKI exhibition hall, ground floor

INTERNET ACCESS AND WIFI
there is Internet access in and near the conference hall

SOCIAL PROGRAM

	BOLSHOI	OPERETTA	HELIKON	MMDM	NOVAYA OPERA	KREMLIN	TABAKOV
9.10	**19.00** historic stage историческая сцена SADKO САДКО	**19.00** KURTIZANKA КУРТИЗАНКА	**19.00** LA SERVA PADRONA / THE TELEPHONE СЛУЖАНКА-ГОСПОЖА		**19.00** THE BARBER OF SEVILLE СЕВИЛЬСКИЙ ЦИРЮЛЬНИК		**19.00** NIGHT IN THE HOTEL НОЧЬ В ОТЕЛЕ
10.10	**19.00** historic stage историческая сцена SADKO САДКО	**13.00, 19.00** MISTER IKS МИСТЕР ИКС	**16.00** LA SERVA PADRONA / THE TELEPHONE СЛУЖАНКА-ГОСПОЖА	**12.00** BACH AND SPANISH BAROQUE. ORGAN MUSIC **19.00** VALAAMSKY MONASTERY MALE CHOIR: YESENIN ХОР ВАЛААМСКОГО МОНАСТЫРЯ	**18.00** TRISTAN & ISOLDA ТРИСТАН И ИЗОЛЬДА		**19.00** KYNASTON КИНАСТОН
11.10						**19.00** BALLET GALA CONSERT ГАЛА-КОНЦЕРТ ЗВЕЗД МИРОВОГО БАЛЕТА	
12.10	**19.00** historic stage историческая сцена DON QUIXOTE ДОН КИХОТ						**19.00** REVIZOR (AUDITOR) РЕВИЗОР
13.10	**19.00** new stage новая сцена TOSCA ТОСКА		**19.00, 20.30** KAFFEEKANTATE КОФЕЙНАЯ КАНТАТА	**19.00** THE FOUR SEASONS ВРЕМЕНА ГОДА	**19.00** FAUST ФАУСТ	**19.00** DON QUIXOTE ДОН КИХОТ	
14.10	**19.00** new stage новая сцена TOSCA ТОСКА			**19.00** LEZGINKA DANCE ENSEMBLE АНСАМБЛЬ ТАНЦА ЛЕЗГИНКА	**19.00** FAUST ФАУСТ	**19.00** TOTO KUTUN`O ТОТО КУТУНЬО	**19.00** NOBODY STAY И НИКОГО НЕ СТАЛО
15.10	**19.00** historic stage историческая сцена LA FILLE DU PHARAON ДОЧЬ ФАРАОНА **19.00** new stage новая сцена TOSCA ТОСКА	**19.00** GRAF ORLOV ГРАФ ОРЛОВ		**19.00** CONCERTO GRANDIOSO		**19.00** KRISTINA ORBAKAYTE КРИСТИНА ОРБАКАЙТЕ, СОЛЬНЫЙ КОНЦЕРТ	
16.10	**19.00** historic stage историческая сцена LA FILLE DU PHARAON ДОЧЬ ФАРАОНА **19.00** new stage новая сцена TOSCA ТОСКА	**19.00** GRAF ORLOV ГРАФ ОРЛОВ			**19.00** RIGOLETTO РИГОЛЕТТО		

BOLSHOI	**bolshoi.ru**	БОЛЬШОЙ ТЕАТР, BOLSHOI THEATRE
OPERETTA	**mosoperetta.ru**	OPERETTA THEATRE, ТЕАТР ОПЕРЕТТЫ
HELIKON	**helikon.ru**	HELIKON OPERA, ГЕЛИКОН ОПЕРА
MMDM	**mmdm.ru**	MOSCOW INTERNATIONAL PERFORMING ARTS CENTER, ДОМ МУЗЫКИ
NOVAYA OPERA	**novayaopera.ru**	NOVAYA OPERA, НОВАЯ ОПЕРА
KREMLIN	**kremlinpalace.org**	STATE KREMLIN PALACE, STATE KREMLIN PALACE
TABAKOV	**tabakov.ru**	TABAKOV THEATRE, SUHAREVSKAYA STAGE, ТЕАТР ТАБАКОВА НА СУХАРЕВКЕ

lUNCH POINTS NEAREST TO IKI



1. **ИНСТИТУТ КОСМИЧЕСКИХ ИССЛЕДОВАНИЙ РАН**,
   столовая, 1 этаж, секция А3
   SPACE RESEARCH INSTITUTE,
   Food center, Ground Floor, Section A3
2. **ТЦ “КАЛУЖСКИЙ”**,
   ул. Профсоюзная, 61А, зона ресторанов, 2 этаж
   “KALUZHSKIY” Market Center,
   Profsoyuznaya Street, 61A, 2 Floor
3. **КАФЕ”АНДЕРСОН”**,
   ул. Обручева, 30/1
   CAFÉ “ANDERSON”,
   Obrucheva street, 30/1
4. **ИНСТИТУТ ПРИКЛАДНОЙ МАТЕМАТИКИ РАН,**
   столовая, 1 этаж
   INSTITUTE OF APPLIED MATHEMATICS,
   Food center, Ground Floor



